ANNUAL REPORT

of

THE INSTITUTE OF PHYSICS
ACADEMIA SINICA

VOLUME 15 DECEMBER 1985

THE INSTITUTE OF PHYSICS, ACADEMIA SINICA
TAIPEI, TAIWAN, REPUBLIC OF CHINA

Annual Report

of

The Institute Of Physics
Academia Sinica

Volume 15 December 1985

The Institute of Physics, Academia Sinica
Taipei, Taiwan, Republic of China

中央研究院物理研究所集刊

發 行 人 (Publisher)
林 爾 康 (E. K. Lin)

執 行 編 輯 (Executive Editor)
李 清 義 (C. Y. Lee)

The Annual Report is published annually by the Institute of Physics, Acadmia Sinica, Taipei Taiwan, 115, Republic of china.

中央研究院物理研究所集刊

第十五卷

中央研究院物理研究所印行

CONTENTS 目 錄

ARTICLES

FLUID MECHANICS AND ATMOSPHERIC PHYSICS

ABSTRACT

THEORETICAL PHYSICS

SOLID STATE PHYSICS AND BIPHYSICS

FLUID MECHANICS AND ATMOSPHERIC PHYSICS

A SMALL ACCELERATOR LABORATORY FOR RESEARCH AND INSTRUCTION

P. K. Teng, C. M. Fou, B. Chen, C. Y. Chen, C. W. Wang,

G. C. Kiang, and E. K. Lin

Institute of Physics, Academia Sinica

Taipei, Taiwan, R. O. C.

I. Introduction

We have recently completed the installation, in the basement of main building of the Institute of Physics, of a 400-kilovolt positive-ion accelerator with slit stabilization. The accelerator has successfully produced ion beams of H^+ and H_2^+ and been tested satisfactorily. We have also completed the design and installation of the beam transport system, the detailed description of which is given in the following sections. The accelerator is now ready to be operational and can be used for research in nuclear physics, atomic physics and solid state physics. It also provides a facility for training, for students to learn about the detailed operation of the Van de Graaff accelerator and auxiliary equipment.

II. The Accelerator

The machine is the HVEC model LC-400 Van de Graaff accelerator of the horizontally mounted type, manufactured by the High Voltage Engineering Corporation. It has been designed to accelerate singly charged ion beams up to 400 keV. The beam produced is of high stability. The max hydrogen ion beam current of 50 microamperes at 400 keV energy can be obtained. The operation of the accelerator is simple and it is esay to vary the beam

energy in the range of 100-400 keV. Fig. 1 shows the installed accelerator and gives a view inside the accelerator room. The operation of the accelerator is controlled in the control and data handling room located at the first floor of the physics building. All control panels and closed-circuit TV are mounted in one rack. A selector switch chooses either belt charge, corona, target or column current, which is then displayed on a meter. The closed-circuit TV can be used to monitor the beam spot at any one of the beam lines. Fig. 2 shows a view of the control and data handling room.

In order to keep the accelerator working on a fail-safe basis, several safety devices have been designed and installed, including the vacuum level trapping electronic circuit to keep the accelerator in operation at vacuum $< 2 \times 10^{-5}$ torr and two micro switches, which are used as interlock to keep the belt in its proper tracking position and will automatically shut down the accelerator otherwise.

III. Beam transport system

1. Beam line arrangement

A sketch of the beam transport system is given in Fig. 3. With the analyzing and switching magnet as described below, we are able to deflect the ion beam to the direction of 15° to the right, zero degree, and 15° to the left, with respect to the central line of the accelerating tube. The right and left beam lines are equipped separately with a gate valve for the convenience of operation. In zero deflection line we installed a quartz viewer for the necessary observation of the beam quality and current. We used a vacon pump to keep constantly this beam transport system under a good vacuum ($< 10^{-6}$ torr).

2. Analyzing and switching magnet

An electromagnet is used to meet the requirement of analyzing and switching beam produced from the accelerator. The mass-energy product is 0.8 at 15° Beams of 800 keV protons and α - articles, and 400

keV deuterons can be deflected to the proper beam lines. The focus point is made at 39" from the center of pole face. In the right beam line we installed a pair of the stabilizing slits, which were set apart at 3 mm. Coaxial cables are connected from the high-energy and low-energy slits to the stabilizing circuit in the control panel for stabilizing the energy of the beam current transmitted. Utilizing the difference of the currents feeding back from high and low energy slits, the stabilizing circuit automatically increase or decrease the discharge current of triode tube from the corona point. We can then stabilize the beam at desired energy. Similar stabilizing slits for the left beam line is now under design and is expected to be completed soon.

3. Beam steering magnetic dipoles

A pair of electromagnetic dipoles are installed for the fine adjustment of the direction of the analyzed beam. They are used for the vertical and horizontal adjustments, respectively, and can be mounted separately outside the beam line tubing. For our purpose, we installed the dipole for the vertical adjustment in front of the analyzing magnet for the vertical adjustment of any one of three beam lines. The dipole for the horizontal adjustment is installed in the right beam line. Only a few volts of d.c. power supply is required for these two dipoles, and the current of no more than one ampere is needed for fine adjustment of deflection 0° - 5° vertically or horizontally. Also, we are designing a similar dipole to be installed in the left beam line.

IV. Energy calibration and alignment of beams

1. Energy calibration

The energy calibration of beam is made for the right beam line by measuring the 340 $\pm$ 2 keV resonance of the $^{19}F(p, \alpha\gamma)$ reaction. The ^{19}F target is prepared by mixing HF and NaOH to form a thin layer of NaF on the surface of a stainless steel blank-off flage. A 3" X 3 "

NaI (T ℓ) detector is used to measure the yields of the 6.13 MeV γ -rays from ^{16}O decay. The result of energy calibration is listed in Table 1. We used the conventional Hall probe and a Hall effect gaussmeter to measure the magnetic field and found E_p = 340 keV at 659 $\pm$ 2 gauss.

2. Alignment of beam

After having completed the energy calibration of the right beam line, we anchored the supports of the analyzing magnet and stabilizing slits firmly to the floor. The alignment of left relative to the right beam line is then obtained with an error of 0.5° by reversing the same magnetic field. Angle relative to zero degree line is determined to an error of 0.1° by optical survey.

Table 1. Result of energy calibration using ^{19}F (p, $\alpha\gamma$) resonance at E_p = 340 $\pm$ 2 keV. Photopeak, single escape and double escape peaks of 6.13 MeV gamma ray were all counted. The integrated charge in milli-coulomb were recorded. Magnetic field was recorded with a Hall probe.

B (Field) gauss	Charge Integration mC	Counts (6.13 MeV gamma) +
705	1.5	2786
700	1.5	2673
691	1.5	2644
685	1.0	1736
681	1.0	1646
671	1.0	1487
661	1.0	1129
655	1.0	79
644	1.0	30
658	1.0	355
668	1.0	1317
678	1.5	2270
688	1.5	2249

V. Results of the beam test

The performance of the installed accelerator is found to be quite satisfactory. The following gives our results of beam test.

Applied voltage : 450 kV max

Beam current : 10 μa for 350 keV H^+ beam

10 μa for 350 keV H_2^+ beam

Focusing : into a spot of 2-4 mm^2 for 350 keV H^+ beam

Resolution : 1.5 keV at 3 mm opening of slits for 340 keV H^+ beam

Vacuum : 5-9 x 10^{-6} torr (beam on)

2 x 10^{-6} torr (beam off)

VI. Scattering chamber

We have also designed and constructed a scattering chamber to be used for various scattering experiments. It has been installed at the end of the right beam line. The chamber is kept at good vacuum ($5x10^{-6}$ torr) by a high speed (140 ℓ/s) turbo molecular pump. Provisions for mounting Faraday cup, detectors, targets, viewer, vacuum guage, and pumping connections are availbale. The detailed description of the scattering chamber will be given in a following paper.

VII. Research projects planned

The first porject planned in the scattering chamber is a simple charge -exchange experiment. The yield of H° as a function of scattering angle, when a solid target is bombarded by a proton beam, will be measured. The result of this experiment will be used to check the importance of velocity matching between the scattered proton and the electron in this charge-pick-up process. Other research projects on radiation damage studies of amorphous metal in the left beam line has been in operation for several months now.

Acknowledgments

The authors would like to express their thanks to Dr. P. T. Wu for his assistance and helpful discussions.

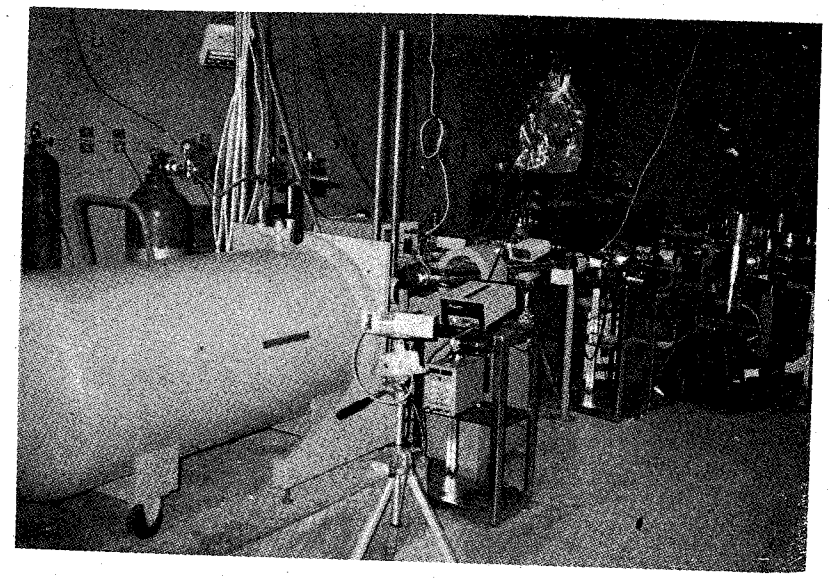

Fig. 1 A view inside the small accelerator laboratory

Fig. 2 A view of the control and data handling room

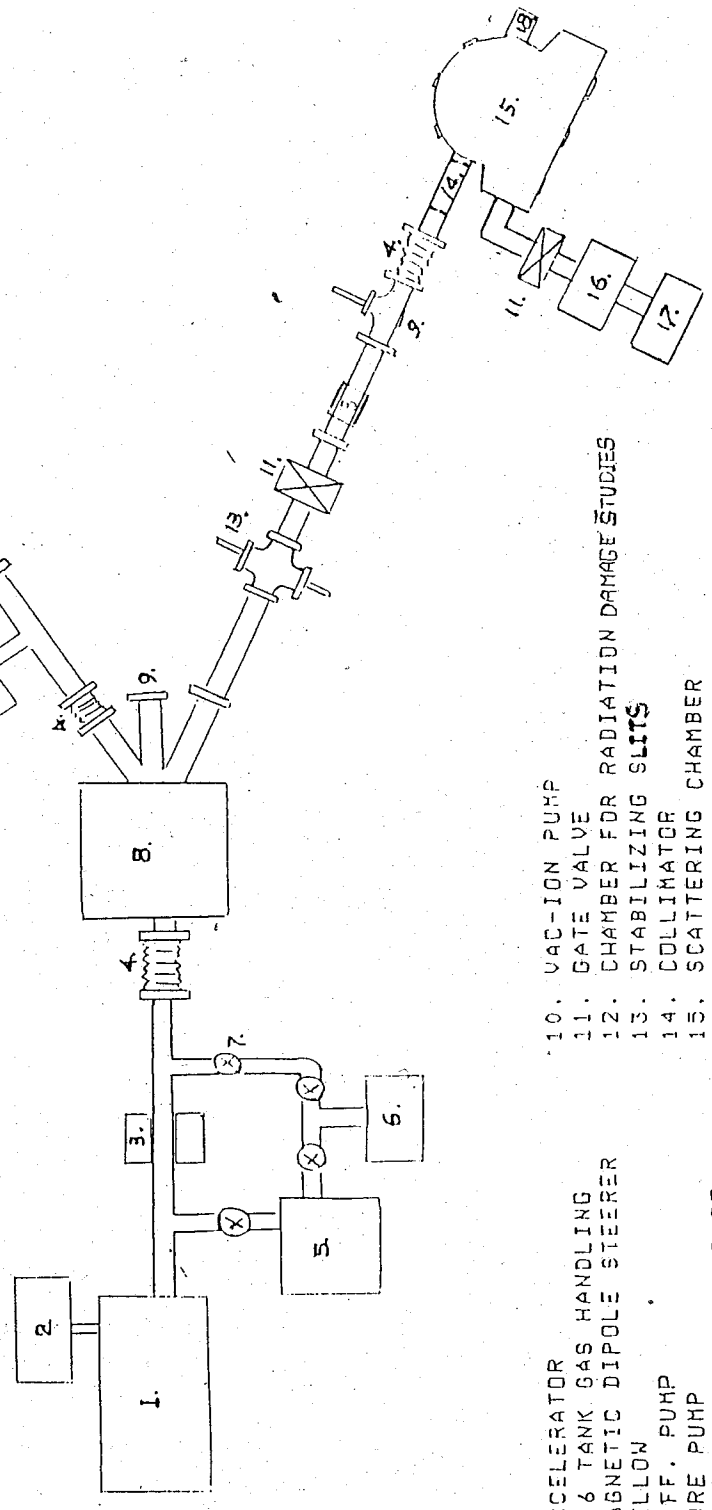

1. ACCELERATOR
2. SF6 TANK GAS HANDLING
3. MAGNETIC DIPOLE STEERER
4. BELLOW
5. DIFF. PUMP
6. FORE PUMP
7. ROUGHING VENTING PORT
8. ANALYZING SWITCHING MAGNET
9. QUARTZ VIEWER
10. VAC-ION PUMP
11. GATE VALVE
12. CHAMBER FOR RADIATION DAMAGE STUDIES
13. STABILIZING SLITS
14. COLLIMATOR
15. SCATTERING CHAMBER
16. TURBO PUMP
17. ROTATRY PUMP
18. FARADAY CUP

Fig. 3. A sketch of the beam transport system.

A SCATTERING CHAMBER FOR ION-ATOM COLLISION EXPERIMENTS

P. K. Teng, C. M. Fou*, G. C. Kiang, C.W. Wang, C. Y. Chen

B. Cheng, and E. K. Lin

Institute of Physics, Academia Sinica

Taipei, Taiwan, R. O. C.

Abstract

A scattering chamber and particle detection system are designed and constructed for the low energy ion-atom collision experiments. The detailed structure of the chamber and experiments to be performed using this facility are described.

I. Introduction

A 400 kV Van de Graaff accelerator and the beam transport system have recently been installed and tested at the institute. The accelerator is now operational and can produce H^+ and H_2^+ ion beams of 10 μa. To utilize this facility to study the charge exchange process in ion-atom collisions, a new scattering chamber and particle detection system have been designed and constructed. In this report, we will describe the structure of the chamber and specific functions it provides. We will also discuss the setup of the particle detection system.

II. Scattering Chamber

The chamber itself consists of a cylinder (target chamber) and an extension (detector chamber). A sketch of the scattering chamber is shown in Figs. 1 and 2. Vacuum requirement of the chamber is designed to be <

10×10^{-6} torr. Provisions for mounting targets, Faraday cup, viewer, detectors, vacuum gauge and pumping connections are available. The scattering takes place at the center of the cylindrical part of the chamber. The cylinarical wall was formed by rolling a 20 am wide strip of 12 mm stainless steel. After rolling into a ring of 40 cm in diameter the joint was arc-welded. Machining of "0" ring groves and ports was done after the welding operation. The bottom part of the cylinder is adapted from an old ORTEC chamber on which two rotatable arms and the rotating mechanism are available. The top plate of 12 mm stainless steel was pinned in position with the flange of the cylinder. It is removable for easy access to the chamber. Targets are fed via a sliding rod through the center of the top plate. Three targets can be mounted, one above the other, on the target holder at the same time. One can easily change target during the experimental time without breaking the vacuum of the chamber. On the side wall of the cylinder opposite to the extension, there are five 2" ports 45° apart. Two of which are used for beam entrance and exit ports. The entrance port is connected to the right beam line of the beam transport system via a 20 cm long beam collimator. The two ends of the collimator are equipped with adjustable aperature holders for beam alignment. Once the positions of these holders are fixed, aperature plates of various diameter for the beam-defining hole at the entrance and anti-scattering slits at the exit port is used to mount a Faraday cup to measure the beam current. The port at 90° with respect to the beam line is used to mount a solid-state detector as a monitor. The other two ports are used presently as viewing windows. In the extension, there is presently a set of parallel electrostatic plates with the shape of a hand-held fan. The detail arrangement and use of it will be described in the next section. On the top wall of the extension part of the chamber, there are two 2" ports and two 3" ports. They are used for mounting HV coaxial cable feed-throughs, vacuum gauge head and roughing valves. In addition to these ports, there is also a 6" access port through which one can put the detector into the chamber. The rear end of the extension is sealed by a 20 mm thick stainless steel plate (22 cm x 87cm) which can be detached to provide us better accesss to the interior of the

chamber. On this plate, there are three 3" windows. The middle one is currently being used as a signal feed-through port. The cylindrical and extension parts were arc-welded together as shown in Figs. 1 and 2. The entire chamber is kept at good vacuum by a high speed turbo-molecular pump which we will describe later.

III. Detection System

The particle detection system consists of a set of slits, an electrostatic deflector and one position sensitive detector. The slits at about 7.5 cm from the target are used to define the direction of the scattered particle to be analyzed. The opening of the slits is adjustable. The electrostatic deflector consists of two fan-shape stainless steel plates of 5 mm thick which are placed parallel to each other with 10.0 mm gap between them. The position, gap, and parallelness of these two plates are adjustable via three supporting screws for the bottom plate and two ceramic insulating spacers plus one lifting screw for the top plate. They are concentric with the target position and extends from 40° to 140° relative to the beam direction. Thus uninterrupted analysis of particles from the target in the angular range of $45° < \theta < 135°$ is possible. A uniform static electric field adjustable from 0-3000 volts/cm is used to separate the charged states of the particles. An ORTEC P-series position sensitive detector (PSD) with a sensitive area of 8 x 10 mm^2 and spatial resolution of 0.1 mm is presently used to detect those deflected charged particles and those undeflected neutral particles after passing through the deflector. The position sensitive detector as well as the slits are mounted on one of the rotatable arms. The flight path from target to the detector is about 36 cm. More PSD and slits can be added onto the rotatable arm allowing simultaneous measurements at several adjacent angles. Besides, for monitoring purpose, a solid-state detector is placed at the port of the chamber at 90° relative to the beam direction.

IV. Vacuum System

The vacuum system consists of a right-angle pneumatic valve and a

pumping system. The valve is used to isolate the chamber from the pumping system. The model 5150 turbomolecular pumping unit of Alcatel is employed. This unit consists of a model 150 turbomolecular pump with a pumping speed of 140 liter/sec and a model 2012A rotary pump. A Penning gauge is used to measure the vacuum pressure. The vacuum in the scattering chamber achieved thus far is 5×10^{-6} mbar.

V. Summary

To summarize, we have constructed and installed a scattering chamber with particle detection system which can be used to study charge exchange process in ion-atom collision. The unique feature of this scattering chamber is the wide fan-shape electrostatic deflector. It would be most useful for the simultaneous measurement of charge states of scattered ions at various angles. Besides, a second rotatable arm in the target chamber makes it possible to do particle-particle coincidence with one of the particle analyzed by the electrostatic deflector. The end plate of the detector chamber can be opened allowing further analyzing setup in the future. The entire chamber can be rotated 45 or 90 degrees and reconnected to the beam line, facilitating charge state seperation of scattered ions down to $0° < \theta < 90°$ or even $-45° < \theta < +45°$ when needed. The removable top plate of the target chamber can be modified for the adaption of windowless gas target. An additional 4" pumping port is provided on the bottom wall of the detection chamber when higher vacuum is needed in the future. The design of this chamber is flexible enough for all forseeable experimental investigation of low energy ion-atom collision with the institute's 400 keV accelerator. Experiments using this facility to study the electron pick-up phenomena due to the velocity matching between the scattered ions and electrons are currently being performed.

Acknowledgments

The authors are grateful to the National Science Council of Republic of China for the partially financial support of this work under Grant Number NSC75-0208-M001-13.

1. Beam entrance port
2. Beam exit port
3. 2" view port
4. Deflector
5. Vacuum gauge port
6. H.V. feedthrough port
7. 3" view port
8. Signal feedthrough port
9. Pneumatic valve
10. Pumping unit

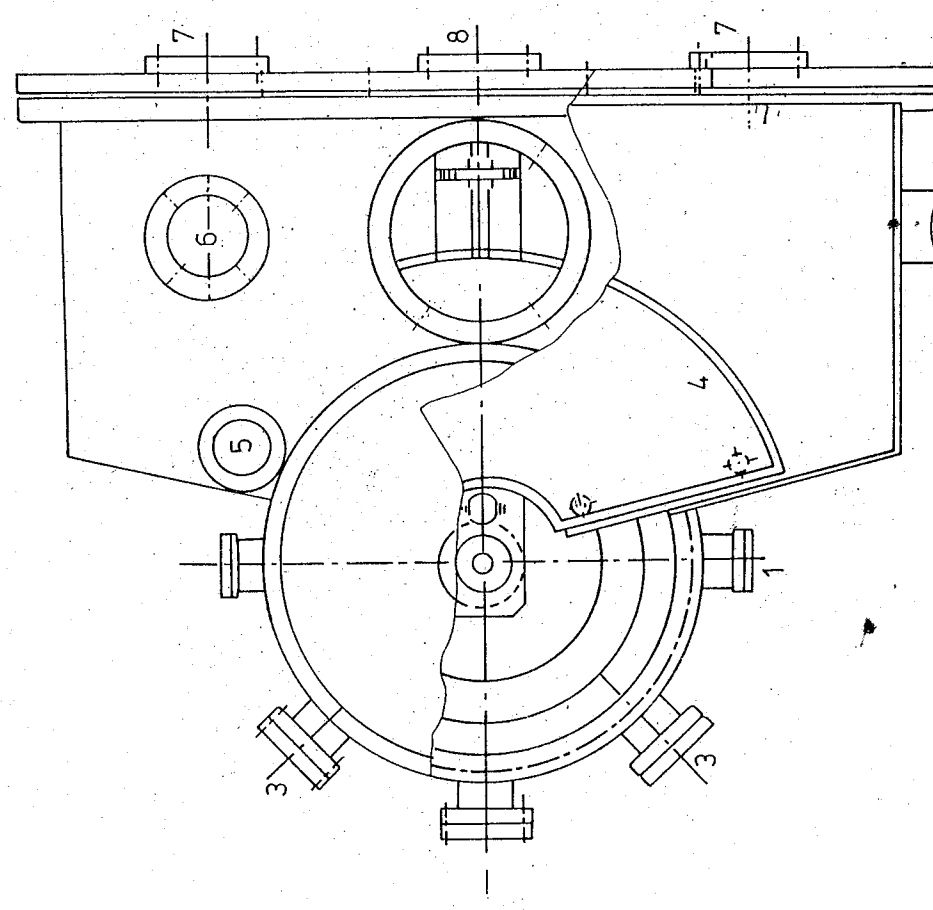

Fig 1 Schematic diagram of the scattering chamber: top view

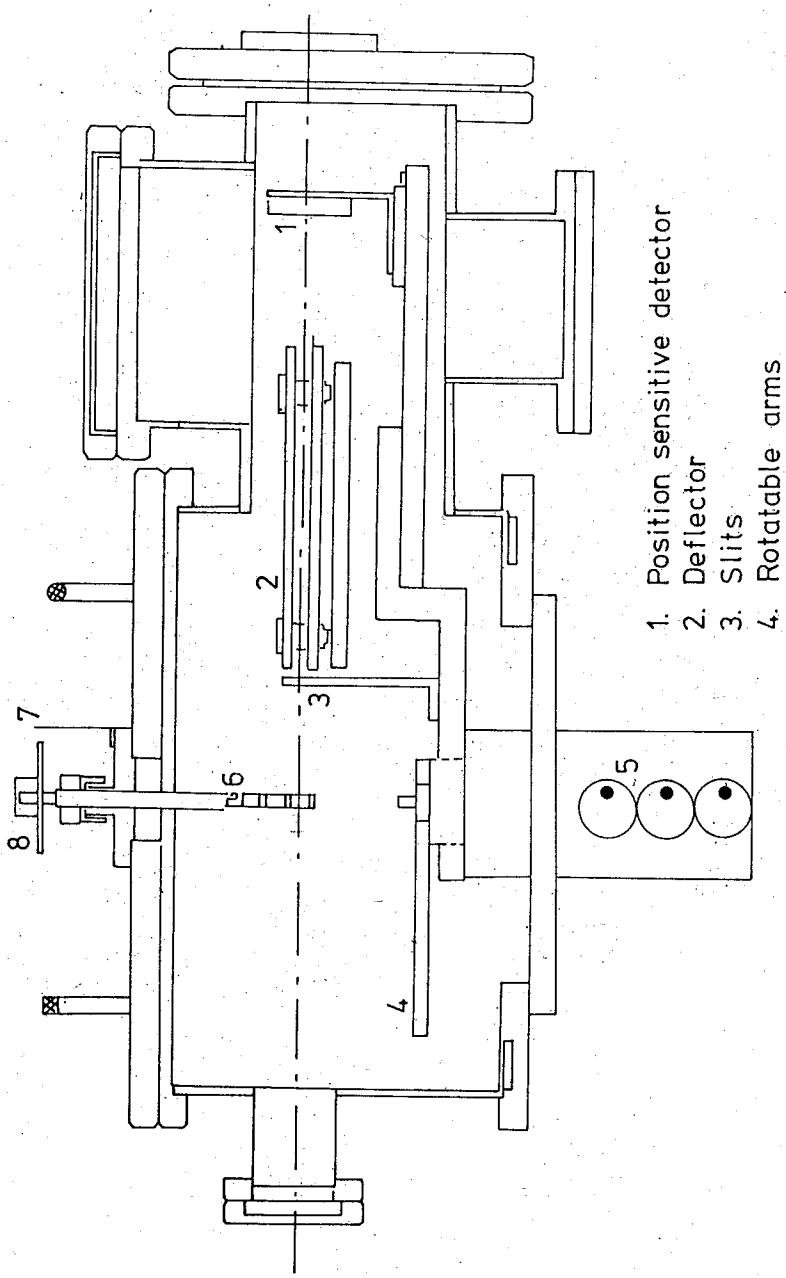

1. Position sensitive detector
2. Deflector
3. Slits
4. Rotatable arms
5. Detector angle setting mechanism
6. Target holder
7. Target angle pointer
8. Potractor

Fig. 2. Schematic diagram of the scattering chamber: side view

THE WALL-ENTROP MECHANISM IN THERMAL DOMAIN DRAG EFFECT

S. U. Jen （任盛源）

Institute of Physics, Academia Sinica

Taipei, Taiwan

R. O. C.

ABSTRACT

At any finite temperature, a magnetic domain wall contains a non-zero entropy S*. When a domain wall moves across a temperature gradient dT/dX, it constitutes a Carnot engine carrying entropy and heat from a hot reservior to a cold reservior, and transforming it into work through the wall-entropy force F. From the basic equivalent Onsager equations, we dervie the result $F = -S^* dT/dX$, which agrees with what predicted in Ref. 1. A rough estimate of wall-entropy drive field H_d is made through the measurement of the wall surface energy. The order of magnitude of H_d is comparable to the bulk pinning force H_c of the material studied. This indicates that wall-entropy mechanism is also active in driving walls into TDD motions.

I. Intvoduction

In previous papers[2-4], we have discussed a new discovered effect, namely the thermal domain drag (TDD) effect. In short, it is a phenomenon associated with the steady, collective, and translational motion of domain walls in a ferromagnet, when a temperature gradient is applied in perpendicular direction to those walls. The motion of walls is always from the hot end to the cold end of the sample.

To have any wall motion, we need to exert pressure on each domain

wall so that it can overcome the pinning force and starts moving. The origins of the drving forces, such as the Nernst-Ettingshausen drive force, the end-drive force, and the isothermal end-drive force, have been discussed before[2-4] The frist force is related to the hydromagnetic force, as electron gas acrosses the domain walls. Clearly, this force, although its magnitude could be quite prominent, is effective only in the metallic materials. For a ferromagnetic insulator, the second and the third forces become possible candidates in the TDD effect. However, recently even a fourth mechanism, called entropy-drive mechanism, also effective for all materials, is proposed[1] Basically, it says that the situation, when domain walls move down a temperature gradient, is similar to that of Carnot engine carrying entropy and heat from a hot reservior to a cold reservior, and performing it partially into work through the entropy-drive force F.

In this paper, we comment on the wall entropy mechanism by using a slightly different approach to the same problem. The result agrees well with what predicted in Ref. 1.

II. Wall Entropy Mechanism

Since TDD effect is a transport of domain walls from the hot end to the cold end of the sample, we may consider the " conduction " of walls and heat lies between a hot reservior at temperature T + ΔT and a cooler reservior at T. Fig. 1. This case is similar to the example illustrated in the Zemansky's thermodynamics textbook[5]. The analogy is that a flow of electric current I maintained in the copper wire by a potential difference $\Delta\xi$ across its ends is analogous to a flow of domain walls I_w in the sample by the work F ΔX performed by the wall entropy force. As to the nature of wall entropy and wall entropy force, Ref. 1 has discussed them. What we present here is just another look or a derivation of the force of the same problem.

Consider the heat conduction of TDD effect alone, due to the heat flow through the sample, the rate of production of entropy within the sample is written as :

$$\frac{dS}{d\tau} = I_Q \frac{\Delta T}{T^2} = I_S \frac{\Delta T}{T}$$

where I_Q stands for a heat current, and I_S is interpeted as an entropy current.

Suppose now that collective motion of TDD type exists, walls are being created at the hot end at a flux rate I_W, and annihilated at the same rate I_W at the cold end. Both ends are assumed to be in thermal contact with their reserviors respectively. Because the force F, which, moves walls a distance ΔX, is perforing work, F·ΔX, this amount of energy F ΔX is dissipated in the sample. Therefore, we obtain the rate of production of entropy from wall motion is :

$$\frac{dS}{d\tau} = I_W \frac{F\Delta X}{T}$$

Note that this entropy and wall flux are all state variables for each heat reservior.

Since in TDD effect, both thermal conduction and " wall current " exist simultaneously the total entropy generated by virture of both processes is :

$$\frac{dS}{d\tau} = I_S \frac{\Delta T}{T} + I_W \frac{F\Delta x}{T}$$

Clearly, what we have now are two irreversible coupled flows, existing by means of a departure from equilibrium conditions in the sample. If this deparature is not too great, it may be assumed that both I_S and I_W are linear functions of ΔT and ΔX. Thus,

$$I_S = L_{11} \frac{\Delta T}{T} + L_{12} \frac{F\Delta x}{T}$$

$$I_W = L_{21} \frac{\Delta T}{T} + L_{22} \frac{F\Delta X}{T}$$

These two equations are equivalent to the Onsager equations.

If ΔT is set equal to zero in both Eqs. (4) and (5) , and then the equations are divided, we get

$$S^* = \frac{I_S}{I_W} = \frac{L_{12}}{L_{21}}$$

The ratio I_S/I_W is a measure of the entropy per wall, $S^* = S/Nw$, that is carried along within the wall when the temperature is uniform.

Further, if there is no wall current $I_W = 0$, Eq. (5) provides the relation

$$F\Delta X = -\frac{L_{21}}{L_{22}} \Delta T$$

Upon insertion of the Onsager reciprocal relation $L_{12} = L_{21}$, and using Eqs (6) and (7) , we obtain

$$S^* = -F\frac{\Delta X}{\Delta T}$$

As the presscre on a domain wall is expressed as

$$P = \frac{F}{A} = 2M_S H_d$$

where H_d is the driving field, A is the wall area, and Ms is the saturation magnetization. From Eqs. (8) and (9), we have

$$H_d = -\frac{S^*}{2M_S A}\frac{\Delta T}{\Delta x}$$

Here we have derived the same result, Eq. (9), as that in Ref. 1 However, this derivation also suffers the disadvantage of not explaining the physical origin of the entropy force and not showing the explicit expression for the entropy S of the wall system. For the continuation of discussion, we simply

quote the result for $S^{(1)}$:

$$S = -AL\frac{d}{dT}\left(\frac{2\sigma}{a}\right)$$

where σ is wall surface energy and a is the equilibrium wall spacing at temperature T. From Eqs. (6), (10), and (11), we obtain

$$H_d = \frac{a}{2M_S}\frac{dT}{dx}\frac{d}{dT}\left(\frac{2\sigma}{a}\right)$$

with the same approximation, $\frac{\sigma}{a} \sim \left(\frac{\sigma}{a}\right)_{T=0}\left[1-\left(\frac{T}{T_C}\right)^n\right]$,

$$H_d \sim -\frac{\sigma}{M_S}\frac{1}{T_C}\frac{dT}{dx}$$

which is a quantity independent of either sample thickness W or sample length L Note, however, the model used to derive Eq. (11) in Ref. 1 is the stripe-wall madel a $\ll$ W, (Fig 2). For the other linit, the single-wall model a $\gg$ W, the calculation for the magnetastatic energy is more difficult because of tits logarithmic divergence. Therefore, the dependence of H_d on sample's dimensions for the single-wall model would be slightly different.

III. Experimental Determination of H_d

Frm Eq. (13), the measurement of H_d is equivalent to the measurement of wall surface energy σ We have devised two methods to measure σ of metglas materials at hand. Both methods involve visual observations of domain walls. We have set up a Kerr microscope, described elsewhere(2), for this purpose,

In the first method, we observe the contrast between domains in a piece of ficld-annealed Metglas, 9mm long and 0.25mm wide, while increasing the external field in the hard direction of the sample. This direction is parallel

to the sample length. The contrast disappears when the domain magnetizations rotate towards the field by 90° The external field needed for that is $H_E = H_k + (D_h M_s) / \mu o$ where H_k is the anisotropy field and D_h is the demagnetizing factor in the hard direction. For this piece of sample, $D_h \sim 1.6 \times 10^{-4}$ (7). From H_E, D_h, and the relation $K_u = (1/2) M_s H_k$, we obtain roughly $K_u \sim 3 \times 10^2$ j/m^3 for 2826MP, and $K_u \sim 1.3 \times 10^2$ j/m^3 for 2705X. Then, assuming the same value of the exchange stiffness constant $A = 1 \times 10^{-11}$ J/m as for crystalline materials such as iron, and using the formula(6) $\sigma = 4 (AK_u)^{1/2}$, we obtain that $\sigma \sim 2.2 \times 10^{-4}$ J/m^2 for 2826MB, and $\sigma \sim 1.4 \times 10^{-4}$J/m^2 for 2705X. Of course, these values aro very rough.

The second method to obtain σ uses the distortion of domain walls by the field of a d. c. current. We know that the " global " field, generated by a d. c. current traversing a wall at right angle, displaces the two ends of the wall in opposite directions by a distance ΔX, Fig. 3. When the current density reaches the value $j_{sat} = (4 \sigma)/(M_s W^2)$, ΔX is predicted to diverge logarithmically. As the current density approaches j_{sat}, ΔX increases rapidly, and adjacent walls touch and annihilate each other. From the measured J_{sat}, we then calculate $\sigma \sim 5.28 \times 10^{-4}$J/m^2 for 2826MB, and $\sigma \sim 3.04 \times 10\text{-}4$ J/m^2 for 2705X. These values are probably more accurate than the ones obtained by the first method, and differ from them by a factor of two.

To estimate H_d, since we obtain $\sigma \sim 5 \times 10^{-4}$J/m^2, $T_c \sim 600$K(8) for two materials, and dT/dx $\sim$ 300K/mm in the TDD experiment, H_d is of the order of 0.2 A/m. This value is of the same order as the bulk pinning field, the coercive field Hc, of these materials.

IV. Conclusion

In this comment, we have showed another approach to obtain the formal expression of wall entropy force. It uses the same principle to derive the

result as in the discusion for the Seebeck effect.

From the measurement of the wall surface energy we have estimated the order of magnitude of the driving field, which is comparable to the pinning field. Although this fact shows that entropy-drive mechanism is a possible candidate to drive walls, other experiments(3,4) have indicated that in those Metglas materials used, the Nerst-Ettingshausen drive mechaniem is dominant over other drive mechanisms. If, however, an insulating ferromagnet can be found, it would be a better material to test this entropy-drive mechanism.

Acknowledgment

We are thankful to Mr. Agarwala and Dr. Hsu for the measurements of wall surface energy, and to Dr. Berger for helpful discussion. This work was supported by NSF Grant DMR-8120769.

References

1. L. Berger, to appear in J. Appl. Phys.
2. S. Jen and L. Berger, J. Appl phys. 53, 2298 (1982).
3. S. U. Jen and L. Berger to appear in J. Appl phys.
4. S. U. Jen and L. Berger to appear in J. Appl. Phys.
5. M. W. Zemansky, Heat and Thermodynamics the ed. (McGraw-Hill, NY 1957).
6. S. Chikazumi, Physics of Magnetism, (Wiley, NY 1964).
7. J. A. Osborn, Phys, Rew. 67 351 (1845).
8. Data Sheet issued by Allied Corporation.

Caption for Figures

Fig. 1 Two ends of a forromagnetic sample are in thermal contact with the heat reserviors at temperature T and T + Δ T. As TDD motion occurs, heat current I_s and wall current Iw run through the sample

continuously.

Fig. 2. A domain structure satisfying the stripe wall model in a ferromagnetic sample.

Fig. 3. Distortions of domain walls by the global field H_{glo}, generated by the uniform part J of the current density, in the Metglas ribbon.

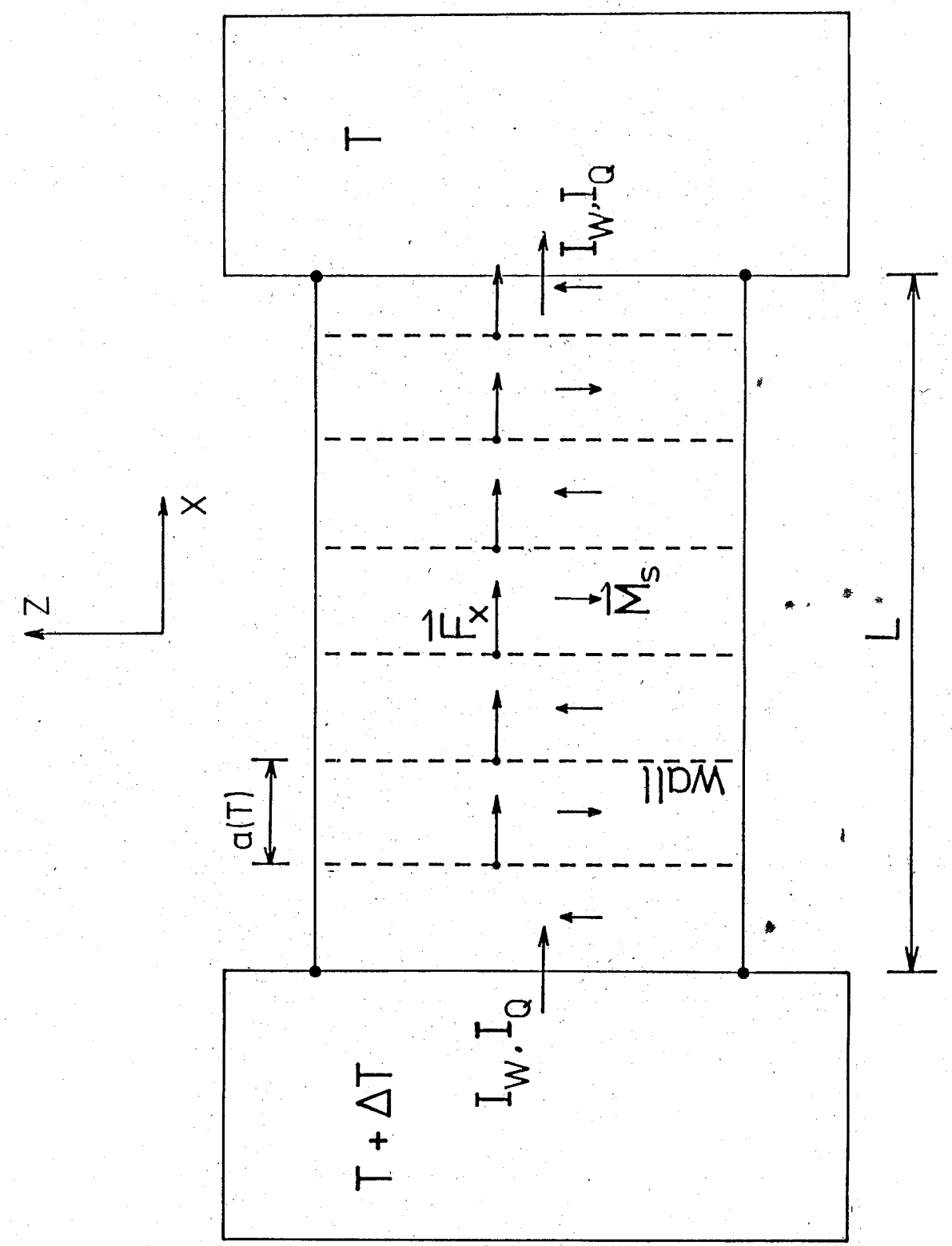

Fig. 1

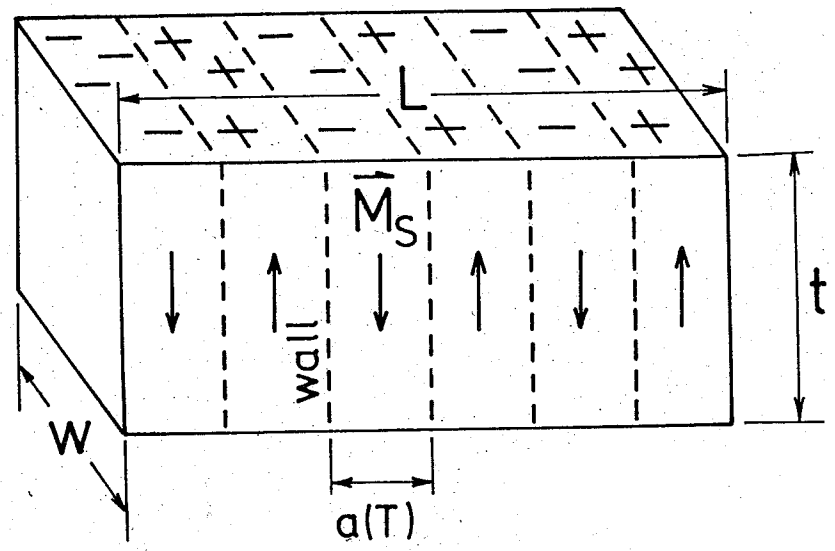

Fig. 2

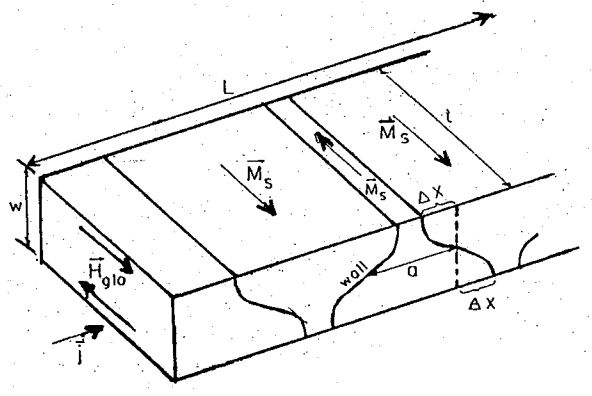

Fig. 3

ANNEALING STUDY OF MULTIFILAMENTARY Cu-Zn THIN WIRES

I-Shin Chen (陳 義 勳)
Taipei Municipal Teachers' College
Taipei, Taiwan, R. O. C.
and
Y. D. Yao (姚 永 德)
Institute of Physics, Academia Sinica
Taipei, Taiwan, R. O. C.

ABSTRACT

Compacts of Cu-50 wt.% Zn powders were reduced in cross section to produce multifilamentary thin wires. Swaging and drawing techniques were used to achieve an areal reduction of about 200 without any intermediate anneals. The temperature-dependent electrical resistivity was studied between 300K and 650K. The isothermal irreversible electrical resistivity changes due to anneal effect was studied at 150 C, 250 C, 350 C and 570 C. According to our experimental data, the alloying effect in multifilamentary CuZn system is completed after annealing at temperatures between 150 C and 350 C for 2 days; and the multifilamentary Cu-Zn thin wire can be annealed at least with a few hours at temperatures below 390K without any alloying effect.

INTRODUCTION :

The annealing effect concerning diffusion of a variety of materials at high temperatures has been studied quite extensively during the past[1-13]. The thin-layer sectioning technique has been widely used for annealing study;

however, the annealing effect concerning alloying observed by changes in the electrical resistivity are very scarce. Any physical property which changes during annealing of a material can be chosen for a rough description of this process. In this paper, the electrical resistivity is used as a probing quantity to trace the process of alloying during annealing.

In recent years, the technology for cold powder metallurgy processing of multifilamentary magnetic materials was pioneered at both National Magnet Laboratory, M. I. T. and Institute of Physics, Academia Sinica[14-17] The equipment and facilities for fabricating multifilamentary thin wires are already set up in Academia Sinica; these facilities can be used whenever it is necessary. Therefore, this made us possible to use this technique to fabricate the multifilamentary Cu-Zn thin wires and to start the research of alloying effect.

According to Hume-Rothery's empirical rule[18], the atomic size is an important factor for two different elements, say A and B, to form solid solution; if the atomic diameters of A and B differ by less than 15 percent, it is favorable to form solid solution. The difference of the atomic size of Cu and Zn is quite small; the atomic diameters[19] of Cu and Zn are 2.55 Å and 2.66 Å, respectively. The solubility between Cu and Zn is quite large[20]. Therefore, we chose Cu-Zn multifilamentary thin wire as a beginning system to observe the alloying effect during high temperature annealing. Our experimental results and their significance are presented below.

EXPERIMENTAL CONSIDERATION :

The multifilamentary Cu-Zn samples were fabricated following the same procedure that developed for multifilamentary magnetic materials[14-17] Figure 1 illustrates the procedure of the cold powder technique which have been used to produce Cu-Zn samples.

The pure copper and pure zinc powders were purchased from Eckart-Werke Co. (West Germany) and May & Baker LTD (England), respectively. Using ~ 100 μm copper powders and ~ 50 μm zinc powders, we mixed

these powders together with 50 percent by weight. Copper tubes with ~ 12.7 mm O. D. and ~ 11.1 mm I. D. were used as an external jacket to contain these powders. The mixed powders were tapped into the Cu tube, the tube was evacuated, and then the compact was swaged and wire drawn to final size. Swaging techniques were used for the preliminary elongation, and the remaining deformation to a wire with a final outer diameter of ~ 0.88 mm was made by wire drawing. Nominal areal reduction ratios of 200 were obtained without any intermediate anneals.

The electrical resistivity of these multifilamentary Cu-Zn thin wires was determined using the conventional four-probe technique. Four copper electrodes were lightly spot welded to each sample, the two central electrodes being used as potential leads and the other two as current leads. A. D. C. current was maintained constant to about one part in 10^5 and the voltage was measured with an accuracy to a few nanovolts. The measurements of the temperature-dependent electrical resistivity between 300K and 650 K were produced by a Marshall vacuum furnace. With a Eurotherm temperature controller (Model #901-2075). Two temperature sensors were placed beneath and above the sample and the average of the readings was assumed to be the temperature of the sample. The measurements of the irreversible electrical resistivity at 150 C, 250 C, 350 C and 570 C were produced by a Lindberg furnace with a vacuum chamber. The temperature was controlled by a Eurotherm temperature controller (Model # 810).

RESULTS AND DISCUSSION:

Fig. 2 shows the temperature-dependent electrical resistivity ρ of the multifilamentary Cu-Zn thin wire in the temperature range between 300 and 650 K. This graph represents three independent experimental runs with the same sample. The rate of temperature change was roughly about 1K/min. Run 1 (open circular points for increasing temperatures, and open square points for decreasing temperatures) was started at 295K and the electrical resistivities were measured with increasing temperatures up to about 426K. After reaching approximately 426K, temperatures were decreased down to

about 300K. It is obvious from Run 1 that the p vs T curves below 390K for both increasing and decreasing temperatures join perfactly well. This suggests that the alloying effect begins roughly around 390K. After the completion of Run 1, the same sample was heated again (Run 2).

Run 2 (Closed circles for increasing temperatures, and cross points for decreasing temperatures) was started at ~ 300K. The highest temperature achieved in this run was ~ 530K. It is obvious from Run 2 that there is a large shift between the ρ vs T curves of increasing and decreasing temperatures. This means that fast diffusion happens between Cu and Zn in the temperature range of 390K and 530K. This indicate that part of the pure copper and zinc becomes Cu-Zn alloys. After completing Run 2, Run 3 (Closed triangular points for increasing temperatures and open triangular points for decreasing temperatures) was measured with the same situation as Run 2, except that the highest temperature achieved in this run was ~ 630K. Again, from Run 2 and Run 3, it is evident that the alloying effect starts roughly above 390K. The values of the electrical resistivity at 300K after Runs 1, 2 and 3 are 3.85 $\mu\Omega$ - cm, 4.10 $\mu\Omega$ - cm and 4,20 $\mu\Omega$ -cm, respectively.

The three ρ vs T curves below 390K in Fig. 2 were fitted to the empirical formula :

$$\rho(T) = \rho_R + A\,T^n$$

where n, ρ_R and A are some constants independent on temperature. Curve a represents the data points for Run 1 and Run 2 with increasing temperatures. Curve b represents the data points for Run 2 with decreasing temperatures and Run 3 with increasing temperatures. Curve c represents the data points of Run 3 with decreasing temperatures. Analysis of these data was carried out by slowly varing the value of n near n = 1 and varying ρ_R and A to produce the best fit curve to the data. The final result, according to the computer analyses, shows that the best values of n and A are roughly

1.03 and 10^{-2}, respectively; the values of ρ_R for curves a, b and c are 0.25, o.55 and o.65, respectively. Usually, the quantity of ρ_R is named the residual electrical resistivity[21] and it is due to the scattering of electrons from chemical and structural imperfections; the term AT^n is assumed to result from the interaction of electrons with phonons etc., The increase of the residual electrical resistivity from 0.25 for curve a to 0.65 for curve c suggests that the effect of alloying takes place significantly after Run 2 and Run 3.

Figs. 3, 4, 5 and 6 show the isothermal irreversible electrical resistivity study at 150 C, 250 C, 350 C and 570 C, respectively. The electrical resistivities of the multifilamentary Cu-Zn samples were measured continuously as a function of time during isothermal annealing. The temperature was maintained to within 2K over a period of several days after an initial transient of 5K which lasted about 20 minutes.

Fig. 3 indicates that the effect of alloying starts roughly after one hour of annealing at 150 C. The electrical resistivity shows logarithmic behavior with respect to time, t, between roughly 100 and 1,000 minutes; after 1,000 minutes, the values of the electrical resistivity is gradually saturated and goes to a asymptotic constant. We stopped this measurement after roughly 10^4 minutes (i. e. roughly one week).

Fig. 4 is the isothermal electrical resistivity study at 250 C. The effect of alloying starts roughly a few minutes of annealing. The electrical resistivity shows logarithmic behavior with respect to t between roughly 10 and 100 minutes. After 100 minutes, it is asymptotically saturated to a constant value.

Fig. 5 represents the isothermal electrical resistivity study at 350 C. It is obvious that the electrical resistivity shows logarithmic behavior with respect to time before roughly 10 minites, after 10 minites, it is gradually saturated and shows a maximum around 1 hour. Five hours later, the electrical resistivity starts decreasing slowly and goas to a stable constant value after roughly two days.

The melting temperatures of Zn and Cu are roughly 420 C and 1,083

C, respectively. The isothermal irreversible electrical resistivity studies of these multifilamentary Cu-Zn thin wires below 420 C can be used to analyze the effect of alloying; however, the study above 420C will include the effects of both alloying between Cu and Zn and melting of Zn itself. This is because that, for multifilamentary CuZn thin wires, the Zn components near the surface of the sample will be easy to evaporate from the surface to the surroundings at temperatures above 420 C. The isothermal irreversible electrical resistivity study at 570 C which is plotted in Fig. 6 shows quite anomalous behavior. This is due to the complicated combinations of the effects of alloying between Cu and Zn and of the melting of Zn etc.

For the sake of studying the saturated alloying behavior, we plot the normalized electrical resistivity, ρ_t/ρ_o , (i. e., the ratio of the electrical resistivity at time t to the electrical resistivity at the beginning of each annealing temperature) as a function of time t in Fig. 7. Except the anomalous behavior for the annealing study at 570 C, the ρ_t/ρ_o vs t curves approach to roughly the same value after 2 days, for these annealing studies below 420 C. This suggests that the effect of alloying seems to be completed after 2 days at annealing temperatures between 150 C and 350 C.

The microstructure of the longitudinal and transverse cross scvtions of an unannealed multifilamentary Cu-Zn sample is shown in Fig. 8 (a) and (b), respectively. From Fig. 8, the roughly uniformed distribution of the ribbon-shaped Cu and Zn filaments can be identified. Fig. 9 (a) and (b) shows the microstructure of the longitudinal and transverse cross sections of an annealed multifilamentary Cu-Zm sample, respectively. It is obvious that the ribbon-shaped Cu and Zn filaments disappear and some kind of CuZn alloys are formed. It is clear from these picture that the effect of alloying occurs for the multifilamentary Cu-50 wt.% Zn thin wire after annealing at temperatures above 150 C.

In conclusion, this is the first time that the effect of alloying of multifilamentary Cu-Zn thin wire studied by means of the isothermal irreversible electrical resistivity technique is reported. We have found that the effect of

alloying in multifilamentary Cu-50wt.% Zn system seems to be completed after annealing at temperatures between 150 C and 350 C for two days. The multifilamentary Cu-50wt.% Zn thin wire can be annealed, at least, with a few hours at temperatures below 390K (i. e. 117C) without any alloying effect.

ACKNOWLEDGEMENTS :

The authors are grateful to the National Science Council of Republic o China for the financial support of this work under contract # NSC75-0208-M001-09.

REFERENCES :

1. B. Goldstein, Phys. Rev. 118, 1024 (1960).
2. M. P. Dariel, G. Erez and G. M. J. Schmidt, Phil. Mag, 19, 1045 (1969).
3. M. P. Dariel, G. Erez and G. M. J. Schmidt, J. Appl. Phys. 40, 2746 (1969).
4. D. L. Kendall and R. A. Huggins, J. Appl. Phys. 40, 2750 (1969).
5. M. P. Dariel, G. Erez and G. M. J. Schmidt, Phil. Mag. 19, 1053 (1969).
6. M. P. Dariel, Phil. Mag. 22, 563 (1970).
7. M. P. Dariel, M. Blumenfeld and G. Kimmel, J. Appl. Phys. 41, 1480 (1970).
8. R. W. Brodersen, J. N. Walpole and A. R. Calawa, J. Appl. Phys. 41 1484 (1970).
9. M. P. Dariel, J. Appl. Phys. 42, 2251 (1971).
10. C. H. Ting and G. L. Pearson, J. Appl. Phys. 42, 2247 (1971).
11. V. Srikrishnan and P. J. Ficalora, Metall. Trans. A 6, 2095 (1975).
12. W. G. Wolfer and M. Ashkin, J. Appl. Phys. 47, 791 (1976).
13. D. Chatenay, W. Urbach, A. M. Cazabat and D. Langevin, Phys. Rev.

Lett. 54, 2253 (1985).

14. Y. D. Yao and S. Foner, Ann. Rep. Nat. Mag. Lab., MIT P. 37 (1981-2).
15. Y. D. Yao and S. Foner, Appl. Phys. Lett. 43, 697 (1983).
16. Y. D. Yao and S. Foner, Proc. 1st CSIR (ROSA) - NSC (ROC) Metal Alloy & Ceramics Workshop, P. 293 (1983).
17. Y. D. Yao and G. Yur, 2nd ROC-ROK Symposium on Solid State Physics, April, 1985.
18. W. Hume-Rothery, Electrons, atome, metals and alloys, Dover, (1963).
19. C. Kittel, Introduction to Solid State Physics, (5th Ed.) John Wiley, (1976).
20. M. Hansen, Constitution of Binary Alloys, (McGraw-Hill Book Co.), (1958).
21. Y. D. [illegible] Phys. Stat. Sol. (b) 94, K137 (1979).

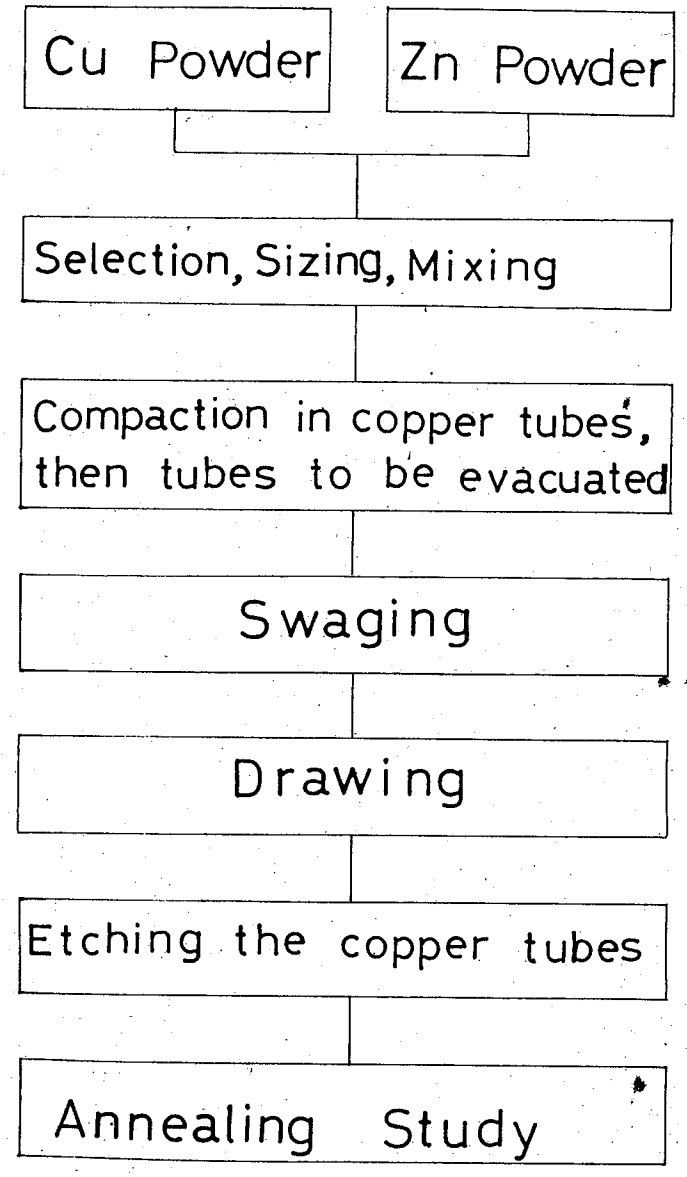

Fig. 1 Cold powder processes.

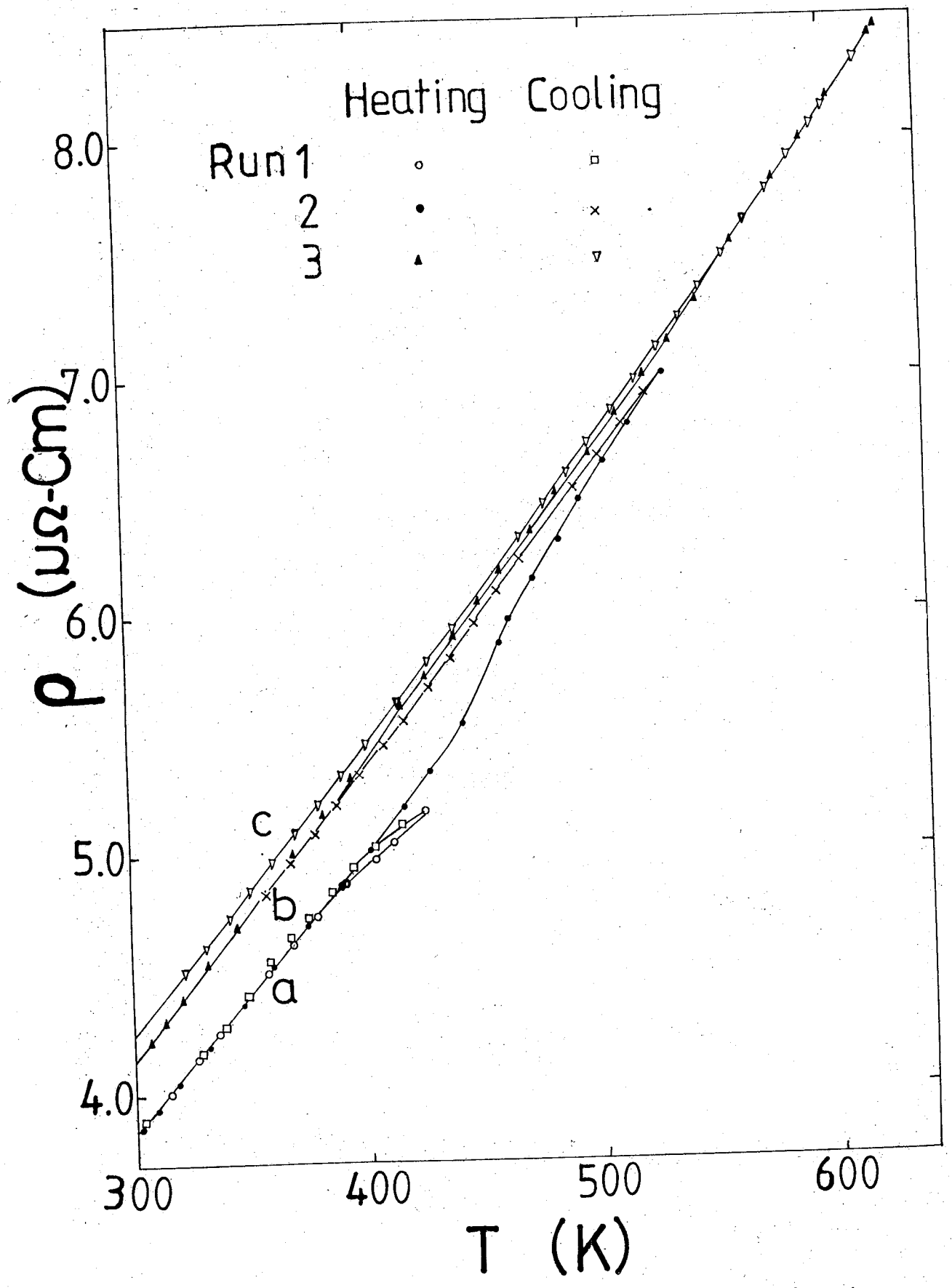

Fig. 2 Electrical resistivity of multifilamentary Cu-50wt.% Zn thin wire as a function of absolute temperature between 300 and 650 K.

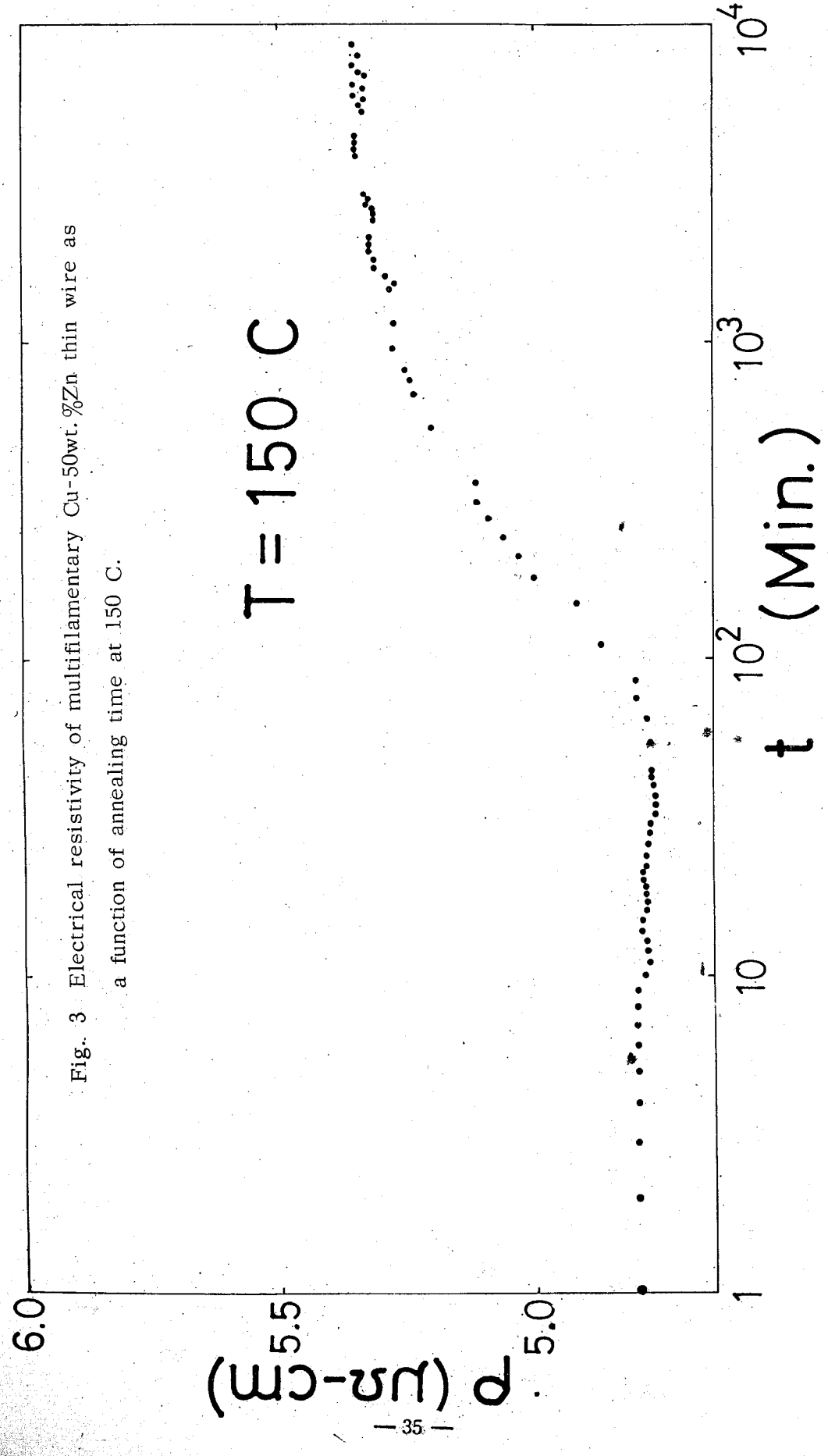

Fig. 3 Electrical resistivity of multifilamentary Cu-50wt.%Zn thin wire as a function of annealing time at 150 C.

Fig. 4 Electrical resistivity of multifilamentary Cu-50wt.%Zn thin wire as a function of annealing time at 250 C.

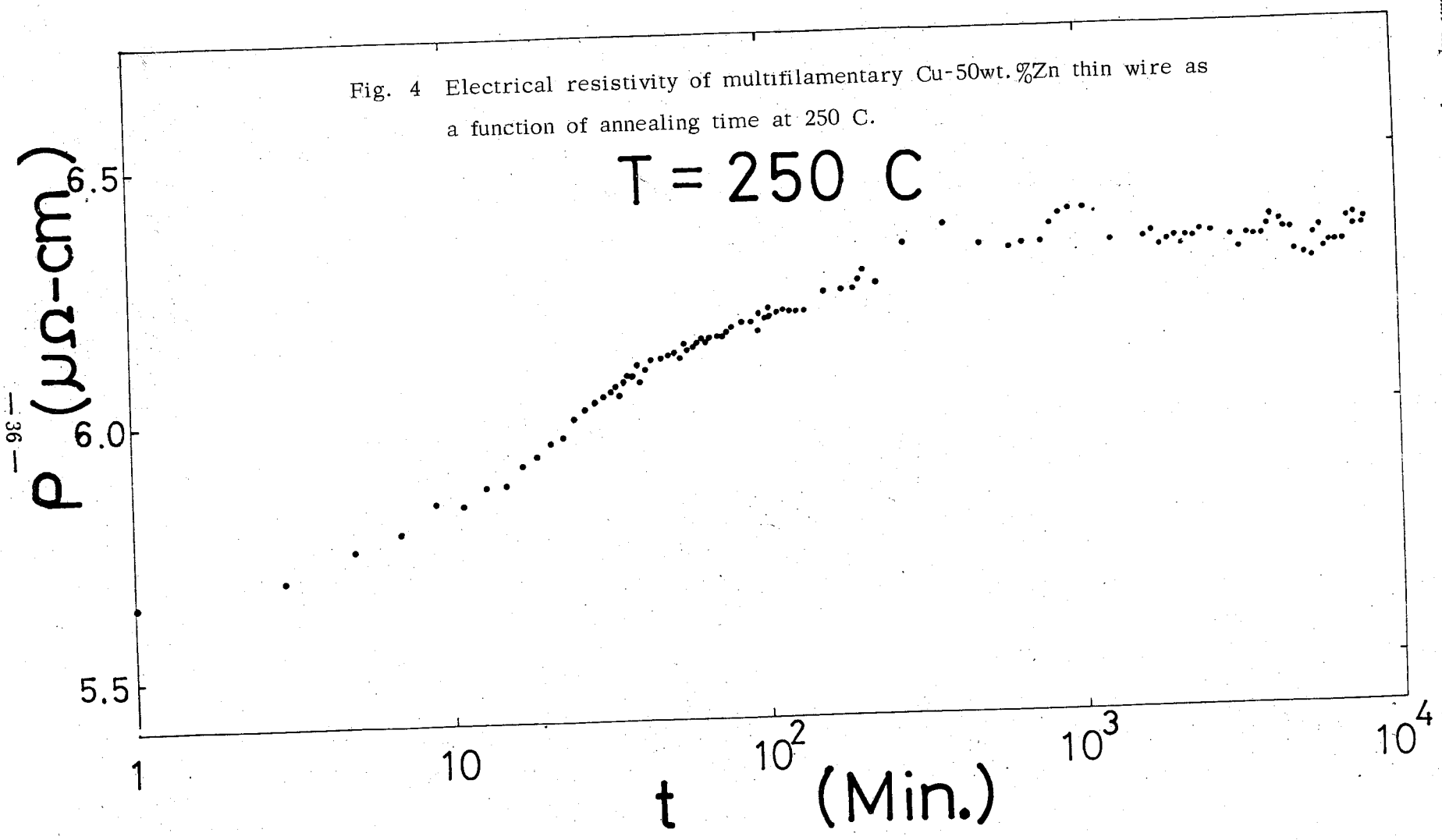

Fig. 5 Electrical resistivity of multifilamentary Cu-50wt.%Zn thin wire as a function of annealing time at 350 C.

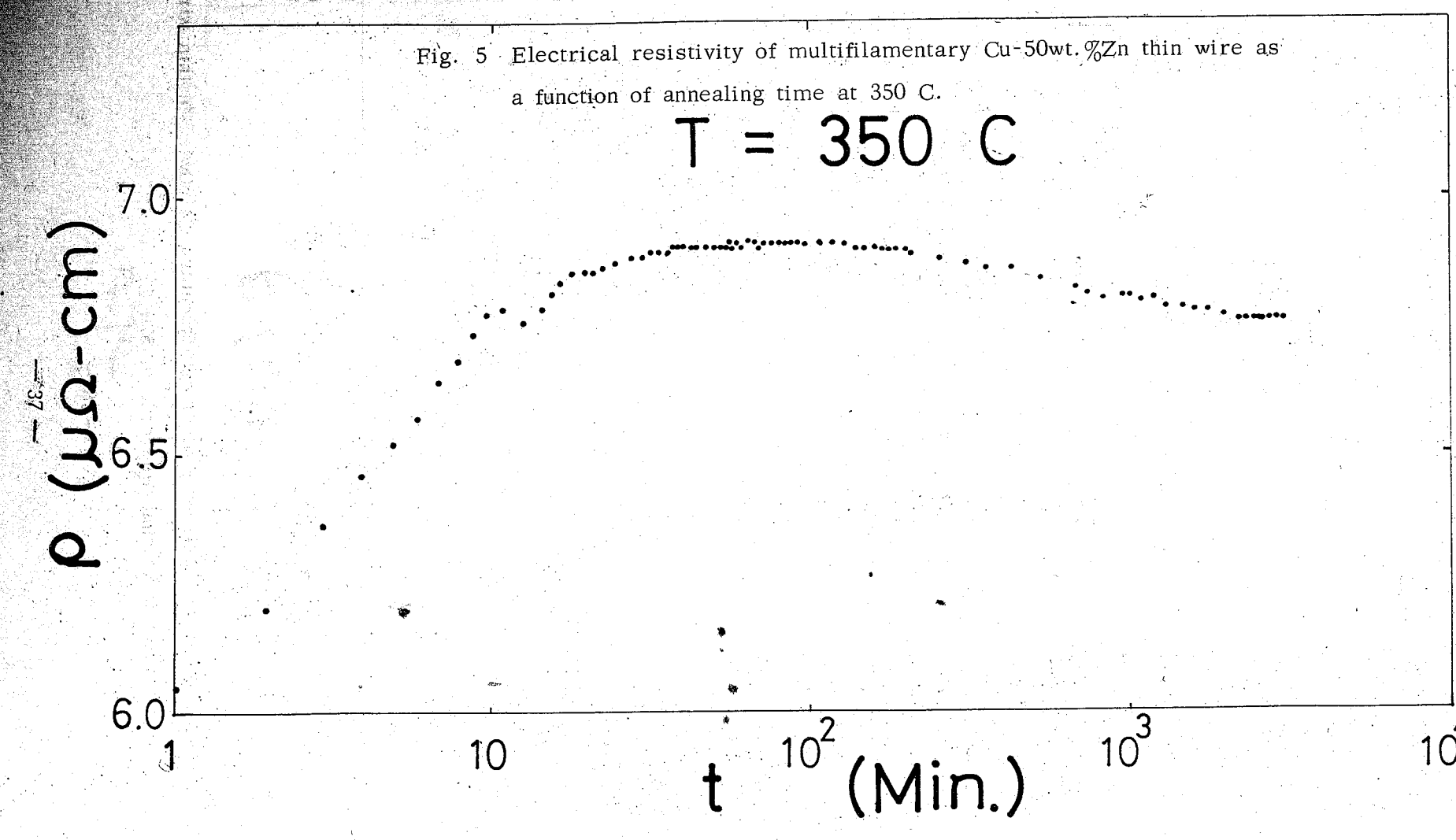

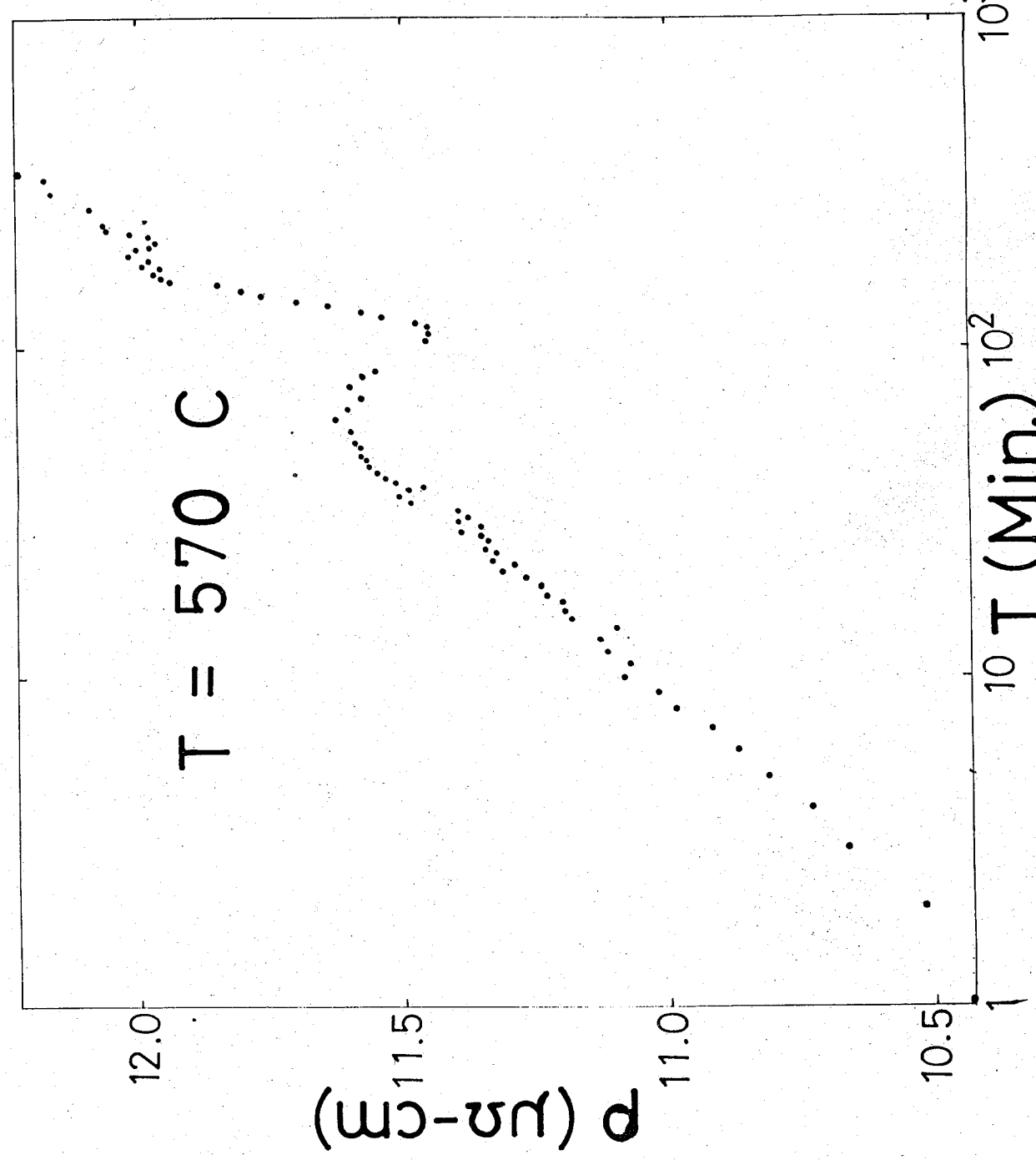

Fig. 6. Electrical resistivity of multifilamentary Cu-50wt.%Zn thin wire as a function of annealing time at 570 C.

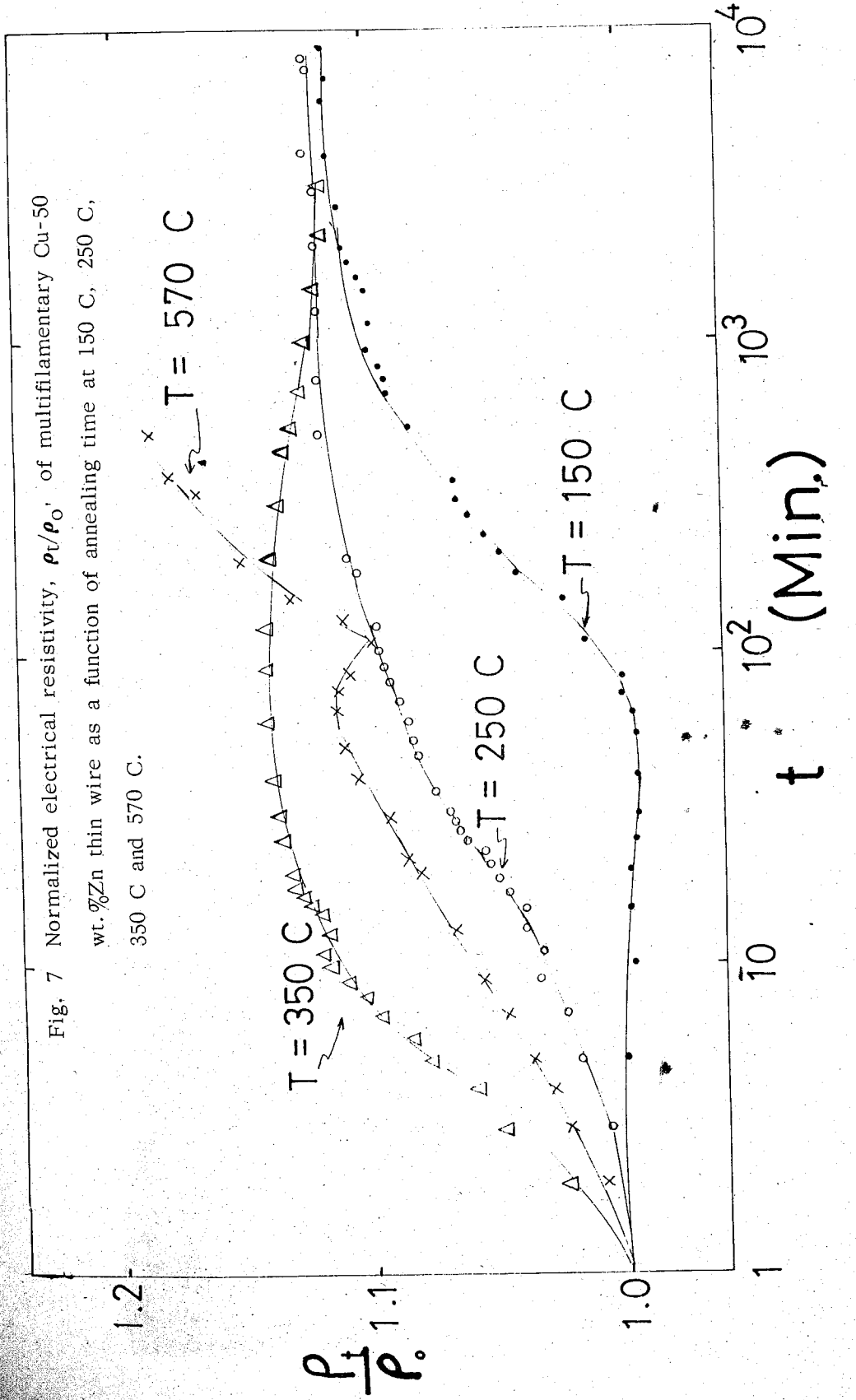

Fig. 7 Normalized electrical resistivity, ρ_t/ρ_o, of multifilamentary Cu-50 wt.%Zn thin wire as a function of annealing time at 150 C, 250 C, 350 C and 570 C.

Fig. 8 Micrographyof polished cross sections (a : longitudinal and b : transverse) of an unannealed multifilamentary Cu-50wt.%Zn thin wire with the magnification of 130.

(a) longitudinal cross section:

(b) transverse cross section:

Fig. 9 Micrograph of polished cross sections (a : longitudinal and b : transverse) of an annealed multifilamentary Cu-50wt.%Zn thin wire with the magnification of 130.

(a) Longitudinal cross section:

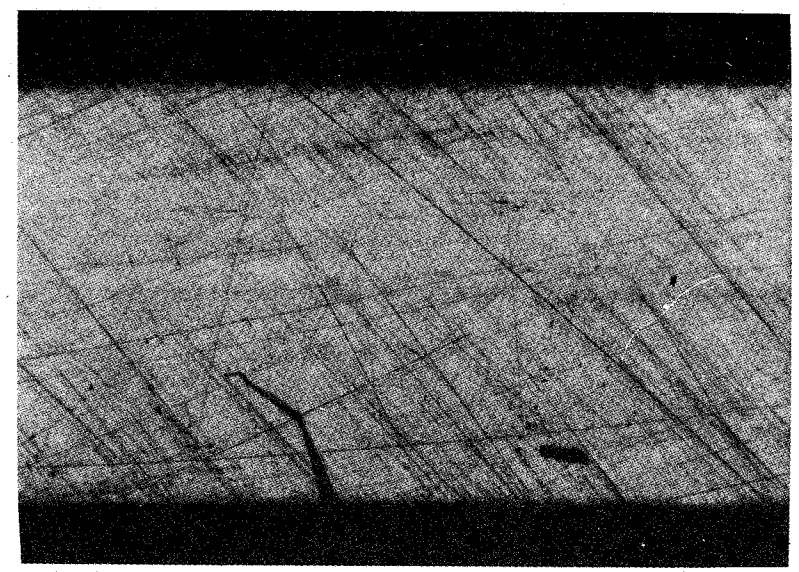

(b) Transverse cross section:

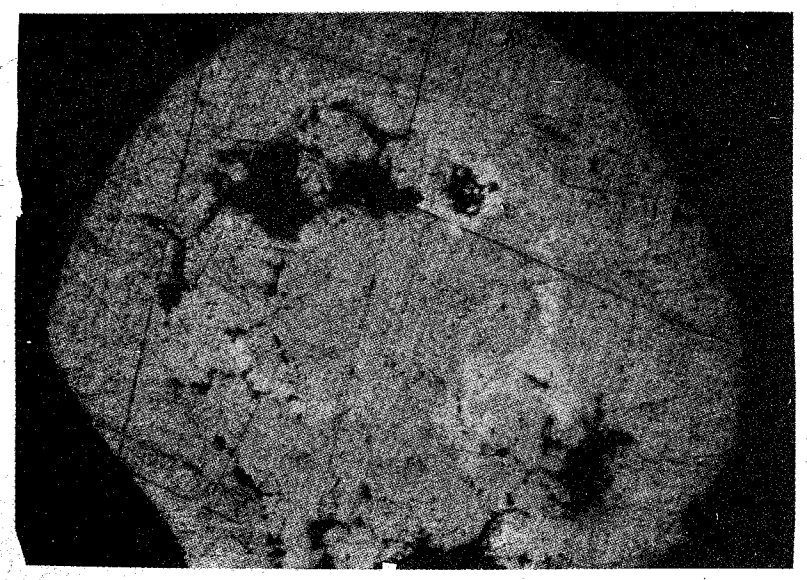

PHASE TRANSITION IN ALLOY SYSTEM

Y. D. Yao（姚 永 德）

Institute of Physics

Academia Sinica

Taipei, Taiwan

R. O. C.

ABSTRACT

Phase transitions in alloy system have been extensively studied both theoretically and experimentally. Several methods and techniques (e. g. the renormalization group, scaling laws and correction to scalings etc.) have been realized to be the indispensable tools for the understanding of the phase transitions in alloy system. However, the numerical results have not been unique yet.

I. Introduction

Phase transitions in alloy system have been extensively studied both theoretically and experimentally. This critical phenomenon has been reviewed by Kadanoff et al [1], Fisher[2], Stanley[3], Ma[4], Fähnle et al[5] and Wilson[6] etc.. In spite of the great amount of theoretical effort that has been devoted to this phenomenon on the basis of idealized models, there are still many unsettled problems with regard to the real alloy materials. During recent years we have already studied experimentally the phase transition problem for quite a few alloy systems (e. g. Fe-Pd[7,8] and Sm-Dy[9]) in our laboratory. In this paper, we will discuss the present situation of phase transition

problem in alloy system.

The phenomena of phase transitions are rather common and furthermore, critical phenomena have a universal character independent of the system. A wide variety of physical systems exhibit phase transitions; usually, we study these critical phenomena by an order parameter, M, which varies from M = 0 (absolute disorder) to M = 1 (absolute order). When the physical system is cooled below a certain temperature, Tc, it begins to change from the disordered state into a partially ordered state. As the temperature is lowered further the state of complete order is finally reached. If the order parameter, M, Changes discontinuously with the change of the temperature near the transition temperature; it is named the first-order phase transition. For the case that M changes continuously, we call it the second-order phase transition. For alloy system, their magnetic phase transitions belong to the second-order phase transition.

II. Relation Between Theoretical Models and Experimental Phenomena

Landau (1937) developed a phenomenological theory of the second-order phase transition from the change of symmetry at the transition temperature. He assumed that the free energy could be expanded in powers of an order parameter. In particular, magnetization M is the order parameter in magnetism and the free energy can be written in a form (for small M, to the fouth order in M) :

$$F(T, M) = F(T, 0) + AM^2 + BM^4 \qquad (1)$$

where A and F are temperature-dependent, and no odd terms of M are included by virtue of the fact that F is invariant under the change of the sign of M. The magnitude of the magnetic field H is given by $H = (\partial F/\partial M)_T$. The true free energy is the minimum of F over all possible values of M. In the absence of an external magnetic field

$$(\frac{\partial F}{\partial M})_T = (2A + 4BM^2)M = 0 \qquad (2)$$

The minimum of F occurs at M = 0 ; this corresponds to temperatures at and above the critical temperature. For temperatures below the critical temperature, we have $M = \sqrt{-A/2B}$. The isothermal susceptibility X_T is given by $(\partial M/\partial H)_T$,

$$X_T^{-1} = (\frac{\partial^2 F}{\partial M^2})_T = 2A + 12BM^2 \qquad (3)$$

Here, in order to get $M \geq 0$ at $T \leq T_c$, one has to consider the coefficient B which has the opposite sign of A ; and the fact that X_T diverges for $T \longrightarrow T_c$ requires $A \longrightarrow 0$ at $T \longrightarrow T_c$. Extensively theoretical works had already been carried out during the past fifty years; and a lot of theoretical models (e. g. Ising model, Heisenburg model etc.) have been developed for a qualitative understanding of the major mechanisms behind phase transitions, and for a basis of quantitative calculations. Mean field theory or Landau theory is one of the simple and old theoretical attempt to explain the critical phenomena, and the values calculated from this theory sometimes disagrees with the experimental evidence, however, it still captures some important features of the critical phenomena. A completely satisfactory theory has not been establishment.

During the past ten years, a considerable amount of progress has been made in the understanding of the critical phenomena. This progress revolves largely around the application and general acceptance of scaling theory and the appearance of the renormalization group, which shows how scaling and homegeneity arise. According to the renormalization group theory, the principal critical point is characterized by two parameters : the dimensi n d and the number of internal components n. Great efforts were made t. ap out cri-

tical behavior as a function of d and n. We summarize the concept of marginal dimensionality as shown in Table I. Critical phenomena occur between the lower marginal dimensionality and upper marginal dimensionality. For dimension which is below the lower marginal dimensionality, no phase transition occur; and above the upper marginal dimensionality, it is the mean field behavior or " classical " behavior. For example, the lower marginal dimensionality is 2, 1, 2 and upper marginal dimensionality is 4 , 4, 4, for isotropic magnet, Ising magnet and ordinary solid, respectively.

For any physical systems undergoing a second-order phase transition, in spite of the complexity of the transition, it is characterized by an asymptotically diverging correlation length :

$$\xi \propto \left| \frac{T - T_c}{T_c} \right|^{-\gamma} \qquad \text{As } T \longrightarrow T_c \qquad (4)$$

which, sufficiently near the critical temperature T_c , is much greater than typical microscopic lengths such as the lattice spacing or the range of interactions. Theoretically, the fluctuations around equilibrium are characterized by a correlation function $\Gamma(\vec{R})$, which, in the magnetic case, is

$$\Gamma(\vec{R}) = \langle [M(\vec{R}) - \langle M(\vec{R}) \rangle] [M(0) - \langle M(0) \rangle] \rangle \qquad (5)$$

$\Gamma(\vec{R}) \longrightarrow 0$ as $R \longrightarrow \infty$. The brackets in Eq. (5) designate a thermodynamic average. The range of $\Gamma(\vec{R})$ is, by definition, the correlation length. Experimentally, the critically varying thermodynamic variables, e.g. M (magnetization) and X (susceptibility) in the magnetic case, are characterized to scale with the correlation length, and for distances short compare to ξ , the details of the interaction are unimportant. Following the scaling ideas, the correlation function and thermodynamic variables are characterized by a number of critical exponents; and a number of important equations relating the critical exponents are obtained. Example of the scaling laws are :

Rushbrooke's scaling law : $\alpha + 2\beta + \gamma = 2$

Widom's scaling law : $\gamma = \beta(\delta - 1)$

Fisher's scaling law : $\gamma = (2 - \eta)\nu$ (6)

Josephson's scaling law : $\nu d = 2 - \alpha$

where d is the dimensionality of space, and other critical exponents will be explained later. Critical exponents have usually served as the common meeting ground between theories and experimental results; and the power-law analysis of the critical behavior has been widely studied both theoretically and experimentally.

III. Critical Exponents

In order to describe the behavior near the phase-transition temperature of certain thermodynamic variables and of the correlation function etc., we define some critical exponents ($\alpha, \beta, \gamma, \delta, \eta, \nu, \lambda$ etc.). Table II shows the relation between these critical exponents and the order parameter, conditions and power laws for magnetic system. The specific heat at constant magnetic field, C_H , and the susceptibility. γ . involve the exponents α , α' , γ and γ' The exponent, β , refers to the variation of the spontaneous magnetization, M. At $T = T_c$, the magnetization is not a smooth function of the external field, and it leads to the exponent δ . Eq. (4) has shown that the exponents for correlation length ξ are ν and ν' The long-distance behavior of the correlation function, $\Gamma(\vec{R})$, defines the exponent η. Finally, the exponents λ and λ' refer to the electrical resistivity, ρ . In most cases, it seems that the primed and unprimed values of the critical exponents are always equal. However, it would be wrong to think that there is perfect symmetry between behavior above and below the phase transition temperature. As an example, the theoretical and experimental values for some critical exponents are listed in Table III. It is evident that different analyzing technique always produces different

results.

IV. Discussion

Theoretically, alloy systems with the same number of degrees of freedom of the order parameter and with the same dimensionality should belong to the same universal class; this means that the values of the critical exponent are the same for any different alloy system. (i.e. the critical phenomena are universal). However, experimentally, nonuniversal features are always observed, such as the value of T_c will depend on the concentration and the kind of the impurities inside the alloy system; and the values of the critical exponents determined experimentally are always the effective critical exponents. According to the correlation to scalings[11], the relation between the effective critical exponent, μ_{eff}, and the exact critical exponent, μ, is defined by

$$\mu_{eff} = \mu - a\Delta \left|\frac{T-T_c}{T_c}\right|^{\Delta} \qquad (7)$$

where a is the amplitude of the confluent singular term and Δ is Wortis-Wegner correction to scaling exponent. From our experimental experiences, we believe that the experimental difficulties for studying the phase transitions in alloy system are as follows : (1) the " relaxation time " (i.e., the time needed to approach thermal equilibrium after a disturbance) is very long when T is near T_c ; this means that we have to spend quite a long time for doing these experimental works accurately. (2) the experimentally attained values of $T - T_c$ have not been small enough for the power law divergence to show up exactly; this means that rounding effect near T_c always happens. (3) the divergence result from large increases in the microscopic fluctuations near T_c ; this means that it is difficult to study macroscopically. (4) other physical effects always co-exist; this means that it is always difficult to separate the background terms besides the singularity exactly.

Basing on the phase transition characteristics, the ferromagnetic alloy systems can be classified into two categories : (1) macroscopically homogeneous random ferromagnets, and (2) inhomogeneons ferromagnets[12]. Macroscopic homogeneous random ferromagnets show the normal critical phenomena near T_c and pseudocritical behavior outside the normal critical region. Normal critical region means that the critical behavior is independent of the details of the atomic structure but depends on the dimensionality of the system and the degress of freedom of the magnetic fluctuation. i.e. the critical exponents are independent of the crystal structure. In the pseudocritical nonlinear region, the critical exponents are varied and depend on the compositional and topological disorder of alloy system. The inhomogeneous ferromagnets show a smeared transition and super-paramagnetic behavior above T_c, For macroscopically homogeneous random ferromagnets, the critical index α for specific heat is negative, so that specific heat plotted against temperature shows a sharp singular behavior at T_c. However, if there is some chemical inhomogeneity such as segregation, the magnetic correlation length does not grow beyond the characteristic wavelength of such an inhomogeneity and the transition becomes smeared with a positive α. This smearing can occar not only because of macroscopic compositional inhomogeneity but also because of spatial inhomogeneity in the degree of structural relaxation, or the large random anisotropy. For example, yamada et al[13] found a well-defined transition for $Fe_{80}P_{13}C_7$, but a smeared transition for $Fe_{70}Ni_{10}B_{13}C_7$ and $Fe_{70}Cr_{10}P_{13}C_7$.

In conclusion, up to date, we have derived a lot of techniques both theoretically and experimentally; e.g. the renormalization group, scaling laws and correction to scalings etc. These methods have been realized to be the indispensable tools for the understanding of the phase transitions in alloy systems. However, the numerical results have not been unique yet. This means that more powerful methods and experimental techniques are definitely required for a complete and unique picture of the phase transition in alloy system.

Acknowledgements

The author is grateful to the National Science Council of Republic of China for the financial support of this work.

References

1. L. P. Kadanoff, W. Götze, D. Haurblen, R. Hecht, E. A. S. Lewis, V. V. Palcianskas, M. Rayl, J. Swift, D. Aspnes, and J. Kane, Rev. Mod. Phys. 39, 395 (1967).
2. M. E. Fisher, Rev. Mod. Phys. 46, 597 (1974).
3. H. E. Stanley, Introduction to Phase Transitions and Critical Phenomena, Oxford Univ. London (1971).
4. S. K. Ma, Modern Theory of Critical Phenomena, Benjamin, Reading, Mass. (1976).
5. M. Fähnle, G. Heszer, H. Kronmüller, R. Meyer, M. Saile and T. Egami, J. Magn. Magnet. Mater. 38, 240 (1983).
6. K. G. Wilson, Rev. Mod. Phys. 55, 583 (1983).
7. Y. D. Yao and S. Arajs, Phys. Stat. Sol. A55, K201 (1979).
8. Y. D. Yao and S. Arajs, Phys. Stat. Sol. A64, 95 (1981).
9. Y. D. Yao, L. T. Ho and C. Y. Young, J. Less-Common Metals, 69, 355 (1980).
10. D. J. Griffiths, D. S. Easton and D. M. Kroeger, Phys. Rev. B31, 287 (1985).
11. F. J. Wegner, Phys. Rev. B5, 4529 (1972).
12. R. Meyer and H. Knonmüller, Phys. Star. Sol. (b) 109, 693 (1982).
13. K. Yamada, Y. Ishikawa, Y. Endoh and T. Masumoto, Solid St. Comm. 16, 1335 (1975).

Table I. The Concept of Marginal Dimensionality.

No Phase Transition	Lower marginal dimensionality	Critical Phenomena	Upper marginal dimensionality	Mean Field Behavior or "Classical" Behavior
Isotropic Magnet	2		4	
Ising Magnet	1		4	
Ordinary Solid	2		4	

Table II. The Critical Exponent, the Order Parameter, Conditions and Power Law for Magnetic Alloy System.

Critical Exponent	Order Parameter	Conditions H	Conditions M	Power Law $\varepsilon \equiv \lvert\frac{T-T_c}{T_c}\rvert$
α,α'	Specific heat (at constant magnetic field)			
	C_H	0	0	$C \propto \varepsilon^{-\alpha}$ $(T>T_c)$
		0	$\neq 0$	$C \propto \varepsilon^{-\alpha'}$ $(T<T_c)$
	Magnetization			
β	M	0	$\neq 0$	$M \propto \varepsilon^{\beta}$ $(T \Rightarrow T_c)$
	Susceptibility			
γ,γ'	χ	0	0	$\chi=\frac{\partial M}{\partial H} \propto \varepsilon^{-\gamma}$ $(T>T_c)$
		0	$\neq 0$	$\chi=\frac{\partial M}{\partial H} \propto \varepsilon^{-\gamma}$ $(T<T_c)$
	Magnetization			
δ	$M_{(T=T_c)}$	$\neq 0$	$\neq 0$	$M \propto H^{1/\delta}$ $(T=T_c)$
	Correlation Length			
ν,ν'	ξ	0	0	$\xi \propto \varepsilon^{-\nu'}$ $(T>T_c)$
		0	$\neq 0$	$\xi \propto \varepsilon^{-\nu}$ $(T<T_c)$
	Correlation Function			
η	$\Gamma(R)$	0	0	$\Gamma(R) \propto 1/R^{d-2+\eta}$
	Electrical Resistivity			
				$\frac{d\rho}{dT}=\frac{A'}{\lambda'}(\varepsilon^{-\lambda'}-1)+B'$
		0	0	$\frac{d^2\rho}{dT^2} \propto \varepsilon^{-(\lambda'+1)}$ $(T>T_c)$
λ,λ'	ρ			$\frac{d\rho}{dT}=\frac{A}{\lambda}(\varepsilon^{-\lambda}-1)+B$
		0	$\neq 0$	$\frac{d^2\rho}{dT^2} \propto \varepsilon^{-(\lambda+1)}$ $(T<T_c)$

Table III. Example of theoretical and experimental values for some critical exponents

Critical exponent	α	β	γ	δ	η	ν
Theory						
Ising (2-dimension)	0(log)	.125	1.75	15.0$\pm$0.07	0.25	1
Ising (3-dimension)	0.013$\pm$0.01	0.312+0.002 -0.005	1.250$\pm$0.002	5.0$\pm$0.05		0.638+0.002 -0.001
Heisenberg (3-dimension)	-0.14 $\pm$0.06	0.38 $\pm$0.03	1.375+0.020 -0.010	4.2		0.703$\pm$0.010
Experiment						
Fe	-0.06 $\pm$0.12	0.37 $\pm$0.03	1.3 $\pm$0.06	4.58$\pm$0.05		
Ni	-0.08 $\pm$0.02	0.37 $\pm$0.04	1.34 $\pm$0.01	3.95$\pm$0.10		
(Ref. 10) $Gd_{70}Pd_{30}$		0.34 $\pm$0.02	1.01 $\pm$0.003			

A RAMAN SPECTRAL STUDY OF ZINC PERCHLORATE HEXAHYDRATE

K. F. Pai, Y. C. Chen

Department of Physics, National Cheng Kung University

Tainan, Taiwan, R. O. C.

W. S. Tse

Institute of Physics, Academia Sinica

Taipei, Taiwan, R. O. C.

Zinc perchlorate hexahydrate, $Zn(ClO_4)_2\ 6H_2O$ (ZnPH), crystallize in triply twined hexagonal form /1/ which rarely occured in crystal physics. An EPR study of Mn^{2+} doped ZnPH single crystal has indicated that there are two phase transitions at 284K (Tc_2) and 346K (Tc_3) /2/. The proton magnetic relaxation /3/ study has shown that there is a possible phase transition at 160K (Tc_1). The Raman spectrum of ZnPH has been recorded earlier at room temperature /4,5/. In this note we report the Raman spectra of ZnPH at various temperatures from 80K to 385K and try to gain some information on the phase transitions in this material.

Polycrystalline ZnPH powder was obtained from ICN pharmaceuticals Inc., and dried at 320K for 30 minutes. The sample was then sealed in a quartz cell and placed in an Oxford Instruments DN 1714 variable temperature liquid nitrogen cryostat. The temperature sensor is a standard 100 ohm platinum resistc resistor mounted on the inside heat exchanger. The temperature resolution is nearly 0.1K. The ZnPH sample was excited using a Coherent Innova 90-4 Argon ion laser, operating at 0.2-0.4 W on the 5145A or 4880A lines. The

light was scattered through 90° and analyzed with J. Y. Ramanor U1000 Spectrometer equipped with a chilled photomultiplier tube (RCA C31034A-02) and Spex DPC-2 Digital Photometer. The spectral slit widths were set to maintain a resolution of about 1 cm^{-1}.

Typical lattice Raman spectra of ZnPH at various temperatures over the range 80-385K are shown in Figure 1. There are several changes observed in the spectra from high temperature phase to low temperature phase through transitions.

In the temperature range between 280K and 345K, significant " softening " of the two lattice modes (45 cm^{-} and 75 cm^{-1}) are observed as the T_{c3} (345 K) is approached from below. Above 345K, the two modes merge to become the shoulder of the broadened Rayleight wing. Since the sample melt above 380K, the transition at 345K many be considered as an order-to-disorder transition. To check the above assertion, we perform the differential scanning calorimetric measurement on the sample. The experiment was done with Perkin-Elmer DSC-4 from room temperature to the melting point of ZnPH. As seen from Figure 2, the anomaly occured at 348K is consistent with our observation from the Raman spectra studies.

As the temperature is raised from 80K, the peak at 28 cm^{-1} gradually soften to 19 cm^{-1} and completely disappear when T_{c2} (280K) is reached. This is summarized in Figure 3. Beyond T_{c2}, the peak does not reappear, this is probably because it is too close to the central Rayleight wing to be observed. It is also noted from Figure 1 that the peaks, 105 cm^{-1}, 166 cm^{-1} and 250 cm^{-1}, at 80K also gradually shifted to low wavenumber and disappear as the temperature pass through T_{c1} (160K). Besides, there is a big shift in the mode 28 cm^{-1} around this temperature, as seen from Figure 3. To justify the existence of the phase transition around this temperature, further investigations by other techniques (e.g. low temperature DSC experiment) are needed.

This research was supported by a grant from the National Science Council of the Republic of China.

REFERENCES

/1/ M. Ghosh and S. Ray, Z. Kristallogr. 145, 146 (1977).

/2/ A. K. Jain and G. C. Upreti, Solid State Communications, 28, 571 (1978).

/3/ I. Svare and B. O. Fimland, J. Chem. Phys. 74, 5977 (1981).

/4/ A. Weil and J. P. Mathien, C. R. Acad. Sci. 238, 2510 (1954).

/5/ M. B. Patel, A. Agarwal and H. D. Bist, J. Raman Spectroscopy 14, 406 (1983).

FIGURE CAPTIONS

Figure 1. Temperature dependent lattice Raman spectra of ZnPH.

Figure 2. Endotherm and Exotherm of ZnPH.

Figure 3. The temperature dependences of the frequency of the lowest lattice mode of ZnPH.

Fig 1

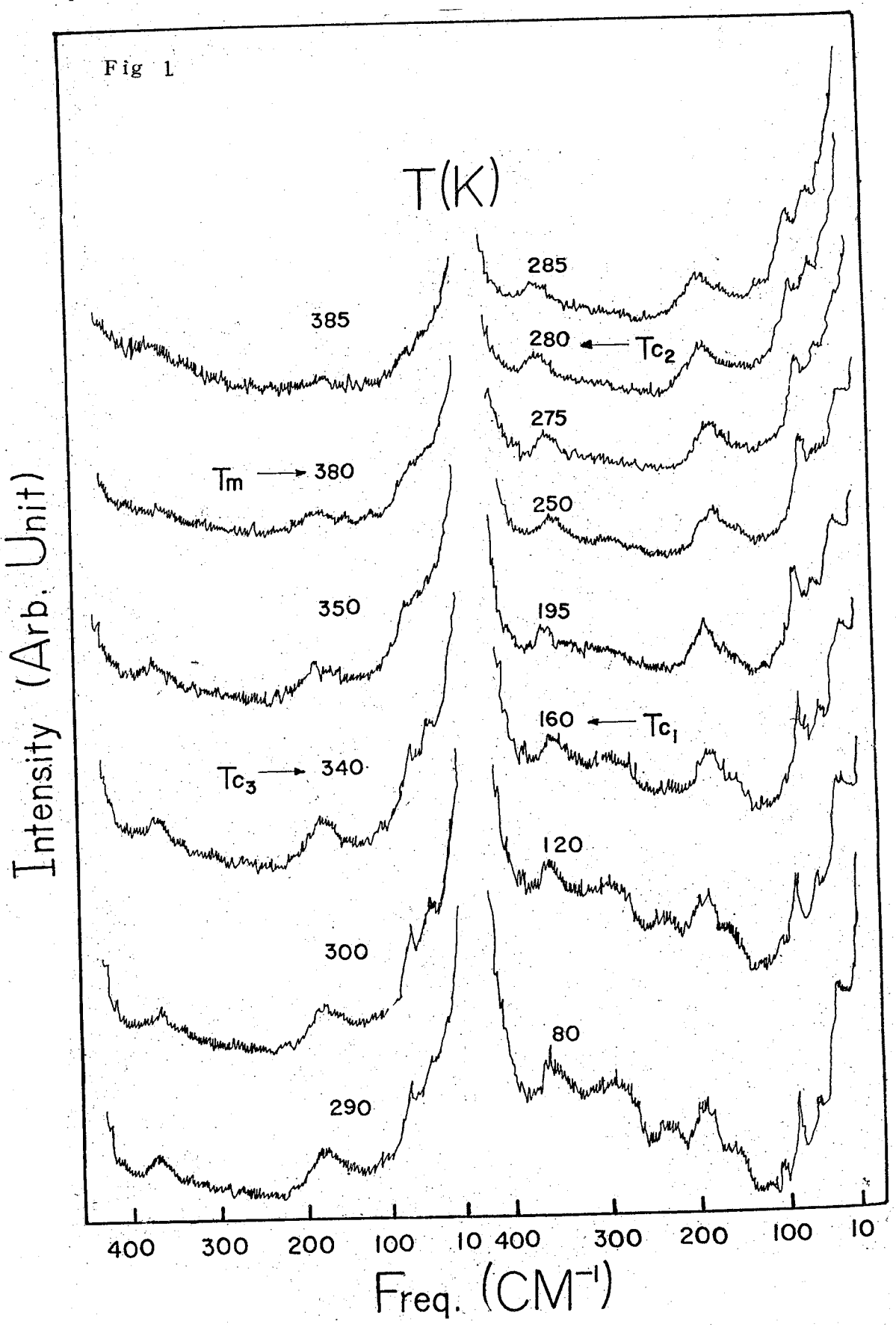
T(K)
385
Tm → 380
350
Tc3 → 340
300
290
285
280 ← Tc2
275
250
195
160 ← Tc1
120
80
Intensity (Arb. Unit)
400 300 200 100 10 400 300 200 100 10
Freq. (CM⁻¹)

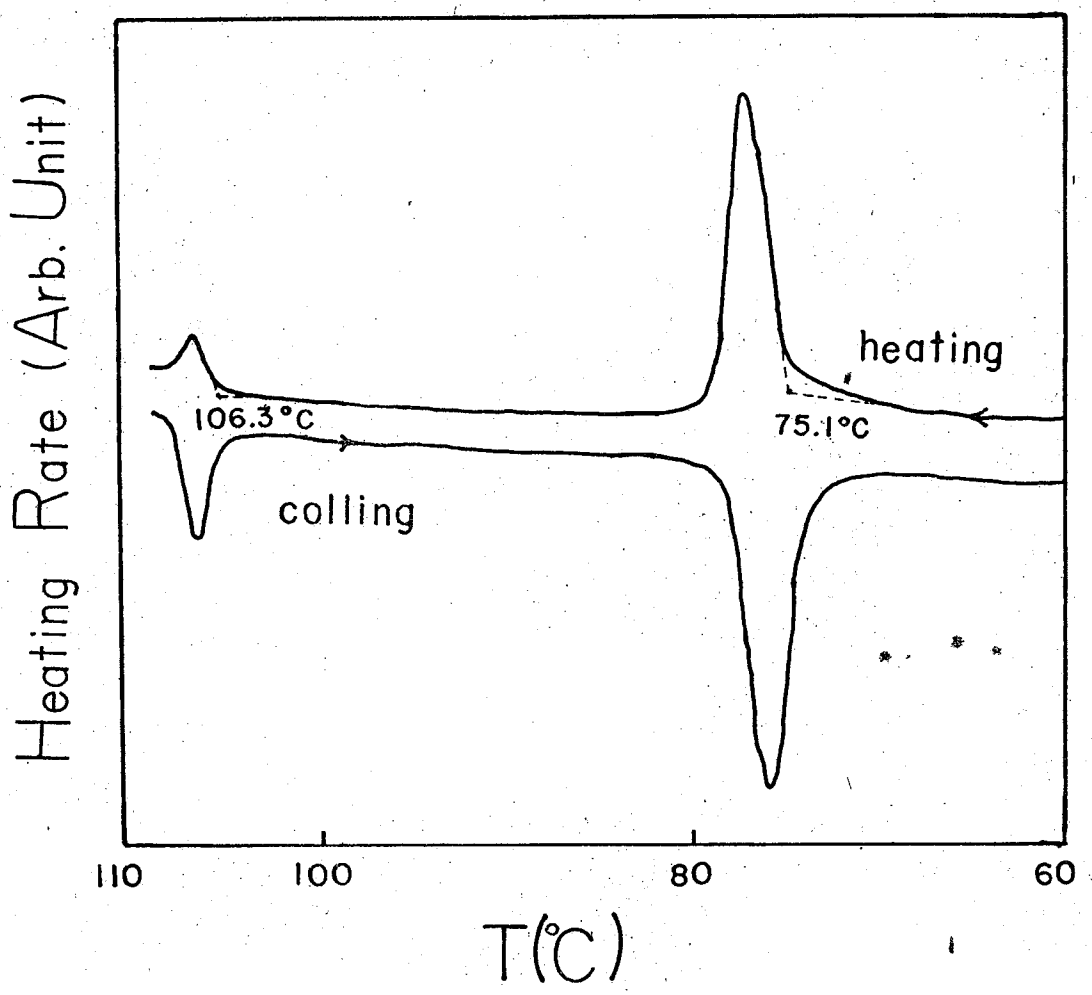
heating
106.3°C
75.1°C
colling
Heating Rate (Arb. Unit)
110 100 80 60
T(°C)

Fig 2

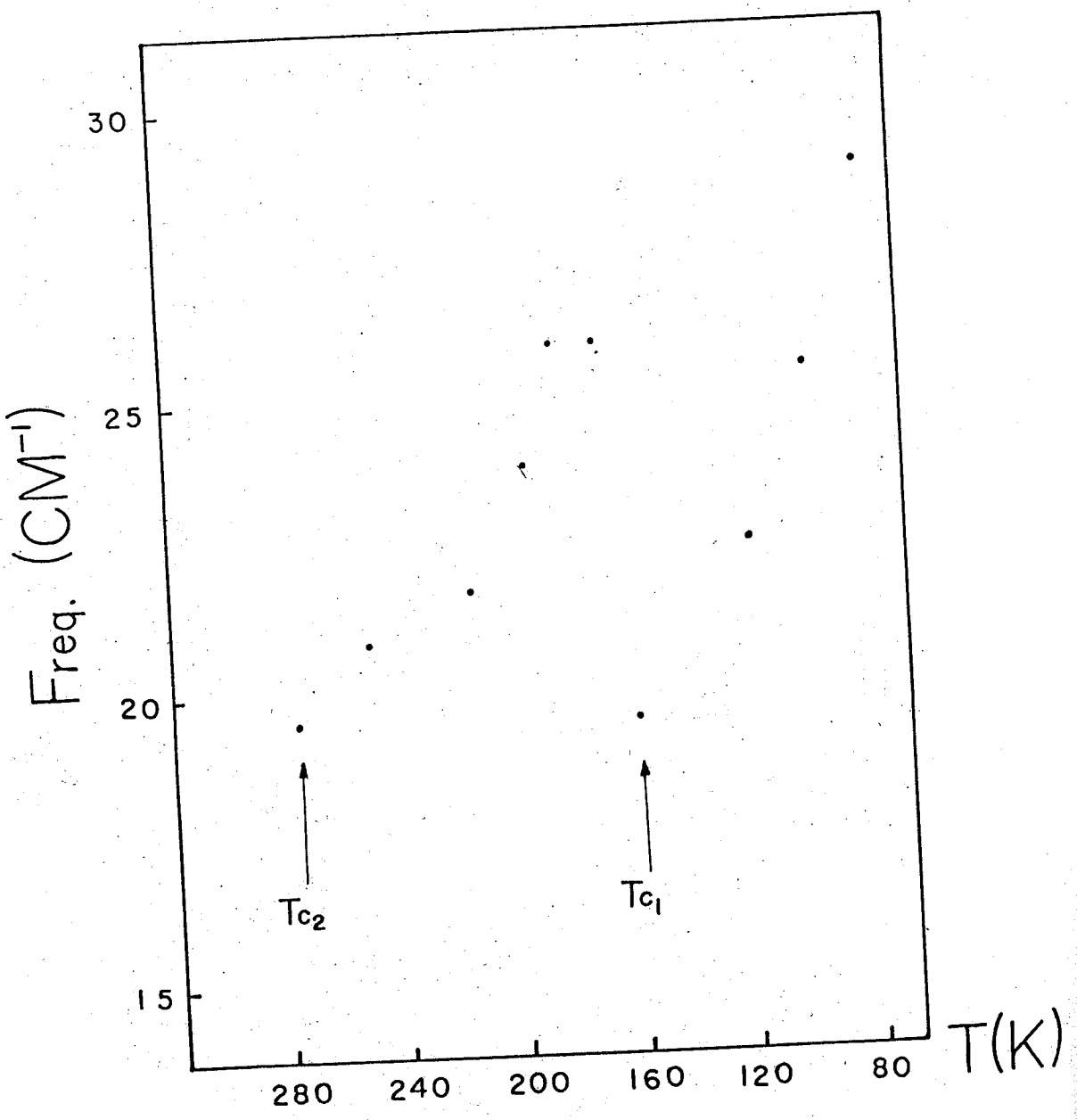

Fig 3

RAMAN SPECTRA OF CRYSTALLINE GERMANIUM AND SILICON TETRABROMIDES

W. S. Tse and G. Yur

Institute of Physics, Academia Sinica

Taipei, Taiwan, R. O. C.

ABSTRACT

The molecular and lattice vibrations of polycrystalline samples of germanium and silicon tetrabromides at temperatures between 80 and 250 K have been investigated by Raman techniques. The observed lattice and molecular modes are discussed according to predictions from the known crystal structure as well as the comparison with other group IV tetrabromides.

INTRODUCTION

Crystalline Raman spectra and crystal structure data for the group IV tetrachlorides are well studied while there are much less documented for group IV tetrabromides. In the literature, a low resolution Raman spectra of solid $GeBr_4$ and $SiBr_4$ in the molecular modes at liquid nitrogen temperature has been reported[1] so far. Only for $SiBr_4$ is reported to be cubic just below its melting and that there appear to be no published crystal data for $GeBr_4$.

The aim of the present work is to obtain more complete and high resolution Raman spectra of the molecular fundamental modes as well as the lattice vibrations of these crystals. This should lead to a better understanding of

the reported crystal structure of $SiBr_4$ and also the most probable structure of the unknown $GeBr_4$ by comparing to other tetrabromide spectra.

EXPERIMENTAL TECHNIQUES

Raman spectra were excited by the 514.5nm line of an argon-ion laser (coherent Innova 90-4 model) with powers up to 400mw. The scattered light was dispersed by J. Y. Ramanor U1000 double monochromator and detected with a cooled photomultiplier (RCA C31034A-02) using photon counting electronics. The output analog signal were then displayed on a Kipp & Zonen DB 40 two-pen strip chart recorder.

Frequencies reported here were estimated to be accurate to $\pm$ 1 cm for sharp features. Periodic calibration checks were made using the known wavelengths of the laser light or other non-lasing plasma lines.

The sample preparation techniques and an conventional optical crystal were similar to those described in an earlier paper in this series[2].

RESULTS AND DISCUSSION

Typical spectra of crystalline $SiBr_4$ and $GeBr_4$ samples at temperatures between 80K and 250K are shown in Figures 1 and 2. Frequencies of maximum intensity are also listed in Table 1. It is found from the temperature variation spectra that there are no further phase changes in any of these compounds as there are not any abrupt spectral changes in the Raman spectra down to 80K.

No exact X-ray structural data are available for crystalline silicon and germanium tetrabromides but $SiBr_4$ is believed to be cubic just below its melting point[3].

As shown in Fig. 1, there are some similarities in spectral band shape and relative intensities between the Raman spectra of $SiBr_4$ in this work and previous Raman work on CBr_4 (I)[2] where CBr_4 (I) at 320K forms the disordered " plastic " crystal in which the center of mass of the tetrahedral

molecules occupy the sites of a face-centered cubic lattice. According to Wyckoff[4], space groups 143m (z = 2) and Pa3 (z = 8) of several tetrahalides are cubic. For space group 143m with 2 molecules per unit cell, the molecules (T_d molecular group) are at Td sites and the group analysis[1] predict no site splitting and a maximum of two components in each fundamental is expected as a result of factor-group splitting. Therefore, there are two Raman active components of ν_1 , ν_2 , ν_3 and ν_4 respectively. The spectra of both compounds, $SiBr_4$ at 80K and CBr_4 (I) at 320K, show only on one sharp peak for ν_1 , ν_2 and ν_4 modes. For ν_3 mode (triply degenerate stretching) only one broad peak present in CBr_4 (I) spectra and three resolved jpeaks in $SiBr_4$, this is because in CBr_4 (I) the temperature is so high (320K) such that all resolved peaks may merged into one broad band due to temperature anharmonic effect. In this work, we also detect no isotopic splitting in totally symmetric stretching ν_1 mode and factor-group splitting of the triply degenerate bending ν_4 mode as observed by Creighton and Sinclar[1].

In the orientationaly disordered CBr_4 (I) phase the molecules are rapidly reorienting about a lattice point. Hence, the lattice Raman spectrum is therefore a broad wind feature[2] compare to the five sharp peaks in the lattice spectrum of $SiBr_4$ at 80K. This feature of sharp peaks in $SiBr_4$ is probably an indication of an ordered cubic phase. The sharp peaks still appear as the sample warming up to high temperatures showing not any reorientational molecular motions as appear in CBr_4 (I).

The above discussions show that the fine structure pattern for $SiBr_4$ (I) are very similar, and it seems an indication that they both may belong to the same cubic space group.

There appear to be no published crystal data for GeBr. However, as shown in Fig. 2, the two spectra of $GeBr_4$ and $SnBr_4$[6] are very similar in band shapes and relative intensities, and it seems probable that these two crystals have similar structures. Complete X-ray data are available for

$SnBr_4$ which belongs to monoclinic space group $P2_1/C$ with four molecules per unit cell. Hence, it is desirable to discuss the spectral features of $GeBr_4$ in terms of the known crystal structure of $SnBr_4$. The group theoretical analysis[2] based on $SnBr_4$ structure predicts two Raman components of ν_1 (A_1) mode; four Raman components of ν_2 (E); six Raman components of ν_3 (T_2); six Raman components of ν_4 (T_2) and also twelve Raman lattice modes. For ν_1 (A_1) mode, the factor-group splitting should give rise two Raman peaks and also ten peaks are observed if taking account of the isotopic splitting. However, only one sharp peak is recorded which means there may be no isotopic and factor-group splittings in this crystal. This fact also suggests that the splittings in other intramolecular modes are not due to isotopic splitting. The degeneracy of ν_2 (E) is removed at the site to give a doublet and further splittings to give four peaks would be factorgroup effect. The observed spectra show that two components are indeed observed suggesting that the splitting arise mainly from site effect. The triply degenerate stretching ν_3 (T_2) mode contains five sharp peaks and are likely five of the six peaks expected from group analysis. The frequency range is nearly 18 cm^{-1} apart and that such large spreading may mainly due to factor-group splitting. On the otherhand the triply degenerate bending ν_4 (T_2) mode gives two peaks only instead of six and this components are mostly due to site effect.

In the lattice region, five of the twelve lattice modes are observed in $GeBr_4$ and that its peak shapes and relative intensities are more or less similar to that of crystalline $SnBr_4$. In this stage it is difficult to assign properly which are translational or librational modes. However, a comparison to the assignment in crystalline CCl_4 (II)[5] and $SnBr_4$[6], the observed lattice spectra are proposed to involve primarily translational motions.

The factor-group analysis based on a monoclinic system with four molecules per unit cell seems to apply reasonably well to the Raman spectra of crystalline $GeBr_4$ indicating its crystal structure may be similar to that

of crystalline $SnBr_4$ of $P2_1/C$ system. Besides, the observed Raman spectra of crystalline $SiBr_4$ is in consistent with the reported cubic crystal structure. The temperature dependent Raman spectra show that both compounds, $SiBr_4$ and $GeBr_4$, exhibit only one phase between 80K and the melting.

ACKNOWLEDGEMENT

This research was supported by a grant from the National Science Council of the Republic of China.

Table 1. Raman frequencies of crystalline $SiBr_4$ and $GeBr_4$ at 80K.

	$SiBr_4$		$GeBr_4$	
	This work	Previous Work[1]	This Work	Previous Work[1]
ν_2 (E)	91	93	79 84	86.5
ν_4 (T_2)	133 246	135 136.5 sh 247.0 sh 247.7	108 110 233	109 111.5 234.6 235.2
ν_1 (A)		248.5 249.3 250.1 sh		236.0 sh 236.7 sh
ν_3 (T_2)	467 471 486	470 475 490	319 325 329 334 337	320 331
	26 32 34 39 42	27 33 sh 42	26 29 35 40 48	34 sh 43 sh 50

REFERENCES

(1) J. A. Creighton and T. J. Sinclar, Spectrochimic Acta, 35A, 137 (1979).

(2) W. S. Tse , N. T. Liang, W. W. Lin and P. Y. Chiang, Chem. Phys. Lett., 119, 67 (1985).

(3) H. Sackmann, D. Demus and D. Penkow, Z. Anorg, Chem. 318, 257 (1962).

(4) R. W. G. Wyckoff, Crystal Structures, Vol. 2, Interscience, New York (1964).

(5) A. Anderson, B. H. Torrie and W. S. Tse, Chem. Phys. Lett., 61, 119 (1979).

(6) W. S. Tse and N. T. Liang Submitted for publication : Chem. Phys. Lett.

Figure 1. Temperature dependent Raman spectra of crystalline $SiBr_4$. The inserted spectra of crystalline CBr_4(I)[2] is used for comparison.

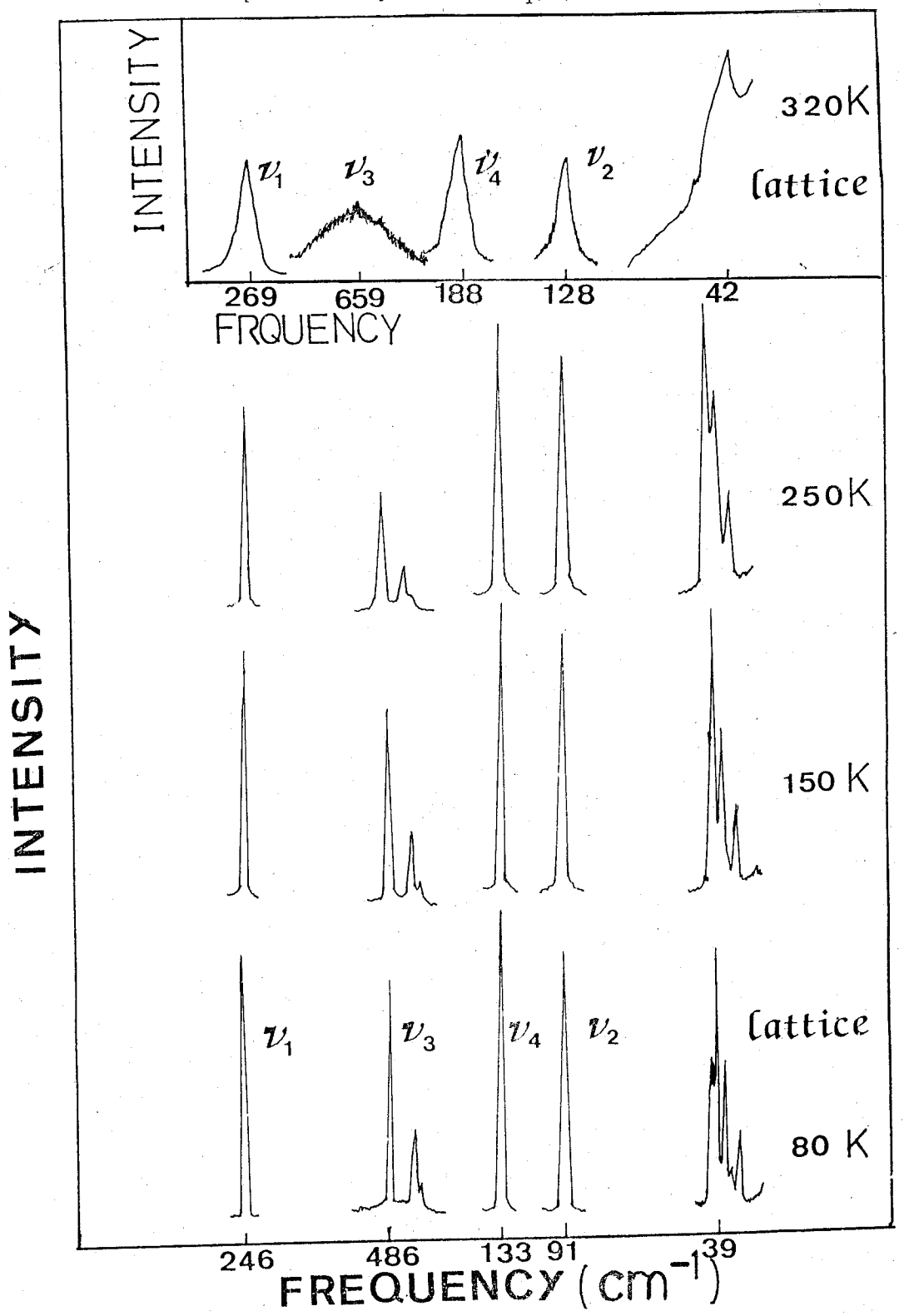

Figure 2. Temperature dependent Raman spectra of crystalline $GeBr_4$. The inserted spectra of crystalline $SnBr_4$[6] is used for comparison.

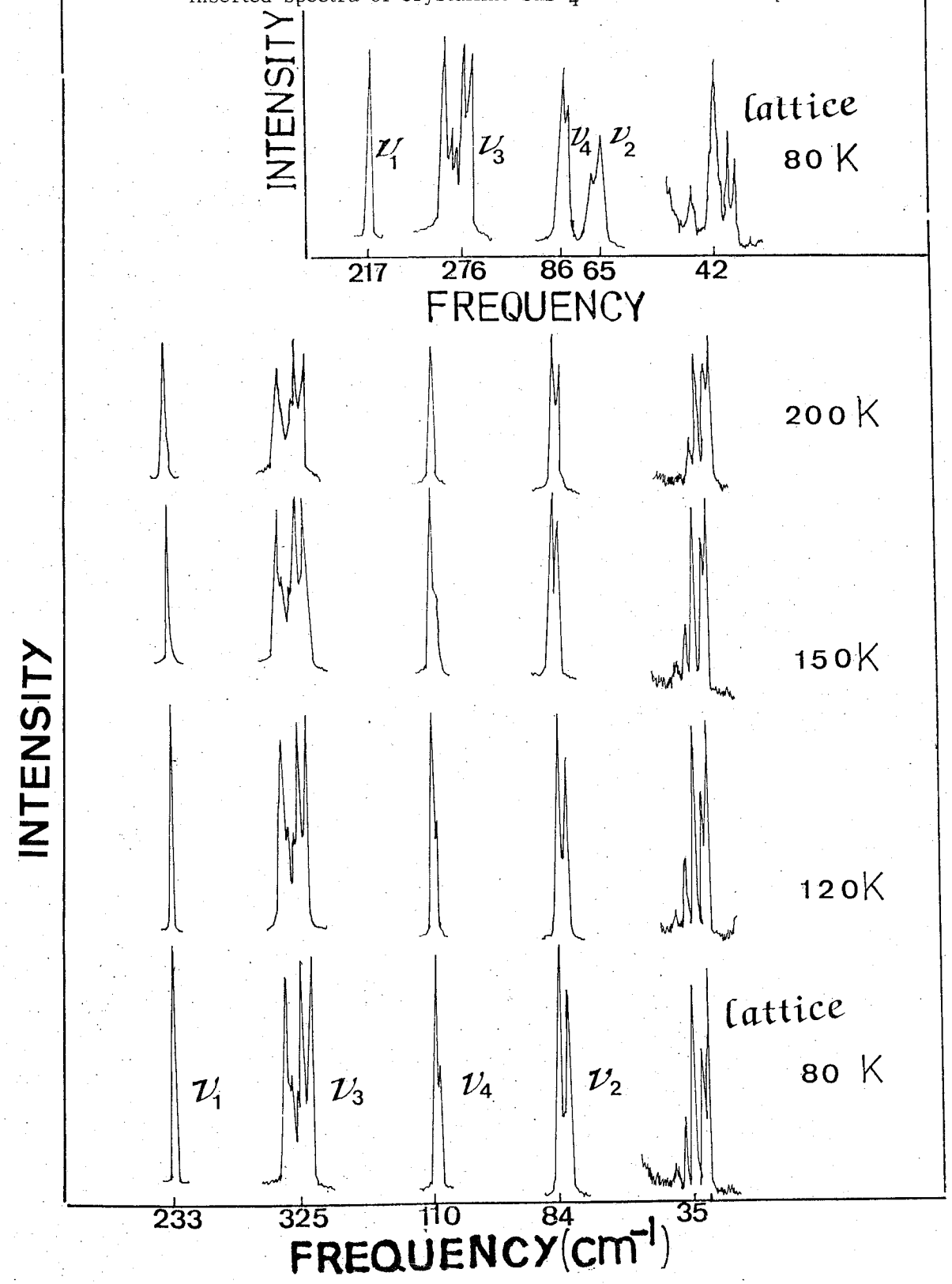

A RAMAN SPECTRAL STUDY OF THE PHASE TRANSITIONS IN CRYSTALLINE POTASSIUM ACETATE

W. S. Tse and P. Y. Chiang
Institute of Physics, Academia Sinica
Taipei, Taiwan (11529), R.O.C.
S. J. Lin
Shu-Teh Junior College of Technology
Taichung. Taiwan, R.O.C.

ABSTRACT

The lattice mode region of the Raman spectrum of polycrystalline Potassium Acetate has been measured over a wide temperature range 80K - 500K. The temperature dependent results are consistent with the X-ray work that two phase transitions occur at 349K and 428K respectively. A new phase transition Tc3 around 500K may exist as detected by thermal expansion study associated with the softening of a low frequency lattice mode.

1. INTRODUCTION

Thermal expansion study of potassium acetate using a dilatometric method has shown at least three interesting phase transitions between room temperatures and their melting point. A crystallographic study[2] indicated that the structure above 428K is orthorhombic (phase I), that from 428K to 349K is monoclinic (phase II) and that from 348K to room temperature is mono-

clinic with an eight-fold increase in cell volume (phase III). The orthorhombic phase I is stable up to the melting point. However, thermal expansion study[1] also reported that there should be a new phase transition near 500K.

The low frequency Raman spectra of potassium acetate at several temperatures above room temperature up to 420K have been recorded[3] but they only discussed qualitatively in terms of their DSC results. Besides, they paid little attention to the detail in the vicinity of the phase transitions. In this work we report a comprehensive study of the high resolution Raman spectra over the temperature tange 80K - 500K and using narrower temperature intervals than in previous studies, especially in the vicinity of the phase transition. A detailed study of the temperature dependent lattice band as the transitions occured confirmed with the X-ray work[2] that two phase transitions occur at 349K and 428K respectively. Besides, a new phase transition Tc_3 around 500K may exist as detected by thermal expansion study[1] associated with the softening of the low frequency lattice mode.

2. EXPERIMENTAL

Raman spectra were obtained with a J. Y. Ramanor U1000 spectrometer and a Coherent Innova 90-4 Argon ion laser, operating at 0.2 - 0.3 W on the 5145A or 4880A lines. Frequencies reported here were estimated to be accurate to $\pm$ cm^{-1} for sharp features. Periodic calibration checkes were made using the known wavelengths of laser line or other non-lasing plasma lines.

Dried polycrystalline potassium acetate with 99% purity was obtained from Ajax. To obtain anhydrous sample, it was dried at $\sim$ 420K for several hours under dry nitrogen atmosphere. The polycrystalline samples were then sealed and placed in an Oxford Instruments DN1714 variable temperature liquid nitrogen cryostat with an economical means of cooling samples in the temperature range 77K and 500K. The temperature sensor is a standard 100

ohm platinum resistor mounted on the inside heat exchanger. The heat exchanger is also fitted with a heater for variable temperature operation in conjunction with a DTC-2 temperature controller and the temperature resolution is nearly 0.1K.

3. RESULTS AND DISCUSSION

Typical lattice spectra of crystalline potassium acetate at various temperatures over the temperature range 80 - 500 K are shown in Figure 1. The lattice spectrum continuously changes its features from high temperature phase to low temperature phase through the phase transitions. As shown in Figure 1, there are three peaks (centred at 100 cm^{-1}, 128 cm^{-1} and 171 cm^{-1}) at 80 K. These are the lattice translational or librational modes of CH_3 COOK molecules on the lattice sites and an exact identification of these peaks can be obtained until more exact crystal structure data are available.

As the temperature is raised gradually to 500K, the two most intense peaks at 128 cm^{-1} and 100 cm^{-1} do not exhibit big changes except normal frequency shift and peak broadening due to temperature effect. However, the peak at 171 cm^{-1} seems slowly " soften " and nearly disappear at 280K. On the otherhand, a low frequency peak near 51 cm^{-1} appears in the spectra around 250K and become more intense and sharpen fairly quickly until Tc1 (349K) is reached. The growth of 51 cm^{-1} and disappearance of 250 cm^{-1} may indicate that monoclinic phase III may exist from 348K down to 250K where another phase may occure below 250K.

According to Hazlewood et al[1], various types of roational or orientational disorder of the non-spherical acetate anions could arise with respect to their neighbours in solid-solid transformations. These disordering may probably due to rotation of the acetate anion or the internal rotation of the CH_3 group about the C - C bond axis. Besides, a head-to-tail rotation of the acetate group might possibly be occured. It seems that the growth of the 51cm^{-1} low frequency mode is associated with the increasing disorder and relaxation

of the strict Raman selection rules. In phases II and III, potassium ocetate forms the monoclinic structure with z = 16 so that the crystal packings are so compact such that barriers to internal rotation of CH_3 group may be very high through intense local repulsion effects. Besides, a head-to-tail rotation of the acetate group is difficult since the acetate ion carry a strong dipole. Hence, the appearance of this low frequency Raman peak may be due to the orientational disorder of the acetate ion about the C-C axis and increases its degree of disordering as the temperature gradually raised up.

The temperature dependence of the frequency, intensity and halfwidths of this lattice modes are shown in Figures 2 to 4. Changes in intensity and linewidth versus temperatures show a discontinuous increase in linewidth and intensity during the phase transitions III $\rightarrow$ II $\longrightarrow$ I due to the increase in the reorientational freedom of the acetate ion and thus may proof the crystal has two phase transitions near 428K and 349K as reported by X-ray method[2]. At temperatures above T_{C2} (428K), the mode frequency obviously keep " softening " fairly quickly and decrease to 24 cm^{-1} at 480K and this may be associated with a new phase transition T_{C3} near 500K is approached as reported by thermal expansion study[1]

The temperature dependent spectra of the ν (CH), ν (COO) and ν(CC) stretching modes are also recorded and that curves of the peak height and halfwidths of these internal modes versus temperatures are also obtained. Some of these results do not give an obvious anomalous dependency of intensity or linewidth during the vicinity of the transition temperatures at T_{C1} and T_{C2} and so details will not be reported here. The significant point is that those results do exhibit fluctuations in intensity and linewidth near T_{C1} and T_{C2} region.

REFERENCES

(1) F. J. Hazlewood, E. Rhodes and A. R. Ubbelohde, Trans. Faraday Soc. 62, 3101 (1966).

(2) J. Hatibarua and G. S. Parry, Acta. Cryst. B28, 3099 (1972).

(3) T. E. Jenkins and P. O'Brien, J. Phys. Chem. Solids. 44, 565 (1983).

HIGURE CAPTIONS

Figure 1. The temperature dependence of the low frequency Raman spectra of crystalline potassium acetate. The asterisk (*) indicates a plasma line. Spectral resolution is 2 cm^{-1}.

Figure 2. The temperature dependence of the frequency of the lowest lattice Raman mode.

Figure 3. The temperature dependence of the peak intensity of the lowest lattice Raman mode.

Figure 4. The temperature dependence of the half-width of the lowest lattice Raman mode.

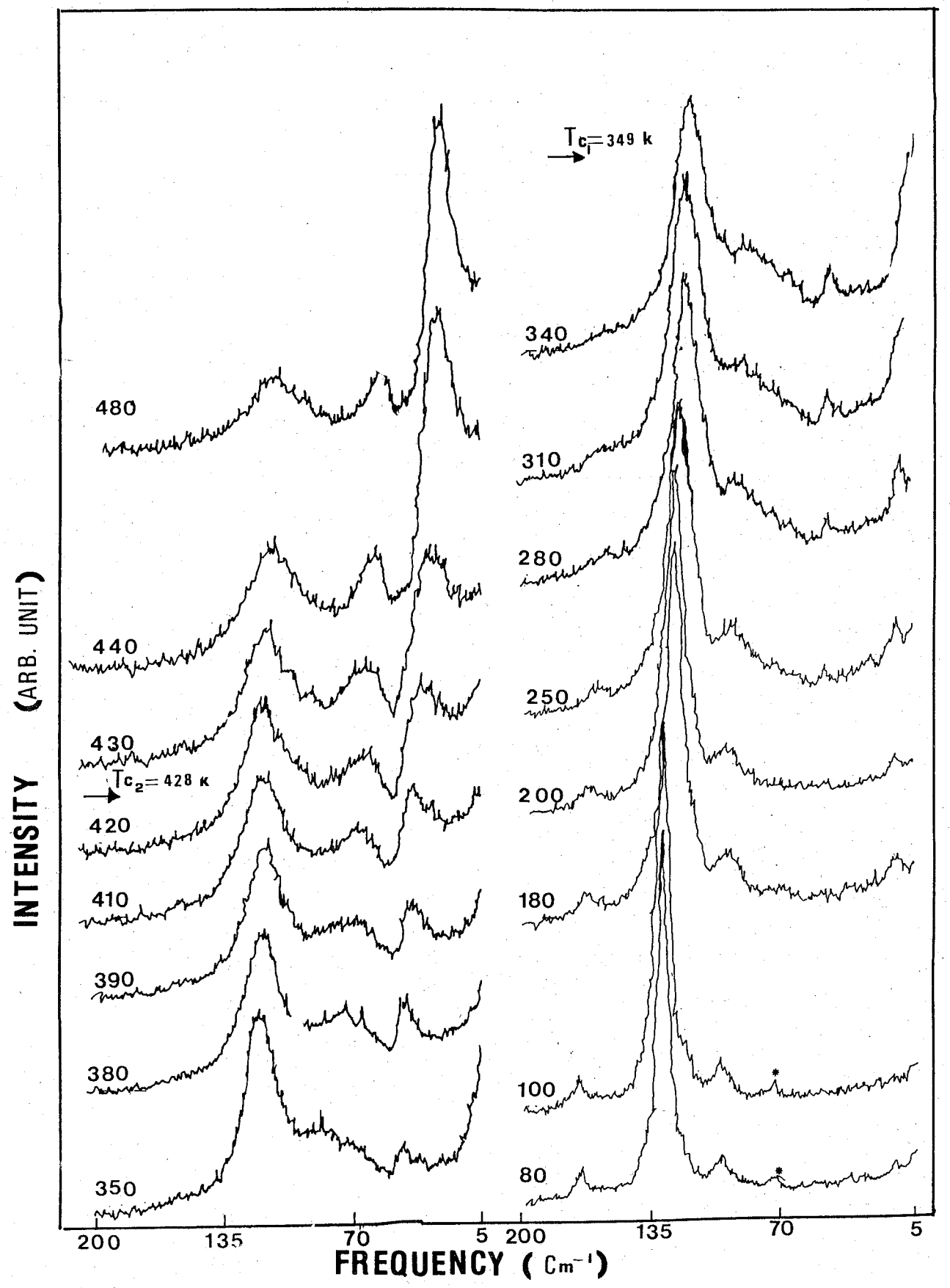
INTENSITY (ARB. UNIT)
T_{c_1}= 349 k
480
440
430
T_{c_2}= 428 K
420
410
390
380
350
340
310
280
250
200
180
100
80
200
135
70
5
FREQUENCY (Cm^{-1})

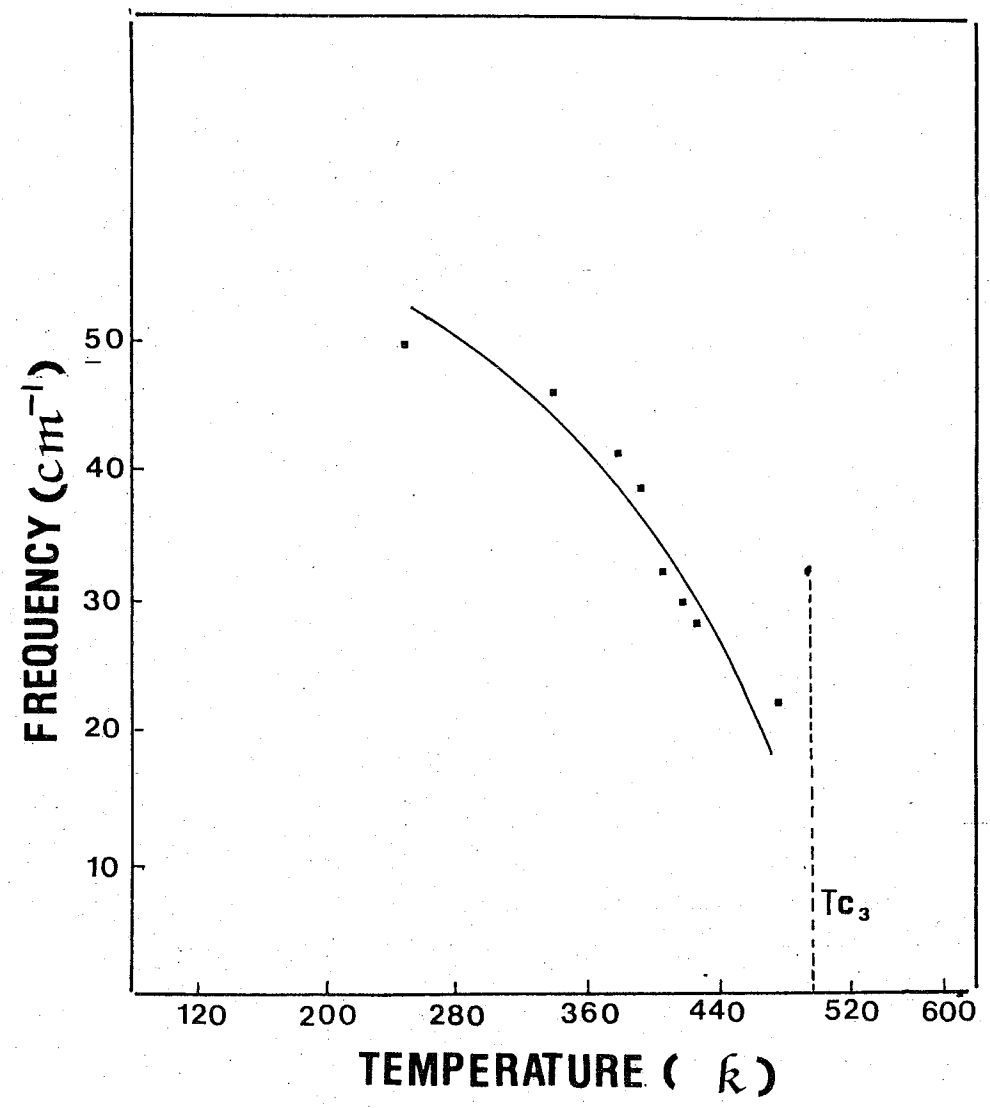
FREQUENCY (cm^{-1})
50
40
30
20
10
T_{c_3}
120
200
280
360
440
520
600
TEMPERATURE (k)

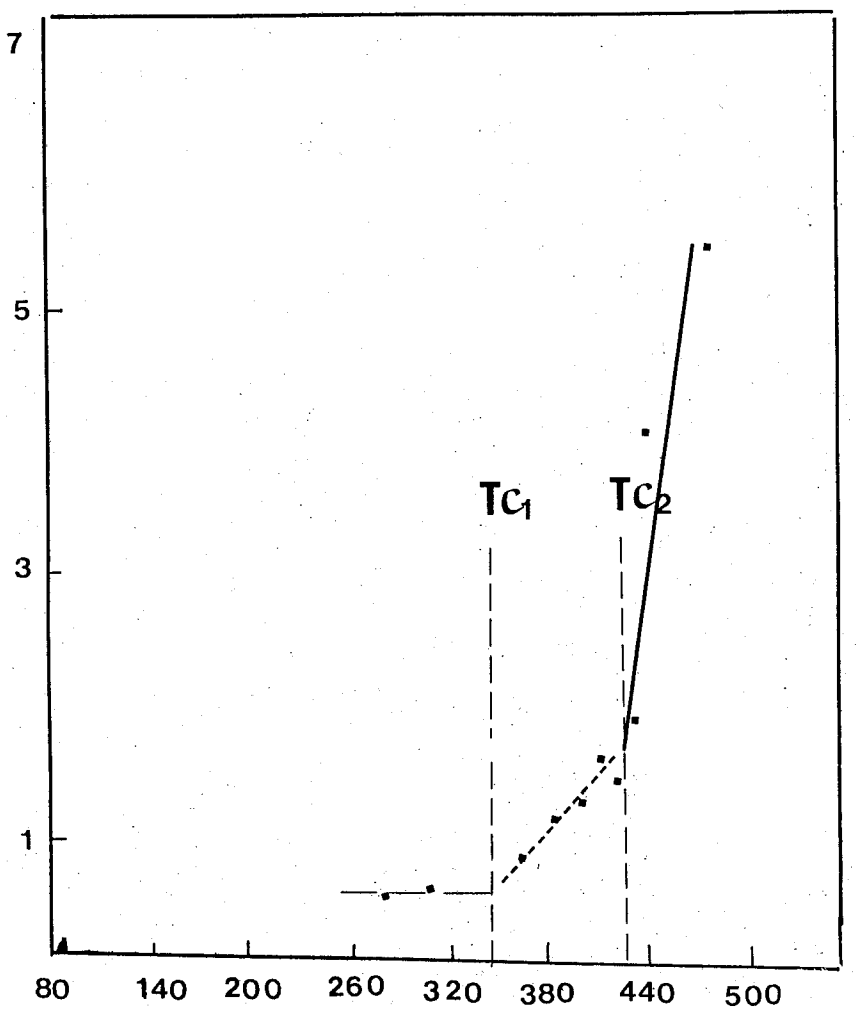
INTENSITY (cm)
7
5
3
1
Tc1
Tc2
80
140
200
260
320
380
440
500
TEMPERATURE (k)

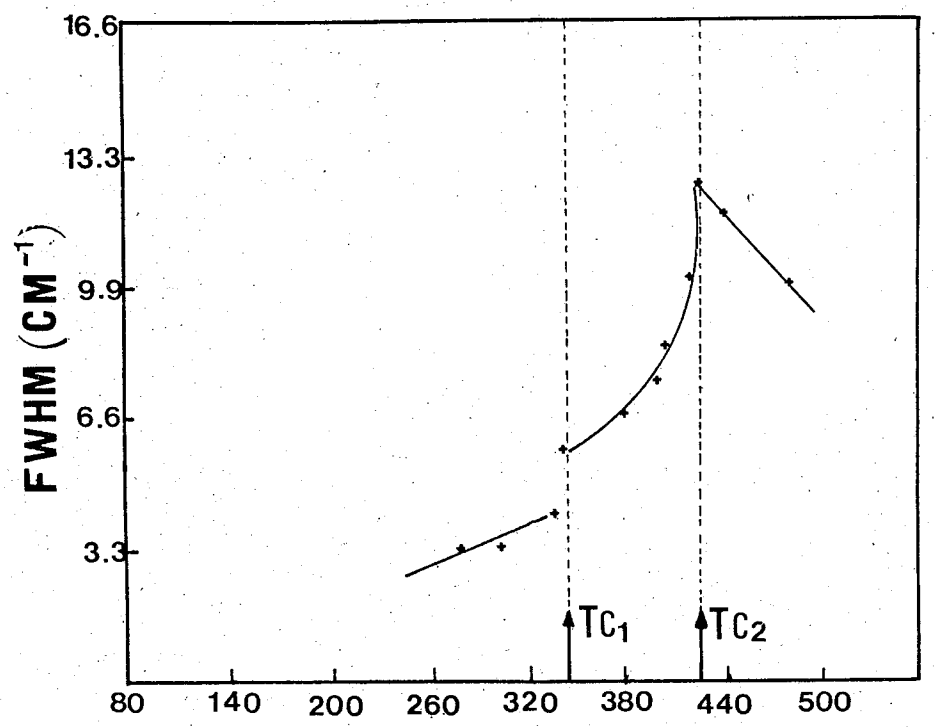
FWHM (CM⁻¹)
16.6
13.3
9.9
6.6
3.3
Tc1
Tc2
80
140
200
260
320
380
440
500
TEMPERATURE (k)

THE RAMAN SPECTRA AND CRYSTAL STRUCTURE OF CRYSTALLINE $SnBr_4$

W. S. Tse and N. T. Liang

Institute of Physics, Academia Sinica

Taipei, Taiwan, (115), R.O.C.

ABSTRACT

The Raman spectra of crystalline tin tetrabromide at various temperatures between 80K and the melting has been studied. There are no evidence of a second phase transition at 223K. In the stretching region, site and factor-group effects determine the modes splittings and that isotopic splittings are not observed compared with those tetrachloride compounds.

I. Introduction

The crystal structure data of $SnBr_4$ at room temperature (293K) has been identified by X-ray method (1) as $P2_1/C$ with four molecules per unit cell, and is the same as is found for other tetrahalides as $TiCl_4$, $TiBr_4$, CCl_4(II) and probably also for $SnCl_4$ (1, 2, 3,). The Raman spectra of solid $SnBr_4$ have been recorded previously by Brutan and Pleshkov (4) between 77K and 318K and the variations in the structure of the stretching modes indicated the presence of a phase transition near 223K, but they did not observe the isotopic splitting of the ν_1 mode. Creighton and Sinclar (5) have reported spectra of $SnBr_4$ at 77K and found that the structure in the ν_1 mode was due mainly to isotope effect. Besides, they found no evidence

from DSC measurement of further phase change down to 190K. Both previous Raman studies were concentrated on the stretching modes only.

The present work reported a comprehensive study of the high-resolution Raman spectra of crystalline SnBr, including the lattice and stretching molecular vibrations, over the temperature range 80K to the melting point, and try to gain further insight into those above mentioned problems.

II. Experimental

The sample $SnBr_4$ obtained from Merck was sealed in a quartz sample cell and placed in an Oxford Instruments DN1714 variable temperature liquid nitrogen cryostat. The structure of the cryostat and the Raman apparatus was described in previous paper (8).

III. Results and Discussion

Figure 1 shows the temperature dependence of the Raman spectra of the crystals in the lattice and stretching region at different temperatures from 80K to 305K and the peak positions at 80K are also listed in Table 1.

The crystal structure of $SnBr_4$ at 293K was reported to be monoclinic with space group $P2_1/C$ and four molecules per unit cell (1) and the site group is C_1 (7). From Fig. 1 it is obviously shown that there are not any abrupt changes in band shapes, intensity or bandwidth of the Raman spectra, both lattice and stretching modes, between 80K and the melting point. It is thus probable to assume that no further phase change occurs in this compound down to 80K as observed by previous Raman work (4). In this work, it is found that a disordered or imperfect crystalline state is produced if the sample is not pure, e.g. react with water vapor. The Raman spectrum thus observed indeed exhibit the variations in the structure of those stretching modes as reported by Brutan and Pleskhov.

In the free molecule (T_d symmetry), all four fundamentals $\nu_1(A_1)$, $\nu_1(E)$, $\nu_3(T_2)$ and $\nu_4(T_2)$ are active in Raman scattering. In

the crystalline monoclinic phase, a splitting of the degenerate fundamental is expected to occur. It is seen that the group theoretical analysis (6) based on known crystal structure predicts two Raman components of the ν_1 (A_1) mode; four Raman components of $\nu_2(E)$; six Raman components of $\nu_3(T_2)$ and also six Raman components of $\nu_4(T_2)$ and that this partly in accord with observed spectra as shown in Figure 1.

The ν_1 fundamental is a totally symmetric stretching mode and contains only one component even at 80K. This is different from the Raman result by Creighton and Sinclar (5) that isotopic components due to ^{79}Br and ^{81}Br of ν_1 symmetric mode are observed as resolved peaks or definits shoulders. In this work and other tetrabromides studies (4, 8) all exhibit one sharp peak of ν_1 mode from 80K to the melting point. This result suggests that the observed splittings of the degenerate fundamentals are not due to isotopic molecules as compared to group IV tetrachlorides (6). Hence, the observed features in ν_2, ν_3 and ν_4 modes are mostly due to site and factor-group effect.

According to factor-group analysis the degeneracy of ν_2 is removed at the site to give a doublet and further splittings to give four bands would be due to factor-group splitting. The observed spectra show that two components are indeed observed in this region which suggests that the two components arise mainly from site effect. The ν_4 mode gives rise to two components, instead of six, which are likely due to site splitting. However, five sharp bands of ν_3 are observed and are likely five of the six bands expected from group anlaysis. The large frequency spread cover 13 cm^{-1} range indicates the factor-group splitting. This observation is in agreement with the predictions of the dipole coupling model, on the basis of which the most intense infrared active fundamental should suffer the greatest factor-group splitting (9).

The group theoretical analysis also predicts six Raman active translational modes and six Raman active librational modes. Various attemps were mode to locate the missing peaks, e.g. recording the spectra as near as possible to the laser line; slow scan rate and a higher resolution to check for further

splitting, shoulder or asymmetry of the Raman band. However, no additional feature was observed. It is difficult to assign properly which are translational or librational modes. Since $SnBr_4$ molecules are near spherical in shape, the librational modes will involve small changes in the polarizability derivatives, and hence the Raman intensities will be low. The observed low frequency lattice peaks are so sharp and intense so that these lattice peaks are therefore postulated to involve primarily translational motions.

The lattice spectra shown in Fig. 1 do not change the features from 80K up to the melting point. The broad Rayleigh wind is due to the random orientational molecular motions in the liquid phase. When monoclinic crystalline phase formed below melting point, orientational disorder of the molecules vanishes and the translational symmetry is imposed so that the Rayleigh wing is replaced by several distinct bands corresponding to lattice vibrational modes.

It is clear from the above discussion that there are no evidence of a further phase transition at 223K, as reported by Brutan and Pleskhov (4), from any of the temperature dependent Raman spectra including both lattice and stretching regions. Besides, this work also excludes the isotope effect as one of the cause of splitting, especially the ν_1 mode, as reported by Creighton and Sinclar (5). The factor-group anlaysis based on a monoclinic system with four molecules per unit cell seems to apply resonably well to the Raman spectra of crystalline $SnBr_4$.

IV. ACKNOWLEDGEMENT

This research was supported by a grant from the National Science Council of the Republic of China.

Reference

(1) P. Brand and H. Sackmann, Acta Cryst. 16, 446 (1963).
(2) P. Brand and H. Sackmann, Z. Anorg. Chem. 321, 262 (1963);

P. Brand and J. Schmidt, Z. Anorg. Chem. 348, 257 (1966).
(3) G. S. Piermarini and A. B. Braun, J. Chem. Phys. 58, 1974 (1973).
(4) E. G. Brutan and A. V. Pleshkov, Izv. Vyssh, Vcheb. Zaved., 14, 29 (1971).
(5) J. A. Creighton and T. J. Sinclar, Spectrochimica Acta. 35A, 137 (1979)
(6) W. S. Tse, C. C. Chen, H. Chang and N T. Liang, J. Raman Spectro. 15, 51 (1984).
(7) " International Tabies for X-ray Crystallography ", Vol. 1, Kynoch Press, Birmingham (1959).
(8) W. S. Tse, N. T. Liang J. W. Lin and P. Y. Chiang, Chem. Phys. Lett., 119, 67 (1985).
(9) D. A. Dows in " Physics and Chemistry of the Organic Solid State ", Interscience, New York, 657 (1963).

Figure Caption

Figure 1. The temperature dependent Raman spectra of crystalline $SnBr_4$ in the lattice and stretching region.

Table 1. Raman frequencies (in cm^{-1}) of crystalline Tin Tetrabromide at 80K.

Mode	Liquid (300K)	Solid	Splitting	Assignment
$\nu_1(A_1)$	216.5	218	-	No isotope effect
$\nu_2(E)$	64	65	4	site splitting
		69		
$\nu_3(T_2)$	275	272	3.5	
		275.5		factor group
		280	4.5	splitting
		282	2	
		284.5	2.5	
$\nu_4(T_2)$	84	84	2	site splitting
		86		
Lattice	-	24		
		28.5		Translational
		35		
		37		
		47.5		

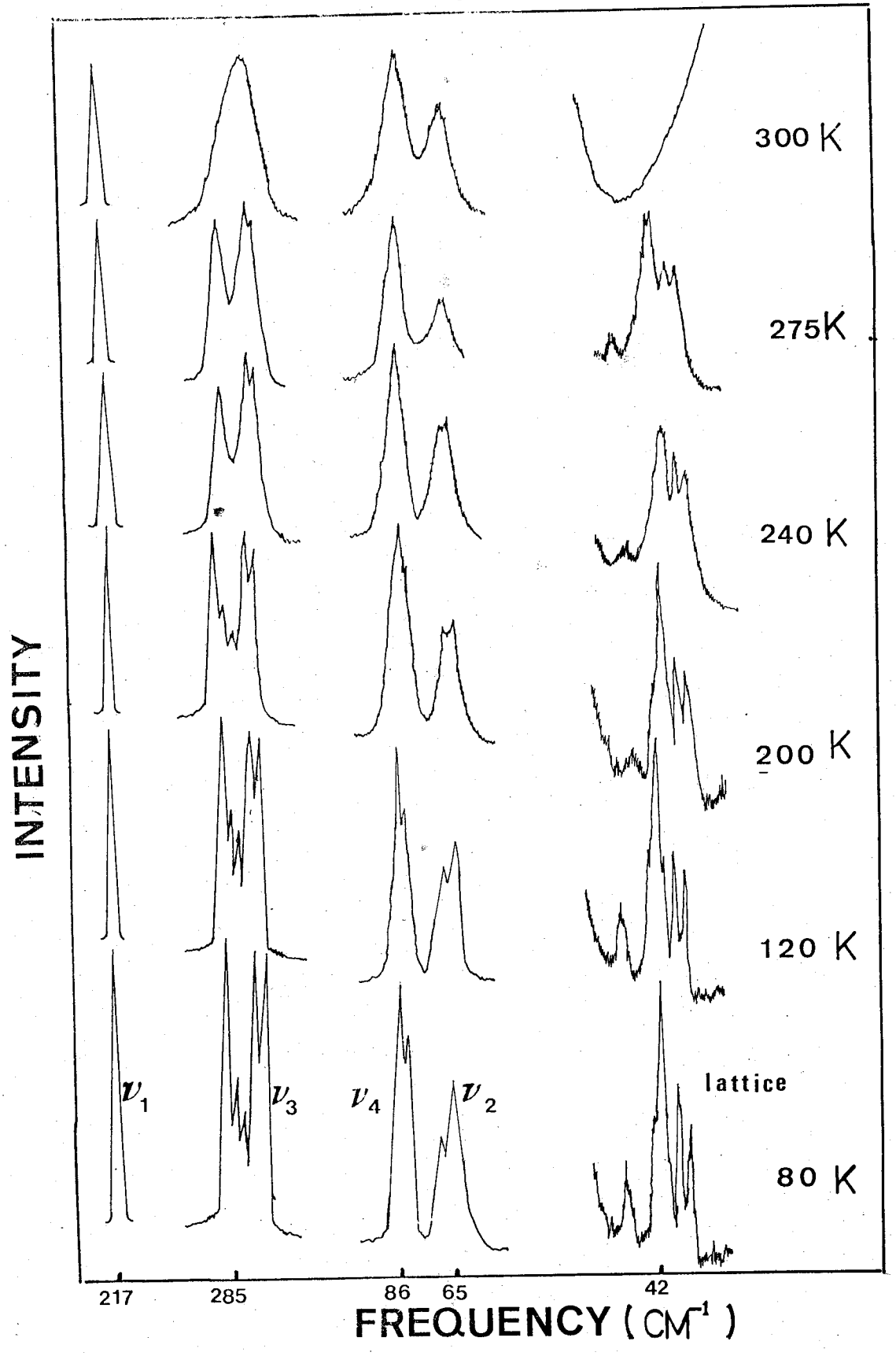

Fig 1

INTRODUCTION OF SODIUM INTO SILICON

L. T. Ho, C. M. Cheng, J. M. Liang
（何侗民） （鄭俊銘） （梁振明）

Institute of Physics, Academia Sinica
Taipei, Taiwan, Republic of China

It is well known that the crystal characteristics can be changed quite dramatically by adding chemical impurities into a semiconductor crystal like silicon. The behavior of the substitutional group III acceptors boron, aluminum, gallium, indium and group V donors phosphorus, arsenic, antimony, bismuth in silicon represents one of the most extensively studied and best understood aspects of semiconductor physics.(1) Chemical impurities belonging to other groups have also been studied. Some of the better known cases are group II elements beryllium(2), magnesium(3), zinc(4), cadmium(5) and group VI elements sulphur(6), selenium(7). Except magnesium, all impurities are substitutional and, therefore, beryllium, zinc and cadmium behave like double aceeptors while sulphur and selenium double donors. When diffused into silicon, magnesium behaves like a double donor rather than a double acceptor, which indicates that it is interstitial rather than substitutional.

Among group I elements, lithium as an impurity has attracted considerable attention as a consequence of its remarkable diffusion properties(8). The diffusion coefficient of lithium in silicon at 800°K is about eight orders of magnitude larger than that of phosphorus in the same host(9). When diffused into silicon, lithium is interstitial and behaves like a shallow donor(10). Another extraordinary property of lithium is its ability to complex with other

chemical impurities which may be present in the crystal[11]. As for other group I elements; copper, silver and gold in silicon have also been studied to some extent. There is no doubt that they are much deeper impurities compared with lithium, Both substitutional and interstitial centers have been reported for these impurities.[12]

Sodium is another group I element with its postition only next to lithium in the periodic table. Since lithium in silicon shows many important features which lead to quite a few industrial applications such as nuclear radiation detector and double-injection diode, the role of sodium as an impurity in silicon should also be quite interesting. Apparently due to doping difficulty, very few research has been made on this subject in the past. Recently, we have made some effort trying to introduce sodium into silicon. In this report we will discuss the experimental procedure and the results we obtained.

It has been known that lithium can be introduced into silicon using the diffusion technique in the following manner[8]. A silicon bar, with a small cube of lithium placed on its broad face, is heated at about 800°C for 30 seconds in a helium atmosphere. During this period the lithium becomes alloyed with silicon and from this alloy lithium diffuses into silicon to form a hemispherical n-type region. If the whole sample surface is covered with lithium and is heated at lower temperature but for longer period, then the lithium can be distributed more homogeneously[10]. Due to the resemblance between sodium and lithium in many features, similar diffusion technique is attempted for sodium. Ultra pure sodium, obtained from Electronic Space Products, Inc., is used for this purpose. But unlike lithium, sodium does not seem to be able to become alloyed with silicon in this way and there is no way to start the diffusion process at all. Similarly, the sandwich method, which has been used for introducing magnesium into silicon successfully[3], also does not work for sodium.

Since the unsuccessful attempt of the conventional method as mentioned above, direct heating of the mixture of silicon and sodium has been tried next. Because of the very low melting point of sodium, which is only 97° C,

sodium is actually in its liquid phase and silicon sample is immersed in the sodium liquid throughout the heat treatment. After several attempts under various temperatures and periods, it is found that almost no any observable change of the sample characteristics can be detected. After removing a very thin surface layer, both the resistivity and the conduction type remain to be the same. Apparently, sodium cannot overcome the surface barrier of the silicon sample in this way. This result also confirms the earlier observation of McCaldin et al.[13] in an experiment trying to determine the solubility of sodium in silicon.

The next doping attempt is to use the electrolysis method. In this method the silicon sample itself is used as the cathod and a piece of either tantalum or molybdenum sheet as the anode. Both the sample and the anode are embedded in the sodium iodide powder obtained from Sigma Chemical Company. Once the furnace temperature is raised above 664° C, the melting point of sodium iodide, the electrilysis process can start in the molten sodium iodide if a voltage of a few volts supplied by a dc battery is applied between the cathode and the anode. During the electrolysis, the sodium diffuses into the silicon from a layer deposited on the silicon sample surface.

By following the above procedure for several hours, all silicon samples examined are found to have converted from p-type to n-type conductivity. Type conversion can be easily checked using a dc thermal probe. The resistivity of the sample, initially more than 1000 ohm-cm, decreases to only a few ohm-cm and is a bout 1000 times less. Specimen subjected to the same heat treatment remains p-type and its original high resistivity if the electrolysis process does not occur by disconnecting the dc battery between the sample and the anode. This check is made to show that the electrolysis does happen and that the change of the electrical properties of the silicon sample is indeed due to the addition of sodium impurities.

From the resistivity of the sample, the room-temperature carrier concentration is estimated to be of the order of 10^{15} cm^{-3}. In order to check the uniformity of the sodium impurity distribution in silicon, the surface resistance of the sample is remeasured continuously after removing each thin

layer from the sample surface. It has been found that the whole sample becomes n-type and that the resistance is the same within experimental error throughout the entire crystal. Clearly the distribution of the sodium impurity is quite uniform in silicon. This indicates that sodium, like lithium, is a fast diffuser in silicon.

The conversion of the sample conduction from p-type to n-type by adding sodium strongly indicates that sodium is a donor in silicon. This suggests that sodium is interstitial rather than substitutional in silicon. Compared with other group I impurities, the behavior of sodium should be similar to that of lithium donor but different from copper, silver or gold acceptors. With its 3s valence electron presumably as the donor electron, the sodium donor can be regarded as a solid-state analog of the hydrogen atom.

In conclusion, we have shown that sodium can be introduced into silcion resulting in interstitial donors. Though the electrical behavior of sodium is similar to that of lithium, its ground state structure, the excitation spectrum, as well as whether it can have the same ability as lithium to complex with other chemical impurities, all remain to be unknown and will be investigated further.

Acknowledgement

We would like to thank the National Science Council of the Republic of China for partial support of this work.

References

(1) W. Kohn, Solid State Physics, Vol. 5, edited by F. Seitz and D. Turnbull (Academic, New York, 1957), p. 257.

(2) R. K. Crouch, J. B. Robertson and T. E. Gilmer, Phys. Rev. B5, 3111 (1972).

(3) L. T. Ho and A. K. Ramdas, Phys. Rev. B5, 462 (1972).

(4) R. O. Carlson, Phys. Rev. 108, 1390 (1957).

(5) M. A. Gulamova, I. Z. Karimova and P. I. Knigin, Sov. Phys. - Semicond. 5, 687 (1971).

(6) W. E. Krag and H. J. Zeiger, Phys. Rev. Lett. 8, 485 (1962).

(7) J. C. Swartz, D. H. Lemmon and R. N. Thomas, Solid State Commun. 36, 331 (1980).

(8) H. Reiss and C. S. Fuller, Semiconductors, edited by N. B. Hannay (Reinhold, New York, 1960), p. 222.

(9) H. F. Wolf, Silicon Semiconductor Data (Pergamon, 1969).

(10) R. L. Aggarwal, P. Fisher, V. Mourzine and A. K. Ramdas, Phys. Rev. 138, A882 (1965).

(11) C. S. Fuller, Semiconductors, edited by N. B. Hannay (Reinhold, New York, 1960), p. 192.

(12) A. G. Milnes, Deep Impurities in Semiconductors (Wiley-Interscience, 1973), p. 17.

(13) J. O. McCaldin, M. J. Little and A. E. Widmer, J. Phys. Chem. Solids 26, 1119 (1965).

NEGATIVE FEEDBACK OF GnRH ON DA MAY CAUSE THE LH PULSATILE RELEASE

W. K. Wang, T. L. Hsu, Y. Chiang

Biophysics Lab. Institute of Physics, Academia Sinica.

ABSTRACT

GnRH was suggested to exert a negative feedback through opiate receptor to suppress dopamine synthesis[16] which might regulate GnRH release (9, 13).

The model, DA $\overset{+}{\underset{-}{\rightleftharpoons}}$ GnRH $\xrightarrow{+}$ LH, was studied by some mathematical derivations. It was found that the concentration of LH should oscillate as a sine wave. This might be the source of the LH pulsatile release[7,8.20].

Due to receptor blocking capabilities, the opiate antagonist naloxone[15] and the dopamine antagonist haloperidol[12.] were chosen to test this model. As expected both were effective in slowing down the LH pulsatile release (lower frequency), suggesting that this feedback model might be correct. Using this model, the age effect of decreasing LH pulsatile release on both frequency and amplitude[4, 19] could also be explained with the evidences that both the pituitary responses to GnRH and the hypothalamic dopaminergic neurons were changed during the aging process[6].

Introduction

The hormonal pulsatile release phenomenon has been found for many years[7, 8, 20] Without the influence from the ovary, the LH concentration in the blood of the female animal would oscillate with a regular frequency and amplitude[1]. The LH concentration of the aged animal would oscillate with a much slower frequency and smaller amplitude[13], No satisfactory explanation of the origin of these phenomena has been given,

Since GnRH may inhibit the dopamine synthesis through the opiatere receptors[16], we present here a negative feedback model between DA and GnRH as DA $\underset{-}{\overset{+}{\rightleftharpoons}}$ GnRH $\xrightarrow{+}$ LH. Mathematical derivations are showing that the concentration of both the GnRH and LH shall oscilalte as a sine wave. Both frequency and amplitude of these will change if the feedback constants between GnRH and dopamine are changed.

Naloxone and HD were tested to check this model. Naloxone is the opiate antagonist[15], which would block the inhibition effect of GnRH on DA synthesis[16]. Haloperidol is the dopamine post-synaptic antagonist[12] however it would not influence the DA auto-inhibition effect on DA presynaptic receptors[17] The effects of these drugs were consistent with the theory. All the problems above could be explained by this model too.

Theory

Assume the negative feedhack model between DA and GnRH, DA $\underset{-}{\overset{+}{\rightleftharpoons}}$ GnRH $\xrightarrow{+}$ LH is correct. The concentration relation can be written as shown :

$$\frac{dx}{dt} = K_1 Y \qquad (1)$$

$$\frac{dy}{dt} = -K_2 X \qquad (2)$$

$$\frac{dz}{dt} = \alpha X - KZ \qquad (3)$$

X : concentration of GnRH $x-C_0$

Y : concentration of dopamine $y - C_1$

Z : concentration of LH $z - C_2$

KZ : LH decay rate in the blood

C_0 : average concentration of GnRH

C_1 : average concentration of dopamine

C_2 : average concentration of LH

From (1), (2). We have $X = A \sin(\sqrt{K_1 K_2}\, t + \phi)$ (4)

$$Z = Ce^{-Kt} + \frac{A\alpha}{\sqrt{K^2 + K_1 K_2}} \sin(\sqrt{K_1 K_2}\, t + \phi + \phi') \qquad (5)$$

$\phi' = \tan^{-1}(-\sqrt{K_1 K_2}/K)$. Since the term Ce^{-Kt} will decay quickly, which suggests that the concentration of LH shall oscillate as a sine wave with the amplitude $A\alpha / \sqrt{K^2 + K_1 K_2}$, this may well be the source of the LH pulsatile release.

Using the model, drug effect can be analysed as following : Naloxone will block the opiate receptor, therefore a larger dose of GnRH will be needed to give similar effect on dopamine. This is equivalent to reduction of K_2 so is the $\sqrt{K_1 K_2}$, which leads the LH concentration to oscillate much slower and with somewhat larger amplitude. Similarly the haloperidol will reduce K_1 The K_1 and K_2 are equivalent in the equation (5). On the contrary if either K_1 or K_2 is increased, then the oscillation shall be much faster and with smaller amplitude.

If none of the K_1 or K_2 is changed, when we added in certain amount GnRH, i.e. increase the initial level of X then we shall see a sharp increase of LH level at that moment, nonetheless this effect will be quickly damped out.

Material and Methods

The bleeding procedure has been described by S. V. Drouva and R. V. Gallo[5]. Briefly, a polyethylene cannula was inserted through the right external jugular vein to approach the right atrium of a young femal ovariectomized Sprauge-Dawley rat. By means of an infusion-withdrawal device that pemitted continuous acess to the venous circulation without the animal

being restrained, two 5 $\mu\ell$ blood samples were taken by way of the catheter every 5 minutes. After 3 hours of control samples, we injected 0.9 mg/rat naloxone or 0.27 mg/rat haloperidol or 200 $\mu\ell$/ rat physiology saline into the rat through the same catheter. 20 mins later another 3 hours samples were taken as comparison. The blood samples were centrifuged with 100 $\mu\ell$ phosphorous buffer with 1 % nomal rabbit serum at 1000 rpm for 10 minutes, 80 ul supernatant were taken and frozen at -70° C until the RIA process started. Buffer was prepared with 10 mM sodium phosphate, 0.15M NaCl and 0.02% NaN_3 at pH 7.5. For RIA, 25 $\mu\ell$ NIADDK anti-r-LH-S-8 of final dilution 1 : 19000 in buffer with 0.05M EDTA was incubated with the sample for 2 days, then 50 $\mu\ell$ ^{125}I-LH about 0.25 ng LH/3500 cpm was added and incubated for another 2 days. Finally the LH-Antibody complex was precipatated with 50 ul second antibody and 180 $\mu\ell$ 10% PEG. This method could detect LH as low as 0.02 ng. NIADDK-rLH-RP-2 was used as standard which was 61 times more potent as NIADDK-rLH-RP-1.

Result

Both of the naloxone and haloperidol would slow down the LH pulsatile release which were shown on Fig. I. The average frequency on pre-drug control was about 30 mins/pulse by eye measurement. The frequency of saline control set was also about 30 mins/pulse , however with the naloxone or haloperidol added, the frequency changed to about 60 min/pulse. No apparent amplitude difference could be measured.

Discussion

These datas were consistent with the theoretical interpretation. Two pharmacologically different drugs, naloxone and haloperidol showed the similar slow-down effect on LH pulsatil release, while α -methyl-tyrosine did not have any effect[5].

Other evidences also support our theory. Direct morphological studies reported that the dopamine neuron and GnRH secreting cells were adjacent

close to each other[11], indicated that they might react with each other. The studies on old animals also showed that both the frequency and amplitude of the LH pulsatile would decrease. Since the pituitary GnRH receptors were decreased, its responses to GnRH were decreased, and the responses and output of hypothalmic dopaminergic neurons were also decreased in old animal[6], according to our theory K_1, K_2, and the α should all be reduced which inturn would reduce both the amplitude and the frequency of the LH oscillation just as what happened.

This feedback mechanism may also explain the difficulty to determine the dopamine effect on LH release. If an external effect that causes the reduction of DA release, this will lead to the reduction of GnRH level which in turn will increase the DA release and therefore stabilize the DA level. We must follow the mathematical derivations to get a more clear picture as to what may happen for an external interference to change the pulsatile release of LH.

Although our model is still a first approximation without considering many complex effects such as the ovary effect[10], the pituitary cells desensitization on GnRH[2,3] and so on, however from the above results it was evident that it is useful to predict the homonal changes during the drug reactions, suggesting that this feedback model might be correct, it might be the framework of the DA, GnRH , and LH relationships.

Finally we shall emphasize that this model will explain not only the LH pulsatile release, but any homone which has the similar pulsatile release, such as growth hormone[18].

We want to thank Dr. W. B. Bee for his generously providing us ^{125}I-LH. Thanks also to Dr. C. E. Finch (Gerontology center at University of South California, L. A.,) for help in this study and NIADDK for supplying the RIA kits.

References

1. Atkinson, L. E., Bhattacharya, A. N., Monroe, S. E., Dierschke, D.J.,

& Knobil, E. Endocrinology 87, 847 (1970).
2. Baird, C. J., Tharandt, L., & Tamarkin, L. Endocrinology 114, 1041 (1984).
3. Belchetz, P. E., Plant, T. M., Nakai, Y., Keogh, E. J., & Knobil, E. Science 202, 631 (1978).
4. Cooper, R. L., Conn, P. M. & Walker, R. F., Biol. Reprod. 23, 611 (1980).
5. Drouva, S. V., & Gallo, R. V., Endocrinology 99, 651 (1976).
6. Finch, C. E., Felicio, L. S., Mobbs, C. V., & Nelson, J. F. Endocrine Rev. 5, 467 (1984).
7. Gallo, R. V. Biol. Reprod. 24, 100 (1981).
8. Gay, V. L., Sheth, N. A. Endocrinology 90, 158 (1972).
9. Kamberi, I. A., Mical, R. S. & Poter, J. C., Endocrinology 89, 1042 (1971).
10. Knobil, E. Rec. Prog. Horm. Res. 30, 1 (1974).
11. McNeill, T. H. & Sladek, J. K. Jr. Science 200, 72 (1978).
12. Miller, R. J., Horn, A. S. & Iversen, L. L. Molec. Pharm. 10, 759 (1974).
13. Mosko, S. S., Erickson, G. F. & Moore, R. Y., Behav. Neural Biol. 28, 114 (1980).
14. Rotsztejn, W. H., Drouva, S. V., Pattoa, E. & Kordon, C. Nature 274, 281 (1978).
15. Snyder, S. H. & Goodman, R. R., J. of Neurochem. 35, 5 (1980).
16. Wang, W. K., Jeng, L. C., Chiang, Y. & Chien, N. K. Nature 296, 354 (1982).
17. Wang, W. K., Hsu, T. L. & Chiang, Y. Annual Report of the Inst. Phys. Acad. Sinica 14, 81 (1984).
18. Werner, S. Acta Endocrinol. Suppl. 216, 179 (1978).
19. Wise, P. M. Proc. Soc. Exp. Biol. Med. 169, 348 (1982).
20. Yen, S.S.C., Tsai, C. C., Naftolin, F., Vandenberg, G. & Ajabor, L. J. Clin. Endocrinol. Metab. 34, 671 (1972).

Figure Caption

Fig. I. Drug effect on LH pulsatile release. 180 minimutes control samples were taken in all three sets. From Time (↓), Rat was injected in (a) 0.2 ml/rat physiology saline (b). 0.27 mg/rat haloperidol (c) 0.90 mg/rat naloxone. NIADDK-rLH-RP-2 was used as RIA reference preparation. The serum LH values presented were 61 times lower than the LH values which used NIADDK-rLH-RP-1 as RIA reference preparation.

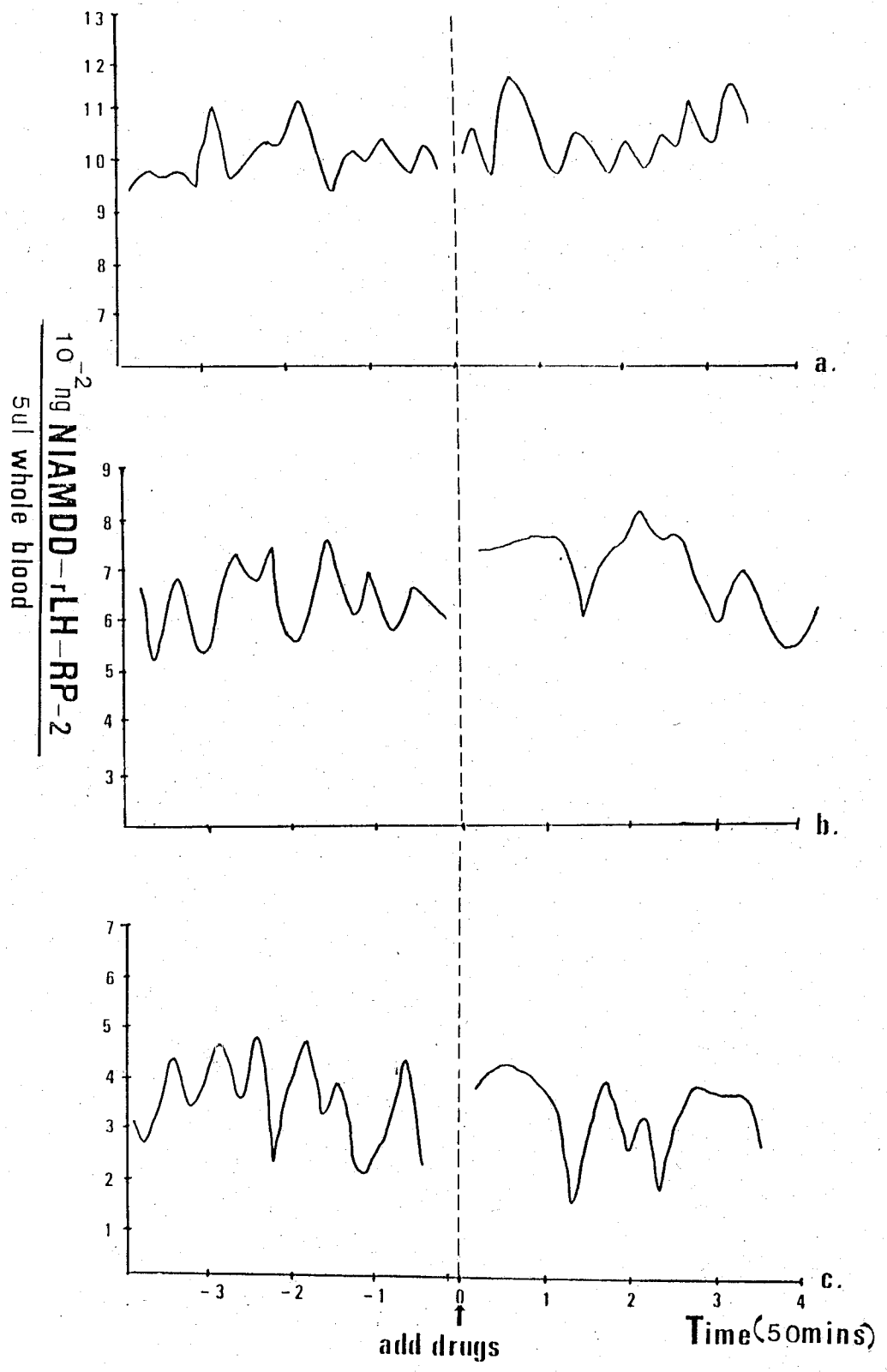

Fig. 1

ANALYSIS OF FLOW DISTRIBUTION AND PULSE SHAPE — A MODEL FOR PULSE FEELING IN CHINESE MEDICINE

Wei Kung Wang and Y. Y. Lo

Biophysics Laboratory

Institute of Physics

Academia Sinica

Taipei, Taiwan

R. O. C.

I. Introduction

For thousands of years, feeling pulse has been used by Chinese physician to diagnose the patient. After the course of illness has been checked, a suitable treatment may be followed. Among this acupuncture which has been well accepted by Western medicine is one of the treatments. In this report we try to give some clue on the physical basis of pulse feeling diagnosis. In the cardiovascular system of a human body, the heart is working like a pump to let blood flow through all parts of body, mainly the liver, the kidney, the spleen and the brain. If there is an organ in trouble, the blood flow through it and the blood pressure across it will be changed. Many papers have discussed the relationships between blood flow and pressure changed in the circulation[1-8], however it seems less research about the relationship between " pulse shape " and blood flow distribution in different parts of the body. The application of the pulse feeling for the Chinese physicians was purely an empirical one, they do not know the physical basis

behind such diagnostic technic and therefore, this branch of art has not been recognized by Western medicine. The purpose of this simple experiment is to investigate the variation of the pulse shape when the distribution of blood flow is changed, and then more experiments will be followed to proof what the Chinese physicians be able to diagnose accurately by feeling the pulse.

Hydrodynamic models of the cardiovascular system[9] have been constructed in the past. (Weber (1850)[10], Marey (1863)[11], Anrep and Harris (1923)[12], Wiggers (1934)[13] and McDowall (1949)[14]). Fig. 1 and Fig. 2 illustrate a model of them.

II. The Systemic Circulation

A unique feature of the systemic circulation is the portion known as the portal circulation, illustrated in Fig. 3[15]. This consists of the hepatic artery which goes directly to the liver and portal vein which feeds blood from the digestive organs, the spleen, the pancreas, and the gallbladder to the liver. The blood also flows through other branching ways such as : kidneys, brain, trunk, legs, arms and head, then finally empties into the right atrium of the heart. This loop, from left ventricle to right atrium, is called the " systemic circulation ".

III. Experimental Model

A similar closed system which was composed of some elastic and distensible tubes,cannulas, clamps and electric pulse pump was built as shown in Fig. 4. The actual working model was shown in Fig. 5. The manometer, used for measuring and recording internal pressure, consists of a U-tube with two vertical limbs about 50 cm in height, which was half-filled with water. Since the water was displaced equally at the beginning, up in one limb and down in the other (we called the upper and lower values in our experiment which mimiced the systole and diastole pressure), it was obvious that any displacement as recorded must be multiplied by two to obtain the actual pressure in terms of a water column. The one limb of mannometer was

opened at the atmosphere and the other limb was connected by a side-branch and a flexible inextensible tube with two 3-way cannulas. The first cannula was only opened at the beginning so that it could give the same water column at the atmosphere but was closed up during operation. The second cannula was tied into the central end of the external tube. The upper and lower values of the jumping water column were then obtained from this position. Distilled water was used as fluid flows through all the tubes and the variable factors could be neglected to simplify the discussion of the main factors of the circulation. The other six clamps, tied respectively on the different diameter tubes, were opened or closed when we needed to get a different flow pattern. For the later explanation, we gave the name for these six clamps such as $1^{\#}$, $2^{\#}$, $3^{\#}$, $4^{\#}$, $5^{\#}$ and $6^{\#}$ respectively (see Fig. 4). The external cycle is about 150 cm. long with 6x8 mm. diameter tube and consists of $1^{\#}$ and $6^{\#}$ clamps. The middle cycle is about 110 cm. long with 5 x 7 mm. diameter tube and consists of $2^{\#}$ and $5^{\#}$ clamps. The internal cycle is about 74 cm. long with 2 x 4 mm. diameter tube and consists of $3^{\#}$ and $4^{\#}$ clamps.

VI Result and Conclusion.

For the various arrangement of $1^{\#}$ to $6^{\#}$ clamps in opened or closed, we obtained the results and shown in Fig. 6, Fig. 7 and Table 1, Table 2. From Table 1, we see that when all the clamps are opened, it means no extra resistance in the circulation, the pressure measured at the $6^{\#}$ tube is about 9.4 cm-H_2O (6.9 mmHg). When some of the clamps are closed, the changes of the upper and lower values of the water column is occured. Because of the hydrostatics of the circulation, the values of the results in Table 2 (the model placed vertical) are less than that in Table 1 (the model placed horizontal). However, we obtained the same conclusion that the pressure changed in the ciuculation was followed with the change of the branched flow. We also see that the branched blood flow may varied when a trouble occurs in an organ, and the pulse feeling is hence different from the normal situation.

* " 6 x 8 mm diameter " means internal diameten is 6 mm and external diameter is 8 mm etc.

Discussion

Although the change of pulse shape cannot be obtained from the experiment with this simple apparatus, still we may conclude that the variation of pulse shape is dependent on the pattern of the branched blood flow. Accurate electric instrument will soon be used to find out the more detailed relationship between the branched blood flow and the pulse shape.

References

1. D. L. Fry, D. M. Griggs, Jr., and J. C. Greenfield, Jr., " In Vivo Studies of Pulsatile Blood Flow : The Relationship of the Pressure Gradient to the Blood Velocity ", Pulsatile Blood Flow, ed. E. O. Attinger, McGraw-Hill, New York, 1964, pp 101-114.
2. V. L. Streeter, W. F. Keitzer and D. F. Bohr, " Pulsatile Pressure and Flow Through Distensible Vessels ", Circulation Research, Vol. 13, 1963, pp 3-20.
3. G. Karreman, " Some Contributions to the Mathematical Biology of Blood Circulation. Reflections of Pressure Waves in the Arterial System ", Bull. Math., Biophys., vol. 14, 1952, pp 327-350.
4. J. R. Womersley, " Method for the Calculation of Velocity, Rate of Flow and Viscous. Drag in Arteries when the Pressure Gradient is Know " , J. Physiol., Vol. 127, 1955, pp 553-563.
5. D. A. McDonald, " Blood Flows in Arteries ", Williams and Wilkins Baltimone, 1960, pp 51-54.
6. A. L. Copley and G. Stainsby, eds., " Flow Properties of Blood and Other Biological Systems ", Pergamon Press, New York, 1960.
7. Joh W. Remington, " Pressure-Flow Relation in the Arterial System ", Medical Engineering, Charles D. Ray, M. D., 1974, pp 232-246.

8. J. E. K. Foreman and W. D. Durie, " Fluid Dynamic Model Studyies of Blood Flow and Artery Dilatation ", Biomedical Fluid Mechanics Symposium, Fluids Eng. Conf., 1916, pp 148-160.
9. Abraham Noordergraaf, " Hemodynamics ", Biological Eng., ed. Herman P. Schwan, 1969, pp 479-509.
10. Weber, E. H. : Uebber die Anwendung der Wellenlehre auf die Lehre vom Kreislaufe des Blutes and ins besondere auf die Pulslehre, Ber. Math. Physik. Cl. Königl, Sächs. Ges. Wiss. (1850); published also as nr. 6, in M. von Frey (ed.), " Ostwalds Klassiker der exakten Wissenschaften ", W. Engelmann, Leipzig, 1889.
11. Marey, E. J. : " Physiologie médicale de la circulation du sang basée sur l'étude graphique des mouvements du coeur et du pouls arteriel " Adrien Delahaye, Paris, 1863.
12. Anrep, G. V., and D. T. Harris : " Practical Physiology ", p. 56, Churchill, London, 1923.
13. Wiggers, C. J. :" Physiology in Health and Disease ", Lea & Febiger, Philadelphia, 1934.
14. McDowall, R. J. S. : " An Artificial Circulation ", J. Physiol., 108 : 2p (1949).
15. Ganong, W. F., Review of Medical Physiology, 5th ed., Lange Med. Publ., Los Altos, California, 1971, p. 415.

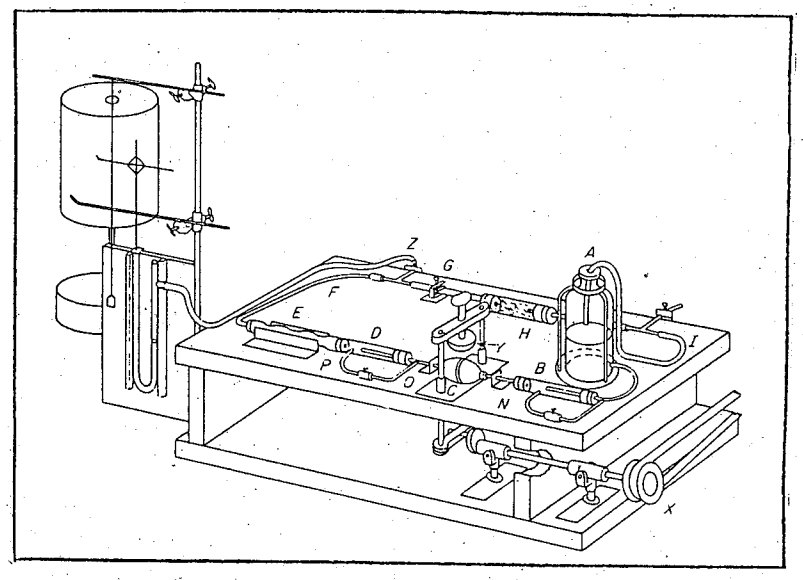

Fig. 1. Hydrodynamic model of part of the circulatory system as used by Wiggers (1934) for student instruction. The loop is closed though right heart and pulmonary tree are omitted. A=auricle, C=ventricle, E=aorta, H=capillaries, I=veins. The motor-driven bulb Y compresses the ventricle C.

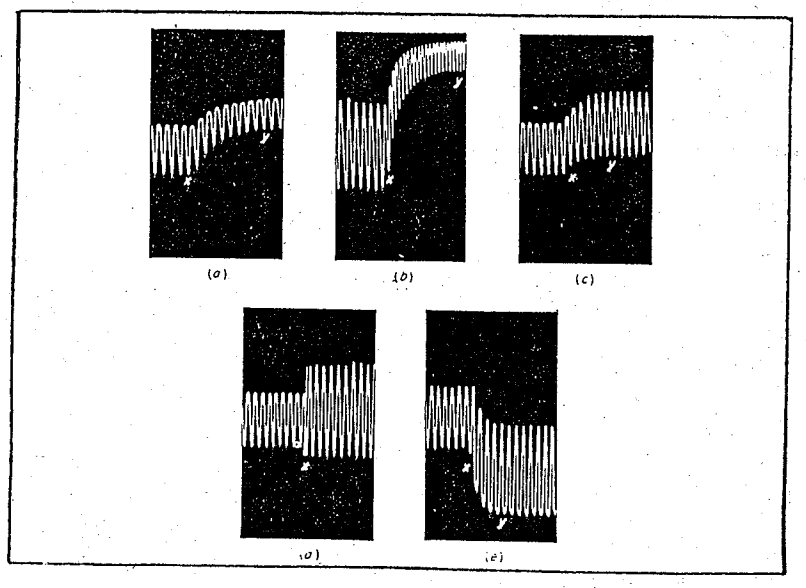

Fig. 2. Records of acterial pressure taken from the hydrodymanic model of Fig. 1 with the effect of changes in parameters. (a) Change in peripheral resistance. (b) Increase in heart rate. (c) Increased stroke volume. (d) Stiffened aorta. (e) Introduction of aortic regurgitation.

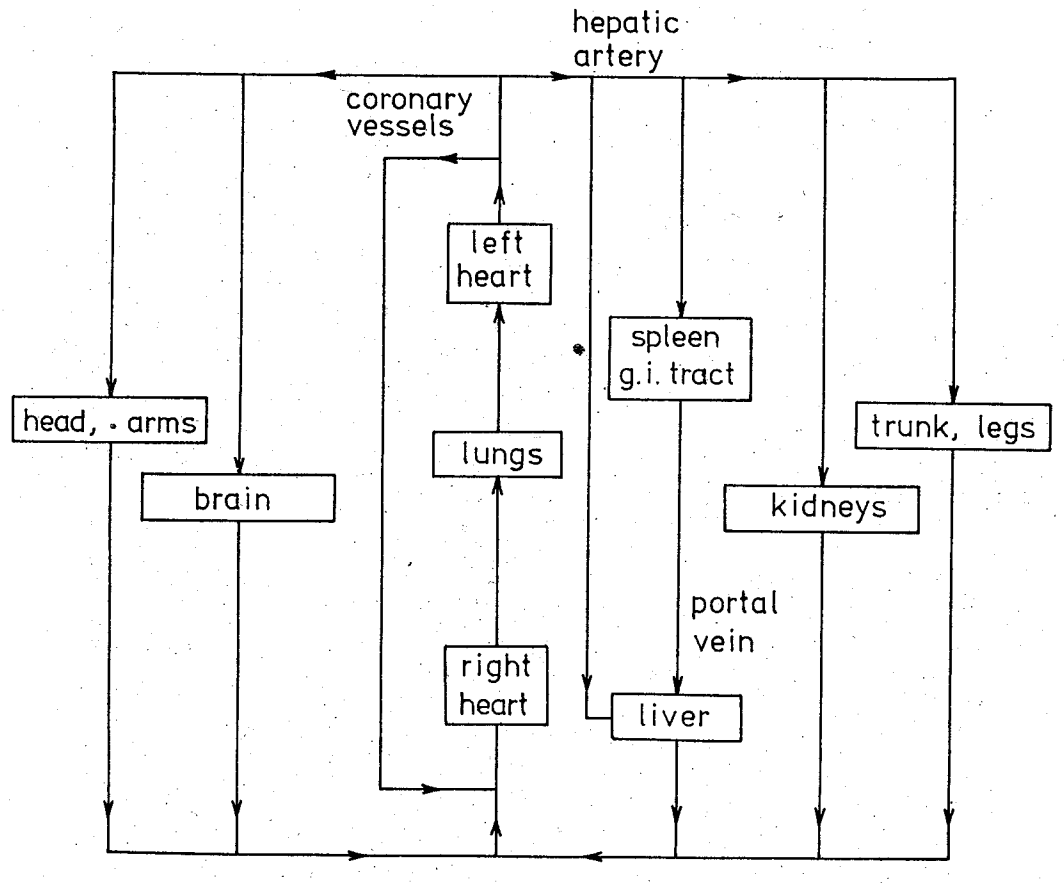

Fig. 3. The adult circulatory system (From Ganong, W. F., Review of Medical Physiology, 5th ed., Lange Med. Publ., Los Altos, California, 1971, p.415).

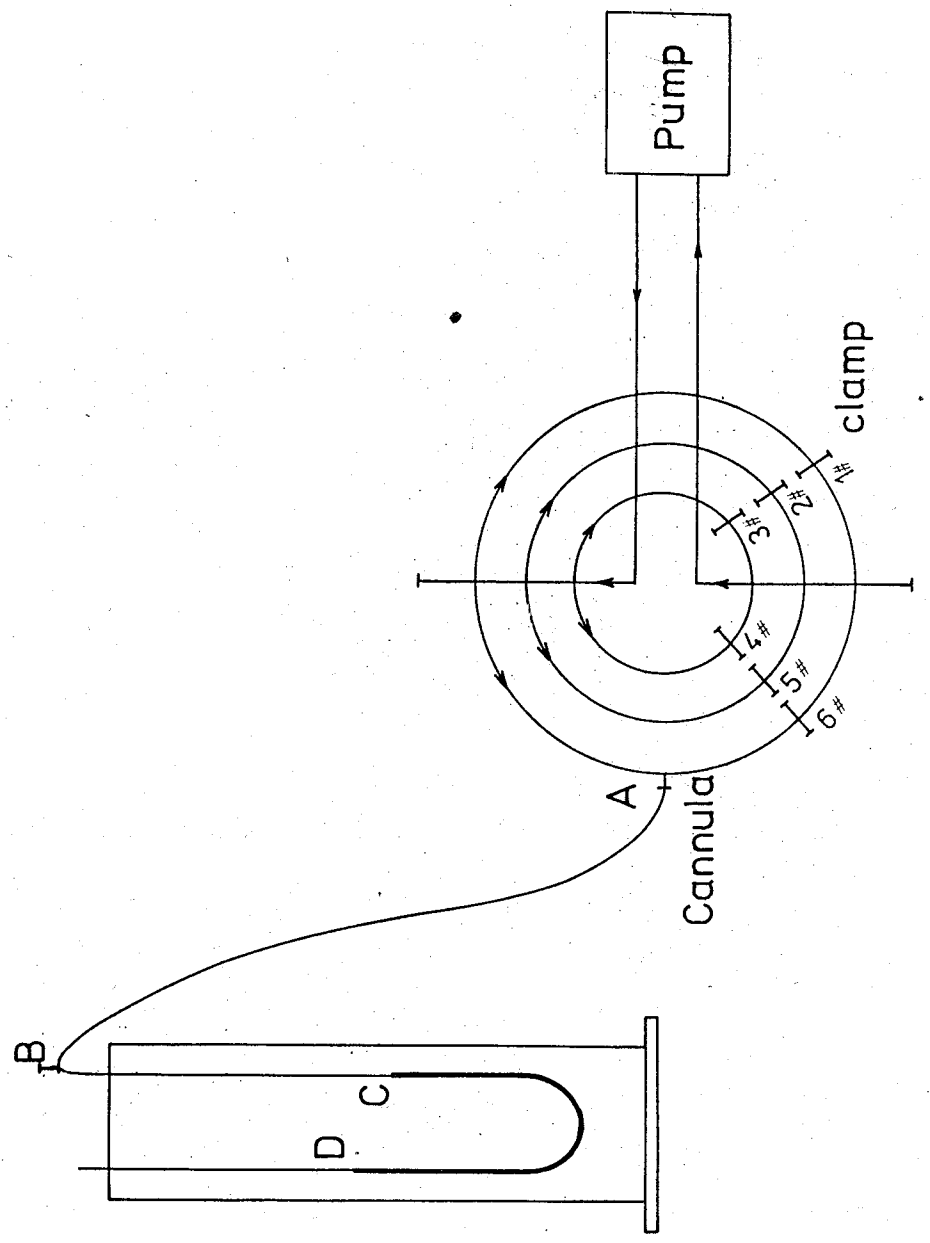

Fig. 4. The modeling diagram of circulatory system.

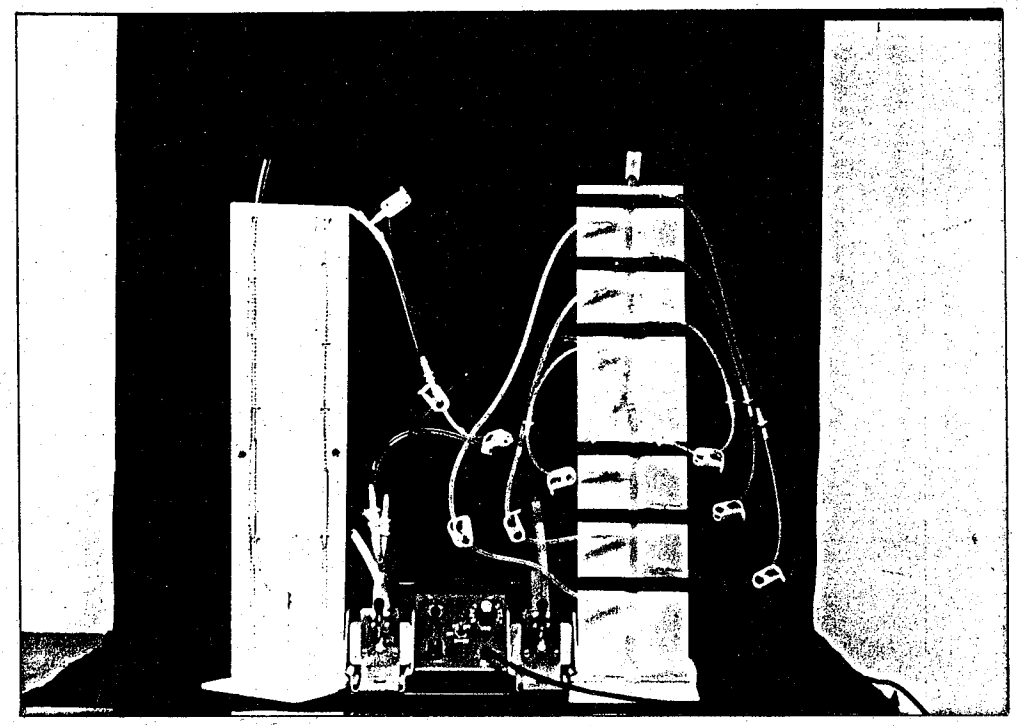

Fig. 5. A photograph of the actual working model in the experiment.

Fig. 5. A photograph of the actual working model in the experiment.

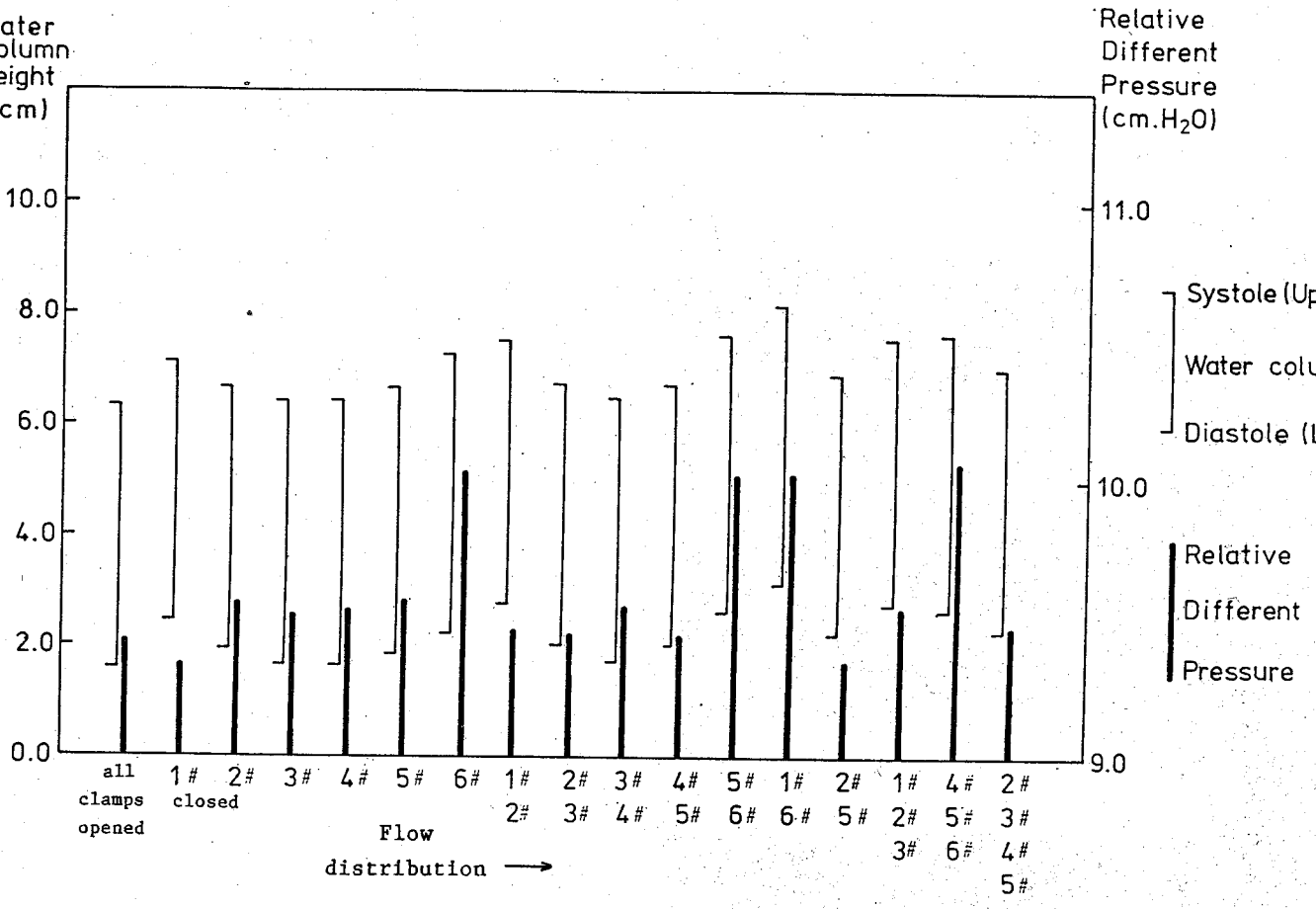

Fig. 6. The result taken from table 1 (model placed horizantal), showing the water column height of upper values (systole), lower values (diastole) and the relative different pressure with effect of changes in various flow distribution. Note : the symmetric flow distribution given the same values of water column height and the same relative different pressure.

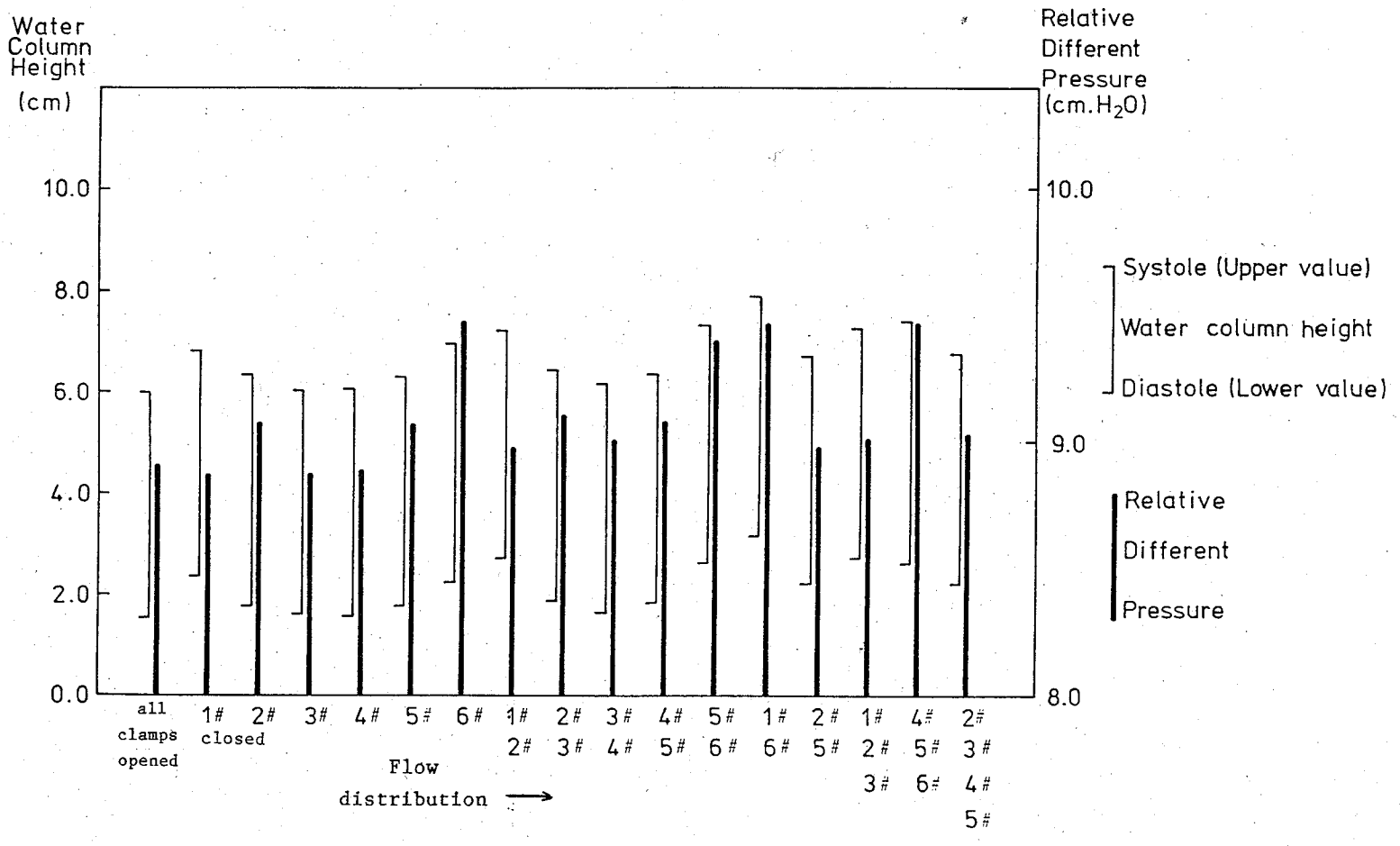

Fig. 7. The result taken from table 2 (model placed vertical), showing the water column height of uppen values (systole), lower values (diastole) and the relative different pressure with effect of changes in various flow distribution. Note : the measured values are less than that of Fig. 6. due to the effect of hydrostatics of the circulation.

Table 1. The data of water column height measured from the water manometer (model placed horizontal) and the values of the computed standard deviation and the relative different pressure to various flow distribution.

Flow distribution	Systole (upper value cm.)	Standard deviation(δ_n)	No.of sample	Diastole (lower value cm.)	Standard deviation(δ_n)	No.of sample	Different pressure(cm-H_2O)
all clamps opened	6.308	0.018	26	1.604	0.024	26	9.408
$1^{\#}$ closed	7.138	0.052	13	2.469	0.046	13	9.338
$2^{\#}$ "	6.681	0.031	13	1.904	0.054	12	9.554
$3^{\#}$ "	6.438	0.035	13	1.681	0.046	13	9.514
$4^{\#}$ "	6.423	0.050	13	1.658	0.043	13	9.530
$5^{\#}$ "	6.662	0.040	13	1.881	0.046	13	9.562
$6^{\#}$ "	7.250	0.039	13	2.235	0.041	13	10.030
$1^{\#},2^{\#}$ "	7.496	0.036	13	2.750	0.028	13	9.492
$2^{\#},3^{\#}$ "	6.742	0.033	13	2.023	0.067	13	9.438
$3^{\#},4^{\#}$ "	6.488	0.040	13	1.715	0.041	13	9.546
$4^{\#},5^{\#}$ "	6.738	0.029	13	2.015	0.066	13	9.446
$5^{\#},6^{\#}$ "	7.627	0.077	13	2.623	0.064	13	10.008
$1^{\#},6^{\#}$ "	8.158	0.051	13	3.150	0.065	13	10.016
$2^{\#},5^{\#}$ "	6.900	0.055	13	2.223	0.025	13	9.354
$1^{\#},2^{\#},3^{\#}$ "	7.550	0.059	13	2.785	0.036	13	9.530
$4^{\#},5^{\#},6^{\#}$ "	7.685	0.057	13	2.654	0.060	13	10.062
$2^{\#},3^{\#},4^{\#},5^{\#}$ "	7.019	0.024	13	2.281	0.024	13	9.476

Table 2. The data of water column height measured from the water manometer (model placed vertical) and the values of the computed standard deviation and the relative different pressure to various flow distribution.

Flow distribution	Systole (upper value cm.)	Standard deviation(δ_n)	No.of sample	Diastole (lower value cm.)	Standard deviation(δ_n)	No.of sample	Different pressure(cm-H_2O)
all clamps opened	5.983	0.031	12	1.529	0.032	12	8.908
$1^{\#}$ closed	6.817	0.037	6	2.383	0.062	6	8.868
$2^{\#}$ "	6.317	0.024	6	1.775	0.025	6	9.084
$3^{\#}$ "	6.033	0.037	6	1.600	0.050	6	8.866
$4^{\#}$ "	6.050	0.058	6	1.583	0.037	6	8.934
$5^{\#}$ "	6.308	0.067	6	1.775	0.048	6	9.066
$6^{\#}$ "	6.967	0.047	6	2.225	0.038	6	9.484
$1^{\#},2^{\#}$ "	7.217	0.047	6	2.725	0.048	6	8.984
$2^{\#},3^{\#}$ "	6.417	0.047	6	1.867	0.069	6	9.100
$3^{\#},4^{\#}$ "	6.158	0.053	6	1.650	0.050	6	9.016
$4^{\#},5^{\#}$ "	6.375	0.063	6	1.833	0.075	6	9.084
$5^{\#},6^{\#}$ "	7.308	0.045	6	2.608	0.034	6	9.400
$1^{\#},6^{\#}$ "	7.892	0.067	6	3.158	0.053	6	9.468
$2^{\#},5^{\#}$ "	6.708	0.045	6	2.217	0.062	6	8.982
$1^{\#},2^{\#},3^{\#}$ "	7.233	0.037	6	2.725	0.048	6	9.016
$4^{\#},5^{\#},6^{\#}$ "	7.400	0.076	6	2.633	0.047	6	9.468
$2^{\#},3^{\#},4^{\#},5^{\#}$ "	6.767	0.047	6	2.250	0.071	6	9.034

FLUOROIMMUNOASSAY ON METAL SURFACE

W. K. Wang, L. T. Ho, Y. Chiang and T. C. Chen

Biophysics Laboratory, Institute of Physics,
Academia Sinica, Taipei, Taiwan 115, R. O. C.

A metal surface is added into a fluorometer to reflect the excited light and to reduce the light scattering. Due to the total separation of the fluorescent signal, the resolution can be improved several order. The same metal surface can also be used for immoblizing biological particles when applied to immunoassay. The detection of rabbit IgG in the human serum is given as an example. The result indicates that the apparatus and the method have many significant advantages.

Non-radioactive labell[1,2,3], such as bacterophages, enzymes, stable free radical, fluorescent groups and chemi-luminescent have been used to replace radioactive isotope for immunoassay. Besides test tube usually used to do an immunoassay test, metal surface has also been reported useful for doing immunoassay as a result that the antibody-antigen reaction can take place at a liquid-solid interface and such reaction can be detected by the use of an ellipsometer[4]. Giaever[5] further developed a visual detection to replace ellipsometer but could only give a qualitative test. In this paper, we will report the basic principle of a high resolution fluorometer which can be used to detect trace amount of fluorescent dye on a metal surface as well as its application to immunoassay to detect antibody quantitatively.

As shown in Fig. 1, the incident light, after proper filtering, hits the

fluorescent dye on a metal surface. The reflected light goes into a black box to be trapped there, while the fluorescent light, after passing through another filter, goes toward the photon counting system. The main purpose of this design is the total separation of the fluorescent light from either the incident or the reflected light. Another advantage is the smooth metal surface causing extremely small amount of light scattering. For example, using a xenon lamp as the light source and single band interference filters with peak at 4880Å and 5200Å for the incident light and the fluorescent light respectively, the count of the photon is less than 10^2 per second for a smooth metal surface prepared by high vacuum sputtering technique. But if the metal surface is replaced by a piece of regular paper, a plastic or a ceramic plate, the increase of the light scattering makes the count to reach as high as 2×10^5, 2×10^4 and 6×10^3 per second, respectively. In order to make sure that the increase originates from scattering and no fluorescence is involved, all the materials have been checked by an argon laser excited fluorometer equipped with double monochromator and no significant fluorescence can be detected at wavelength shorter than 5400Å for ceramic and 6000Å for paper and plastic. Adding this design to a fluorometer, the signal-to-noise ratio can thus be increased several order and very high resolution can be obtained. Another way to prove its high resolution is to directly measure the fluorescence arising from the fluorescein isothiocyanate (FITC) as an example. FITC was first diluted to 0.5 ng/ml and a drop of 5 ul of this solution was then put on the metal surface and let dry. The photon count is about 5×10^2 per second. Since the count of the metal surface itself, i.e. the noise, is less than 10^2 per second, such a small amount of FITC can thus be detected. In other words, the resolution in this case is about 5 ul X 0.5 ng/ml = 2.5 pg of FITC ! If argon laser is used as light source, the resolution can be further improved.

To show the high resolution performance of such a fluorometer when applied to immunological test, the detection of rabbit IgG mixed with human serum were given as an example. Goat IgG anti rabbit IgG was first dissolved in saline then diluted with bicarbonate buffer with pH = 9.6 to 0.1 mg/cc. A drop of 10 ul and about 3mm in diameter was then put on the surface of metal slide. After incubation for about an hour it was rinsed with distilled water and gently blow dry. 8 ul of solution containing FITC conjugated rabbit IgG, which was mixed with 1/40 human serum together with unknown amount of rabbit IgG were added to the same spot, After incubation for about 4 hrs in a moisture chamber, it was again rinsed and blow dry.

The result of a typical test is shown in Table I. From this data it is evident that this method can detect antigen quantitatively. However this competitive assay is not so good as the sandwich assay. To perform a sandwich fluorescent Immuno-test, the FITC conjugated rabbit IgG was omitted from the second incubation step. A third step, which used FITC conjugated goat IgG anti rabbit IgG, of incubation was needed to bind the FITC conjugated goat IgG to the rabbit IgG which were on the metal surface. Some data are also shown in Table I.

In conclusion, both competitive method and sandwich method may be used for the antigen detection, while the sandwich method have somewhat better resolution.

References

1. Simpson, J. S. A., Campbell, A. K., Ryall, M. E. T., & Woodhead, J. S., Nature 279, 646-647 (1979).
2. Schroeder, H. R., Hines, C. M., Osborn, D. D. Moore, R. P., Hurtle, R. L., Wogoman, F. F., Roger, R. W., & Vogelhut, P. O., Clin. Chem. 27, 1378-1384 (1981).
3. Petterson, K., Sutari, H., Hemmila, I., Soini, E., Lorgren, T., Hanninen, V., Tanner, P., Stennan, U., Clin. Chem. 29/1 60-64 (1983).
4. Rothern, A., Physiol. Chem. Phys. 5, 243-258 (1973).
5. Giaever, I., & Laffin, R.J., Proc. Nat. Acad. Sci. USA 71/4533-4535 (1974).

Table and Figure Caption

Table I. The dependence of the fluorescent photon count on the amount of rabbit IgG. Two results were given (a) for competitive test (b) for the sandwich test. Data shown here is the average of 3 tests with the standard deviation.

Fig. 1. Schematic diagram of the high resolution fluorometer. 1 : light source, 2 and 6 : filters, 3 : sample and sample holder, 4 : reflected photon directed toward a photon trap, 5 : fluorescent photon, 7 : photon counting system.

Table I

Amount of rabbit IgG	Fluorescence photon count
0	4200 ± 1390
3 ng	3442 ± 562
10 ng	3323 ± 584
30 ng	2964 ± 149
100 ng	2071 ± 351

(a)

Amount of rabbit IgG	Fluorescence photon count
0	2731 ± 134
5 ng	6951 ± 384
25 ng	8039 ± 1624
75 ng	8739 ± 1132
150 ng	17547 ± 2222

(b)

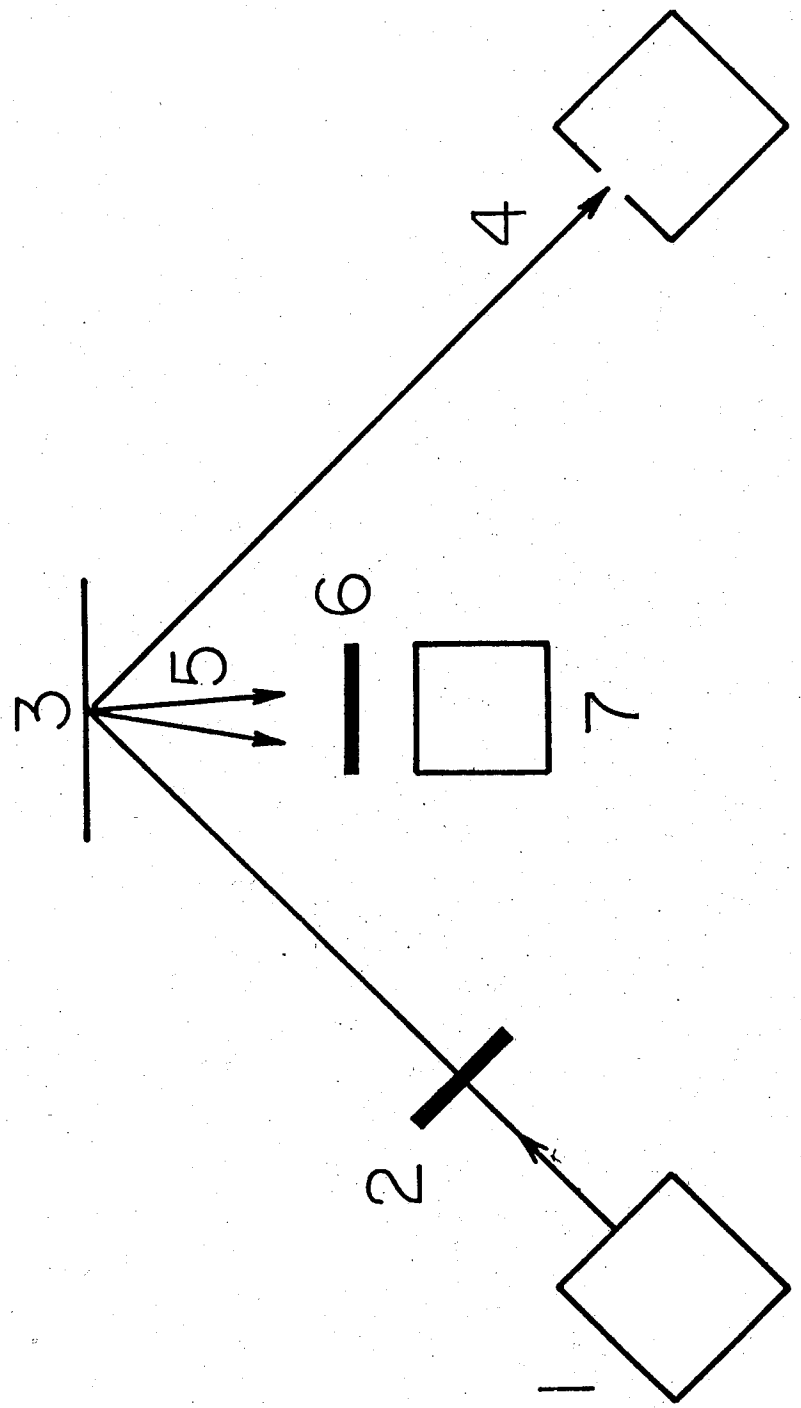

Fig. 1

非壓縮性黏滯流通過圓柱體的渦漩分離研究

黃 榮 鑑（Robert R. Hwang）
中央研究院物理研究所
台灣大學造船工程研究所
趙茂吉（M.T.Chio）
中山科學研究院

摘 要

本文利用物形調協座標轉換以數值方法解析漩度方程式及流函數—漩度關係方程式以探討二維非壓縮性黏滯流通過圓柱體流場的渦漩分離及流況變化。流場之雷諾數分別爲 100 ， 200 及 500 。數值計算過程採用一特別設計之交替方向隱式法（ ADI methed ）以求解漩度函數，並用SOR（ successive over-relaxation ）方法求解流綫函數。研究流場之物理量包括速度、壓力、阻力、昇力、轉矩和渦漩分離的頻率。研究結果並和各相關研究作比較。

Abstract

In this study, numerical solutions of the equations governing time-dependent viscous, incompressible fluid flow past a circular cylinder are presented for Reynolds numbers of 100, 200 and 500. These solutions are based on the use of body-fitted coördinate systems having a coordinate line coincident with the body contour regardless of its shape.

The implicit solution utilizes the vorticity-stream function formulation. All field equations are approximated using central differences and solved simultaneously at each time step by ADI method and SOR iteration. Comparisons of the present study with the existing results are also made and good agreement is obtained.

Annual Report of the Institute of Physics, Academia Sinica, Vol. 15, 1985

一、緒　論

流體流經圓柱體的流場研究在流體力學上是一個古老而基本的問題。由於它具有簡單的幾何形狀但却含有複雜的流場變化現象，因而一直成爲實驗及理論研究者竭力研究的題目之一。流場在其雷諾數值（$R_e = 2aU/\nu$，a爲圓柱體半徑，U爲均勻流之流速以及ν爲流體之運動黏滯係數）超過某極限值時，流場開始會有渦漩分離現象發生，根據實驗顯示當雷諾數達40～50時，會有此等的現象。尤其當$R_e > 100$時愈容易產生。這種渦漩分離（vortex shedding）現象是由於邊界層從圓柱分離，引發分離點下游附近流體作逆向廻流，造成渦漩運動。

當雷諾數較小時，這時渦漩僅對稱地在圓柱後方成長，若入流速度增加（雷諾數增大），這對渦漩便以某一固定的頻率交替地脫離圓柱體散流而去，渦漩一離開圓柱，隨即造成一個反向環流環繞該圓柱，於是圓柱便受到與入流速度方向垂直的外力作用。這些渦漩交替地從圓柱分離出去的頻率可定義史徹荷數，$S \equiv 2af/U$，表示之。史徹荷數和雷諾數有關，由於渦漩交替分離使得作用在圓柱體上之阻力和昇力等也出現週期性的振盪。

過去，已有很多學者從事有關二維均勻流通過圓柱體的研究，其中大部分爲穩定狀態解或非穩定狀態的對稱流場解(1)—(7)。僅有少數的研究探討有渦漩分離的渦漩系列發展情形(8)—(10)。在上述流場的數值研究，其數值方法大多使用有限差分法或有限元素法，利用這兩種數值方法直接來研討二維均勻流通過圓柱體，有下列的缺點：

(1)採用極座標的數值方法雖可完整的描述圓柱體的邊界，但差分網格點數須相當多才足以描述流場的變化。

(2)如使用傳統的座標系統，須在邊界附近密佈甚多的網格點，增加內外插值的程序以設定邊界條件。

(3)靠近圓柱體附近及流場變化較劇烈處須更細的網格點因而增加計算機時間及容量。

針對上述的缺失，本文捨棄傳統座標系統而採用物形調協座標系統(11)（body-fitted coordinate system）。在此座標系統的轉換下，物體的邊界變成一座標綫，而能輕易地完整描述邊界條件，另外利用OC型的外邊界更能將流場變化較劇烈處更有效地在計算平面上予以描述而不須增加網格點數。應用ADI及SOR的數值方法分別對渦度擴散方程式及渦度流函數方程式作數值分析以求解流場之渦度（vorticity）、流函數（stream function）及流況變化。流場之雷諾數分別爲100，200及500以研討雷諾數增加所造成流場內各物理量變化之傾向，同時並探討渦漩分離前後流場內各重要物理量變化之歷程，並與各有關研究結果作比較。

二、基本方程式

考慮一半徑爲a的圓柱體位於一無限大，均質非壓縮流體中，在$t = 0$時以一定之

均勻流U平行流過圓柱體。以a，U及a／U分別爲特性長度，速度及時間，則控制這個二維流場的運動方程式無因次化後可寫爲：

$$\frac{\partial \zeta}{\partial t} + \frac{\partial \psi}{\partial y}\frac{\partial \zeta}{\partial x} - \frac{\partial \varphi}{\partial x}\frac{\partial \zeta}{\partial y} = \frac{2}{R_e}\left(\frac{\partial^2 \zeta}{\partial x^2} + \frac{\partial^2 \zeta}{\partial y^2}\right) \qquad (1)$$

式中ζ爲渦度，$R_e = 2Ua/\nu$。

流函數φ，渦度ζ及速度分量u，v之關係，由渦度之定義及連續方程式，可寫爲：

$$\frac{\partial^2 \varphi}{\partial x^2} + \frac{\partial^2 \varphi}{\partial y^2} = -\zeta \qquad (2)$$

及

$$u = \partial \varphi / \partial y \quad , \quad v = -\partial \varphi / \partial x \qquad (3)$$

其他作用於圓柱體物理量，如壓力、昇力係數、阻力係數及轉矩係數可由渦度與流函數之求得計算如下：

$$C_p = \frac{2}{R_e}\int_0^{\phi} \partial \zeta / \partial \gamma \quad d\phi \qquad (4)$$

$$C_L = -\int_0^{2\pi} C_p \sin\phi \, d\phi + \frac{2}{R_e}\int_0^{2\pi} \zeta \cos\phi \, d\phi \qquad (5)$$

$$C_D = -\int_0^{2\pi} C_p \cos\phi \, d\phi - \frac{2}{R_e}\int_0^{2\pi} \zeta \sin\phi \, d\phi \qquad (6)$$

及

$$C_T = \frac{2}{R_e}\int_0^{2\pi} \zeta \, d\phi \qquad (7)$$

式中，$C_p = P/\rho U^2$，$C_L = L/\rho U^2 a$，$C_D = D/\rho U^2 a$及$C_T = M/\rho U^2 a^2$。

方程式(1)及(2)爲控制流場的基本方程式，流場之求解還須滿足下列之啓始條件及邊界條件：

(1)啓始條件：在$t = 0$之啓始流場爲非旋流之勢流場（potenial flow），即

$$\varphi(x, y, 0) = \varphi_p(x, y)$$
$$\zeta(x, y, 0) = 0 \qquad ; \forall (x, y) \in \Omega \qquad (8)$$

式中Ω爲流場區域，φ_p爲勢流流函數。

(2)邊界條件：

在圓柱體上，

$$\varphi_b = 0 \quad , \quad \zeta_b = -\frac{\partial^2 \psi}{\partial n^2}\Big|_b$$

在遠離圓柱體無限遠處，

$$\varphi = \varphi_p \quad , \quad \zeta = 0 \qquad (9)$$

三、物形調協座標之研成

「物形調協座標轉換」係藉一組橢圓型偏微分方程式以關聯原卡氏座標和物形調協座標相對應平面之關係，使得物形調協座標綫能順著障礙物形狀自動形成分布(11)—(12)。

較常用的爲以Poission 方程式將卡氏座標的物理面轉換至計算面（ computation domais ）。其過程爲先指定物理面與計算面邊界點之對應關係，其餘內部各點的對應由下列偏微分方程式來決定：

$$\zeta_{xx}+\zeta_{yy}=P(\zeta,\eta),\ \eta_{xx}+\eta_{yy}=Q(\zeta,\eta) \qquad \cdots\cdots(10)$$

式中（ ζ ， η ）爲物形調協座標，P，Q爲網格疏密控制函數。

爲使數值計算在（ ζ ， η ）面上進行，將(10)式中之他變數與自變數相互調換，轉換方程式可寫成：

$$\begin{aligned} x\chi_{\xi\xi}-2\beta\chi_{\xi\eta}+\gamma\chi_{\eta\eta}&=-J^2(P\chi_\xi+Q\chi_\eta) \\ x y_{\xi\xi}-2\beta y_{\xi\eta}+\gamma y_{\eta\eta}&=-J^2(Py_\xi+Qy_\eta) \end{aligned} \qquad \cdots\cdots(11)$$

式中，$\alpha=x_\eta^2+y_\eta^2$，$\beta=x_\xi\chi_\eta+y_\xi y_\eta$，$\gamma=\chi_\xi^2+y_\xi^2$，及

$$J=\frac{\partial(x,y)}{\partial(\zeta,\eta)}=x_\xi y_\eta-x_\eta y_\xi$$

將(11)式以有限差分法之數值解析過程中，在（ ζ ， η ）面選擇均勻的正方形網格，應用中央差分將所有微分項差分化，並以SOR（ successive overrelaxation ）數值方法反覆運算以得出相對於所有（ ζ ， η ）點之（ x ， y ）值。圖(一)爲求得之相對應於計算面上之物理面的座標綫。

四、數值解析與運算程序

由於原（ x ， y ）座標與轉換後之物形調協座標（ ζ ， η ）有(10)式或(11)式之轉換關係，根據微分鏈鎖法則，控制方程式(1)，(2)及(3)式可寫成：

$$\zeta_t+(\varphi_\eta\zeta_\xi-\varphi_\xi\zeta_\eta)/J=\frac{2}{J^2R_e}(\alpha\zeta_{\xi\xi}-2\beta\zeta_{\xi\eta}+\gamma\zeta_{\eta\eta})+2(Q\zeta_\eta+P\zeta_\xi)/R_e \qquad \cdots\cdots(12)$$

$$(\alpha\varphi_{\xi\xi}-2\beta\varphi_{\xi\eta}+\gamma\varphi_{\eta\eta})/J^2+Q\varphi_\eta+P\varphi_\xi=-\zeta \qquad \cdots\cdots(13)$$

及 $$u=(x_\xi\varphi_\eta-\chi_\eta\varphi_\xi)/J,\ v=(y_\xi\varphi_\eta-y_\eta\varphi_\xi)/J \qquad \cdots\cdots(14)$$

邊界條件在物形調協座標（ ζ ， η ）爲：

(1)在 Γ_1^* 段（ $1\le\xi\le NZ$ ， $\eta=1$ ），

$$\varphi(\xi,1,t)=0 \qquad \cdots\cdots(15)$$
$$\zeta(\xi,1,t)=-\gamma\varphi_{\eta\eta}/J^2$$

(2)在 Γ_3^* 、 Γ_4^* ， Γ_6^* 及 Γ_7^* 段（流場外邊界），

$$\varphi(\xi,\eta,t)=\varphi_p \qquad \cdots\cdots(16)$$
$$\zeta(\xi,\eta,t)=0$$

(3)在 Γ_5^* 段，

$$\varphi_\eta=0 \quad 及 \quad \zeta_\eta=0 \qquad \cdots\cdots(17)$$

由於(12)式中含有對 ζ 及 η 同時微分之混合項，無法直接應用ADI數值方法將其差

分化。本文經調整設計一個差分式，使能保有ADI 方法的程序將(12)式差分化。對空間之變化採用中心差分，對時間變化則以前進差分，得出控制方程式(12)之有限差分式爲：

$$\begin{aligned} &(\frac{\varphi_\eta}{2J}-\frac{P}{R_e}-\frac{2\alpha}{J^2R_e})_{ij}\zeta^*_{i+1,j}+(\frac{4\alpha}{J^2R_e}+\frac{1}{\Delta t})_{i,j}\zeta^*_{i,j}-(\frac{\varphi_\eta}{2J}-\frac{P}{R_e}+\frac{2\alpha}{J^2R_e})_{i,j}\zeta^*_{i-1,j}=-(\frac{\varphi_\eta}{2J}-\frac{P}{R_e}-\frac{2\alpha}{J^2R_e})^{\dagger}_{ij}\zeta^n_{ij}+(\frac{\varphi_\eta}{2J}-\frac{P}{R_e}+\frac{2\alpha}{J^2R_e})\zeta^n_{i-1,j}+(\frac{\varphi_\xi}{2J}+\frac{Q}{R_e}+\frac{2\gamma}{J^2R_e})_{ij}\zeta^n_{i,j+1}-(\frac{\varphi_\xi}{2J}+\frac{Q}{R_e}-\frac{2\gamma}{J^2R_e})_{ij}\zeta^n_{i,j-1} \\ &-(\frac{2\beta}{J^2R_e})_{ij}(\zeta^n_{i+1,j+1}+\zeta^n_{i-1,j-1}-\zeta^n_{i+1,j-1}-\zeta^n_{i-1,j+1}) \qquad \cdots(18a) \end{aligned}$$

及

$$\begin{aligned} &-(\frac{\varphi_\xi}{2J}+\frac{Q}{R_e}+\frac{2\gamma}{J^2R_e})_{ij}\zeta^{n+1}_{i,j+1}+(\frac{4\gamma}{J^2R_e}+\frac{1}{\Delta t})_{ij}\zeta^{n+1}_{ij}+(\frac{\varphi_\xi}{2J}+\frac{Q}{2R_e}-\frac{2\gamma}{J^2R_e})_{ij}\zeta^{n+1}_{i,j-1}=\zeta^*_{i,j} \qquad \cdots\cdots(18b) \end{aligned}$$

(13)式應用SOR數值法，可得出方程式之有限差分式爲：

$$\begin{aligned} \varphi^{(m+1)}_{ij}=&(\frac{J^2}{2(\alpha+\gamma)})_{ij}\{(\frac{\alpha}{J^2}+\frac{P}{2})_{ij}\varphi^m_{i+1,j}+(\frac{\alpha}{J^2}-\frac{P}{2})_{ij}\varphi^{m+1}_{i-1,j} \\ &+(\frac{\gamma}{J^2}+\frac{Q}{2})_{ij}\varphi^m_{i,j+1}+(\frac{\gamma}{J^2}-\frac{Q}{2})_{ij}\varphi^{m+1}_{i,j-1}-(\frac{\beta}{2J^2})_{ij}(\\ &\varphi^m_{i+1,j+1}+\varphi^{m+1}_{i-1,j-1}-\varphi^{m+1}_{i+1,j-1}-\varphi^m_{i-1,j+1})+\zeta_{i,j} \qquad \cdots\cdots(19a) \end{aligned}$$

及 $$\varphi^{m+1}_{ij}=\lambda\varphi^{(m+1)}_{ij}+(1-\lambda)\varphi^m_{ij}$$

式中，λ 爲收斂參數，其值爲大於1，上標m表反覆運算之次數。(14)式對空間採用中心差分，則速度場之有限差分式爲：

$$u^{n+1}_{ij}=\frac{1}{4}\{(x_{i+1,j}-x_{i-1,j})(\varphi^{n+1}_{i,j+1}-\varphi^{n+1}_{i,j-1})-(x_{i,j+1}-x_{i,j-1})(\varphi^{n+1}_{i+1,j}-\varphi^{n+1}_{i-1,j})\}/J_{ij} \qquad \cdots\cdots(20a)$$

及

$$v^{n+1}_{ij}=\frac{1}{4}\{(y_{i+1,j}-y_{i-1,j})(\varphi^{n+1}_{i,j+1}-\varphi^{n+1}_{i,j-1})-(y_{i,j+1}-y_{i,j-1})(\varphi^{n+1}_{i+1,j}-\varphi^{n+1}_{i-1,j})\}/J_{ij} \qquad \cdots\cdots(20b)$$

式中 $$J_{ij}=\frac{1}{4}\{(x_{i+1,j}-x_{i-1,j})(y_{i,j+1}-y_{i,j-1})-(x_{i,j+1}-x_{i,j-1})(y_{i+1,j}-y_{i-1,j})\}$$

啓始條件及邊界條件由上述(15)，(16)及(17)式中決定後，控制方程式(18)，(19)及(20)之求解，經數值差分法之方程式寫成電腦程式後，利用高速電子計算機CDC-CYBEK170-825解出。其數值解步驟如下：(1)由流函數之拉普拉方程式解出勢能流流場。(2)由(15)式求得

在圓柱體表面之漩量值，ζ_{i1} 。

(4)由啓始流場及圓柱體面之漩量，解漩量方程式（18a）及（18b）分別對 ζ 及 η 雙向掃瞄，加入邊界條件求得新時段的漩量，ζ_{ij}^{n+1} 。

(4)由求得之漩量代入流函數—漩量關係式（19a）及（19b），利用 SOR 法循序收斂以求得該新時段之流函數，收斂之是否完成，則由是否滿足下式爲判斷依據

$$ABS\left[\left(\varphi_{ij}^{m+1}-\varphi_{ij}^{m}\right)/\varphi_{ij}^{m}\right]<5\times10^{-3} \qquad \cdots\cdots(21)$$

(5)新時段之速度則由（20a）及（20b）式求得。

(6)重覆步驟(2)－(5)以求解各個不同新時段流場的變數值。

本文研討之流場經物形調協座標轉換後在計算面爲一凸形，如圖(一)所示，取正方形網路 $\Delta\zeta=\Delta\eta=1$ ，其中 NZ＝66 ，NE=55 ，NZ1 ＝ 13 ，NZ2 ＝ 14 ，NZ3 ＝ 52 ，NZ4 ＝ 54 ，NEZ ＝ 30 ，共計 3046個差分格點。由於網路已夠濃密，未再作網格疏密度的控制，即 P＝Q＝ 0 。計算中時間增量 Δt 的選取並未固定，其變化如下：

$$\Delta t=\begin{cases}0.005 & t=0\\ 2\times\Delta t_f & 0<t<0.05\\ 0.05 & t>0.05\end{cases}$$

式中 Δt_f 爲前一時段所用之 Δt 。

雖然控制方程式(1)爲非對稱，但由於流場及邊界條件均爲上下對稱，從勢流流場開始要解析到不對稱之渦漩分離發生，需要很長的計算時間，爲使流場早些產生渦漩分離，以往的研究 (7) 爲在圓柱表面上下對稱之兩點加上大小相同，方向相反之人爲渦度（artificial vorticity）的小擾動，以激發促進渦漩分離的發生。本文採用的方式爲在外邊界作擾動。設外邊界點之流函數值爲 φ_b ，該點若爲勢流流場，流綫函數值爲 φ_b^F ，則定外邊界之擾動邊界條件爲：

$$\varphi_b=\varphi_b^F+F(t)$$

式中 F(t) 表示外邊界之流綫被提高或降低之值，隨 t 而變化，藉此擾動來促進渦漩之分離。其中之微小擾動量 F(t) 由下式求得，

$$F(t)=\left[\sum\left(\varphi_{b-1}(t)-\varphi_{b-1}^{F}\right)\right]/N$$

式中，N爲外邊界點之總數，∑爲對N個點作總和。

五、結果與討論

爲印證本文數值模式計算之準確性，將本文之部分計算結果與相關研究結果作比較。圖(二)及圖(三)分別爲 $R_e=100$ 及 200 時渦漩長度（wake length）之比較，圖(四)爲渦漩分離角度 θ_s 隨時間變化的計算結果與 Collins & Dennis (6) 結果之比較。結果顯示本文之數值計算與前人之實驗和計算結果，皆甚爲吻合。

在解析 $R_e=100$ 流場時，流場之變化由勢流流場開始，隨時間增加，在圓柱體下游區，由於負渦漩值的增大而逐漸形成渦漩，其渦漩長度起先隨時間之增加而增長，而

後發展到一定長度而漸趨穩定。圖四所示爲 t＝20時，流場之流綫等渦漩綫。爲從使流場早些產生渦漩分離（vortex shedding），應用前述方法當尾流渦漩長度趨近穩定時，在流場外邊界產生輕微擾動迫使流場產生不對稱而發生渦漩分離。圖五爲在圓柱後渦漩交替地依某固定頻率分離的流綫變化。圖六爲分離週期內相對時間之渦漩量變化。圖七爲分離週期中之速度場變化。圖八爲圓柱體面上之阻力昇力及轉矩隨時間之變化，由上述之振盪週期得出渦漩交替分離之 S 爲 0.16 。

爲瞭解流場雷諾數變化對於渦漩分離及其他現象之影響，本文的流場分析亦分別對 R_e ＝ 200 及 500 作系列數值探討。計算結果與 R_e ＝ 100的流場一樣，有渦漩交替分離的現象發生，而且隨著 R_e 的增加其交替發生之頻率亦隨之增大（S增大）。圖九、圖十、圖十一分別爲 R_e ＝200時，流場中渦漩分離週期內之流綫、速度及渦漩變化。流場之發展與 R_e ＝100時相似，當時稱流場隨時間增加趨近穩定時作用於圓柱之阻力亦愈小，直到渦漩分離現象出現時反而增加，而且作振盪式的增加，振盪週期約爲昇力和轉矩振盪週期的一半，後兩者和渦漩分離的週期相同，從振盪變化曲綫波峯間隔知振盪週期爲 11，故史徹荷數 S ＝ 0.182 。

有關 R_e ＝500之流場如圖(十)及(十一)分別爲渦漩分離週期內之流綫及速度變化。流場雷諾數增加，影響渦漩分離的週期減小，因而其史徹荷數亦隨之增大，圖(十二)爲 S 與 R_e 之關係。另外，流場 R_e 的變化亦會影響圓柱體所受之阻力，昇力及轉矩之大小及振盪情形，圖(十三)所示爲 R_e 變化對 C_D ，C_L 及 C_T 的變化。有關本文計算結果與其他相關研究結果之比較如表一所示(13)－(15)

六、結　論

利用物形調協座標以探討二維壓縮黏滯流通過圓柱體之流場特性，經由數值分析就 R_e ＝ 100 ，200 及 500 的系列計算結果，可獲致下列之結論：

(1)利用物形調協座標轉換可使座標綫順著流綫分佈，提高有限差分式之準確性並減少網格數量。

(2)流場因渦漩分離現象的發生，將使流場內諸物理量（如速度、壓力、漩度、阻力、昇力及轉矩等）產生週期性之振盪變化。

(3)流場中渦漩交替分離的頻率（或史徹荷數）隨雷諾數之增加而增大。

(4)本文之計算結果與其他研究結果之比較顯示，本文數值模式相當良好。

參考文獻

1. Keller, H. B. and Takami, H 1966 : Numerical Solutions of Non-linear Differential Equations, edited by D. Greenspan, Wiley, New York, p.115.

2. Hamielec, A. E. and Real, J. D. 1969 : Numerical studies of viscous flow around circular cylinders, Physics of Fluids 12, 11-17.
3. Son, J. S. and Hanratty, T. J. 1969 : Numerical solution of flow around a cylinder, J. Fluid Mech. 35, 369-386.
4. Underwood, R. L. 1969 : Calculation of incompressible flow past a circular cylinder at moderate Reynolds numbers, J. Fluid Mech. 37, 95-114.
5. Dennis, S. C. R. and Chang, G. Z. 1970 : Numerical solution for steady flow past a circular cylinder at Reynolds number up to 100, J. Fluid Mech 42, 471-488.
6. Collin, W. M. and Dennis, S. C. R. 1973 : Flow past an impulsively started circular cylinder, J. Fluid Mech 60, 105-126.
7. Loc, T. P. 1980 : Numerical analysis of unsteady secondary vortices generated by an impulsively started circular cylinder, J. Fluid Mech. 100, 111-132.
8. Jordan, S. K. and Fromm, J. E. 1972 : Oscillatory drag, lift, and torque on a cirvular cylinder in a uniform flow, Physics of Fluids, 15, 3, 371-376 376.
9. Gresho, P. M., Lee R. L. and Sani, R. L. 1980 : On the time-dependent solution of the incompressible Navier-stokes equations, Recent Advances in Numerical Methods in Fluids, edited by C. Taylor, Pineridge Press, 27-80.
10. Deffenbangh, F. D. and Marshall, F. J. 1976 : Time development of the flow about an impulsively started cylinder, AIAA Journal, 14, 7, 908-913.
11. Thames, F. C., Thompson, J. F. et al 1977 : Numerical solution for viscous and potential flow about arbitary two dimensional bodies using body-fitted coordinate system, J. Comput. Phys. 24, 245-273.
12. Thompson, J. F., Thames, F. C. and Mastin, C. W. 1977 : TOMCAT, J. Comput. Physics 24, 274-302.
13. Lin C. L. Pepper, D. W. and Lee, S. C. 1976 : Numerical methods for seperated flow solutions around a circular cylinder, AIAA J. 14,

900-907.
14. Thoman, D. and Szewczyk, A. 1969 : Time dependent viscous flow over a circular cylinder. Phys. Fluid, suppl II. 79-86.
15. Lecointe, Y. and Piguet, J. 1984 : On the use of several compact methods for the study of unsteady incompressible viscous flow round a circular cylinder. Computer & Flnids, 12, 255-280.

表一　阻力、昇力及史徹荷數之比較

R_e	C_D	C_L	S	Author(s)
100	1.28	±0.54	0.16	Jordan and Fromm(8)
	1.39	±0.69	0.174	Swanson and Spanlding
	1.43	±0.50	0.166	Smith and Brebbia
	1.27	±0.6	0.161	Gresho and Lee (9)
	1.30	±0.45	0.16	This study
			0.18	Lin etal (13)
200	1.17		0.19	Martinez
	1.27	±0.4	0.15	Thoman and Szewczyk (14)
	1.17		0.194	Lecointe and Piguet (15)
	1.46	±0.7	0.182	This study
	1.35	±0.6		

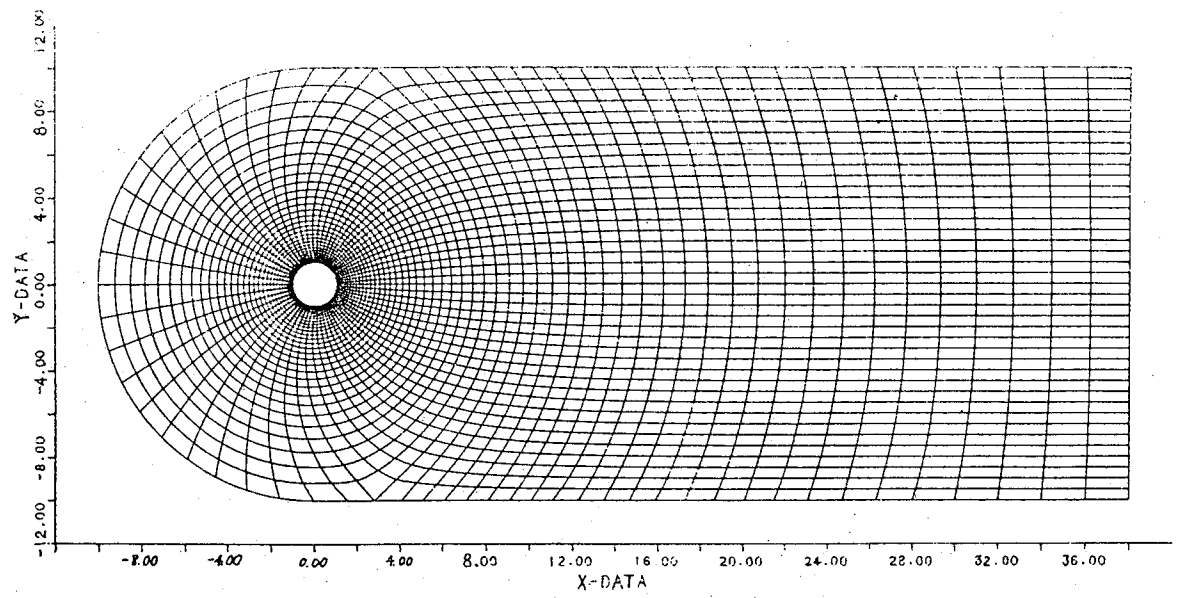

(a)物理面之物形調協座標綫

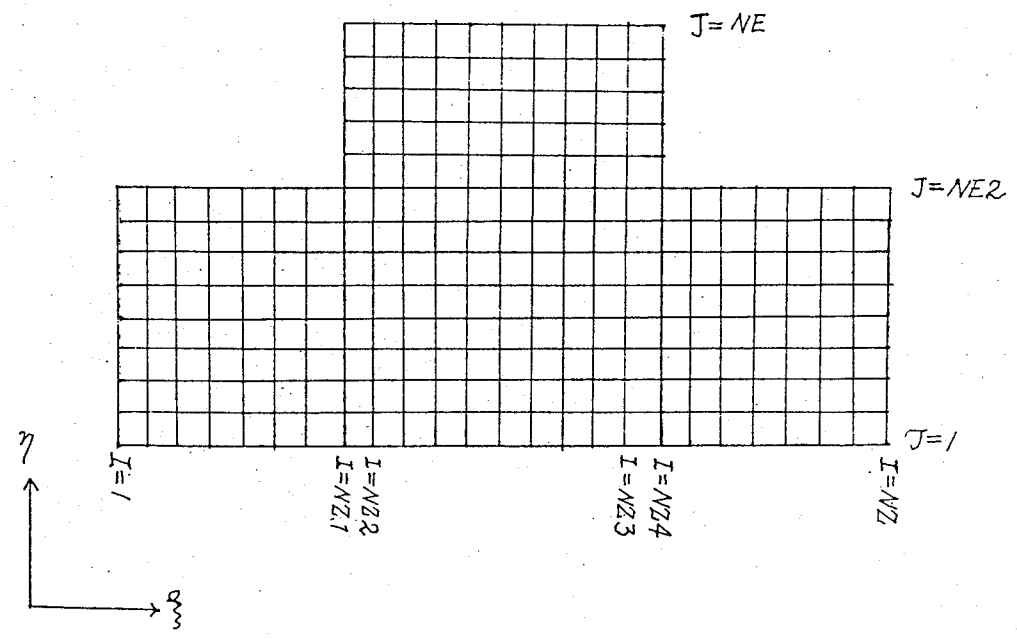

(b)計算面之物形調協座標網路

圖一　流場的物形調協座標網路

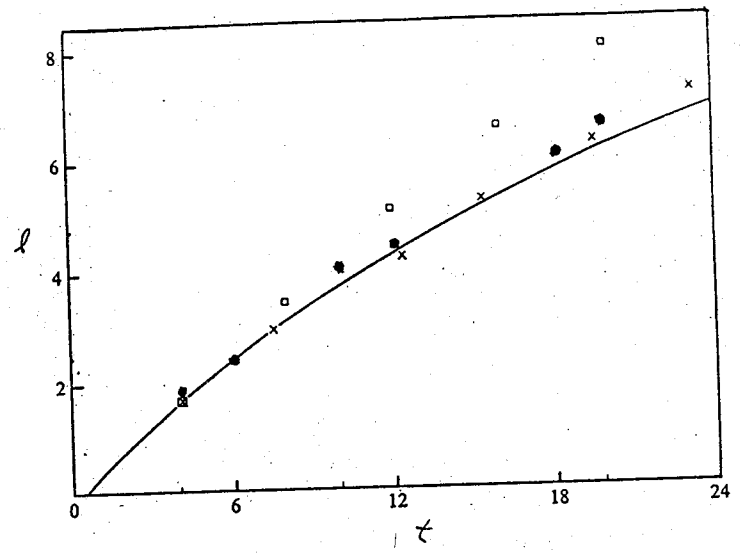

圖二　R_e =100 渦漩長度之比較：—Collin & Dennis ，×Honiz & Taneda ，□Kawaguti & Jain ，·本文之計算結果

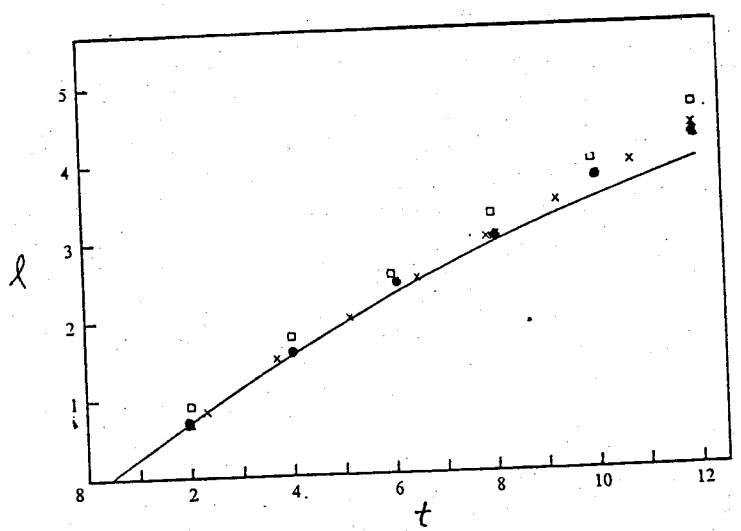

圖三　R_e =200 渦漩長度之比較：—Collin & Dennis ，×Honji & Taneda ，□Kawaguti & Jain ，·本文之計算結果

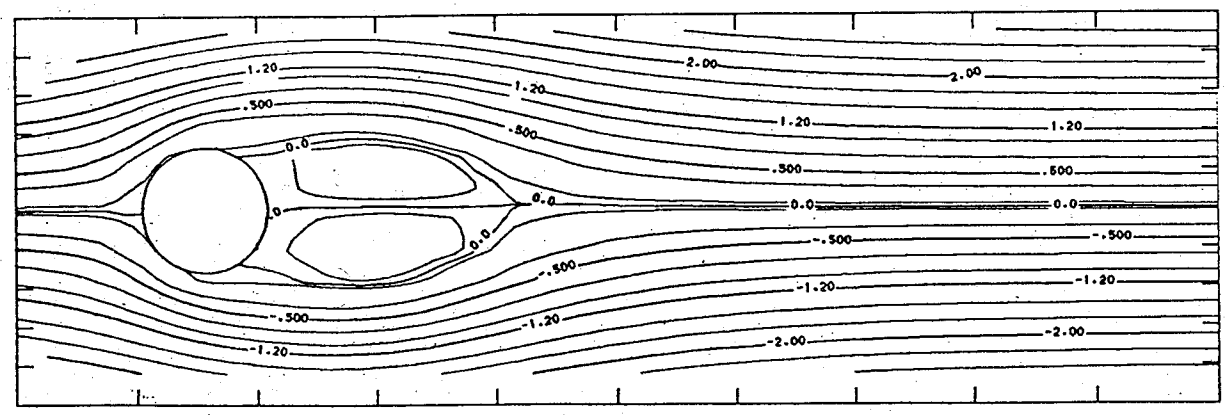

(a) R_e = 100 ， t = 20 之流綫

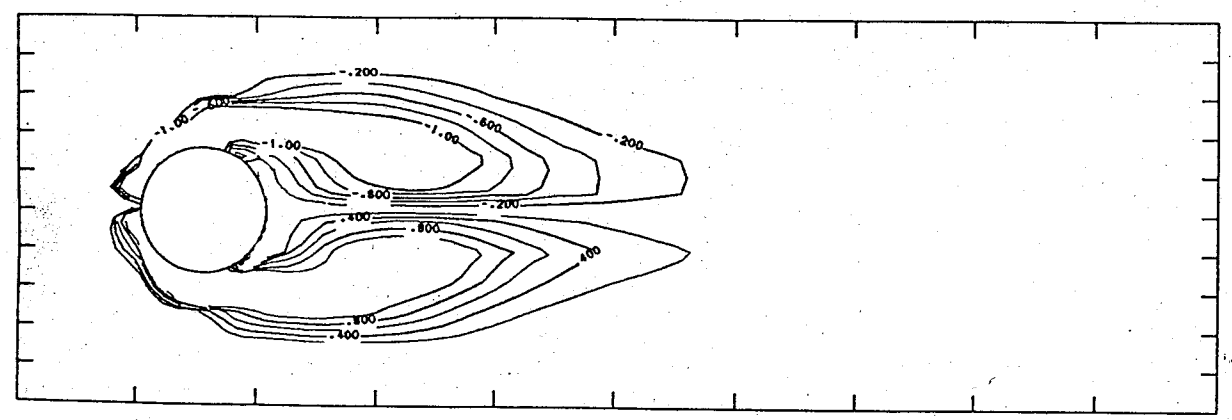

(b) R_e = 100 ， t = 20 之等渦漩綫

圖四　R_e =100 ， t = 20 之流綫及等渦漩綫

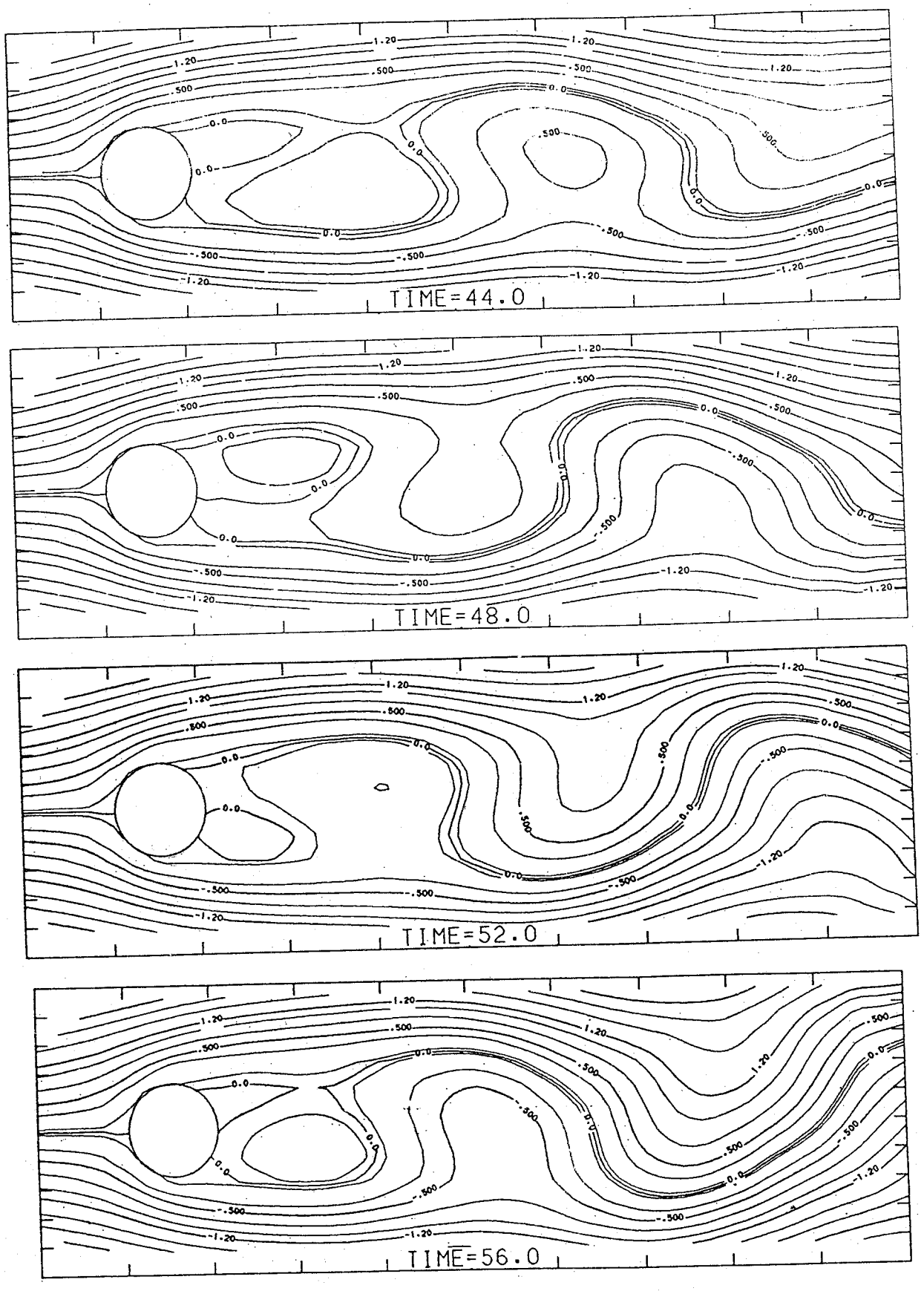

圖五　$R_e = 100$ 流場渦漩分離週期中之流綫變化

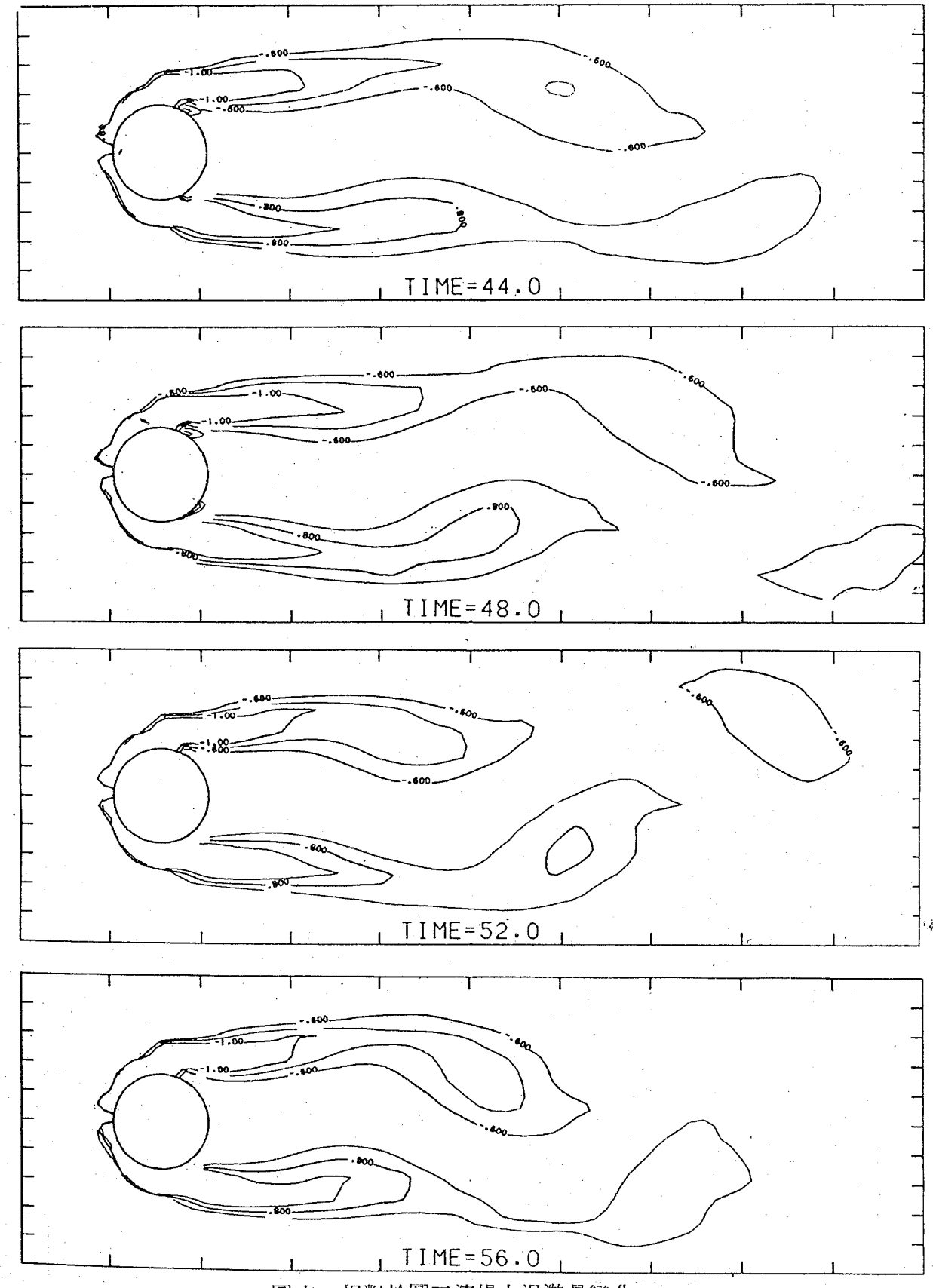

圖六　相對於圖五流場之渦漩量變化

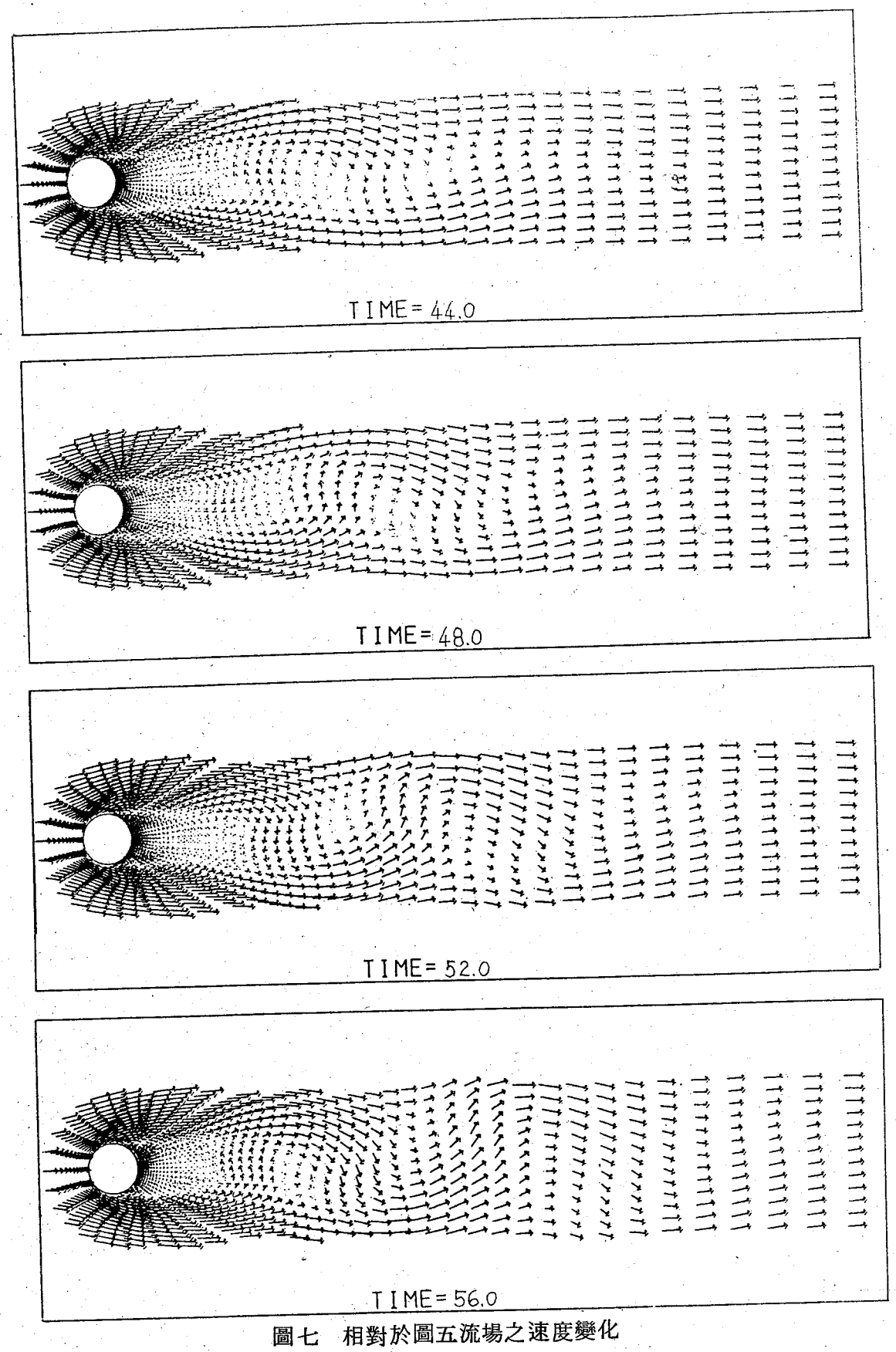

圖七　相對於圖五流場之速度變化

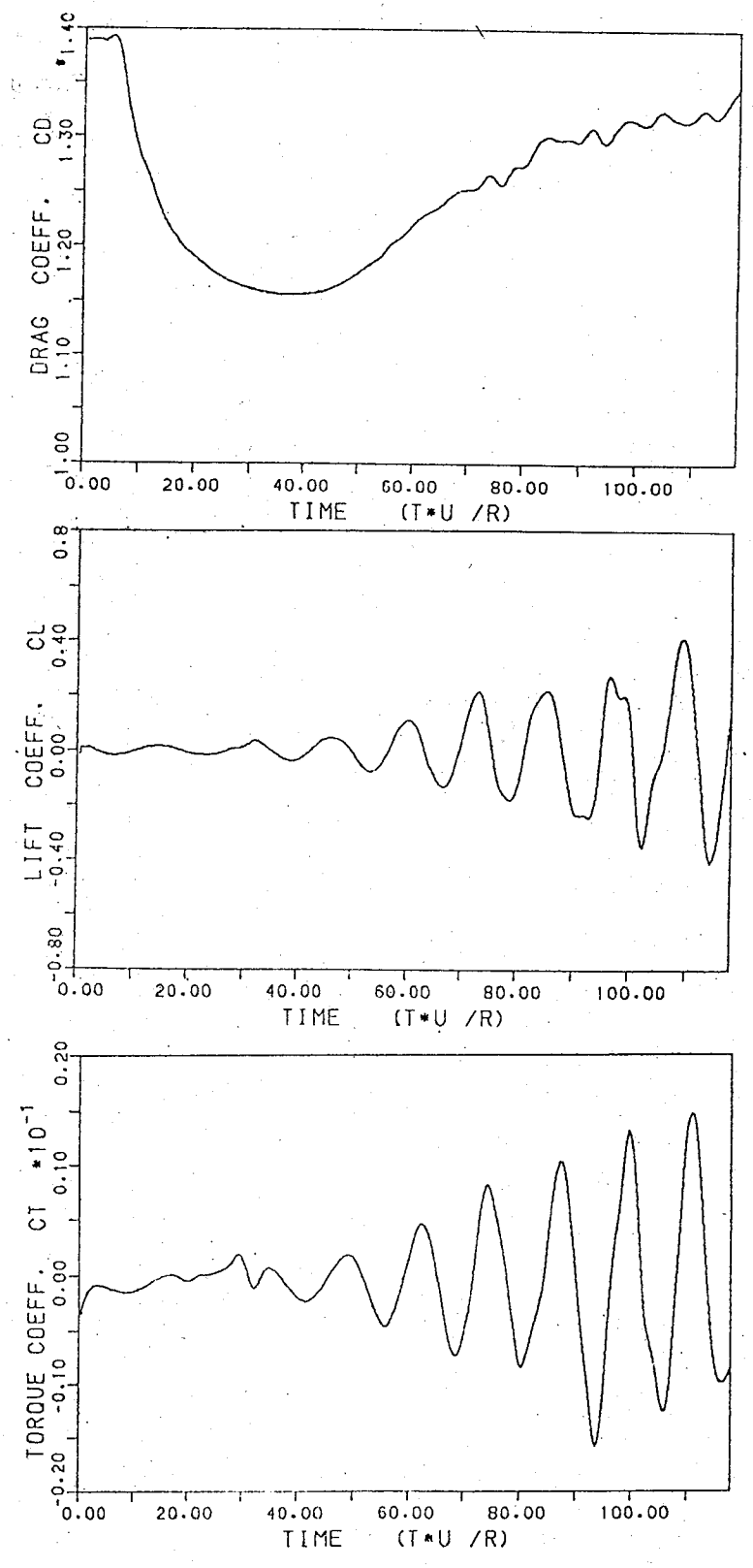

圖八　R_e =100 圓柱體之阻力、昇力及轉矩之變化

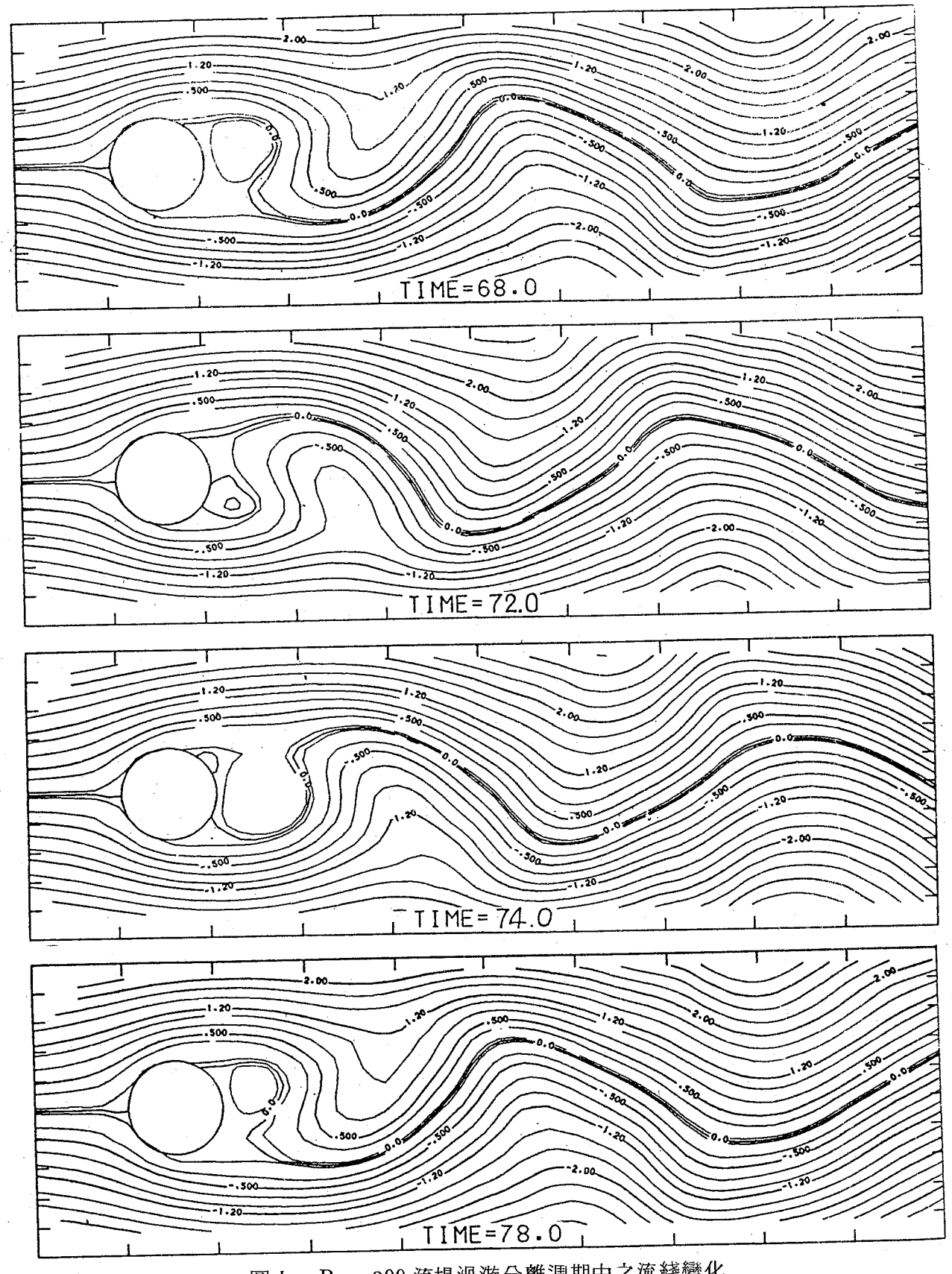

圖九　$R_e = 200$ 流場渦漩分離週期中之流綫變化

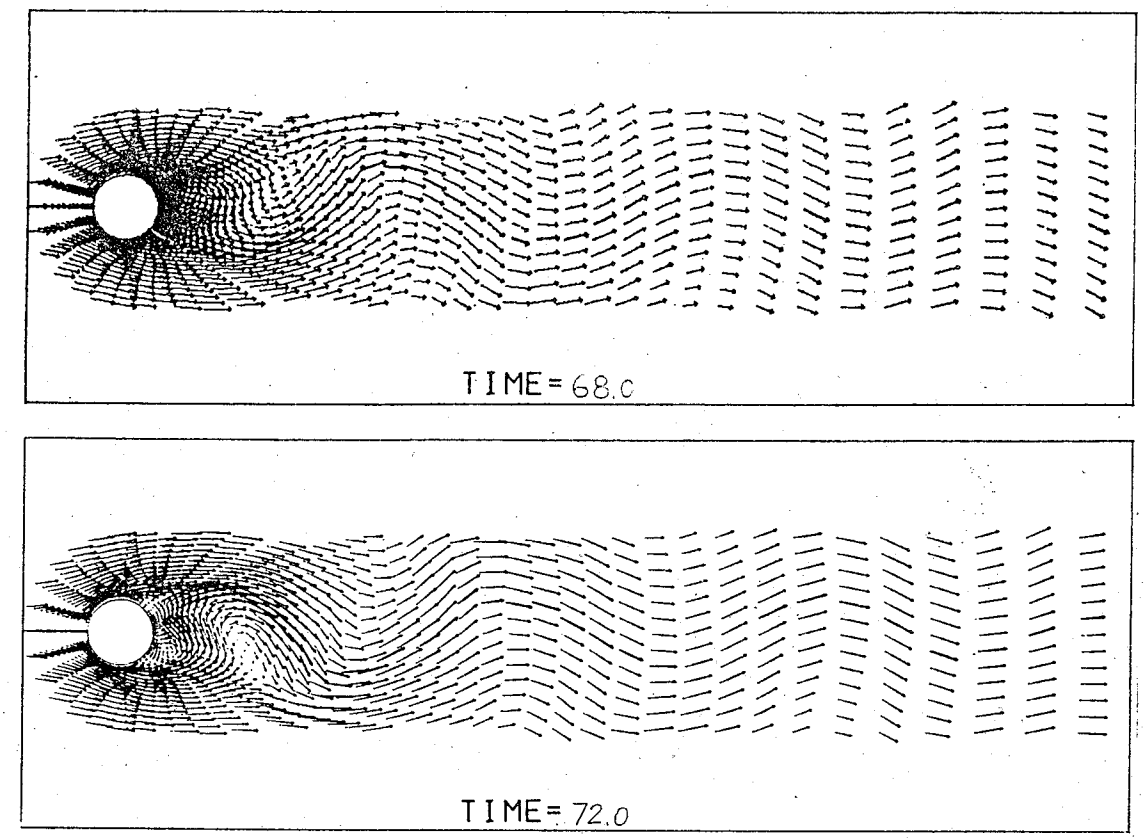

圖十　相對應於圖九流場之速度變化

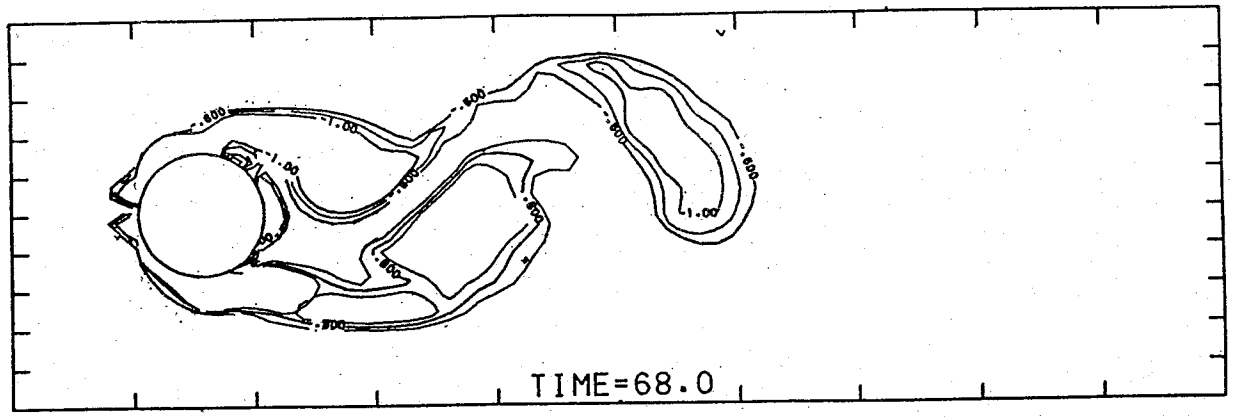

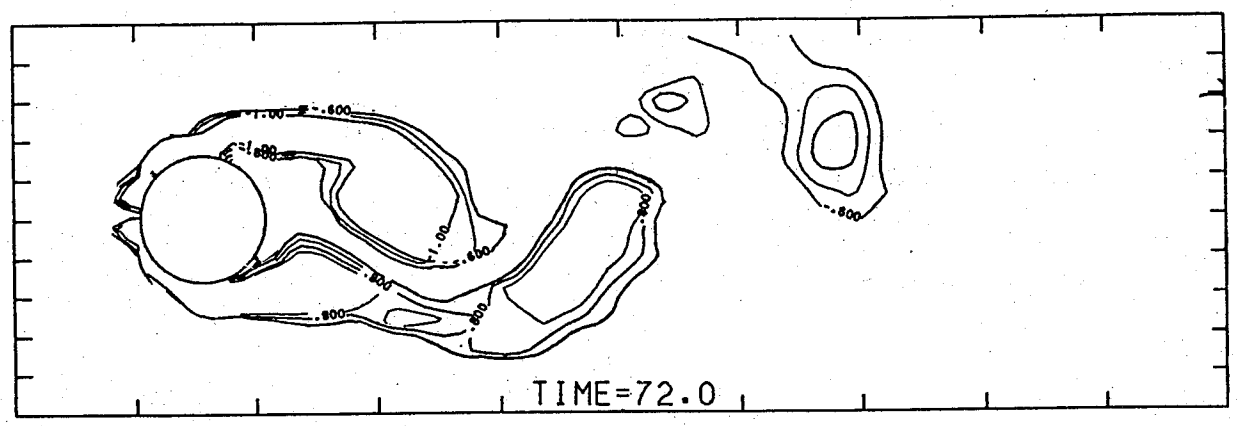

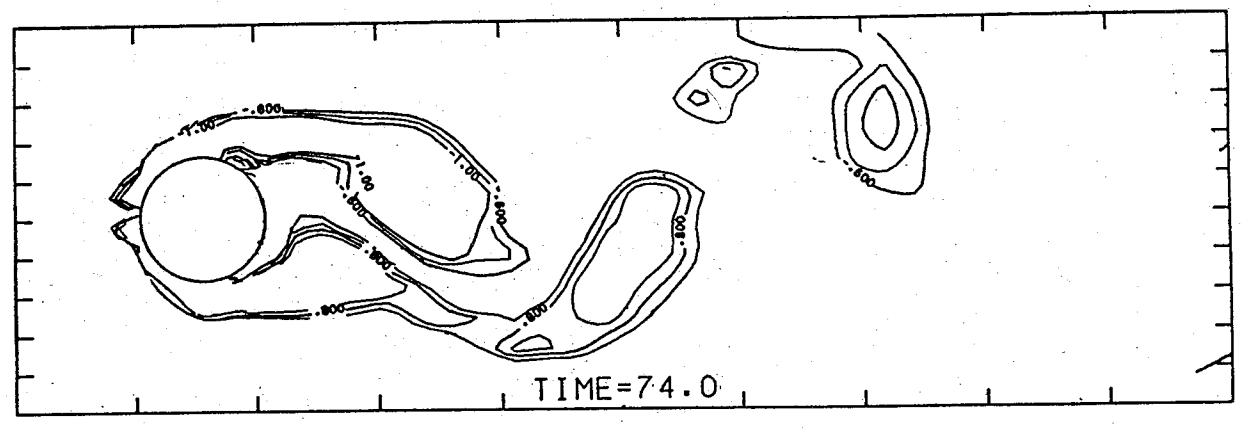

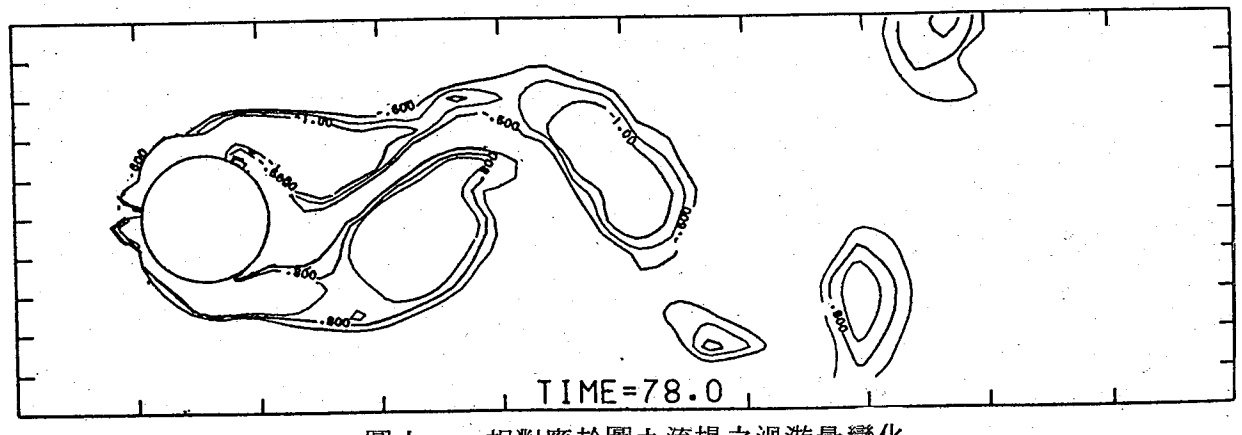

圖十一　相對應於圖九流場之渦漩量變化

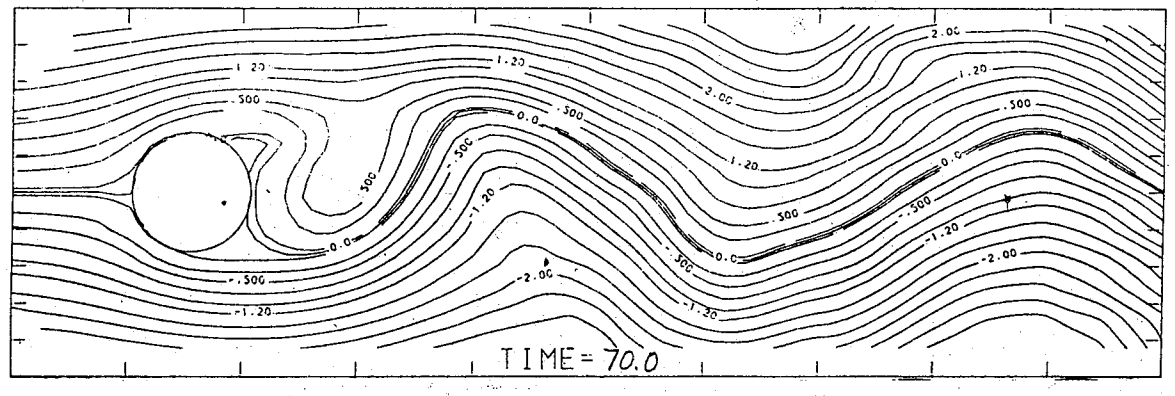

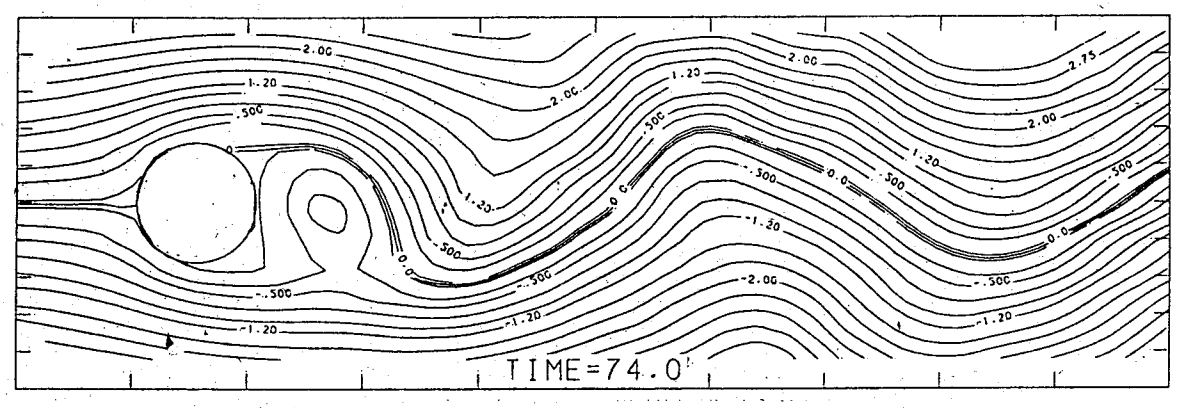

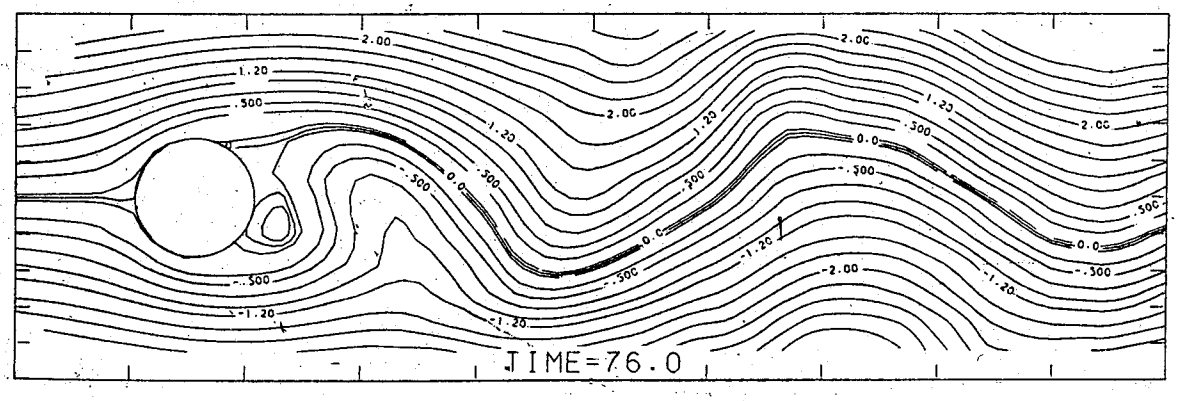

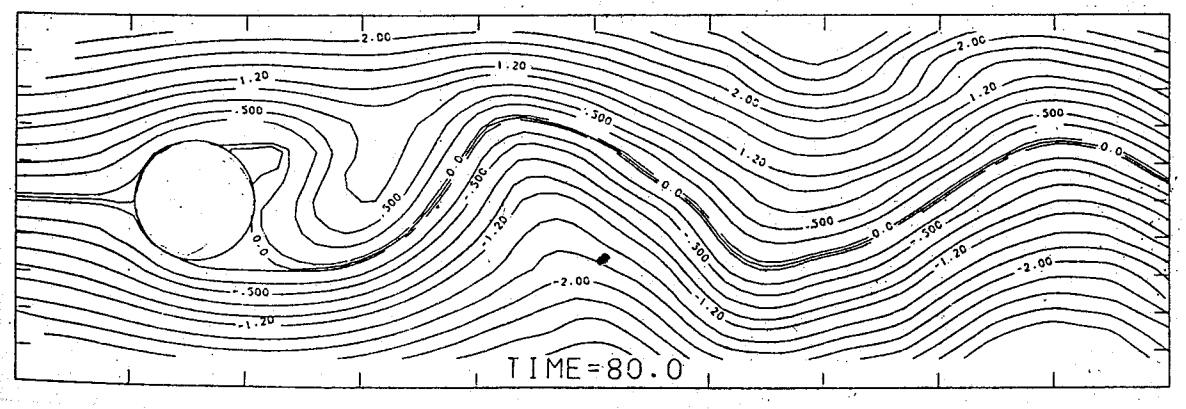

圖十二　R_e ＝500 流場渦漩分離週期中之流綫變化

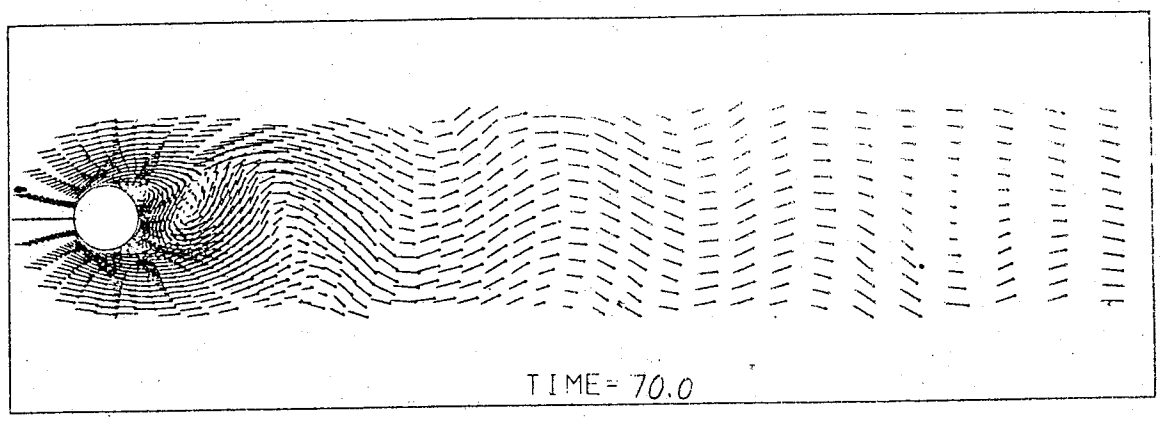

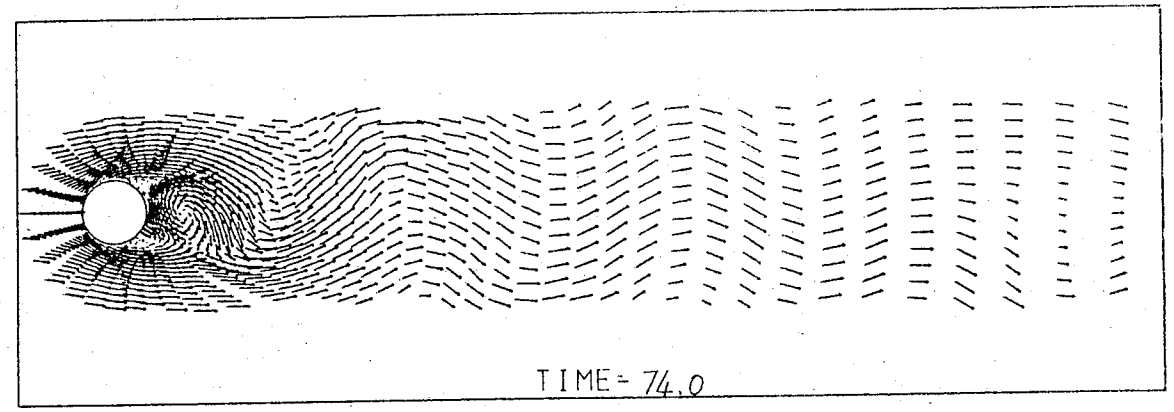

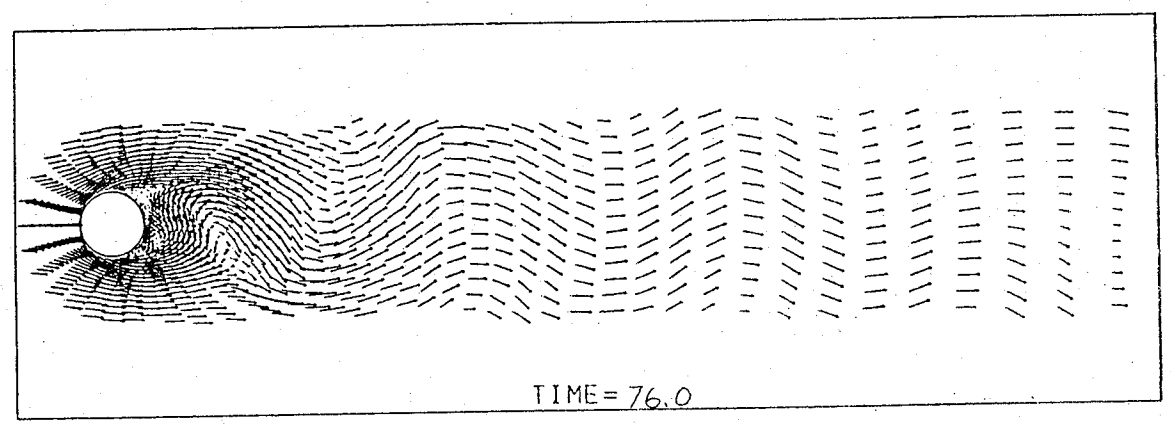

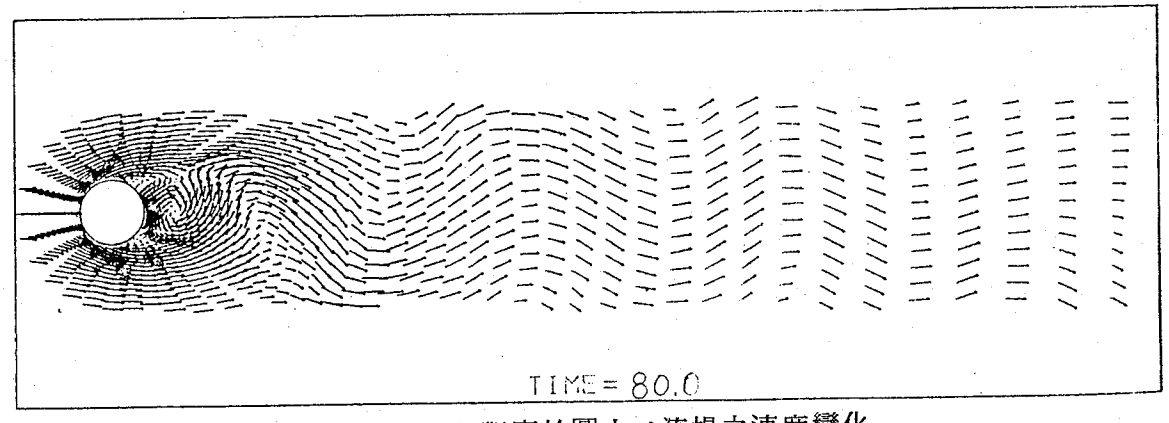

圖十三　相對應於圖十二流場之速度變化

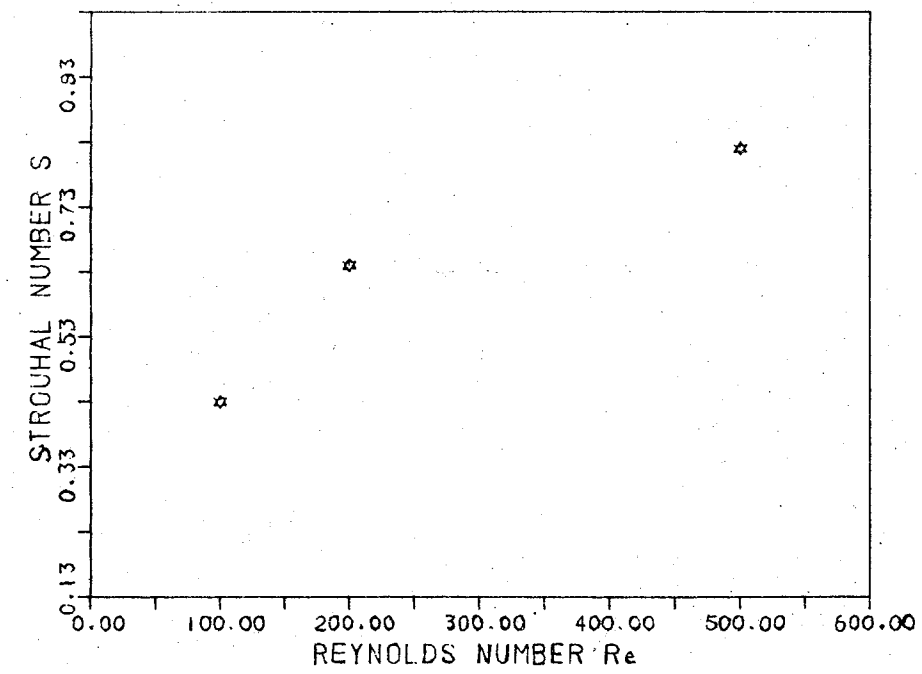

圖十四　流場R_e對渦漩分離頻率S之影響

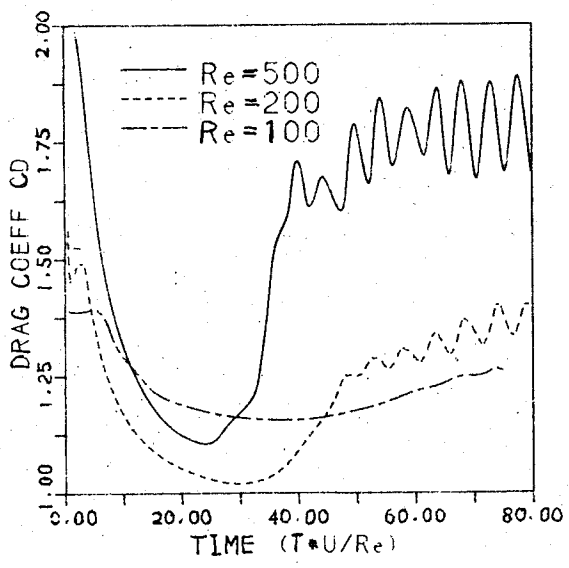

圖十五　(a)流場R_e對C_D之影響

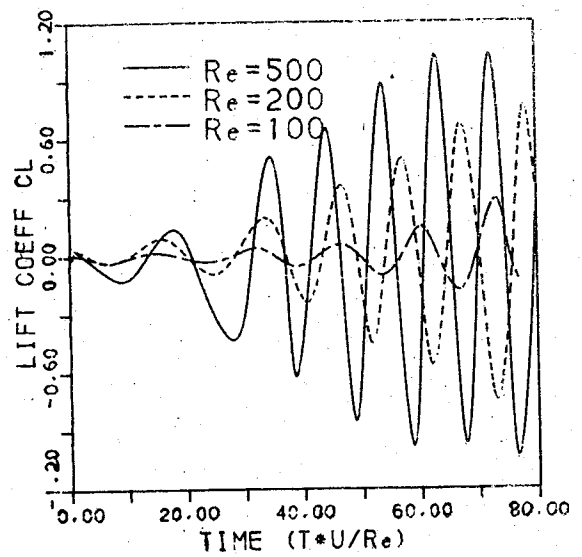

圖十五(b)　流場 R_e 對 C_L 之影響

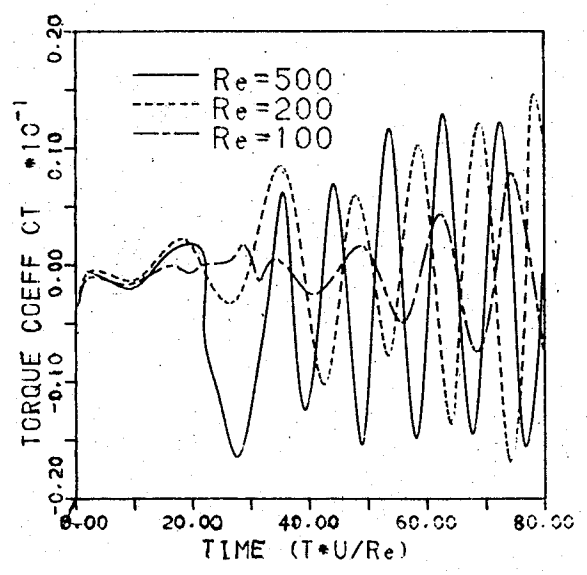

圖十五(c)　流場 R_e 對 C_T 之影響

圖十五　流場 R_e 對 C_D，C_L 及 C_T 之影響

紊流層變流中浮昇效應對尾流之影響

(Buoyancy Effect on Turbulent Wake After Flat Plate)

黃 榮 鑑

中央研究院物理研究所

台灣大學造船工程研究所

方　疇

中山科學研究院

摘　要

本文以紊流 K－ϵ 模式探討平板尾流在浮昇效應之影響下，所產生之物理現象。此種浮昇效應由流場中溫度層變所引發，與傳統的加熱平板所造成的浮昇效應完全不同，本文之控制方程式，包含連續方程式，動量方程式，能量方程式及紊流 K-ϵ 模式。利用有限差分法求得控制方程式之數值解，以了解流場中速度、溫度之變化，在結果中發現，穩定溫度層變對尾流的發展有抑制作用，長度尺度減少，平均速度減慢，紊流能量降低。而不穩定溫度層亦有相反的效果。

Abstract

In this essay, turbulence k-ϵ model together with Navier-Stokes equations, continuity equation and energy equation constitute governing equations. A numerical algorithm based on these equations was examined by using data from Chevray and Kovasnay and proved to be satisfactory. Discussions on mean velocity, temperature, length scale, Reynolds stress and turbulence kinematic energy were made for both stable and unstable stratification.

Results showed that, in general, stable stratification will induce damping effects in wake developement process while unstable amplifying. Both eddy viscosity and eddy conductivity are strongly related to stratification, and play a crucial roll in the process.

一、前　言

本文主要的目的在探討浮昇對流與尾流發展的關係。在以往的研究中，以圓柱體，平板等障礙物置於流場中，對障礙物以加熱或冷却的方式所產生的結果，不但在尾流區域內有浮昇效應，同時在物體邊界層內亦有浮昇對流，當後者隨流動帶入下游後，兩者作用混合，在下游由於溫度的變化造成一個不對稱的浮昇效應影響，如圖 1 所示。在這類流場中，浮昇效應的發生有兩個來源，來自上游的及尾流本身的。因而產生複雜的作用。爲了能探討浮昇效應在尾流區域內的獨立效應，而無上游的影響，因此假設一個絕緣平板，板上下的溫度分別控制，使之保持恒定，分別爲 Tu , Td。如圖 2 所示。在邊界層發展時，平板上下溫度因平板的絕緣性質可各自保持固定，所以沒有浮昇對流發生。離開平板後，從板尾端開始，尾流形成。此時溫度開始擴散，因爲溫度的變化浮昇對流引入尾流區域內。這種浮昇效應是單純的，穩定或不穩定層變。因此所得結果祇受單一的溫度層變效應控制，而沒有上游邊界層影響。

有關應用 K - ϵ 模式以模擬紊流特性的研究，較著名的爲 Launder et. al [1]的研究，由對 K－ϵ 模式原型式（ Exact Equation ）中各項的物理意義的了解，提出各項的模擬，並以數值分析對照各種實驗結果。對照的實驗包括均質流（ Homogeneous flow ），自由剪力流（ free shear flow ）及射流（ jet ）等，結論顯示，模式預測自由剪力流的能力最好，但在特別強或弱的應力區，由於壓力應變項模擬的缺陷或是實驗量測不準確，常造成較大誤差，文中並提出最佳係數以使模式與實驗最接近。

溫度層變所引發的浮昇對流最主要的是一種熱傳導現象，Launder [2] 針對紊流 K－ϵ 模式中雷諾應力傳輸式。（ Reynolds stress transport equation）及熱通量傳輸式（ heat flux transport equation）加入浮昇對流項後，重新檢討壓力應變項的模擬。

從事實驗的探討，研究紊流熱效應較早期的有 Webster [3] 所做的實驗。在風洞中加上穩定溫度層變，同時以網格產生均勻紊流，量測紊流動能的三個分量，雷諾應力，熱通量與理察森數之間的關係。在穩定層變垂直方向的紊流動能明顯的被壓抑，順流水平向的增加，而側流水平向的約與層變無關。被壓抑的垂直紊流動能在極端穩定時約是在均質流場的二分之一。從實驗中可知渦滯性係數（ eddy viscosity ）及渦熱導係數（ eddy conductivity ）與理察森數成反比，渦傳導係數約在 $R_f = 0.35$ 降爲零，也就是紊流熱傳導在極端穩定的情形下會停止。

另外 Alexoponlos et. al. [4] 亦有類似的實驗，研究被動的紊流熱效應。以一個線性的穩定溫度層變加於圓柱體後的實驗，量測尾流流場的紊流特性，所加的溫度層變爲 0.22 ℃ / cm，流場中典型的理察森數爲 0.005。因此浮昇對流被忽略，溫度視爲流場中被帶動的物質，結果顯示平均速度剖面與均質流場的相比幾乎相同，流場中心軸上平均速度及尾流長度尺度均與 $(X-X_0)^{1/2}$ 成正比，平均溫度剖面與溫度振動值均與

$K(\eta) = \eta^2 \exp(1-\eta^2)$ 成比例，而具有此種關係的相似剖面。

本文經由連續方程式，運動方程式及能量方程式組成的控制方程式，並利用 k－ϵ 紊流模式以模擬流場之紊流效應來探討浮昇效對尾流發展的影響。這組方程式以包氏近似法（ Boussinesq approximation ）將浮昇效應考慮進入運動方程式及 k－ϵ 模式中，並以邊界層假設簡化方程式組。以 ADI (altenative direction implicit) 的數值方法將方程組差分化並求得數值解。分別對穩定及不穩定溫度層變的流場進行探討，並以各種不同溫差及層變流場所獲得的結果，比較平均速度、長度尺度、中心軸速度、雷諾應力及熱通量之變化，從而獲得溫度層變在尾流發展中的影響。

貳、基本方程式

本文主要在探討溫度層變對尾流之影響，故主要流場在尾流區域。流體通過水平平板後，在板尾後方產生尾流，同時上、下溫度分別爲 Tu及 Td 。當流體通過平板時，溫度保持不變，因此浮昇效應由板尾端開始產生。以平板尾端爲原點，流場以此爲起點，向下游延伸，直至現象無顯著變化爲止。流場並向上下方延伸，以包含整個尾流。流場中採用卡氏座標， x 軸爲平板的延伸方向， y 軸爲垂直向上。流場以紊流現象爲主要控制因素並爲均勻重力場，同時流場在完全發展後，其平均量會保持穩定的狀態。經由 k－ϵ 模式以模擬紊流效應，並以邊界層理論簡化其方程組後，描述流場的控制方程式組可寫成下列形式：

熱通量：
$$-\overline{v\theta} = \left(\Upsilon t \frac{\overline{v}^2}{K}\right)\frac{K^2}{\epsilon}\frac{\partial T}{\partial y} = \left(\frac{0.3125}{1+0.25\,B}\frac{\overline{v}^2}{K}\right)\frac{K^2}{\epsilon}\frac{\partial T}{\partial y}$$

雷諾應力：
$$-\overline{uv} = \left(\nu_t \frac{\overline{v}^2}{K}\right)\frac{K^2}{\epsilon}\frac{\partial U}{\partial y} = \left(\frac{0.2}{1+0.0625\left(1+\frac{0.5}{\sigma_t}\right)B}\frac{\overline{v}^2}{K}\right)\frac{K^2}{\epsilon}\frac{\partial U}{\partial y}$$

浮昇力參數：
$$B = \beta g \left(\frac{K}{\epsilon}\right)^2 \frac{\partial T}{\partial y}$$

流普朗特數：
$$\sigma_t = 0.64\,\frac{1+0.2\,B}{1+0.0625\,B}$$

紊流動能分量：
$$\frac{\overline{u}^2}{K} = 0.93 + 0.4\,\frac{\beta g(-\overline{v\theta})}{\epsilon}$$

$$\frac{\overline{v}^2}{K} = 0.53 - 0.4\,\frac{\beta g(-\overline{v\theta})}{\epsilon}$$

$$\frac{\overline{w}^2}{K} = 0.53$$

浮昇力參數 β 表示浮昇力大小，溫度梯度愈大，浮昇力愈強，穩定層變時 $\frac{\partial T}{\partial y} > 0$ ，故 $B > 0$ ，反之， $B < 0$ 。因此 Υt 及 ν_t 在穩定層變流場與溫度梯度成反比，在不穩定層變與溫度梯度之絕對值成正比。在極端穩定或極端不穩定時，Υt 及 ν_t 之變化可利用通量理察森數（ flux Richardson number ）得到確定的結果，通量理察森數爲質點對浮昇力作用與紊流能量生成量之比，可度量浮昇對流大小[12]，在穩定層變時其值大於零。反之，小於零。其定義如下：

$$\frac{\partial U}{\partial x} + \frac{\partial v}{\partial y} = 0 \tag{1}$$

$$U\frac{\partial U}{\partial x} + V\frac{\partial U}{\partial y} = \frac{\partial}{\partial y}(-\overline{uv}) - \beta g \frac{\partial}{\partial x}\int_{-\infty}^{y}(T - Ts)\,dy + \frac{\partial}{\partial x}\overline{v}^2 \tag{2}$$

$$U\frac{\partial T}{\partial x} + V\frac{\partial T}{\partial y} = \frac{\partial}{\partial y}(-\overline{v\theta}) \tag{3}$$

$$U\frac{\partial k}{\partial x} + V\frac{\partial k}{\partial y} = \frac{\partial}{\partial y}\left(C_k \frac{K^2}{\epsilon}\frac{\partial k}{\partial y}\right) + \beta g\,\overline{v\theta} - \overline{uv}\frac{\partial U}{\partial y} - \epsilon \tag{4}$$

$$U\frac{\partial \epsilon}{\partial x} + V\frac{\partial \epsilon}{\partial y} = \frac{\partial}{\partial y}\left(C_\epsilon \frac{K^2}{\epsilon}\frac{\partial \epsilon}{\partial y}\right) + C_{\epsilon_1}\frac{\epsilon}{k}\left(-\overline{uv}\frac{\partial U}{\partial y}\right) + C_{\epsilon_3}\frac{\epsilon}{k}\beta g\,\overline{v\theta} - C_{\epsilon_2}\frac{\epsilon^2}{k} \tag{5}$$

邊界條件爲：

$U(y), V(y), T(y), K(y), \epsilon(y)$ 已知，當 $x = 0$

$$\frac{\partial}{\partial x}\{U, V, T, K, \epsilon\} = 0 \text{ ，當 } x \to +\infty$$

$$\frac{\partial}{\partial y}\{U, T, K, \epsilon\} = 0 \text{ ，當 } y \to \pm\infty$$

$$V\Big|_{y\to+\infty} = -V\Big|_{y\to-\infty}$$

利用 $k-\epsilon$ 模式以模擬流場的紊流效應，則控制方程式中各紊流項可由下列式子予以閉合：

$$-\overline{uv} = \frac{\frac{1-C_2}{C_1}}{1 + \frac{1-C_3}{C_1}\frac{1}{C_{1T}}\left(1 + \frac{1-C_{2T}}{\sigma_t}\right)B}\,\frac{k\overline{v}^2}{\epsilon}\frac{\partial U}{\partial y} \tag{6}$$

$$= \left(\nu_t \frac{\overline{v}^2}{k}\right)\frac{k^2}{\epsilon}\frac{\partial U}{\partial y} \tag{6,a}$$

$$-\overline{v\theta} = \frac{\frac{1}{C_{1T}}}{1 + \frac{1-C_{3T}}{C_{1T}C_\theta}B}\,\frac{k\overline{v}^2}{\epsilon}\frac{\partial T}{\partial y} \tag{7}$$

$$= \left(\Upsilon t \frac{\overline{v}^2}{k}\right)\frac{k^2}{\epsilon}\frac{\partial T}{\partial y} \tag{7,a}$$

$$\frac{\overline{v}^2}{k} = \left(\frac{2C_2}{3C_1} + \frac{2}{3}\frac{C_1 - 1}{C_1}\right) - \left(\frac{6 - 4C_3}{3C_1} - \frac{2}{3}\frac{C_2}{C_1}\right)\frac{\beta g(-\overline{v\theta})}{\epsilon} \tag{8}$$

$$B = \beta g \left(\frac{K}{\epsilon}\right)^2 \frac{\partial T}{\partial y} \tag{9}$$

$$\sigma_t = \frac{\nu_t}{\Upsilon t} = \sigma_{t_0}\,\frac{1 + \left(\frac{1-C_{3T}}{C_{1T}C_\theta} - \frac{1-C_3}{1-C_2}\frac{1-C_{2T}}{C_{1T}}\frac{1}{C_{1T}}\right)B}{1 + \frac{1-C_3}{C_1}\frac{1}{C_{1T}}B} \tag{10}$$

$$\sigma_{t_0} = \frac{\frac{1-C_2}{C_1}}{\frac{1}{C_{1T}}} \tag{11}$$

(9)式爲浮昇力參數，可代表浮昇力大小。σ_t 爲紊流普朗特數（ turbulence Prandtl number ），是渦滯性係數（ eddy viscosity ）與渦熱導係數（ eddy conductivity ）之比。σ_{t_0} 爲無溫度層變紊流普朗特數(6)—(11)式中各項常數，可由實驗結果檢驗得知，本文使用Launder et. al.[1], Launder[2]陳[5]之建議，分列如下：

$C_1 = 2.0$ ， $C_2 = C_3 = 0.6$ ， $C_{1T} = 3.2$ ， $C_{2T} = C_{3T} = 0.5$ ，

$C_\theta = 0.625$ ， $C\epsilon = 0.08$ ， $C\epsilon_1 = 1.44$ ， $C\epsilon_2 = C\epsilon_3 = 1.90$ ， $C_k = 0.09$

參、數值分析

本文以ADI法（ Alternative Direction Implicit method ）求得數值解，雖然ADI原用於求解時變問題（ transient problem ），但在方程組中加入時變項（即 $\frac{\partial U}{\partial t}$ ， $\frac{\partial k}{\partial t}$ ， $\frac{\partial \epsilon}{\partial t}$ ， $\frac{\partial T}{\partial t}$ ）後，求得穩定解（ steady state solution ）。因此依照雙向掃描原則[6, 7]將控制方程組化爲差分式。由於差分式單調而冗長，在此不另敍述[8]而只描述計算過程。

計算開始時，祇有在上游邊界各點變數爲已知，其步驟如下：

(1)輸入上游邊界條件。

(2)由x方向運動式計算下時段U值。

(3)由亂流動能傳輸式計算下時段 k 值。

(4)由消散率傳輸式計算下時段 ϵ 值。

(5)由能量方程式計算下時段 T 值。

(6)由連續方程式計算下時段 V 值。

(7)檢查每個因變數之變化量是否小於精度要求，若否由步驟 2 開始重覆。精度要求爲 $\frac{\max|f_{ij}^{n+1}-f_{ij}^{n}|}{\max|f_{ij}^{n+1}|}<\zeta$。

(8)達到精度要求，輸出結果，結束計算。

本文發展的計算程序專注於求得穩定解，因此並不考慮每一時段的收斂問題，非線性項之處理可以單純化，各方程式之間的關聯也減弱。相對的，建立的過程也較簡易。在不同的流況計算中，平均疊代（interation）125 次可獲得穩定解，每次疊代約需15秒（VAX/780）。

肆、結果與討論

4—1 模式測驗

本文模式的正確性以 R. Chevray 及 S.G. Kovasnay[9]的實驗結果作檢驗。其實驗爲量測均質，無壓力梯度流中平板尾流的各種紊流物理量，包括水平平均速度、長度尺度、雷諾應力及紊流動能分量。因爲他們的實驗符合本文所討論的流場狀況，所以各項數據可以很方便的應用於檢驗無溫度層變時模式的正確性。計算以平板尾端（Trailing edge）斷面上各項數據爲上游邊界條件。在 5 cm，20 cm，50 cm，150 cm 及 240 cm 等位置上的水平平均速度及雷諾應力的計算值與實驗值之比較如圖 3 及圖 4 所示。速度以自由流速度 U_0 爲速度尺度無因次化，y 軸座標以平板尾端動量厚度（momentum thickness）θ_0 無因次化，雷諾應力以速度尺度的平方無因次化，比較結果顯示紊流模式計算所得吻合性相當良好。

4—2 渦帶性係數及渦熱導係數（eddy viscosity and eddy conductivity）

將各係數之實驗值代入雷諾應力，熱通量及各項相關參數的代數式中可得如下結果

通量理察森數：
$$R_f=\frac{\beta g(-\overline{v\theta})}{-\overline{uv}\frac{\partial U}{\partial y}}$$

將 B 化爲 R_f 之函數，代入 Υt

$$B=\beta g\left(\frac{K}{\epsilon}\right)^2\frac{\partial T}{\partial y}$$

$$\Upsilon t=\frac{0.167-0.54R_f}{0.53-0.93R_f}$$

由上式可得 $R_{ferit}=0.31$ 時 $\Upsilon t=0$。很接近Webster[3]之結果，$R_{ferit}=0.35$。Turner[13]指出在穩定層變，質點抵抗浮昇力作功總是小於紊流能量之生成量，因此 R_f 不會達到 1，而且遠離此值。因此可期待在極端穩定的狀態下熱通量爲零，在極端不穩定時，取 $R_f\to-\infty$，可得 $(\Upsilon t)_{max}=0.58$，在流場達到平衡時，$\epsilon=-uv\frac{\partial U}{\partial y}+\beta g\,v\theta$ 代入紊流動能各分量中可得：

$$\frac{\overline{u^2}}{K}=0.93+0.4\frac{R_f}{1-R_f}$$

$$\frac{\overline{v^2}}{K}=0.53-0.4\frac{R_f}{1-R_f}$$

$$\frac{\overline{w^2}}{K}=0.53$$

由以上各式可以判斷，穩定浮昇對流增加 u^2 分量之比例，而其來源是從 $\overline{v^2}$ 分量取得，因此穩定層變對質點在垂直方向的運動有壓抑作用。但因 $R_f\ll1$，故各分量之變化爲有限值。在另一方面，取 $R_f\to-\infty$，可得如下結果：

$$\overline{u^2}:\overline{v^2}:\overline{w^2}=0.53:0.93:0.53$$

與 $R_f=0$ 時之比例比較，可知不穩定浮昇對流可促進垂直方向的動量傳遞。

$$\left(\frac{\overline{v^2}}{K}\right)_{max}=0.93$$

紊流普朗特數在穩定層變當 $R_f\to R_{ferit}$ 時，$\sigma_t\to\infty$。在不穩定層變可由下式探討。

$$\sigma_t=0.64\frac{\Upsilon t\frac{\overline{v^2}}{K}-(\Upsilon t\frac{\overline{v^2}}{K}-0.2)R_f}{\Upsilon t\frac{\overline{v^2}}{K}-(\Upsilon t\frac{\overline{v^2}}{K}-0.0625)R_f}$$

取 $R_f\to-\infty$，$(\sigma_t)_{max}=0.46$。另外 $R_f=0$ 時，$\sigma_{t_0}=0.64$，爲均質流場紊流普朗特數。ν_t 在穩定層變時，無臨界值，但將 ν_t 轉換成下式後可得最大值。

$$\nu_t=0.2-0.03125\frac{R_f}{1-R_f}\frac{K}{\overline{v^2}}-0.0625\sigma_t\frac{R_f}{1-R_f}\frac{K}{\overline{v^2}}$$

取 $R_f\to-\infty$，$(\nu_t)_{max}=0.26$。

4 — 3　平均速度與尾流長度尺度

圖 5 至圖 8 顯示不同溫差的穩定層變，各水平平均速度的分佈情形。它們並與均質流場作比較。當溫差加大時，平均速度亦開始減少，同時可比較出速度剖面中缺陷的部分比均質流場的凹入現象漸趨明顯。這種現象可由(2)式，動量式中找到答案。(2)式中右側浮昇力項 $-\beta g \frac{\partial}{\partial x}\int_{-\infty}^{y}(T-Ts)\,dy$ ，在考慮溫度層變隨流動變化之後，如圖 2，以整個過程而言，在穩定層變時此項爲負值，在不穩定層變爲正值，若將浮昇力項與 $-\frac{1}{\rho}\frac{\partial p}{\partial x}$ 互相比擬，穩定層變相似於流場中有一正向壓力梯度作用，而不穩定則爲負，因此在穩定層變作用下水平平均速度會減少，而不穩定增加，圖 9 及圖10爲不穩定層變的平均速度分佈圖與上面的推論有相符的結果。隨著溫差的增加及距離的增加，浮昇對流越來越強，速度的變化越明顯。在穩定層變流場中，速度剖面有凹入的現象，尾流的區域也縮小。顯示穩定溫度層變不只是類似正向壓力梯度的效果，同時也抑制尾流的發展。在不穩定溫度層變，情形剛好相反，速度增加，範圍擴大。

平均速度的變化也可用中心軸速度剖面表達，見圖 11，與前述現象有一致的結果。另外如圖12所示，尾流長度尺度可表現尾流被壓抑或增加的情形。其變化約與溫差成比例。在 $dT=-20$ ℃時，圖 10 發現平均速度不規則現象。一個合理的解釋是不穩定層變會增加紊流的程度，強烈的混合作用可使原本小尺度的渦流擴大。較大的溫差引發更大尺度的渦流時，垂直方向的運動將會與水平方向的同等重要。在本文理論推演的過程中所做邊界層假設的限制下垂直速度將祇能維持一個次要的量。因此本文的模式在這方面遭遇最大的限制。

4 — 4　溫度分佈、雷諾應力與熱通量

圖13至圖16顯示不同溫度及層變時溫度分佈的情形，圖中溫度以溫度尺度 T_0 無因次化後減去 1 以放大溫度的變化。一般而言，溫度以紊流擴散的方式變化。其中圖 24，$dT=-20$ ℃時，溫度也有如同速度的不規則情形出現顯示溫度也受較大尺度渦流影響。因之可預期，雷諾應力與熱通量有相似的現象發生。圖17比較穩定層變流場中的雷諾應力的變化。圖中雷諾應力以速度尺度的平方無因次化，由於壓抑的效果，使應力也減少。圖18比較不穩定層變流場中的情形。應力有增強的趨勢，在 $dT=-20$ ℃時，有類似平均速度，溫度的波動現象發生。

熱通量的變化可見於圖19至圖22，圖中熱通量以速度尺度、溫度尺度無因次化。在不同層變及溫差之間除了數值上的差別外，有相同的趨勢。在上游熱通量最強，但範圍最小，漸向下游熱通量減小，範圍增大，與溫度的梯度及擴散的範圍有吻合的關係。在下游的熱通量分佈曲線漸趨平緩，其對溫度造成的影響可從線性化的能量方程式得知。

$$U_0\frac{\partial T}{\partial x}=\frac{\partial}{\partial y}(-\overline{v\theta})$$

若 $\frac{\partial}{\partial y}(-\overline{v\theta})=0$，則 $\frac{\partial T}{\partial x}=0$ 。因此溫度的分佈將維持穩定從圖13至圖16中可證實這個結果。

4 — 5　紊流動能及消散率

紊流動能及消散率與前面所討論各項物理量有相同的變化。在穩定層變流場中，動能及消散率均減小，見圖23及圖24。反之，在不穩定層變時則爲增加，見圖25及圖26。圖中紊流動能及消散率均已無因次化，紊流動能及消散率的分佈曲線均有峯值出現於尾流長度尺度的位置（比較圖12），雷諾應力分佈曲線也有類似的情形。

這個結果可以證明在級序分析中引用這個尺度是正確的。

伍、結　論

當尾流向下游發展時，紊流能量的生成量減少，使浮昇對流有機會佔優勢。以通量理察森數可說明浮昇對流的變化，又因穩定層變有 $R_{f\,crit}$ 存在，值得提出特別討論。圖 27 是 R_f 在穩定層變流場中之變化。從圖中可知 R_f 愈往下游愈大，顯示浮昇對流逐漸控制流場。再對照熱通量分佈（圖 21 及 22 ）以後可知極端穩定的流況並未發生，浮昇對流在尾流中心區域以最大可能的方式發生。又由於尾流的對稱特性，中心軸上的紊流能量的生成量必爲零，而浮昇力却總是存在，因之浮昇對流是從中心軸開始生成，逐漸向外擴大影響範圍。浮昇對流是一種局部性（ Local ）的現象，需要由速度梯度，溫度梯度雷諾應力及熱通量之間巧妙的平衡才能決定。由於尾流區域外 $\sigma_{t_0}=0.64$，因此溫度的擴散較快。因之 R_f 在尾流邊緣有上昇的現象。

穩定層變對各項物理量均有衰減作用，抑制了尾流的發展。但同時由於發展的緩慢尾流會在較長而窄的範圍內存在。不穩定層變則有相反的作用，促進尾流的發展，可使之在較短的距離內消失。

本文所討論的尾流發展過程在邊界層假設的限制下，浮昇對流所引發的垂直方向運動小於水平方向的，因此無法涵蓋從無浮昇對流到浮昇對流控制流場的整個範圍。雖然如此，討論浮昇效應的主要影響已經完成。更進一步的探討，如渦流、內波的發生，則需取消邊界層假設來改進模式，以使垂直方向與水平方向的運動有等量的考慮。

參考文獻

1. Launder, B. E., Reece, G. J. and Rodi, W. 1975 : Progress in the development of a Reynolds - stress turbulence closure, J. Fluid Mechanics 68, 537-566.
22. Launder, B. E. : 1975 : On the effect of a gravitational field on the turbulent transport of heat and momentum, J. Fluid Mech 67, 569-581.
3. Webster, C A. G. 1965 : An experimental study of trubulence in a density - stratified shear flow, J. Fluid Mech. 19, 221-245.
4. Alexopoulos, C. C. and Keffer, J. F. 1971 : Turbulent wake in a passively stratified field, Physics of Fluids 14. 216-224.
5. Chen, C. J. 1983 : Turbulence modelling and its applications, manuscript.
6. Rodi, W. 1980 : Turbulence Models and Their Applications in Hydraulics, IAHR Publications.
7. Roache, P. J. 1972 : Computational Fluid Dynamics, Hermosa Publishers, 64-69 and 91-99.
8. Taylor, T. D. and Peyret, R 1983 : Computational Methods for Flnid Flow, Springer-Verlag New York Inc., 66-75.
9. 黃榮鑑，1985：溫度層變對紊流平板尾流之影響，國科會研究計畫研究報告 FM 303 。
10. Chevray, R. and Kovasnay, S. G. 1969 : Turbulence measurements in the wake of a thin flat plate, AIAA J. 7, 1641-1643.

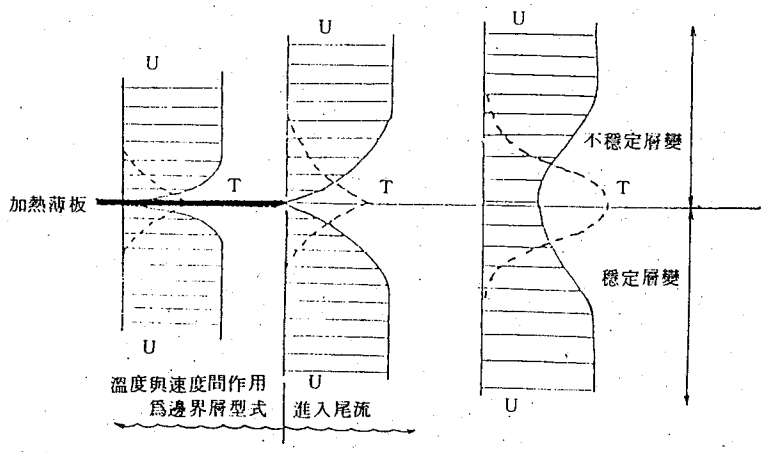

圖 1　非對稱溫度層變尾流流場

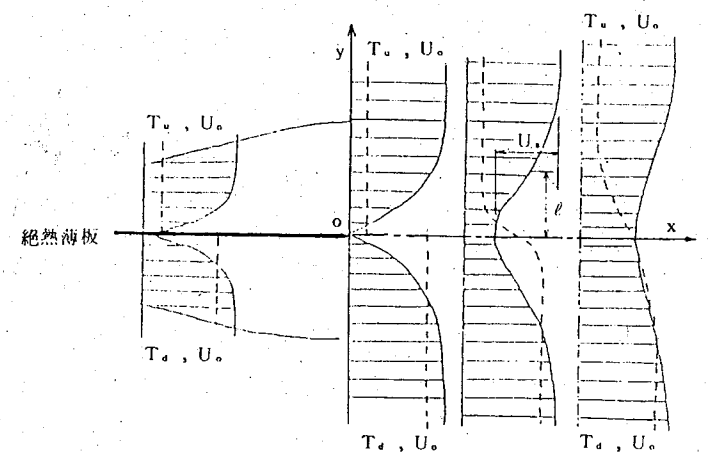

圖 2　本文所討論的溫度層變尾流流場

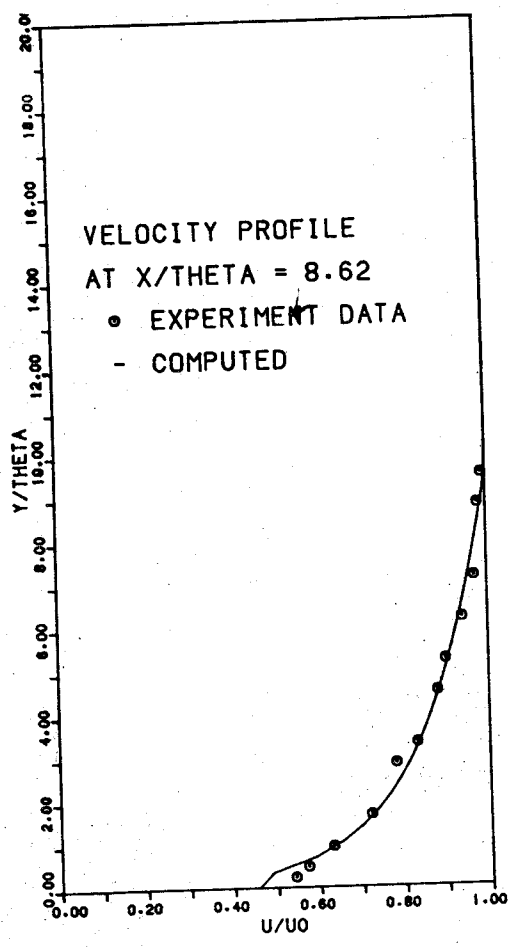

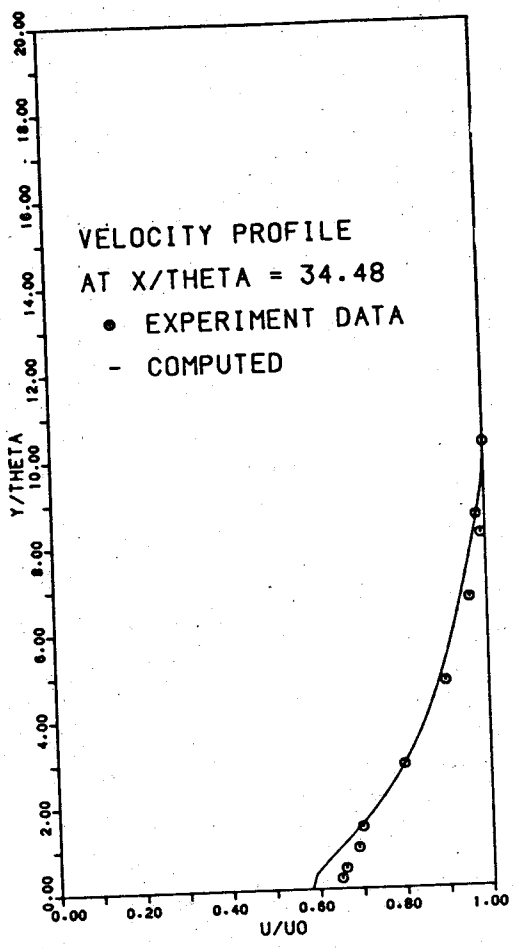

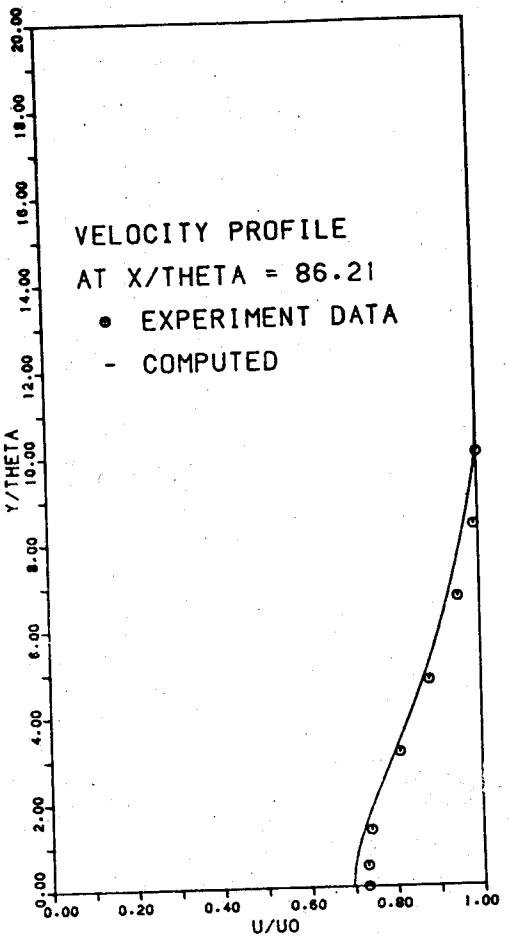

圖 3　水平平均速度計算值與實驗值比較

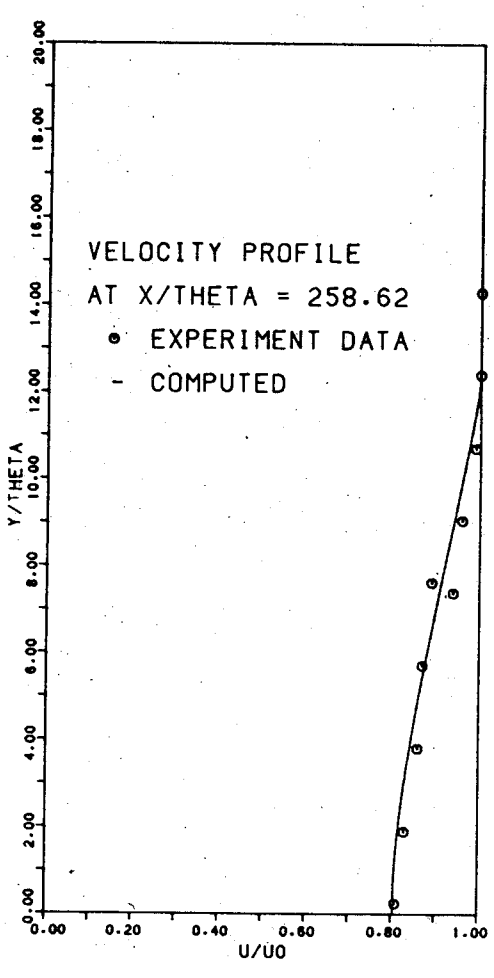

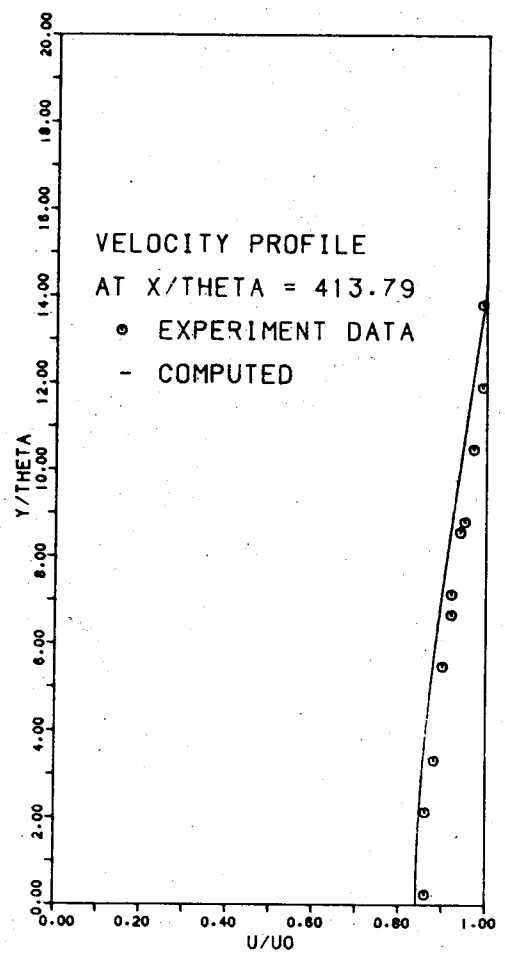

圖 3　水平平均速度計算值與實驗值比較（續）

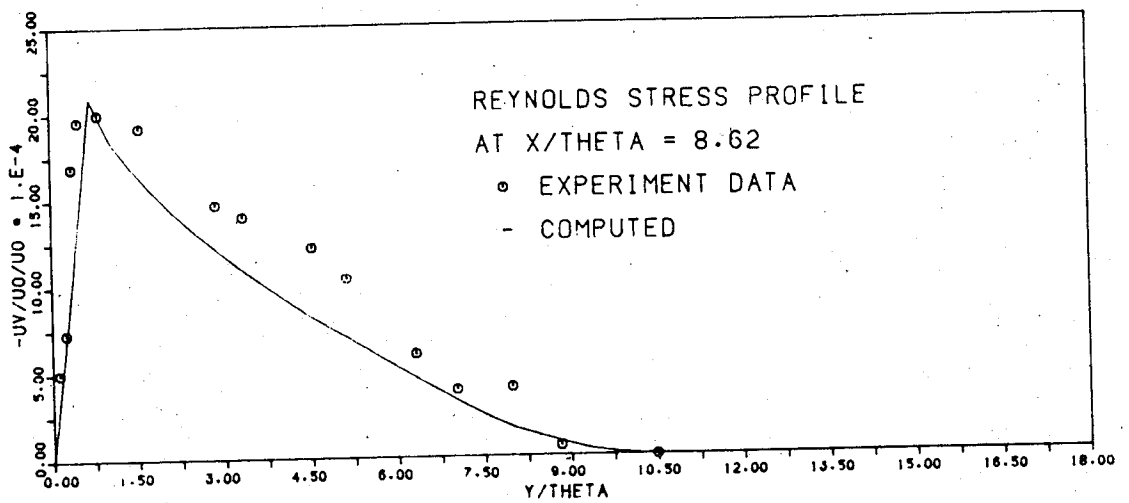

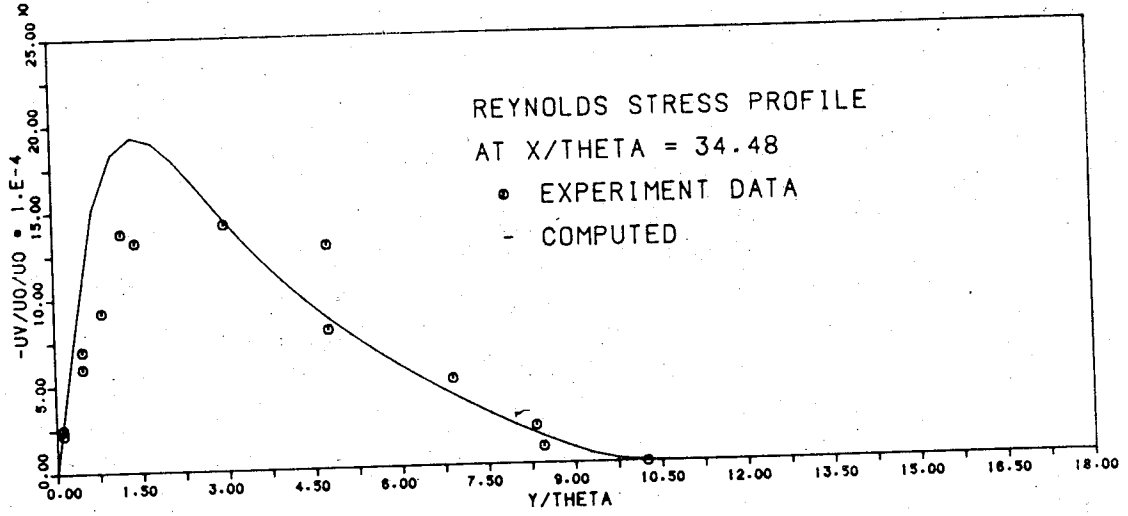

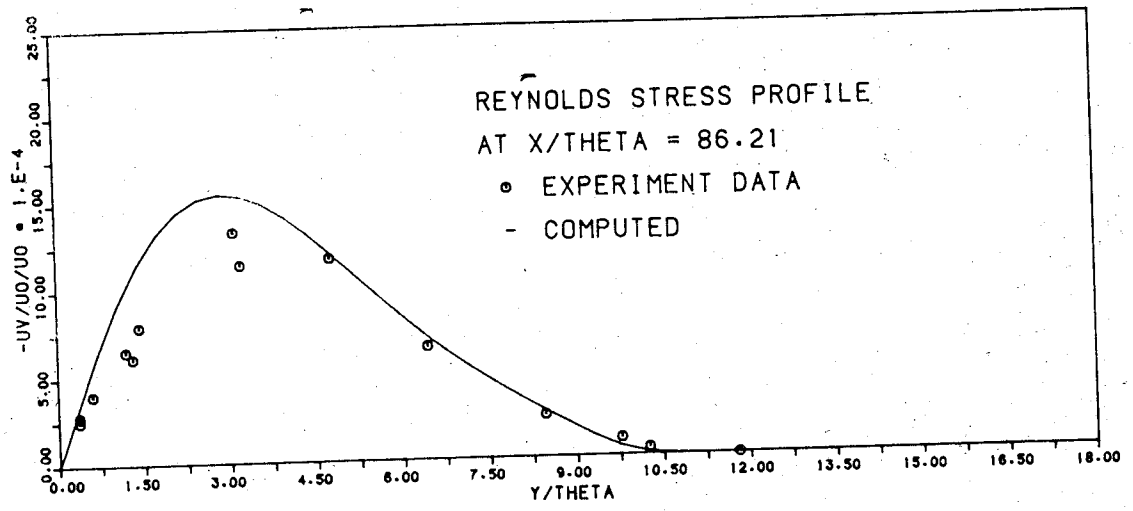

圖 4　雷諾應力計算值與實驗值比較

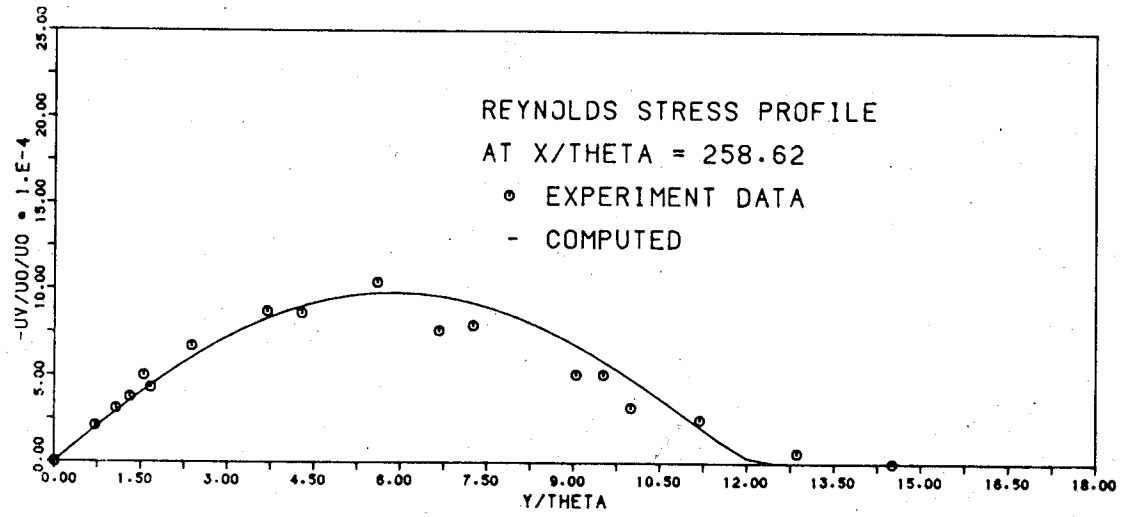

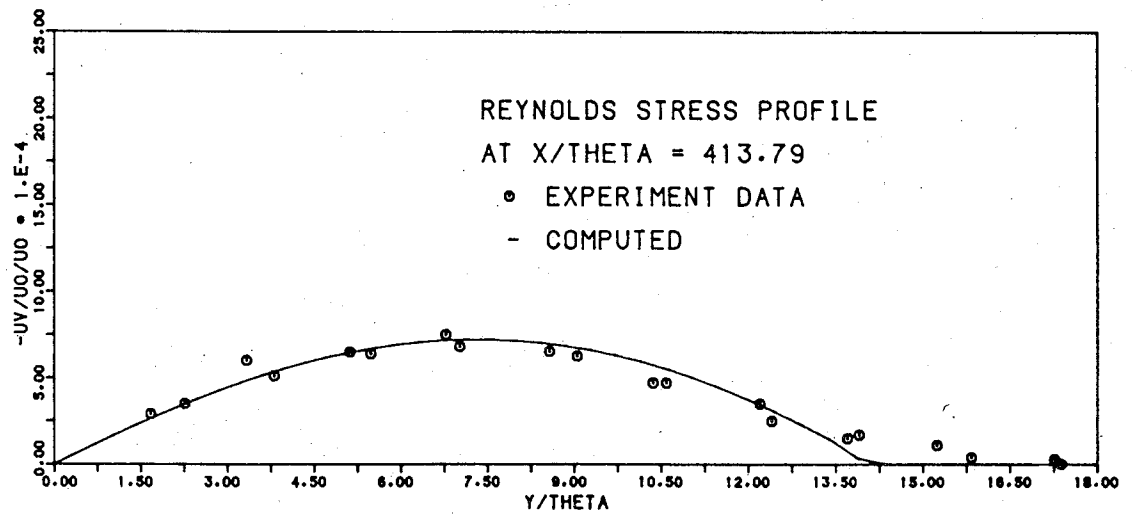

圖 4　雷諾應力計算值與實驗值比較（續）

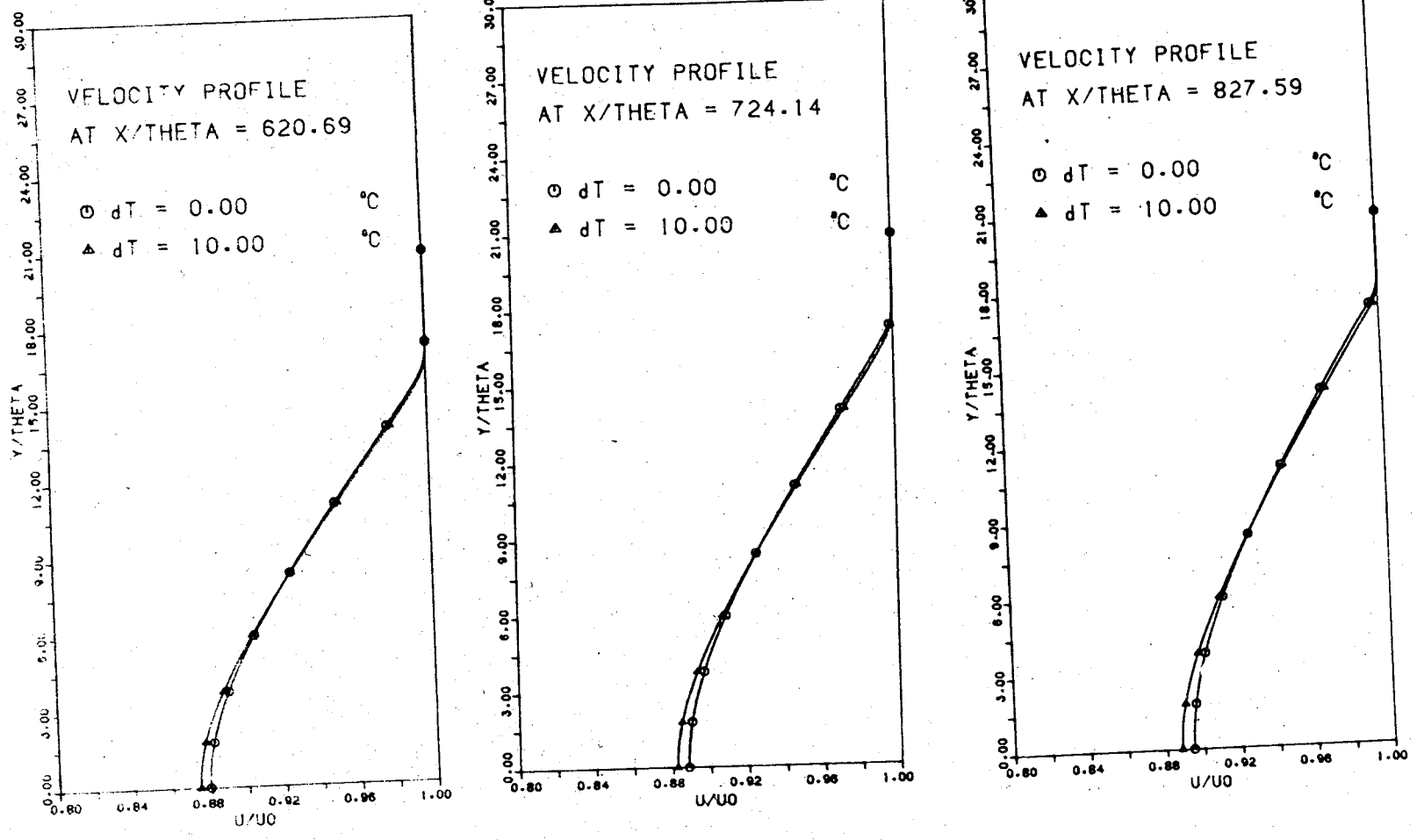

圖 5　穩定層變（dT = 10 ℃）與均質流場水平平均速度之比較

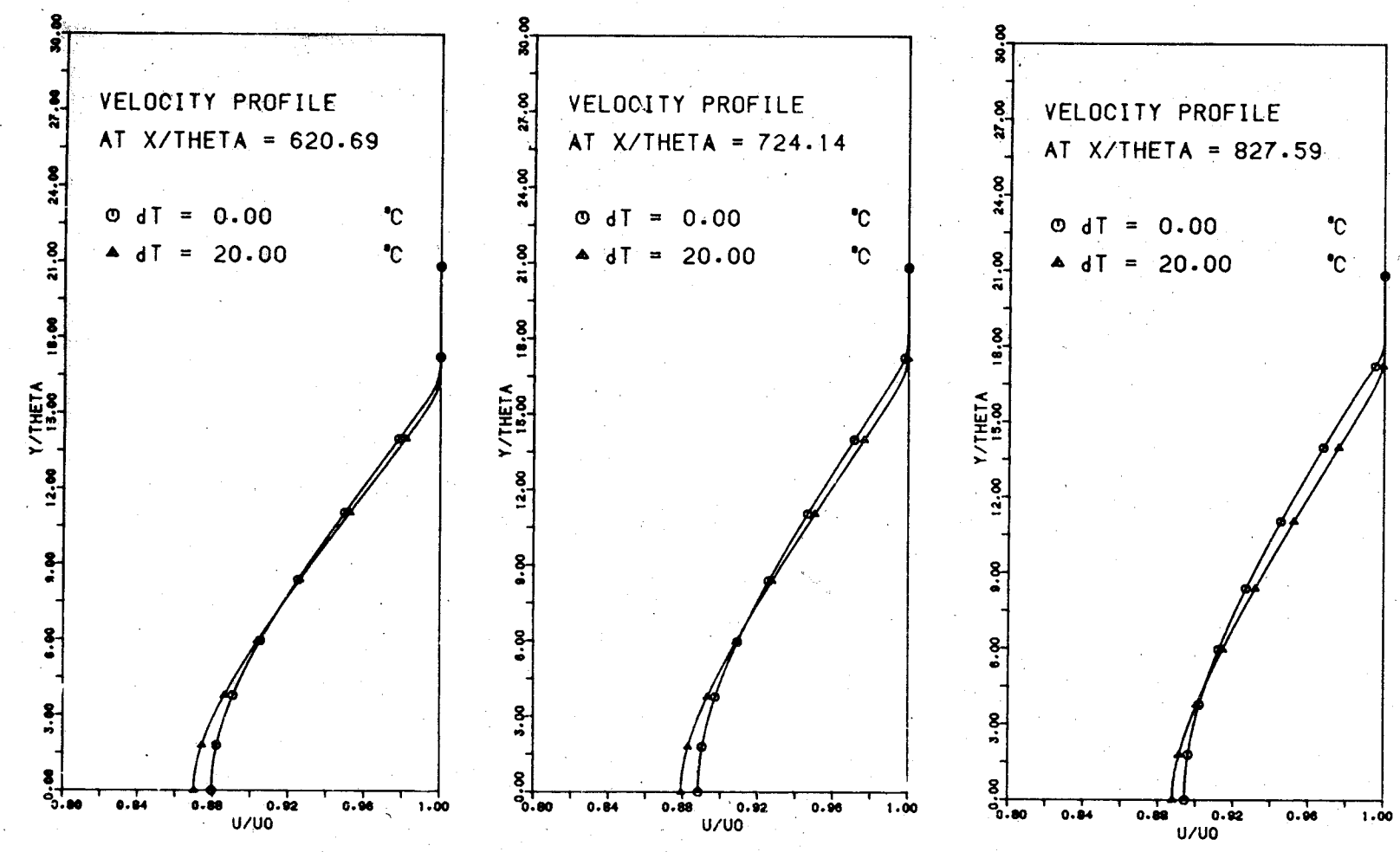

圖 6　穩定層變（dT = 20 ℃）與均質流場水平平均速後之比較

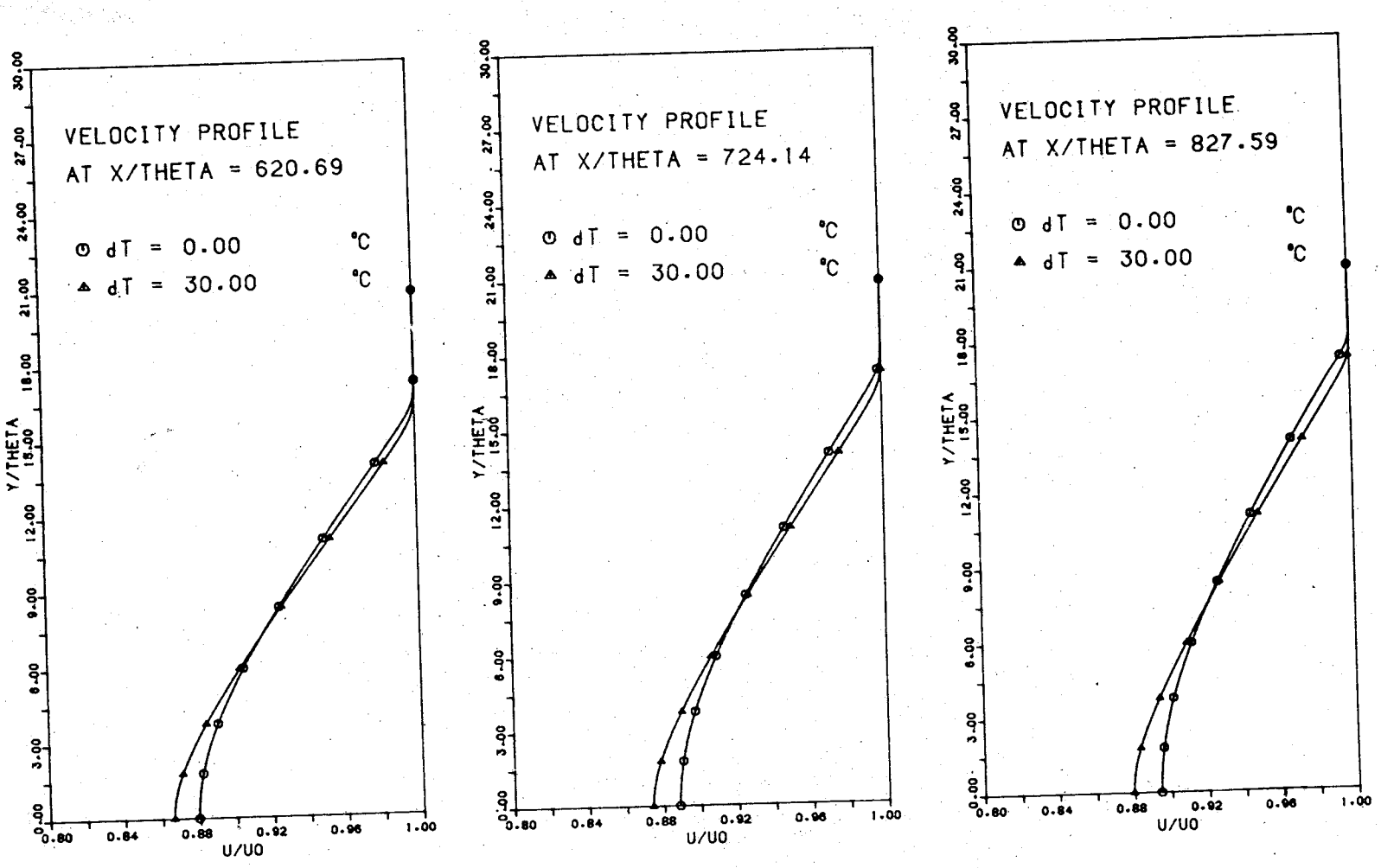

圖 7　穩定層變（ d T = 30 ℃ ）與均質流場水平平均速度之比較

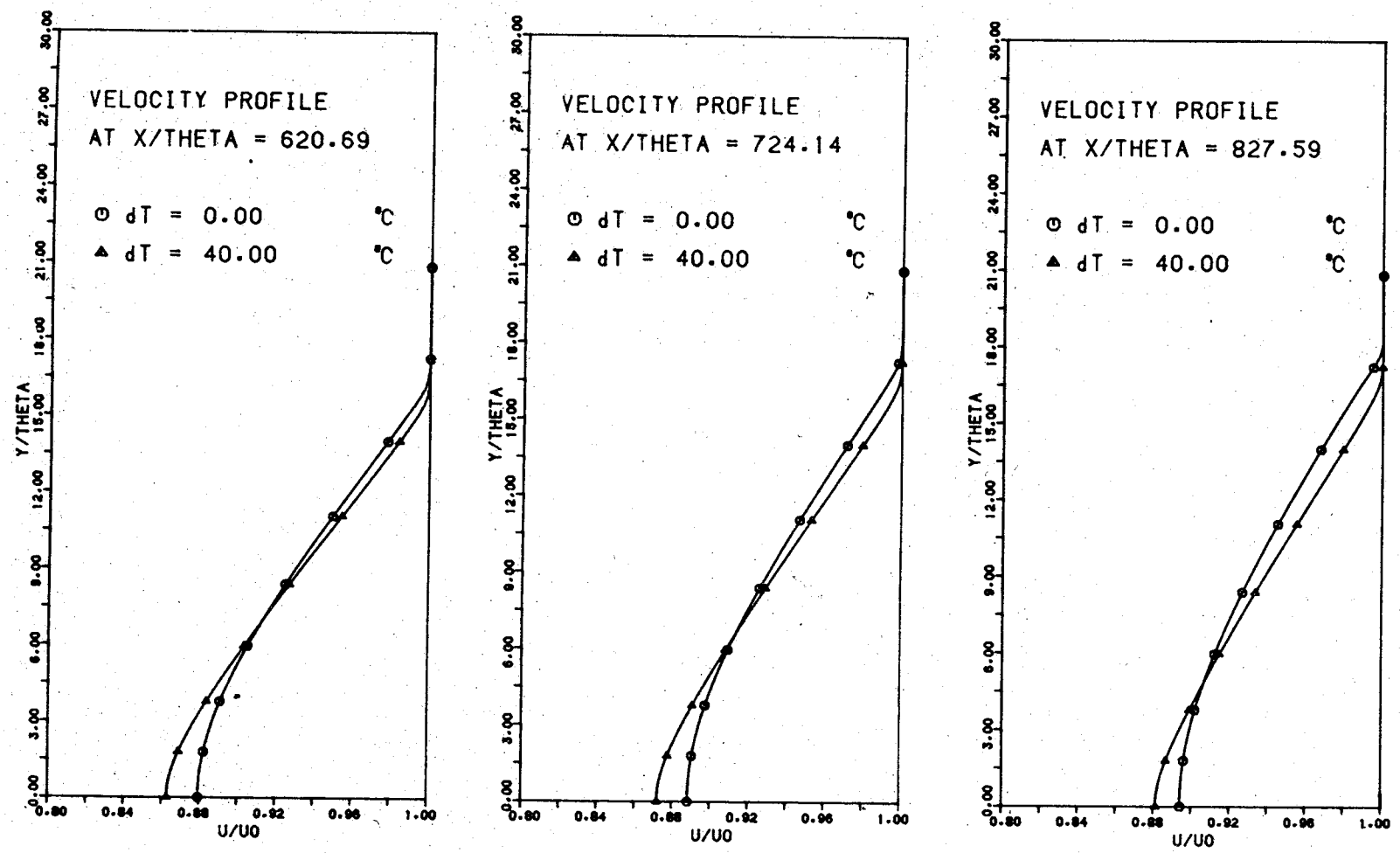

圖 8　穩定層變（ d T = 10 ℃ ）與均質流場水平平均速度之比較

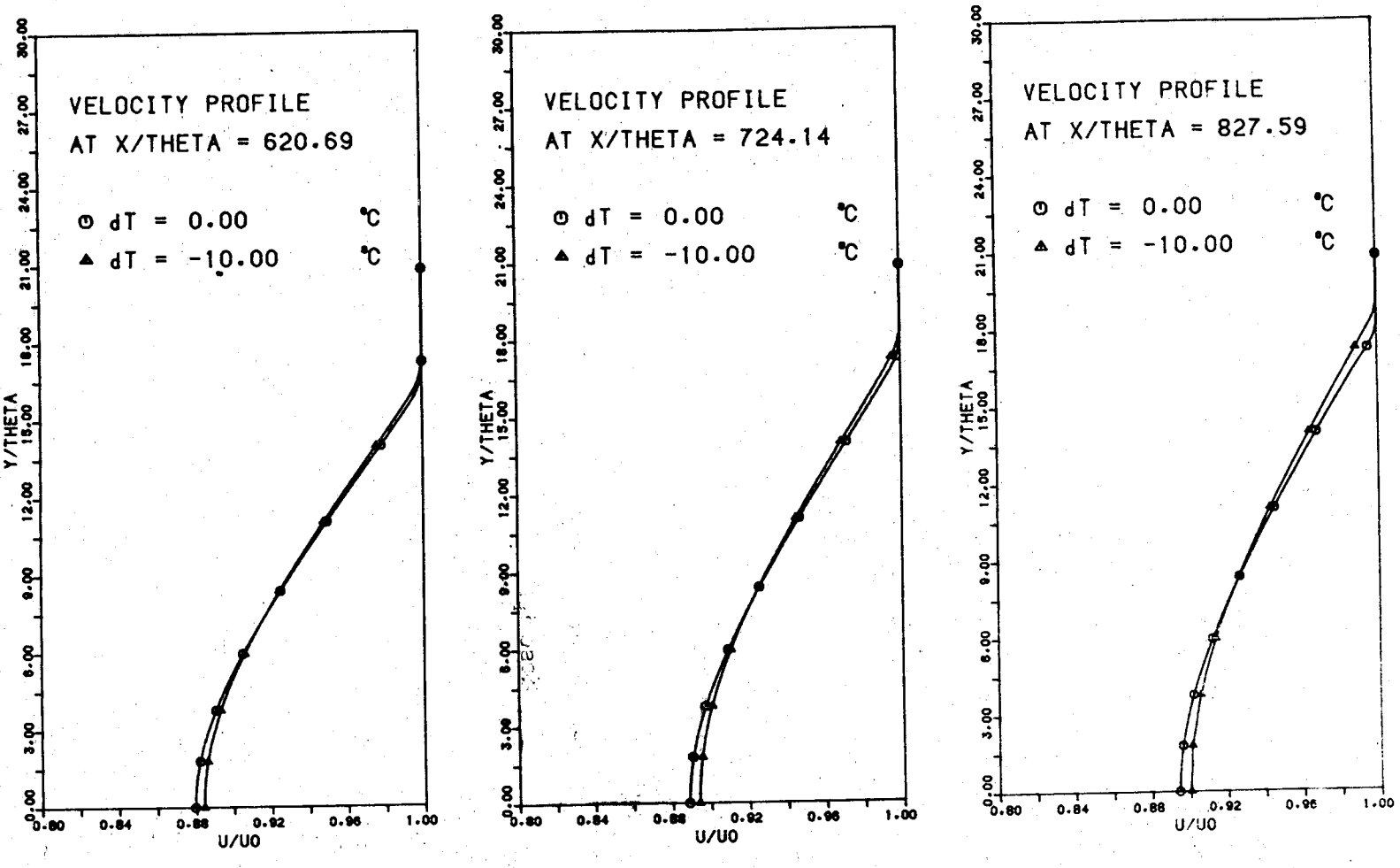

圖 9　不穩定層變（dT＝－10℃）與均質流場水平平均速度之比較

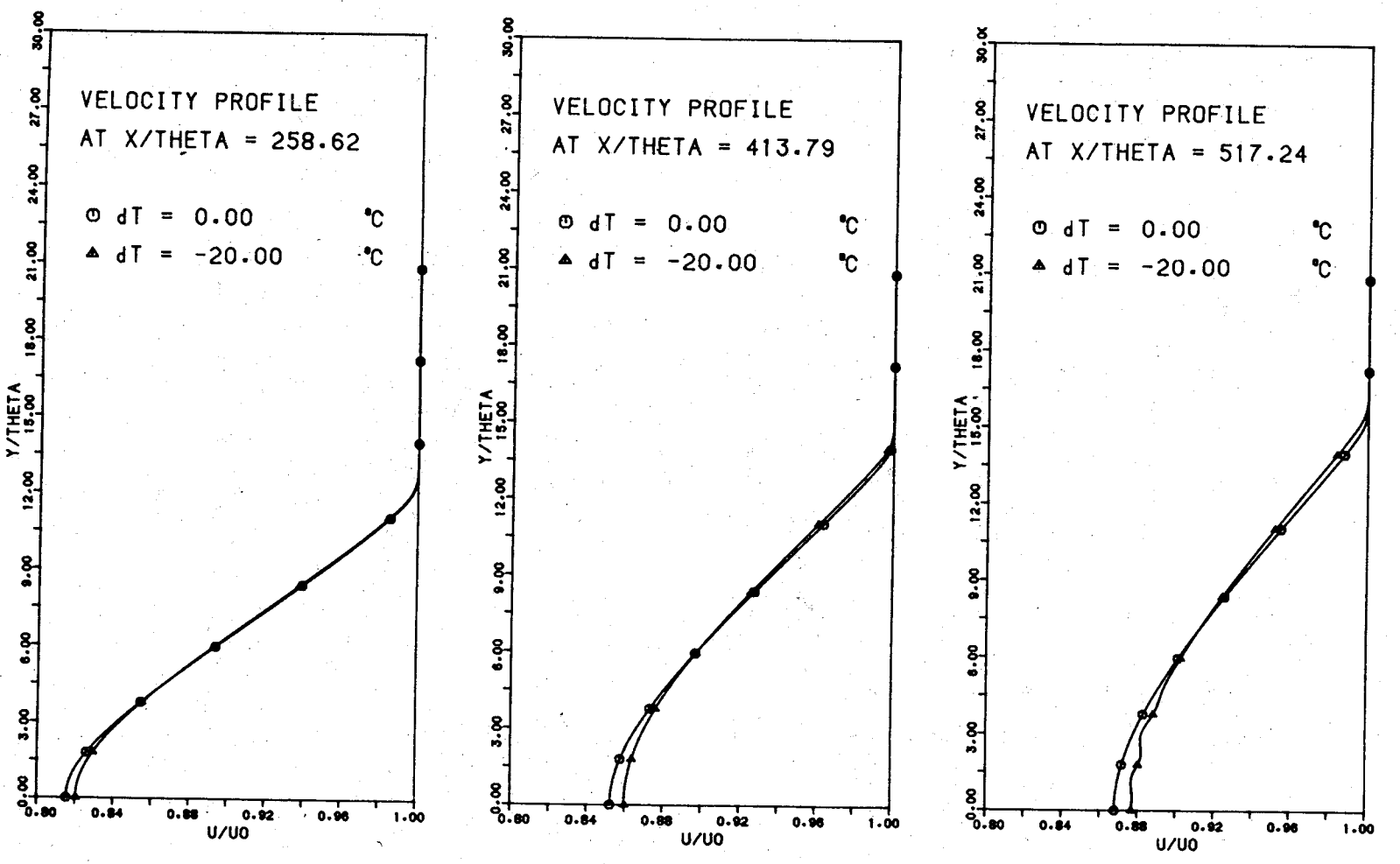

圖 10　不穩定層變（dT＝－20℃）與均質流場水平平均速度之比較

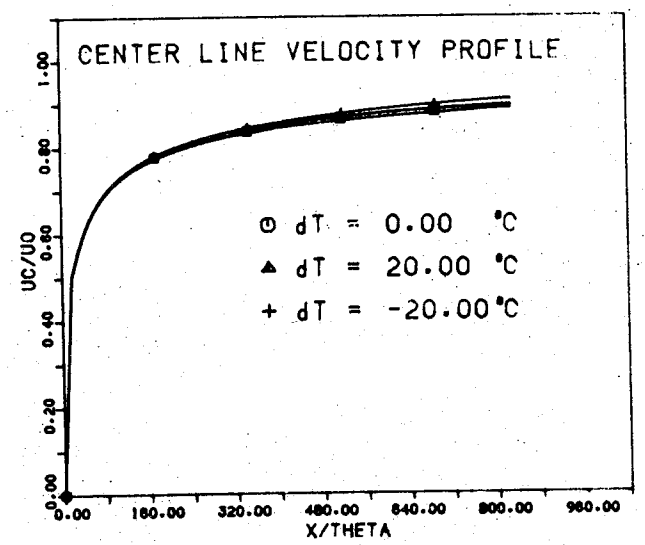

圖 11　中心軸速度剖面

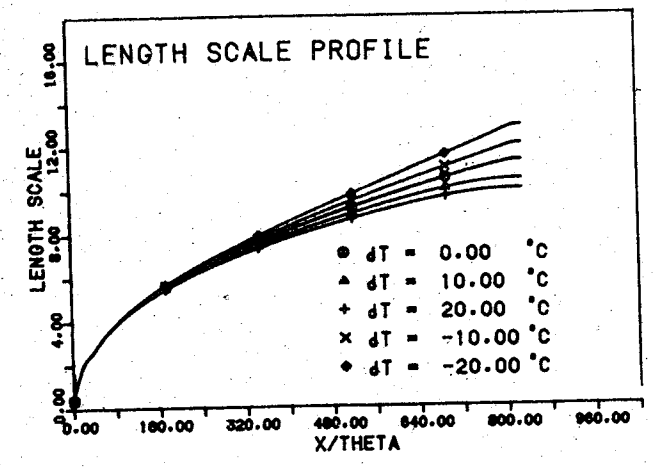

圖 12　尾流長度尺度變化

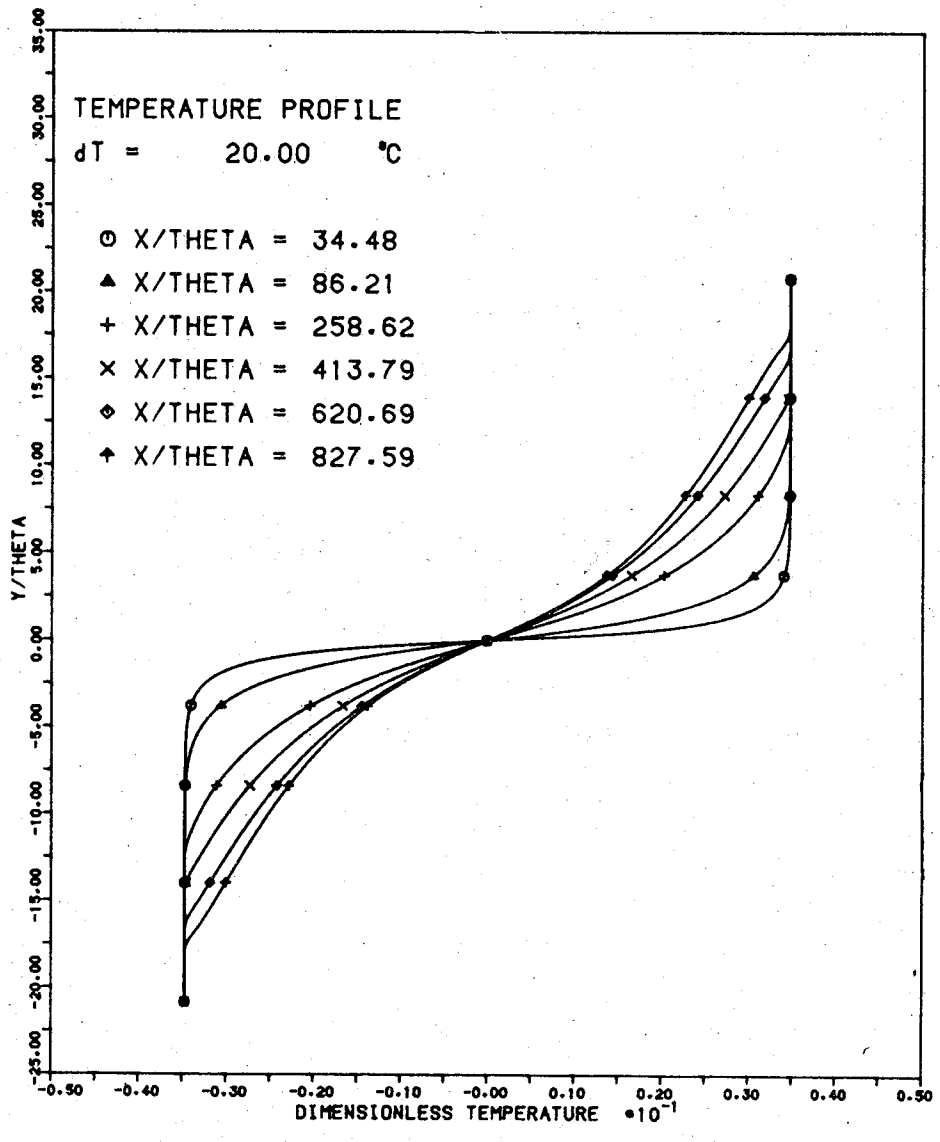

圖 13　穩定層變（ dT = 20 ℃ ）溫度分佈

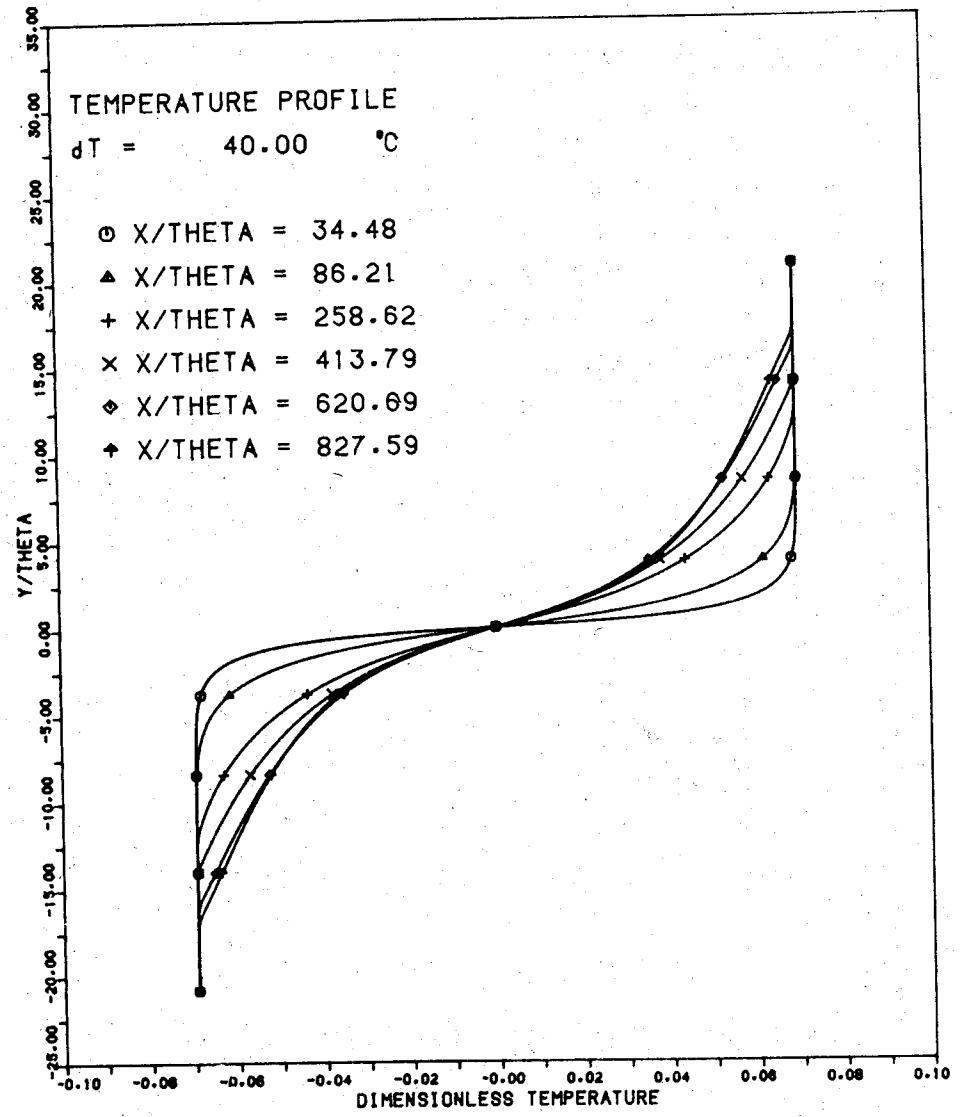

圖 14　穩定層變（ dT = 40 ℃ ）溫度分佈

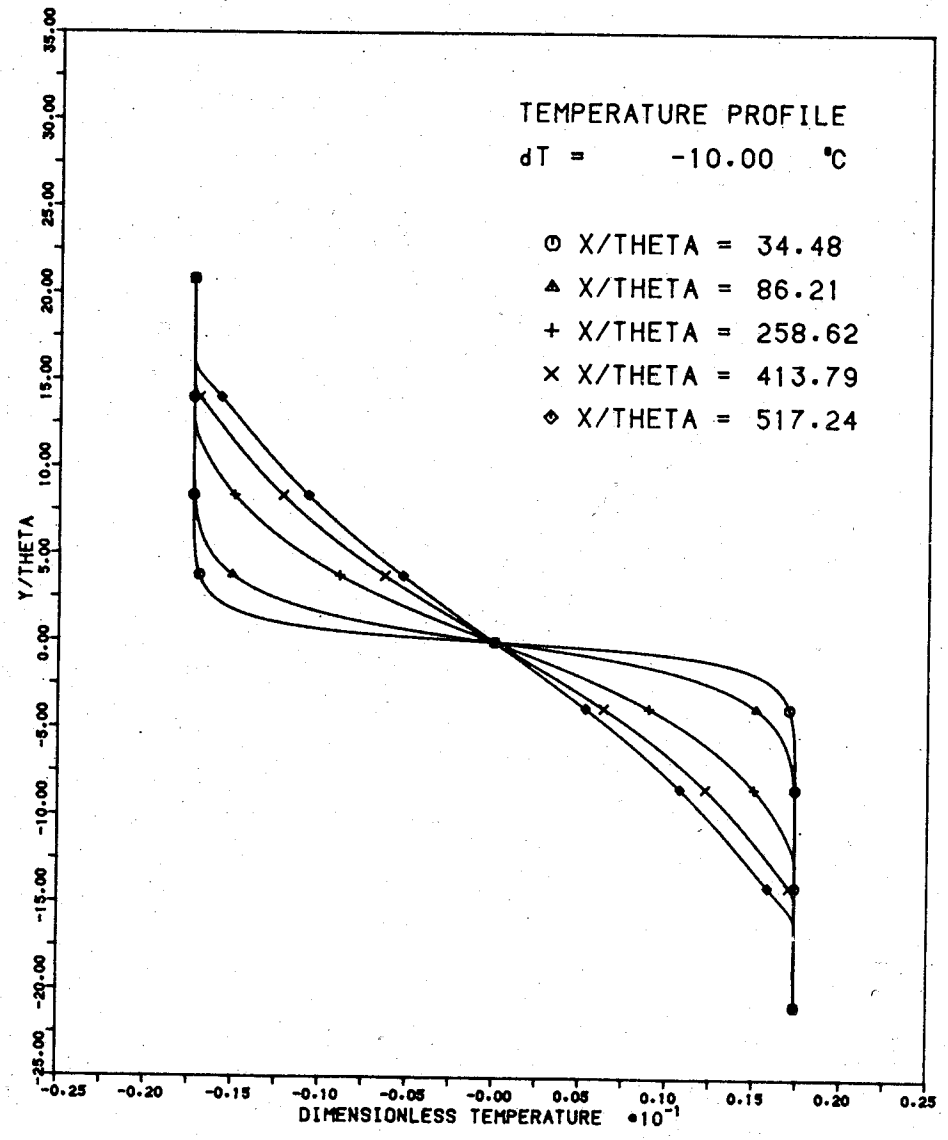

圖 15　不穩定溫度（ dT = − 10 ℃ ）溫度分佈

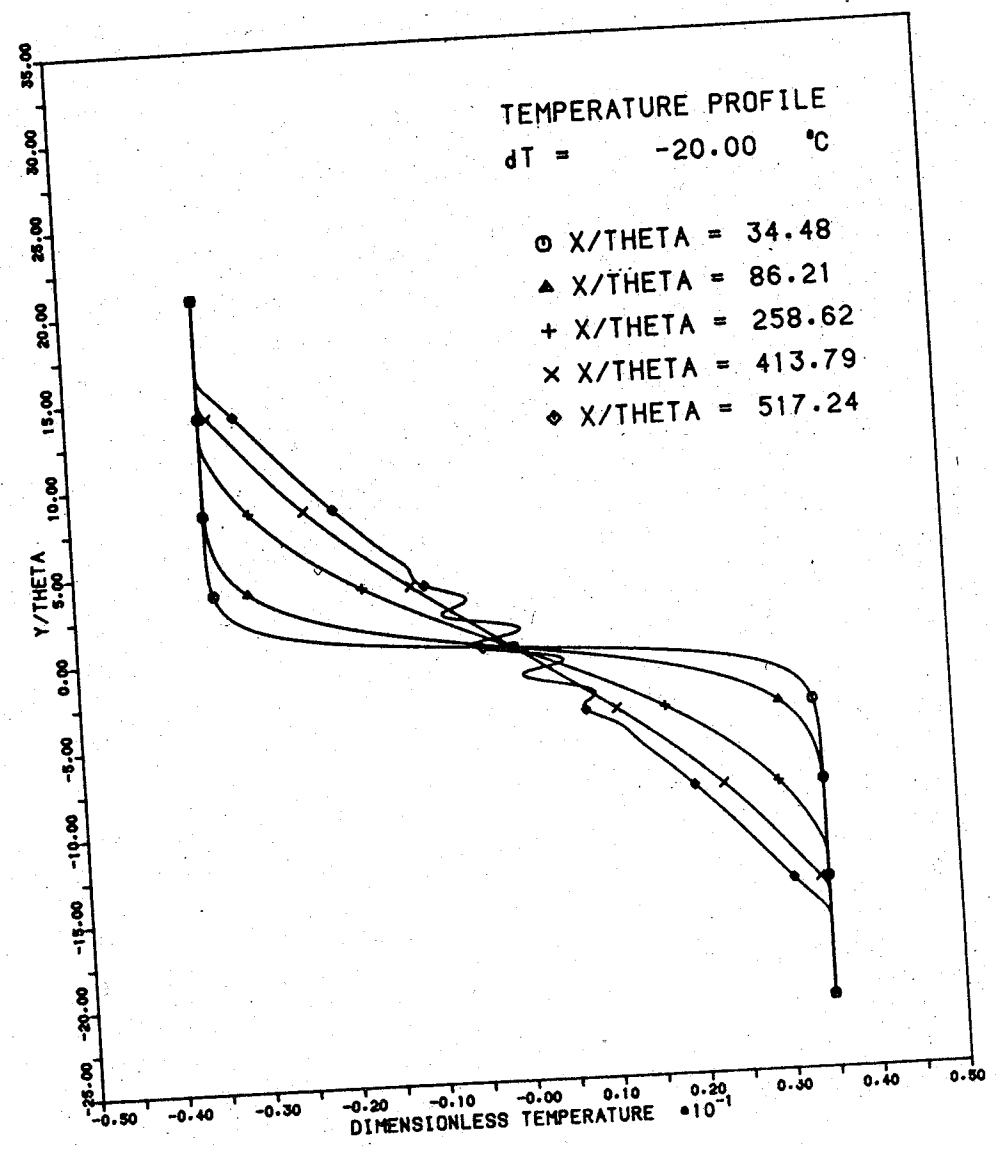

圖 16　不穩定層變（ dT = − 20 ℃）溫度分佈

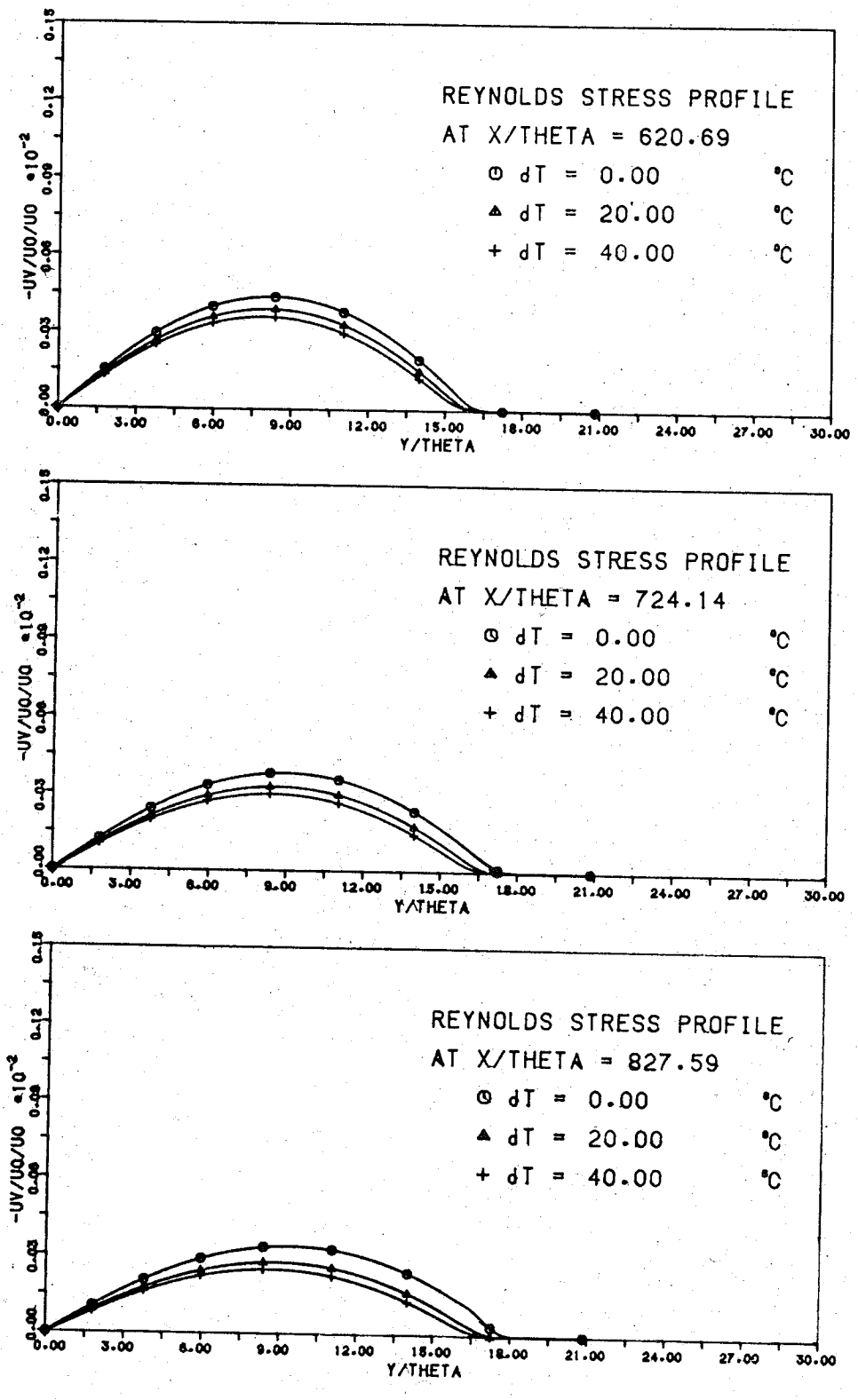

圖 17　穩定層變雷諾應力分佈

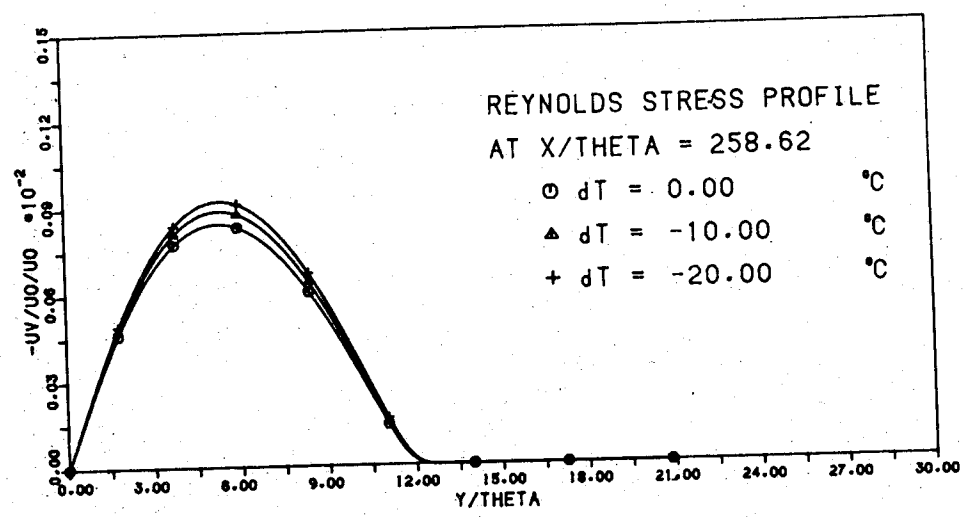

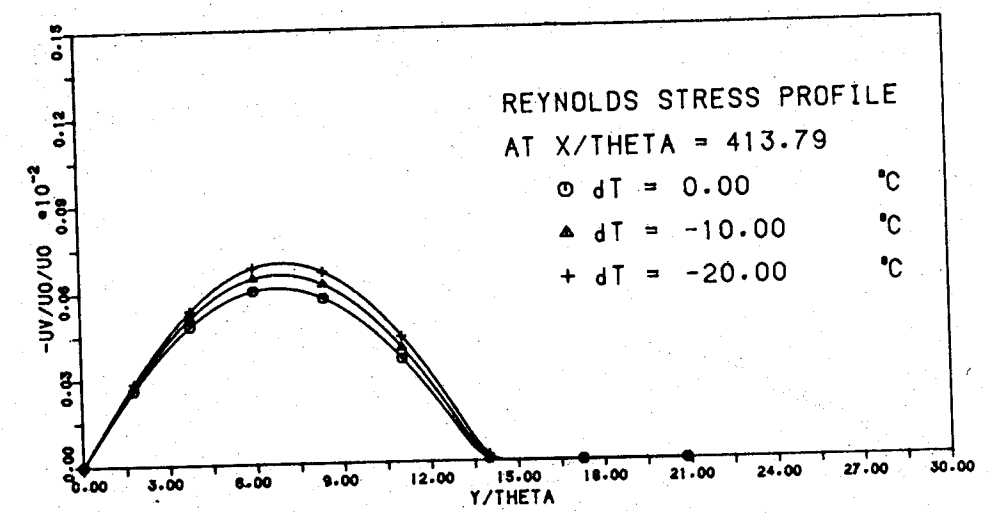

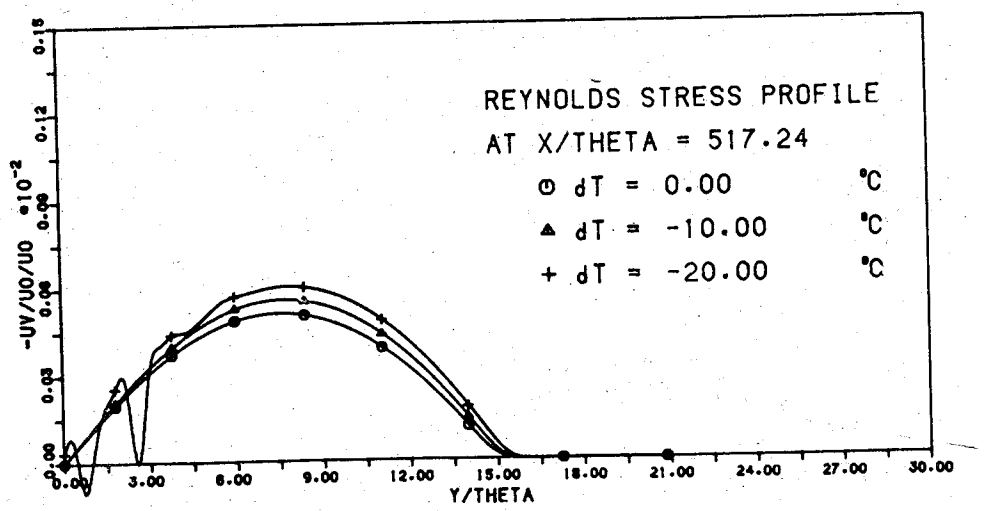

圖18　不穩定層變雷諾應力分佈

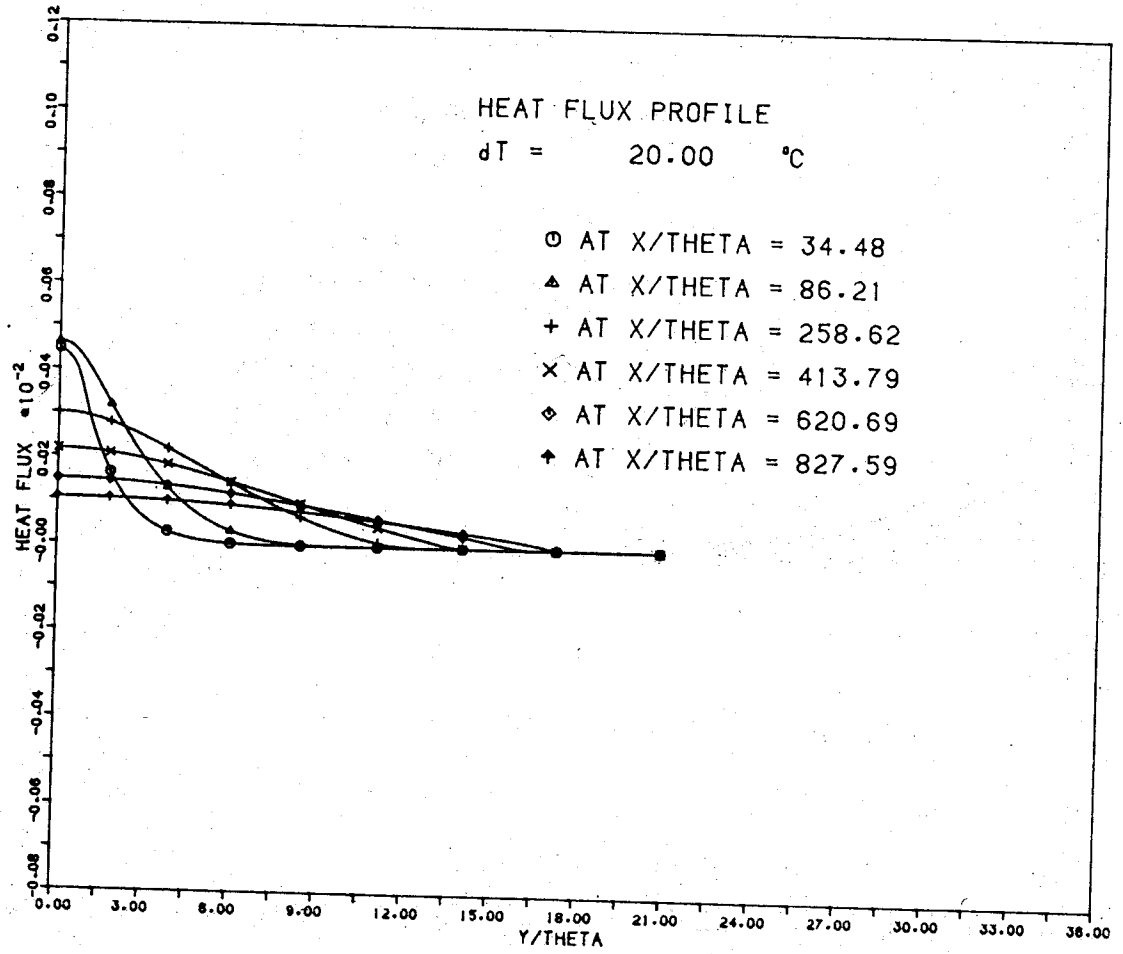

圖19　穩定層變（ dT = 20 ℃ ）熱通量分佈

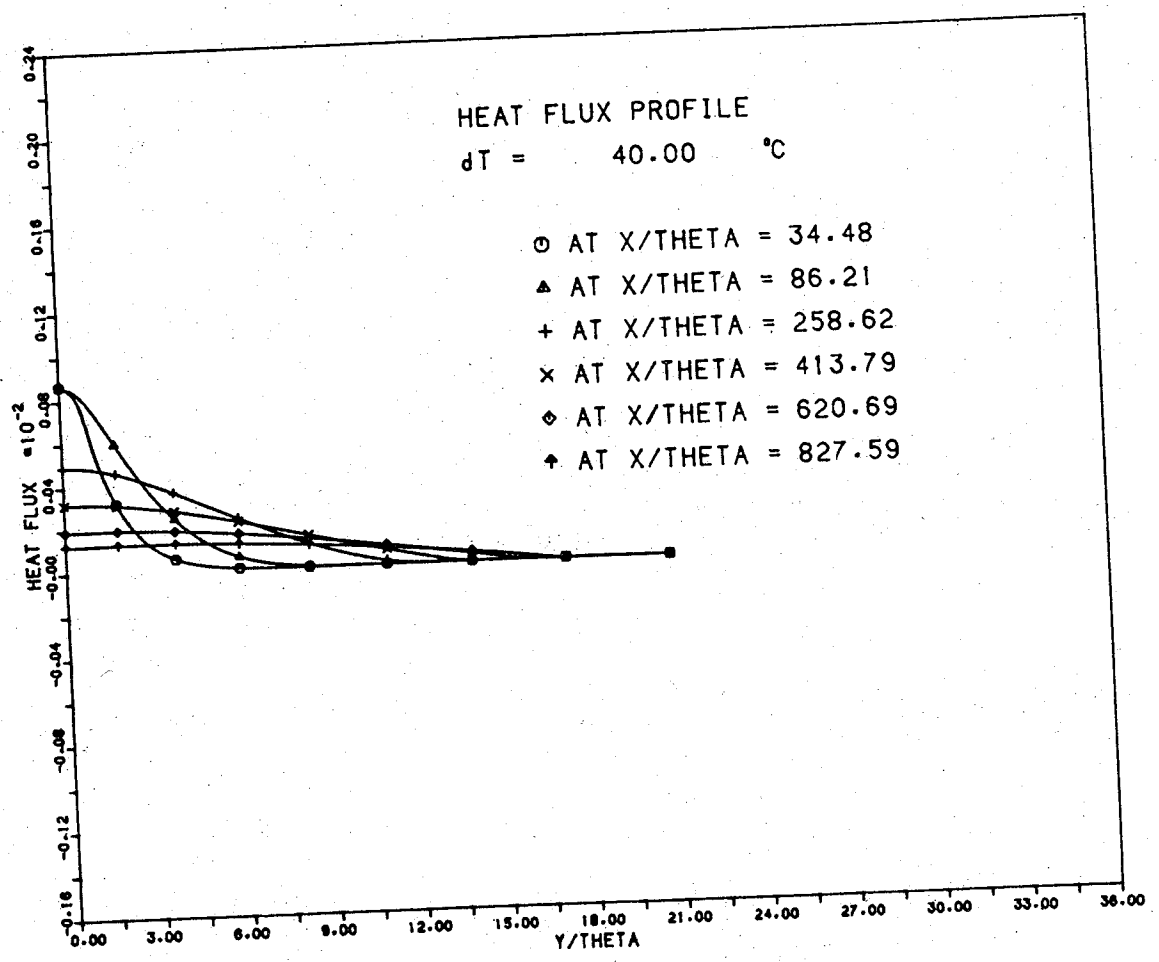

圖 20　穩定層變（ d T = 40 ℃ ）熱通量分佈

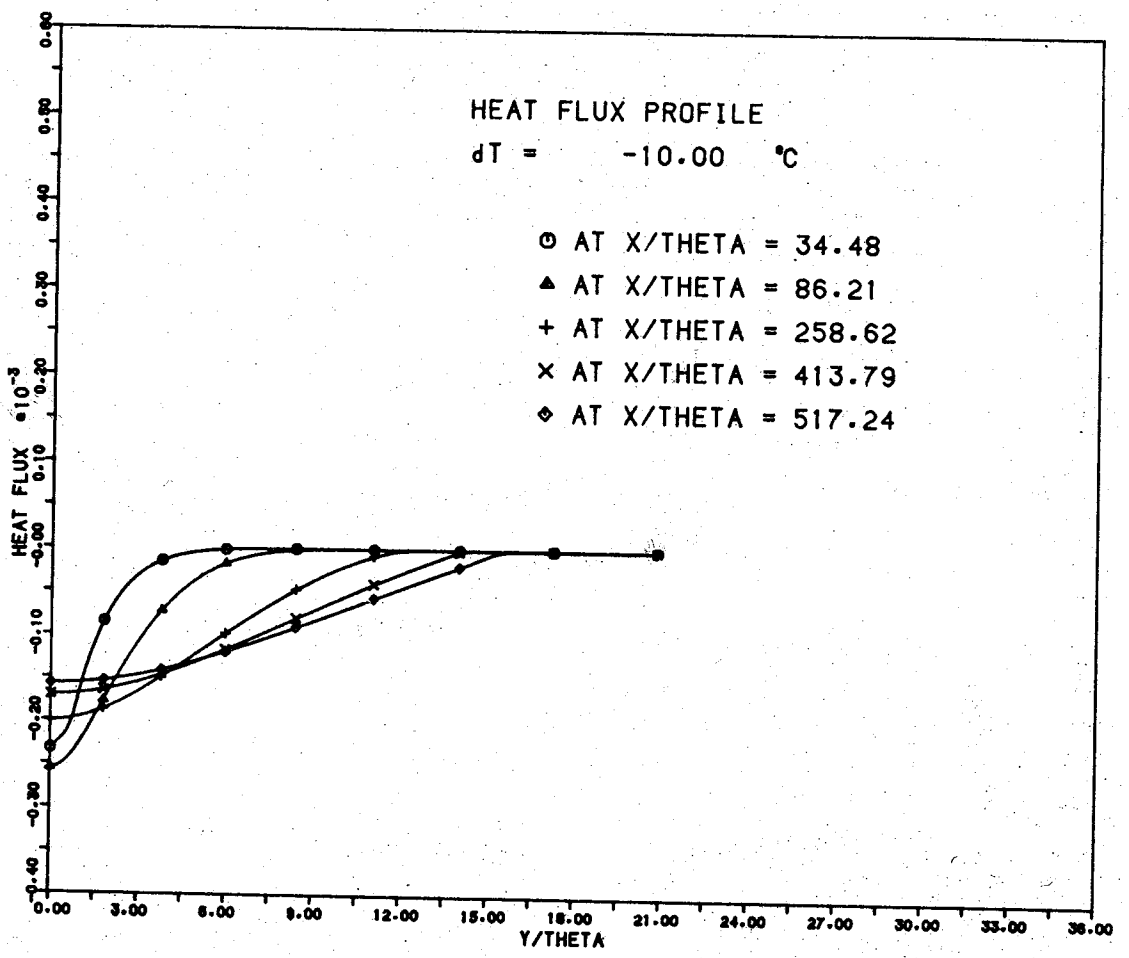

圖 21　不穩定層變（ d T = − 10 ℃ ）熱通量分佈

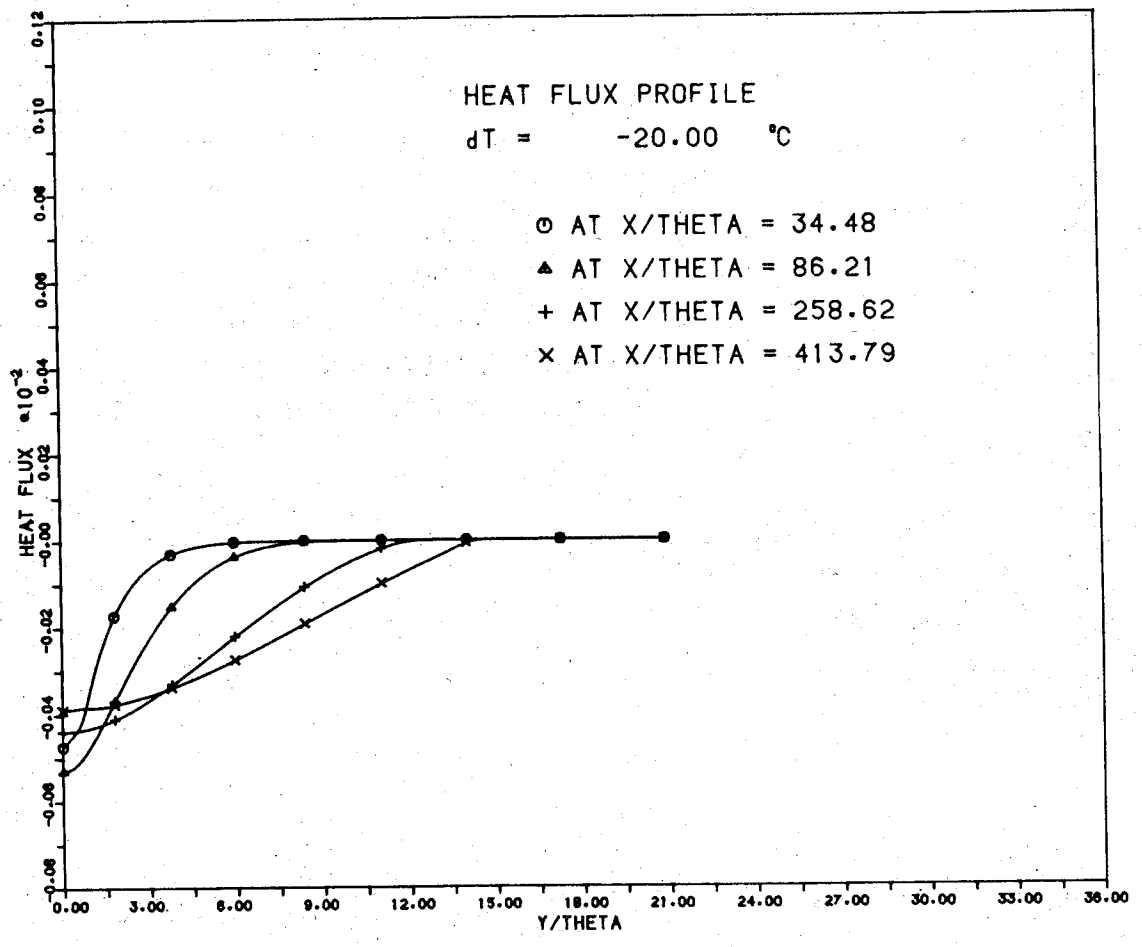

圖 22　不穩定層變（ dT = − 20 ℃ ）熱通量分佈

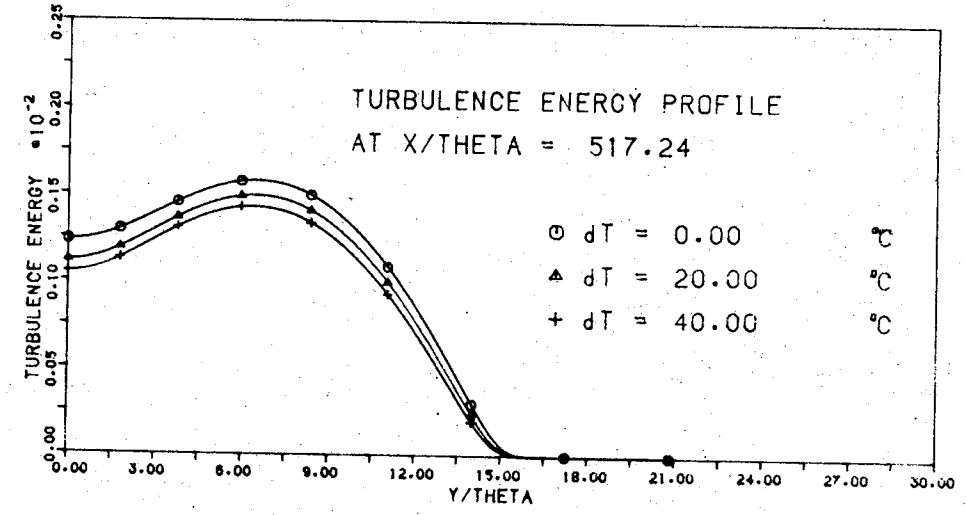

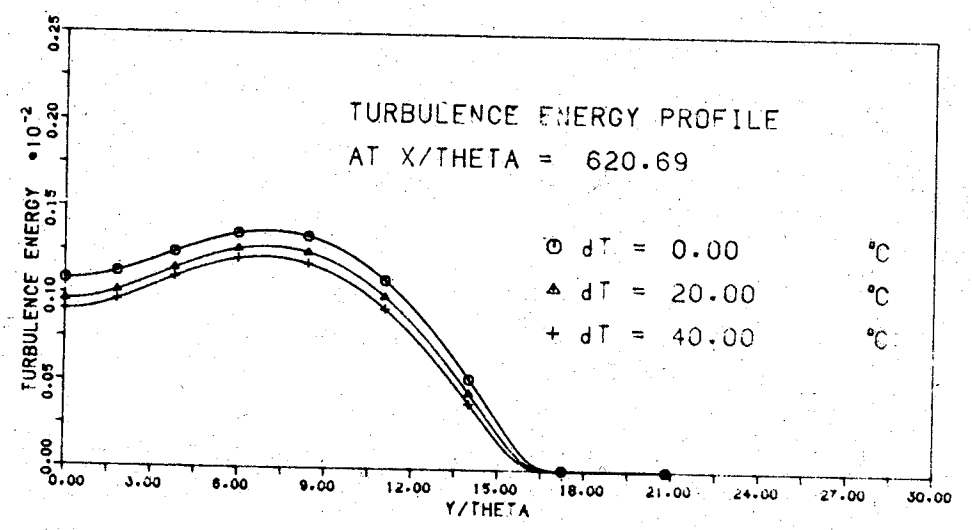

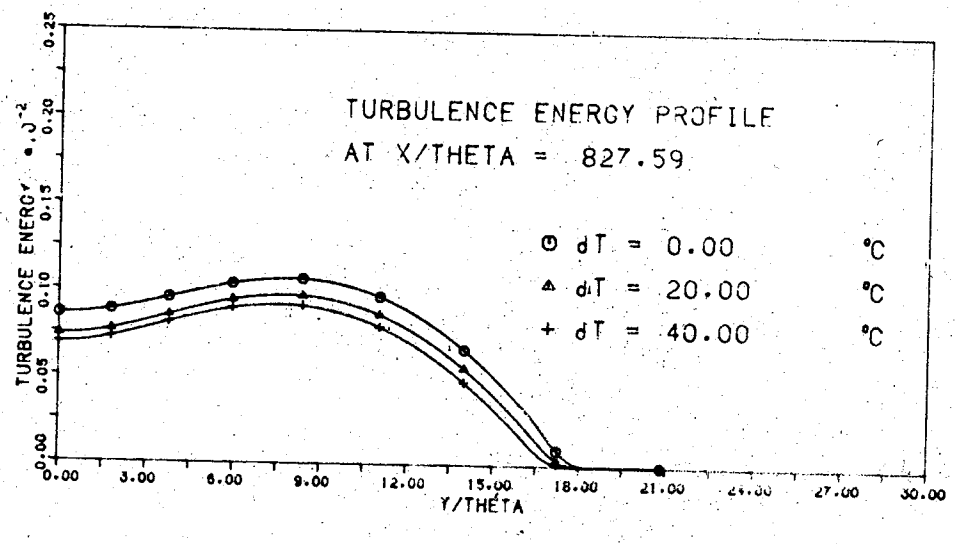

圖 23　穩定層變紊流動能分佈圖

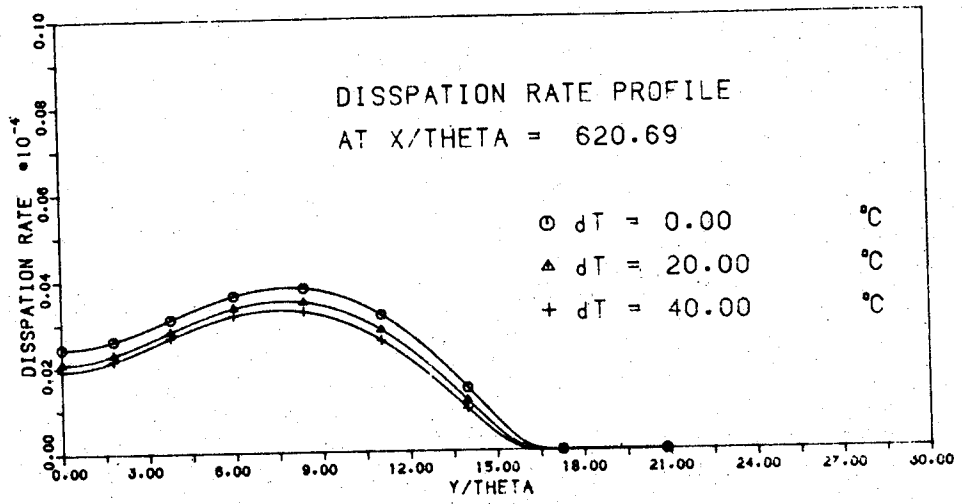

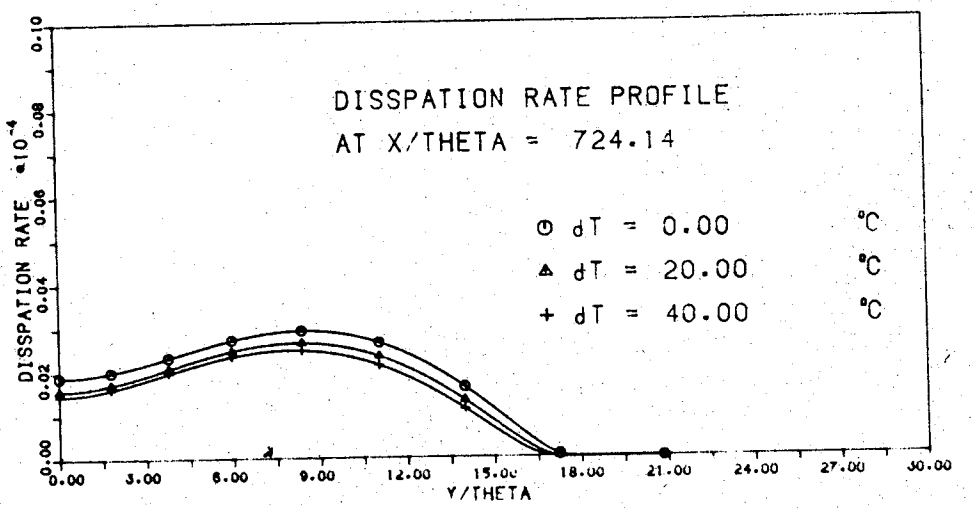

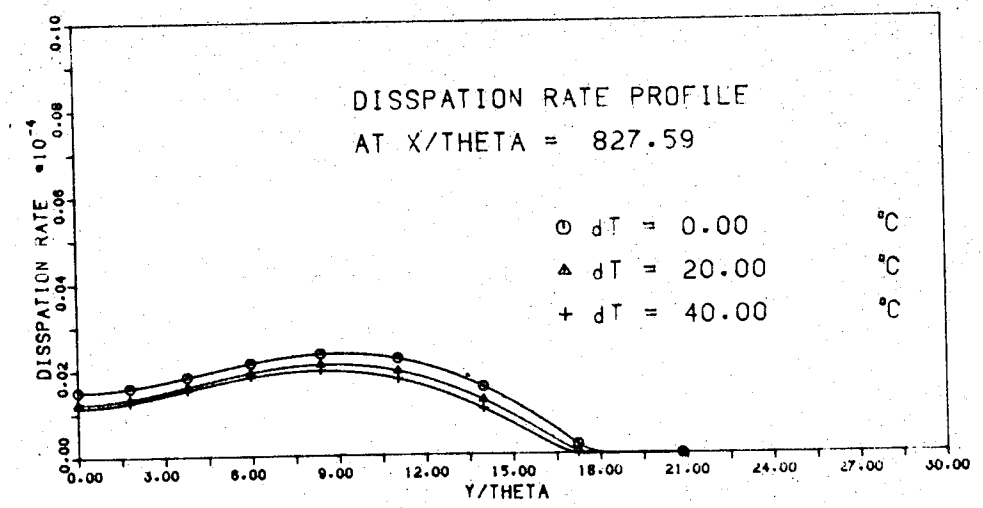

圖 24　穩定層變消散率分佈

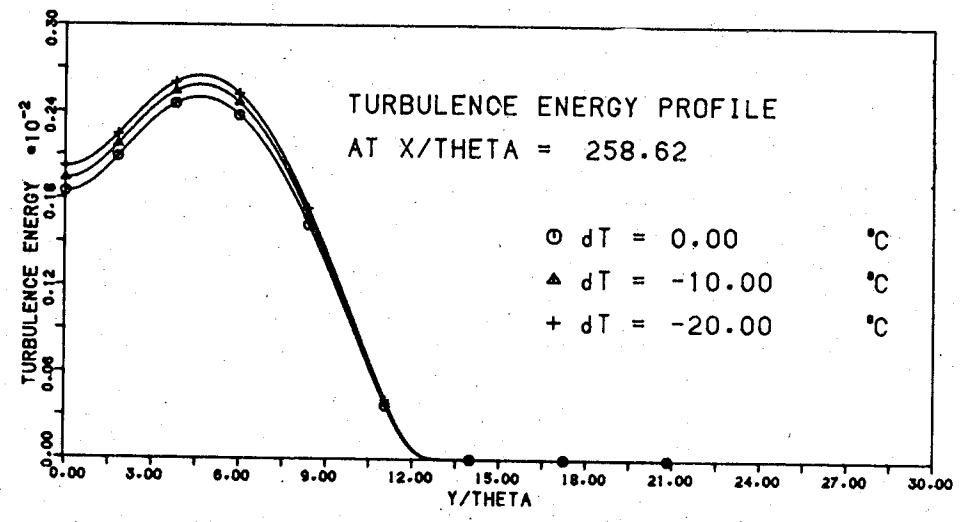

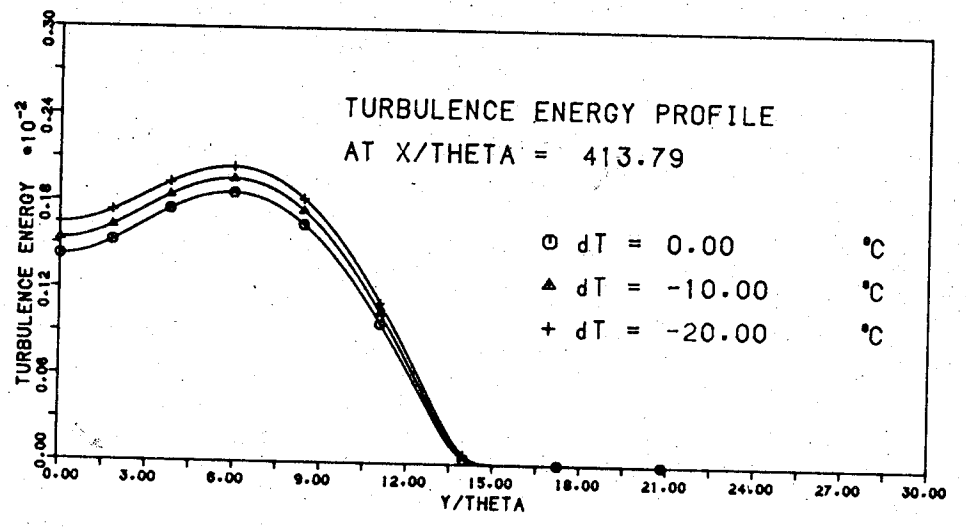

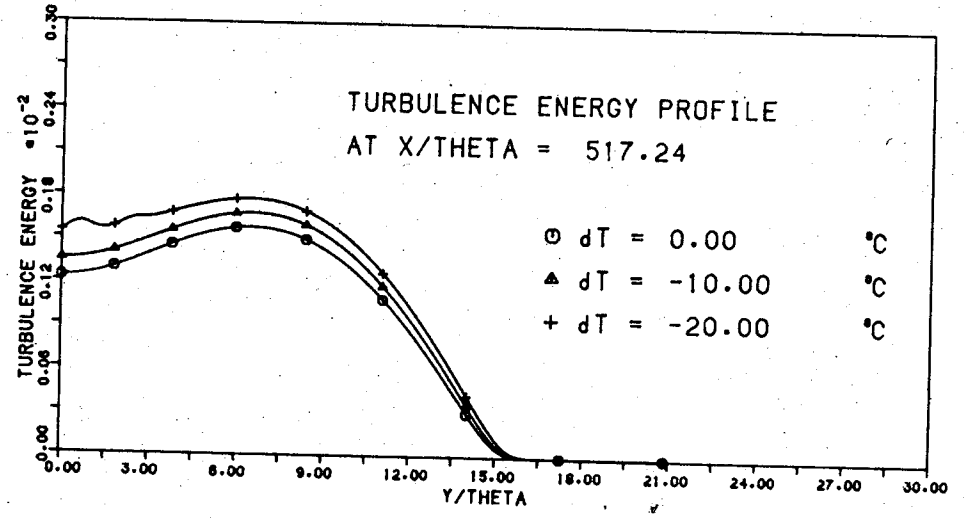

圖 25　不穩定層變紊流動能分佈

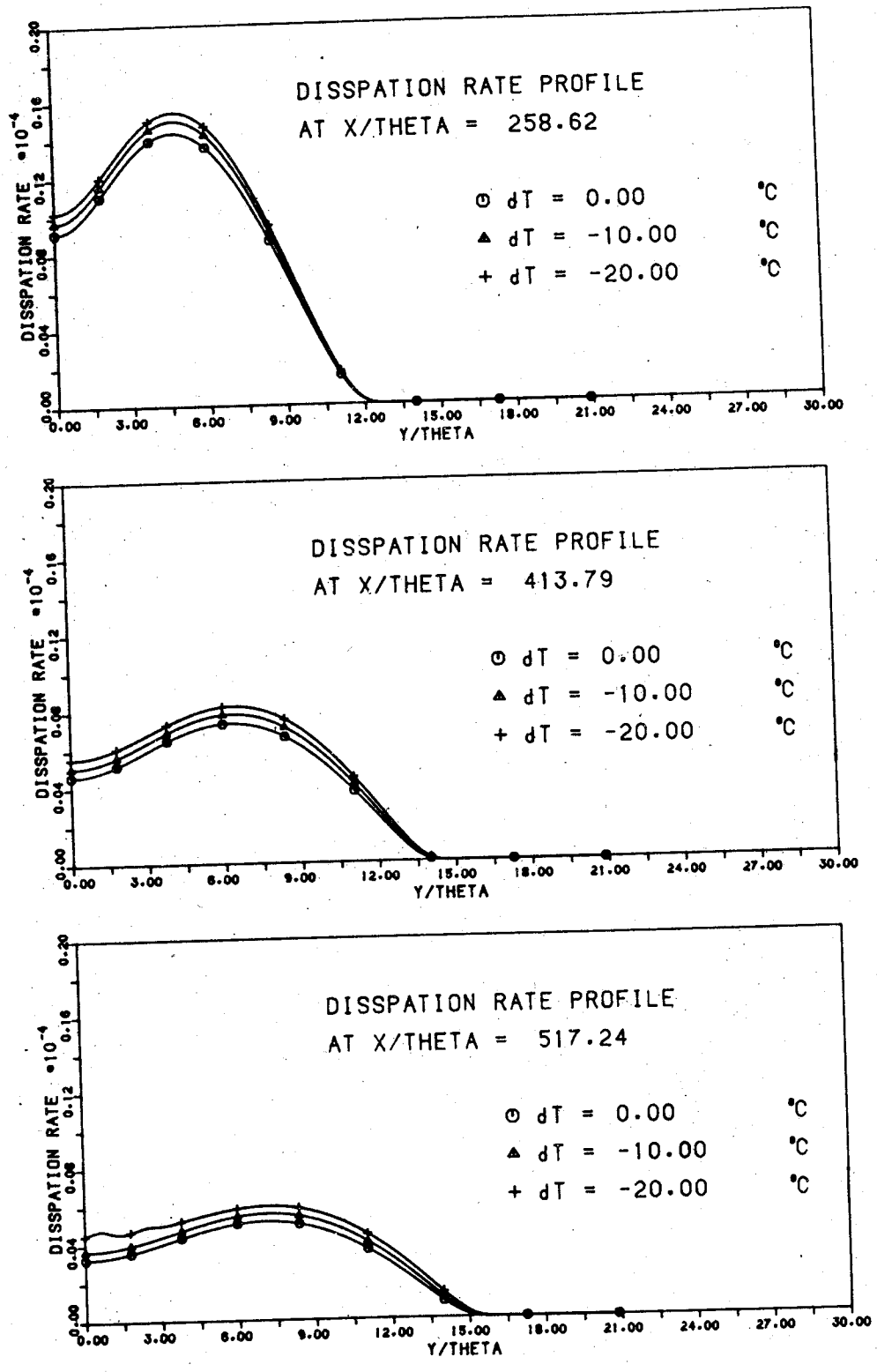

圖 26　不穩定層變消散率分佈

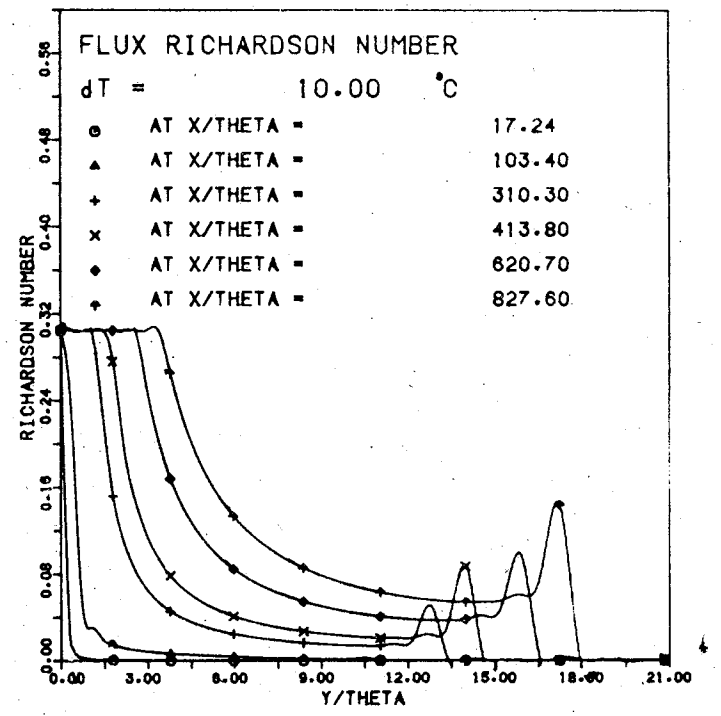

圖 27　穩定層變通量理察森數分佈

大氣環境風洞中對稱紊流跡流之量測

黃 榮 鑑
趙 勝 裕
蕭 葆 義

中 央 研 究 院
物 理 研 究 所

摘 要

本文旨在利用定溫式熱線探針風速儀，類比數位轉換器與數位電腦連線，由電腦線上控制及處理分析大氣環境風洞中對稱紊流跡流之量測。量測數據經電腦分析後顯示結果趨勢良好。同時由實驗量測數據說明了一些對稱紊流跡流之特性；(1)愈遠離平板尾端，紊流能量愈減少，平均流速剖面逐漸趨近於均勻流。(2)軸向及垂向之紊流強度之最大值發生於稍偏離中心軸向線之最大剪應力處。(3)在接近平板尾端處，垂向擾動速度因受到平板抑制作用故其紊流強度僅約爲軸向紊流強度之一半，而愈往下游，二者則愈接近。此外由本文紊流之量測也顯示了大氣環境風洞中進行基本紊流現象量測之可行性。

壹、前 言

自然界中到處充滿非常複雜之紊流現象，欲控制自然，捨其弊而求其利，則需對各類型紊流現象有透澈之了解。複雜之紊流現象可由多種簡單紊流組合而成借助於簡單紊流之實驗與數值解析即可求解自然界之複雜紊流問題。

紊流實驗爲解析紊流問題中非常重要之一環：在數值模型建立前，可先借其觀測紊流結構，以作爲理論分析之憑據。數值模型建立後，則因未知數多於控制方程式，亦需借助實驗提供某些參數初始值以滿足閉合條件，且實驗亦可驗證數值分析之正確性。

本文針對上述目的，利用大氣環境風洞（汪黃 1983〔1〕）試驗段第一號轉盤進行平板紊流跡流之量測，藉以明瞭紊流跡流之一些紊流統計特性，提供數值模式演算之參考；同時測試實驗室電腦線上控制處理紊流量測系統與大氣環風洞中進行基本紊流現象量測之可行性。

貳、理論基礎

一、紊流量測儀器

現今量測紊流之二種主要儀器，其動作原理簡述如下：

(1)雷射都卜勒風力計（ Laser Doppler Anemometer ）： 如圖㈠，應用都卜勒效應，流體通過雷射光束，速度變化會造成雷射光之頻率改變，由此頻率改變即可測得流速。

(2)熱風力計（ Thermal Anemometer ）：如圖㈡之惠斯登電橋（ Wheat stone Bridege ）、熱線探針（ Hot Wire ）或熱膜探針（ Hot Film ）爲電橋之一臂，若電橋平衡（ $R_1/R_2 = R_3/R$ ），則A，B端之電位相等，放大器無電壓差輸出。熱風力計即應用此原理，以電流加熱探針，增加其電阻值至電橋平衡。若通過探針之流速改變，因熱傳作用，探針之溫度改變，電阻值亦改變，造成電橋不平衡，則A，B端之電位不相等，放大器將輸出電壓，由此輸出電壓即可對應得流體速度。熱風力計又可分爲下列二種形式：

(a)定電流熱風力計（ Constant Current Anemometer ）：電源供應至探針之電流保持定值，爲較早期使用之系統。

(b)定溫度熱風力計（ Constant Temperature Anemometer）：如圖㈢，以一回饋網路（ Feedback Loop ）保持探針於固定之操作溫度（ Operating Temperature ）。電橋平衡後，若通過探針之流速改變，則探針之溫度之電阻亦將改變，爲保持探針於固定之操作溫度，回饋網路需增減其輸至探針之電流值，定溫度放大器之輸出電壓即爲供應探針足夠電流以保持其溫度於一定所需之電壓。由E（電壓）＝I（電流）R（電阻），因R＝常數，故$E \propto I$，又I值之大小與流速有關，故亦可由放大器之輸出電壓值對應得流體速度。此爲較進步之電路系統。本紊流跡流量測實驗即採用此種定溫度電路系統，以下所述均針對定溫度電路系統而言。

二、理論依據：

以圓柱形探針之熱傳遞爲例，在單位時間內由長度ℓ，直徑d之探針傳至周圍氣體之熱量爲：$h\pi d\ell(Q_w - Q_g)$，

h：熱傳遞係數（ Heat Transfer Coefficient ）

Q_w：探針溫度

Q_g：氣體溫度

由熱平衡條件，此單位時間之熱傳損失應等於單位時間內由電流供應至探針之電能：I^2R_w

R_w：探針之電阻值

若引進一無因次Nusselt 參數，$Nu = hd/k_g$

k_g：氣體在溫度爲Q_g時之熱傳導係數（ Heat Conductivity ）

則可得圓柱形探針之熱平衡公式：

$$I^2R_w = h\pi d\ell(Q_w - Q_g) = \pi\ell k_g (Q_w - Q_g) \cdot Nu \quad \cdots\cdots(2.1)$$

由Kramers 經驗公式：

$$N_u = 0.42P_r^{0.2} + 0.57P_r^{0.33}R_e^{0.5} \quad \cdots\cdots(2.2)$$

P_r：Prandtl 數，$P_r = \dfrac{C_p u_g}{K_g}$

R_e：Reynold 數，$R_e = \dfrac{\ell_g U_d}{u_g}$

u_g：氣體溫度Q_g時之黏性係數（ Dynamic Viscosity ）

C_p：定壓比熱係數

U：流體速度

ℓ_g：氣體溫度Q_g時之密度

應用上式時，各氣體特性值應取溫度爲$Q_f = \dfrac{Q_w + Q_g}{2}$ 又探針之電阻值受溫度之影響可表示爲：

$$R_w = R_0\{1 + b(Q_w - Q_0) + b_1(Q_w - Q_0)^2 + \cdots\cdots\} \cdots(2.3)$$

R_0：溫度爲0時探針之電阻值。

b_0, b_1：探針電阻之溫度係數

通常b_1遠較b值小，故二次以上之非線性項可忽略，則溫度差$Q_w - Q_g$可表示爲：

$$Q_w - Q_g = \frac{R_w - R_g}{bR_0} \quad \cdots\cdots(2.4)$$

故（2．1）式可表爲：

$$I^2R_w = \frac{\pi\ell k_f}{b}\frac{R_w - R_g}{R_0} \cdot Nu \quad \cdots\cdots(2.5)$$

代入Krame r's 式得

$$I^2R_w = \frac{\pi\ell k_f}{b}\frac{R_w - R_g}{R_0}\{0.42(P_r)_f^{0.2} + 0.57(P_r)_f^{0.33}(R_e)_f^{0.5}\} \quad \cdots\cdots(2.6)$$

上式適用於$R_e > 40$之流況

爲方便計，可將上式化爲：

$$\frac{I^2R_w}{R_w - R_g} = A + B\sqrt{U} \quad \cdots\cdots(2.7)$$

$$A = 0.42\frac{\pi\ell k_f}{bR_0}(P_r)_f^{0.2}$$

$$B = 0.57\frac{\pi \ell k_f}{bR_0}\left(\frac{\ell_f d}{u_f}\right)^{0.5}(P_r)_f^{0.33}$$

實用上A，B值並非由此二式求得，U亦非爲固定之0.5次方，此次方值隨流速大小，探針形狀等因素而變，故現今之作法都寫爲：

$$\frac{I^2R_w}{R_w-R_g} = A + BU^n \quad \cdots\cdots(2.8)$$

n值之範圍約爲 0.3 ～ 0.6 間

於定溫度電路系統下，R_w = 常數

$$\therefore \frac{R_w}{R_w-R_g} = \text{常數}$$

$$\therefore I^2 \propto A + BU^n \quad \cdots\cdots(2.9)$$

又由 $E = IR$ 知，$E \propto I$

$$\therefore E^2 \propto A + BU^n \quad \cdots\cdots(2.10)$$

則由實驗所得數據，分別以E^2及U^n爲縱、橫座標，以試誤法（Try and Error）求得一適當之n值，使其成一簡單之線性關係如圖㈣。則截距A，斜率B即可求得，風速與電壓值之對應關係亦可由此求得。詳見蕭〔2〕。

三、溫度校正

若校正探針時之流場溫度與實驗時之流場溫度不同，或實驗過程中流場溫度發生變化，將會影響探針之熱傳效應，進而影響放大器之輸出電壓，即同一風速將因流場溫度之改變而得到不同之輸出電壓。故需作溫度校正。於低速風洞中，不會因超音速震波（Shock Wave）造成流場溫度之急驟變化，可由下列簡單運算求得溫度校正因子：

由（2．8）式可導得：

$$E^2 \propto (A + BU^n)(Q_w - Q_g) \quad \cdots\cdots(2.11)$$

於不同流場溫度Q_{g1}, Q_{g2}，可得不同輸出電壓值E_1, E_2，

即
$$E_1^2 \propto [A + BU^n](Q_w - Q_{g1})$$
$$E_2^2 \propto [A + BU^n](Q_w - Q_{g2})$$
$$\therefore \frac{E_1^2}{E_2^2} = \frac{Q_w - Q_{g1}}{Q_w - Q_{g2}}$$

$$\therefore E_2 = E_1\left(\frac{Q_w - Q_{g2}}{Q_w - Q_{g1}}\right)^{\frac{1}{2}} \quad \cdots\cdots(2.12)$$

即乘一溫度校正因子$\left(\frac{Q_w - Q_{g2}}{Q_w - Q_{g1}}\right)^{\frac{1}{2}}$而得溫度校正值，於一般之操作狀態下，2°C之溫差約會產生1％之輸出電壓誤差。

四、流向校正：

若流場之流向並不垂直於探針，則須作流向校正。如圖㈥，實際平均流速U與有效冷却

流速Ueff間有一餘弦函數關係：

若傾斜角a小時，：$U^2eff = U\cos a$ ……（2．13）

傾斜角a大時　：$U^2eff = U^2(\cos^2 a + k^2 \sin^2 a)$ …（2．14）

k sin a 爲平行於探針之有效冷却係數

k值受探針$\frac{\ell\text{（長度）}}{d\text{（直徑）}}$比值之影響，由$\frac{\ell}{d} = 200$，$k \fallingdotseq 0.2$降至$\ell / d = 600$，$k \fallingdotseq 0$

五、X型熱線探針

利用二根熱線排列成X型，可量測二維柒流特性，詳見蕭 1985〔2〕。今將其理論原理簡述如下：

如圖㈦，二根相互垂直，成“X”型之熱線探針同置於流場中，與流場流向成45°角由方向校正知，探針1之輸出電壓E_1對應之有效風速爲：$U\cos 45° + V\sin 45°$ 同理探針2之輸出電壓E_2對應之有效風速爲：

$$U\cos 45° - V\sin 45°$$

由校正曲線之特性知：

$$E_1^2 = A_1 + B_1(U\cos 45° + V\cos 45°)^{n1}$$
$$= A_1 + B_1'(U+V)^{n1}\cdot\left(\frac{1}{\sqrt{2}}\right)^{n1} = A_1 + B_1(U+V)^{n1}$$
$$\cdots\cdots(2.15)$$

同理：$E_2^2 = A_2 + B_2'(U-V)^{n2}\left(\frac{1}{\sqrt{2}}\right)^{n2} = A_2 + B_2(U-V)^{n2}$ …（2．16）

解上述聯立方程式得：

$$U = \frac{1}{2}\left[\left(\frac{E_1^2 - A_1}{B_1}\right)^{\frac{1}{n1}} + \left(\frac{E_2^2 - A_2}{B_2}\right)^{\frac{1}{n2}}\right] \quad \cdots\cdots(2.17)$$

$$V = \frac{1}{2}\left[\left(\frac{E_1^2 - A_1}{B_1}\right)^{\frac{1}{n1}} + \left(\frac{E_2^2 - A_2}{B_2}\right)^{\frac{1}{n2}}\right] \quad \cdots\cdots(2.18)$$

再由平均原理得：

$$\overline{U} = \frac{\sum_{i=1}^{N} U_i}{N} \quad \cdots\cdots(2.19)$$

$$\overline{V} = \frac{\sum_{i=1}^{N} V_i}{N} \quad \cdots\cdots(2.20)$$

且振動速度 $u' = U - \overline{U}$ ……（2．21）

$v' = V - \overline{V}$ ……（2．22）

故　$\overline{u'^2} = \overline{(U-\overline{U})^2} = \overline{U^2} - (\overline{U})^2$ ……（2．23）

$$\overline{V'^2} = \overline{(V-\overline{V})^2} = \overline{V^2} - (\overline{V})^2 \quad \cdots\cdots (2.24)$$

$$\overline{u'v'} = (U-\overline{U})(V-\overline{V}) = (\overline{UV} - \overline{U}\,\overline{V}) \quad \cdots\cdots (2.25)$$

由上列各式即可求得平均速度U，V，紊流強度

$$\frac{\sqrt{u'^2}}{U_\infty}, \frac{\sqrt{v'^2}}{U_\infty}$$ 及雷諾應力 $$\frac{\overline{u'v'}}{U_\infty^2}$$ 。

參、實驗儀器之配置

大氣環境風洞試驗段長 18.5 公尺，寬 3 公尺高 2.1 公尺爲開放吸入式之風洞。該風洞之規劃設計，可參考汪黃 1983〔1〕。本實驗採用長 2.4m，寬1.2m厚 1.6 cm 之夾板，垂直懸吊於大氣環境風洞中第一號轉盤上。空風洞時邊界層厚度約爲 15 cm，平板懸吊於風洞之正中間，可確保其處於均勻流段。爲使實驗符合二維度之基本假設，量測斷面取於平板寬之½處，分別由距平板兩端 60 cm 處起，由平板二面向二端對稱削炭＝底端之板厚約爲 1mm。於距板前端 60 cm 處平貼一直徑約爲 1 cm 之彈簧條當紊流產生器以便於平板尾端產生一較厚且穩定之紊流邊界層。紊流尾流之量測則於距板尾端 5 cm，20 cm，50 cm，150 cm，240 cm等五處斷面以“X”型熱線探針量測之。風洞之均勻流速爲 4.45m／sec，以邊界層厚度 δ 計算之雷諾數爲：

$$\frac{\delta U_\infty}{} = 2.1 \times 10^4$$ 。

紊流之量測採用DISA TYPE 56Co1 CTA & CTA Bridge 56 C16 定溫式熱線探針風速計，DISA Probe Type 55 P61 X型熱線探針，ANDS-5400 A／D 轉換器及 PDP 11／23plus電腦連線，由電腦線上操作控制流場之取樣及數據分析處理。電腦線上控制操作，可參考蕭 1985〔2〕。利用TSI Model 1125／1125R 風速校正儀校正X型熱絲線探針而獲得率定曲線（calibration curve）。

肆、結果與討論

在平板尾端X＝0cm 斷面所量測得之紊流邊界層各特性值如下：邊界層厚度（$U/U_\infty = 0.99$）$\delta = 17.5$ cm，動量厚度（Momentum Thickness）$\theta_0 = 8.01$ cm，位移厚度（Displacement Thickness）$\delta^* = 10.99$ cm，形狀參數（Shape Parameter）$H = \delta^*/\theta_0 = 1.37$ 。

實驗結果以均勻流速度 U_∞ 爲速度尺度，動量厚度 θ_0 爲長度尺度，分別對速度值及垂直座標無因次化後，所得之速度剖面，軸向紊流強度，垂向紊流強度，及雷諾應力曲線，如圖(八)～（十一）所示。

圖(八)爲尾流速度剖面變化情形，其對稱性良好。愈往下游，紊流能量愈減，逐漸趨近於均勻流。在往下游流動過程中，並未有任何障礙物增加其能量損失，故速度剖面變

化甚爲緩慢。

比較圖(九)、(十)、(十一)知，軸向及垂向紊流強度之最大值發生於稍離平板中心線之最大剪應力處。在接近平板尾端處，垂向振動速度受到平板之抑制作用，故其紊流強度僅約爲軸向之一半，愈往下游則二者愈爲接近。圖(九)、(十)曲線尾端未趨近於 0 之值，爲空風洞本身所具之紊流強度值，二者均約爲 0.5 %。

伍、結　論

紊流量測實驗，爲解析各類紊流問題中，非常重要之一環，所得實驗結果，既可供數值模型應用，提供初始條件，（Initial Conditions）以滿足閉合問題（Closure Problem）又可作數值模型之驗證，於數值模型未建立之時，亦可借實驗對各種紊流特產有一適當之了解，以供建立數值模型之參考。故精確之紊流量測實爲有效解析紊流問題所必需，本紊流尾流量測實驗在開放吸入式大氣環境風洞中進行，此類型風洞易受外界氣候影響流場，故實驗之進行需選定穩定之氣候爲宜。由上節實驗結果顯示，量測結果尚屬良好。亦即肯定了在大氣環境風洞中進行基本紊流現象量測之可行性。

參考文獻

〔1〕汪群從、黃榮鑑、“大氣邊界層風洞之規劃與設計研究”行政院國家科學委員會研究報告 NSC-72-0414-P-001-02 AEWT-001，中央研究院物理研究所 1983

〔2〕蕭葆義，“應用數位型電腦線上控制及處理分析熱絲／熱膜量測紊流之研究”中央研究院物理研究所大氣環境風洞實驗室研究報告 AEWT-006　1985

〔3〕Hinze, J.O. “Turbulence” Chapter 2 Mc Graw Hill, 1975

〔4〕Chevray, R; Kovasznay, L.S.G, “Turbulence Measurements in the wake of a Thin Flat Plate”, Journal of AIAA August 1969 pp 1641-1642

〔5〕黃榮鑑、趙勝裕、蕭葆義“平板紊流跡流之量測”行政院國家科學委員會研究報告 NSC-74-0202-M-001-10 FM 304 AEWT-007 中央研究院物理研究所 1985

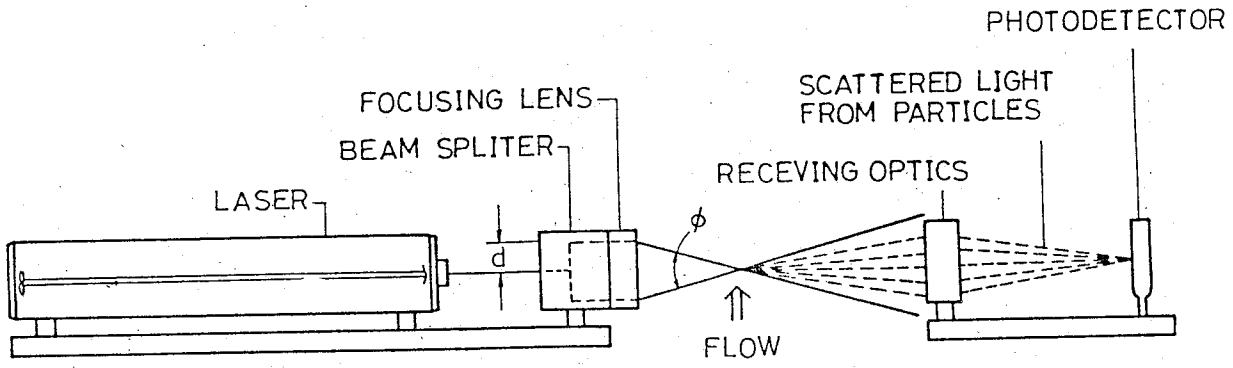

圖一　雷射都卜勒風力計示意圖

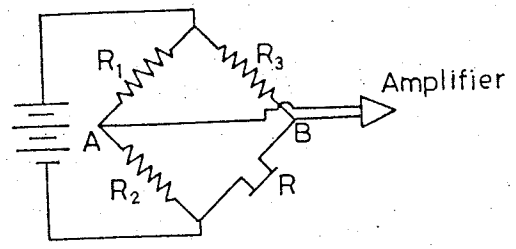

圖二　惠斯登電橋

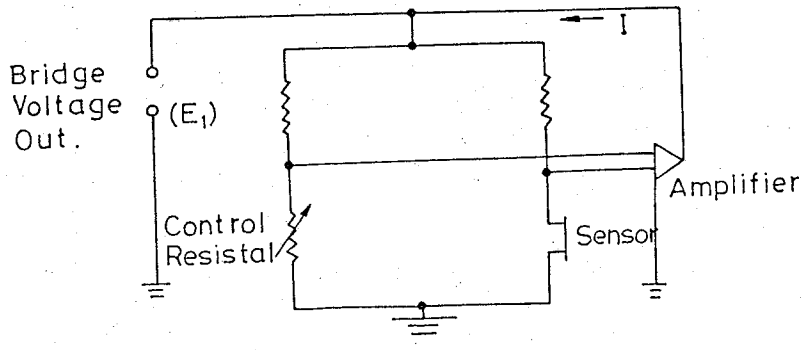

圖三　定溫度風力計電路圖

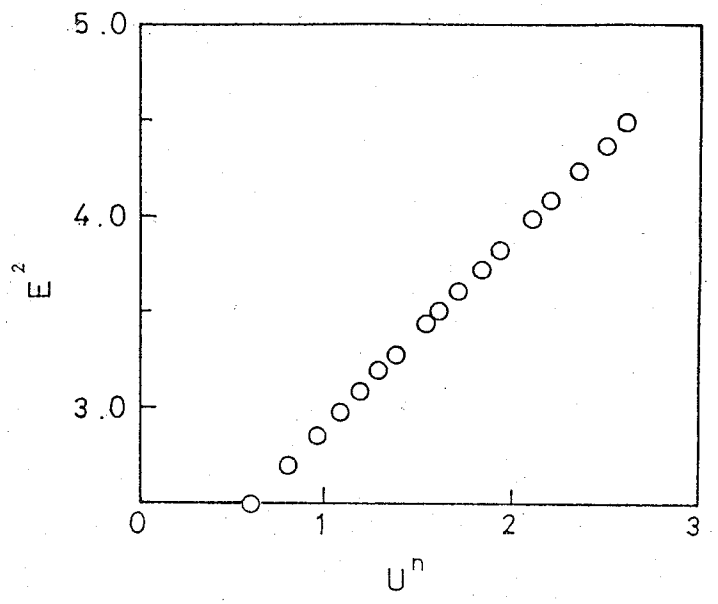

圖四　以金氏定律表示之風速——電壓率定曲線

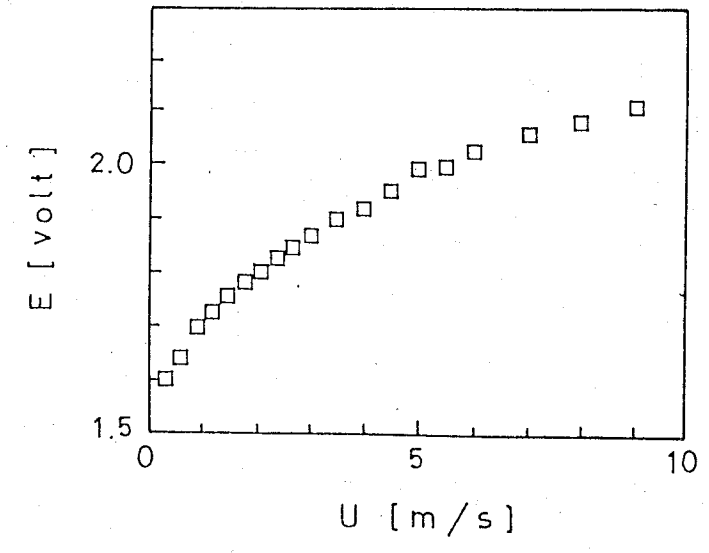

圖五　風速——電壓校正曲線

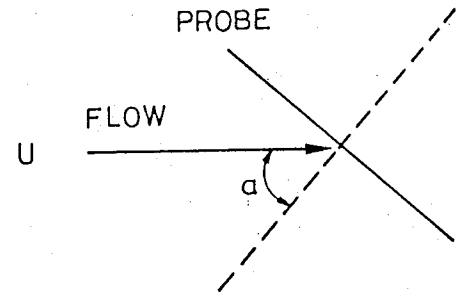

圖六　流向校正

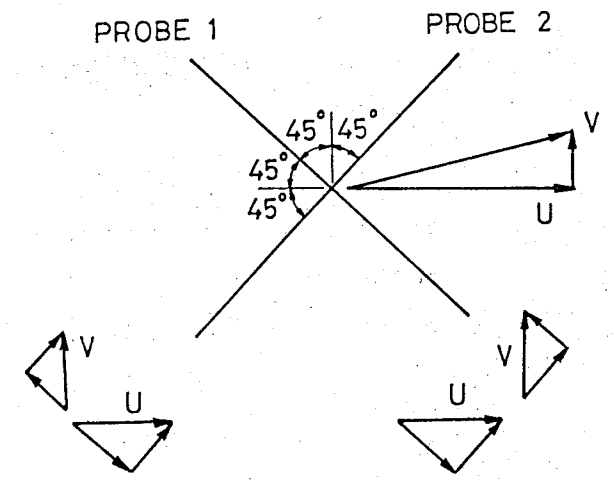

$E_1^2 \sim U\cos 45° + V\sin 45°$　　$E_2^2 \sim U\cos 45° - V\sin 45°$

圖七　X型探針示意圖

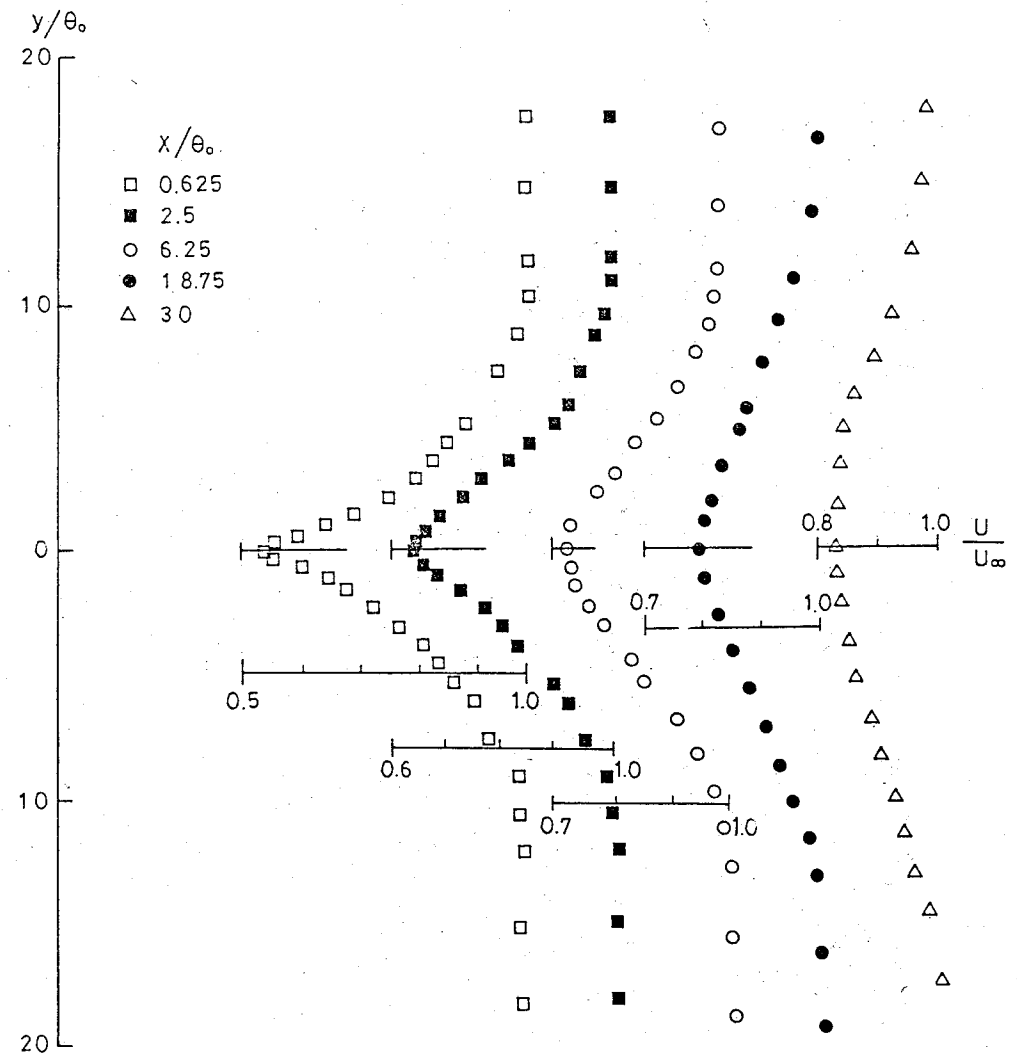

圖八　跡流速度剖面

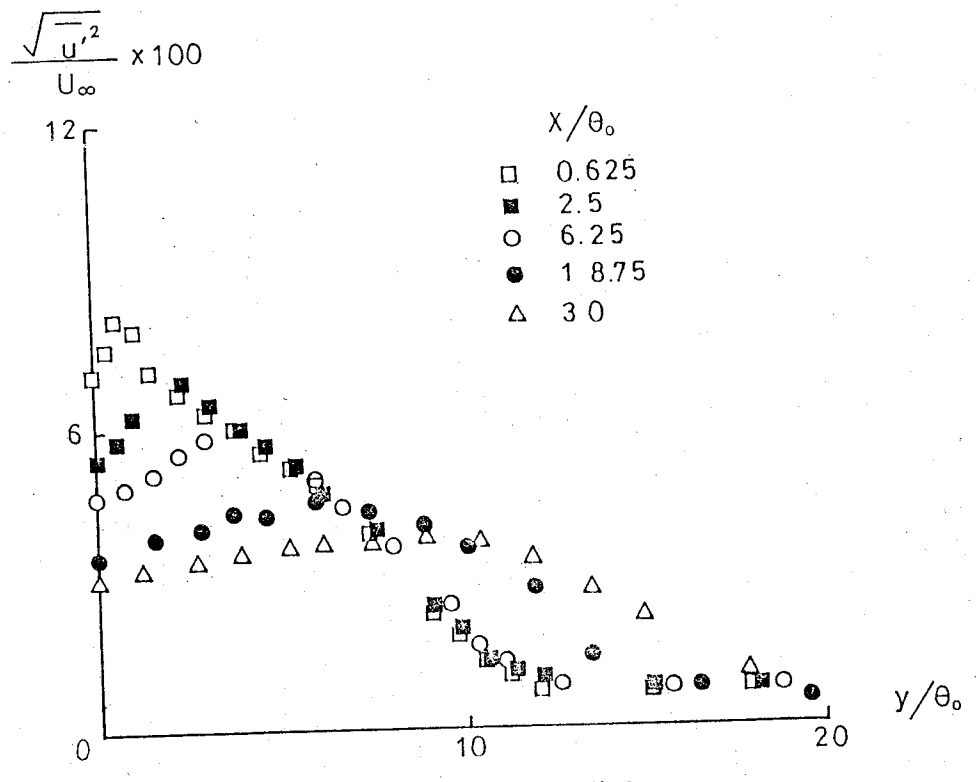

圖九　軸向紊流強度

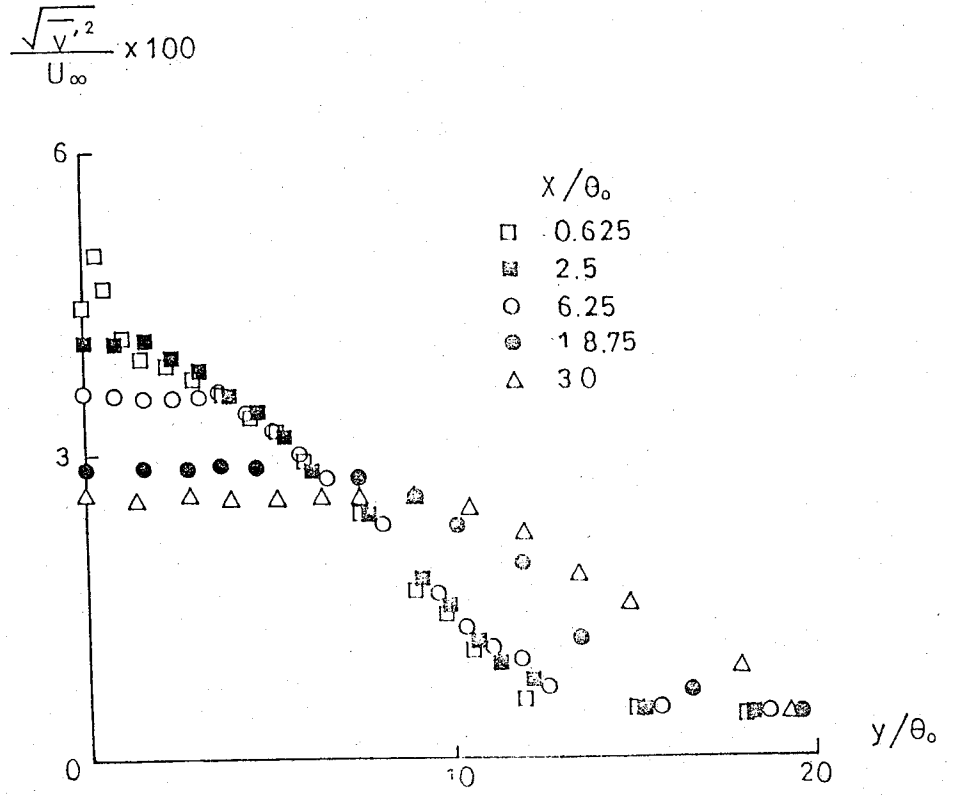

圖十　垂向紊流強度

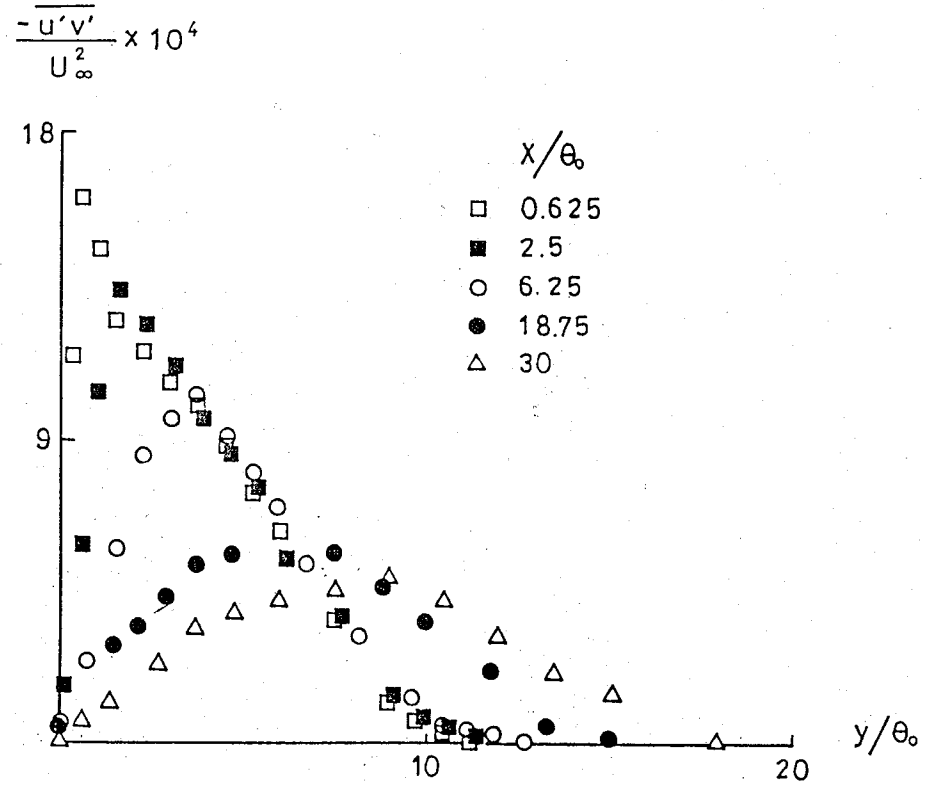

圖十一　雷諾應力分佈

Annual Report of the Institute of Physics, Academia Sinica, Vol. 15, 1985

MEASUREMENT OF SYMMETRIC TURBULENT WAKE FLOW BEHIND A FLAT PLATE IN THE ATMOSPHERIC EN'/IRONMENT WIND TUNNEL

Robert R. Hwang

S. Y. Jaw

B. S. Shiau

Institute of Physics

Academia Sinica

Nankang, Taipei, Taiwan

R. O. C.

ABSTRACT

Atmospheric environment wind tunnel (AEWT) is an open suction type wind tunnel with test section 18.5m long, 3 m wide and 2.1 m hight. In this paper we measure the symmetric turbulent wake flow behind a flat plate in the AEWT. The measured turbulent quantities tell us some characteristics of the symmetric turbuleat wake flow. Also the successful measurements verify the feasibility of experimental study turbulent flow in the AEWT.

大氣邊界層風洞中建築物比較試驗之研究

汪群從、張能復、黃榮鑑

梁文傑、李陽琛

中央研究院物理研究所

摘　要

爲了進一步瞭解利用中研究物理所建造完成之大氣環境風洞中進行建築結構物試驗之可能性，本研究院取已在國外六座不同風洞中測試過之CAARC標準高樓建築，製作模型於風洞中進行試驗，其結果爲：

1. 利用欄柵並輔以地面PVC 管組成之粗糙物，在大氣環境風洞3號轉盤處之邊界層厚度可達150公分以上。邊界層內垂向平均風速成指數分佈，利用不同之地面粗糙物，指數 n 可控制於 0.20至 0.36 的範圍內。
2. 利用壓力孔與皮托管量度CAARC高樓模型之流速與壓力分佈，在不同吹風角度所得 Cp 分佈情形大致上與國外實驗室量計值類同。

本研究顯示中研院物理所之大氣環境風洞應可供風洞中建築結構物試驗使用。

一、前　言

風力對於建築結構物之影響爲風力工程學（ wind engineering ）中重要課題。爲了從事風力工程之研究工作，中研究物理所流力組同仁設建了一座大氣環境風洞（詳請參閱汪氏等（ 1983 ）（ 1985 ）研究報告）。該風洞爲開放吸入式，試驗段全長18公尺，寬3.048公尺（ 10英呎），高2.133公尺（ 7英呎）。

本文擬進一步探討利用風洞進行建築結構物試驗之可能性，選取已在國外六座不同風洞中測試過之CAARE標準高樓建築（ Melbourne ， 1980），製作模型於大氣環境風洞中測計其壓力分佈，並與國外風洞試驗結果比較，以了解該風洞從事建築物試驗之能力。

二、邊界層之形成

欲在風洞中探討風力對建築結構物之影響，首先必需能在風洞中控制邊界層之生成。

本計劃進行時，首先利用 spire（ Peterka & Cermak ， 1974 ）產生邊界層，或許由於 spire 製作不完全正確，或許由於風洞形成式不同，製成的邊界層不合用。

其後參考 Ponsford（ 1982 ） 文中所用欄柵式（ graded grid ）裝置產生邊界層。圖 1 顯示此欄柵式裝置的基本尺寸，氣流流過欄柵，輔以地面的粗糙裝過，於建築物試驗截處處形成足夠的邊邊層厚度與恰宜的速度分佈曲綫。

本計劃中風速量測或藉熱膜測針（ hot film probe ）或藉皮托管（ pitot-tube ）量度，量度數據之分析如圖 2 所示，圖 3 顯示一組風速與電壓之校驗關係，使用熱膜測針進行實驗時，圖 4 顯示試驗 1 如圖 5 所示欄柵配以磚塊爲粗糙物時，量測之平均風速資料。每塊磚塊尺寸大約爲 21 cm × 12 cm × 9 cm，磚塊在地面之佈置如圖 5 上方所示。在量測位置垂向平均速度分佈如圖 4 所示成一 n = 0.318 之指數速度分佈

$$\frac{U}{U\infty} = \left(\frac{Z}{\delta}\right)^{n}$$

式中 U 爲 Z 處之平均風速，U∞代表邊界層厚度 δ 處以外之自由流場（ free stream ）流速。

將地面粗糙物改用厚度較小的 PVC 管時，試驗數據顯示 n 值可控制於 0.24 至 0.36 一帶。圖 6 顯示試驗 17 如圖 7 所示欄柵配以 PVC管做爲粗糙物時，量得之垂向平均風速分佈，其 n ～ 0.265 。垂向紊流強度分佈如圖 8 所示。

雖然以上二組系列試驗顯示使用欄柵配以適當的地面粗糙物時，應可在大氣環境風洞 3 號轉盤處獲得足夠的邊界層厚度以及適宜的指數速度分佈曲綫。不過由於在進行試驗時，觀察到同一個熱膜測針之校驗曲綫隨著試驗之進行有相當程度的變異，是由於測針逐漸損耗，抑或環境空氣之濕度等變動，抑或校驗方式本身有問題，尚不得而知。

改用較不受環境影響之皮托管爲量測風速工具。圖 9 顯示試驗 18 如圖 10 所示欄柵配以 PVC 圓管爲地面粗糙物時，量測的平均風速資料。垂向平均風速分佈顯示 n ～ 0.204 。紊流強度分佈如圖11所示。值的注意的是皮托管量度風速與熱膜測針量度值有相當的不同，由於皮托管之量度直接，同時量度數據重複性甚佳，因之計劃中之壓力計測部分中相關之風速量計採用皮托管量計者。

三、建築物模型

CAARC 標準高樓爲一長方型建築，高 600 呎、截面爲 100 呎× 150 呎，四週平坦。計劃中使用壓克力製作二種比例的模型。一爲 $\frac{1}{240}$，一爲 $\frac{1}{400}$，前者放置於 3 號轉盤時，由於發生振動，暫時無法使用。將半徑 140 cm 的 3 號轉盤支架全面加強後，$\frac{1}{240}$ 的建築物模型可置於 3 號轉盤上進行試驗。模型如圖12所示。在 2 ／3 高度處沿截面四周頭有小孔量度壓力，壓力孔編號如圖12右下方所示。轉盤固定時盤面的突出地面 0.4

cm。

四、壓力量計

將圖 12 所示建築物模型置於風洞中 3 號轉盤處，如圖 10 所示位置，當氣流流經上游 351.5 cm 處之欄柵，並受地面 PVC 管所構成的粗糙物影響，流至模型處時邊界層厚度 δ 大於 150 cm，因之此個模型處於大氣邊界層內。

各壓力孔處之壓力由 scanivalve 控制，經由差壓式壓力感應器可量得各壓力孔處壓力。模型頂處靜壓與流速之量測亦可藉圖 13 所示系統量得。圖 14 顯示一些壓力實際量測值。

在不同吹風角度 β = 0°, 15°, 30°, 45°, 60°, 75°, 90° 時所量得的壓力差值可據以計算而得壓力係數 C_p 值。值得一提的是在數日內重複試驗所得 C_p 值相當接近。

$$C_p = \frac{P - P_H}{\frac{1}{2}\rho U_H^2}$$

式中 P_H 與 U_H 分別爲模型頂處靜壓與流速。

五、壓力分佈之比較

表 1 顯示本計劃所得之壓力係數 C_p 值，依吹風角度 β 及孔口位置列出，與表 2 國外其他實驗室所量計壓力係數值比較，可看出其大小尚稱吻合。同一孔口在相同吹風角度時之壓力係數差異值並不大於圖外其他實驗室量計壓力係數值彼此間之差異值。

表 3 顯示量計壓力之標準差分係數 $C_{\sigma p}$

$$C_{\sigma p} = \frac{\sigma_p}{\frac{1}{2}\rho U_H^2}$$

式中 σ_p 爲壓力之標準差分，與國外其他實驗室量計之 $C_{\sigma p}$比較（ Melbourne ， 1980 ），大氣環境風洞中量計值略小，此與流場中基本紊流強度（圖 8 B ）較國外其他實驗室風洞流場紊流強度爲小有關。

六、結論與建議

1. 利用欄柵並輔以地面 PVC 管組成之粗糙物，在大氣風洞 3 號轉盤處之邊界層厚度可達 150 cm 以上，邊界層內平均風速成指數分佈，利用不同之地面粗糙物，指數 n 可控制於 0.20 至 0.36 的範圍內。
2. 利用壓力孔與皮托管量度 CAARC 高樓模型之流速與壓力分佈，在不同吹風角度所得 C_p 分佈情形大致上與國外實驗室量計值類同。

爲能使紊流問題獲得更好的了解，需要設置一座小型風洞，供熱膜測針校驗用。同

時宜再改良欄柵構造，使形成之紊流具較大的紊流強度。

誌　謝

本計劃承行政院國科會NSC74-0414-P001-05計劃經費支援得以完成，謹致謝意。

參考文獻

1. Melbourne, W. H., 1980 : Comparison of Measurements on the CAARC Standard Tall Building Model in Simulated Model Wind Flows , J. Wind Engr. & Indus. Aerodynamics, 6 , 73-88.
2. Peterka, J.A. & J.E.Cermak, 1974; Simulation of Atmospheric Flow in Short Wind Tunnel Test Section , FDDL, CER 73-74 JAP-JEC 32, Colorado State University.
3. Ponsford , P. J., Wind Tunnel Measurements of Aerodynamic Forces and Moments on a Model of a Semi-Submersible Offshore Drilling Rig , NMI R34 , 1982.
4. 汪群從、黃榮鑑、張能復、梁文傑、曾忠一、簡來成、呂幸源，1983. 大氣邊界層風洞規劃與設計研究、國科會研究報告，NSC72-0414-P-001-02, AEWT-001
5. 汪群從、張能復、黃榮鑑、梁文傑、林俊男、劉國棟，1985 大氣邊界層風洞系統特性之研究，國科會防災科技研究報告 73-33 號

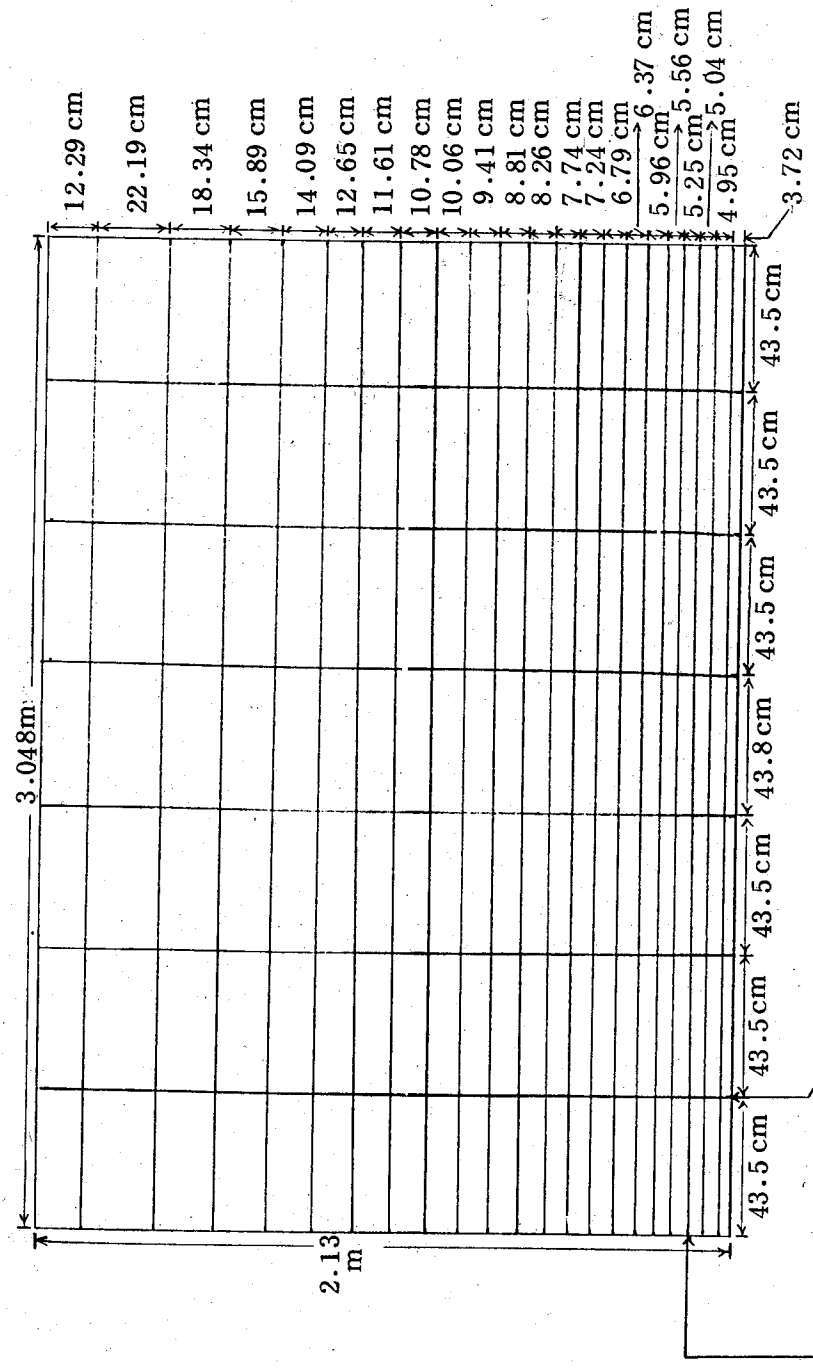

圖 1　欄柵裝置

圖 2　流場計測分析流程圖

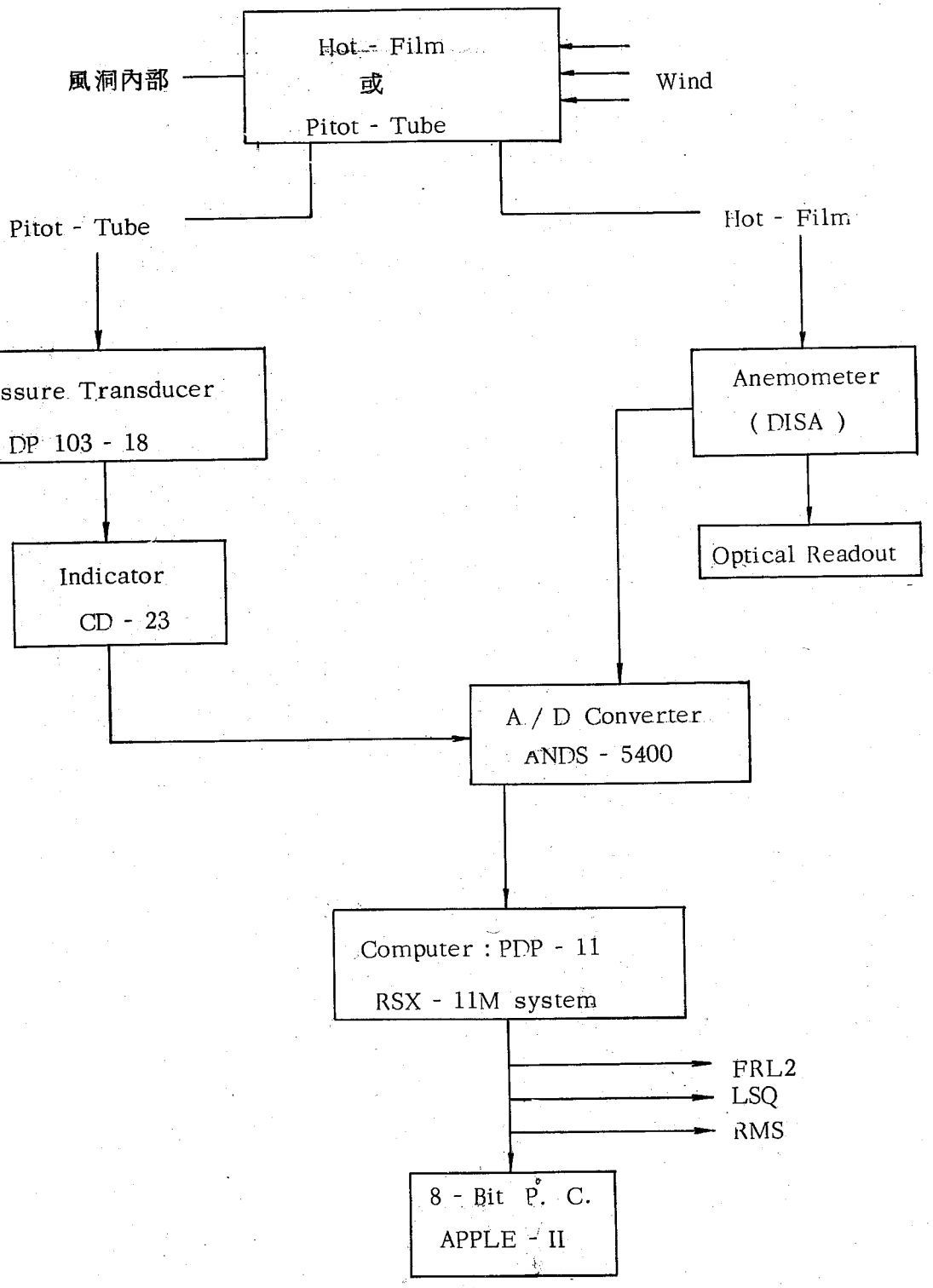

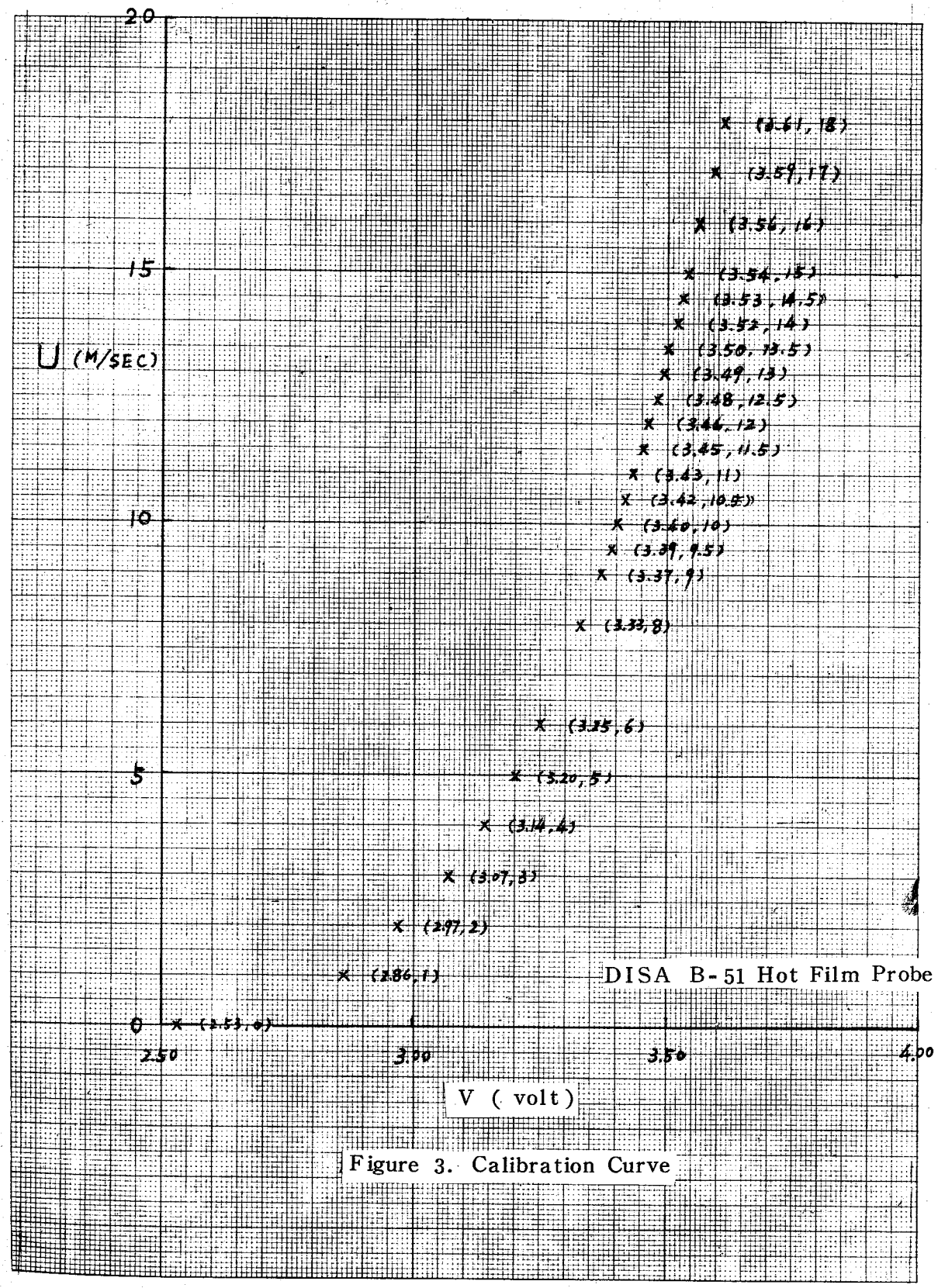

Figure 3. Calibration Curve

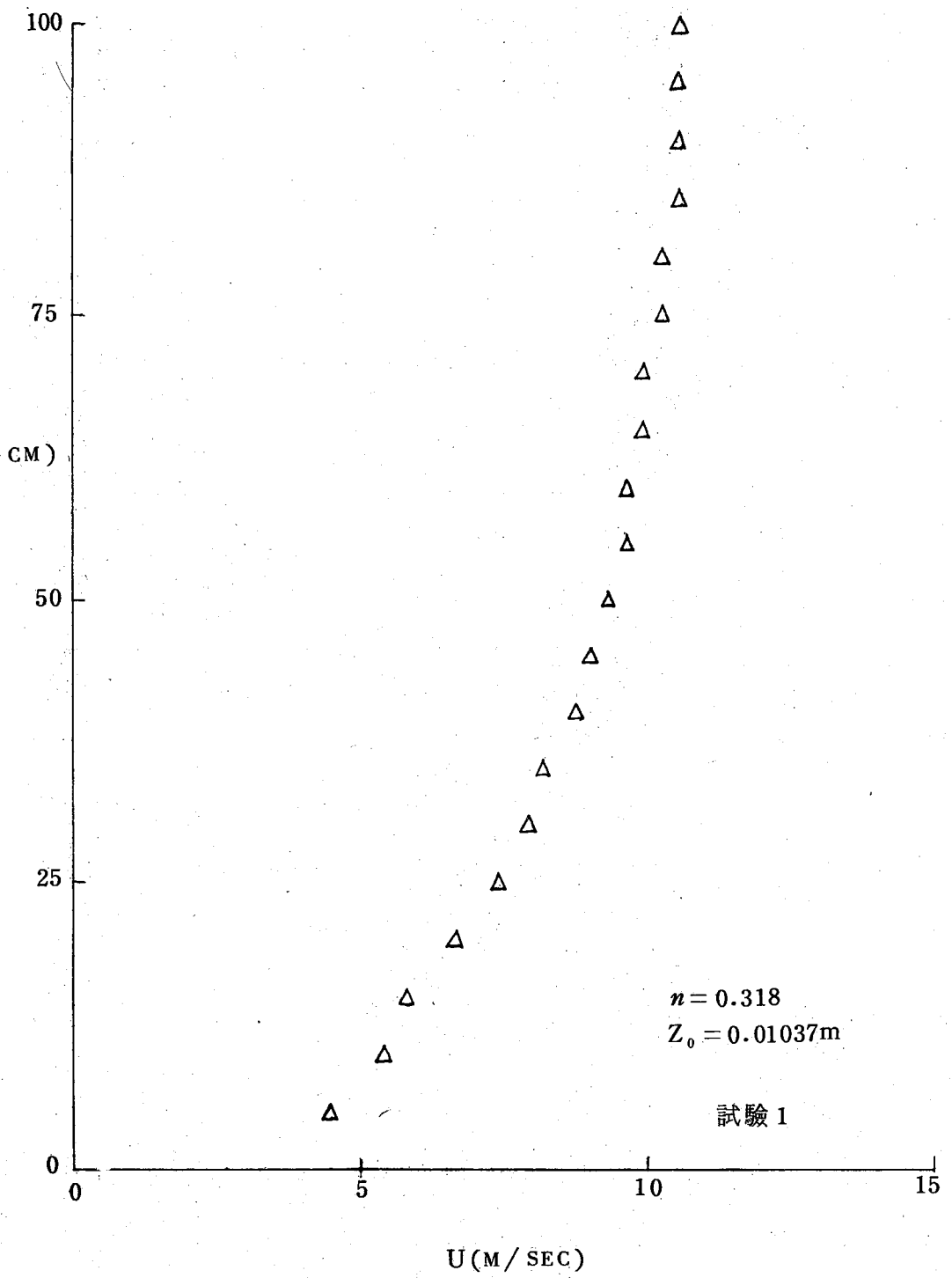

Figure 4. Velocity Distribution

Wind-tunnel

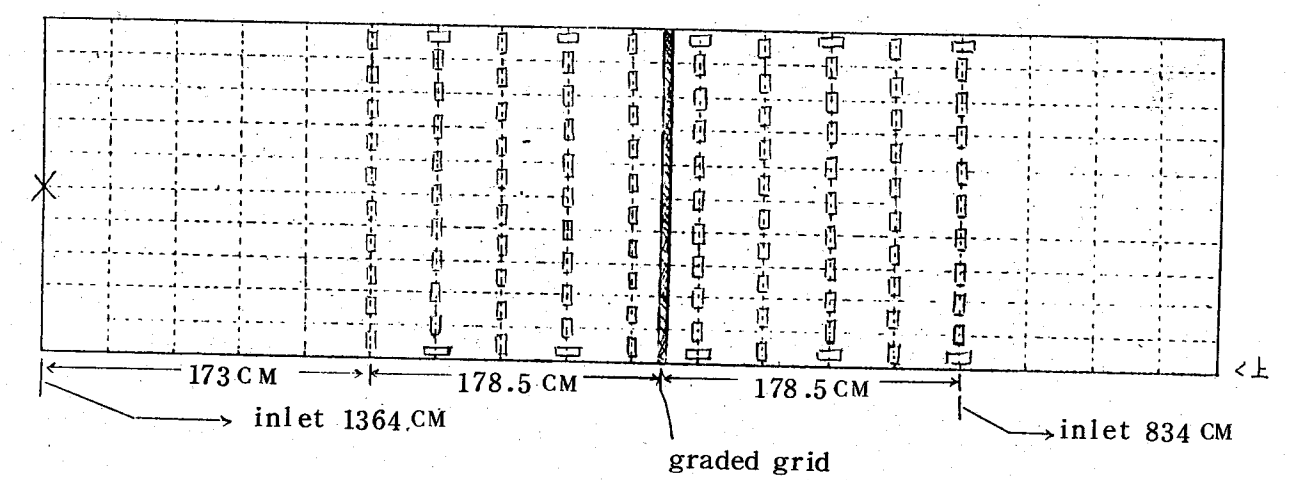

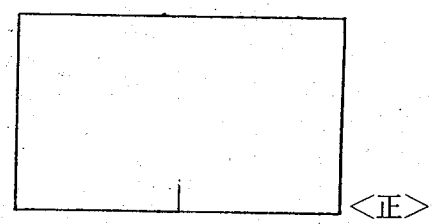

Srrangement in Wind-tunnel

Roughness : 磚塊
Graded Grid : 固定式
Barrier : 無

圖 5 試驗佈置

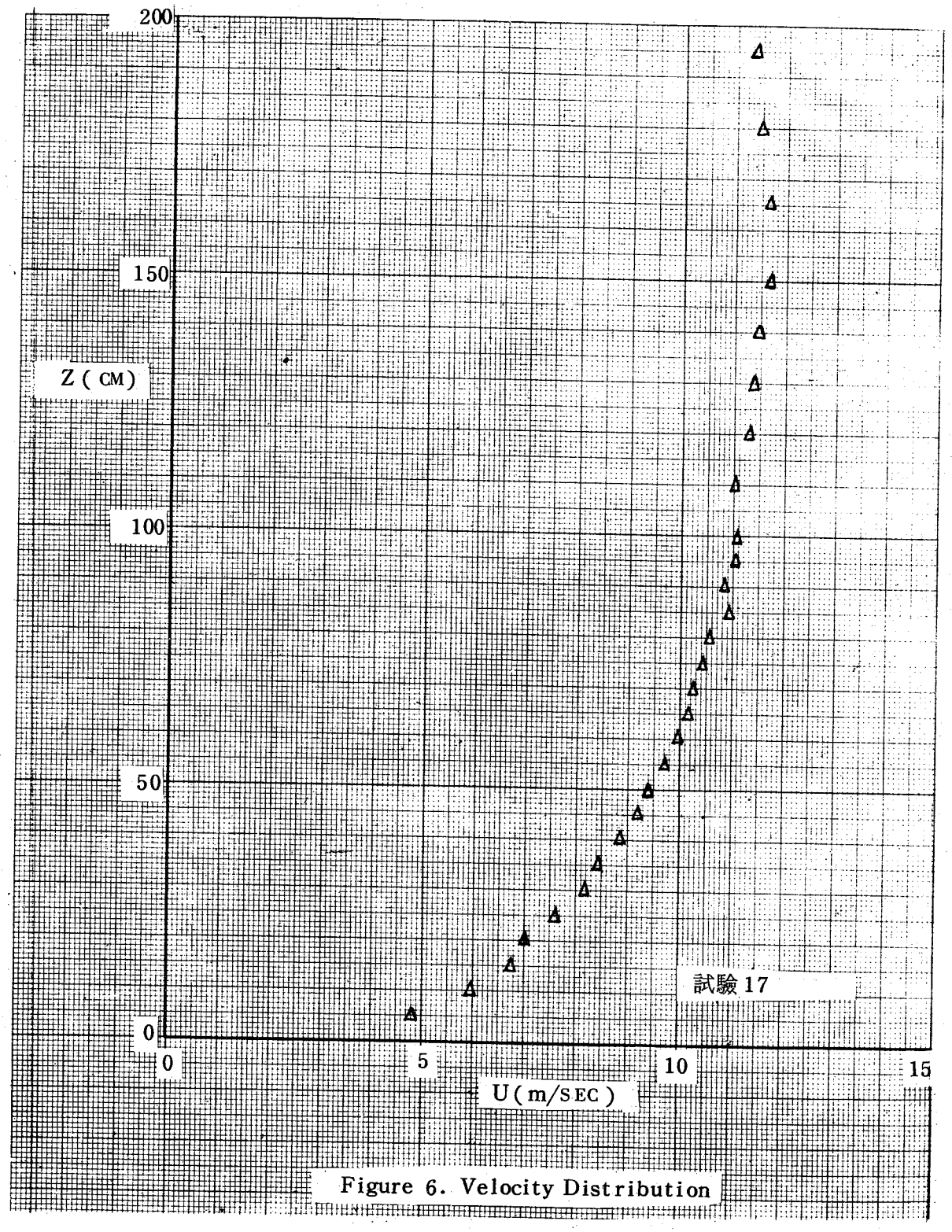

Figure 6. Velocity Distribution

Wind-tunnel

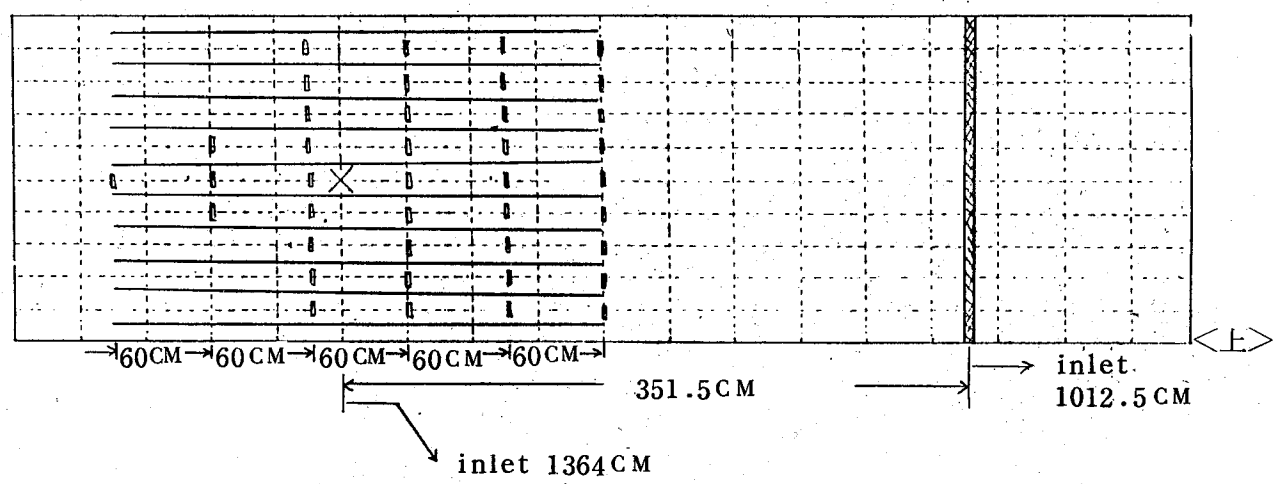

Arrangement in Wind-tunnel

ROUGHNESS: ① 1" PVC 圓管，長 300 CM 10 枚直排
② ½" PVC 圓管，長 5.6 CM 40 段橫排

GRADED GRID: 固定式

BARRIER: 無

圖 7 試 驗 佈 置

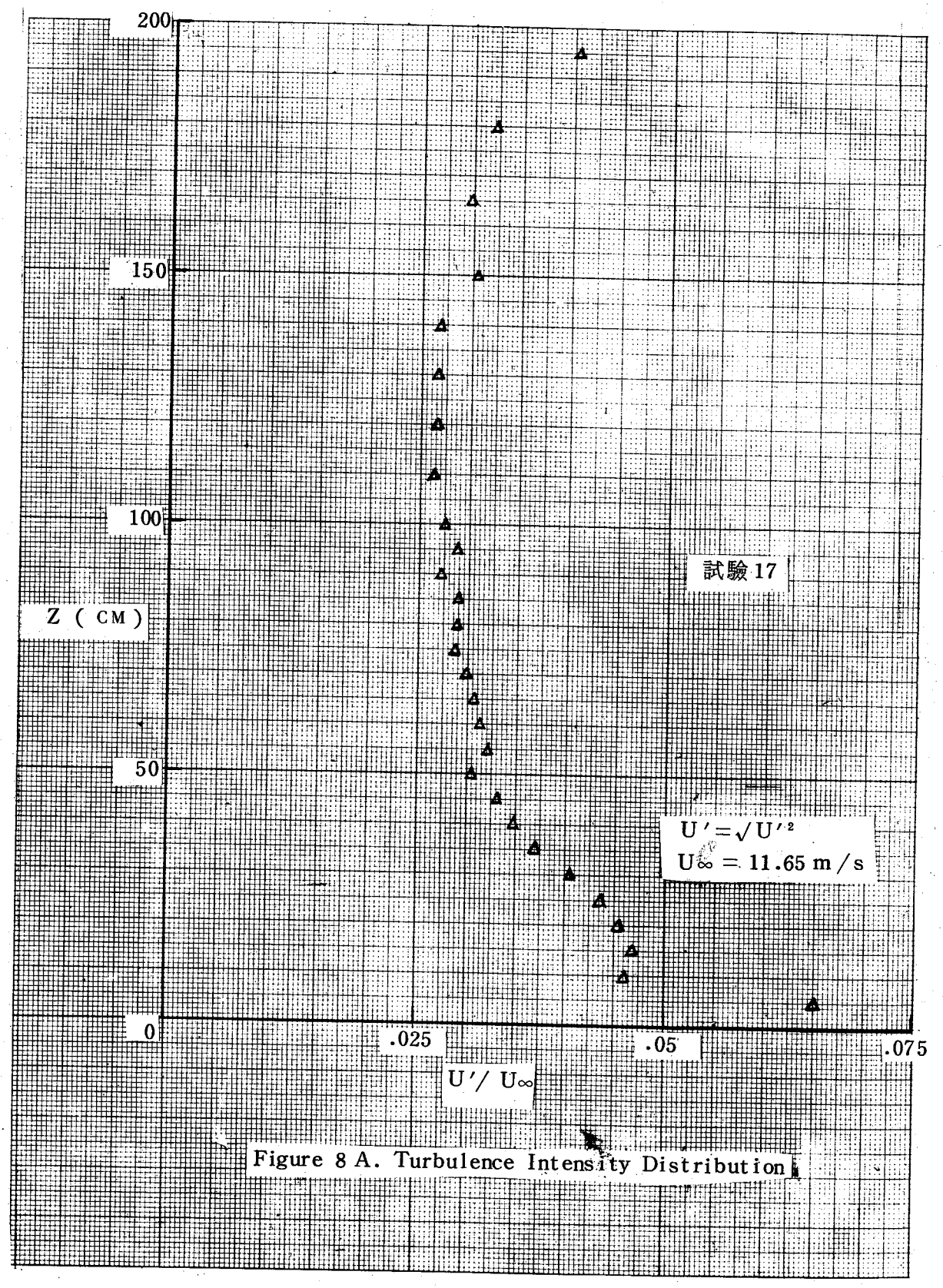

Figure 8 A. Turbulence Intensity Distribution

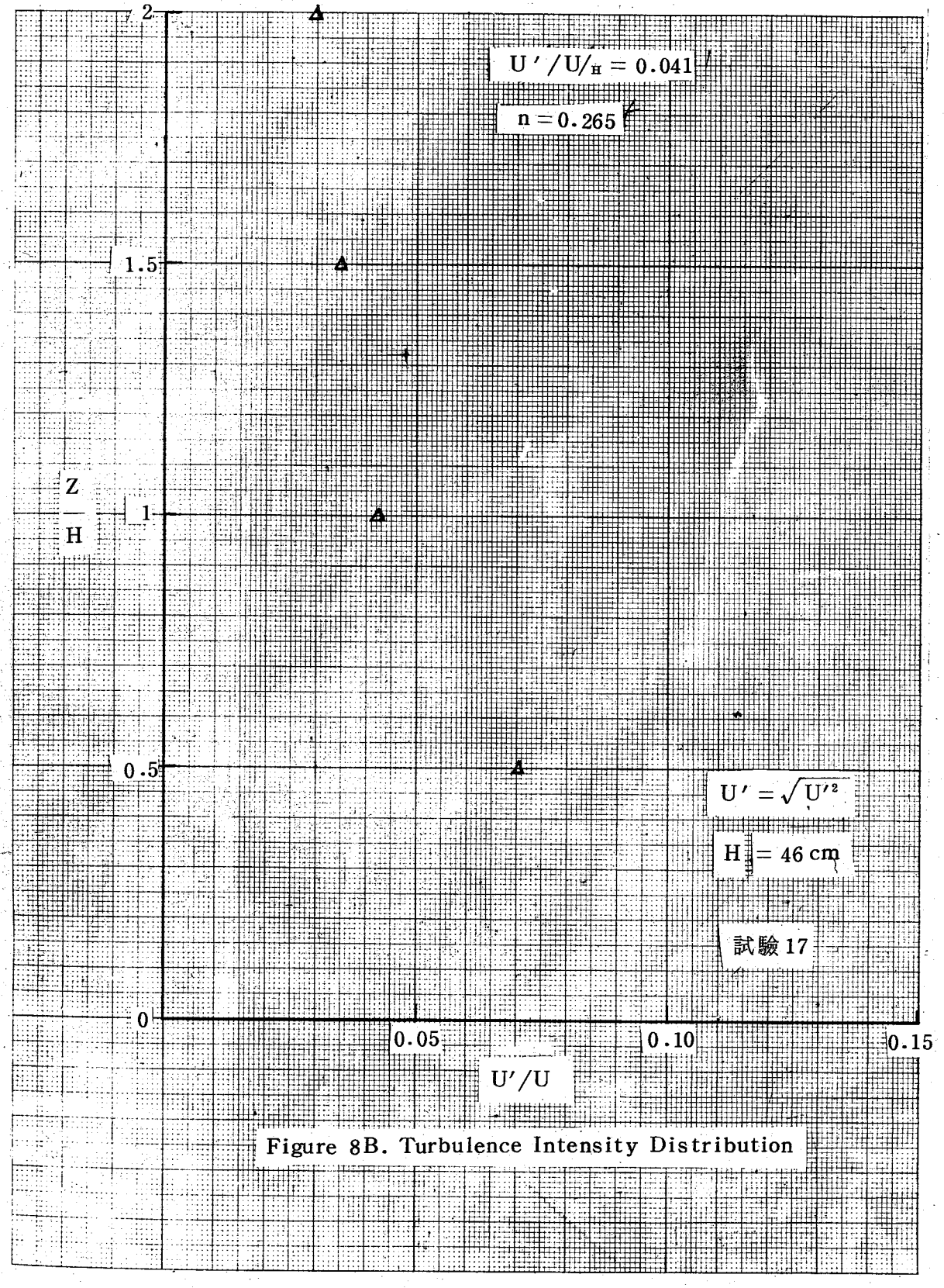

Figure 8B. Turbulence Intensity Distribution

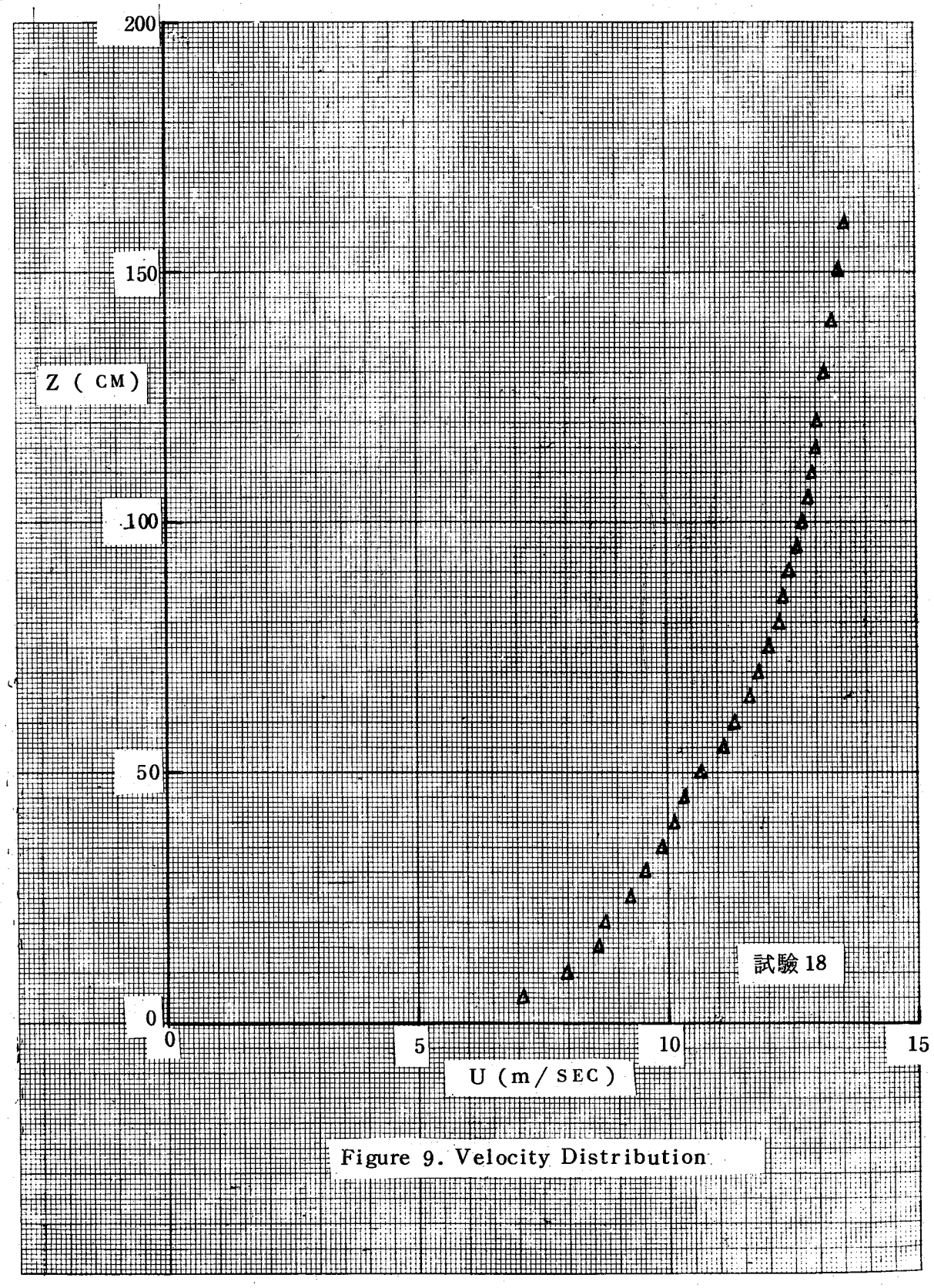

Figure 9. Velocity Distribution

Wind-tunnel

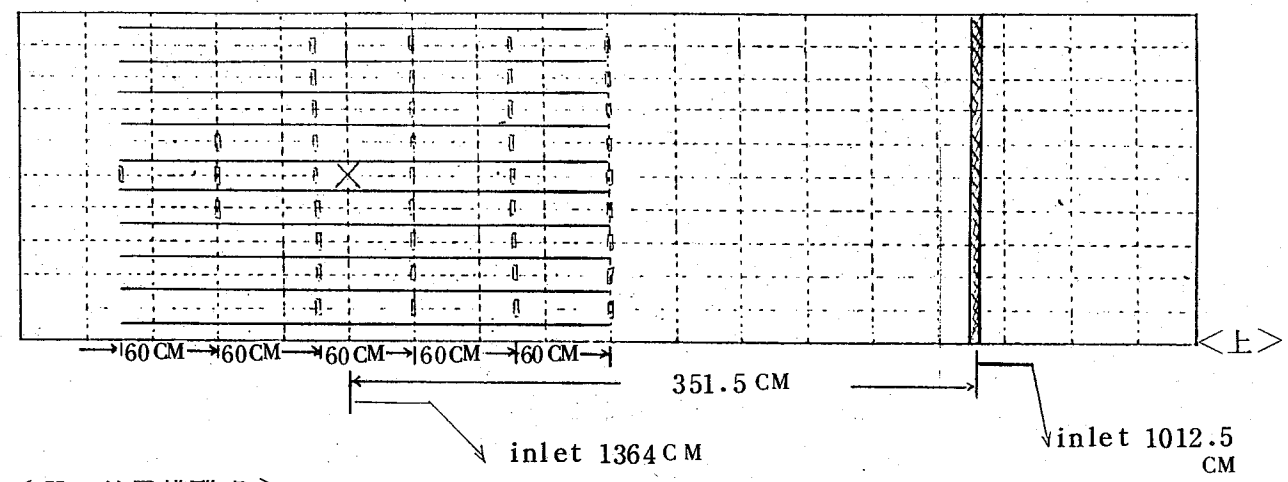

〔X：放置模型處〕

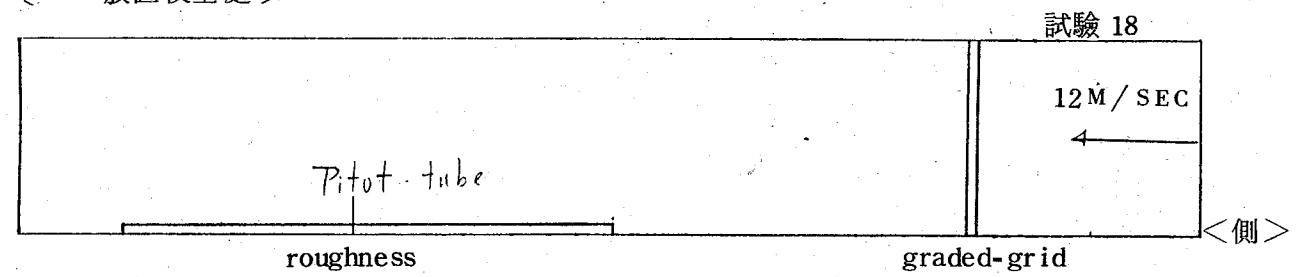

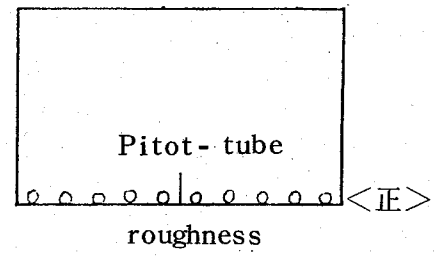

Arrangement in Wind-tunnel

ROUGHNESS： ① 1" PVC 圓管，長 300 cm　10根直排
② ½" PVC 圓管，長 5.6 cm　40段橫排

GRADED GRID： 固定式

BARRIER： 無

圖 10　試　驗　佈　置

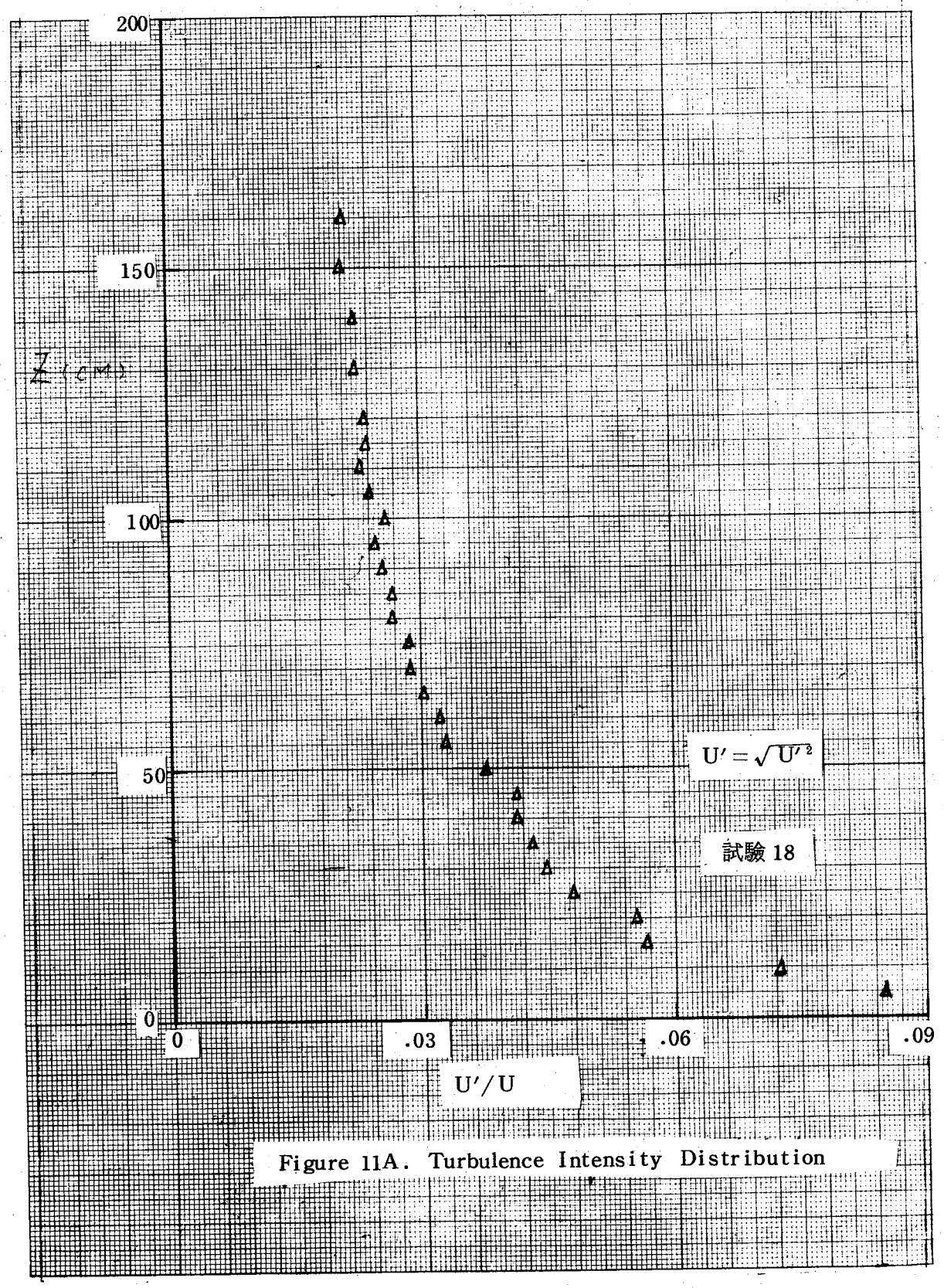

Figure 11A. Turbulence Intensity Distribution

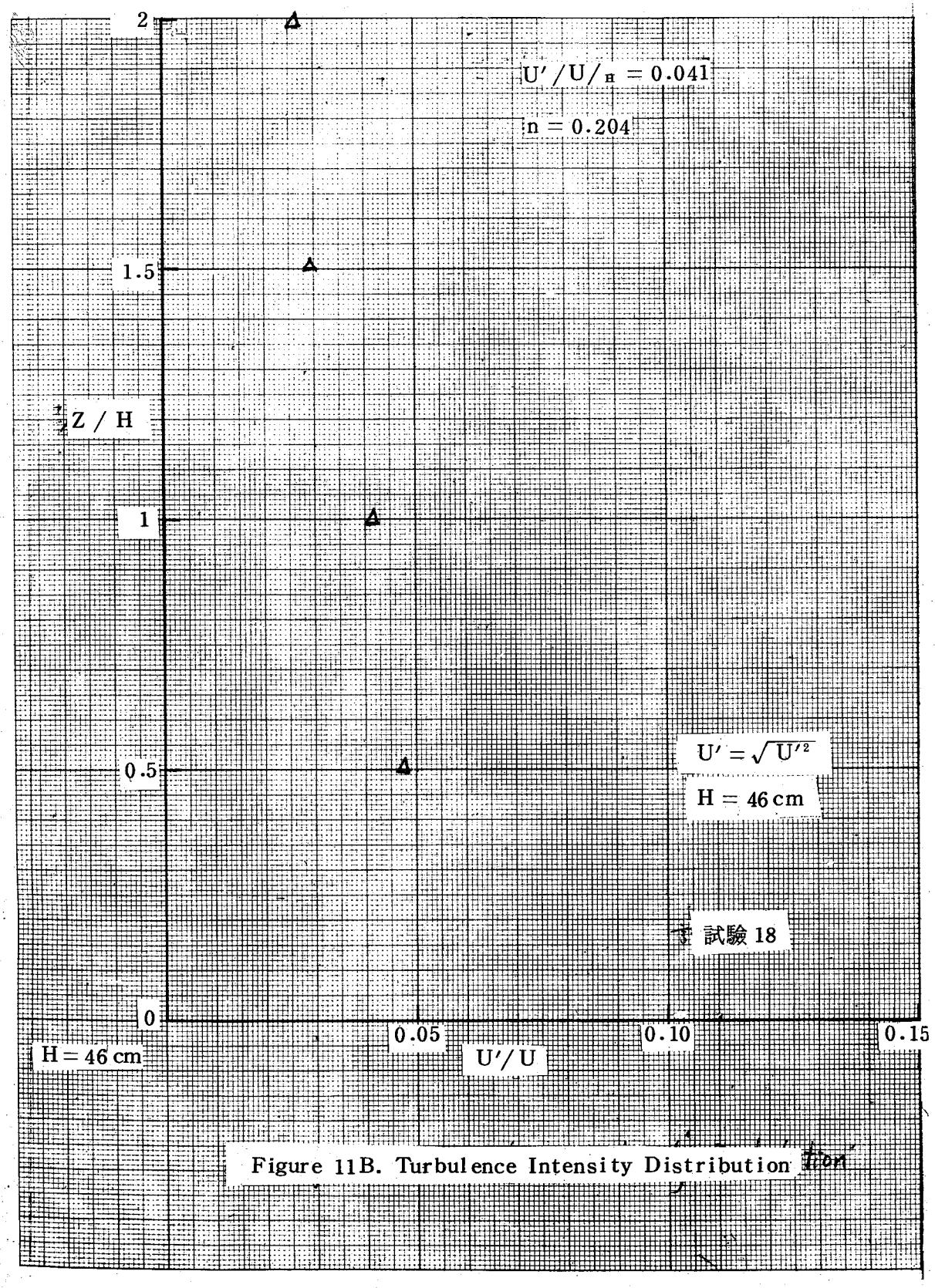

Figure 11B. Turbulence Intensity Distribution

圖12 建 築 物 模 型

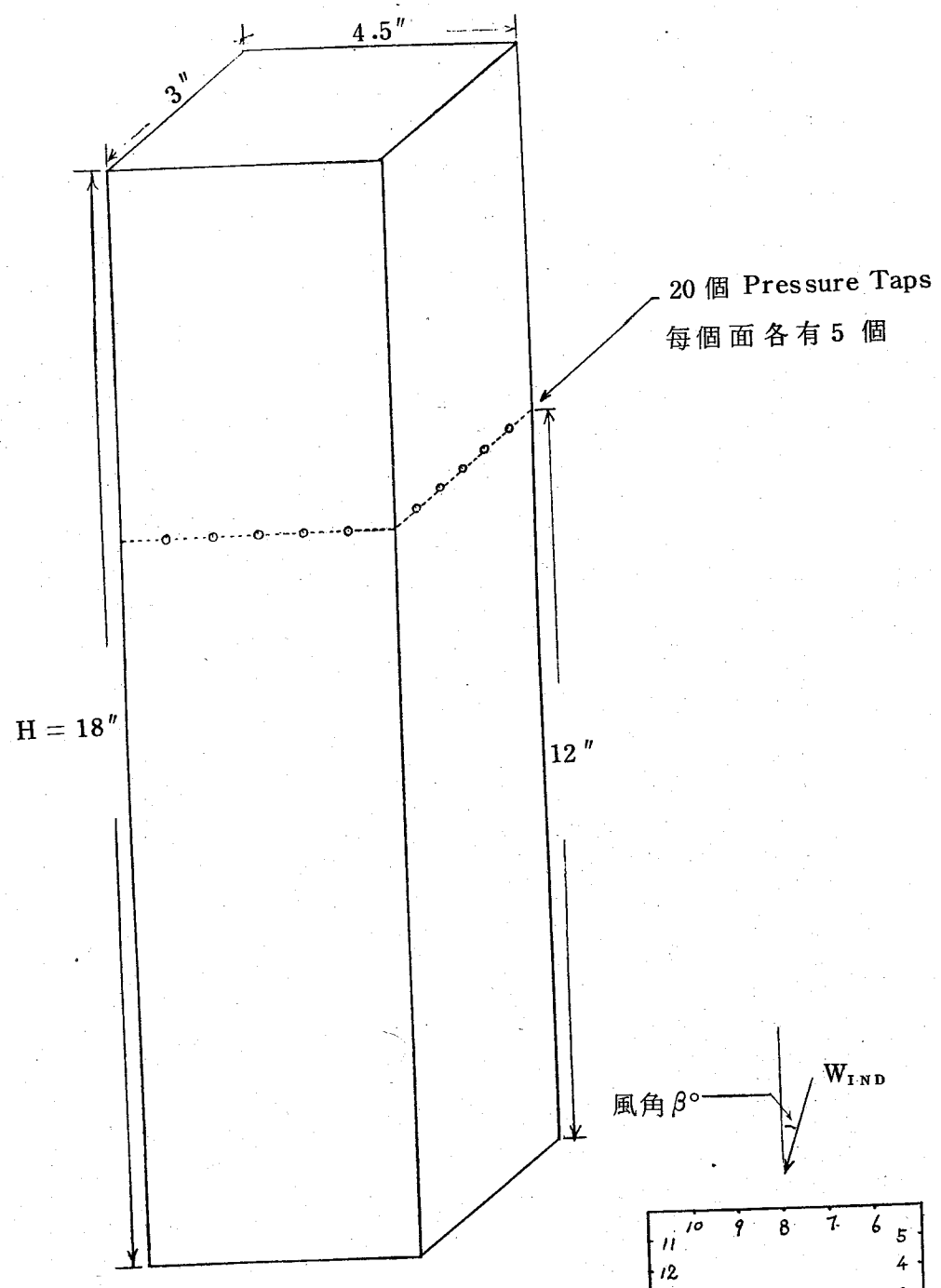

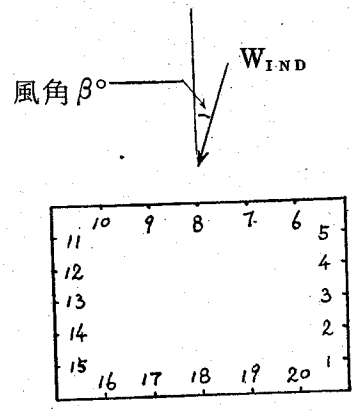

PRESSURE TAPS
20 個，在⅔H(12″)高處

模型：比例：$\frac{1}{400}$
尺寸：18″× 4.5″×3″
材質：壓克力板製

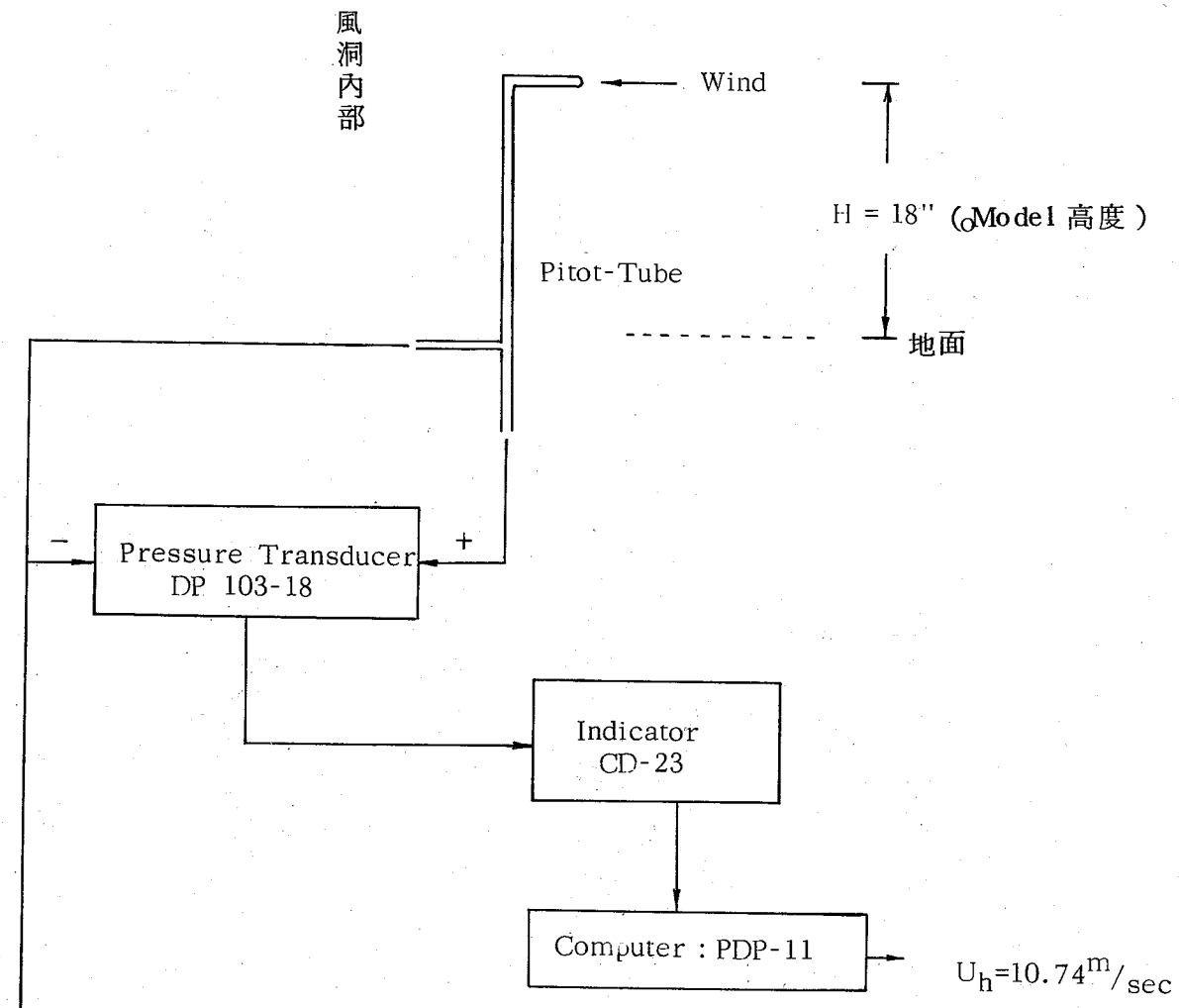

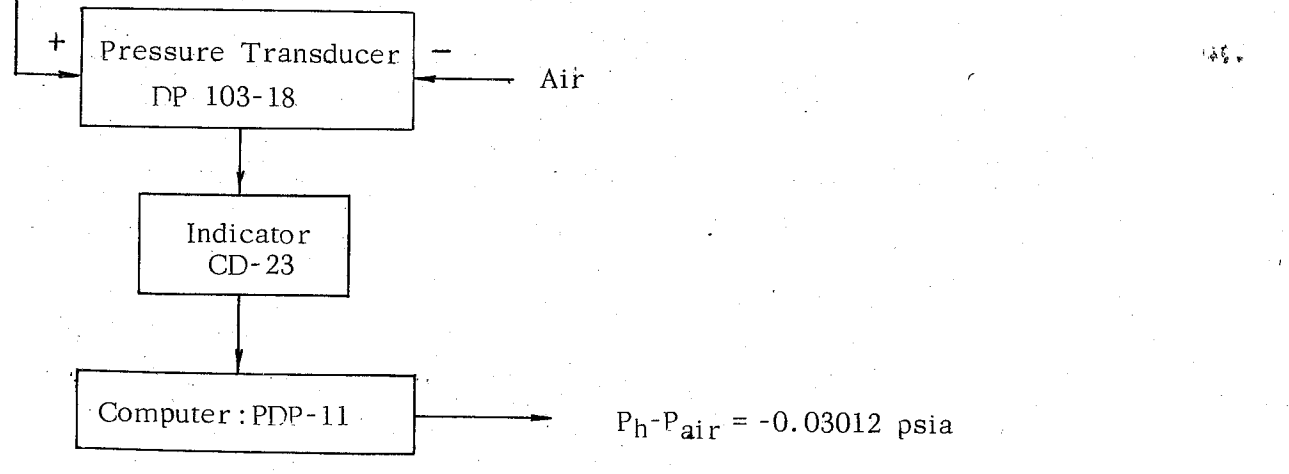

圖13 靜壓與流速量測系統

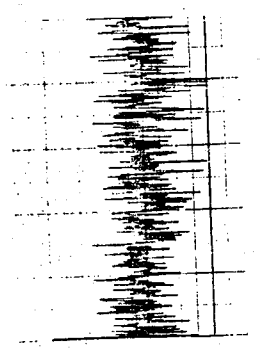

#3 β : 90°

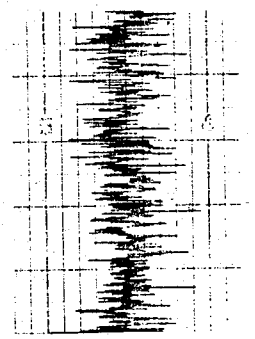

#4 β : 75°

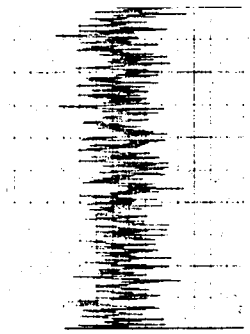

#1 β : 60°

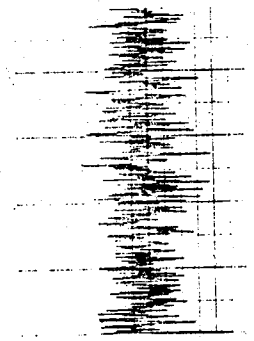

#7 β : 45°

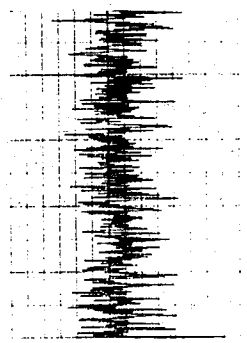

#8 β : 30°

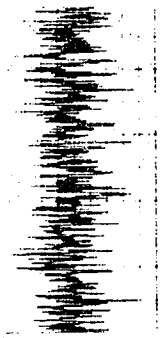

#7 β : 15°

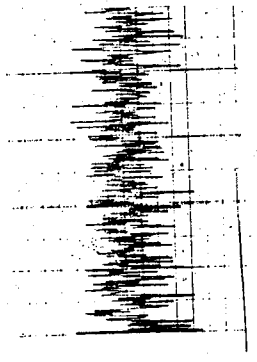

#6 β : 0°

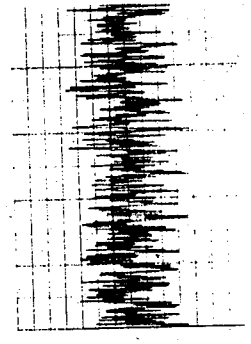

#13 β : 90°

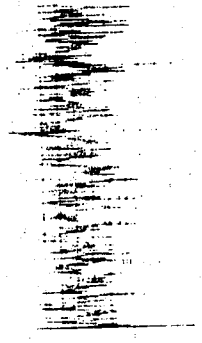

#17 β : 45°

圖14 壓 力 測 量 值

表1 壓力係數，C_p，值

$U_H = 10.7414 m / sec = 35.2408 ft / sec$ —— static velocity at H.

$P_H - Pair = -0.03012$ psia —— static pressure diff at H.

$H = 46$ cm —— building model height

$\rho = 0.076314\ \ell bm / ft^3$ —— density of air

$C_p = [(P - Pair)_{tap} - (P_H - Pair)] / \frac{1}{2}\rho U_H^2$ —— pressure coeff.

$C_{\sigma p} = P_{rms} / \frac{1}{2}\rho U_H^2$ —— pressure fluctuations coeff

C_p 值

孔口	β = 0°	β = 15°	β = 30°	β = 45°	β = 60°	β = 75°	β = 90°
1.	-0.92	-0.74	-0.21	-0.10	0.17	0.37	0.55
2.	-0.77	-0.88	-0.03	0.12	0.51	0.74	0.73
3.	-0.72	-0.97	0.06	0.27	0.68	0.82	0.81
4.	-0.70	-0.91	0.16	0.42	0.85	0.85	0.79
5.	-0.72	-0.87	-0.58	0.51	0.88	0.72	0.52
6.	0.40	0.65	0.83	0.79	0.02	-0.85	-0.72
7.	0.71	0.80	0.82	0.61	0.24	-0.88	-0.71
8.	0.80	0.82	0.70	0.48	0.07	-0.40	-0.81
9	0.74	0.68	0.55	0.28	0.00	-0.26	-0.77
10.	0.50	0.41	0.12	0.00	-0.21	-0.32	-0.71
11.	-0.76	-0.59	-0.53	-0.51	-0.54	-0.37	-0.51
12.	-0.72	-0.61	-0.53	-0.53	-0.54	-0.44	-0.39
13.	-0.77	-0.63	-0.61	-0.57	-0.52	-0.42	-0.39
14.	-0.81	-0.66	-0.58	-0.58	-0.48	-0.45	-0.42
15.	-0.85	-0.70	-0.58	-0.56	-0.47	-0.52	-0.44
16.	-0.66	-0.58	-0.55	-0.58	-0.59	-0.63	-0.74
17.	-0.65	-0.59	-0.50	-0.48	-0.56	-0.60	-0.74
18.	-0.58	-0.57	-0.55	-0.46	-0.52	-0.48	-0.74
19.	-0.65	-0.58	-0.53	-0.52	-0.64	-0.52	-0.71
20.	-0.64	-0.58	-0.50	-0.47	-0.51	-0.51	-0.70

表2　壓力係數 C_p 值

孔　口	$\beta = 0°$	$\beta = 15°$	$\beta = 30°$	$\beta = 45°$	$\beta = 60°$	$\beta = 75°$	$\beta = 90°$
1.	-0.77	-0.47	-0.23	0.01	0.20	0.40	0.54
2.	-0.73	-0.67	0.04	0.25	0.53	0.74	0.78
3.	-0.70	-0.89	0.01	0.39	0.70	0.84	0.84
4.	-0.69	-0.97	-0.01	0.51	0.84	0.86	0.77
5.	-0.66	-0.92	-0.47	0.67	0.88	0.74	0.50
6.	0.53	0.73	0.86	0.78	-0.03	-0.72	-0.75
7.	0.80	0.88	0.83	0.61	0.24	-0.56	-0.79
8.	0.80	0.84	0.71	0.46	0.14	-0.23	-0.77
9	0.76	0.77	0.53	0.30	0.01	-0.15	
10.	0.49	0.43	0.20	0.03	-0.16	-0.19	-0.59
11.	-0.66	-0.47	-0.46	-0.40	-0.41	-0.31	-0.42
12.	-0.70	-0.48	-0.47	-0.41	-0.42	-0.31	-0.39
13.	-0.70	-0.51	-0.48	-0.43	-0.43	-0.32	-0.34
14.	-0.71	-0.54	-0.50	-0.44	-0.43	-0.32	-0.37
15.	-0.76	-0.58	-0.52	-0.45	-0.43	-0.34	-0.40
16.	-0.59	-0.44	-0.44	-0.46	-0.53	-0.57	-0.61
17.	-0.53	-0.43	-0.43	-0.45	-0.50	-0.50	-0.69
18.	-0.50	-0.44	-0.43	-0.45	-0.47	-0.48	-0.78
19.	-0.51	-0.45	-0.44	-0.42	-0.47	-0.44	-0.77
20.	-0.58	-0.43	-0.43	-0.41	-0.45	-0.43	-0.73
實驗室	Bristol	N.A.E.	Bristol	N.A.E.	Bristol	N.A.E.	Bristol

表3　壓力標準差分係數值

$C_{\sigma p}$ 值：

孔口	$\beta = 0°$	$\beta = 15°$	$\beta = 30°$	$\beta = 45°$	$\beta = 60°$	$\beta = 75°$	$\beta = 90°$
1.	0.12	0.08	0.08	0.07	0.09	0.07	0.08
2.	0.11	0.10	0.11	0.09	0.11	0.08	0.08
3.	0.12	0.09	0.08	0.07	0.06	0.08	0.08
4.	0.09	0.09	0.07	0.09	0.09	0.09	0.07
5.	0.09	0.09	0.10	0.10	0.09	0.08	0.07
6.	0.09	0.06	0.06	0.05	0.14	0.09	0.08
7.	0.07	0.06	0.07	0.06	0.08	0.08	0.06
8.	0.09	0.07	0.08	0.06	0.07	0.09	0.10
9	0.07	0.07	0.07	0.08	0.09	0.10	0.07
10.	0.08	0.07	0.07	0.08	0.07	0.11	0.07
11.	0.11	0.08	0.08	0.06	0.10	0.08	0.10
12.	0.10	0.10	0.08	0.08	0.08	0.11	0.08
13.	0.13	0.09	0.09	0.09	0.07	0.09	0.09
14.	0.09	0.11	0.09	0.10	0.08	0.09	0.07
15.	0.11	0.09	0.09	0.07	0.09	0.08	0.09
16.	0.10	0.10	0.07	0.08	0.08	0.10	0.08
17.	0.10	0.08	0.08	0.10	0.07	0.08	0.07
18.	0.09	0.08	0.09	0.13	0.10	0.09	0.08
19.	0.09	0.08	0.09	0.09	0.08	0.10	0.07
20.	0.12	0.09	0.08	0.09	0.09	0.08	0.08

Model : $\frac{1}{400}$　　$18'' \times 4.5'' \times 3''$

Wind velocity : 12m／sec

應用數位電腦於風洞中量測紊流之研究

蕭 葆 義

中央研究院物理研究所

摘 要

本文旨在應用數位型電腦線上控制及處理分析風洞中各類紊流流場之量測。利用熱絲／熱膜、平衡電橋、風速校正儀、類比數位轉換器及數位電腦等連線形成一套系統，運用自行發展之電腦軟體程式，在數位電腦線上操作控制風洞中各類紊流流場之取樣及數據儲存與分析。該系統經實際應用驗證結果良好。

壹、前 言

風洞中流場之量測，可使用雷射儀（ Laser Doppler Velocimetry ）或熱絲／熱膜風速儀（ Hot Wire ／Film Anemometer ），然而前者價格昂貴，而後者便宜，且在適當範圍內使用，亦不失精確，故能普遍使用。

傳統上使用熱絲／熱膜量測紊流（ turbulent flow ）均以類比法處理，然而類比處理法有諸多缺失：例如易受電源供應品質影響類比處理結果；類比處理儀器無法多功能一般化，亦即一儀器一功能。反之電腦數位處理法則可免除上述缺失，並且電腦具有快速處理操作大量資料的能力，再加上各類資料處理分析之電腦應用程式可隨不同分析目的而自行撰寫，方便異常且彈性大。電腦數位處理法較諸類比處理法具如上之優點，再加上近年來，電腦的普遍化價格大衆化，故數位處理法漸有取代類比處理法之趨勢。

基於電腦數位處理法之優點，乃利用PDP-11 ／23 plus電腦爲主機做爲主要控制器，配合ANDS-5400 14 Bit 類比數位轉換器（ Analog to Digital converter），熱絲／熱膜風速儀等連線（ on line ）構成一套系統，再運用自行發展之應用程式，使該系統於線上操作控制以及處理分析以熱絲／熱膜量測風洞中之紊流。

貳、基本理論

一、熱風力計（ thermal anemometer ）原理

如圖一之惠斯登電橋（ wheatstone bridge ），其中熱絲（ hot wire ）探針或熱膜（ hot film ）探針爲電橋之一臂，若電橋平衡，亦即$R_1 / R_2 = R_3 / R$ ，則A,B

端電位相等，放大器（ amplifier ）無電壓差輸出。熱風力計即應用此原理以電流加熱探針，增加其電阻值至電橋平衡。若流體以某一流速通過探針，帶走部份熱量，故探針溫度改變，電阻值亦改變，造成電橋不平衡，則A，B端電位不相等，放大器將輸出電壓，此輸出電壓即可對應某一流速。熱風力計一般分成二種：定電流熱風力計（ Constant current anemometer ）與定溫度熱風力計（ Constant Temperatare anemometer）。本文系統則採定溫度熱風力計，其原理概述如下：

如圖二，以一回饋網路（ Feedback Loop ）保持探針於固定之操作溫度（ Operating Temperature）。電橋先是保持平衡狀態，若通過探針之流速改變，則探針之溫度及電阻亦將改變，爲保持探針於固定之操作溫度，回饋網路需增減其輸至探針之電流值。定溫度放大器之輸出電壓即爲供應探針足夠電流以保持其溫度於一定所需之電壓。又E（電壓）= I（電流）× R（電阻），因R＝常數，故E∝I，又I值與流速大小有關，故亦可由放大器之輸出電壓值對應某一流速。

二、探針熱傳理論

以圓柱形探針之熱傳遞爲例，在單位時間內由長度ℓ，直徑d之探針傳至周圍氣體之熱量爲：

$$h\pi d\ell\,(Q_w-Q_g) \qquad \cdots\cdots(2\cdot1)$$

式中：h ：熱傳係數（ Heat Transfer Coefficient ）

Q_w 探針溫度　　Q_g ：周圍氣體溫度

由熱平衡條件，此單位時間之熱傳損失應等於單位時間內由電流供應至探針之電能I^2R_w，R_w 爲探針之電阻值。若引入一無因次參數N_u

$$N_u=\frac{hd}{k_g} \qquad \cdots\cdots(2:2)$$

式中 k_g ：氣體右溫度爲Q_g時之熱導係數（Heat Conductivity）則可得圓柱形探針之熱平衡公式：

$$I^2R_w=h\pi d\ell\,(Q_w-Q_g)$$
$$=\pi\ell K_g\,(Q_w-Q_g)\,N_u \qquad \cdots\cdots(2\cdot3)$$

又由Kramers經驗公式

$$N_u=0.42Pr^{0.2}+0.57Pr^{0.33}Re^{0.5} \qquad \cdots\cdots(2\cdot4)$$

式中：$P_r=\frac{C_p\mu_g}{k_g}$　　$Re=\frac{\rho_g Ud}{\mu_g}$

其中　C_p ：定壓比熱係數

U ：流體流速

μ_g ：氣體溫度Q_g時之黏性係數（ dynamic viscosity ）

ρ_g ：氣體溫度Q_g時之密度

應用上式時，各氣體特性值應取溫度　Q_f

$$Q_f=\frac{1}{2}(Q_w+Q_g) \qquad \cdots\cdots(2\cdot5)$$

又探針之電阻值受溫度之影響可表示如下

$$R_w=R_o\,[\,1+b\,(Q_w-Q_o)+b_1\,(Q_w-Q_o)^2+\cdots\cdots\,] \qquad \cdots\cdots(2\cdot6)$$

式中：R_o ：溫度爲0時探針之電阻值

b_o，b_1 探針電阻之溫度係數

一般情形b_1遠小於b，故二次以上非線性項可略去，則Q_w-Q_g可表示爲

$$Q_w-Q_g=\frac{R_w-R_g}{bR} \qquad \cdots\cdots(2\cdot7)$$

將（2．7）式代入（2．3）式得

$$I^2R_w=\frac{\pi\ell K_f}{b}\cdot\frac{R_w-R_g}{R_o}\cdot N_u \qquad \cdots\cdots(2\cdot8)$$

再將Kramer 經驗公式（2．4）代入（2．8）式，得

$$I^2R_w=\frac{\pi\ell K_f}{b}\,\frac{R_w-R_g}{R_o}\,[\,0.42\,(P_r)_f^{0.2}+0.57\,(Pr)_f^{0.33}\,(R_e)_f^{0.5}\,] \qquad \cdots\cdots(2\cdot9)$$

上式適用於$R_e>40$之流況。

爲方便計，可將上式化爲

$$\frac{I^2R_w}{R_w-R_g}=P+Q\sqrt{u} \qquad \cdots\cdots(2.10)$$

式中：$P=0.42\frac{\pi\ell K_f}{bR_o}(P_r)_f^{0.2}$ $\cdots\cdots(2.11)$

$$Q=0.57\frac{\pi\ell K_f}{bR_0}\left(\frac{f_fd}{u_f}\right)^{0.5}(P_r)_f^{0.33} \qquad \cdots\cdots(2.12)$$

然而應用上P，Q值並非由（2．11）（2．12）式求得，且U亦非固定之0.5次方，而係隨流速大小，探針形狀等因素而變，故一般均表示爲：

$$\frac{I^2R_w}{R_w-R_g}=P+QU^n \qquad \cdots\cdots(2.13)$$

於定溫度電路系統下，R_w＝常數，故R_w/R_w-R_g亦爲常數，又E＝IR ，亦即$E\propto I$，故（2．13）式簡化爲

$$E^2=A+BU^\alpha \qquad \cdots\cdots(2.14)$$

此即所謂之金氏定律（King's Law）。爲探針訊號電壓值線性化（ linearize ）爲風速值之重要依據。

三、類比數位訊號轉換器及電腦

第一節述及當流體通過熱絲／熱膜，因而帶走了部份熱量，然而熱絲／熱膜爲了維

持一定溫度，反饋系統隨之產生補償電流（壓）加熱熱絲／熱膜使之維持定溫，該補償電流（壓）對應某一類比電壓值，使用纜線（cable）將之輸出。由於採用數位型電腦處理資料，所以輸出之類比電壓值必須先經過轉換爲數位電壓值，才能變成有用資料，可爲數位型電腦處理分析。

今使用美國 ANALOGIC 公司訊號搜集系統（data acquisition system）ANDS-5400 系列之類比數位轉換器，連接 PDP-11／23 plus 電腦，由電腦線上操作控制信號轉換速率及訊號搜集時間，再以直接記憶取存（Direct Memory Access；DMA）方法，將轉換完成之數位訊號（digital signal）存放於磁碟中。圖三爲上述系統運作示意圖。

參、電腦控制程式之原理

由於該量測紊流系統均由線上操作控制，故需建立各種工作程式，以利運用 PDP-12／23 plus主機進行紊流流暢取樣之控制及資料處理分析。首先應用電腦中之作業系統起動電腦後，由已建立完成之取樣程式控制將熱絲／熱膜探針感應流場之變化，透過平衡電橋，把輸出之類比電壓訊號，經由A／D轉換器，變爲數位訊號，利用電腦之 DMA 功能存入磁碟。以下說明各類工作程式之原理，程式之內容與操作使用方法，詳見蕭 1985〔8〕。

(1)使用單熱絲／熱膜取樣之資料處理分析電腦程式原理

由於使用之熱絲／熱膜爲單線，故爲單頻道輸入。因爲經類比數位轉換器轉換後之數位訊號爲電壓值，電壓值與風速值爲非線性關係，故須線性化方能進行分析，以求得平均速度，紊流強度。

熱絲／熱膜因流體通過經平衡電橋感應輸出之電壓值與流速之間，滿足金氏定律（King's law）

$$E^2 = A + BU^{\alpha} \quad \cdots\cdots (3.1)$$

式中 E：電壓值（伏特）

U：流速（公尺／秒）

A，B爲係數

α爲熱絲／熱膜之形狀係數

(1)式亦可寫成

$$U = \{ (E^2 - A) / B \}^{1/\alpha} \quad \cdots\cdots (3.2)$$

(2)式即爲電壓值線性化爲速度值之依據

流場量測前，須先對熱絲／熱膜進行校驗工作，亦即率定出風速值與電壓值之關係，該關係可由(1)式之A，B，α 決定，而最佳A，B，α 可由校驗時之風速值與電壓值以最小二乘法（Least Square Method）定之。

設若等時距取樣之電壓值均依(2)式線性化爲速度值後，則平均速度值（Mean

velocity），擾動速度均方根值（Root Mean Square of velocity fluctuation），依下述可計算求得。

令U_i 表示爲：

$$U_i = \overline{U} + u_i \quad \cdots\cdots (3.3)$$

$i = 1 \sim N$　N爲取樣數目

則

$$\overline{U} = \sum_{i=1}^{N} U_i / N \quad \cdots\cdots (3.4)$$

$$u' = \sqrt{\overline{u_i^2}} = \sqrt{|\overline{U_i^2} - \overline{U}^2|}$$

$$= \sqrt{|\sum_{i=1}^{N} U_i^2 / N - (\sum_{i=1}^{N} U_i / N)^2|} \quad \cdots\cdots (3.5)$$

式中 U_i：瞬間流速（公尺／秒）

$\overline{U_i}$：平均流速（公尺／秒）

u_i：瞬間流速擾動值（公尺／秒）

u_i'：擾動速度均方根值（公尺／秒）

(2)使用X型熱絲／熱膜取樣之資料處理分析電腦程式原理

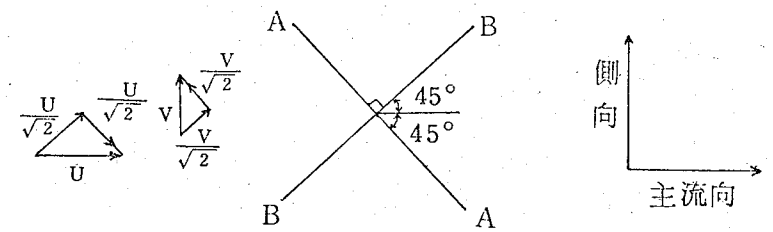

對於AA熱絲／熱膜，$\frac{U}{\sqrt{2}}$與$\frac{V}{\sqrt{2}}$二正向風速之和使其產生一輸出電壓值E_A；對於BB熱絲／熱膜，$\frac{U}{\sqrt{2}}$與$\frac{V}{\sqrt{2}}$二正向風速之差使其產生一輸出電壓值E_B。

在做熱絲／熱膜之校驗工作時，假設由校正儀（Calibrator）孔口之噴氣流爲單向均勻流，即$V = 0$，對於AA熱絲／熱膜代入金氏定律得

$$E_A^2 = A_A + B_A^* \left[\frac{U}{\sqrt{2}}\right]^{\alpha_A}$$

$$= A_A + B_A U^{\alpha_A} \quad \cdots\cdots (3.6)$$

同理對於BB熱絲／熱膜

$$E_B^2 = A_B + B_B^* \left[\frac{U}{\sqrt{2}}\right]^{\alpha_B}$$

$$= A_B + B_B U^{\alpha_B} \quad \cdots\cdots (3.7)$$

利用校驗時之風速值與電壓值，使用最小二乘法，則分別可決定出最佳之A_A，B_A，α_A

與A_B，B_B，α_B值。

設若等時距取樣，使用X型熱絲／熱膜量測二維流場，則U，V分別可依下述方法計算求得。

設AA熱絲／熱膜與BB 熱絲／熱膜置於風場中，其平衡電橋之輸出電壓值爲E_{Ai}，E_{Bi}，$i=1\sim N$，N爲取樣數目。由金氏定律知

$$E_{Ai}^2 = A_A + B_A^* \left[\frac{1}{\sqrt{2}} (U_i + V_i) \right]^{\alpha_A}$$

$$= A_A + B_A \left[U_i + V_i \right]^{\alpha_A} \quad \cdots\cdots (3.8)$$

$$E_{Bi}^2 = A_B + B_B^* \left[\frac{1}{\sqrt{2}} (U_i - V_i) \right]^{\alpha_B}$$

$$= A_B + B_B \left[U_i - V_i \right]^{\alpha_B} \quad \cdots\cdots (3.9)$$

(8)(9)式聯立，求解U_i，V_i，如下：

$$U_i = \frac{1}{2} \left[\left(\frac{E_{Ai}^2 - A_A}{B_A} \right)^{\frac{1}{\alpha_A}} + \left(\frac{E_{Bi}^2 - A_B}{B_B} \right)^{\frac{1}{\alpha_B}} \right] \quad \cdots\cdots (3.10)$$

$$V_i = \frac{1}{2} \left[\left(\frac{E_{Ai}^2 - A_A}{B_A} \right)^{\frac{1}{\alpha_A}} - \left(\frac{E_{Bi}^2 - A_B}{B_B} \right)^{\frac{1}{\alpha_B}} \right] \quad \cdots\cdots (3.11)$$

式中 U_i：主流向瞬間速度（公尺／秒）

V_i：側向瞬間速度 （公尺／秒）

(10)(11)式之A_A，B_A，α_A與A_B，B_A，α_B爲做熱絲／熱膜校驗時決定出之最佳係數。E_{Ai}，E_{Bi}爲平衡電橋之輸出電壓值，故由(10)(11)式即可將電壓值線性化爲速度值。令U_i，V_i分別表示爲：

$$U_i = \overline{U} + u_i \quad \cdots\cdots (3.12)$$

$$V_i = \overline{V} + v_i \quad \cdots\cdots (3.13)$$

則

$$\overline{U} = \sum_{i=1}^{N} U_i / N \quad \cdots\cdots (3.14)$$

$$\overline{V} = \sum_{i=1}^{N} V_i / N \quad \cdots\cdots (3.15)$$

$$u' = \sqrt{\overline{u_i^2}} = \sqrt{| \overline{U_i^2} - \overline{U}^2 |} \quad \cdots\cdots (3.16)$$

$$= \sqrt{| \sum_{i=1}^{N} U_i^2 / N - (\sum_{i=1}^{N} U_i / N)^2 |} \quad \cdots\cdots (3.17)$$

$$v' = \sqrt{\overline{v_i^2}} = \sqrt{| \overline{V_j^2} - \overline{V}^2 |}$$

$$= \sqrt{| \sum_{i=1}^{N} V_i^2 / N - (\sum_{i=1}^{N} V_i / N)^2 |} \quad \cdots\cdots (3.18)$$

$$\overline{uv} = \overline{(U_i - \overline{U}) (V_i - \overline{V})}$$

$$= \overline{U_i V_i} - \overline{U}\,\overline{V}$$

$$= \sum_{i=1}^{N} U_i V_i / N - (\sum_{i=1}^{N} U_i / N) (\sum_{i=1}^{N} V_i / N) \quad \cdots\cdots (3.19)$$

式中 $\overline{U}$：主流向平均流速（公尺／秒）

$\overline{V}$：側向平均流速（公尺／秒）

u_i：主流向瞬間流速擾動值（公尺／秒）

v_i：側向瞬間流速擾動值（公尺／秒）

u_i'：主流向擾動速度均方根值（公尺／秒）

v_i'：側向擾動速度均方根值（公尺／秒）

$\overline{uv}$：主流向與側向相關性或紊流應力（公尺／秒）^{2}

(3)最小二乘法之電腦程式原理

熱絲／熱膜校驗工作完成，電壓值與速度值之關係符合金氏定律而該定律若視爲E^2與U^α之關係，則爲一次方程式，故方程式斜率與截距B，A可利用最小二乘法求得如下。

給定α值，利用下式求出A，B

$$A = \{ \sum_{j=1}^{N} (E_j^2) \sum_{j=1}^{N} (U_j^\alpha)^2 - \sum_{j=1}^{N} (U_j^\alpha) \sum_{j=1}^{N} (U_j^\alpha) (E_j^2) \} / \Delta \quad \cdots\cdots (3.20)$$

$$B = \{ N \sum_{j=1}^{N} (U_j^\alpha) (E_j^2) - \sum_{j=1}^{N} (U_j^\alpha) \sum_{j=1}^{N} (E_j^2) \} / \Delta \quad \cdots\cdots (3.21)$$

式中 $\Delta = N \sum_{j=1}^{N} (U_j^\alpha)^2 - [\sum_{j=1}^{N} (U_j^\alpha)]^2$

$j = 1 \sim N$ N爲校驗量測數目

A，B求出，則方程式$E^2 = A + BU^\alpha$亦定出，再比較由該方程式計算值與校驗之量測值之誤差，選出最小之誤差平方和，該組即是最佳之A，B,α。

(4)溫度效應之校正

當熱絲／熱膜進行校驗工作時之室溫與熱絲／熱膜置於風洞中進行量測時之溫度不同時，須進行溫度效應校正，蓋熱絲／熱膜對於溫度之感應相當靈敏。校正時，將風洞中進行量測之取樣電壓值乘以一係數修正。該修正系數如下：

$$f = \left(\frac{T_s - T_c}{T_s - T_e} \right)^{0.5} \quad \cdots\cdots (3.22)$$

式中 T_s：熱絲／熱膜操作溫度（ sensor operatrng temperature ）°C 。

T_c：熱絲／熱膜進行校驗時之室溫（ room temperature of calibration ）°C。

T_e：熱絲／熱膜置於風洞中進行量測之氣溫（ wind tunnel room temper-

ature ）°C。

肆、紊流量測系統之應用程序

一、紊流流場取樣與分析之程序：

1. 調整平衡電橋，調整方法可參考平衡電橋儀器操作手册〔 1 ，2 〕。
2. 利用校正儀由空壓機送氣設定不同風速值，設定方法參考校正儀操作手册〔 3 〕，使用經調整後之平衡電橋，配合 PDP-11 ／ 23 plus 電腦，執行FRL 2 與MEAN 程式對熱絲／熱膜進行校驗，亦即決定率定曲線。
3. 利用最小二乘法，由電腦執行 LSQ 程式而定出最佳 A ，B ，α 。
4. 定出 A ，B ，α 值後，將熱絲／熱膜置於風洞中，由電腦執行 FRL 2 程式控制取樣之時距與取樣之時間，再將平衡電橋之輸出類比電壓值轉換爲數位電壓值接存入磁碟。
5. 執行電腦中預先建立之各種程式，線上操作處理分析取樣之數據，結果以列表機印於報表紙上。
6. 程序示意流程圖參考圖四(a)(b)。

二、電腦控制及線上處理分析數據程式：

依照不同目的亦即流場取樣之控制或取樣數據的處理分析，經撰寫測試後建檔之電腦工作程式分成三類：訊號搜集；訊號轉換及檢驗；訊號處理及資料分析。各類處理程式之名稱分別表示如下：

(1)訊號搜集：FRL2

(2)訊號轉換及檢驗：RRL2 ，VEL

(3)訊號處理及資料分析：MEAN ，LSQ ，RMS, STRESS

伍、應用實例與結果

使用前述設立完成之紊流量測系統，可應用於風洞中進行各類紊流量測。

下述以平板尾端二維紊流跡流（ Two-Dimensional turbulent wake flow ）及大氣邊界層（ Atmospheric Boundary layer ）風速剖面模擬爲例，利用自行設立發展之量測系統進行紊流量測，量測之取樣數據由數位電腦線上處理分析，結果及討論如下：

㈠應用之結果：

大氣邊界層之風洞模擬，經常於空風洞內加設粗糙度（ roughness ）或欄柵（grid ），以增加邊界層厚度，而該等模擬是否合乎個別實驗目的，必先量測平均風速剖面及紊流強度剖面。應用本文所述開發設立之紊流量測系統，參照圖四(a)所示流程，即可完成該工作。

平板跡流之量測係採用 240 公分長、120 公分寬、1.6 公分厚之三合板，前後端均

削尖，豎吊於風洞試驗段前端處，以平均風速 4 公尺／秒通過平板。亦即雷諾數（ Reynolds' no. ）爲 $R_e = U_0 L / \nu \approx 530000$ ，L 爲平板長，U_0 爲自由流速，ν 爲黏性係數，量測平板尾端下游 5 公分，20 公分，50 公分處之二維紊流跡流平均特性。同樣應用前述之紊流量測系統，參照圖四(b)所示之流程，即可完成二維紊流平均特性之量測工作。

㈡討論：

採用DISA Probe Type 55 R31 單熱膜使用校正儀校驗，並由數位電腦執行LSQ 程式，計算出最佳 A ，B ，α 值。校正結果繪定率定曲線，示如圖五。圖六則爲率定曲線以金氏定律表示之結果。使用上述之DISA單熱膜進行風洞大氣邊界層風速剖面模擬之量測，由數位電腦PDP-11 ／ 23 plus 執行FRL2 程式進行取樣，之後再由數位電腦執行RMS 程式，以處理分析取樣數據，結果繪於圖七，亦即圖七爲平均風速剖面與紊流強度剖面之結果。

採用DISA Probe Type 55 P61 X 型熱絲使用校正儀校驗該熱絲，並由電腦執行MEAN程式，計算出二根熱絲在不同之風速下所對應之電壓值，結果繪於圖八(a)、(b)，分別得二根熱絲之率定曲線。又執行LSQ 程式計算出二根熱絲最佳 A ，B ，α 值。結果繪於圖九(a)、(b)，分別得二根熱絲之率定曲線以金氏定律表示之結果。使用上述校驗完成之DISA X型熱絲於風洞中進行平板尾端二維紊流跡流之量測，由電腦執行FRL2 程式進行取樣，之後再執行 STRESS程式以處理分析取樣數據，結果分別繪於圖十、圖十一及圖十二。圖十爲平板尾端下游 5 公分、20 公分及 50 公分處之平均速度剖面圖，由該圖可以很明顯地看出二維紊流跡流之平均流速特性，隨著遠離平板尾端（ trailing edge ）而中心點速度漸增；以及跡流區之擴大。圖十一爲平板尾端下游 5 公分、20 公分及50公分處之主軸流向之紊流強度分佈圖。該圖很清楚的告訴吾人，各斷面之最大紊流強度均偏離中心軸（或對稱軸）；又隨著遠離平板尾端各斷面之最大紊流強度均遞減且更偏離中心軸。圖十二爲平板尾端下游 5 公分、20 公分、50 公分處之紊流應力（ Reynolds' stress ）分佈圖。由該圖可以知道隨著遠離平板尾端各斷面之最大紊流應力均遞減且更偏離中心軸。比較圖十一與圖十二可以發現各斷面之最大紊流強度均發生於最大紊流應力區域內。

陸、結　論

由以上應用實例驗證運用熱絲／熱膜風速儀，A／D 轉換器及 PDP電腦等連線構成之系統應用於風洞中進行紊流流場量測爲可行，且結果良好。該系統之資料處理工作程式隨需要可再行補充，如計算紊流相關函數，能譜，各種尺度等，非常具有彈性，誠爲量測紊流之有效工具。

誌　謝

本文進行期間，蒙黃榮鑑教授張能復教授熱心提供儀器設備，謹誌謝忱。

參考文獻

〔1〕Instruction Manual DISA 56C16
General Purpose Bridge 1983

〔2〕Instruction Manual IFA 100 System
TSI Incorporated 1983

〔3〕Instruction Manual Model 1125／1125R
Calibrator／Probe Rotator

〔4〕Focus 5000 System 1983

〔5〕Manuals of RSX-11M of PDP-11 1984

〔6〕Doebelin , E.O.“Measuremt System Application and Design ”, Mc Graw-Hill 1983

〔7〕Hinze , J.O. “ Turbulence ” Chapter 2 1975

〔8〕蕭葆義，“應用數位型電腦線上控制及處理分析熱絲／熱膜量測紊流之研究”中央研究院物理研究所大氣環境風洞實驗室研究報告AEWT-006 ，中華民國七十四年六月

〔9〕黃榮鑑、趙勝裕、蕭葆義，“平板紊流跡流之量測”，行政院國家科學委員會研究計劃研究報告NSC-74-0202-M-001-10 FM304 AEWT-007 中華民國七十四年七月

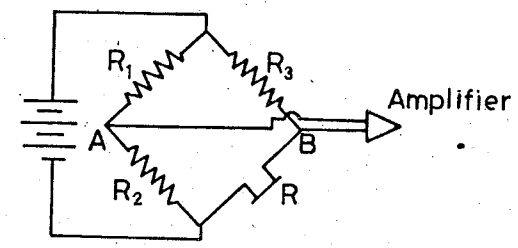

圖一　惠斯登電橋示意圖

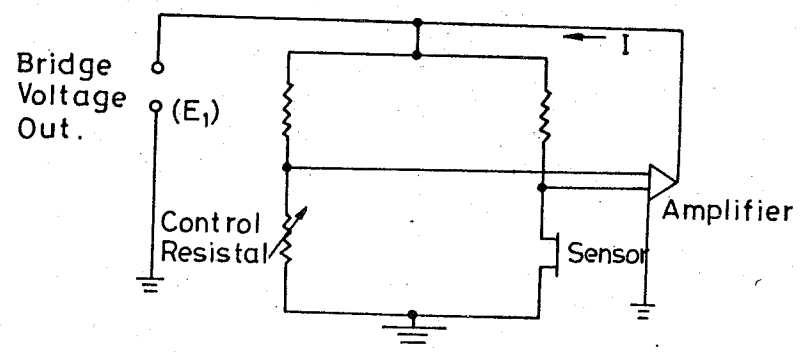

圖二　定溫度風力計電路示意圖

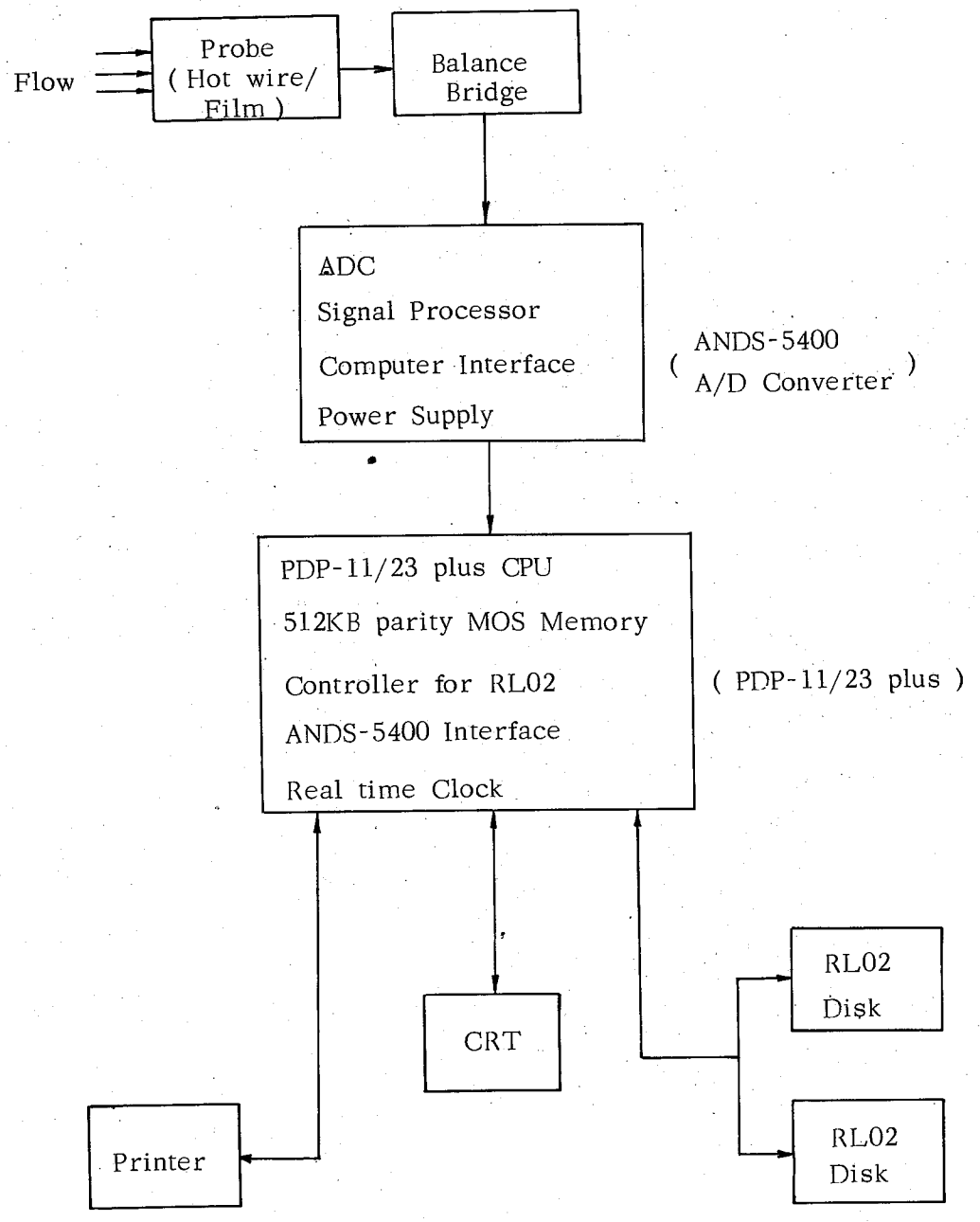

圖三　紊流流場取樣系統示意圖

流　程	說　明
RUN FRL2	（單熱絲／熱膜置於校正儀噴口取樣）
RUN MEAN	（分析上述取樣結果，計算平均電壓值）
RUN LSQ	（由平均電壓值及速度值之量測結果，計算出最佳A，B，α值）
RUN FRL2	（單熱絲／熱膜置於風洞紊流流場中進行取樣）
RUN RMS	（將執行LSQ計算出之最佳A，B，α輸入分析上述取樣結果，計算出平均流速、速度擾動均方根植）

圖四(a)　單熱絲／熱膜量測紊流之電腦程式使用程序示意圖

流　　程	說　　明
RUN FRL2	（X型熱絲／熱膜置於校正儀噴口取樣）
RUN MEAN	（分析上述取樣結果，計算平均電壓值）
RUN LSQ	（由平均電壓值及速度值之量測結果，計算出最佳之A_1, B_1, α_1, A_2, B_2, α_2 值）
RUN FRL2	（X型熱絲／熱膜置於風洞紊流流場中進行取樣）
RUN STRESS	（將執行LSQ計算出之最佳A_1, B_1, α_1, A_2, B_2, α_2 輸入分析上述取樣結果，計算出主流向及側向之平均流速、速度擾動均方根值及紊流應力）

圖四(b)　X型熱絲／熱膜量測紊流之電腦程式使用程序示意圖

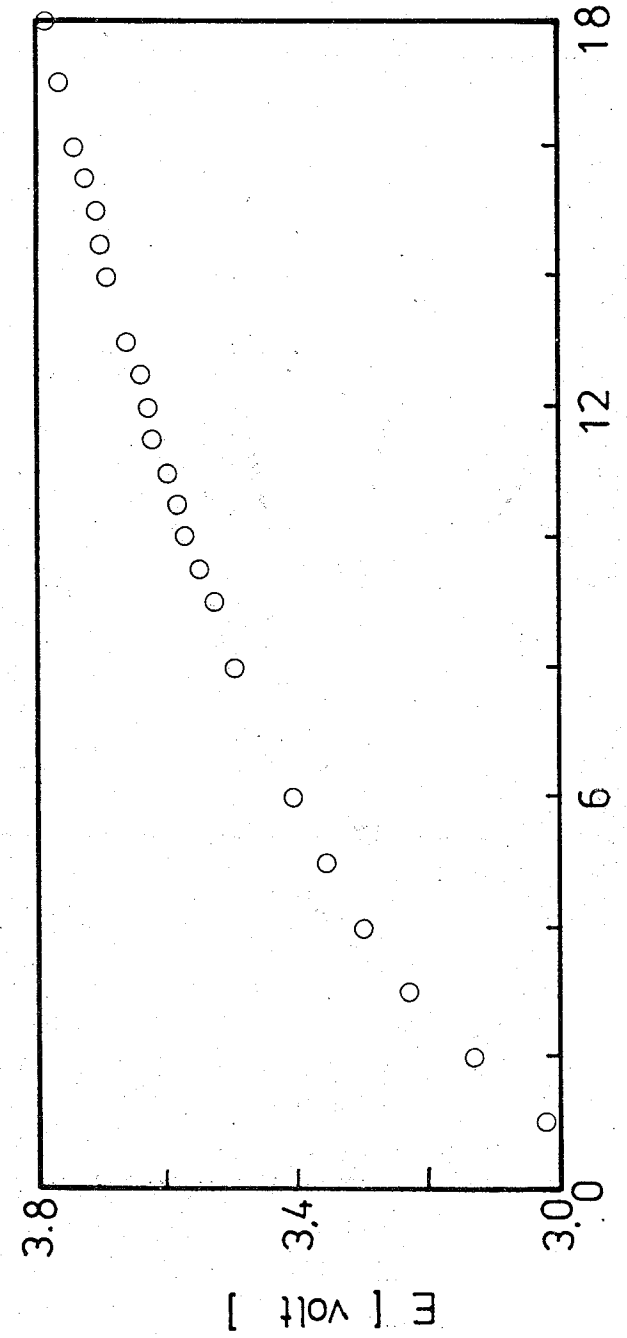

圖五、DISA Probe Type 55 R31 單熱膜之風速值與電壓值之率定曲線

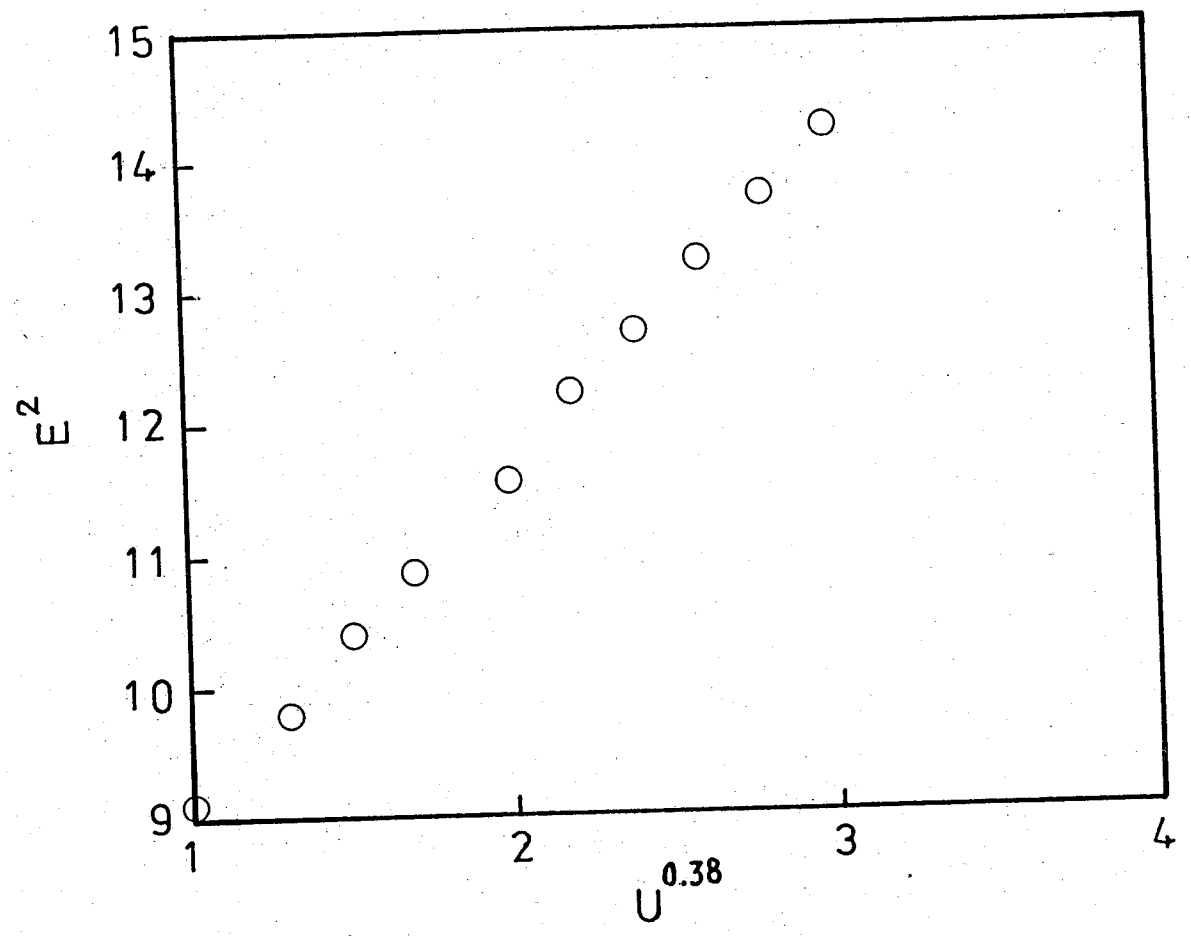

圖六　DISA Probe Type 55 R31 單熱膜之率定曲線以金氏定律表示

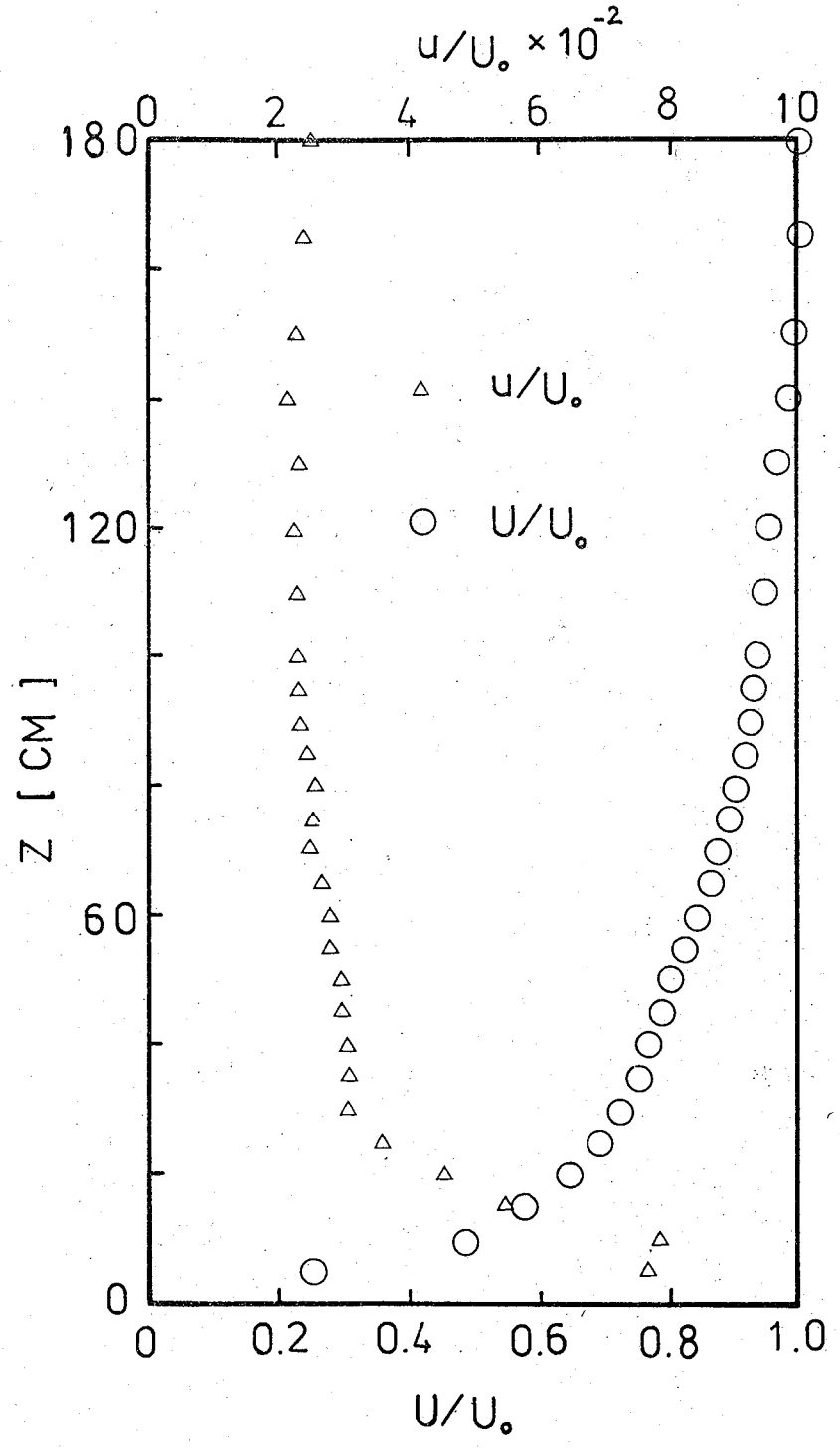

圖七　以DISA Probe Type 55 R31 單熱膜量測平均風速剖面及紊流強度剖面

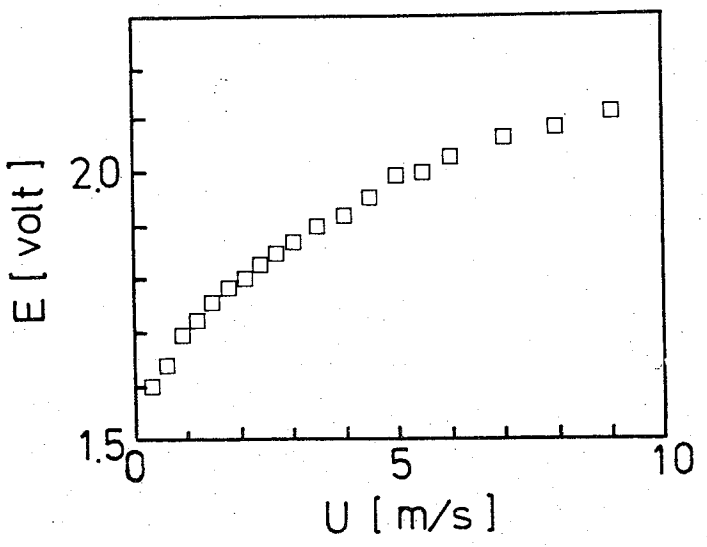

圖八(a) DISA Probe Type 55 P61 X型熱絲之第一根熱絲之電壓值與風速值之率定曲線

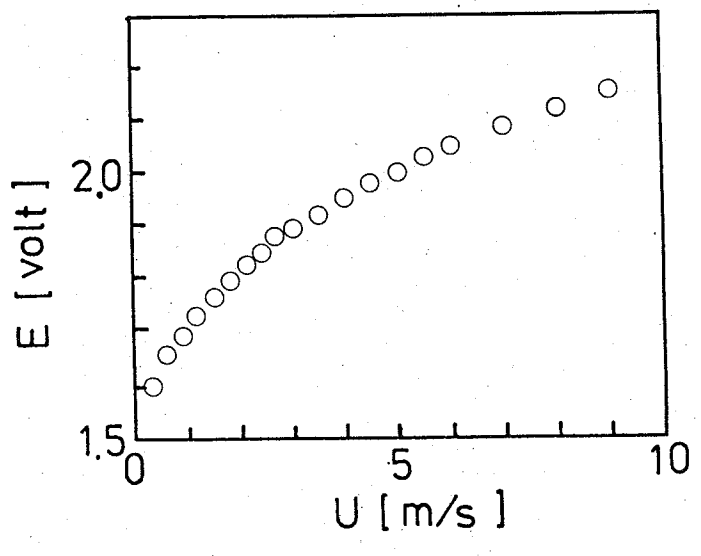

圖八(b) DISA Probe Type 55 P61 X型熱絲之第二根熱絲之電壓值與風速值之率定曲線

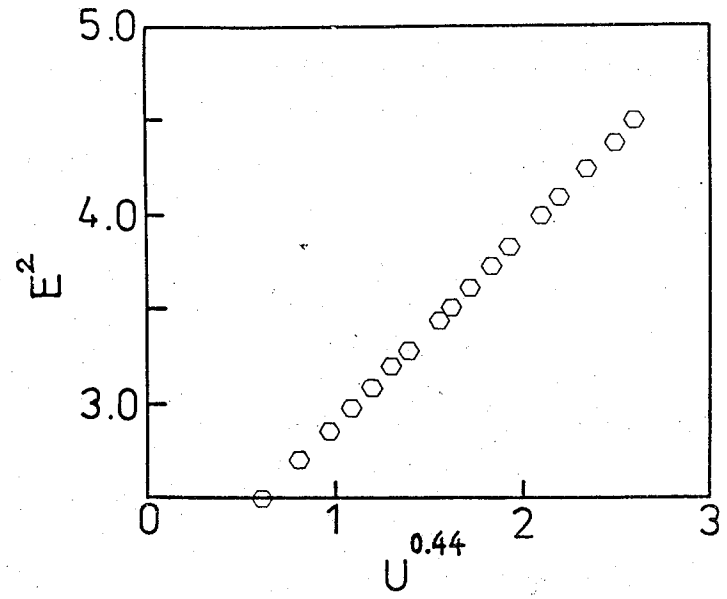

圖九(a) DISA Probe Type 55 P61 X型熱絲第一根熱絲之率定曲線以金氏定律表示

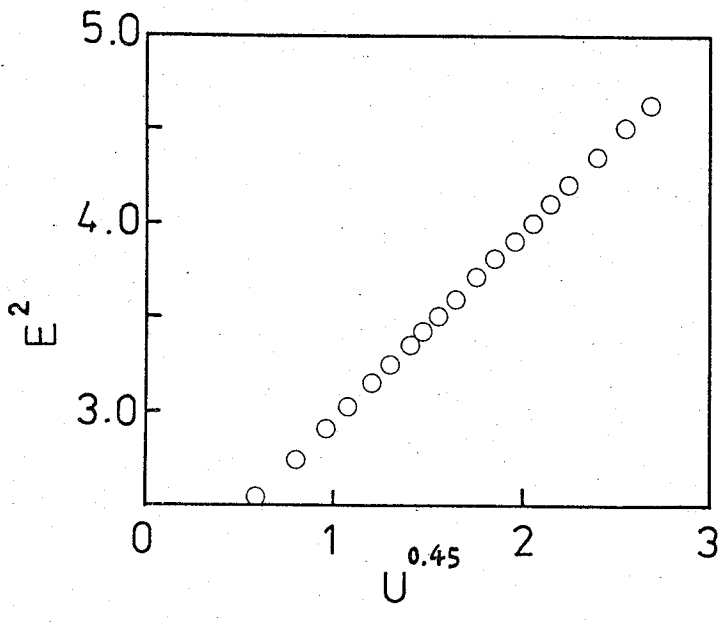

圖九(b) DISA Probe Type 55 P61 X型熱絲第二根熱絲之率定曲線以金氏定律表示

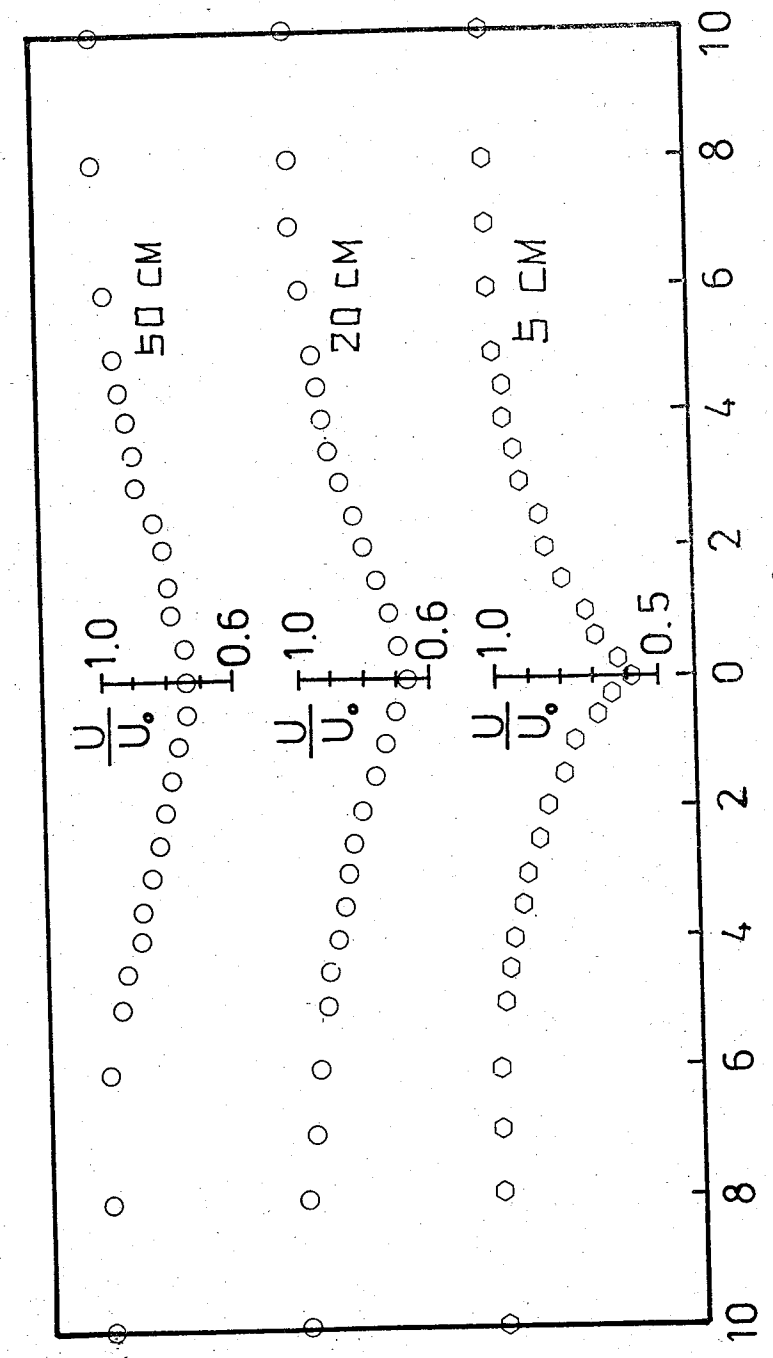

圖十　以DISA Probe Type 55 P61 X型熱絲量測平板尾端下游5公分、20公分及50公分處之平均流速剖面

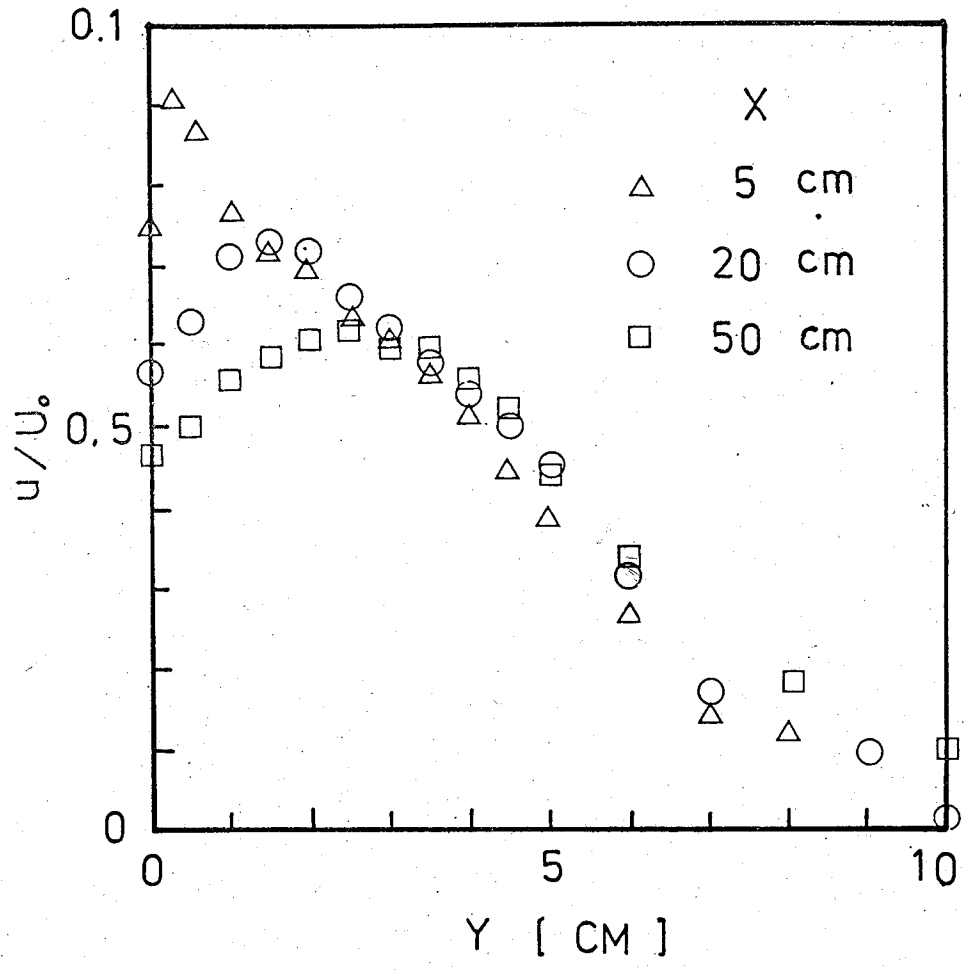

圖十一　以DISA Probe Type 55 P61 X型熱絲量測平板尾端下游5公分、20公分及50公分處之紊流強度分佈

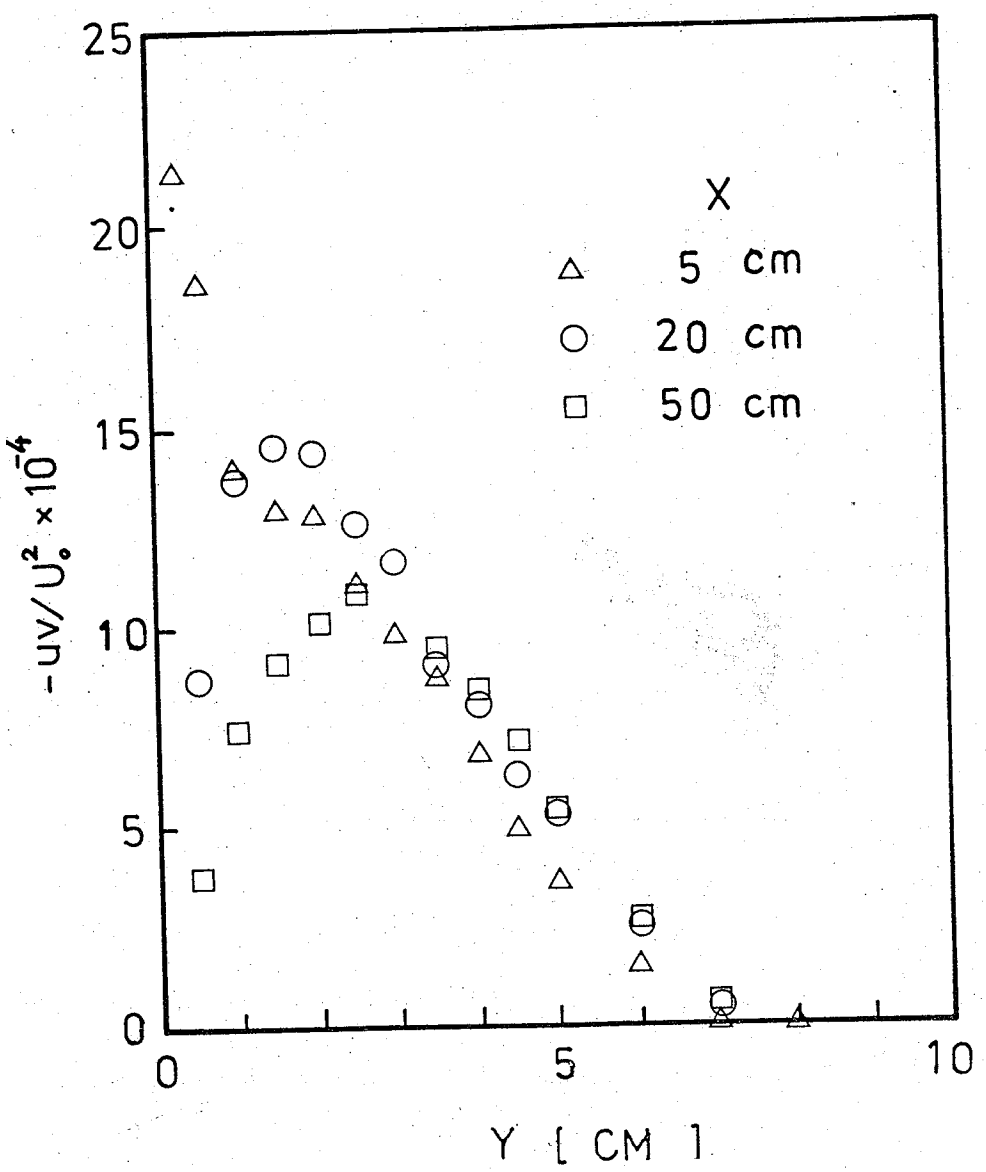

圖十二　以DISA Probe Type 55 P61 X型熱絲量測平板尾端下游5公分、20公分及50公分處之紊流應力分佈

A STUDY ON APPLICATION OF DIGITAL COMPUTER IN TURBULENCE MEASUREMENT

B. S. Shiau

Institute of Physics

Academia Sinica

Nankang, Taipei, Taiwan

R. O. C.

ABSTRACT

This study presents a system which is suitable for turbulence measurement. The system consists of a hot wire anemometer, 14-Bit analog-digital converter and a digital computer. Together these instruments on line, the system is set up. Running the programs which were developed by author himself the system firstly converts the analog signals output from hor wire anemometer to digital signals by A/D converter and records them on hard disk, then analyzes these digital data and finally prints the results. This system has been applied successfullyin turbulence measurement at the Atmospheric Environment Wind Tunnel of the Institute of Physics, Academia Sinica

邊界層線源擴散的雙程式紊流模式

梁文傑　張瓊雄

中央研究院物理研究所

台灣大學機械工程學系暨研究所

摘　要

本研究將k－ϵ模式與擴散方程式合併來分析紊流中污染物的擴散現象，並就平滑板上穩定的（steady）二維邊界層流場作實際的計算，溫度分佈設爲中性穩定（netunrlly stable），污染爲惰性且濃度甚小不致干擾流場。將流場與線源在地面高度產生的濃度分佈計算值與實驗值比較，顯示除在極近板面處外，平均速度、動能與雷諾應力的估算值與實驗值相當吻合，摩擦係數與形狀因子的誤差則在動量厚度雷諾數大於2500時約小於1%，而濃度分佈曲線、擴散半寬及地面濃度曲線均與實驗曲線頗爲接近。另計算線源在不同高度時的擴散情形，由於模式的擴散係數分佈在某高度處有最大值，致使當線源高度低於該高度時，線源以上的濃度擴展得較快使最大濃度的位置下移；當線源高度漸高於該高度時，線源以上的擴展作用漸弱使最大濃度的位置漸轉向上移。在下游遠處，濃度的分佈型態逐漸一致，不因原線源高度而異。

壹、引　言

流體力學的領域中，與工程應用有關的流場多爲紊流。由於這種流體運動呈現高度的不規則性與不穩定性且爲三度空間，所以要描述或預測其瞬間動量、質量或熱的傳遞十分困難。研究紊流的理論區分爲三類，即統計分析法（statistical approachment）、動力論（kinetic theory）及現象分析法（phenomenal approachment）；其中以現象分析法的使用最爲普遍。該理論係假設紊流運動滿足Navier-Stokes方程式，但是此程式無解析解；若利用數值方法，因紊流運動基本單元（渦旋）的尺度常遠小於全流域的尺度，典型的約10^{-3}倍，要充分的解全部的運動情形（三度空間），則至少需要10^{9}個網格點，處理這些網格點所需要的儲存空間與運算時間遠超過現今計算機的能力。爲應用的需要，乃根據Osborne Reynolds的作法，將紊流的瞬間物理量分解爲（對時間的）平均量與變動量（fluctuating quantities）的和，再將原方程式對適當的時間間

距（應大大於紊流運動的時間尺度）取平均得到時間平均方程式，由於平均量變化的尺度約與流域的尺度相若，可望在計算機的容量內解這些方程式。但這些方程式包含代表紊流傳遞量的未定相關項在數學上爲未封閉系統（未知數個數不等於方程式個數），因此必須建立紊流模式，利用（半）實驗式來近似這些未定項與平均量的關係，使成爲封閉、可解的系統。

好的紊流模式應該具備廣泛的通用性而不致於太複雜。前者的意義是指模式所用的經驗常數及函數要盡量的爲固定的通式而能適用於各種型態的流場；後者的意義則是指模式所含的微分方程式個數要愈少愈好。Rodi〔1〕即根據微分方程式的數目作爲模式分類的標準，並依序介紹其整個發展的大致過程。零程式模式（Zero-Equation Model），包括混合長度模式的形式最爲簡單，但使用的係數隨流場型態而不同，故其通用性不佳，僅適用於較簡單型式的流場。單程式模式（One-Equation Model）係將紊流的平均動能K，由模式方程式來表示，因爲K代表與紊流傳遞作用有關的特性速度V（$V=\sqrt{K}$），故其通用性較零程式模式爲佳，但另一個與紊流傳遞作用有關的物理量，即渦旋特性長度L，則仍須靠實驗來獲得。雙程式模式（Two-Equation Model）則除K模式方程式外，另加模式方程式來描述代表該特性長度的物理量Z，其中$Z=K^m \cdot L^n$。這兩個特性尺度可用來近似紊流的傳遞情形，因此其通用性乃大大的提昇。根據比較的結果（〔1〕，p.27；〔2〕），當$Z=K^{3/2} \cdot L^{-1}$，即$Z=\epsilon$（散逸速率）時爲最佳的形式（近牆的適用性最好且微分方程式所含的項數最小），此即所謂的$K-\epsilon$模式。另外尚有紊流應力／通量模式（Turbulence Stress / Flux Model），係將紊流應力及其它傳遞量以模式方程式來表示，除在極複雜的狀況外，此類模式的計算值並不比$K-\epsilon$模式的計算值準確很多，但其所含的微分式遠較$K-\epsilon$模式爲多，因此在一般的狀況下乃以$K-\epsilon$模式應用得最爲廣泛。

由模式解出的流場分佈可配合擴散方程式來預測污染物在紊流中的擴散情形。污染物在輸散過程會產生化學變化而影響濃度分佈者，稱爲非惰性污染物，不發生化學反應而以輸送與擴散爲濃度擴散的主要機構者，稱爲惰性污染物。本研究討論污染物在流場中的擴散情形，不涉及化學反應，故對象爲惰性污染物。

倘若計算的狀況爲邊界層流場，則可比擬大氣擴散的問題。研究大氣惰性污染物的擴散現象，目前仍多借重實驗方法，但一則由於實驗的不易（因爲外場實驗的參數，如風向、穩定性等，不易控制得當，風洞實驗中尺度比例的限制等因素），一則由於污染防制的需要，有必要建立完整的理論模式以補實驗的不足並供分析之用。現有的理論包括梯度傳導理論（gradient-transfer theory）、相似性理論（similarity theory）及統計理論（statistical theory）[3]，以最前者的應用能力最佳。該理論係導出污染物的平均擴散方程式（大氣擴散方程式），再假設或由實驗得到速度與擴散係數的分佈代入制御方程式解平均濃度的分佈[4],[5],[6],[7]。

本文擬以$K-\epsilon$模式系統解平板上的邊界層流場，並配合擴散方程式預測其中污染物的擴散情形，期應用於大氣擴散現象的研究。爲簡明起見，討論的狀況定爲二度空間

的穩定（steady）狀況，即爲平滑板上中性穩定（nturally stable）的不可壓縮流場，且惰性污染物的重力作用可予忽略。第一部分計算流場的分佈，將結果與實驗值作比較以探討$K-\epsilon$模式的可信性。第二部分考慮線污染源置於板面時的擴散情形，並與對應的實驗值（包括大氣實驗與風洞實驗）作比較。同時另討論線源在不同的高度對擴散作用與濃度分佈的影響。

貳、基本理論

(一)流場的統制方程式

不可壓縮流體的連續方程式爲

$$\frac{\partial u_i}{\partial x_i}=0 \quad , \tag{1}$$

動量方程式（Navier-Stokes方程式）爲

$$\frac{\partial \tilde{u}_i}{\partial t}+u_j\frac{\partial \tilde{u}_i}{\partial x_j}=-\frac{1}{\rho}\frac{\partial \tilde{p}}{\partial x_i}+\nu\frac{\partial^2 \tilde{u}_i}{\partial x_j \partial x_j} \tag{2}$$

其中$\tilde{u}_i$，$\tilde{p}$代表瞬間速度與壓力，將之分解爲平均量與變動量的和，令

$$\tilde{u}_i=U_i+u_i \quad ,$$
$$\tilde{p}=P+p \quad ,$$

其中U_i，P爲時間平均速度與壓力，即

$$U_i=\frac{1}{\Delta t}\int_0^{\Delta t}\tilde{u}_i\,dt \quad ,$$

$$P=\frac{1}{\Delta t}\int_0^{\Delta t}\tilde{p}\,dt \quad ,$$

Δt爲取平均的時間間距，應大大於紊流運動的時間尺度。u_i，p分別爲速度與壓力的平均值爲零，即

$$\int_0^{\Delta t}u_i\,dt=0 \quad ,$$

$$\int_0^{\Delta t}p\,dt=0 \quad ,$$

將上述關係代入(1)，(2)式，再對時間取平均，則得到時間平均連續方程式

$$\frac{\partial U_i}{\partial x_i} = 0 \quad , \tag{3}$$

及時間平均動量方程式

$$\frac{\partial U_i}{\partial t} + U_j \frac{\partial U}{\partial x_j} = -\frac{1}{\rho}\frac{\partial P}{\partial x_i} + \frac{\partial}{\partial x_j}\left(\nu \frac{\partial U_i}{\partial x_j} - \overline{u_i u_j}\right) \tag{4}$$

上式包含有未定的二階相關項，即$-\overline{u_i u_j}$，稱爲雷諾應力或紊流應力，必須使用適當模式來描述它。根據Boussinesq's (1877) 渦旋黏滯係數的關念 (eddy-viscosity concept)，假設紊流應力與層流黏滯力相似，均正比於平均速度的梯度，則在一般的狀況下，可以寫爲 (〔1〕, P.10)：

$$-\overline{u_i u_j} = \nu_t \left(\frac{\partial U_i}{\partial x_j} + \frac{\partial U_j}{\partial x_i}\right) - \frac{2}{3} K \cdot \delta_{ij} \quad , \tag{5}$$

右邊第一項代表紊流應力之正比於平均速度的梯度 (或更一般性的，爲正比於應變率，即Stokes' Law)；第二項則是爲使 i = j 時該式仍能成立；K代表紊流的平均動能，當 i = j 時，上式變爲

$$\frac{1}{2}\left(u_1^2 + u_2^2 + u_3^2\right) = K$$

在(5)式中的ν_t稱爲渦旋 (或紊流) 黏滯係數，相對於層流中的分子黏滯係數ν。根據氣體動力論，可推得ν正比於分子的平均速度與平均自由路徑 (〔8〕, Ch.2)。比照這個觀念，在紊流中若將渦旋視爲動量傳遞的單位體，即將之類比於一個分子，則ν_t應正比渦旋運動的特性速度V及特性長度L，即

$$\nu_t \propto V \cdot L \tag{6}$$

但事實上，紊流中的渦旋並非如分子一般，可視爲是一個剛體，它們並不能維持固定的特徵；而渦旋彼此間的相互作用亦相當複雜，並非單純的碰撞而已，且動量的傳遞主要發生於大渦旋中，其"自由路徑"並不遠小於流域的特性長度。這些現象都與氣體動力論的假設不合，致使上述推論在理論上頗有缺陷。縱然如此，在實際的應用中，若能給予適當的V、L值，由(5)，(6)式算出的結果，在許多狀況下常能滿足應用的要求，故此關係式乃被沿用下來。一般的模式，即在以適當的平均量來近似特性度量V及L。

其他的紊流傳遞量 (如熱鍋或質量等)，亦可比照(5)式，假設正比於平均量的梯度，並設定"渦旋擴散係數"C_ϕ爲比例常數，則可寫爲

$$-\overline{u_i \varphi} = C_\phi \frac{\partial \phi}{\partial x_i} \quad ,$$

其中ϕ代表平均物理量，φ爲變動物理量。C_ϕ可以表示爲$C_\phi = \nu_t / \sigma_t$；$\sigma_t$稱爲"紊流Prandtl數"，或"紊流Schmidt數"。根據實驗的結果，在一般的情況下 (如無浮力、離心力效應等)，其值在整個流場或在不同的流場變化均不大，可視爲常數 (〔1〕, P.12)。

在$K-\epsilon$模式中，係以紊流平均動能的平方代表渦旋運動的特性速度，即$V \sim \sqrt{K}$；而以散逸率ϵ代表其特性長度，因爲ϵ的級數約爲$V^3 \cdot L^{-1}$，或$K^{3/2} \cdot L^{-1}$的級數 (〔8〕, Ch.3)，將這些關係式代入(6)式中，再設定比例常數爲C_μ，可得

$$\nu_t = C_\mu \frac{K^2}{\epsilon} \tag{8}$$

其中K，ϵ值欲由方程式解出，故需推導其傳遞方程式。先將(2)式乘$u_i/2$及(4)式乘$U_i/2$後兩式相減，再對時間取平均，則可得到平均動能 ($= \frac{1}{2}\overline{u_i u_i}$) 的傳遞方程式

$$\frac{\partial K}{\partial t} + U_j \frac{\partial K}{\partial x_j} = A_k + B_k + C_k + D_k \quad , \tag{9}$$

其中

$$A_k = \frac{\partial}{\partial x_j}\left(-\frac{1}{2}\overline{u_i u_i u_j} - \frac{\overline{p u_j}}{\rho}\right) \quad ,$$

$$B_k = \frac{\partial}{\partial x_j}\left(\nu \frac{\partial K}{\partial x_j}\right) \quad ,$$

$$C_k = -\overline{u_i u_j}\frac{\partial U_i}{\partial x_j} \quad ,$$

$$D_k = -\nu \overline{\frac{\partial u_i}{\partial x_j}\frac{\partial u_i}{\partial x_j}} \quad ,$$

A_k稱爲紊流擴散項，B_k爲分子擴散項，C_k爲產生項，D_k爲散逸項。

另將(2)式減去(4)式後，整式對x_j微分，再乘上$2 \cdot \frac{\partial u_j}{\partial x_j}$，對時間取平均，則可得到散逸率$\epsilon$ ($= \nu \overline{\frac{\partial u_i}{\partial x_i}\frac{\partial u_i}{\partial x_j}}$) 的傳遞方程式

$$\frac{\partial \epsilon}{\partial t} + U_j \frac{\partial \epsilon}{\partial x_j} = A_\epsilon + B_\epsilon + C_\epsilon + D_\epsilon \tag{10}$$

其中

$$A_\epsilon = \frac{\partial}{\partial x_j}\left(-\overline{\frac{\partial u_i}{\partial x_j}\frac{\partial u_i}{\partial u_j}u_j} - \frac{2\nu}{\rho}\overline{\frac{\partial u_j}{\partial x_l}\frac{\partial p}{\partial x_l}}\right) ,$$

$$B_\epsilon = \frac{\partial}{\partial x_j}\left(\nu\frac{\partial \epsilon}{\partial x_j}\right) ,$$

$$C_\epsilon = -2\nu u_j\frac{\partial u_i}{\partial x_l}\frac{\partial^2 U_i}{\partial x_j \partial x_l} - 2\nu\frac{\partial U_i}{\partial x_l}\cdot\left(\overline{\frac{\partial u_j}{\partial x_i}\frac{\partial u_i}{\partial x_l}} + \overline{\frac{\partial u_i}{\partial x_j}\frac{\partial u_l}{\partial x_j}}\right) ,$$

$$D_\epsilon = -2\nu\overline{\frac{\partial u_i}{\partial x_l}\frac{\partial u_i}{\partial x_j}\frac{\partial u_l}{\partial x_j}} - 2\overline{\left(\nu\frac{\partial^2 u_i}{\partial x_j \partial x_l}\right)^2} ,$$

A_ϵ 爲紊流擴散項，B_ϵ 爲分子擴散項，C_ϵ 爲產生項，D_ϵ 爲破壞項。

但是要直接從這些方程式連同連續及動量方程式（共六個方程式）來解流場是不可能的，因爲除了六個基本未知數 U_i，$i=1,2,3$，P、K、ϵ 外，在(9)、(10)式中又包括一些未定的相關項。倘若再進一步導出這些相關項的傳遞方程式，其中將包含更高階的未定相關項，而整個系統始終未能成爲封閉的系統（即未知數與方程式數目相同）。爲避免引入更多的方程式，乃擬以基本未知數的關係式來近似這些未定項，使方程式得以封閉。因爲 K 與 ϵ 均爲二階的相關項，故此步驟稱爲“二階完封（2nd order closure）”。

(1) K之模式方程式

在K方程式中，紊流擴散項爲未定項，其中壓力擴散項 $\frac{\partial}{\partial x_j}\left(\overline{\frac{p u_j}{\rho}}\right)$ 的作用並不甚被了解，因此 Hanjalic' 及 Launder〔9〕僅根據在非對稱平面流道的實驗結果，建議可以省略該項，雖然不盡合理，却是目前常用而可行的作法。另一項爲動能的變動傳遞量，根據(7)、(8)兩式表示爲

$$-\frac{1}{2}\overline{u_i u_i u_j} = \frac{C_\mu}{\sigma_k}\cdot\frac{K^2}{\epsilon}\cdot\frac{\partial K}{\partial x_j} = C_k\cdot\frac{K^2}{\epsilon}\cdot\frac{\partial K}{\partial x_j} ,$$

將上式代回(9)式可得到 k 的模式爲

$$\frac{\partial K}{\partial t} + U_j\frac{\partial K}{\partial x_j} = \frac{\partial}{\partial x_j}\left(C_k\frac{K^2}{\epsilon}\frac{\partial K}{\partial x_j} + \nu\frac{\partial K}{\partial x_j}\right) - \overline{u_i u_j}\frac{\partial U_i}{\partial x_j} - \epsilon \qquad (11)$$

(2) ϵ 之模式方程式[10]

ϵ 方程式中右邊除分子擴散項外全爲未定項，均需建立模擬關係式。因模擬的項數

頗多，是K—ϵ 模式系統中較難把握的一部分。

紊流擴散項中的壓力項，仍比照K模式中的作法予以省略[9]，餘項爲 ϵ 的變動傳遞量，仍依照(7)，(8)兩式寫成

$$-\overline{\left(\nu\frac{\partial u_i}{\partial x_j}\frac{\partial u_i}{\partial x_j}\right)u_j} = \frac{C_\mu}{\sigma_\epsilon}\frac{K^2}{\epsilon}\frac{\partial \epsilon}{\partial x_j} = C_\epsilon\frac{K^2}{\epsilon}\frac{\partial \epsilon}{\partial x_j}$$

產生項包括兩項，先將前項，即 $2\nu\overline{u_j\frac{\partial u_i}{\partial x_l}}\frac{\partial^2 U_i}{\partial x_j \partial x_l}$，與破壞項中的 $2\nu\overline{\frac{\partial u_i}{\partial x_l}\frac{\partial u_i}{\partial x_j}\frac{\partial u_l}{\partial x_j}}$ 項作級數的比較，得到

$$2\nu\overline{u_j\frac{\partial u_i}{\partial x_l}}\frac{\partial^2 U_i}{\partial x_j \partial x_l} \sim \nu\cdot\frac{V^2}{L}\cdot\frac{U}{x}$$

$$2\nu\overline{\frac{\partial u_i}{\partial x_l}\frac{\partial u_i}{\partial x_j}\frac{\partial u_l}{\partial x_j}} \sim \nu\cdot\frac{V^3}{L^3}$$

其中U，x 代表平均量的特性速度與長度，而 L / x ≪ 1。由上述關係可知前者約爲後者的 $\left(\frac{L^2}{x^2}\frac{U}{V}\right)$ 倍，假設 $\left(\frac{L}{x}\frac{U}{V}\right) \ll 1$，則可省略該產生項。當流場中的紊流運動只有一個特性速度與長度時，可得到 L / V ～ x / U 的關係[8]，故上述作法可以成立，但在一般的狀況下則尚有疑問。對於另一個產生項，即 $\nu\frac{\partial U_i}{\partial x_l}\left(\overline{\frac{\partial u_j}{\partial x_i}\frac{\partial u_i}{\partial x_l}} + \overline{\frac{\partial u_i}{\partial x_j}\frac{\partial u_l}{\partial x_j}}\right)$，當 $i \neq l$ 時，若考慮爲等向散逸則括符內之項爲零，當 $i = l$ 時，則由連續方程式得到 $\frac{\partial U_i}{\partial x_l} = 0$，故亦令之爲零。

致於破壞項，根壞 Lumley 的說法，當流場中達到局部平衡，即動能產生率等於散逸率時，散逸率本身亦維持不變，即其破壞項應等於其產生項（已設爲零）。因此可由下列的關係式來表示：

$$-2\nu\overline{\frac{\partial u_i}{\partial x_l}\frac{\partial u_i}{\partial x_j}\frac{\partial u_l}{\partial x_j}} - 2\overline{\left(\nu\frac{\partial^2 u_i}{\partial x_j \partial x_l}\right)^2}$$

$$= (\text{常數})\cdot\left[\frac{\epsilon}{t}\right]\cdot\left(\frac{\text{K之產生項}}{\epsilon} - 1\right) ,$$

其中〔 〕內的量表示單位因子，〔 t 〕代表時間單位，可由〔 t 〕= K / ϵ 來表示。則上式可轉化爲

$$C'_{\epsilon 1}\left[\frac{1}{t}\right]\left(-\overline{u_i u_j}\frac{\partial U_i}{\partial x_j}\right)-C'_{\epsilon 2}\left[\frac{\epsilon}{t}\right]=-C_{\epsilon 1}\frac{\epsilon}{K}\cdot\overline{u_i u_j}\frac{\partial U_i}{\partial x_j}-C_{\epsilon 2}\frac{\epsilon^2}{K}$$

將以上各式代回⑽式，得到 ϵ 的模式爲

$$\frac{\partial \epsilon}{\partial t}+U_j\frac{\partial}{\partial x_j}=\frac{\partial}{\partial x_j}\left(C_\epsilon\frac{K^2}{\epsilon}\frac{\partial \epsilon}{\partial x_j}+\nu\frac{\partial \epsilon}{\partial x_j}\right)-C_{\epsilon 1}\frac{\epsilon}{K}\overline{u_i u_j}\frac{\partial U_i}{\partial x_j}-C_{\epsilon 2}\frac{\epsilon^2}{K} \tag{12}$$

綜觀以上的推導過程（如使用⑸式時係數爲純量及在模擬 ϵ 的產生項時所作的假設等），可發現其中隱含一個假設，即流場具有局部等向的性質，也就是在高雷諾數的情況下，因此使用 k—ϵ 模式時亦當受限於這個條件。K—ϵ 模式中的經驗告常數是根據實驗與實際應用的結果所決定[1]、[10]，一般適用的範圍列於表一；表二則爲本文中所選用的值。

二維穩定邊界層的流場（圖一），可由⑶、⑷、⑸、⑾、⑿等式化簡爲以下各式：

$$\frac{\partial U}{\partial x}+\frac{\partial V}{\partial y}=0 \quad , \tag{13}$$

$$U\frac{\partial U}{\partial x}+V\frac{\partial U}{\partial y}=-\frac{1}{\rho}\frac{dP_0}{dx}+\frac{\partial}{\partial y}\left(-\overline{uv}+\nu\frac{\partial U}{\partial y}\right) \quad , \tag{14}$$

$$-\overline{uv}=C_\mu\frac{K^2}{\epsilon}\frac{\partial U}{\partial y} \quad , \tag{15}$$

$$U\frac{\partial K}{\partial x}+V\frac{\partial K}{\partial y}=\frac{\partial}{\partial y}\left(C_k\frac{K^2}{\epsilon}\frac{\partial K}{\partial y}+\nu\frac{\partial K}{\partial y}\right)-\overline{uv}\frac{\partial U}{\partial y}-\epsilon \tag{16}$$

$$U\frac{\partial \epsilon}{\partial x}+V\frac{\partial \epsilon}{\partial y}=\frac{\partial}{\partial y}\left(C_\epsilon\frac{K}{\epsilon}\frac{\partial \epsilon}{\partial y}+\nu\frac{\partial \epsilon}{\partial y}\right)-C_{\epsilon 1}\frac{\epsilon}{K}\overline{uv}\frac{\partial U}{\partial y}-C_{\epsilon 2}\frac{\epsilon^2}{K} \tag{17}$$

這些式子就是本文中計算流場所使用的統制方程式。

㈡污染物擴散的統制方程式

設 $\tilde{c}$ 代表惰性污染物在紊流中單位體積的質量（即濃度），則其質量守恒式爲

$$\frac{\partial \tilde{c}}{\partial t}=-\frac{\partial(\tilde{u}_i\tilde{c})}{\partial x_i} \tag{18}$$

將 c 分解爲其平均量C及變動量c′的和，代回⑱式，對時間間距取平均，則得到

$$\frac{\partial C}{\partial t}+U_j\frac{\partial C}{\partial x_j}=-\left(\frac{\overline{\partial u_j c'}}{\partial x_j}\right) \quad , \tag{19}$$

其中 $u_j c'$ 爲可依照⑺式寫成

$$-\overline{u_j c'}=(\text{常數})\cdot\frac{\partial C}{\partial x_j} \quad ,$$

因爲該傳遞作用並非是等向性的，所以上式中的常數亦隨不同的方向而不同，分別設爲 K_x，K_y，K_z，則⑲式變爲

$$\frac{\partial C}{\partial t}+U_j\frac{\partial C}{\partial x_j}=\frac{\partial}{\partial x}\left(K_x\frac{\partial C}{\partial x}\right)+\frac{\partial}{\partial y}\left(K_y\frac{\partial C}{\partial y}\right)+\frac{\partial}{\partial z}\left(K_z\frac{\partial C}{\partial z}\right) \tag{20}$$

此方程式就是所謂的大氣擴散方程式。

根據一般邊界層中的級數分析，⑳式可化簡爲

$$U\frac{\partial C}{\partial x}+V\frac{\partial C}{\partial y}=\frac{\partial}{\partial y}\left(K_y\frac{\partial C}{\partial y}\right) \quad , \tag{21}$$

上式即爲本文用以計算平均濃度的統治方程式。若進一步作級數分析可得

$$U\frac{\partial C}{\partial x}\sim U\cdot\frac{C}{x_c} \quad ,$$

$$V\frac{\partial C}{\partial y}\sim V\cdot\frac{C}{y_c} \quad ,$$

後者約爲前者的 $\left(\frac{V}{U}\cdot\frac{x_c}{y_c}\right)$ 倍，其中 x_c，y_c 各代表濃度擴散延 x，y 方向的特性長度（圖三），x_c 可取爲 x 方向與線源的距離；y_c 可取爲四倍的半寬 σ_y（即濃度爲最大濃度一半時的寬度）。根據計算數值的比較，$O\left(\frac{V}{U}\cdot\frac{x_c}{y_c}\right)<0.1$（表三），可再省略 $V\frac{\partial C}{\partial y}$ 項，前㉑式變爲

$$U\frac{\partial C}{\partial x}=\frac{\partial}{\partial y}\left(K_y\frac{\partial C}{\partial y}\right) \quad , \tag{21a}$$

此爲其它文獻[5]、[6]、[7]使用的方程式。根據實際的計算，兩式的結果相差在百分之一以內。

擴散係數 K_y 可定爲 $K_y=\nu_t/\sigma_{tc}$；σ_{tc} 爲污染物擴散的 Prandtl 數，在一般大氣擴散及熱傳的理論中，其值介於 0.6 至 1.0 之間。本文採用 Nieuwstadt 與 Van Ulden [6]的建議值，即 $\sigma_{tc}=0.74$。若令 $\sigma_{tc}=0.6$ 或 1.0，則產生 10％～20％的差距。

㈢邊界條件

前面導出的主要偏微分方程式，⑭、⑯、⑰及㉑等，均爲邊界層型態的微分方程式

，即延主要流動方向（x 座標）爲拋物線型；延橫方向（y 座標）爲橢圓型，因此共需三個邊界條件：一個在流場的上游；另兩個分別在橫向的上、下限處（圖一）。

(1)上限邊界條件（在 $y = y_u$ 處）

將上限邊界定在邊界層外，因爲該處爲無旋流動，故可令流場的變數爲 $U = U\infty$；$K = \epsilon = 0$。而污染物濃度分佈的上限邊界條件原爲“ $\partial C / \partial y = 0$，在 $y \to \infty$ 處”，若要在此處設爲 $\partial C / \partial y = 0$，則應另要求此處的濃度很小，以配合“無窮遠處”的物理意義，程式中設定應小於該處最大濃度的百分之一，當濃度大於此數值時，則標示說明或終止計算。

(2)下限邊界條件（在 $y = y_L$ 處）

由於 K—ϵ 模式僅適用於高雷諾數的情況下，不宜用以計算極靠近牆壁的區域，因此下限邊界必須定在離牆壁夠遠的地方，設在 $y = y_L$ 處。中間的部分可由一組經驗通式（在壓力梯度不太且無分離現象的情況下都適用），即牆函數來描述〔1〕〔2〕〔10〕。牆函數爲

$$\frac{U}{u} = \frac{1}{k} \ell n \, E \, y^+ \quad ,$$

$$K = u^2_* / \sqrt{C_\mu} \quad ,$$

$$\epsilon = u^3_* / (k \cdot y) \, ,$$

$$- \overline{uv} = u^2_* \quad ,$$

其中 E 爲代表牆面粗糙度的參數，若 k_s 爲粗糙度的均方根（rms），則

$$\ell n \, E = k \cdot B - \ell n \left(\frac{u_* \cdot k_s}{\nu} \right) ,$$

B 爲粗糙度雷諾數（$u_* \cdot k_s / \nu$）的函數，其關係曲線可查閱參考文獻〔11〕，P620，若爲光滑表面則 $E = 9.0$。u 爲摩擦速度；$k = 0.41$，爲 Von k'arm'an 常數；$y^+ = u_* \cdot y / \nu$。牆函數的適用範圍在 $10 < y^+ < 100$ 之間〔8〕〔12〕，故 y_L^+（$= u_* \cdot y_L / \nu$）亦應在此範圍內。在本文中選定 $y_L^+ = 50$，則流場變數的邊界條件爲

$$U = \frac{u^*}{K} \ell n \, E \cdot y_L^+ \quad ,$$

$$K = u^2_* / \sqrt{C_\mu} \quad ,$$

$$\epsilon = u^4_* / (k \cdot \nu \cdot y_L^+) \, ,$$

$$- \overline{uv} = u^2_* \, ,$$

濃度分佈的下限邊界原爲“ $K_y \cdot \frac{\partial C}{\partial y} = V_g \cdot C$ ，在 $y = 0$ 處”，其中 V_g 爲沈澱速率。爲配合流場的計算，乃將此條件定在 $y = y_L$ 處，因爲 y_L 均甚小於邊界層厚度（小於百分之一），故對計算結果然甚影響。當地面爲全反射時，$V_g = 0$。

(3)起始邊界條件（在 $x = x_0$ 處）

此邊界條件爲給予各相關變數（記爲 ϕ）的分佈曲線，記爲 P（ϕ）。本文第一部分求流場本身的解時，定在 $x = x_{01}$（$= 0$）處，並設 U、K、ϵ 爲等分佈曲線（圖二），$P(U) = U$，$P(K) = P(\epsilon) = 0$。

第二部分爲考慮污染物擴散的情形，設將線源置於 $x = x_{02}$ 處，高度爲 h（圖二），則流場變數（U、K、ϵ）的起始分佈曲線採用第一部分裡在 $x = x_{02}$ 處的解；若假設爲穩定的線源，強度爲 Q，則濃度的起始分佈曲線可設爲(5)，(7)

$$P(C) = \frac{Q}{U(h)} \, \delta(y - h) \quad ,$$

$\delta(y - h)$ 爲 Dirac delta 函數。作數值分析時，以下式來近似：

$$P(C) = \begin{cases} \dfrac{Q}{U(h)(\triangle y_L + \triangle y_L)/2} \, , & h - \dfrac{\triangle y_L}{2} \leq y \leq h + \dfrac{\triangle y_L}{2} \, , \\ 0 \, , & \text{其它各處。} \end{cases}$$

其中 $\triangle y$ 代表網格點間的距離（圖四）。

因爲大氣邊界層中是完全發展的流場，故相對的，在計算域中線源之所在（即 $x = x_{02}$ 處）亦應爲完全發展的流動型態。x_{02} 值的選定係根據給定的初邊界層厚度 δ_0（即線源所在的邊界層厚度）而定。在不同的自由流速度下，給定的 δ_0 值與對應的 x_{02} 值將列於表四。

參、數值方法分析

㈠數值公式

本文使用的數值方法爲 Patankar 控控制體積法與冪次方法則〔12〕。首先定出網格點，因爲在全流場中以靠近牆壁及授施源附近區域的物理量變化較大，所以在這些地方定出較密的網格點（詳見附錄 C）。再將流場劃分爲許多個不重疊的“控制體積”（圖五），使除上下限的點外各包含一個網格點，並將其界面定在兩網格點的正中處。

然後將微分方程式轉化爲對應的差分式。由於(14),(16),(17)及(21)式均爲同型式的方程式，可用一標準式(22)來代表，連同連續方程式可寫爲

$$\frac{\partial U}{\partial x}+\frac{\partial V}{\partial y}=0 \quad , \tag{13}$$

$$\frac{\partial J_x}{\partial x}+\frac{\partial J_y}{\partial y}=S \quad , \tag{22}$$

其中

$$J_x=\rho U\phi \quad ,$$

$$J_y=\rho V\phi-\Gamma_y\frac{\partial \phi}{\partial y} \quad ;$$

$$\Gamma_y=\rho\left(C\phi\frac{K^2}{\epsilon}+\nu\right) ,$$

ϕ 代表平均物理量，Γ_y爲其擴散係數，餘項併入S項中視爲授施項(表五)。將(13)、(22)兩式對控制體積(圖六)積分，並依冪次方法則近似界面上的通量(J_x, J_y)，最後可得到

$$(U_e-U_w)\triangle y+(V_n-V_s)\triangle x=0 \quad , \tag{23}$$

$$a_P\phi_P=a_W\phi_W+a_N\phi_N+a_S\phi_S+b \quad , \tag{24}$$

對於整個流場(圖五)，(24)式可寫成

$$a_{i,j}\phi_{i,j}=a_{i-1,j}\phi_{i-1,j}+a_{i,j+1}\phi_{i,j+1}+a_{i,j-1}\phi_{i,j-1}+b_{i,j} \quad , \tag{25}$$

$$i=2,3,4,\cdots\cdots;\ j=2,3,\cdots\cdots,N .$$

上式的係數，$a_{i,j}$等，本身也包含變數ϕ，因此爲非線性方程式。但對邊界層型態的流場(有一主要的流動方向)而言，上、下游的性質變化不大，故係數中的物理量可由上游的值來近似，則(25)式可改寫爲

$$\phi_{i,j}=A_i\phi_{i,j+1}+B_i\phi_{i,j-1}+C_i \quad , \tag{26}$$

$$i=2,3,\cdots\cdots;\ j=2,3,\cdots\cdots,N .$$

其中

$$A_i=\frac{a_{i,j+1}(\phi_{i-1,})}{a_{i,j}(\phi_{i-1,})} \quad ,$$

$$B_i=\frac{a_{i,j-1}(\phi_{i-1,})}{a_{i,j}(\phi_{i-1,})} ,$$

$$C_i=\frac{a_{i-1,j}(\phi_{i-1,})\phi_{i-1,j}+b_{i,j}}{a_{i,j}(\phi_{i-1,})}$$

倘若上游的值爲已知，則(26)式成爲準線性方程式，可用Thomas方法(〔12〕, P52)解而不需作疊代。爲配合此作法，應將(23)式改寫爲

$$(U_P-U_W)\triangle y+(V_n-V_s)\triangle x=0 \quad , \tag{27}$$

或

$$(U_{i,j}-U_{i-1,j})\triangle y_j+(V_{i,j+\frac{1}{2}}-V_{i,j-\frac{1}{2}})\triangle x_i=0 \quad , \tag{28}$$

$$i=2,3,\cdots\cdots;\ j=2,3,\cdots\cdots,N .$$

(26)、(28)式即爲程式中使用的差分方程式。

㈡守恒性、一致性、穩定性的討論

(1)守恒性

控制體積法是將微分方程式對一有限的控制體積積分，故在這個體積內本就滿足守恒性質；而在Patankar的推導過程中，要求界面上的通量一致，因此可以確定在任一部分或全部的控制體積中，都能滿足守恒性質。

(2)一致性

Patankar的方法相當於是先把(22)式展開爲

$$\frac{\overline{J_e}-\overline{J_w}}{\triangle x}+\frac{\overline{J_n}-\overline{J_s}}{\triangle y}+Q(\triangle x^2,\triangle y^2)=S , \tag{29}$$

再根據冪次方法則將界面上的平均通量($\overline{J}$)表示成差分式，這個方法事實上是種高階的近似法，因此可以寫成

$$\overline{J_e}-\overline{J_w}=\triangle\overline{J_x}(\phi_E,\phi_P,\phi_W)+\theta(\triangle x^m) \quad ,$$

$$\overline{J_n}-\overline{J_s}=\triangle\overline{J_y}(\phi_N,\phi_P,\phi_S)+Q(\triangle y^{m\prime}) \quad ,$$

其中$\triangle J$代表差分關係式，而m，m則至少是大於3。將之代回(29)式則得到

$$\frac{\triangle J_x(\phi_E,\phi_P,\phi_W)}{\triangle x}+\frac{\triangle J_y(\phi_N,\phi_P,\phi_S)}{\triangle y}$$

$$=S_c+S_p\phi_p+Q(\triangle x^2,\triangle y^2) \tag{30}$$

式中已令$S=S_c+S_p\phi_p$(表五)。這個式子即相當於(24)式，只是加入誤差項。對於在K、ϵ程的方程式中，$S_c\propto(\partial U/\partial y)^2$，若使用中心差分式來算速度梯度，則誤差爲$O(\triangle y^2)$，或寫成$S_c=S'_c+O(\triangle y^2)$，可代回(30)式中，但由於主體形式不變，故仍由(30)式來表示其結果。

當$\triangle x$，$\triangle y\to 0$時，

$$\frac{\triangle J_x}{\triangle x}\to\frac{J_e-J_w}{\triangle x}\to\frac{J_e-J_w}{\triangle x}\to\frac{\partial J_x}{\partial x} ,$$

$$\frac{\triangle J_y}{\triangle y} \rightarrow \frac{J_n - J_s}{\triangle y} \rightarrow \frac{J_n - J_s}{\triangle y} \rightarrow \frac{\partial J_y}{\partial y} \quad ,$$

$$S_c + S_p P_p + O(\triangle x^2, \triangle y^2) \rightarrow S \quad ,$$

故(30)式趨近於原微分方程式(22)，即合乎一致性質。

(3)穩定性

根據Patankar的第四個基本原則〔12〕，(26)式中的係數滿足以下關係：

$$1 \geq |A_i| + |B_i| \tag{31}$$

如果用Thomas方法來解(26)式，(31)式即爲維持穩定性質的充分條件。

㈢程式流程

在整個計劃中共包括六個方程式，即(13)、(14)、(15)、(16)、(17)及(21)等式，前五個爲流場的統制方程式，先用以解出流場的形式後，再將結果代入(21)式以計算污染物的平均濃度分佈。其過程如下（參考圖五）：

(1)設定起邊界條件。在 $i = I_U = 1$ 處給予U、K、ϵ、C起始分佈曲線（$j = 1, 2, \cdots, N+1$）。

(2)設定下游，即 $i = I_U + 1$ 處的上、下限邊界條件（在 $j = N+1$ 及 $j = 1$ 處U、K、ϵ、C的值）。需假設 $u*$ 值以由牆函數計算下限邊界條件，包括第一點（$j = 1$）的雷諾應力，$-uv(1)$。

(3)由連續方程式(13)及動量方程式(14)，配合(15)式解出在 $i = I_U + 1$ 處的速度分佈，U及V（$j = 2, 3, \cdots, N$）。由於此步驟是解兩個聯立方程式(13)、(14)，故須構成迴路作疊代的工作，詳細說明於後。

(4)計算新的速度梯度分佈，$\partial U / \partial y$（$i = I_U + 1$, $j = 2, 3, \cdots, N$），代入K、ϵ模式(16)、(17)式解出該處K、ϵ的分佈（$j = 2, 3, \cdots, N$）。

(5)根據(3)、(4)的結果，以(15)式算出在 $i = I_U + 1$ 處，第二點起的雷諾應力分佈（$j = 2, 3, \cdots, N$），記爲 $-uv(j)$。

(6)由(2)、(5)的結果判斷原先假設的 $u*$ 值是否正確（詳細說明於後），是則往下一步；否則回到步驟(2)並重覆其後各步驟。

(7)以 $i = I_U + 1$ 處的流場變數分佈代入(21)式中解該處的平均濃度分佈（$j = 2, 3, \cdots, N$），並將結果輸出。

(8)如果要繼續往下游計算，則重令 I_U 等於目前的i值，然後回到步驟(2)，重覆以下過程；否則即執行完畢。

圖九爲流程圖。在全流程中有幾個疊代的迴路，其收斂條件與疊代值的更替將予說明。

在迴路一中，是由兩個聯立方程式來解U及V，其中(14)式的差分式可寫成（參考(24)式）

$$U_P = \frac{a_W U_W + a_N U_N + a_S U_S + b}{(a_W + a_N + a_S)} \quad ,$$

因爲 $a_W \sim O(U)$；a_N、$a_S \sim O(V)$，且 $U \gg V$，故由上式可看出V的變化對U的影響很小，因此在此疊代過程中應先假設速度V的分佈，然後由動量方程式解速度U的分佈，再由連續方程式修正V的值，代回動量方程式重覆各步驟，直至V收斂爲止。其收斂條件的數學式可寫成

$$\left| \frac{\text{V新值} - \text{V舊值}}{\text{V舊值}} \right| \leq (\text{常數}) \quad ,$$

該常數經選定爲0.01，在此範圍內U、K、$-uv$、C等預測值的誤差均在百分之一以內，已在一般應用上允許的誤差範圍之內。

迴路二是 $u*$ 的疊代迴路。由於使用牆函數作爲邊界條件，故需要先設 $-u*$ 值，因爲牆函數的應用範圍是在等應力區域，即其（第一網格點的）應力斜率應爲零，所以該 $u*$ 值必須滿足此物理現象。若用第一網格點與第二網格點雷諾應力值的差來近似第一點的應力斜率，則收斂條件可寫成

$$\frac{[-\overline{uv}(1)] - [-\overline{uv}(2)]}{[-\overline{uv}(1)]} \leq (\text{常數}) \quad ,$$

此常數若定爲0.1，則雷諾應力的預測值與實驗值相差達百分之十；若定在0.01以下，則不易收斂（須作十次以上的疊代）或無法收斂，因此合適的值在此範圍之內，愈小則應力的預測準度較高；愈大則疊代次數較少。本文選定其值爲0.03。其它物理量受此常數的影響很小，變化量在百分之一以內。

$u*$ 的疊代值先以掃描法來選定，掃描範圍的最小值爲零；最大值則須滿足所算出的第一點平均速度要小於或等於自由流速度。根據數值實驗的結果，假設的 $u*$ 值愈小則 $-\overline{uv}$ (2)有偏高（大於 $-\overline{uv}(1)$）的趨勢；反之則有偏低（小於 $-\overline{uv}(1)$）的趨勢，其中存在有一平衡點。因此可憑此訊號（$-\overline{uv}(2)$大於或小於 $-\overline{uv}(1)$）來作進一步的修正，直至滿足(32)式。

迴路三的結速與否端看是否已達計算的終點（圖一）。據程式本身的要求，終點處的邊界層厚度不得大於計算域的高度（y_U），且該處上限邊界的網格點的濃度亦不得大於設定的極限值。此外，可視爲意所需，訂定任意參數（如雷諾數、x座標或計算的步數i等）作爲終止的指標。

肆、結果與討論

㈠流場的計算結果：

圖十至十四爲二維光滑平板上紊流邊界層流場中物理量分佈的預測值與實驗值的比較。圖十至十二分別爲平均速度、平均動能及雷諾應力的分佈圖形，實驗值爲Klebanoff〔13〕的實驗結果。Klebanoff 的實驗使用 4 ½－ft 的風洞；利用長12ft、寬 4½ ft、厚¼ in.，對稱而爲鋒緣頂邊（ pointed leading edge ）的平滑鋁板垂直置於風洞中以產生邊界層流。自由流速度爲 50ft／s（ 15.24 m／s ），量測位置在距離頂邊 10ft 處，由於採取加寬邊界層厚度的方法（在鋁板的前·2 ft 覆蓋 No. 16 的砂紙造成粗糙面使邊界層加速發展，以使量測儀器尺寸產生的誤差相對減少），故邊界層厚度爲 3in（ 0.076 m ），若全爲平滑板面的狀況，對應的位置在離頂邊 14.2ft（ 4.33m ）處，其長度雷諾數（長度尺度爲與頂邊的距離），R_θ 爲 4.2×10^6 ，或動量厚度雷諾數（長度尺度爲動量位移（ momentum displacement ）），R_2 爲 6955（〔11〕，（ 21.12）式）。風洞內壁可調整使漸擴大，以保持平均壓力梯度爲零。除在量測位置的板中心處外，klebanoff 並在中心線以下，以下各 10in 處量取平均速度分佈，均與中心線爲平均速度分佈極爲一致，所以可確認該實驗爲二維的狀況。平均速度與雷諾應力直接取自實驗值，平均動能值則爲三個變動速度平方和的一半。預測值的狀況爲：$U\infty=15.24/s$，$X=4.5m$，$\delta=0.077m$，$R_2=7025$。由圖顯示，除靠近牆壁的平均動能與雷諾應力外，其餘部分的預測值與實驗值的吻合情況均稱良好。圖十一中近牆處處的平均動能預測值所以會產生偏差，可歸因於使用牆函數作爲邊界條件之故。因爲在該函數使用的範圍（ $10<y_+<100$ ），所提供的平均動能邊界值恆爲 $K=u*^2/\sqrt{c_u}=3.333\,u*^2$；但實驗值約在 $4\,u*^2$ 至 $5\,u*^2$ 之間，因此造成此誤差。圖十二的雷諾應力分佈在靠牆處發生下陷狀況，與物理現象不合。倘若再增加網格點（達90點），情形依舊，而且在 $y/\delta\geq0.05$的預測情形一直良好，故似可排除數值計算產生誤差的因素；另一方面，改變 $y_L{}^+$值則有影響。當 $y_L{}^+=30$，下陷偏差幾達百分之廿（但平均速度與動能變化不大），$y_L{}^+=50$ 以上則在百分之五以內，因此推斷產生下陷的原因可能是 $K-\epsilon$ 模式與牆函數的配合問題，這部分需要再作研究分析。雖然存在有此問題，摩擦係數，$C_f=2(u*/U\infty)^2$，的預測值仍有相當的準度。

圖十三爲摩擦係數 C_f 與形狀因子（ shape factor ）H對雷諾數R_2的關係圖，使用 Coles 的實驗結果（節錄自〔14〕）作比較。當雷諾數大於約 2500 時兩者預測值與實驗值的差距在百分之一以內，但雷諾數小於此數值時偏差逐漸增加。對於形狀因子，在低雷諾時量測值本身即隨造成過度（ transition ）的機構而不同，因此這部分的差異並無甚緊要。對於摩擦係數，當雷諾數愈小時偏差愈大，預測值愈小於實驗值，此現象可根據圖十四予以說明。圖十四爲在 $u^+\sim y^+$ 座標系統中的平均速度分佈圖，其中 $u^+=U/u*$，$y^+=u*y/\nu$。從圖中可發現預測曲線在一般邊界層中所謂的“通式區域（ universal region ）“裡（在該區域的平均速度均滿足通式

$$u^+=\frac{1}{0.41}\ln y^+ + 5.0\,, \qquad (33)$$

其範圍約在 $30<y^+<200$ 之間），是隨雷諾數而不同。但 Coles 的實驗中假設(33)式恆成立，故在量得U～y 的分佈後，俱由該式計算 u* 與 C_f 的值。如果實際的情形（u*，U，y 三者的反應的關係）與預測結果相似，則由圖十四可看出 Coles 估計的u* 值（及 C_f 值）比原值偏高，其差距隨雷諾數減小而增大，正如圖十三的情形一般。

㈡濃度擴散的計算結果：

圖十五至廿三爲線源置於地面的擴散情形。使用的實驗數據爲Nieuwstadt 與Van Ulden〔 7 〕及Poreh 與Cermak〔15 〕的結果。前者係根據Barad的實驗數據（Prairie Grass實驗）而來，原實驗是在大氣中將穩定點源置於離地 0.5m 的高度（視爲地面高度），再於下游 100m 處設置六個測量塔分別量取變數的分佈（0.5m高至 17.5m 高的範圍）。Nieuwstadt 與 Van Ulden將六個塔各別的量測結果相加，代表水平衡向（相當本文座標系統的 z 方向，與 x、y 方向均垂直。）的積分，得到近似的二維分佈曲線，再以一族經驗式來表示這些曲線，即

$$\frac{C}{C_0}=\exp\left\{-\ln 2\left(\frac{y}{\sigma_y}\right)^s\right\}\,,$$

C_0 爲最大濃度（即地面濃度），σ_y 爲擴散半寬；s 與大氣的穩定性（ stability ）有關，愈大代表愈穩定。s＝1.4 時，$L^{-1}=0.005$（L 爲Monin-Oboukhov長度 ），爲中性稍趨穩定的狀況；s＝1.3 時，$L^{-1}=-0.005$，爲中性稍趨不穩定的狀況，而中性穩定狀況（ $L^{-1}=0$ ）的 s 值則在兩者之間。此實驗的地面爲草原狀況，相當於平滑表面（ u*／U∞ 值在 0.037～0.045 間；平均速度與高度的 1／7 次方成正比），故可與計算的狀況比較。

Poreh 與 Cermak 的風洞實驗爲光滑平板上穩定的（ steady）二維邊界層流場（壓力梯度爲零，平均速度與高度的 1／7 次方成正比），污染源置於板面上（地面高度），爲穩定的線源。三種實驗狀況的自由流度分別爲 9，12，16ft／s（ 2.74，3.66，4.88 m／s ），對應的初邊界厚度依次爲 6.88，6.36，5.33 in（ 0.175，0.162，0.135m ）。該實驗依擴散的範圍延下游方向劃分爲四個區域，即超始區域（擴散作用主要發生在邊界層內），過渡區域與末尾區域（擴散作用已發展至邊界層外）。其中中間區域的擴散型態與大氣層者相同，故取其濃度分佈的實驗值作比較，此區範圍爲 $x/\delta_{av}\leq18$（ x/δ_{av} 的定義參見圖八）。在三種實驗狀況下，擴散半寬與地面平均濃度的發展情形可寫成經驗式爲

$$\sigma_y=0.076\,x^{0.8}\,,$$

$$C_0U\infty=26.2\cdot Q\cdot x^{-0.9}\,,$$

上兩式使用 c. g. s. 單位系統；x 爲下游方向與線源的距離，適用的範圍爲 $x\leq4$ m。

圖十五爲平均濃度的分佈圖形，預測曲線爲中性穩定的狀況，位置在 $x/\delta_0=17$ 處（ $x/\delta_{av}<17$），和Nieuwstadt 與 Van Ulden的實驗曲線（ s 爲 1.3 及 1.4 ）、Poreh 與Cermak 的實驗值均相當一致。同時可推測後者的實驗是中性稍偏穩定的狀況

，可以合理的用其結果與預測值作更多的比較。

圖十六、十七分別爲半寬與地面平均濃度延流向的變化情形，預測值對應的狀況爲 $U\infty = 5.0m/s$ ， $\delta_0 = 0.136m$ 。此外另就 $U\infty = 10$ ， $15.24m/s$ ； $\delta_0 = 0.077$ ， $0.096m$ 等狀況加以計算，圖十八、十九爲當 $\delta_0 = 0.077$ ， $0.096m$ 等狀況加以計算，圖十八、十九爲當 $\delta_0 = 0.077m$ 時，在不同自由流速度下半寬與地面平均濃度的變化圖；圖廿、廿一爲當 $U_\infty = 5.0m/s$ 時，在不同的 δ_0 值下半寬與地面平均濃度的變化圖。由這些結果得知，當自由流速度愈低及初邊界層厚度愈大時，污染物的擴散作用愈強（較大的半寬及較低的濃度）。這些曲線在無因次座標中相差極爲有限，可視爲通用的曲線，如圖廿二、廿三所示，可應用於大氣擴散的分析。無因次的擴散半寬定義爲 σ_y/δ ，無因次濃度爲 $C_0 U\infty \cdot \delta / Q$ ，因次下游座標爲 x/δ_0 。

圖廿四至廿六分別爲線源在不同高度時的平均濃度分佈圖。紊流的輸送與擴散作用使下游遠處的平均濃度漸呈均等分佈，但在近線源的區域濃度分佈的型式隨線源高度而有差別，當 $h/\delta_0 = 0.2$ 時（圖廿四）污染物濃度擴展的速率在線源以上的部分較快；當 $h/\delta_0 = 0.6$ 時則在線源以下的部分較快。造成此差異是因爲使用 $K-\epsilon$ 模式的紊流擴散係數分佈之故，其約在 $h/\delta_0 = 0.41$ 處有最大值（圖廿七）。在 $h/\delta_0 = 0.2$ 的狀況，線源附近的平均速度與擴散係數均隨高度增加，代表輸送與擴散作用漸強，故以上半部的擴展速率較快。在 $h/\delta_0 = 0.4$ 的狀況，平均速度仍隨高度增加，但擴散係數過最大值後開始下降，使兩邊的擴展速率約若相等。至 $h/\delta_0 = 0.6$ 的狀況，擴張係數隨高度遞減，大過平均速度的輸送作用，故以下半部的擴散速率較快。一般計算大氣擴散時假設紊流擴散係數正比於高度的 n 次方，即 $v_t \propto y^n$ ，則無此現象。

圖廿八爲不同線源高度時地面平均濃度延下游方向的變化情形。在近距離內，在相同的下游距離，線源高度愈高濃度愈低；但在下游遠處（ $x/\delta_0 > 56$ ）地面濃度的發展呈現一致的情形，顯示下游污染物的分佈將逐漸擺脫原來分佈的影響。圖廿八可應用於污染物濃度的預測或決定線源高度的規劃。例如，假設在 $x/\delta_0 < 1$ 的範圍中污染物的（無因次）濃度不得超過 1 ，則線源高度 h/δ_0 應在 0.16(圖中虛線）以上。圖廿九、卅爲前圖的輔助圖形，圖廿九表示改變線源高度時，地面最大平均濃度的變化情形，高度愈小，尤其在 $h/\delta_0 < 0.2$ 的範圍，濃度變化愈大，若稍加高線源位置即可大幅降低濃度值。圖卅表示地面最大濃度所在位置的變化，高度愈大離線源愈遠且隨高度的變化愈，唯不若濃度值變化之巨。

伍、結論與建議

$K-\epsilon$ 模式在本研究的應用情形大體良好，預測的物理量包括平均速度、平均動能、雷諾應力、平均濃度的分佈，以及形狀因子、摩擦係數，半寬與地面濃度的發展。根據本文的計算結果，自 流速度愈小及線源所在的邊界層厚度愈大則污染物的擴散作用愈強。若紊流擴散係數在 $y/\delta = 0.41$ 處有最大值，則此高度以上的擴散作用隨高度減

弱，以下隨高度增強；而平均速度的輸送的輸送作用均隨高度增強，最後的效果使平均濃度成均等分佈。近線源的區域，線源愈高地面發生的最大濃度值愈低，所在位置愈遠，在較低的線源高度時前者的變化較大，後者的變化較小。至下游遠度（ $x/\delta_0 > 56$ ）地面最大濃度的發展呈現一致現象，與原線源高度無關。

本文僅計算中性穩定的狀況，如果要考慮穩定性的影響，$K-\epsilon$ 模式應擴展爲（〔1〕，P.28 ）。

$$\frac{\partial K}{\partial t} + U_i \frac{\partial K}{\partial x_j} = \frac{\partial}{\partial x_j}\left[C_k \frac{K^2}{\epsilon} \frac{\partial K}{\partial x_j} + \nu \frac{\partial K}{\partial x_j} \right] + P + G - \epsilon \quad ,$$

$$\frac{\partial \epsilon}{\partial t} + U_j \frac{\partial \epsilon}{\partial x_j} = \frac{\partial}{\partial x_j}\left[C_\epsilon \frac{K^2}{\epsilon} \frac{\partial \epsilon}{\partial x_j} + \nu \frac{\partial \epsilon}{\partial x_j} \right]$$

$$+ C_{1\epsilon} \frac{\epsilon^2}{K} (P+G)(1 + C_{3\epsilon} R_f) - C_{2\epsilon} \frac{\epsilon^2}{K} \quad ,$$

$$P = -\overline{u_i u_j} \frac{\partial U_i}{\partial x_j} \quad ,$$

$$G = -\beta g_i \overline{\theta u_j} \quad ,$$

其中 β 爲體積膨脹係數，g_i 爲重力，T爲平均溫度，$C_{3\epsilon} = 0.8$ ，爲經驗常數，R_f 爲 Richardson 數，代表穩定的狀況，與L的關係爲

$$R_f = \frac{x^3}{L} \quad ,$$

x_3 爲垂直地面的高度。此時統制方程式應包括平均溫度的方程式

$$\frac{\partial T}{\partial t} + U_j \frac{\partial T}{\partial x_j} = \frac{\partial}{\partial x_j}\left(\gamma \frac{\partial T}{\partial x_j} - \overline{\theta u_j} \right)$$

$$+ \frac{1}{C_p}\left[\nu \left(\frac{\partial U_i}{\partial x_j} + \frac{\partial U_j}{\partial x_j} \right) \frac{\partial U_i}{\partial x_j} + \epsilon \right] ,$$

θ 爲溫度變動量，γ 爲熱的分子擴散係數，C_p爲單位質量的等壓比熱。並在動量方程式(4)中增加浮力項成爲

$$\frac{\partial U_i}{\partial t} + U_j \frac{\partial U_i}{\partial x_j} = -\frac{1}{\rho} \frac{\partial P_i}{\partial x_i} + \frac{\partial}{\partial x_j}\left(\nu \frac{\partial U_i}{\partial x_j} - \overline{u_i u_j} \right) - \frac{T - T_0}{T} g_i \ ,$$

T_0 爲中性穩定時的溫度，ρ 爲對應的密度。

原則上本理論模式可擴展到三度空間及更複雜區域的狀況，唯擴散係數 K_x，K_y，K_z 與 ν_t 的關係需要作更廣泛的研究，或使用紊流應力通量方程式模式（Turbulent stress / flux-equation Models）來描述 $-\overline{u_i u_j}$、$\overline{\varphi_i u_j}$ 等紊流傳遞量。

參 考 文 獻

1. Rodi, W., Turbulent Modles and Their Application in Hydraulics, Karlsruhe, Federal Republic of Germany (1980).
2. Launder, B. E. and D. B. Spalding, " The Numerical Computation of Turbulent Flows ", Comp. Meth. Appl. Mech. Eng., 3, 269-289 (1974).
3. Pasquill, F., Atmospheric Diffusion, 2 nd Edn., John Wiley, New York (1974).
4. Smith, F. B., " The Diffusion of Smoke From a Continuous Elevated Point-Source into a Turbulent Atmosphere ", J. Fluid Mech., 2, 49-76 (1956).
5. Wengle, H., Bruno Van Den Bosch and John H. Seinfeld, " Solution of Atmospheric Diffusion Problems by Pseudo-Spectral and Orthogonal Collocation Method ", Atmos. Envior., 12, 1021-1032 (1978)
6. Robin, A.G., " Plume Dispersion From Ground Level Source in Simulated Atmospheric Boundary Layers ", Atmos. Enviro., 12, 1033-1044 (1978).
7. Nieuwstadt, F. T. M. and A. P. Van Ulden, " A Numerical Study on the Vertical Dispersion of Passive Contaminants From a Continuous Source in the Atmospheric Surface Layer ", Atmos. Envir., 12, 2119-2124 (1978).
8. Tennekes, H. and J. L. Lumely, A First Course in Turbulence, MIT, Massachusetts (1972).
9. Hanjalic, K. and B. E. Launder, " A Reynolds Stress Model of Turbulence and Its Application to Thin Shear Flows ", J. Fluid Mech., 52, 609-638 (1972).
10. Chen, C. J., Lecture of Turbulence Modelling and Its Applications, Institute of Physics, Academia Sinica, Taipei (1983).

11. Schlichting, H., Boundary Layer Theory, 7th Edn., McGRAW-HiLL New York (1979).
12. Patankar, S. V., Numerical Heat Transfer and Fluid Flow, Hem s here, New York (1980).
13. Klebanoff, P. S., " Characteristics of Turbulence in a Boundary Layer With Zero Pressure Gradient ", NACA Rep. No. 1247 (1955).
14. Jones, W. P. and B. E. Launder, " The Prediction of Lam nar zation with a Two-Equation Model of Turbulence " , Int. J. Heat Mass Transfer, 15, 301-314 (1972).
15. Poreh, M. and J. E. Cermak, " Study of Diffusion From a Line Source in a Turbulent Boundary Layer ", Int. J. Heat Mass Transfer, 7, 1083-1095 (1964).

表一　$k-\epsilon$ 模式經驗常數的適用範圍

C_μ	C_k	C_ϵ	$C_{\epsilon 1}$	$C_{\epsilon 2}$
0.09 ∿0.11	0.09	0.07	1.44 ∿1.45	1.90 ∿2.0

表二　本文使用的模式常數值

C_μ	C_k	C_ϵ	$C_{\epsilon 1}$	$C_{\epsilon 2}$
0.09	0.09	0.07	1.44	1.92

表三　級數 $O\left(\frac{V}{U}\frac{x_c}{y_c}\right)$ 的典型計算值。$x=\hat{x}_c$，$4\cdot SIGMA=\hat{y}_c$，ORDER $=O()$

	X	SIGMA	MAX.[V/U]	ORDER
	0.10000E-01	0.38188E-03	0.46879E-02	0.30690E-01
	0.51000E+00	0.14795E-01	0.18468E-02	0.15914E-01
	0.10100E+01	0.25439E-01	0.18595E-02	0.18456E-01
	0.15100E+01	0.34941E-01	0.18267E-02	0.19736E-01
U_∞=15.24 m/s	0.20100E+01	0.43670E-01	0.17458E-02	0.20088E-01
δ_0=0.077 m	0.25100E+01	0.51770E-01	0.17245E-02	0.20903E-01
	0.30100E+01	0.59343E-01	0.17563E-02	0.22271E-01
	0.35100E+01	0.66465E-01	0.16860E-02	0.22260E-01
	0.40100E+01	0.73210E-01	0.16653E-02	0.22804E-01
	0.45100E+01	0.79635E-01	0.16544E-02	0.23423E-01
	0.50100E+01	0.85789E-01	0.16223E-02	0.23686E-01
	0.10000E-01	0.62743E-03	0.48755E-02	0.19426E-01
	0.51000E+00	0.16903E-01	0.18644E-02	0.14063E-01
	0.10100E+01	0.27591E-01	0.17502E-02	0.16017E-01
	0.15100E+01	0.36911E-01	0.16822E-02	0.17204E-01
U_∞=5.0 m/s	0.20100E+01	0.45013E-01	0.16126E-02	0.18002E-01
δ_0=0.077 m	0.25100E+01	0.52708E-01	0.19987E-02	0.23795E-01
	0.30100E+01	0.59824E-01	0.21737E-02	0.27342E-01
	0.35100E+01	0.66271E-01	0.21934E-02	0.29043E-01
	0.40100E+01	0.72204E-01	0.22448E-02	0.31168E-01
	0.45100E+01	0.77721E-01	0.63577E-03	0.92232E-02
	0.50100E+01	0.82929E-01	0.58168E-03	0.87853E-02
	0.20000E-01	0.90391E-03	0.46512E-02	0.25728E-01
	0.52000E+00	0.16846E-01	0.45158E-03	0.34849E-02
	0.10200E+01	0.27602E-01	0.46003E-03	0.42500E-02
	0.15200E+01	0.37195E-01	0.24359E-02	0.24886E-01
U_∞=5.0 m/s	0.20200E+01	0.45928E-01	0.42762E-03	0.47019E-02
δ_0=0.136 m	0.25200E+01	0.54079E-01	0.42418E-03	0.49415E-02
	0.30200E+01	0.61681E-01	0.48670E-03	0.59575E-02
	0.35200E+01	0.68865E-01	0.48997E-03	0.62611E-02
	0.40200E+01	0.75625E-01	0.54529E-03	0.72465E-02
	0.45200E+01	0.82035E-01	0.54807E-03	0.75495E-02
	0.50200E+01	0.88079E-01	0.57185E-03	0.81481E-02

表四　放置線源起始處的物理狀況分列表

U_∞(m/s)	15.24	10.0	5.0	5.0	5.0
δ_0(m)	0.077	0.077	0.077	0.096	0.136
X_{02}(m)	4.50	4.22	3.28	4.32	6.96
R_2	7025	4773	2500	3001	4137

表五　各平均物理量的授施項其中 $S=S_c+S_p$ ϕ

ϕ	S	S_c	S_p
U	$-\frac{dP_0}{dx}$	$-\frac{dP_0}{dx}$	0
K	$\rho[C_\mu \frac{K^2}{\epsilon}(\frac{\partial U}{\partial y})^2-\epsilon]$	$\rho C_\mu \frac{K^2}{\epsilon}(\frac{\partial U}{\partial y})^2$	$-\rho\cdot\frac{\epsilon}{K}$
ϵ	$\rho[C_{\epsilon 1}C_\mu K(\frac{\partial U}{\partial y})^2-C_{\epsilon 2}\frac{\epsilon^2}{K}]$	$\rho C_{\epsilon 1}C_\mu K(\frac{\partial U}{\partial y})^2$	$-\rho C_{\epsilon 2}\frac{\epsilon}{K}$
C	0	0	0

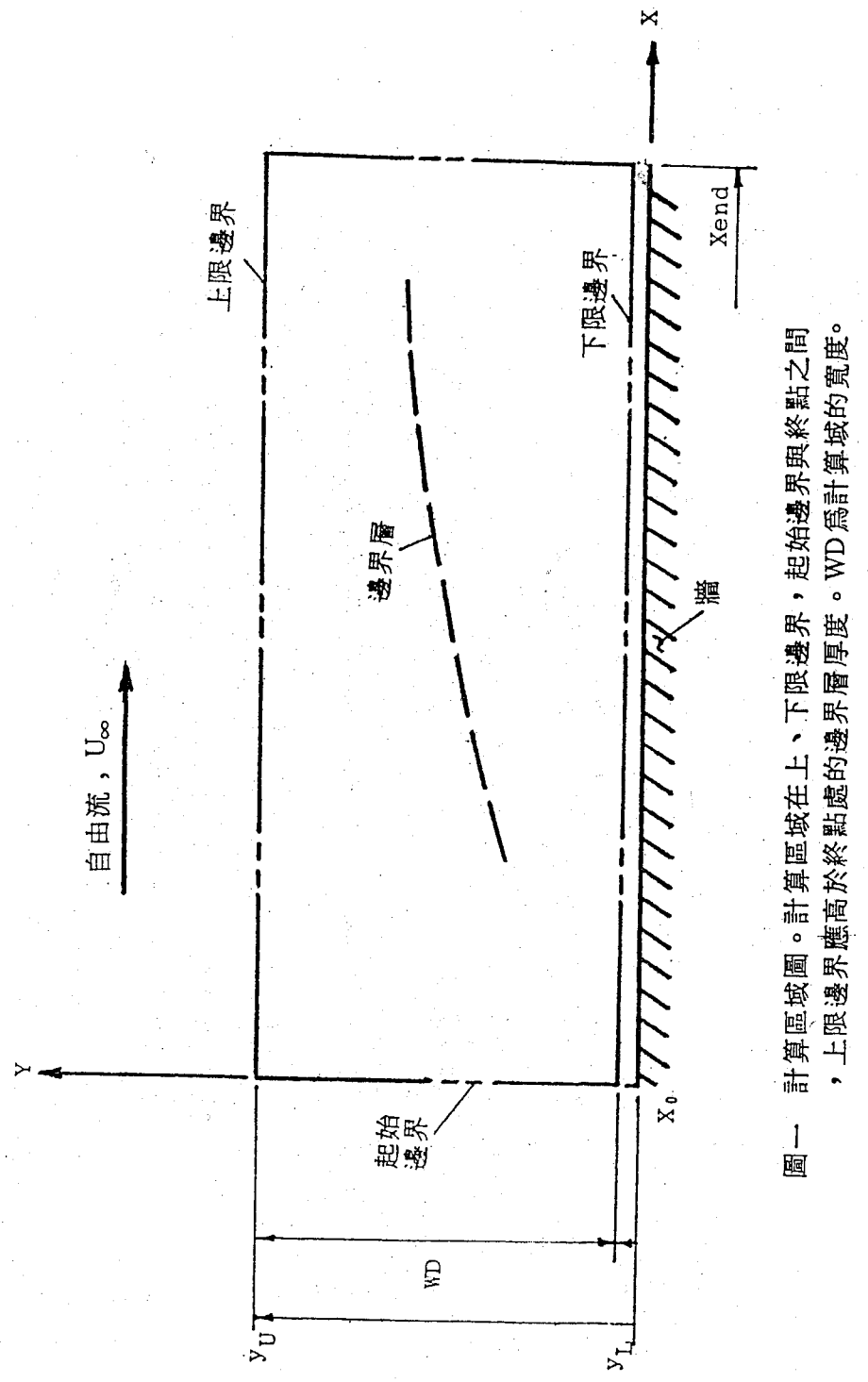

圖一　計算區域圖。計算區域在上、下限邊界，起始邊界與終點之間，上限邊界應高於終點處的邊界層厚度。WD為計算域的寬度。

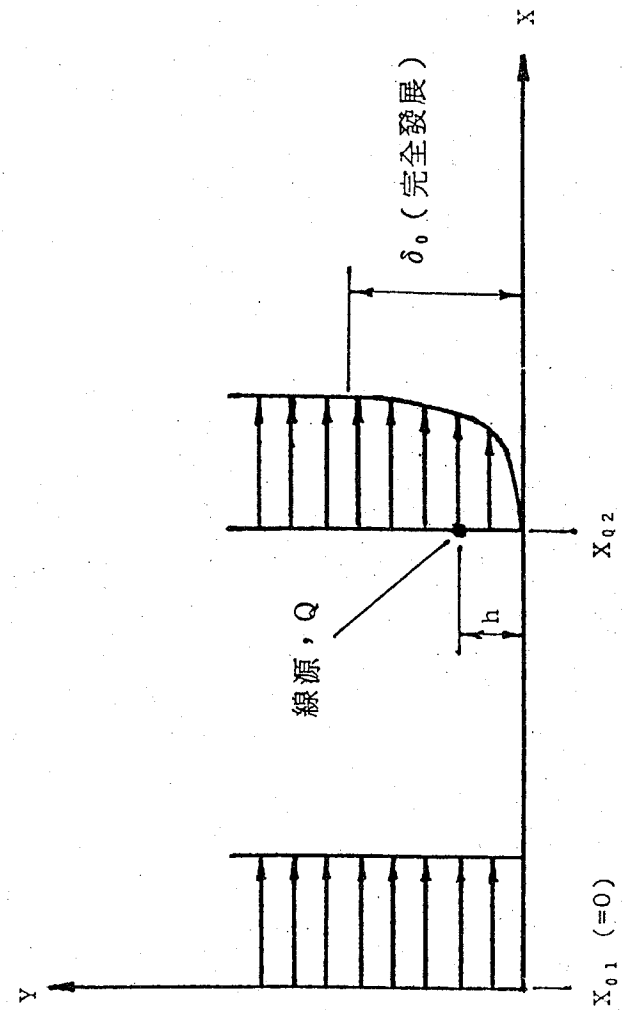

圖二　線源位置圖。X_{01} 爲計算流場分佈時的起始邊界，變數設爲均等分佈，X_{02} 爲計算濃度分佈時的起始邊界條件，即線源所在。根據要求的邊界層厚度 δ_0 決定 X_{02} 之值，線源強度爲 Q，高度爲 h。

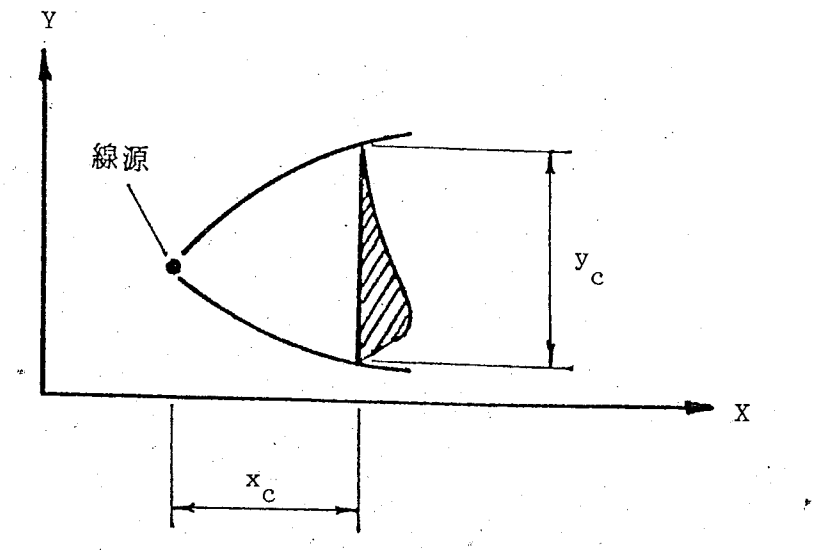

圖三　濃度擴散的特性長度圖。X 方向的特性長度取爲與線源的距離 x_c，y 方向的特性長度取爲四倍的半寬 y_c。

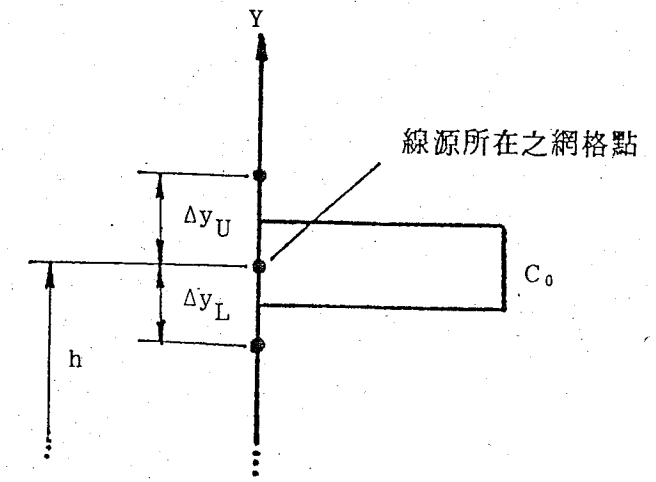

圖四　初濃度分佈的數值似近圖，其中 $C_0=Q/[U(h)(\Delta y_U+\Delta y_L)/2]$

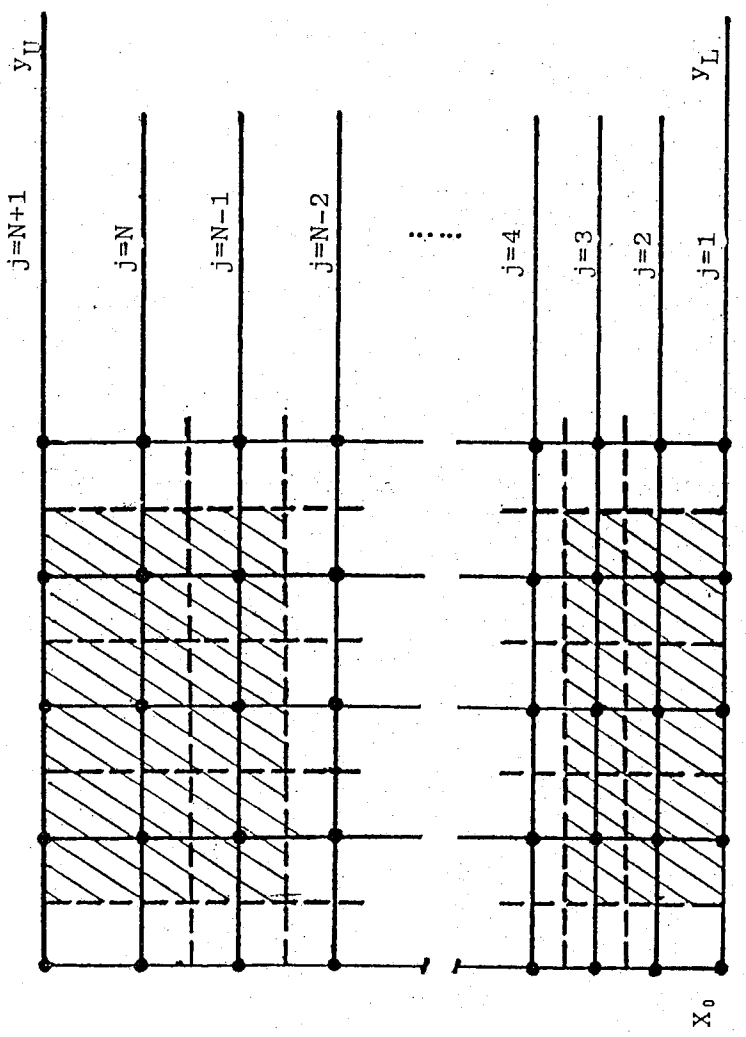

圖五　網格點與控制體積積分佈圖。• ：網格點；----：控制體積的界面。

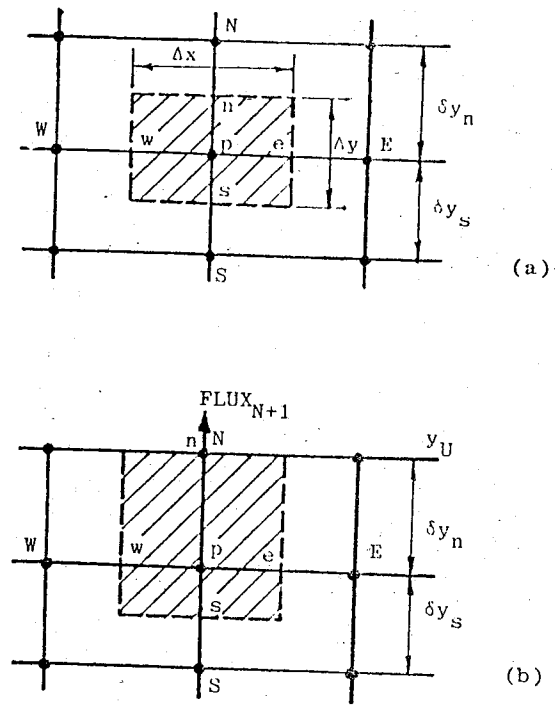

圖六　控制體積詳細圖。(a)爲一般的控制體積，(b)爲上限界限爲控制體積，(c)爲下限邊界的控制體積。其中P，E，W，S，N代表網格點；e，w，n，s代表控制體積的界面；$FLUX_{N+1}$，$FLUX_1$ 各爲上、下限界面的物理通量。

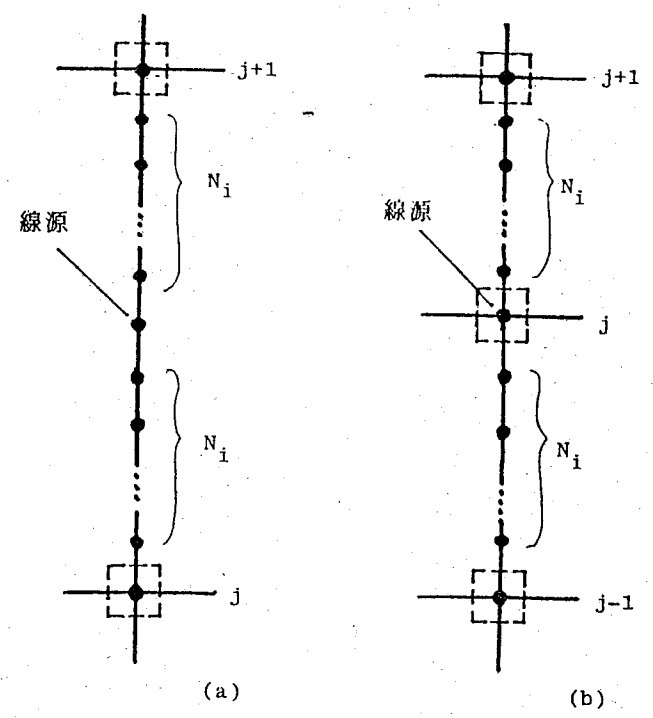

圖七　內插網格點分佈圖。●，內插的網格點；⊡，原網格點；N_i 爲內插網格點數。(a)爲線源在原相鄰網格點間的狀況，(b)爲線源在原網格點上的狀況。

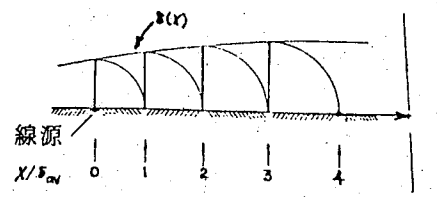

圖八　$X/\delta_{.v}$ 值的定義圖〔15〕

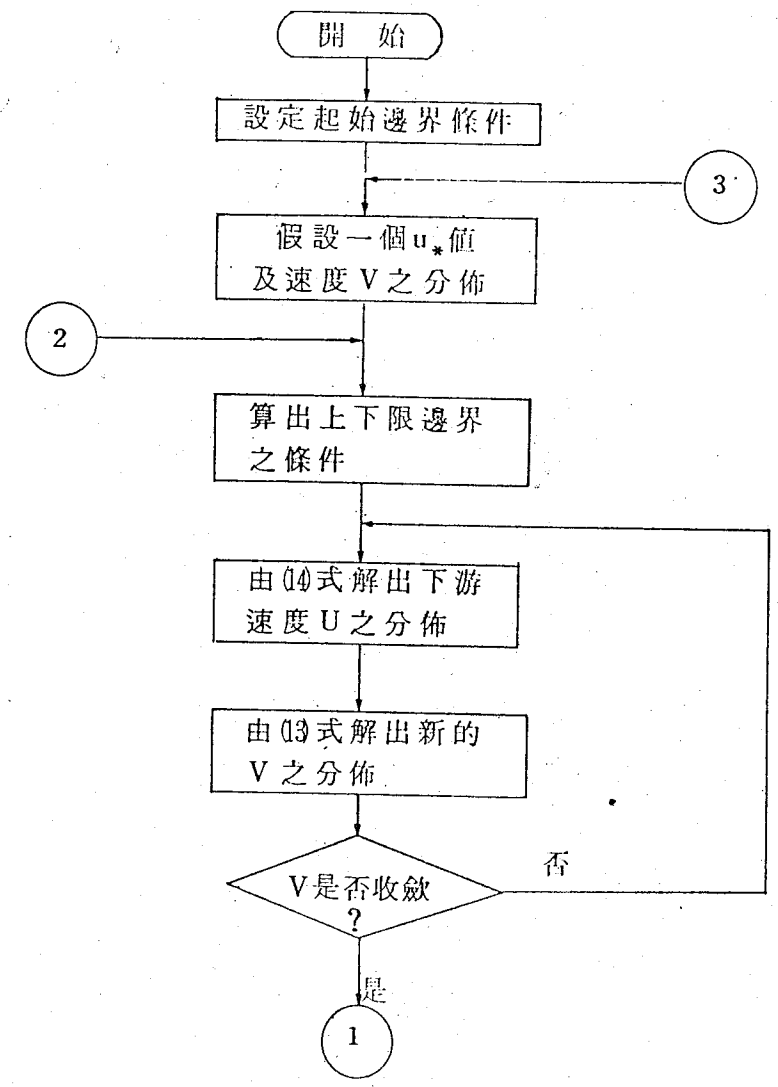

圖九　程式流程圖，包括三個迴路，第一迴路中聯解速度U、V的分佈，第二迴路K、ε，$-\overline{uv}$ 的分佈，第三迴路解C的分佈並決定是否繼續計算。

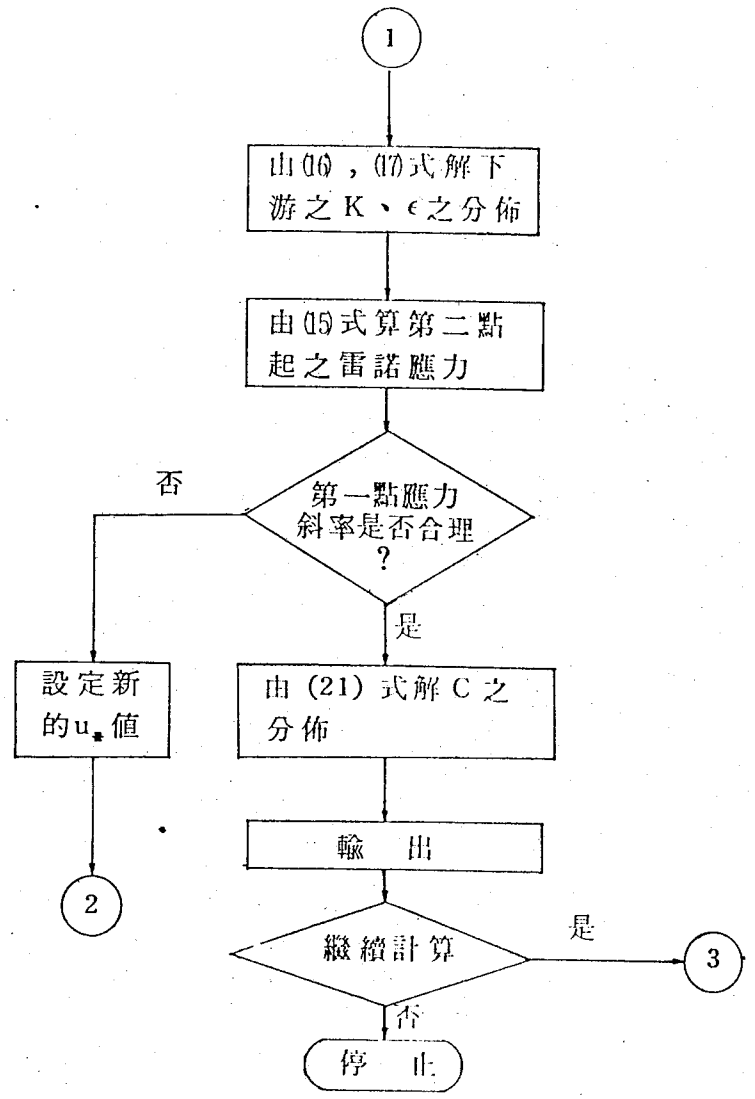

圖九（續） 程式流程圖

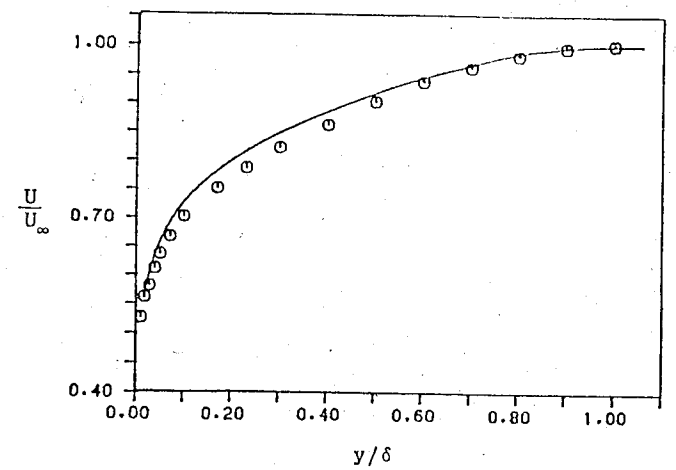

圖十　平均速度分佈圖。o，klebanoff〔13〕實驗值，在動量厚度雷諾數$R_2=6955$的狀況；—，計算值，$R_2=7025$，U_∞為自由流速度，δ為邊界層厚度。

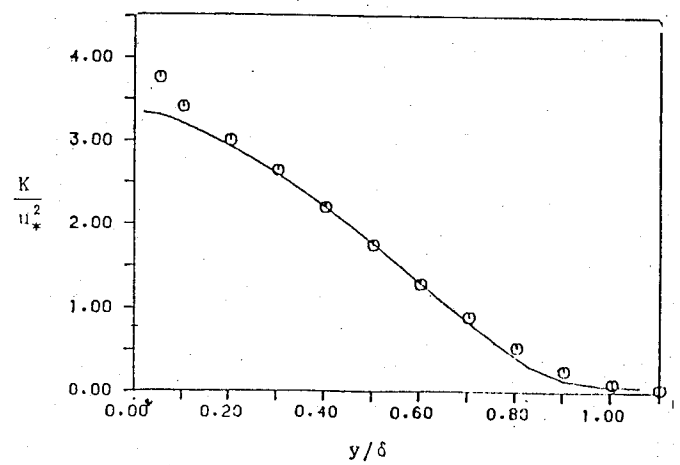

圖十一　平均動能分佈圖。符號同圖十。

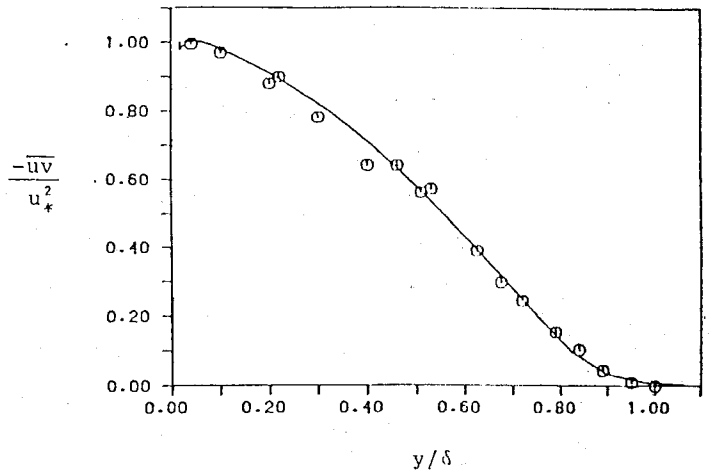

圖十二　雷諾應力分佈圖。符號同圖十。

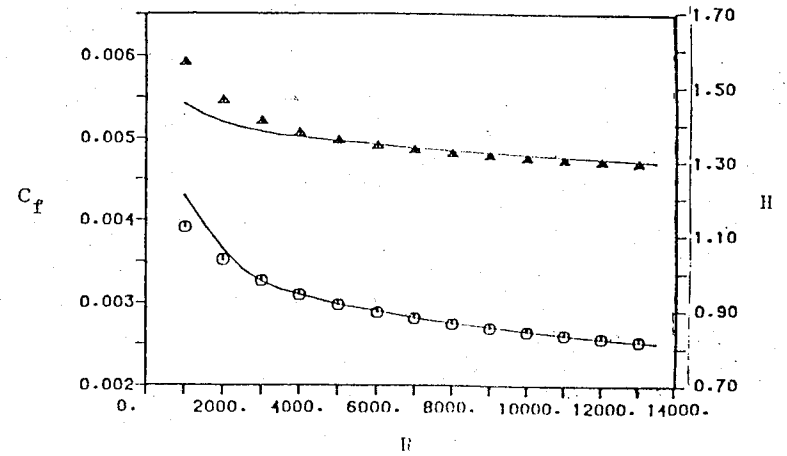

圖十三　摩擦係數C_f與形狀因子H對雷諾數R_2的關係圖。—，Coles〔14〕實驗值；o，C_f計算值；△，H計算值。

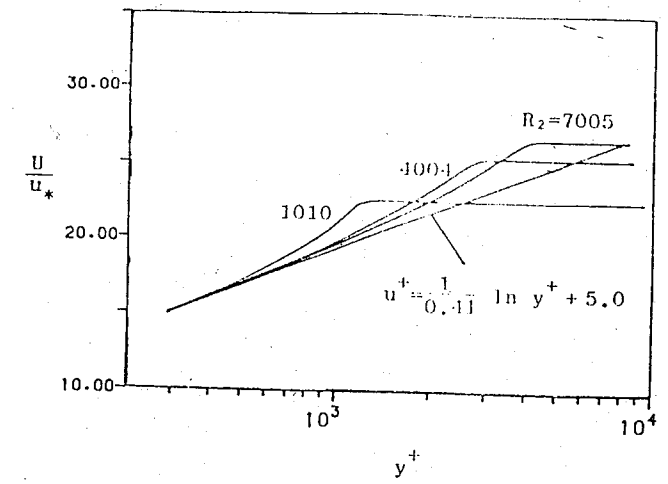

圖十四　無因次座標的平均速度分佈圖。三種不同雷諾數時的計算曲線與根據通式所作曲線的比較，$y^+ = y \cdot u_* / \nu$。

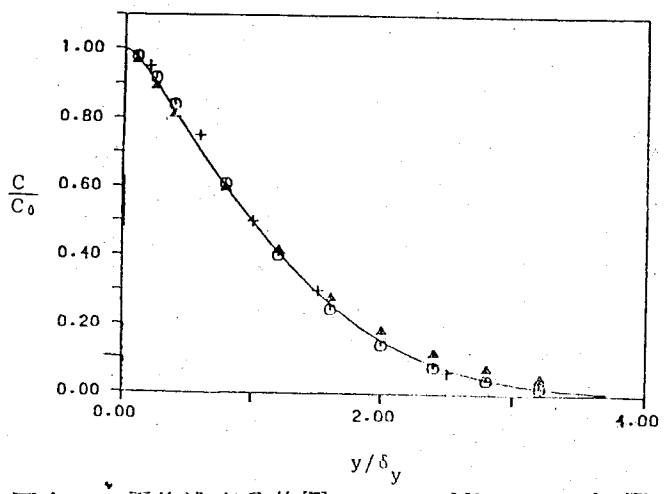

圖十五　平均濃度分佈圖。o，△，Nieuwstadt 與 Ven Ulden〔7〕的實驗值，o：s=1.4，△：s=1.3；＋，Poreh 與 Cermak〔15〕的實驗值；—，計算值。C_0為地面濃度，σ_y為擴散半寬。

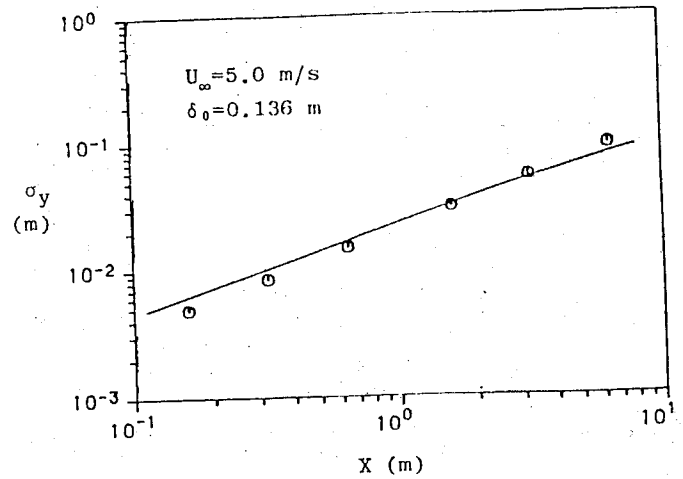

圖十六　擴散半寬發展圖。o, Poreh 與 Cermak〔15〕的實驗值；—，計算值。σ_y 爲擴散半寬，δ_0 爲初邊界層厚度，即線源所在的邊界層厚度。

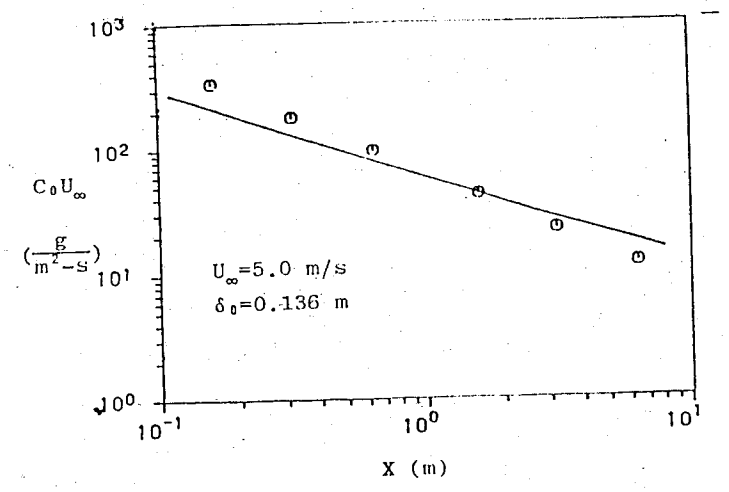

圖十七　地面平均濃度發展圖。o, Poreh 與 Cermak〔15〕的實驗值；—，預測值。C_0 爲地面濃度。

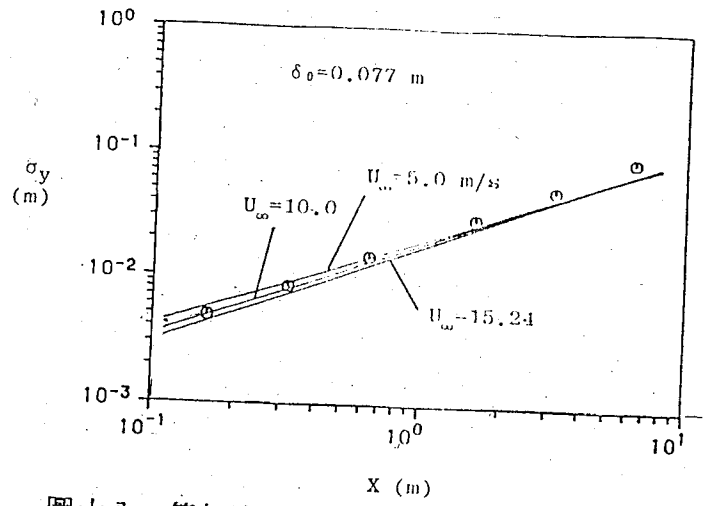

圖十八　等初邊界層厚度，不同自由流速度下的半寬發展圖。符號同圖十六。

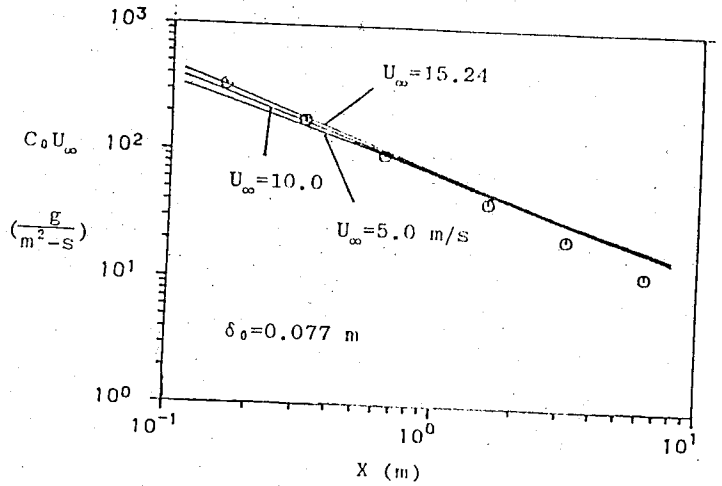

圖十九　等初邊界層厚度，不同自由流速度下的地面平均濃度發展圖，符號同圖十七。

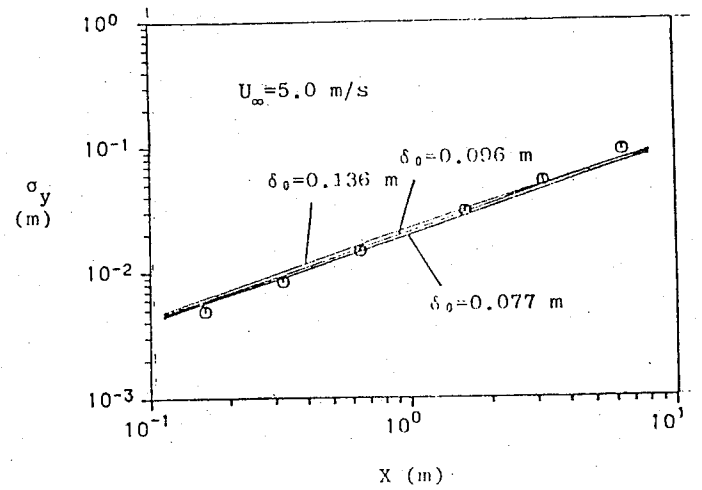

圖二十　等自由流速度，不同初邊界層厚度下的半寬發展圖，符號同圖十六。

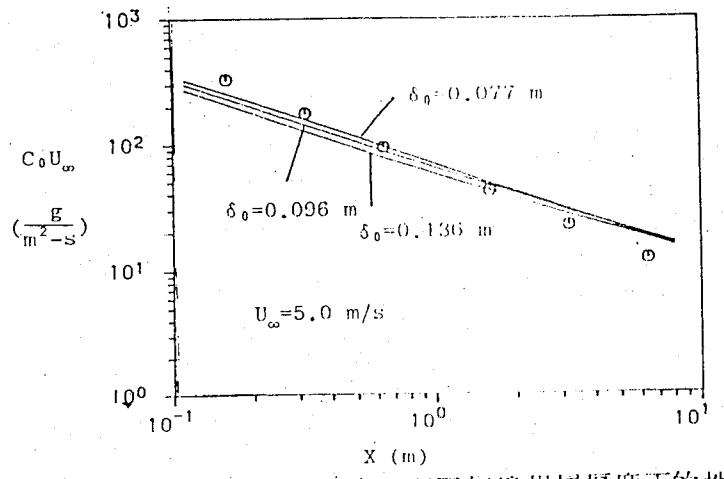

圖廿一　等自由流速度，不同初邊界層厚度下的地面平均濃度發展圖，符號同圖十七。

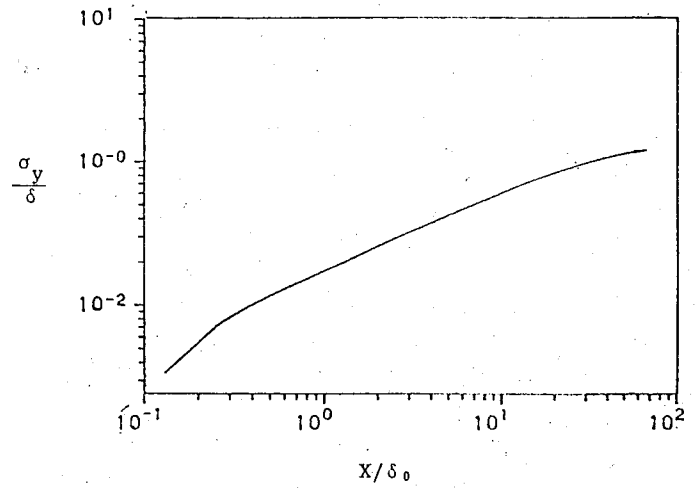

圖廿二　無因次的半寬發展曲線圖。σ_y為半寬，δ為邊界層厚度，δ_0為線源所在的邊界層厚度。

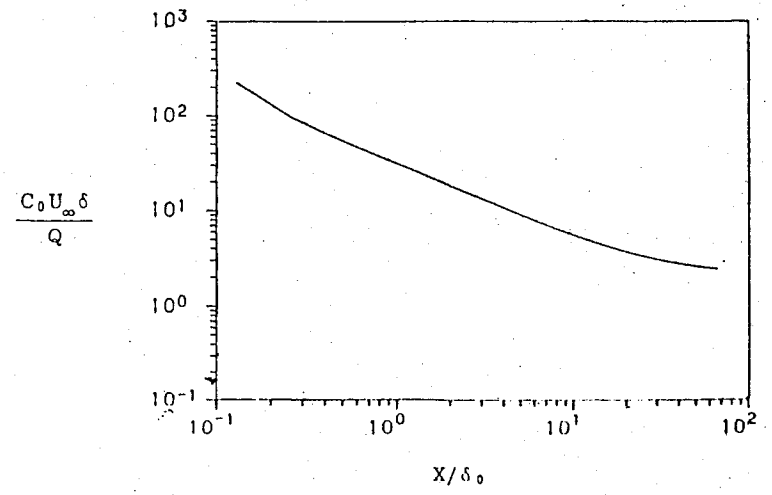

圖廿三　無因次的地面平均濃度發展曲線圖。C_0為地面濃度，δ為邊界層厚度，δ_0為線源所在的邊界層厚度，Q為線源強度。

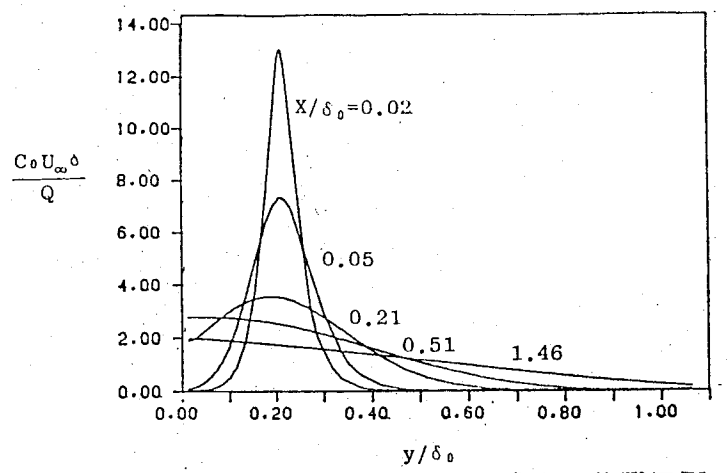

圖廿四　線源高度 $h/\delta_0=0.2$時的濃度分佈發展圖。在 $h/\delta_0>0.2$的部分擴展速率較快，符號同圖廿三。

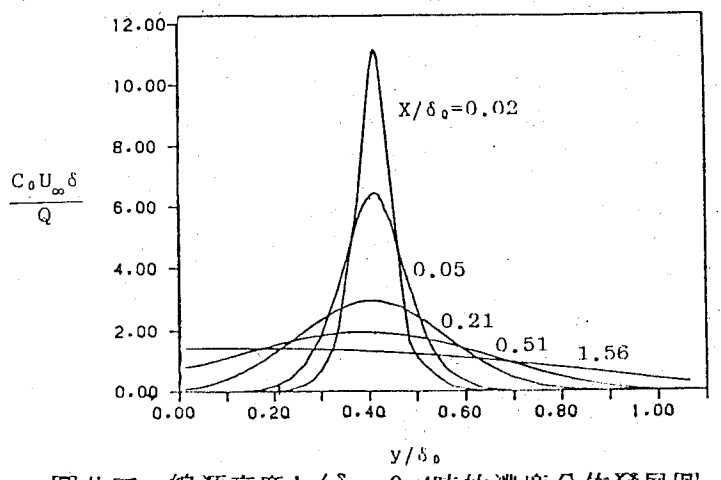

圖廿五　線源高度 $h/\delta_0=0.4$時的濃度分佈發展圖。在 $h/\delta_0>0.4$ 的部分擴展速率稍快，符號同圖廿三。

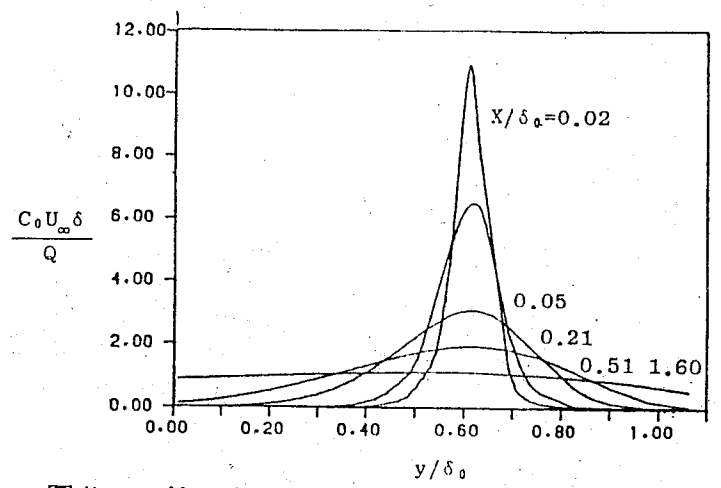

圖廿六　線源高度 $h/\delta_0=0.6$時的濃度分佈發展圖。在 $h/\delta_0<0.6$的部分擴展速率較快，符號同圖廿三。

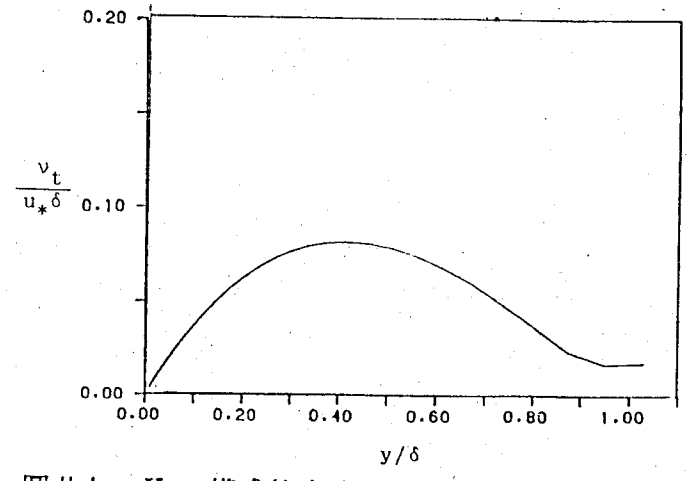

圖廿七　K—ε模式的紊流擴散係數分佈圖。約在 $y/\delta=0.41$ 處有最大值。ν_t，紊流擴散係數，δ，邊界層厚度。

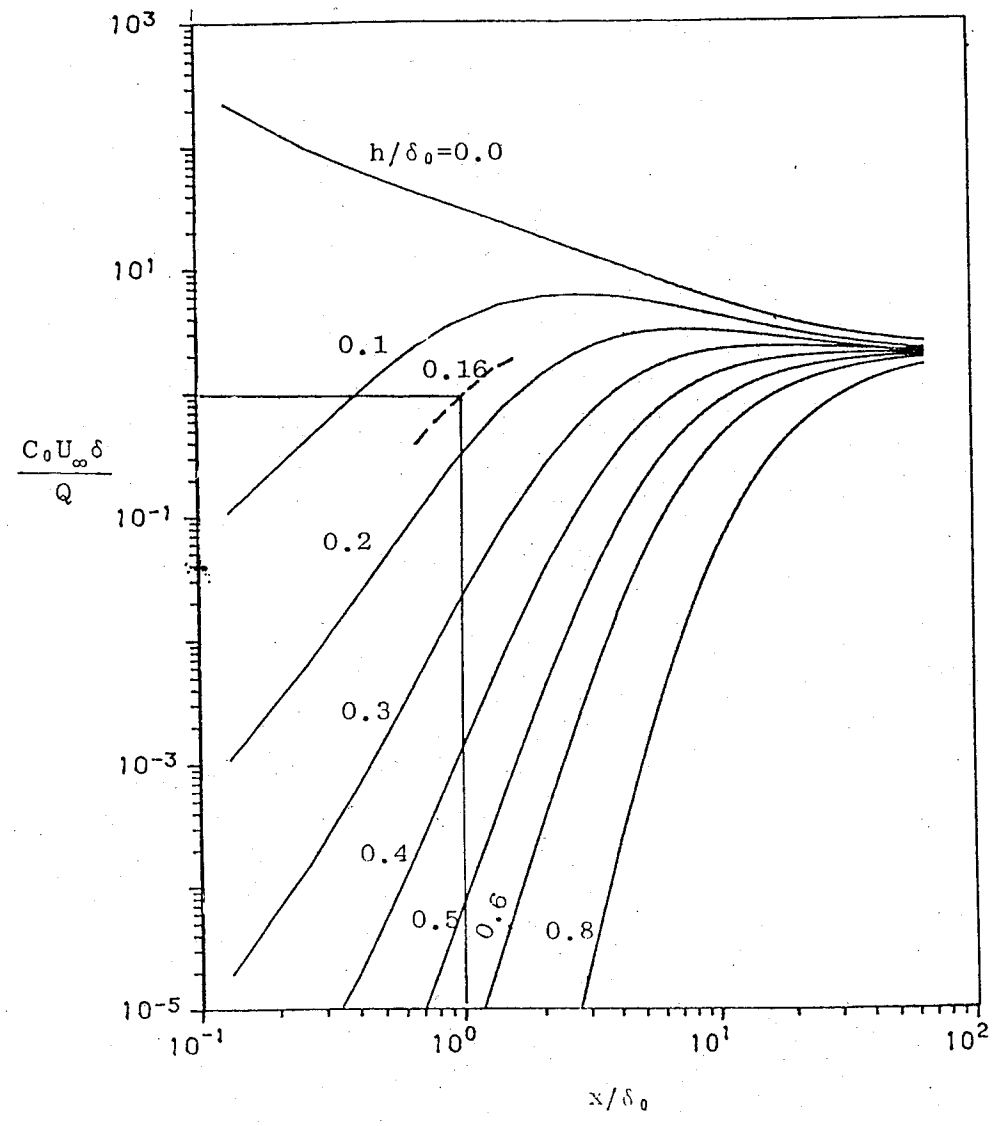

圖廿八　不同線源高度時的地面平均濃度發展圖。可應用於濃度控制的規劃。設在$X/\delta_0<1$的範圍內，須維持地面濃度$C_0U_\infty\delta/Q<1$，最線源高度最少爲$h/\delta_0=0.16$，如虛線所示，符號同圖廿三。

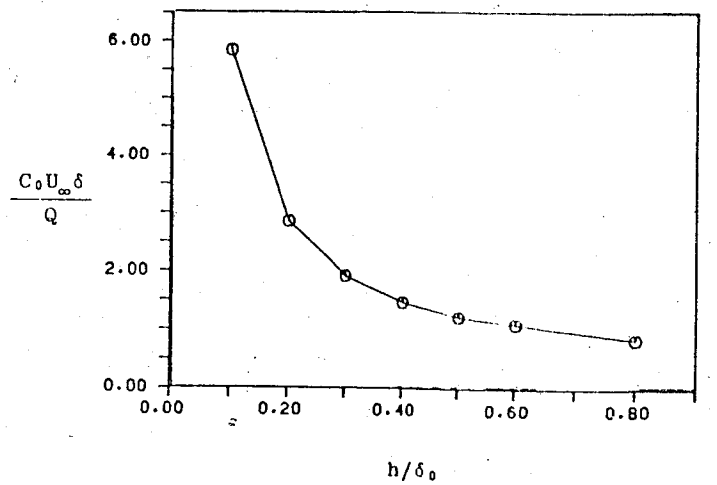

圖廿九　最大地面平均濃度對線源高度的關係圖。在$h/\delta_0<0.2$時變化率極大，符號同圖廿三。

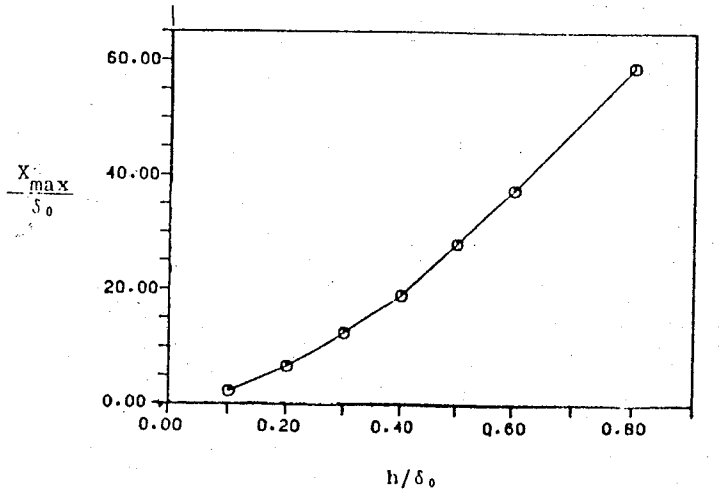

圖三十　最大地面平均濃度所在位置對線源高度的關係圖。X_{max}爲最大濃度所在位置。

平板間線擴散的雙程式紊流模式

梁文傑　黃明璋

中央研究院物理研究所

台灣大學機械工程學系暨研究所

摘　要

本文以K－ε紊流模式爲基礎，發展解析渠壁均爲水力平滑之二維完全發展渠流流場及擴散現象之數學模式，數值方法採用史氏（D. B. SPALTING），巴氏（S. V. PATANKAR）所發展的控制體積法（control volume method），文中以紊流長度尺度，時間尺度，速度尺度，及其他相關尺度探討流場特性，得知在中心線上，長度尺度，時間尺度有極大值，速度尺度有極小值。

本文利用等濃度線與截面濃度分佈等探討擴散之特性，得知對稱線源與單一線源分別在高度 0.7 與 1.0 半渠寬時，濃度分佈在線源附近有局部對稱性，使最大濃度點的連線保持水平。渠壁之存在使其附近之擴散分佈較不均勻。

壹、引　言

以微分輸送方程式（differential transport eguation），詮註紊流（turbulence）狀況，爲目前工程上解決紊流問題使用最多之型式，其中以雙方程式模式（Two eguation model）之使用最廣泛；雙方程式模式又因求解尺度因子（length scale）之變數不同而有形形色色之雙方程式模式，各種求解尺度因子變數有，歇氏（kolmogorov）之$K^{1/2}/L$，眞氏（Jones-launder）、哈氏（Harlow-Nakayama）、德氏（Davidov）之$K^{3/2}/L$、也就是ε，羅氏（Rotta）史氏（Spalding）之L，及史氏（Spalding）之K/L^2，因ε方程式在固體邊界上之型式比其他上列物理量簡單，所以K－ε模式爲最受歡迎之模式，且K－ε模式在薄剪力層（thin shear layer）上之使用已被多位研究者確定爲合理(1)。

完全發展二維渠流，因已完全發展，紊流邊界層厚度即爲渠道之半寬，亦即延渠道方向紊流邊界層將不再增長，所以完全發展二維渠流爲薄剪力層之流動狀態；固體邊界爲許多有界流場（bounded fluid flow）之共同特性，而動量方模式，K－ε紊流模式，

又是解紊流流場常用到之工具，因此本文擬偏重另一邊界條件效果之探討，即該流場對稱之特性，此特性在數學上被表示爲梯度爲零；因有此特性，使得某些物理量被壓抑（速度尺度、等等），某些物理量會在該邊界爲最大值（平均速度，紊流黏性係數，等），某些則爲最小值（紊流平均動能，等）；綜合這些特性，將使該流場表現出離固體邊界某一距離時，流場對擴散物產生擴散上近似對稱之效果。

在高雷諾數下，紊流漩渦的擴散能力，一般而言是分子擴散能力的數個數量階（order）(2)，因此在紊流裡，紊流狀態對非活性擴散物（passive contaiment）之擴散有很大影響，此效果，將使流場對擴散物之局部對稱性，在整個二維渠流擴散現象上，顯得很特別；在該局部對稱發生之高度以上之線源，固體邊界上發生之最大濃度，將是均勻混合濃度。

在分析靜電集塵器（ESP, Electrostatic precipitators）之污染物受電荷（Electric charge），慣性（Inertia effect），擴散（diffusion），重力（Gravitaticnal effect）等諸效應作用時，前人(3)(4)(5)(6)(7)均只用不可壓縮，穩定，均勻混合流場作爲分析之基礎，擴散效應被過份簡，如今ESP的除塵效率要求超過99.99％，詳細探討除塵機制（包括擴散效應）的需求日益迫切，本文模擬渠流擴散之定性特性，以爲後續研究ESP者比較之基礎。

貳、數學模式

本文以K－ε紊流雙方程式模式，分析完全發展二維渠流，並以此流場特性，探討擴散物質（Passive contaminant）在完全發展二維渠流之擴散特性；爲了簡化計算之繁複，本文作如下之假設：

(a)不考慮溫度梯度之效應，即不考慮浮力之效果。

(b)假設承載流體爲不可壓縮，且密度均勻。

(c)假設流體流場爲，穩定，且在順流向爲等壓力梯度，及完全發展，因風洞實資料爲在此狀況下量得，爲了比較流場之計算結果，及簡化計算，所以作此假設。

(d)忽略順流向流紊流擴散效果，因爲此項和擴散方程式中其它項相比，其數值階（order）較小。

(e)假設擴散物爲線源。

(f)不考慮擴散物之粒徑效應，亦即不爲考慮粒子間之互碰，及各種外力引起之終端速度（terminal velocity）效應。

(g)假設擴散物爲純粹之被載體（Passive material），即不考慮其對流場之作用，亦不考慮化學反應，即其爲惰性污染物（inert pollutants）。

㈠傳輸方程式

因本文只計算兩渠壁均爲水力平滑（hydraulically smooth）之狀況，整個流場性質有對中心線對稱之特性，所以只取中心線至渠壁爲計算區。根據質量不滅定律，可得流體的連續性方程式爲

$$\frac{\partial \rho}{\partial t} + \nabla \cdot (\rho \vec{v}) = 0 \qquad [1]$$

式中ρ爲密度，$\vec{v}$爲流速，t爲時間，∇爲梯度運算子。

由假設(b)、(C)，若把(1)式表成直角坐標，則可簡化成下式

$$\frac{\partial \tilde{U}}{\partial x} + \frac{\partial \tilde{V}}{\partial y} = 0 \ ,$$

式中$\tilde{U}$爲水平方向的速度分量，$\tilde{V}$爲垂直方向的速度分量。

因本文設定順流向爲完全發展，順流向流場物理量之梯度爲零，上式可簡化爲

$$\frac{\partial \tilde{U}}{\partial x} = 0 \ ,$$

$$\frac{\partial \tilde{V}}{\partial y} = 0$$

採用雷諾（Osborne Reynolds）之建議，把紊動物理量化爲平均量（mean value），及變動量（fluctuating value）之和，令

$$U = \frac{1}{T}\int_0^T \tilde{U}\, dt,$$

$$V = \frac{1}{T}\int_0^T \tilde{V}\, dt,$$

$$W = \frac{1}{T}\int_0^T \tilde{W}\, dt,$$

式中T可表時間，或空間座標等。則

$$\vec{V} = (U + u', V + v', W + w')$$

因此平均流速之連續方程式可寫爲

$$\frac{\partial U}{\partial x} = 0 \ , \qquad [2]$$

$$\frac{\partial V}{\partial y} = 0 \ 。 \qquad [3]$$

動量方程式爲

又是解紊流流場常用到之工具，因此本文擬偏重另一邊界條件效果之探討，即該流場對稱之特性，此特性在數學上被表示爲梯度爲零；因有此特性，使得某些物理量被壓抑（速度尺度、等等），某些物理量會在該邊界爲最大值（平均速度，紊流黏性係數，等），某些則爲最小值（紊流平均動能，等）；綜合這些特性，將使該流場表現出離固體邊界某一距離時，流場對擴散物產生擴散上近似對稱之效果。

在高雷諾數下，紊流漩渦的擴散能力，一般而言是分子擴散能力的數個數量階（order）(2)，因此在紊流裡，紊流狀態對非活性擴散物（passive contaiment）之擴散有很大影響，此效果，將使流場對擴散物之局部對稱性，在整個二維渠流擴散現象上，顯得很特別；在該局部對稱發生之高度以上之線源，固體邊界上發生之最大濃度，將是均勻混合濃度。

在分析靜電集塵器（ESP, Electrostatic precipitators）之污染物受電荷（Electric charge），慣性（Inertia effect），擴散（diffusion），重力（Gravitaticnal effect）等諸效應作用時，前人(3)(4)(5)(6)(7)均只用不可壓縮，穩定，均勻混合流場作爲分析之基礎，擴散效應被過份簡，如今ESP的除塵效率要求超過99.99％，詳細探討除塵機制（包括擴散效應）的需求日益迫切，本文模擬渠流擴散之定性特性，以爲後續研究ESP者比較之基礎。

貳、數學模式

本文以K－ϵ紊流雙方程式模式，分析完全發展二維渠流，並以此流場特性，探討擴散物質（Passive contaminant）在完全發展二維渠流之擴散特性；爲了簡化計算之繁複，本文作如下之假設：

(a)不考慮溫度梯度之效應，即不考慮浮力之效果。

(b)假設承載流體爲不可壓縮，且密度均勻。

(c)假設流體流場爲，穩定，且在順流向爲等壓力梯度，及完全發展，因風洞質資料爲在此狀況下量得，爲了比較流場之計算結果，及簡化計算，所以作此假設。

(d)忽略順流向流紊流擴散效果，因爲此項和擴散方程式中其它項相比，其數值階（order）較小。

(e)假設擴散物爲線源。

(f)不考慮擴散物之粒徑效應，亦即不爲考慮粒子間之互碰，及各種外力引起之終端速度（terminal velocity）效應。

(g)假設擴散物爲純粹之被載體（Passive material），即不考慮其對流場之作用，亦不考慮化學反應，即其爲惰性污染物（inert pollutants）。

㈠傳輸方程式

因本文只計算兩渠壁均爲水力平滑（hydraulically smooth）之狀況，整個流場性質有對中心線對稱之特性，所以只取中心線至渠壁爲計算區。根據質量不滅定律，可得流體的連續性方程式爲

$$\frac{\partial \rho}{\partial t} + \nabla \cdot (\rho \vec{v}) = 0 \qquad [1]$$

式中ρ爲密度，$\vec{v}$爲流速，t爲時間，∇爲梯度運算子。

由假設(b)、(C)，若把(1)式表成直角坐標，則可簡化成下式

$$\frac{\partial \tilde{U}}{\partial x} + \frac{\partial \tilde{V}}{\partial y} = 0 \ ,$$

式中$\tilde{U}$爲水平方向的速度分量，$\tilde{V}$爲垂直方向的速度分量。

因本文設定順流向爲完全發展，順流向流場物理量之梯度爲零，上式可簡化爲

$$\frac{\partial \tilde{U}}{\partial x} = 0 \ ,$$

$$\frac{\partial \tilde{V}}{\partial y} = 0$$

採用雷諾（Osborne Reynolds）之建議，把紊動物理量化爲平均量（mean value），及變動量（fluctuating value）之和，令

$$U = \frac{1}{T}\int_0^T \tilde{U}\, dt,$$

$$V = \frac{1}{T}\int_0^T \tilde{V}\, dt,$$

$$W = \frac{1}{T}\int_0^T \tilde{W}\, dt,$$

式中T可表時間，或空間座標等。則

$$\vec{V} = (U + u', V + v', W + w')$$

因此平均流速之連續方程式可寫爲

$$\frac{\partial U}{\partial x} = 0 \ , \qquad [2]$$

$$\frac{\partial V}{\partial y} = 0 \ 。 \qquad [3]$$

動量方程式爲

$$\frac{\partial \vec{v}}{\partial t}+(\vec{v}\cdot V)\vec{V}=-\frac{1}{\rho}VP+\mu V^2\vec{v} \qquad [4]$$

式中P爲壓力仿連續方程式之處理程序，可得順流向及垂直流向動量方程式

$$O=-\frac{1}{\rho}\frac{\partial P}{\partial x}+\frac{\partial}{\partial y}\left[\nu\frac{\partial U}{\partial y}-\overline{u'v'}\right], \qquad [5]$$

$$O=-\frac{1}{\rho}\frac{\partial p}{\partial y}-\frac{\partial}{\partial y}\left[-\overline{v'^2}\right] \qquad [6]$$

令式(6)對 y 軸積分，可得

$$\frac{P}{\rho}+\overline{v'^2}=\frac{P_0}{\rho}, \qquad [7]$$

$$P_0=P_0(x),$$

式中P_0爲壓力場在渠壁之值，由假設（ c ）可知

$$\frac{\partial}{\partial x}\overline{V'^2}=0,$$

所以式(7)可化爲

$$\frac{dp}{dx}=\frac{dp_0}{dx},$$

即壓力場在流向之梯度，在整個截面上均同，又由假設（ C ）

$$\frac{dp}{dx}=\frac{dp_0}{dx},$$

$$=\text{常數}$$

將上式代入式(5)，再對 y 積分，可得

$$O=-\frac{y}{\rho}\frac{dp_0}{dx}+\nu\frac{dU}{dy}-\overline{u'v'}-\left[-\overline{u'v'}+\nu\frac{dU}{dy}\right]_{\text{渠壁}} \qquad [8]$$

因在渠壁上無紊流，故

$$\left(-\overline{u'v'}\right)_{\text{渠壁}}=0,$$

即，在渠壁上之剪應力純粹由黏滯性提供，若定義

$$\left(\nu\frac{dU}{dy}\right)_{\text{渠壁}}=u_*^2,$$

$$u_*=\sqrt{\frac{\tau_0}{\rho}}$$

$$=\text{摩擦速度（ friction velocity ）},$$

τ_0 爲渠壁剪刀，式(8)可化爲

$$O=-\frac{y}{\rho}\frac{dp_0}{dx}-\overline{u'v'}+\nu\frac{dU}{dy}-u_*^2 \qquad [9]$$

因流場對中心線有對稱之特性，所以在中心線上

$$\frac{dU}{dy}=0,$$

$$\overline{u'v'}=0.$$

所以式(11)在中心線上爲

$$u_*^2=-\frac{H}{\rho}\frac{dp_0}{dx}, \qquad [10]$$

式中H爲渠道半寬。將式(10)代入式(9)，可得

$$-\overline{u'v'}+\nu\frac{dU}{dy}=u_*^2\left(1-\frac{y}{H}\right) \qquad [11]$$

上式爲常微分方程式，式中雷諾應力（ $-\overline{u'v'}$ ）與U皆爲未知量，因未知量個數比方程式多，式(11)需要紊流模式，解決此閉塞問題（ closure problem ）。

㈡紊流模式

本文採用RODi[8]建議之K－ϵ 模式，此模式以紊流動能（ turbulent kinetic energy ）K，及紊流動能消散率（ dissipation rate of turbulent kinetic energy ）ϵ，詮註紊流狀態；K及 ϵ 物理意義表示式如下

$$K=\frac{1}{2}\left[\overline{u_i'^2}\right],$$

$$\epsilon=\nu\overline{\frac{\partial u'_i}{\partial x_j}\frac{\partial u'_i}{\partial x_j}},$$

大部份的單一方程式紊流模式，及雙方程式紊流模式，採用梯度型之表示法，因此也都採用渦漩黏滯／擴散觀念（ eddy viscosity／diffusivity concept ），及格普關係式（ Kolmogorov－Prandtl relation ），把雷諾應力，及紊流黏滯係數 ν_t 表爲下列式子

$$-\overline{u'_i u'_j} = \nu_t \left(\frac{\partial U_i}{\partial x_j} + \frac{\partial U_j}{\partial x_i}\right) - \frac{2}{3} K \delta_{ij} ,$$

$$\nu_t = C' \mu \sqrt{K} \cdot L$$

式中 L 爲大漩渦之長度尺度；K－ϵ 雙程式模式，也採用如上之處理方式，又 ϵ 在尺度方面可以下式表之

$$\epsilon \alpha \frac{K^{\frac{3}{2}}}{L} ,$$

所以 K－ϵ 模式之雷諾應力以下式表之

$$\nu_t = C\mu \frac{K^2}{\epsilon} ,$$

$$-\overline{u'_i u'_j} = \nu_t \left(\frac{\partial U_i}{\partial x_j} + \frac{\partial U_j}{\partial x_i}\right) - \frac{2}{3} K \delta_{ij} ,$$

K－ϵ 模式以兩個微分方程式表示 K 及 ϵ 在流場中之變化，

$$\frac{\partial K}{\partial t} + U_i \frac{\partial K}{\partial x_i} = \frac{\partial}{\partial x_i}\left(\frac{\nu_t}{\sigma k} \frac{\partial K}{\partial x_i}\right) - \overline{u'_i u'_j} \frac{\partial U_j}{\partial x_j} - \epsilon ,$$

$$\frac{\partial \epsilon}{\partial t} + U_i \frac{\partial \epsilon}{\partial x_i} = \frac{\partial}{\partial x_i}\left(\frac{\nu_t}{\sigma \epsilon} \frac{\partial \epsilon}{\partial x_i}\right) - C\epsilon_1 \frac{\epsilon}{K} \overline{u'_i u'_j} \frac{\partial U_i}{\partial x_j} C\epsilon_2 \frac{\epsilon^2}{K}$$

令

$$A = \frac{\partial K}{\partial t} 或 \frac{\partial \epsilon}{\partial t} ,$$

$$B = U_i \frac{\partial K}{\partial x_i} 或 U_j \frac{\partial \epsilon}{\partial x_j} ,$$

$$C = \frac{\partial}{\partial x_i}\left(\frac{\nu_t}{\sigma k} \frac{\partial K}{\partial x_j}\right) 或 \frac{\partial}{\partial x_j}\left(\frac{\nu_t}{\sigma_t} \frac{\partial \epsilon}{\partial x_j}\right) ,$$

$$D = \overline{u'_i u'_j} \frac{\partial U_i}{\partial x_j} , 或 C\epsilon_1 \frac{\epsilon}{K} \overline{u'_i u'_j} \frac{\partial U_i}{\partial x_j} ,$$

$$E = \epsilon , 或 C\epsilon_2 \frac{\epsilon^2}{K} ,$$

A表時變項，B表對流向，C表擴散向，D表製造向，E表消散向；由假設(b)、(c)，及式(3)，及增加考慮分子擴散效應，上二式可化爲

$$O = \frac{\partial}{\partial y}\left(\frac{\nu_t}{\sigma_k} \frac{\partial K}{\partial y} + \nu \frac{\partial K}{\partial y}\right) - \overline{u'v'} \frac{\partial U}{\partial y} - \epsilon , \qquad (12)$$

$$O = \frac{\partial}{\partial y}\left(\frac{\nu_t}{\sigma \epsilon} \frac{\partial \epsilon}{\partial y} + \nu \frac{\partial \epsilon}{\partial y}\right) - \epsilon_{g1} \frac{\epsilon}{K} u'v' \frac{\partial U}{\partial y} - C\epsilon^2 \frac{\epsilon^2}{K} , \qquad (13)$$

$$\sigma_k = 1.0 ,$$

$$\sigma \epsilon = 1.3 ,$$

$$C\mu = 0.09 ,$$

$$C\epsilon_1 = 1.45 ,$$

$$C\epsilon_2 = 1.9 。$$

由物質連續方程式，基於假設(f)，可得

$$\frac{\partial \widetilde{C}}{\partial t} = -\left(\frac{\partial}{\partial x} \widetilde{U}\widetilde{C} + \frac{\partial}{\partial y} \widetilde{V}\widetilde{C} + \frac{\partial}{\partial z} \widetilde{W}\widetilde{C}\right)$$
$$+ D\left(\frac{\partial^2 \widetilde{C}}{\partial x^2} + \frac{\partial^2 \widetilde{C}}{\partial y^2} + \frac{\partial^2 \widetilde{C}}{\partial z^2}\right)$$
$$- K_n''' C_A{}^n , \qquad (14)$$

$$A = \frac{\partial \widetilde{C}}{\partial t} ,$$

$$B = -\left(\frac{\partial}{\partial x} \widetilde{U}\widetilde{C} + \frac{\partial}{\partial y} \widetilde{V}\widetilde{C} + \frac{\partial}{\partial z} \widetilde{W}\widetilde{C}\right) ,$$

$$C = D\left(\frac{\partial^2 \widetilde{C}}{\partial x^2} + \frac{\partial^2 \widetilde{C}}{\partial y^2} + \frac{\partial^2 \widetilde{C}}{\partial z^2}\right) ,$$

$$D = -K_n''' C_A{}^n ,$$

A表時變項，由假設(c)、(g)，此項爲零；B表對流項；C表擴散項；D表第幾 n 階均勻反

應項，由假設(g)，此項爲零；由假設(d)，略去C之第一項；由假設(e)，略去B之第三項，及C之第三項；仿照連續方程式

$$\widetilde{C} = C + c' \,, \qquad [15]$$

$$C = \frac{1}{T}\int_0^T \widetilde{C}\ dt$$

(15)式代入(14)式，取平均，可得

$$O = -\left(\frac{\partial}{\partial x} U C + \frac{\partial}{\partial y} V C\right) - \left(\frac{\partial}{\partial x}\overline{u'c'} + \frac{\partial}{\partial y}\overline{v'c'}\right) + D\frac{\partial^2 \overline{C}}{\partial y^2} \qquad [16]$$

,

$$A = \frac{\partial}{\partial x} UC \,,$$

$$B = \frac{\partial}{\partial x} V C \,,$$

$$C = \frac{\partial}{\partial x}\overline{u'v'} \,,$$

$$D = \frac{\partial}{\partial y}\overline{v'c'}$$

$$E = D\frac{\partial^2 \overline{C}}{\partial y^2}$$

A爲順流向，平均流場對平均濃度之對流效應；B爲垂直渠壁之平均流場，對平均濃度之對流效應，由式(3)可得

$$\frac{\partial}{\partial y} V C = V\frac{\partial C}{\partial y} \,,$$

令(3)式均對y積分，

$$V = V_0(x)$$
$$= 0$$

式中$V_0(x)$爲渠壁之垂直向平均流速，

$$\frac{\partial}{\partial y} V C = V_0(x)\frac{\partial C}{\partial y} = 0$$

C爲順流向，紊流效應，由假設(d)此項爲零；D爲垂直渠壁向紊流效應；E爲分子擴散效應；由K－ϵ模式之漩渦擴散系數，配合上菲克擴散定律（Fick's law of diffusion ），可得

$$\frac{\partial}{\partial y}\overline{v'c'} = -\frac{\partial}{\partial y}\left(\frac{\nu_t}{S_c}\frac{\partial C}{\partial y}\right) \,,$$

式中S_c爲紊流斯密特常數（turbulent schmidt number ），其值爲0.885
由式(2)以及上之討論，式(16)，可化爲

$$U\frac{\partial C}{\partial x} = \frac{\partial}{\partial y}\left(\frac{\nu_t + \nu}{S_c}\frac{\partial C}{\partial y}\right)$$

㈢邊界條件

(a)對稱綫源狀況

因所考慮之流場爲完全發展，制御方程式爲常微分方程式流場不需入口條件；就擴散而言，其入口即爲線源所在，所以入口條件爲

$$C_{(o,h)} = \frac{Q}{U_{(o,h)} \cdot \triangle y} \cdot \delta(y - h) \,, \qquad [18]$$

$C_{(o,h)}$表綫源濃度，h表綫源高度，$U_{(o,h)}$表綫源所在之流速，△y表數值化後之格點距，Q表單位長度綫源之施放量，$\delta(y-h)$爲柯涅克函數（kronecker delta function ）

$$\delta(y-h) = 0 \,,\ y \neq h \,,$$
$$\delta(y-h) = 1 \,,\ y = h$$

因流場在中心線有對稱之特性，且線源亦對稱，所以

$$\frac{\partial C}{\partial y} = \frac{\partial K}{\partial y} \,, \qquad [19]$$

$$= \frac{\partial \epsilon}{\partial y} \,, \qquad [20]$$

$$= \frac{\partial U}{\partial y} \,, \qquad [21]$$

$$= 0 \qquad [22]$$

由於K－ϵ樣式本身不適用於低紊流雷諾數（turbulent Reynold number ）

$$Re_T = \frac{\nu_t}{\nu},$$

之區域，所以必需使用壁函數（Wall function）以使模式計算之第一個格點，位於低紊流雷諾數之層性副流區（viscous sublayer）之外，本文採⑻建議之壁函數

$$\frac{\partial C}{\partial y} = 0,$$

$$\frac{U}{u_*} = \frac{1}{K} \ln [Ey^+], \quad (23)$$

$$\frac{K}{u_*^2} = \frac{1}{\sqrt{C\mu}}, \quad (24)$$

$$\epsilon = \frac{u_*^3}{Ky}, \quad (25)$$

式中

$$y^+ = y \cdot u^* / \nu,$$

$K = 0.41$，爲逢卡門常數（Von Karman Constant），$E = 9.0$，爲水力平滑面糙度因子（Hydraulically Smooth Wall Roughness Factor）。

⑹單一線源狀況

因此狀況二邊界均爲渠壁，所以二邊界條件即爲式⑲，㉓，㉔，㉕，入口條件爲⑱式。

㈣無因次傳輸方程式

取渠道半寬H，流體動力黏滯係數ν，線源格點濃度$C_{S\phi urce}$，與摩擦速度u^*爲無因次基，定義諸無因次參數與變數如下：

$$y = \frac{y}{H},$$

$$x = \frac{x}{H},$$

$$U = \frac{U}{u_*},$$

$$K = \frac{K}{u_*^2},$$

$$\nu t = \frac{\nu_t}{\nu},$$

$$\epsilon = \frac{\epsilon}{u_*^3 / H},$$

$$C = \frac{C}{C_{S\phi urce}},$$

$$Re = \frac{u_* H}{\nu},$$

$$S_c = \frac{\nu_t}{D_t},$$

式中D_t爲紊流擴散係數，則無因次傳輸方程式爲

$$\frac{\partial}{\partial x}\hat{U} = 0 \quad (26)$$

$$O = Re + \frac{\partial}{\partial \hat{y}}\left[(1+\hat{\nu}_t)\frac{\partial \hat{U}}{\partial \hat{y}}\right], \quad (27)$$

$$O = \frac{\partial}{\partial \hat{y}}\left[(1+\hat{\nu}_t)\frac{\partial K}{\partial y}\right] + \hat{\nu}_t\left[\frac{\partial \hat{U}}{\partial \hat{y}}\right]^2 - Re \cdot \hat{\epsilon}, \quad (28)$$

$$O = \frac{\partial}{\partial \hat{y}}\left[\frac{(1+\hat{\nu}_t)}{\sigma\epsilon}\frac{\partial \hat{\epsilon}}{\partial \hat{y}}\right] + C\epsilon_1 \frac{\hat{\epsilon}}{\hat{K}} \cdot \hat{\nu}_t \left[\frac{\partial \hat{U}}{\partial \hat{y}}\right]^2 - C\epsilon^2 \cdot Re \cdot \frac{\hat{\epsilon}^2}{\hat{K}}, \quad (29)$$

$$\hat{U} = \frac{\partial \hat{c}}{\partial \hat{x}} = \frac{1}{Re \cdot S_c}\frac{\partial}{\partial \hat{y}}\left[(1+\hat{\nu}_t)\frac{\partial \hat{c}}{\partial \hat{y}}\right] \quad (30)$$

相配合之無因次邊界條件爲

入口處，

$$\hat{C} = \delta(y-h), \quad (31)$$

中心線處，

$$\frac{\partial \hat{U}}{\partial \hat{y}} = 0, \quad (32)$$

$$\frac{\partial \hat{K}}{\partial \hat{y}} = 0, \quad (33)$$

$$\frac{\partial \hat{\epsilon}}{\partial \hat{y}} = 0 \quad , \qquad [34]$$

$$\frac{\partial \hat{C}}{\partial \hat{y}} = 0 \quad , \qquad [35]$$

渠壁處，

$$\hat{U} = \frac{1}{K} \ln \left(Ey^{+} \right) , \qquad [36]$$

$$\hat{K} = \frac{1}{\sqrt{C\mu}} \quad , \qquad [37]$$

$$\hat{\epsilon} = \frac{Re}{Ky^{+}} \quad , \qquad [38]$$

$$\frac{\partial \hat{C}}{\partial \hat{y}} = 0 \quad .$$

參、結果與討論

本文採用史氏（D.B. SPALDING），及巴氏（S.V.PATANKAR ）所發展的控制體積法（control volume method ）[9]；控制體積法，先對微分方式，在控制體上的積分，再用通量表示法，化方程式爲最後之數值式。

㈠基本流場

本文與拉氏（JOHN LAUFER ）[10] 平均速度之實驗結果相比較。拉氏之實驗是在主要量測區全長 23英尺之渠道上進行，該渠道之進口區爲 3 吋寬，寬高比 12 ：1 之截面，在隨後 7 英呎，渠道截面逐漸變爲 5 吋寬，寬高比 12 :1 ；該實驗以直徑 0.00005 英吋至 0.00024 英吋之熱絲（ hot wire ），於進口風速每秒 3 、5 、7 米之狀況下進行量測；圖 1 爲計算結果和拉氏實驗之比較，由圖可見計算結果和實驗相當相當近似；表 1 爲平均流速度計算誤差之比較，由表可見，誤差隨無因次高度之增加而減小。

在渠壁附近剪應力計算值的可靠性可借動量方程式來探討。動量方程式(11)之左手邊可改寫爲

$$\text{剪應力} = -\overline{u'v'} + \nu \frac{dU}{dy}$$

$$= (\nu_t + \nu) \, dU / dy \, ,$$

所以無因次剪應力可以表成

$$\text{無因次剪應力} = (\nu_t + \nu) \frac{dU}{dy} / u_*^2$$

$$= 1 - y \, ,$$

y 爲無因次高度，由上式知，本文之動量方程式，即表無因次剪應力和無因次高度之關係爲線性；圖 2 爲無因次剪應力之計算結果，在無因次高度大於 0.15 時，相當脗合(39)式線性之要求，但是在渠壁附近則有些許誤差，此乃因使用壁函數而來；因假定分子子黏滯係數和紊流擴散係數相比顯得較小，所以

$$\nu + \nu_t = \nu + C\mu K^2 / \epsilon$$

$$\approx C\mu K^2 / \epsilon \, ,$$

所以本文之剪應力以下式表之，

$$\text{剪應力} = C\mu \cdot \frac{K^2}{\epsilon} \cdot \frac{dU}{dy} \quad ,$$

因本文採用之壁函數爲(23)，(24)，(25)式，所以在壁函數使用點上，

$$dU / dy = u_* / (K \cdot y) \, ,$$

因次在該點之無因次剪應力爲，

$$\text{無因次剪應力} = C\mu \frac{\frac{u_*^4}{C\mu}}{\frac{u_*^3}{Ky}} \cdot \frac{u_*}{Ky} / u_*^2$$

$$= 1 \, ,$$

但是動量方程式要求在該點之剪應力則爲(39)式，因此在該點無因次剪應力之誤差爲，

$$\frac{y}{1-y} = y \cdot \frac{\frac{u_*}{\nu}}{\frac{u_*}{\nu}} / \left(1 - y \cdot \frac{\frac{u_*}{\nu}}{\frac{u_*}{\nu}} \right)$$

$$= \frac{y^+}{Re} / \left(1 - \frac{y^+}{Re} \right) \, ,$$

在本文之計算中 y^+ 採用 50 ，所以在該點之無因次剪應力誤差如表 2 ；由此表知，誤差隨雷諾數之增加，因黏性副流區之貼近渠壁，而降低，雖然在低雷諾時，此誤差頗大，但是本文使用之 $K - \epsilon$ 模式可以使其迅速降低，在計算區第一格點之誤差如表 3 ，由表

知，高雷數時，有較慢之無因次剪應力誤差遞減速率，低雷諾則反之，其他格點之誤差情形可在圖 3 看到，由此圖知，在渠壁均爲水力平滑之完全發展渠流，K－ϵ 紊流模式有使高雷諾數時剪應力起始誤差小，誤差遞減慢，低雷諾數則反是之特性，因此本文之計算區在渠壁雷諾 300 至 900 之間剪應力最大誤差在 1.8 %以下。

渠壁均爲水力平滑之二維完全發展渠流有對中心線對稱之特性，物理上，此現象爲上渠壁往下輸送之各物理量，和下渠壁往上輸送之各物理量，在中心線互相平衡，在數學上，即以梯度爲零表示且因在二維完全發展渠流中，各流場物理量，至多僅爲無因次高度之函數，而單一自變數函數，在梯度爲零處，有可能爲局部極大，或極小，因此在中心線上將可期待，有某些物理量爲局部極大，或極小；漩渦之長度尺度（ length scale ）受流場幾何因素之影響，亦即在渠壁附近，受此邊界之不等向性（ anisotropy ）之影響，在渠壁附近只能存在小尺度之漩渦，隨著高度之增加，漩渦之平均尺度亦增加，在中心線上有最大之長度尺寸，如圖 4 。

紊流動能之產生大概和剪應力及平均速度梯度之乘積成正比，K－ϵ 模式之動能方程式之製造項即爲此物理概念，而在二維完全發展渠流，由動量方程式可看出剪應力由渠壁之最大值遞減至中心線爲零，又流場爲等壓梯度，因此在平均速度曲綫上，將不會發生反曲點，又中心綫之對稱性，使該處速度斜率爲零，因此平均速度斜率亦是自渠壁逐漸降爲零；圖 5 爲速度斜率之計算值；由上知在計算區中，第一格點有最大之紊流動能製造能力，逐次遞減，至中心線則已無比能力，但在中心線上仍有小長度尺度之漩渦存在，因此仍有動能之消耗，所以中心綫上紊流狀態之維持，主要是由其相鄰區擴散紊流動能而得，由此知在第一格點上可能有整個計算區最大之紊流動能，因而有最大之速度尺度，而在中心綫則最小，紊流動能及速度尺度之計算值於圖 6 與 7 ；在圖 8 可看到由長度尺度，及速度尺度推算之時間尺度；由圖 4 ，7 與 8 知二維完全發展渠流紊流流場之大漩渦有較大時間尺度，較小速度尺度；小漩渦則反是。綜合以上漩渦之特性，則有圖 9 之紊流擴散特性，於圖可見，擴散係數在中心線有最大值。

㈡擴散現象

(1)綫源高度及渠壁雷諾數之效果

因擴散方程式在中心綫及渠壁之邊界條件均爲零梯度，所以在此二邊界附近之綫源的擴散情形，有較不對稱之圖形；圖 16爲渠壁雷諾數 300 與 900 ，無因次高度 0.3 與 0.9 之等濃度線，由圖可見在高度 0.7 時有較對稱之擴散圖形，且距綫源相等距離時，相對應之等濃度綫有較廣之涵蓋範圍。

雖然由圖 9 知高雷諾比低雷諾有較強之漩渦擴散能力，但圖⑽(c)(d)卻比(a)(b)有較狹長之圖形，可見高雷諾數之狀態，可保留高濃度區至較遠之下游，即對流效應對雷諾數之增長率，比擴散效應大。

因本文探討之擴散物爲對流場無反向作用之被載體，流場之特性對擴散行爲有很強烈之影響，因此可預期單一綫源之擴散情形和對稱綫源有相當程度的相似；圖 11 與 12 爲渠壁雷諾 300 ，及 900 線源在無因次高度爲 0.3 與 0.9 處之等濃度線，由圖可見線源

在高度 0.9 處有較對稱之擴散。

(2)連續截面擴散比較

因本文之擴散方程式的邊界條件均設定爲梯度爲零，此即在邊界之擴散不穿透邊界，因此延順流向，在邊界附近，擴散物之質量有累積之效果，在邊界上將發生濃度截面分佈曲綫之局部極大值，當綫源貼近下渠壁時，將於下渠壁發生局部極大值，逐次地當綫源往上升，最後將在上邊界發生局部極大值；因此可預期在某一高度之線源有最大濃度點不偏向之特性。

圖13爲對稱綫源於渠壁雷諾 300 時線源高度 0.3 ， 0.5 ， 0.7 ， 0.9 ，之相續截面擴散情形，於圖可見，所有之截面擴散曲綫均爲單一尖峯，所以局部最大濃度，即爲截面最大濃度；且區域性近似對稱性發生在無因次高度 0.7 時；最大濃度點濃度之下降速率，隨擴散物濃度之均勻化，而降低；且當綫源高度小於 0.7 時，截面之最大濃度點終將發生在渠壁上；綫源高度大於 0.7 則終將發生在中心綫上；因此當綫源高度大於 0.7 時，渠壁上之最大濃度爲均勻濃度，而達此濃度之點將在無窮遠處之下游。

圖 14爲單一綫源於渠壁雷諾 300 時，綫源高度 0.3 ， 0.9 ， 1.1 ， 1.7 ，之相續截面擴散情形，此二圖之特性和圖　相似，但是其對稱點爲無因次高度 1.0 ；即最大濃度點不偏不倚之高度爲 1.0 。

(3)截面最大濃度點比較

圖15.爲渠壁雷諾 300 與 900 綫源高度 0.3 ， 0.5 ， 0.7 ， 0.9 之最大濃度點偏向圖；圖之擴軸長 12 cm ，上有50個點，所以點距 2.4 mm ，縱軸 8 cm 50 個點，所以點距 1.6 mm ，即綫源高度 0.5 之折綫爲數值網路之對角綫，即能看出最大濃度點偏向效應之最小單位；於圖可見越近渠壁之綫源其最大濃度點偏向渠壁越早，至高度 0.7 時，則不偏向； 0.7 以上時，偏向中心綫。

圖16爲渠壁雷諾 300 ， 900 綫源無因次高度 0.3 ， 0.5 ， 0.7 ， 0.9 之最大濃度點偏向圖，此二圖之特性和圖15相似，但此狀況之擴散對稱點在無因次高度 1.0 ，因此於圖可見在無因次高度 0.9 時，於計算區內，已無偏向。

肆、結論

本文以K－ϵ 紊流模式爲基礎，發展解析渠壁均爲水力平滑之完全發展渠流之流場，及擴散場之數學模式；在分析剪應力誤差時，本文發現，在渠壁雷諾 300 至 900 間，剪應力誤差有高雷諾數時，起始誤差小，誤差遞減速率慢，而在低雷數時，則反此之特性，因此在本文之數值化計算區內，剪應力之最大誤差在 1.8 %以下，由此可見K－ϵ 紊流模式，適用於渠壁均水力平滑之二維完全發展紊流之計算。

在中心線上，本文之流場有一對稱性，且紊流長度尺度，時間尺度，紊流黏性系數有極大值，紊流速度尺度有極小值。雖高雷諾時有較大擴散能力，但是對流效應對雷諾數之增長率，比擴散效應快，所以高雷諾之等濃度線較狹長，且因層性副流區較低雷諾

數貼近渠壁，因而近渠壁之線擴散較低電諾時稱且均勻。

因本文之邊界條件均設定濃度梯度爲零，此即在邊界上擴散物不穿透邊界，因此延順流向，擴散物之質量在邊界上有累積之效果，所以近渠壁之線源，截面最大濃度點終將發生在渠壁上，但當線源在適當高度處，最大濃度點既不上飄，也不下移，高於此對稱點之線源，截面最大濃度點終將發生在上邊界反之則在下邊界。在對稱線源情況，此對稱點在無因次高度 0.7 處，在單一線源情況，此對稱點在中心線上。高於對稱點之線源，其下渠壁之最大濃度爲均勻濃度。

參考文獻

1. W. RODI, " Examples of turbulence models for incompressible flows ", AIAA, Vol. 20, No. 7, p. 872-879, (1982).
2. H. Tennekes and J L. Lumley, " A first course in turbulence ", The MIT Press, (1972).
3. R. Y. CHEN, " Diffusive diposition of Particles in a short channel ", Powder Technology 16, P. 131-135, (1977).
4. R. . CHEN, " Deposition of aerosol particles in a channel due to diffusion and electric charge " J. Aerosol Sci., Vol. 9, P. 253-260, (1978).
5. R. Y. CHEN and H. E, PAWEL and W. C. CHEN, " Inertia effect on deposition of charged particles in a parallel-plate channel ", Powder Technology 34, P. 249-253, (1983).
6. R. Y. CHEN and M. W. GELFER, " Deposition of particles in a parallel-okate cgabbek due to electrostatic charge, diffusion and gravitational effects ", Powder Technology 28, P. 229-234, (1982).
7. D. B. INGHAM , " A note on the deposition of aerosol particles in a channel due to diffusion and electric charge ", J. Aerosol Sci., Vol. 11, P. 517-520, (1980).
8. W. RODI, " Turbulence models and their application in hydraulics ", Iahr, (1980).
9. SUHAS V. PATANKAR, " Numerical heat transfer and fluid flow ", Hemisphere publishing conporation.
10. JOHN LAUFER, " Investigation of turbulent flow in a two-dimensional channel", California Institute of Technology, report 1053, (1951).

H	A	B	誤差%
0.3	0.875	0.847	3.3
0.4	0.912	0.875	4.2
0.5	0.937	0.911	2.8
0.6	0.962	0.944	1.9
0.7	0.981	0.972	0.09

表 1　平均流速計算誤差（與 Lanfer[10] 實驗值比較），H 表無因次高度，A 表渠壁雷諾 500 之平均流速計算值，B 表中心雷諾 12300 之平均流速實驗值。

Re	A	B	誤差%
300	1.	0.833	20
500	1.	0.9	11.1
700	1.	0.929	7.7
900	1.	0.94	5.9

表 2　y^+ 爲 50 處無因次剪應力誤差值，Re 表渠壁雷諾，A 爲以壁函數計算之無因次剪應力，B 爲以動量方程式計算之無因次剪應力。

Re	A	B	誤差%
300	0.817	0.816	0.0367
500	0.885	0.882	0.32
700	0.919	0.91	0.92
900	0.942	0.926	1.798

表 3. 第一個網格點處（無因次高度爲$\frac{1}{15}$）之剪應力誤差值

Re 表渠壁雷諾，A爲以數值計算之無因次剪應力，B爲以動量方程式計算之無因次剪應力。

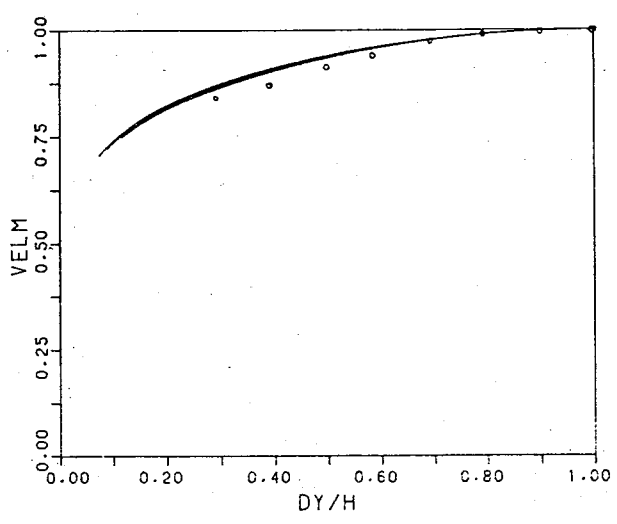

圖 1. VELM表U／U_c，U爲平均速度，U_c爲中心線平均速度，。爲 JOHN LAUFER 於中心線雷諾 12300 之實驗值；固體線爲計算值，由下往上依序爲渠壁雷諾 300、500、700、900；H表渠道半寬。

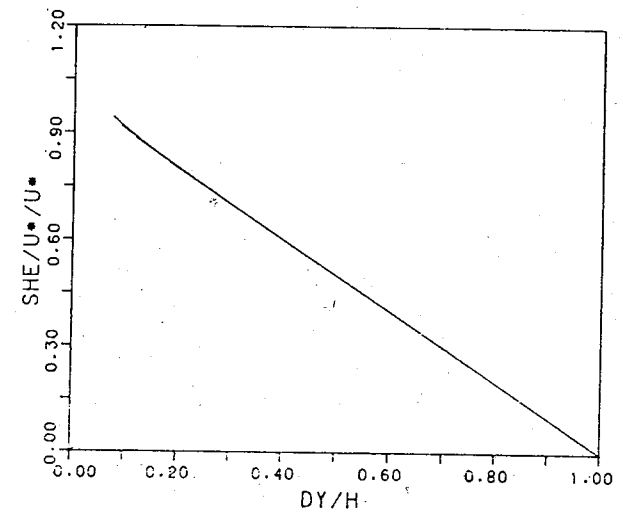

圖 2. U_* 爲摩擦速度，SHE表$C\mu \cdot \frac{k^2}{\epsilon}\frac{dU}{dy}$之計算值，圖中共有 4 條線，由下往上分別爲渠壁雷諾 300，500，700，900。

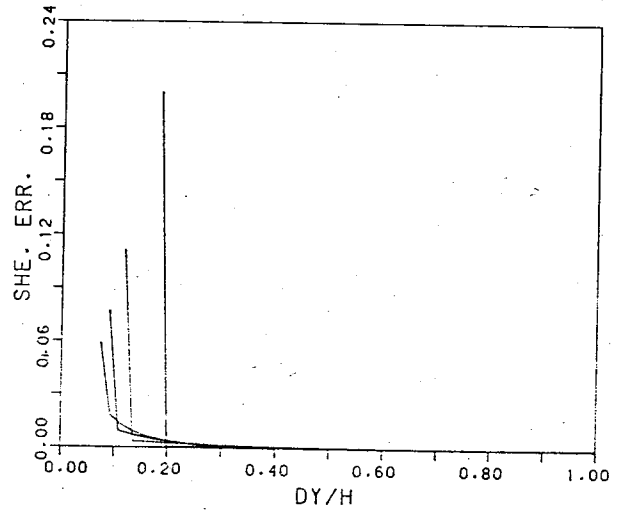

圖 3. SHE.ERR 表計算剪應力之誤差百分比，圖中共有 4 條線，線之起始點由左而右，分別對應於渠壁雷諾 300、500、700、900 之狀況。

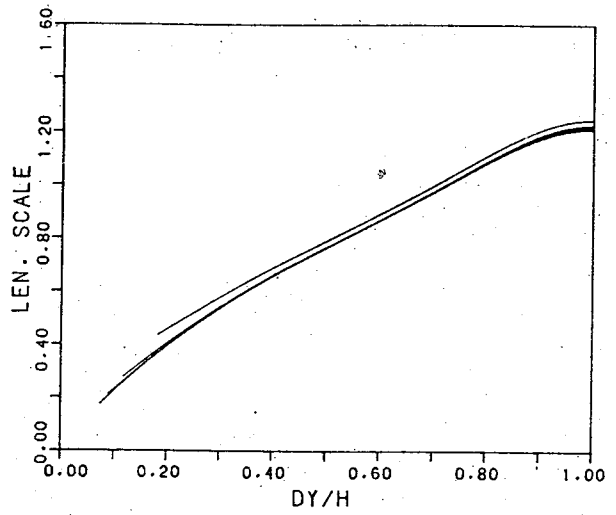

圖 4　LEN SCALE 表漩渦長度尺度，圖中之線由下而上，分別爲渠壁雷諾 900 、 700 、 500 、 300 。

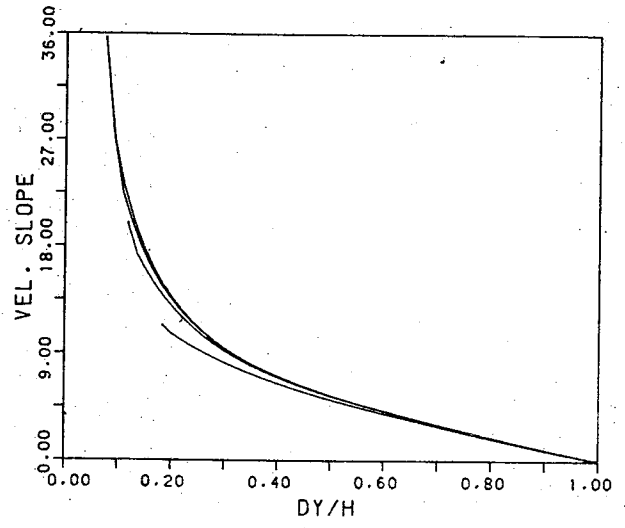

圖 5.　VEL . SLOPE 爲平均速度斜率之計算值，圖中之線由下往上，分別爲渠壁雷諾 300 、 500 、 700 、 900 。

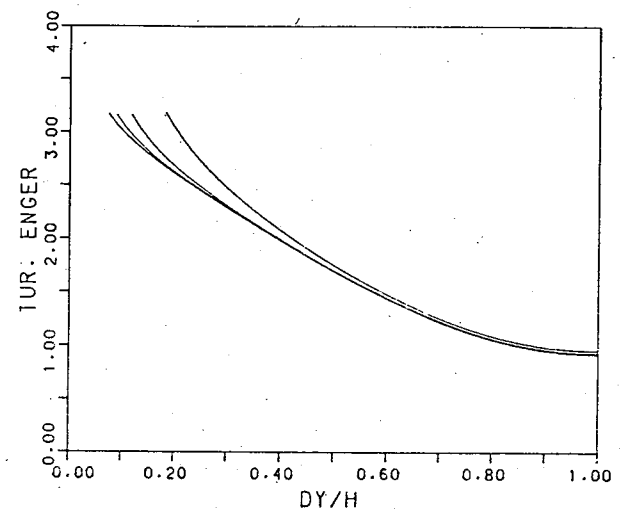

圖 6　TUR . ENGER 爲紊流動能之計算值，圖中之線由上往下爲渠壁雷諾 300 、 500 、 700 、 900 。

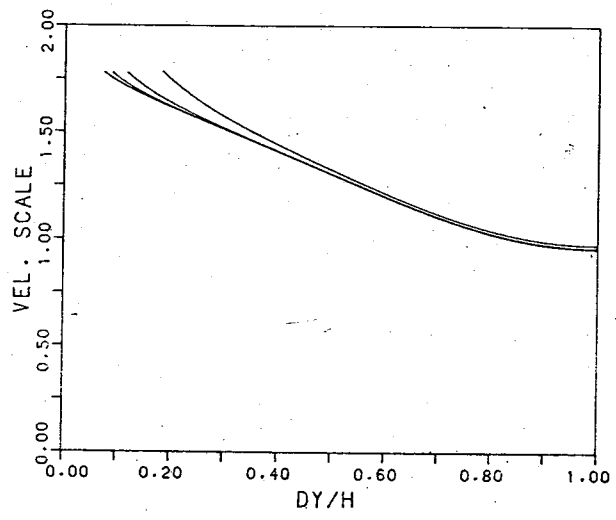

圖 7.　VEL . SCALE 表漩渦速度尺度，圖中之線，由上往下爲渠壁雷諾 300 、 500 、 700 、 900 。

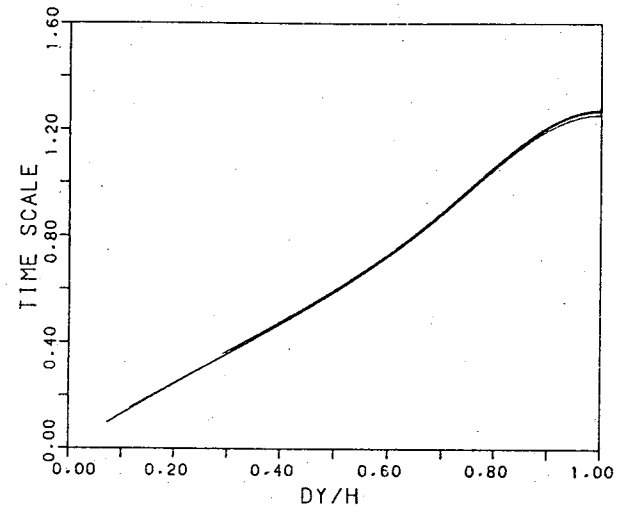

圖 8. TIME SCALE 表漩渦時間尺度，圖中之線，由上往下爲渠壁雷諾 300 、500 、700 、900 。

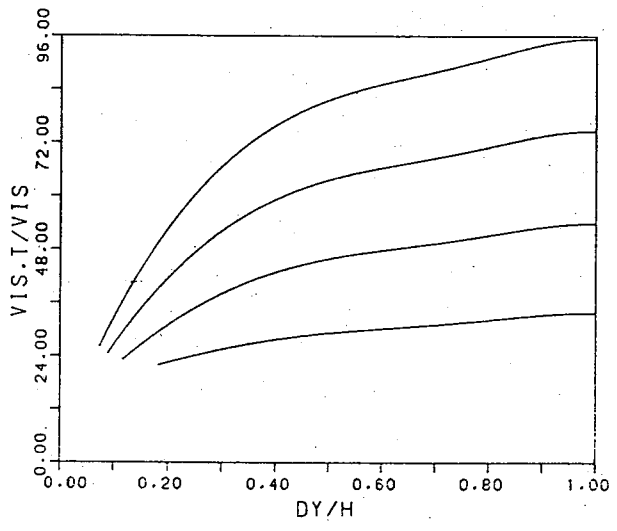

圖 9 VIS.T／VIS表因無次紊流漩渦擴散係數；圖中之線由下往上，分別爲渠壁雷諾 300 、500 、700 、900 。

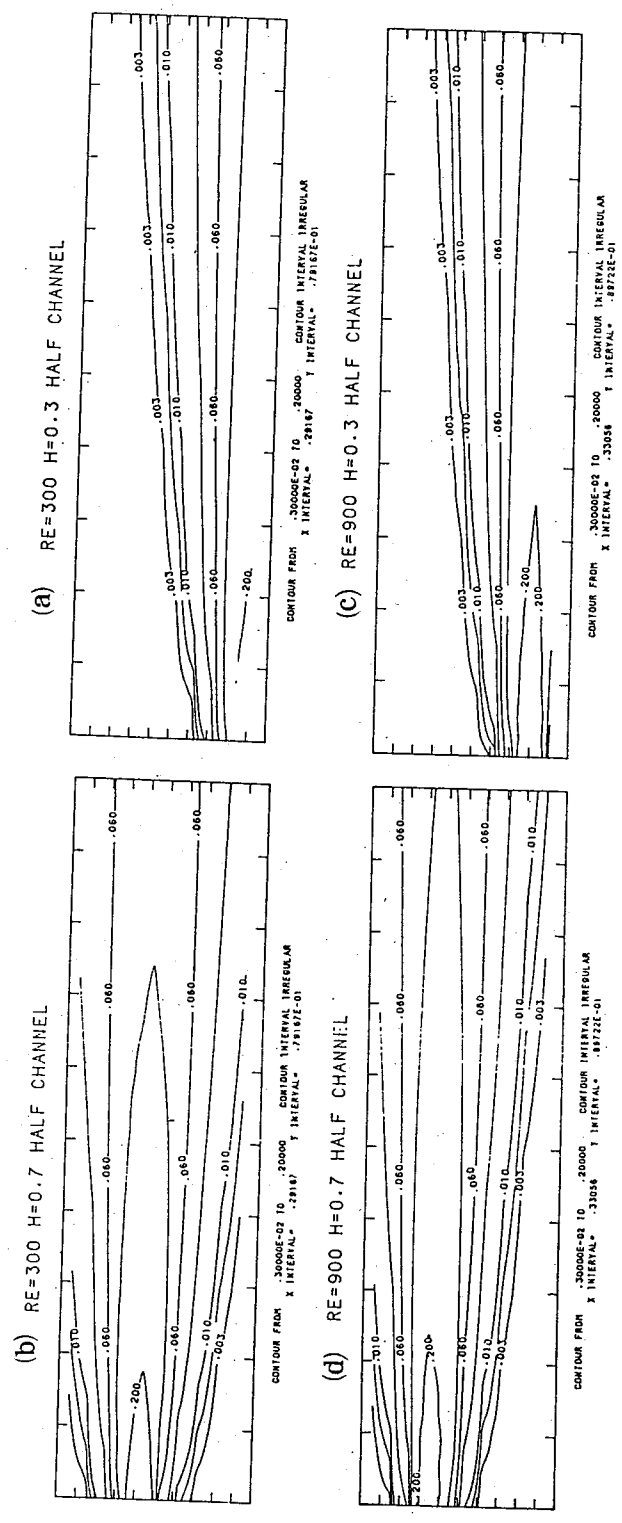

圖10. RE表渠壁雷諾，H表線源無因次高度，圖中線斷間之數字表無次濃度；縱軸表高度，全長爲渠通半寬；橫軸表計算之擴散長度，共長 1.25 渠通半寬。

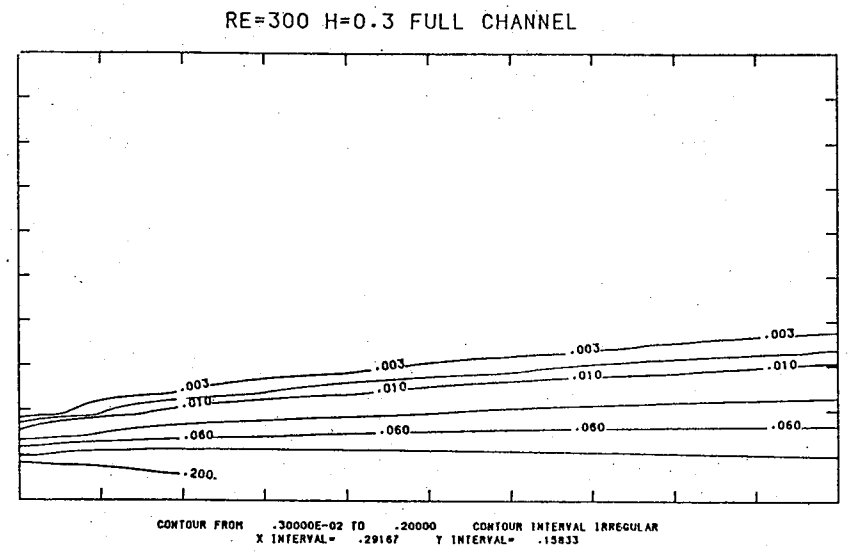

(a)

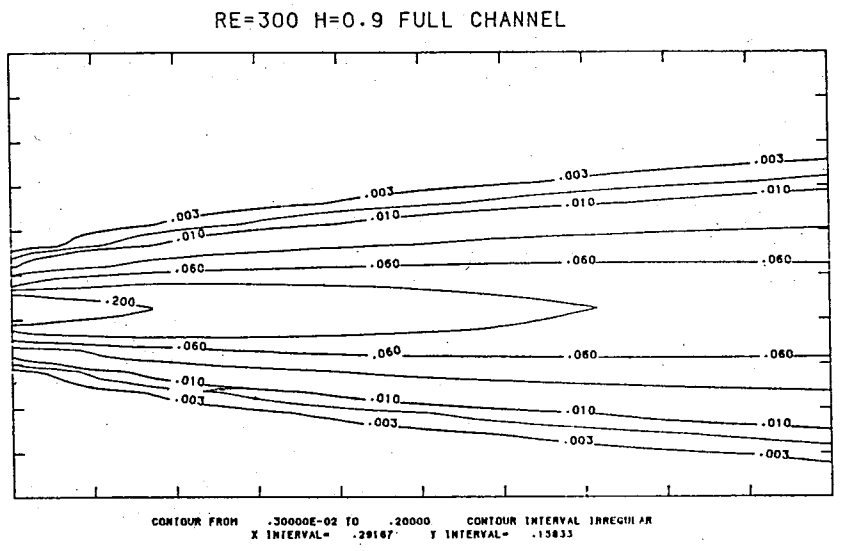

(b)

圖11. ＲＥ表渠壁雷諾，Ｈ表線源無因次高度，圖中線斷間數字表無因次濃度，縱軸表高度，全長二個渠道半寬；橫軸表計算之擴散長度，全長 1.28 個渠通半寬。

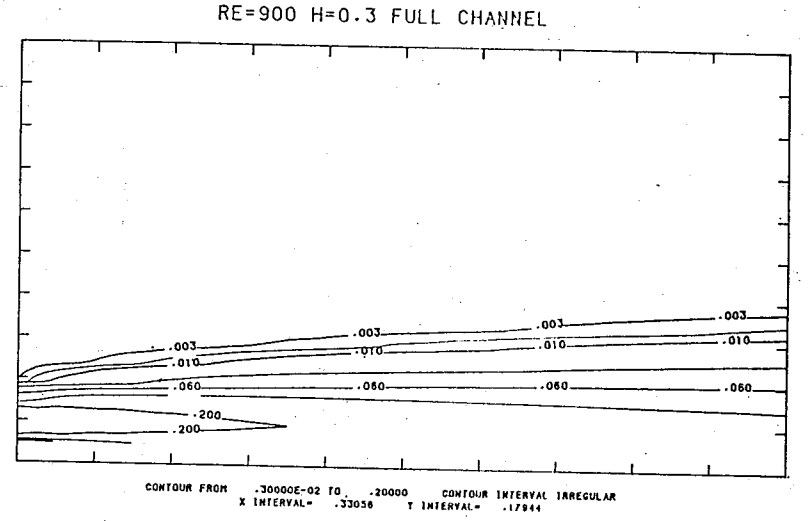

(a)

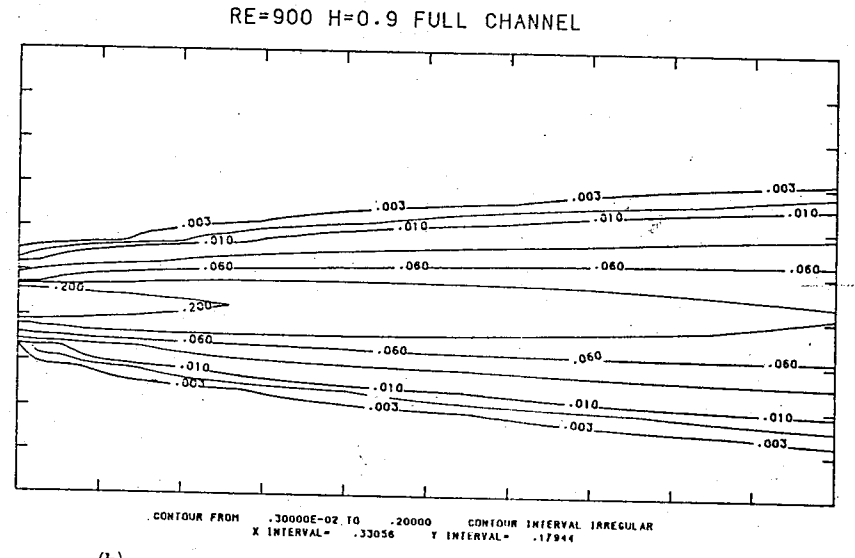

(b)

圖12. ＲＥ表渠壁雷諾，Ｈ表線源無因次高度，圖中線斷間數字表無因次濃度，縱軸全長，二個渠通半寬，橫軸全長，1.4 個渠道半寬。

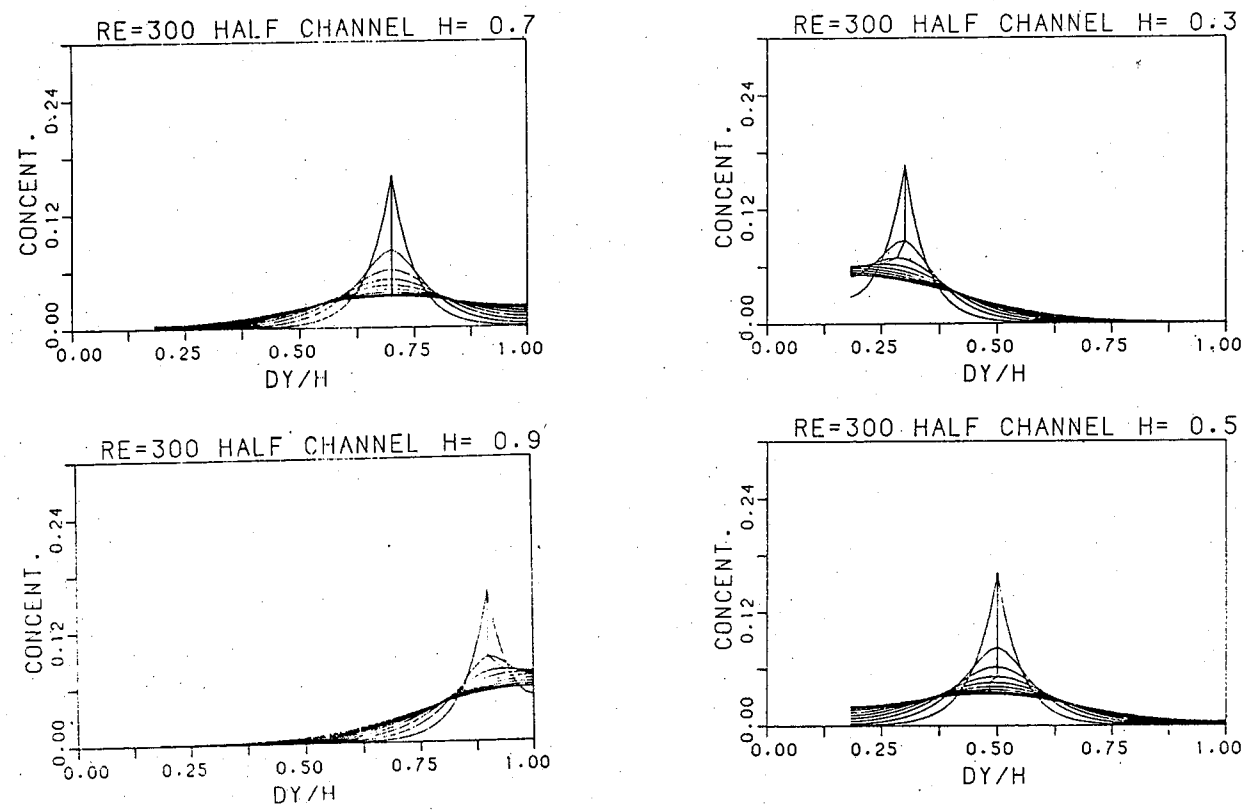

圖13. RE表渠壁雷諾，H表線源無因次高度，縱軸爲無因次濃度，橫軸爲無因次高度。濃度分佈曲線由上往下，距線源由 0.5 渠道半寬，至 4.5 渠道半寬。

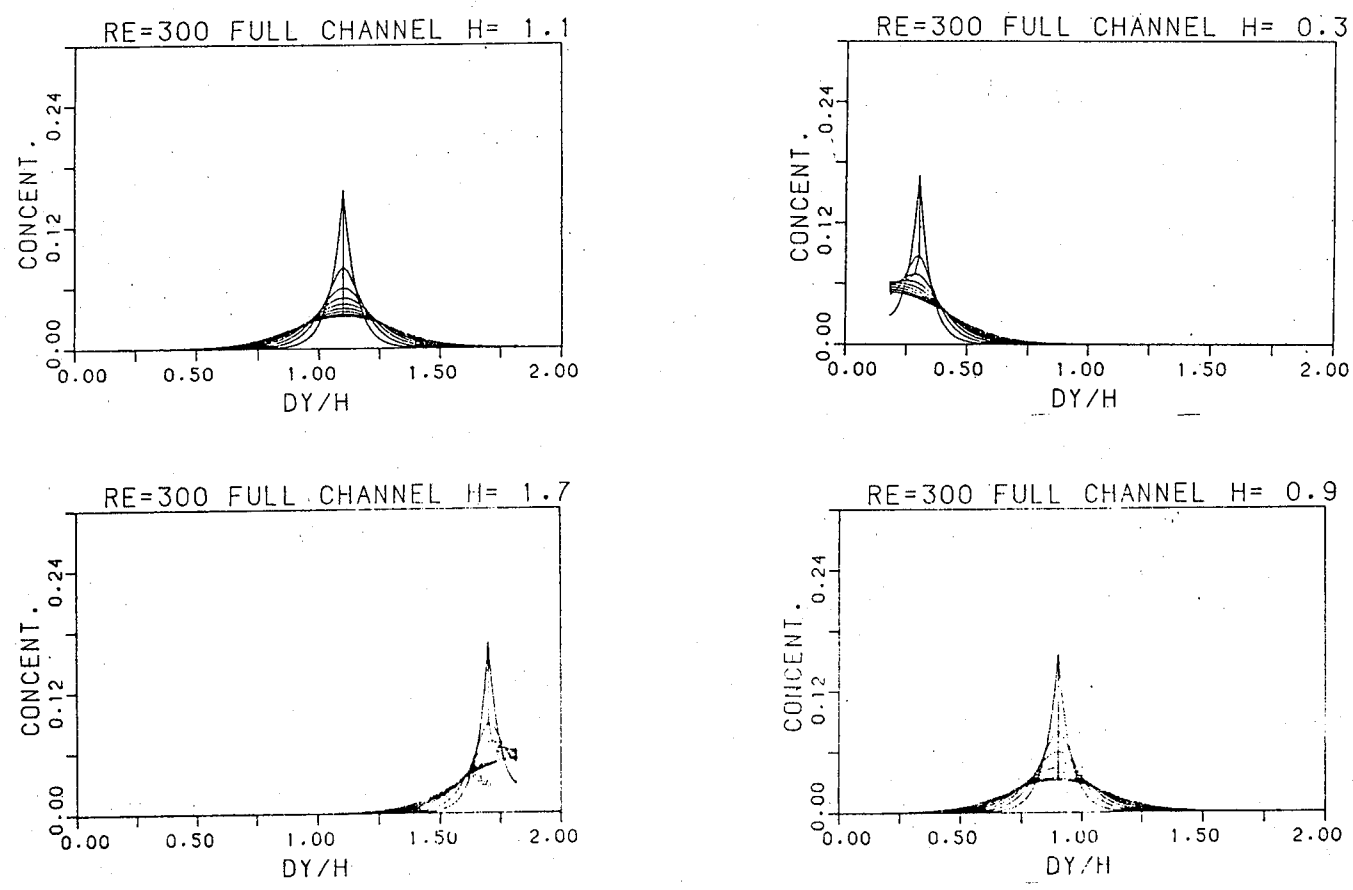

圖14. RE表渠壁雷諾，H表線源無因次高度，縱軸表無因次濃度，橫軸表無因次高度，濃度分佈曲線由上往下，距線源由 0.5 渠道半寬至 4.5 渠道半寬。

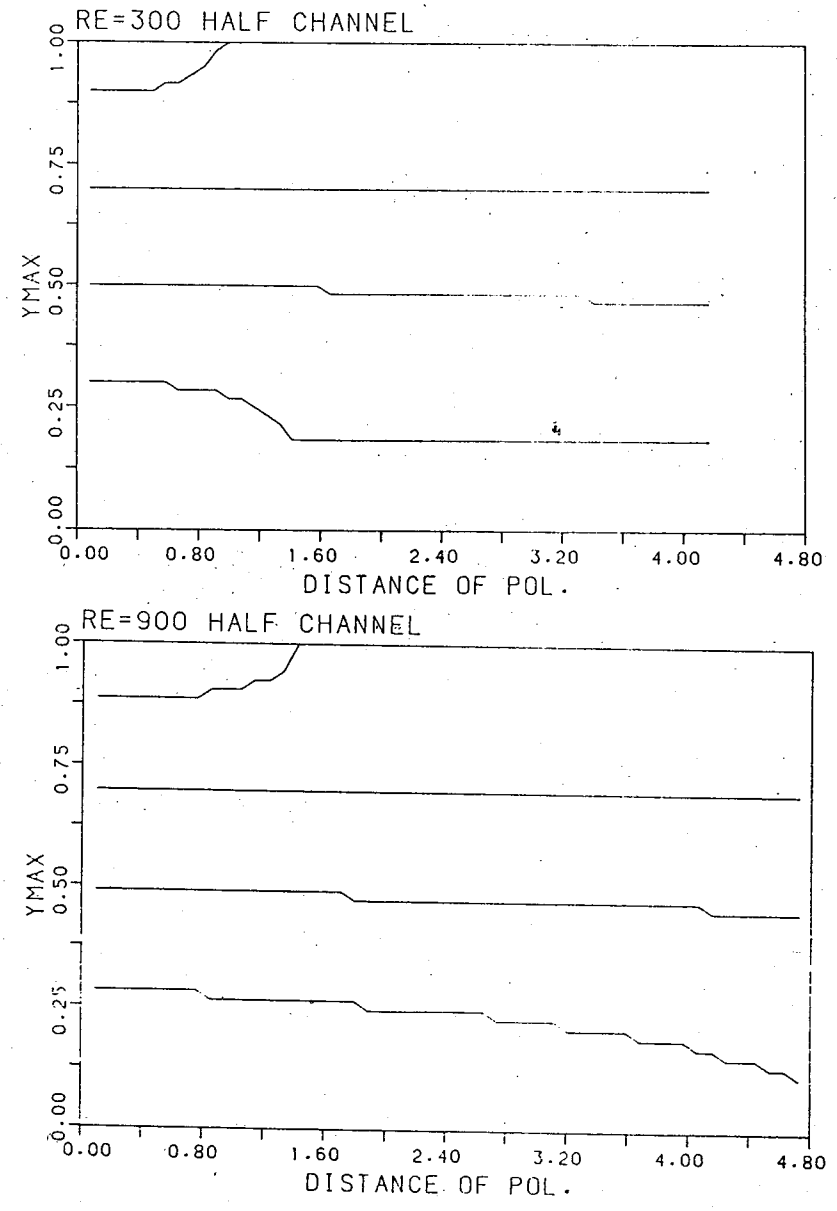

圖15. ＲＥ表渠壁雷諾，YMAX 表最大濃度點高度，橫軸表離線源之距離，圖中之線由下而上，相對於線源無因次高度 0.3 、0.5 、0.7 、0.9 。

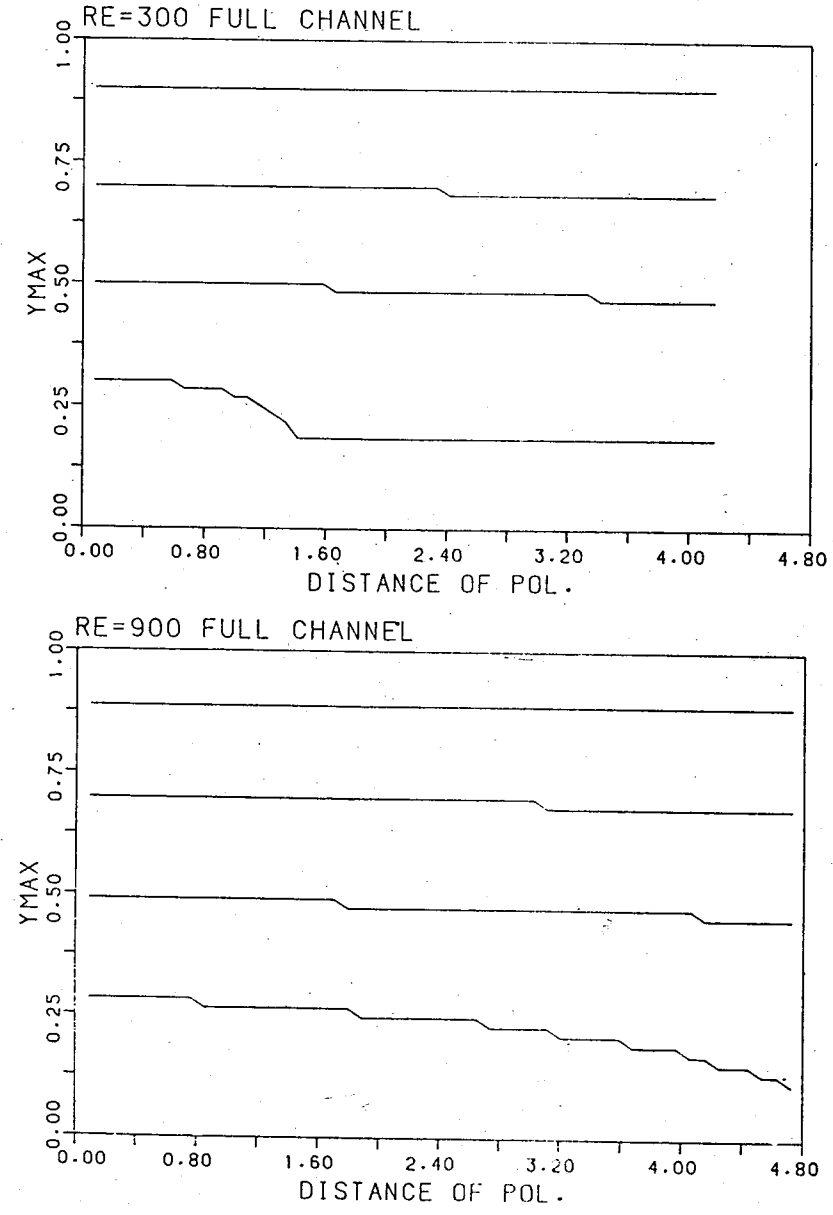

圖16. ＲＥ表渠壁雷諾，YMAX 表最大濃度點高度，橫軸表離線源之距離，圖中之線由下往上，相對於線源無因次高度 0.3 、0.5 、0.7 、0.9 。

雲參數和海面溫度的衛星紅外遙控

曾 忠 一

中央研究院物理研究所　台大大氣科學系

黃 一 成

台大大氣科學研究所

摘　要

海面溫度的衛星紅外遙測中最主要的問題是濾雲和水汽訂正。本文設計一種篩選步驟，以便檢定輻射計各頻道的資料是否正確，同時確定一個視場是晴天，或是完全被雲所遮蔽，還是部分被雲所遮蔽，然後用多頻道濾雲法除去雲的影響，以便求出裂雲區中的雲頂溫度和海面溫度。

現在氣象衛星的輻射計有三個窗區頻道，可用來進行更精確的水汽訂正。本文使用簡單的大氣模式，給定氣溫和水汽含量的垂直分布、海面溫度、視角等，計算出觀測到的輻射強度。然後利用這些大量的海面溫度和輻射強度的統計資料建立廻歸模式，確定海面溫度和各頻道亮度溫度之間的關係。最後用實際觀測的衛星資料決定海面溫度。研究結果顯示，經過濾雲和水汽訂正後的海面溫度和十日平均海溫的觀測結果相當符合。

壹、前　言

海面溫度是重要的海洋參數，同時也是不可缺少的氣象參數，因爲在大氣海洋的熱收支問題、霧的形成以及熱帶氣旋的形成等方面，它都扮演極爲重要的角色。此外在數值天氣預報模式和大氣環流模式中，海面溫度更是重要的參數。簡單的說，由於海面和大氣的溫差，從海洋輸送到大氣的顯熱影響了整個大氣的運動和環流，進而調節了氣候。

過去海面溫度的觀測主要依賴於船舶和浮標，但用這些傳統的方法時，觀測範圍相當有限，而且花費相當昂貴，已經不能滿足目前對海面溫度的需求。氣象衛星能在很短的時間內對廣大的海域進行海面溫度遙測，已經逐漸取代傳統方法，成爲最重要的海面溫度觀測法。

在紅外區，海面可視爲黑體。因此，在沒有雲或大氣的削弱下，氣象衛星攜帶的輻射計所觀測到的窗區頻道亮度就是海面溫度。可是雲的存在和大氣的吸收通常使窗區頻道的資料難以解釋，因此海面溫度遙測中最重要的問題是如何濾除雲的影響及進行大氣訂正。濾雲法及大氣訂正法和輻射計的演進有很大的關係，早期的氣象衛星只有一個窗

區頻道，現在已有多頻道的觀測了，可以進行更準確的濾雲和大氣訂正。

Smith等人（1970）首先利用統計直方圖來濾除雲的影響，以便求得海面溫度。Rao等人（1972）利用Smith的方法，由衛星資料求出全球的海面溫度分布。他認爲誤差主要由於儀器雜訊、大氣訂正的不夠完善所引起的。McMillin（1978）使用多頻道濾雲法求取海面溫度，以便求出更準確的值。他認爲誤差主要來自水汽吸收的影響。

另外，Anding and Kauth（1970）首先提出多頻道濾雲法，認爲可以不必使用其他氣象資料就能做水汽訂正。Deschamps and Phulpin（1980）利用三個頻道或其中兩個頻道的資料進行水汽訂正。他發現儀器誤差小於0.1°K時，使用三個頻道得到的結果較好。Barton（1983）也用兩個頻道的資料來進行水汽訂正。他的研究結果顯示，求得的海面溫度當視角在60°以內時均根方差大約在0.2°K到0.5°K之間。Strong and McClain（1984）也用多頻道法進行水汽訂正，求得的海面溫度和浮標測定值之間的均根方差大約爲0.6°K。

我國中央氣象局在七十一年四月間解讀出繞極軌道衛星NOAA-6攜帶的計AVHRR（Advanced Very High Resolution Radiometer 所觀測到的輻射資料（曹氏，1982），並立即用簡單的方法計算出海面溫度。後來苟氏（1984）和劉氏（1984）也都做過類似的研究。本文再仔細探討多頻道濾雲法的適用性，並使用簡單的大氣模式求出水汽訂正的廻歸方程，以便求得更準確的海面溫度。此外，在用濾雲法求出裂雲區海面溫度的同時，我們也求出了雲頂溫度。

貳、紅外幅射傳遞方程

衛星上輻射計所接收到的輻射強度 $I_\nu(\theta)$ 可用下式表示（曾氏，1983）：

$$I_\nu(\theta) = I_{\nu s} e^{-\tau_1 \sec\theta} + \int_0^{\tau_1} B_\nu(T)\, e^{-\tau \sec\theta} \sec\theta \, d\tau \qquad (1)$$

其中 ν 是波數。θ 是視角，在平行平面大氣的假設下它就是衛星天頂角。$I_{\nu s}$ 是地表放出的輻射強度，$B_\nu(T)$ 是Planck函數，τ_1 是整個大氣的光程。在(1)式中我們使用光程 τ 爲垂直坐標，其定義爲（圖1）：

$$\tau = \int_z^\infty k_\nu \rho \, dz'$$

在上式中 k_ν 和 ρ 分別爲吸收氣體的吸收係數和密度。整個大氣的光程 τ_1 就是在地表上的 τ 值，即：

$$\tau_1 = \int_0^\infty k_\nu \rho \, dz$$

(1)式有簡單的物理意義。到達衛星上輻射計的上升輻射強度由兩部分組成。第一部

分是地表輻射 $I_{\nu s}$ 經過整個大氣的削弱後到達衛星的部分，即(1)式右邊的第一項。另一部分是各層大氣所放出的輻射經過其上大氣的吸收後到達衛星的部分，即右邊的第二項。

在紅外區，地表可視爲黑體，其放射率接近於1，故地表放出的輻射強度爲：

$$I_{\nu s} = B_\nu(T_s)$$

其中 T_s 是地表溫度。定義透射函數 $\mathcal{T}_\nu$ 爲：

$$\mathcal{T}_\nu(\tau) = e^{-\tau}$$

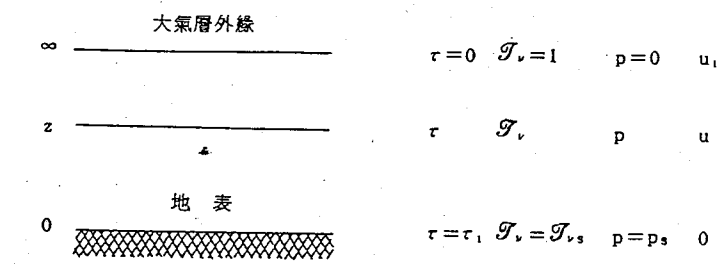

圖1　五種垂直坐標的關係

那麼(1)式可改寫爲：

$$I_\nu = B_\nu(T_s)\, \mathcal{T}_{\nu s}^{\sec\theta} + \int_{\mathcal{T}_{\nu s}}^{1} B_\nu[T(\mathcal{T}_\nu)]\, d\mathcal{T}_\nu^{\sec\theta} \qquad (2)$$

這是以透射函數爲坐標的紅外輻射傳遞方程，其中 $\mathcal{T}_{\nu s}$ 就是整個大氣的透射率：

$$\mathcal{T}_{\nu s} = \mathcal{T}_\nu(\tau_1) = e^{-\tau_1}$$

在大氣窗區，吸收很少，即 $k_\nu \approx 0$，$\tau_1 \approx 0$，故 $\mathcal{T}_{\nu s} = 1$。因此，由(2)式我們有：

$$I_\nu = B_\nu(T_s)$$

由上式可知，在沒有大氣的削弱下，衛星攜帶的輻射計所觀測到的亮度溫度就是表面溫度。可是雲的存在和窗區中微量水汽的吸收通常使窗區頻道的資料難以解釋。海面溫度的紅外遙測中最主要的問題是下面兩個：

㈠雲的濾除：從海面溫度遙測的觀點來看，雲是雜訊，要如何濾除觀測區域內雲的影響是相當重要的。因此必須發展出一種濾雲法，以便除去雲的影響，但這種濾雲法有其侷限性，只能適用於視場一部分被雲遮蔽的情況，也就是說只能適用於裂雲的情況。假如一個視場完全被雲遮蔽，就無法濾除，除了使用微波頻道外幾乎沒有其他辦法。

㈡水汽訂正：我們說過，在沒有大氣的削弱下，衛星觀測到的窗區亮度溫度就是海面溫度。可是從海面到衛星高度處存在着種種物質，諸如水汽、二氧化碳和氣懸膠體等，由於這些物質的影響，窗區頻道的亮度溫度和眞正的海面溫度之間仍有若干差異，最大差異甚至可達到10°C左右。海面溫度和亮度溫度的差值稱爲大氣訂正值，因爲水汽

吸收的影響最大，故又稱爲水汽訂正值。

最後我們附帶一提，Planck 函數可用下式表示：

$$B_\nu(T) = \frac{c_1 \nu^3}{e^{c_2 \nu / T} - 1}$$

其中 c_1 和 c_2 分別稱爲第一和第二輻射常數，其值分別爲：

$$c_1 = 2hc^2 = 1.191066 \times 10^{-5}\ mW / m^2 - cm^{-4} - sr$$

$$c_2 = hc / K = 1.438833\ deg - cm$$

在上式中 c、h、K 分別爲光速、Planck 常數和 Boltzmann 常數。觀測到的輻射強度 I_ν 和對應的亮度溫度 T_B 之間有如下的關係：

$$I_\nu = B_\nu(T_B)$$

解出 T_B 我們得到：

$$T_B = \frac{c_2 \nu}{\ln(c_1 \nu^3 / I_\nu + 1)}$$

參、多頻道濾雲法的原理

設一視場的一部分被雲遮蔽，則上升輻射強度爲：

$$I(\nu) = N I_{cd}(\nu) + (1 - N) I_{cl}(\nu)$$

其中N表示部分雲量，$I_{cd}(\nu)$ 和 $I_{cl}(\nu)$ 分別爲雲區和晴空區的上升輻射強度。上式也可寫爲：

$$I(\nu) - I_{cl}(\nu) = N\,[\,I_{cd}(\nu) - I_{cl}(\nu)\,] \qquad (3)$$

或

$$I(\nu) - I_{cd}(\nu) = (N-1)\,[\,I_{cd}(\nu) - I_{cl}(\nu)\,] \qquad (4)$$

現在我們考慮兩個相鄰的視場。假設雲是不透明的，而且在同一氣壓層上。因此上升輻射強度的不同只是由於兩視場中雲量的不同而已。也就是說，在兩視場中 $I_{cd}(\nu)$ 及 $I_{cl}(\nu)$ 都是相同的（見圖 2）

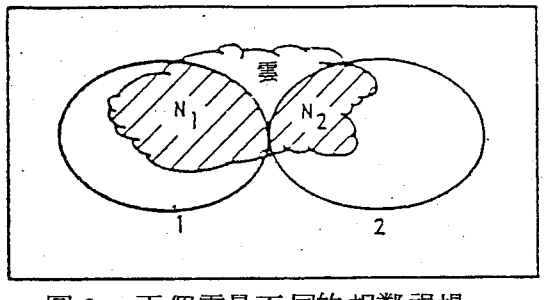

圖 2　兩個雲量不同的相鄰視場

在這個假設下，在這兩視場中(3)式可分別寫爲：

$$I_1(\nu) - I_{cl}(\nu) = N_1\,[\,I_{cd}(\nu) - I_{cl}(\nu)\,]$$

$$I_2(\nu) - I_{cl}(\nu) = N_2\,[\,I_{cd}(\nu) - I_{cl}(\nu)\,]$$

上二式相除，就有：

$$\frac{I_1(\nu) - I_{cl}(\nu)}{I_2(\nu) - I_{cl}(\nu)} = \frac{N_1}{N_2} = N^* \qquad (5)$$

對已經做過水汽訂正的窗區晴空輻射強度而言，它只是波數 ν 和表面溫度 T_S 的函數，即

$$I_{cl}(\nu) = B_\nu(T_S)$$

若有兩個窗區頻道 ν_1 和 ν_2，那麼因爲雲量和波數完全無關，所以由(5)式我們就有：

$$\frac{I_1(\nu_1) - B_{\nu_1}(T_S)}{I_2(\nu_1) - B_{\nu_1}(T_S)} = \frac{I_1(\nu_2) - B_{\nu_2}(T_S)}{I_2(\nu_2) - B_{\nu_2}(T_S)}$$

上式經過一些演算後可以得到：

$$B_{\nu_1}(T_S) = A_0 + A_1 B_{\nu_2}(T_S) \qquad (6)$$

其中

$$A_0 = \frac{I_1(\nu_1) I_2(\nu_2) - I_1(\nu_2) I_2(\nu_1)}{I_2(\nu_2) - I_1(\nu_2)} \qquad (7)$$

$$A_1 = \frac{I_1(\nu_1) - I_2(\nu_1)}{I_1(\nu_2) - I_2(\nu_2)} \qquad (8)$$

用完全同樣的方法，由(4)式我們也可得到：

$$B_{\nu_1}(T_C) = A_0 + A_1 B_{\nu_2}(T_C) \qquad (9)$$

其中 T_C 爲雲頂溫度，A_0 和 A_1 就是(7)和(8)式中所定義的常數。在導出(9)式時已設：

$$I_{cd}(\nu) = B_\nu(T_C)$$

由(6)和(9)二式可知，方程

$$B_{\nu_1}(T) = A_0 + A_1 B_{\nu_2}(T) \qquad (10)$$

有兩個解，其中一個解是表面溫度 T_S，另一個解是雲頂溫度 T_C，根據實際情況可知，$T_S > T_C$。

令　$I(\nu_1) = B_{\nu_1}(T)$　　$I(\nu_2) = B_{\nu_2}(T)$ (11)

則(10)式變爲：

$$I(\nu_1) = A_0 + A_1 I(\nu_2) \qquad (12)$$

現在若以 $I(\nu_1)$ 爲縱座標，$I(\nu_2)$ 爲橫座標，則(12)式是一條直線，已知兩個視場的 $I(\nu_1)$ 和 $I(\nu_2)$ 值，就可完全決定這條直線，即圖 3 中的虛線。(11)式消去T後代表 $I(\nu_1)$ 和 $I(\nu_2)$ 的函數關係，即圖 3 中的實線。實線和虛線的交點就是(10)式的解了

。必須注意，(10)式有兩個解，因此圖 3 中必須有兩個交點，高溫的代表表面溫度，低溫的代表雲頂溫度。

表面溫度和雲頂溫度求出以後，從(3)式和(4)式我們又可得到另一個重要的氣象變數，即雲量 N_1 和 N_2。

底下我們再把(11)式寫成更簡便的形式。根據 Planck 函數的定義，(11)式可寫爲：

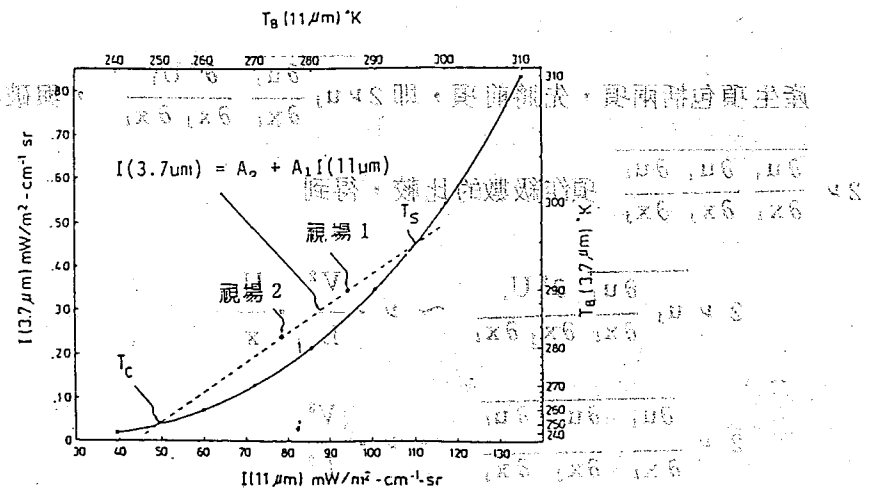

圖 3　這個圖表示(10)式的解法。虛線代表 $I_{\nu_1} = A_0 + A_1 I_{\nu_2}$，而實線表示聯立方程式 $I_{\nu_1} = B_{\nu_1}(T)$ 和 $I_{\nu_2} = B_{\nu_2}(T)$ 的解。實線和虛線的交點就是(10)式的解。較高溫處的交點代表表面溫度，而較低溫的交點代表雲頂溫度（曾氏，1983）。

$$I(\nu_1) = \frac{c_1 \nu_1^3}{e^{c_2 \nu_1 / T} - 1}$$

$$I(\nu_2) = \frac{c_1 \nu_2^3}{e^{c_2 \nu_2 / T} - 1}$$

由上面兩個式子解出 T 就有：

$$T = \frac{c_2 \nu_1}{\ln(c_1 \nu_1^3 / I(\nu_1) + 1)} = \frac{c_2 \nu_2}{\ln(c_1 \nu_2^3 / I(\nu_2) + 1)}$$

也就是說，$I(\nu_1)$ 和 $I(\nu_2)$ 有如下的關係：

$$I(\nu_1) = \frac{c_1 \nu_1^3}{(c_1 \nu_2^3 / I(\nu_2) + 1)^{\nu_1 / \nu_2} - 1} \quad (13)$$

上式就是圖 3 中的實線。解出方程組(12)和(13)二式我們可以得到兩個 $I(\nu_1)$ 的解，然後再求出其亮度溫度，我們就可求出 T_S 和 T_C 來。

當我們實際處理衛星資料時，對一特定的視場而言，通常有 8 個相鄰視場，如圖 4 所示。也就是說，對某一特定的視場而言，圖 3 中的虛線有 8 條，我們必須從這 8 條虛線選擇其中的一條，以便求出海面溫度和雲頂溫度。

由圖 3 可知，圖中的虛線是由兩個相鄰視場的兩個窗區頻道的輻射強度值決定的。這兩點必須相當準確才能決定出準確的海面溫度和雲頂溫度。可是在這個濾雲法中我們做了下面的假設：

㈠大氣的削弱可以完全略去不計，或者已做水汽訂正。

㈡海面是完全的黑體，即其放射率等於 1。

㈢兩相鄰視場中雲是完全的黑體，而且在同一高度上。

㈣陽光反射可完全略去不計。

只要上面的假設中的一個不成立，那麼我們得到的 T_S 和 T_C 就有問題。因此，在實際從事濾雲時，我們必須注意下面幾點：

㈠在進行濾雲以前，必須先做水汽訂正。

㈡對衛星觀測的輻射強度資料必須先做檢定工作，例如 3.7 μm 頻道的亮度溫度一定要大於 11 μm 的亮度。也就是說，在 I（11 μm）- I（3.7 μm）的平面上，所有的點必須落在曲線的上方。

7	6	5
8	中央視場	4
1	2	3

圖 4　中央視場及其相鄰視場

㈢兩個相鄰視場中若有一個是晴天或完全被雲所遮蔽，則上述濾雲法就不能用了。在這情況下，我們可立刻求出 3.7 μm 頻道的亮度溫度，它就代表海面溫度或雲頂溫度。因此，我們必須有一個方法判斷一個視場是晴天、部分被雲遮蔽或完全被雲遮蔽。

肆、多頻道水汽訂正法的原理

較高級的輻射計具有兩個以上的窗區頻道，這樣就可以對水汽的吸收進行更精確的訂正。在太空中飛行的氣象衛星上所觀測到的上升輻射強度爲：

$$I_\nu = B_\nu(T_S)\,\mathcal{T}_{\nu S}^{\sec\theta} + \int_{\mathcal{T}_{\nu S}}^{1} B_\nu\left[T(\mathcal{T}_\nu)\right] d\mathcal{T}_\nu^{\sec\theta} \tag{14}$$

利用中值定理，(14)式變爲：

$$I_\nu = B_\nu(T_S)\,\mathcal{T}_{\nu S}^{\sec\theta} + B_\nu\left[T(\overline{\mathcal{T}}_\nu)\right](1-\mathcal{T}_{\nu S}^{\sec\theta}) \tag{15}$$

其中 $\overline{\mathcal{T}}_\nu$ 在 $\mathcal{T}_{\nu S}$ 和1之間。$T(\overline{\mathcal{T}}_\nu)$是大氣的一個平均溫度，可用$\overline{T}$表示；$B_\nu[T(\overline{\mathcal{T}}_\nu)]$是一種平均的Planck 函數，可用$\overline{B}_\nu$ 表示。一般說來，$\overline{T}$大致爲 850mb 層的氣溫。

在吸收很微的窗區頻道，我們做下列近似：

$$\mathcal{T}_{\nu S}^{\sec\theta} = e^{-\tau_1 \sec\theta} \approx 1 - \tau_1 \sec\theta \tag{16}$$

將(16)式代入(15)式，我們有：

$$I_\nu = B_\nu(T_S) + \tau_1 \sec\theta\left[\overline{B}_\nu - B_\nu(T_S)\right] \tag{17}$$

再假設吸收係數 k_ν 和高度無關，那麼

$$\tau_1 = \int_0^\infty k_\nu \rho\, dz$$

$$= k_\nu \int_0^\infty \rho\, dz = k_\nu u_1$$

其中 u_1 爲可降水量，因此(17)式變爲：

$$I_\nu = B_\nu(T_S) + k_\nu u_1\left[\overline{B}_\nu - B_\nu(T_S)\right]\sec\theta \tag{18}$$

因爲 $B_\nu(T_S)$ 和 I_ν 相接近，而且 $B_\nu(T_S)$ 和 $\overline{B}_\nu$ 也幾乎相等，我們可進行下列泰勒數列展開：

$$I_\nu - B_\nu(T_S) \approx \left(\frac{\partial B_\nu}{\partial T}\right)_S (T_B - T_S) \tag{19}$$

$$\overline{B}_\nu - B_\nu(T_S) \approx \left(\frac{\partial B_\nu}{\partial T}\right)_S (\overline{T} - T_S) \tag{20}$$

將(19)和(20)二式代入(18)式得到（Anding and Kauth, 1970 和 Prabhakara et al, 1974）

$$T_B = T_S - (T_S - \overline{T})\, u_1 \sec\theta\, k_\nu \tag{21}$$

上式可說是一個相當重要的結果。必須記得，上式中 T_B、$\overline{T}$ 和 k_ν 是隨頻道變動而變動的。我們若能假設平均溫度 $\overline{T}$ 不依賴於頻道，那麼由(21)式可知，亮度溫度 T_B 和吸收係數 k_ν 之間有線性關係，同時海面溫度 T_S 就是 $k_\nu = 0$ 時的亮度溫度（圖 5）。若以 k_ν 爲橫座標，T_B 爲縱座標，則(21)式是一條直線，T_S 代表截距，$(T_S - \overline{T})\, u_1 \sec\theta$ 代

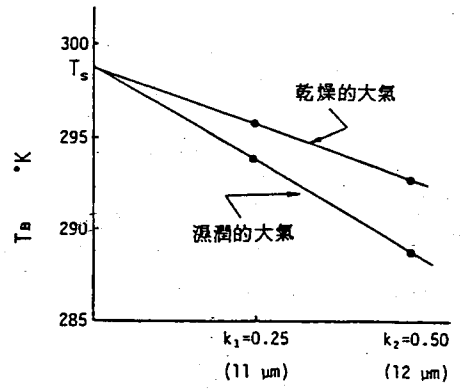

圖 5　多窗區頻道水汽訂正法的圖解

表斜率，因此只要有兩個頻道的（k_ν, T_B）值，我們就可完全決定截距和斜率。也就是說，理論上而言，只要有兩個頻道的亮度溫度觀測值，我們就可以決定出海面溫度值 T_S。現在若有兩個窗區頻道，則由(21)式我們有：

$$\frac{T_S - T_B(\nu_1)}{T_S - T_B(\nu_2)} = \frac{k_{\nu_1}}{k_{\nu_2}} = \frac{k_1}{k_2}$$

爲簡化符號起見，令 k_1 代替 k_{ν_1}，k_2 代替 k_{ν_2}。我們可以由上式求出海面溫度：

$$T_S = \frac{k_2}{k_2 - k_1} T_B(\nu_1) - \frac{k_1}{k_2 - k_1} T_B(\nu_2) \tag{22}$$

對具有三個窗區頻道的輻射計來說，我們可用最小平方法由(21)式求得截距和斜率。求得的截距可用下式表示：

$$T_S = T_B(\nu_1) + \frac{k_1}{2(k_2 - k_1)}\left[T_B(\nu_1) - T_B(\nu_2)\right] + \frac{k_1}{2(k_3 - k_1)}\left[T_B(\nu_1) - T_B(\nu_3)\right] \tag{23}$$

這種多頻道窗區法是 Anding 和 Kauth（1970）首先提出的。

由(22)和(23)式可知，海面溫度很容易由兩個或三個頻道的亮度溫度求出來，因爲各頻道水汽的吸收係數 k_ν 是已知的。可是事實上我們很少直接利用(22)和(23)式進行水汽訂正，最主要的原因是我們無法事先計算出足夠準確的吸收係數 k_ν。因此必須用別的方法進行水汽訂正。

一般說來，表面溫度可用窗區頻道亮度溫度的線性組合表示（特例爲(22)式和(23)式）

$$T_S = A_0 + \sum_{i=1}^{n} A_i T_B(\nu_i) \quad (24)$$

其中 n 爲窗區頻道個數。也就是說，根據上面的理論，表面溫度和各窗區頻道亮度溫度之間有線性關係。可是(24)式中的 A_1 ，A_2 ，……，A_n ，我們不把它們和吸收係數連繫，而把(24)式當做廻歸方程，然後用大量的（T_S , $T(\nu_i)$）統計樣品來求出廻歸係數。必須注意，由(22)和(23)式可知，(24)式中的 A_0 應當等於零。可是我們若把(24)式視爲廻歸方程，則可放鬆 A_0 的限制，讓它不一定等於零。最主要的原因在於 T_S 實際上並不完全是 $T_B(\nu_i)$ 的線性函數，我們若用線性廻歸模式，則 A_0 就不一定等於零了。這樣一來，對某一地點上已知的海面溫度 T_S ，我們必須找出其對應的各窗區頻道亮度溫度值 $T_B(\nu_i)$ 來，而且必須有大量的（T_S , $T_B(\nu_i)$）統計樣品，才能用最小平方法求出(24)式中的廻歸係數 A_0 , A_1 , ……, A_n 。然後對某一定的一組亮度溫度觀測，就可以由(24)式計算出海面溫度。這種方法在許多物理問題中經常使用。也就是說，我們先用理論導出各物理變數之間的函數關係，以便建立廻歸模式，然後再用大量的統計樣品決定廻歸係數、確定各物理變數之間的關係。

上面說過，我們必須收集大量的海面溫度和對應的窗區頻道觀測值的統計資料，以便求出廻歸係數。可是在廣大的海洋中有船測海面溫度的地點很少。在另方面，即使已經知道某一地點的海面溫度，要從極爲龐大的衞星資料中找出對應的亮度溫度值也是相當麻煩而費力的事。因此必須尋求別的途徑。最方便的方法莫過於用計算機製造出大量的衞星資料。也就是說，對一給定的海面溫度 T_S ，我們利用(14)式計算出不同窗區頻道的輻射強度，此時必須先給定(14)式右邊所有的物理量，除了 T_S 外還須給定氣溫垂直分布 T 和透射函數 $\mathcal{T}_\nu$ ，而透射函數 $\mathcal{T}_\nu$ 又取決於吸收係數 k_ν 和吸收氣體的混合比 q 。因此，我們只要使用某一地區某一季節的探空資料 T 和 q ，對給定的不同的視角 θ 和海面溫度 T_S ，就可以求出對應的輻射強度 I_ν 。這樣就可得到大量的（T_S , $T_B(\nu_i)$）的統計樣品。

用上面的方法進行統計分析，除了需要探空資料之外，還需要一個計算透射函數 J_ν（或吸收係數 k_ν ）的程式。現在最常被使用的是北美空軍地球物理實驗室（Air Force Geophysics Laboratory）發展出來的 LOWTRAN-5（Kneizys et al, 1980）和 LOWTRAN-6（Kneizys et al, 1983）。這兩個程式可計算出從波數 350 cm^{-1} 到 40000 cm^{-1} ，每隔 5 cm^{-1} 的大氣透射函數。本文爲方便起見使用較簡單的透射函數，不用 LOWTRAN-5 或 LOWTRAN-6 。

伍、資料來源

本文採用衞星 NOAA-7 上 AVHRR 輻射計的資料。NOAA-7 屬於美國繞極軌道氣象衞星的第三代 TIROS-N 衞星系列。本系列衞星在 1978 年發射，以代替第二代繞

極氣象衞星 ITOS / NOAA 系列。TIROS-N 衞星系列中，預計發射八枚衞星，平均每枚衞星壽命是二年。衞星的飛行高度平均是 850 公里，每 24 小時繞地球 14.18 圈，沿地球近似南北向不斷的繞經南北兩極附近運轉。每繞地球一周約需 102 分鐘。任何時刻太空中同時有兩枚作業衞星，目前作業衞星是 NOAA-7 和 NOAA-8 。一枚在當地太陽時上午 7 時左右南下穿越赤道，另一枚則於當地太陽時下午 3 時左右北上穿越赤道。以我國中央氣象局衞星接收站而言，約每 6 小時就有一枚衞星飛到台灣附近上空，即本地時間上午 7 時左右，下午 3 時左右，下午 7 時左右，凌晨 3 時左右。繞極軌道衞星因飛行高度較低，有較好的解像力，但觀測區域則隨軌道而有所變動。

AVHRR 是衞星 NOAA-7 上主要觀測儀器之一。AVHRR 的掃瞄速率是每秒 6 條掃瞄線，掃瞄範圍在衞星正下方左右各 55.4 度，整個掃瞄線包括有 2048 個像元（Pixel），在衞星正下方的解像力是 1.1 公里。AVHRR 有 5 個觀測頻道，第一頻道波長是從 0.58 到 0.68 微米，屬於可見光頻道，可用來決定雲的存在；第二頻道波長從 0.725 到 1.1 微米，屬於近紅外輻射波段，可用來辨別雲系、水陸及冰雪的分布；第三頻道波長從 3.55 到 3.93 微米，第四頻道波長從 10.3 到 11.3 微米，第五頻道波長從 11.5 到 12.5 微米，這三個頻道都在紅外區，可用來計算雲頂及地表溫度。但是第三頻道在白天時受陽光反射的影響很大，只適用於夜間。併用第三和第四頻道可濾除雲的影響；併用第四和第五頻道，可做水汽訂正（Schwalb, 1978）。本文所採用的資料即是第三、四、五頻道的紅外波段。

爲了避免第三頻道受陽光反射的影響，本文取用 NOAA-7 軌道編號第 12416 的資料。衞星在民國 72 年 11 月 19 日格林威治時間 18 時 48 分 2.285 秒經過升交點，升交點位於西經 52.043 度赤道上空。升交範圍在西半球，到達本省附近時已是南下，由北向南運動。接收站的天線追踪時間由格林威治時間 19 時 24 分 11.251 秒至 19 時 39 分 24.763 秒。衞星在格林威治時間 19 時 38 分 59.855 秒到達降交點。降交點位於東經 115.217 度赤道上空。圖 6 是衞星 NOAA-7 的經過範圍。

本文研究目的是求在裂雲區中視場部分有雲時的海水溫度，所以研究範圍取在 25°N — 33°N， 122.5°E — 130.5°E 。此範圍在我國東北部的海面，如圖 7 所示。

我們從當時衞星圖片（圖 8）上可看出，有雲的地方位在左下角至右上角的連線及右下角一帶，相對應的亮度溫度如圖 9 到圖 11（分別代表 3.7 μm 、11 μm 、12 μm 頻道的亮度溫度，是每隔 0.3 個經緯度選一點畫出的）。這三張圖在等溫線的型態上非常相似，溫度值 3.7 μm 頻道者最高， 11 μm 和 12 μm 二頻道則較低，較 3.7 μm 約低 4.2 °C 到 18°C 左右，後二者的溫度值非常接近。三張圖溫度較低的區域，都是在左下角到右上角的連線及右下角一帶，和衞星雲圖是非常符合的。其中右下角的溫度最低，衞星雲圖在這塊區域也正是雲多且厚的地方。

從 1983 年 11 月 19 日 1800 Z 地面天氣圖（圖 12）可以很明顯看出，當時正好有一高壓在長江口出海，我們的研究區正好在高壓的籠罩下。而衞星雲圖上研究區中間的小朵狀積雲及右側的大片雲帶，也正是在高壓之中及前緣的表徵。

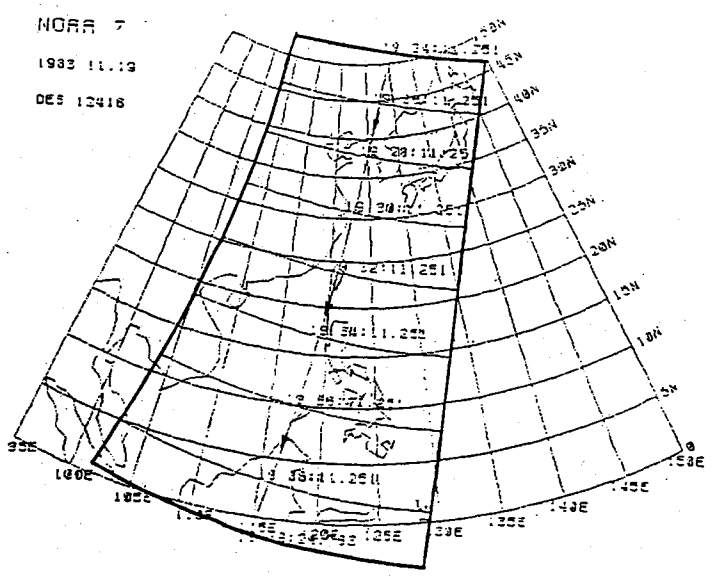

圖 6　軌道衛星NOAA-7軌道編號 12416所經過的區域及掃瞄範圍（苟氏，1983）

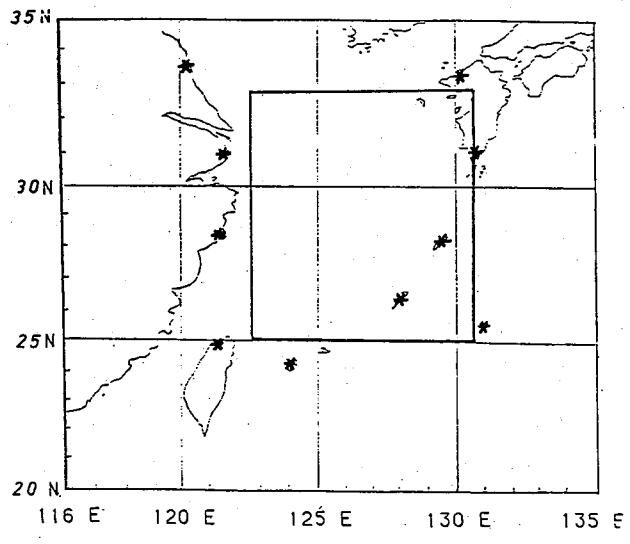

圖 7　本文研究範圍

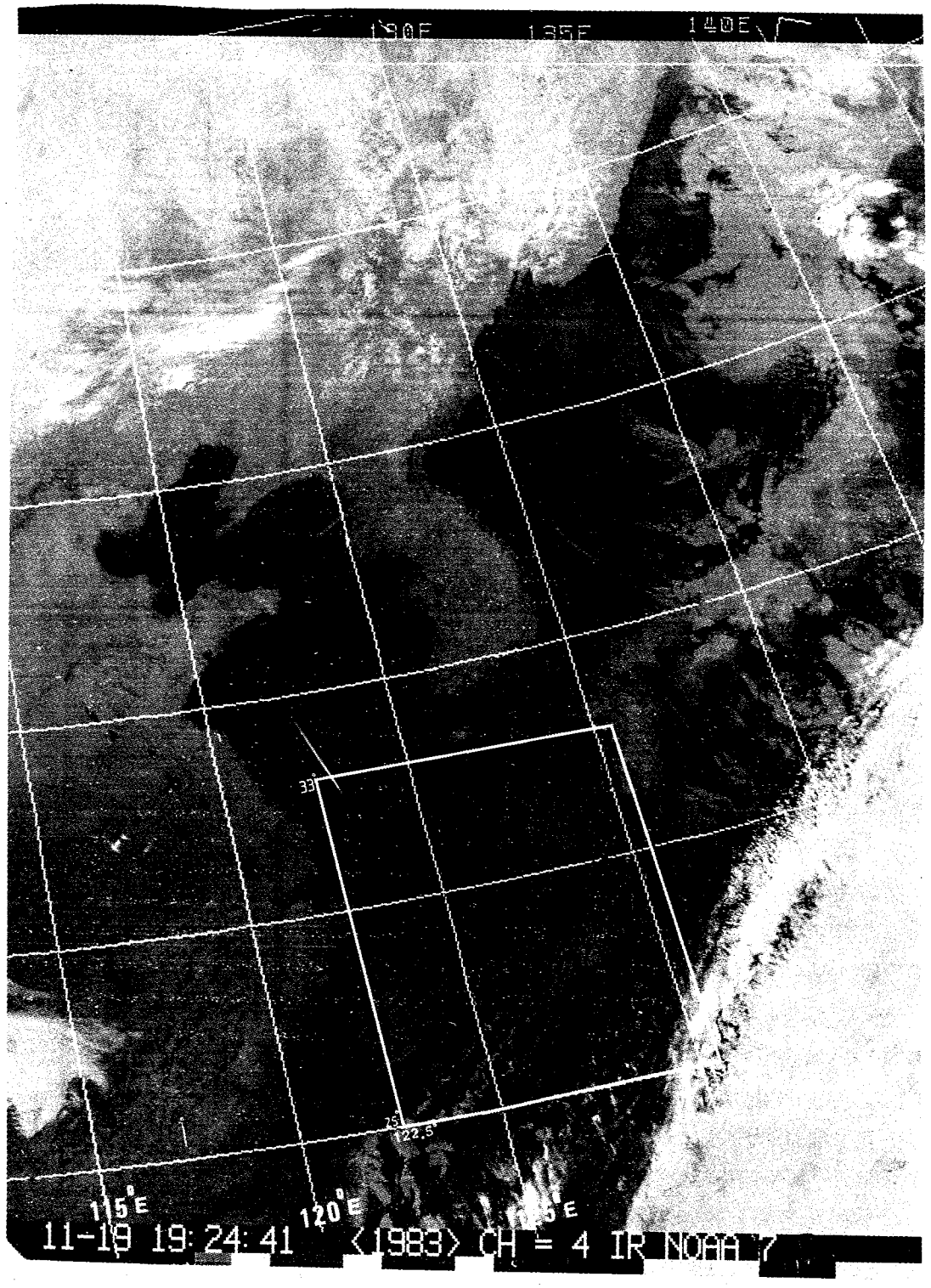

圖 8　1983 年 11 月 19 日 1924 Z 衛星雲圖

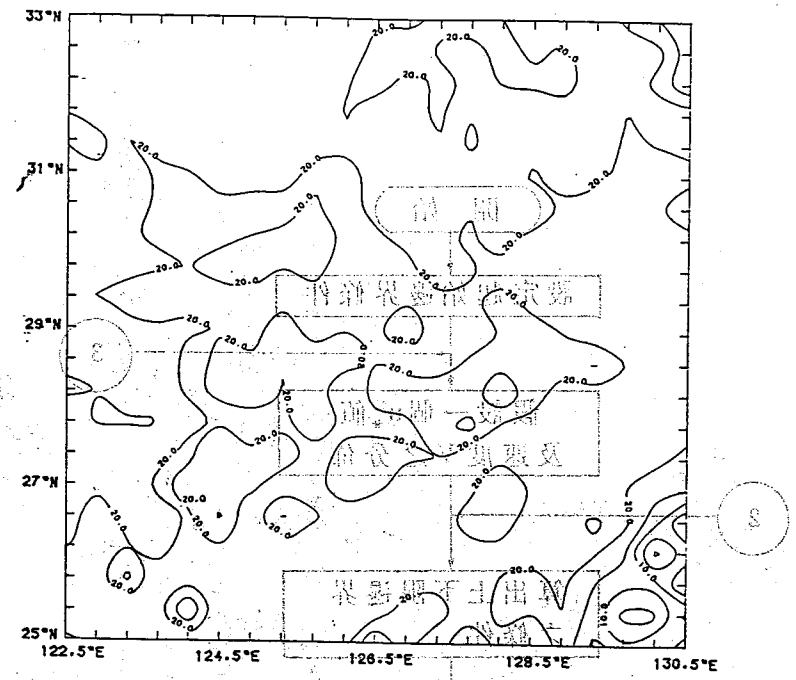

圖 9　3.7 μm頻道的亮度溫度

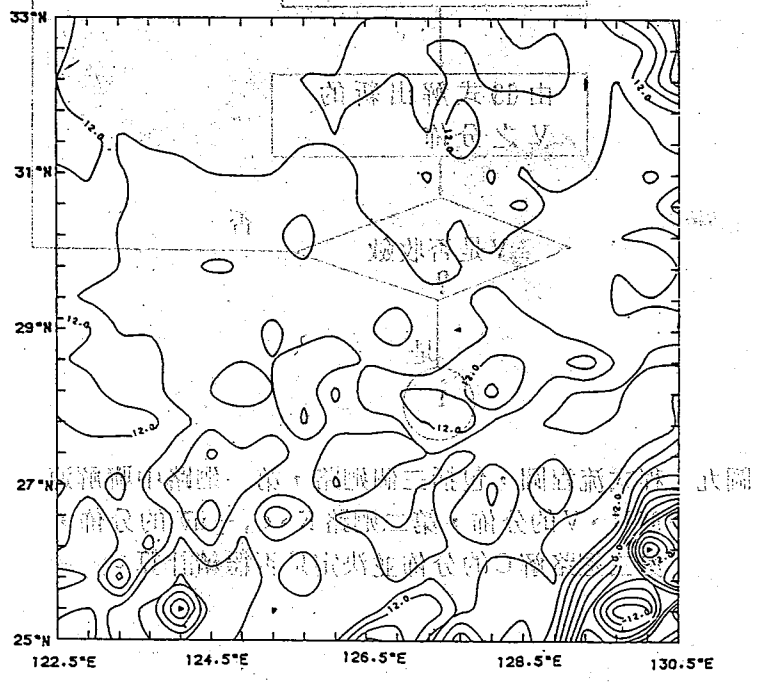

圖 10　11 μm頻道的亮度溫度

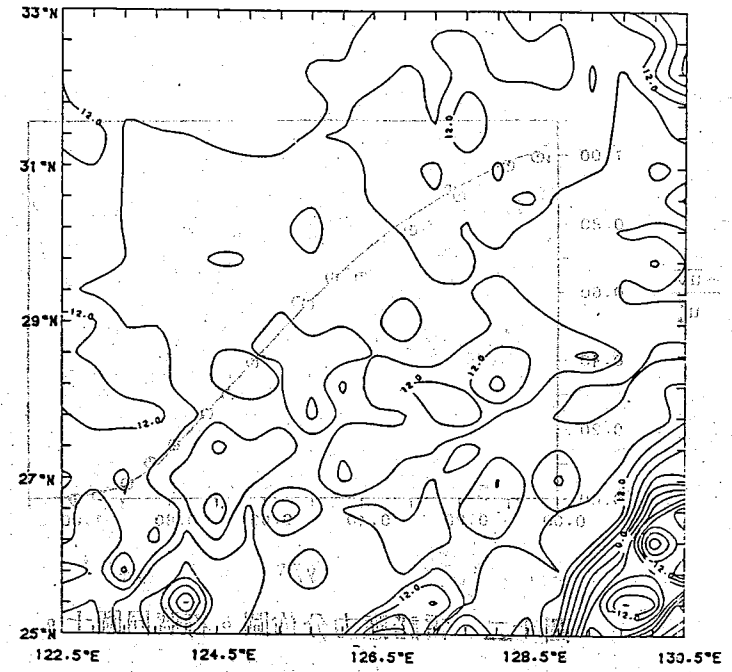

圖 11　12 μm頻道的亮度溫度

陸、濾雲法的步驟

由(11)式可知，消去$B_{3.7}(T)$和$B_{11}(T)$二者之間的T，並以I（3.7 μm）爲縱座標，I（11 μm）爲橫座標，則這二頻道的函數關係式爲一向上凹的曲線（圖3）。對於完全晴天且大氣無任何吸收作用存在時，任何一視場的輻射強度值必會落在該曲線上；另外當天空完全被雲遮蔽而大氣中也無吸收作用時，該視場的輻射強度也會落在曲線上。如果視場中有部分雲遮蔽，使該視場的輻射強度無法達到完全晴天的值，那麼不能滿足I（3.7 μm）和I（11 μm）函數關係的那些點會落在曲線以外的地方。此外雲對3.7 μm 頻道的影響比較小，使3.7 μm 的亮度溫度高於11 μm的亮度溫度，更接近於表面溫度（曾氏，1983）。因此那些落於曲線外的點就一定位於曲線的上方。利用這個原理，對於任何相鄰二視場而言，當它們都部分爲雲遮蔽時，它們的點都會落在曲線上方（圖3），由這二點就可以決定一條直線。這條直線在合理的條件下，必會和向上凹的曲線有兩個交點。較高處的交點溫度較高，就是海面溫度的解，較低處的交點溫度較低，就是雲頂溫度的解。

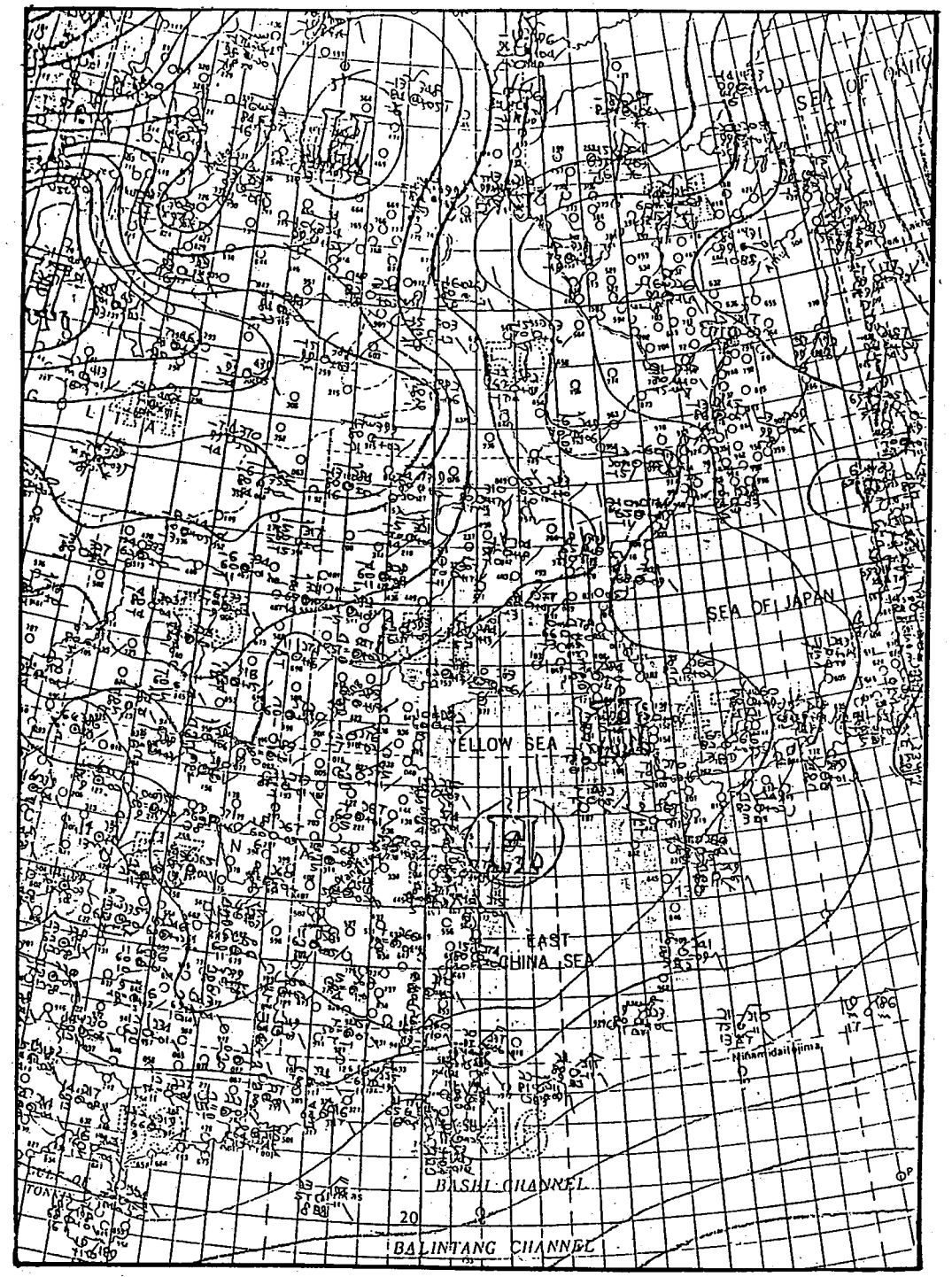

圖 12　1983年11月19日1800Z地面天氣圖

以上理論我們是假設大氣中沒有水汽或它其氣體的吸收作用才能求解的。因爲當大氣中有水汽或其它氣體的削弱作用時，它們對 3.7μm 和 11μm 頻道的輻射強度影響不一樣，會使得原爲晴天或陰天的視場不滿足(11)式的函數關係，而落於曲線以外的地方。同時更會使得那些原爲部分雲遮蔽的視場（不落在曲線上）所落的位置難以解釋，由其決定的直線斜率也會偏差太多，無法求得合理的解，這樣問題就複雜多了。因此，使用上述濾雲理論前，應先除去水汽等吸收作用的影響。

以下是我們的求解步驟：

㈠大氣訂正：

大氣吸收效應的影響不同，3.7μm 所受的影響比 11μm頻道小，11μm頻道的大氣訂正值要比 3.7μm 頻道的大氣訂正值來得大。依此原理，我們先對 3.7μm和11μm分別作大氣訂正。

㈡直線斜率上下限：

由實際狀況知，雲頂溫度範圍爲 $-65°C < T_c < 5°C$，海面溫度範圍爲 $5°C < T_s < 35°C$，由此決定(12)式中直線斜率 A_1 的上、下限。若斜率高於或低於此上下限，則捨棄不要。

㈢天氣狀況判斷：

我們對研究區每一視場作天氣狀況判斷原則如以下幾個方法。若爲晴天或陰天，直接以 Planck 定律求出海面、雲頂溫度；若爲部分雲遮蔽時，則用濾雲法求出海面溫度及雲頂溫度。

1. 鄰近點檢驗法（McMillin and Dean 1982）：

(1)中央視場若比周圍八個視場都低於 10°K 以上時，則中央視場爲陰天。

(2)中央視場若比周圍八個視場有的低於 10°K，有的高於 10°K時，則中央視場爲部分雲遮蔽。

2. 頻道特性檢驗法：

在經過水汽訂正後的所有視場，當 3.7μm 頻道的亮度溫度低於 5°C 時，該視場視爲陰天。

3. 數學殘差檢定法：

在晴天、陰天的視場其輻射強度應滿足(13)式，但在部分雲的視場不會滿足(13)式，而會有一殘差 R：

$$R = I(\nu_1) - \frac{c_1 \nu_2^3}{\left[\frac{c_1 \nu_2^3}{I(\nu_2)} + 1\right]^{\nu_1/\nu_2} - 1}$$

大氣中除水汽吸收外，還有其他氣體吸收作用，及儀器誤差等因素，故若 $R < 0.05\ mW/m^2 \cdot cm^{-1} \cdot sr$ 則爲晴天或陰天，反之爲部分雲遮蔽的視場。

㈣求解方程式：

由(7)和(8)二式就可決定視場 1 和視場 2 之間的直線；當直線斜率在我們所定的斜率上下限之間時才取用。

㈤直線斜率的決定：

對於部分被雲遮蔽的視場而言，該點的直線斜率是由其周圍八個部分被雲遮蔽的視場來決定。先由周圍的視場以(8)式決定 n 個（ $n \leq 8$ ）斜率，再由此 n 個斜率中求衆數來代表中央視場的斜率。

㈥求解裂雲區的海面溫度和雲頂溫度：

解出方程組(12)和(13)二式就可得到兩個 I（ ν_i ）的解，然後再求出其亮度溫度，這就是海面溫度或雲頂溫度。

柒、濾雲法的結果

爲了便於研究分析，我們把原始資料 3.7μm和 11μm 二頻道的輻射強度和亮度溫度放在圖13上。從這張圖可以發現，所有 3.7μm、11μm 頻道的點都不在由 I(3.7μm）和 I（ 11μm ）構成的函數關係曲線上。很明顯的，這是因爲所有的點皆受到大氣削弱和雲的影響，以致於它們不滿足(13)式的函數關係，而落在曲線之外。若這些點不先作大氣訂正，則我們可以從其上任意二點連線所決定的直線看出，有的直線斜率太大和曲線的交點偏高，求出的溫度也太高；有的直線斜率太小和曲線只有一個交點。因此，若不先作大氣訂正，本文所述的濾雲法將無法得到合理的海面溫度和雲頂溫度。

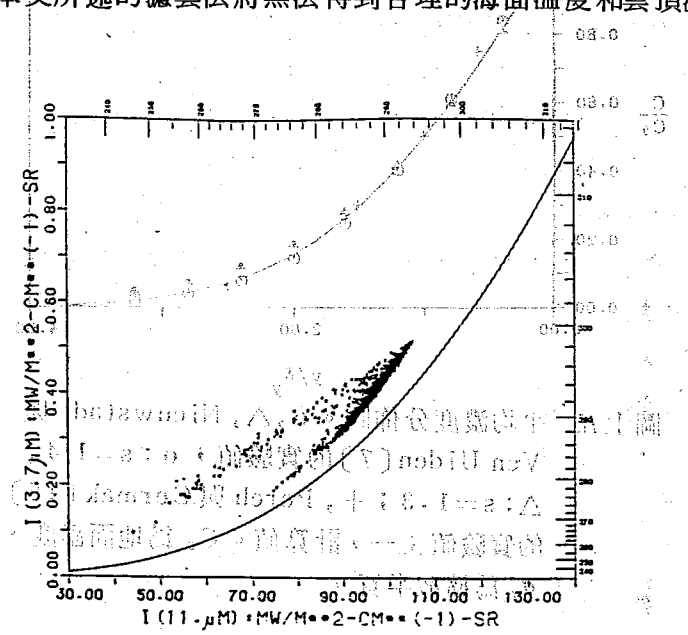

圖 13　未經大氣訂正前研究區各視場的輻射強度分布

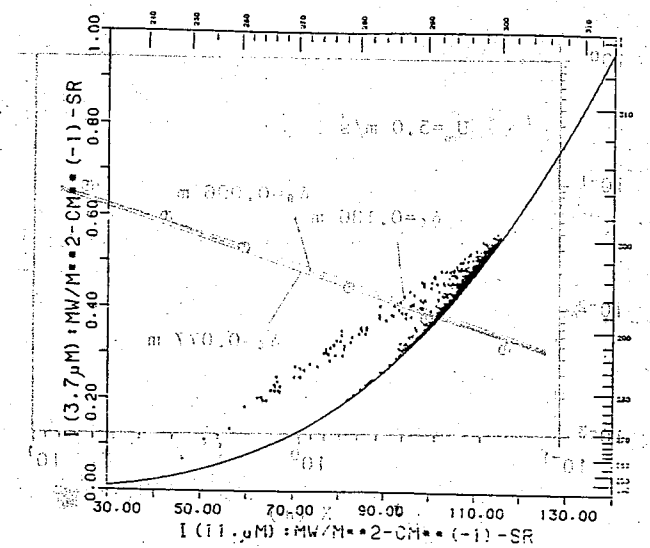

圖 14　經大氣訂正後研究區各視場的輻射強度分布

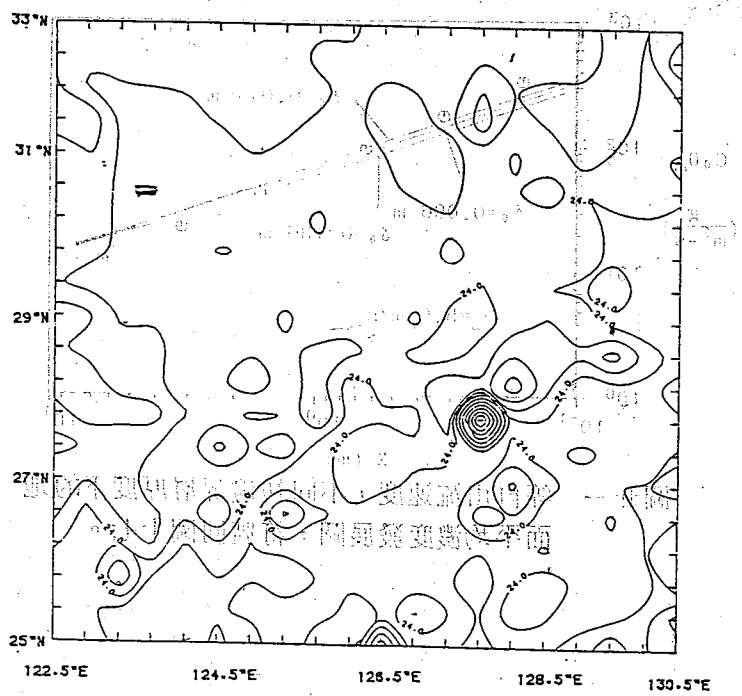

圖 15　濾雲後的海面溫度

若將原始資料每一點的3.7μm、11μm 輻射值作大氣訂正，其結果如圖14所示。很明顯的，有許多的點都非常靠近曲線，有的正好在其上，也有不少的點仍離曲線很遠，這些點是因仍受到雲的影響所致。

圖15是我們用多窗區頻道濾雲法所得的海面溫度圖（每隔3°C劃一等溫線），等溫線大致呈東北、西南向，西側溫度低，最低約15.8°C左右，東側溫度高，最高約28°C，溫度梯度呈東南向。中間偏右下側有一區域溫度比較低，約14.5°C 左右。一般而言，濾雲後的溫度較未濾雲前的3.7μm 亮度溫度，在無雲區高1.8°C～2.8°C，而在雲區溫度高出較多，約5°C～18°C左右；原來3.7μm 亮度溫度在雲區溫度低，且不平滑的情形。濾雲後溫度增高許多，和周圍沒有雲的溫度很接近，等溫線較原來平滑，顯然雲的雜訊已被濾除掉。

圖16是濾雲法得到的雲頂溫度，溫度由—4.1°C～—64.0°C。可以發現有雲頂溫度的區域（也就是有雲的地方），正是在左下角至右上角一帶連線和右下角的區域，就是衛星雲圖中有雲的地方。且右下角的雲頂溫度比較低，對應在衛星雲圖上的這塊區域正是雲較厚較多的位置（雲層應該較高）。

由圖15和圖16的結果，使我們對於多窗區頻道濾雲法有相當良好的評價，這方法可以把那些沒有被雲全部覆蓋住的視場，作濾除雲雜訊的工作，而得到眞實的海面溫度及雲頂溫度，而且從雲頂溫度的高低可以幫助我們作雲高的判斷。

由於沒有相對應的船測海溫資料可作校驗工作，因此我們取日本1983年11月11日到20日的十日平均海溫圖，來作我們檢驗時的參考（圖17）。

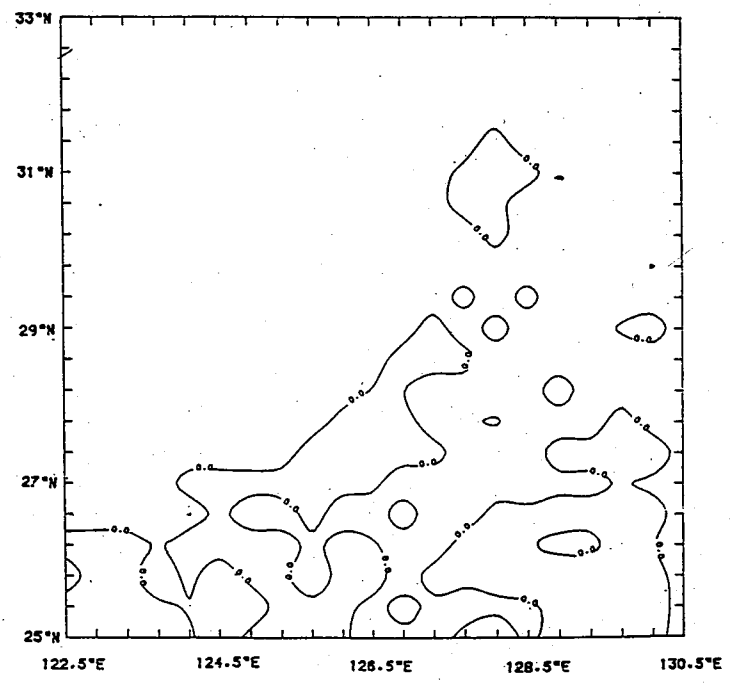

圖16　濾雲法得到的雲頂溫度

日本十日平均圖等溫線皆呈東北、西南向，溫度由16 ℃左右到26 ℃左右。本文所得的結果和此溫度範圍非常接近。不過此十日平均圖，並不能顯示出19日高壓出海的情形；而且日本十日平均圖是用GMS-2的衛星觀測值以直方圖的方法做出來的，自然無法和本文用NOAA-7的3.7μm和11μm觀測值以多窗區頻道濾雲法得到的結果一一作詳細的比較。然而，在型態和數值上，本文所得到的結果和日本十日平均圖都很接近。

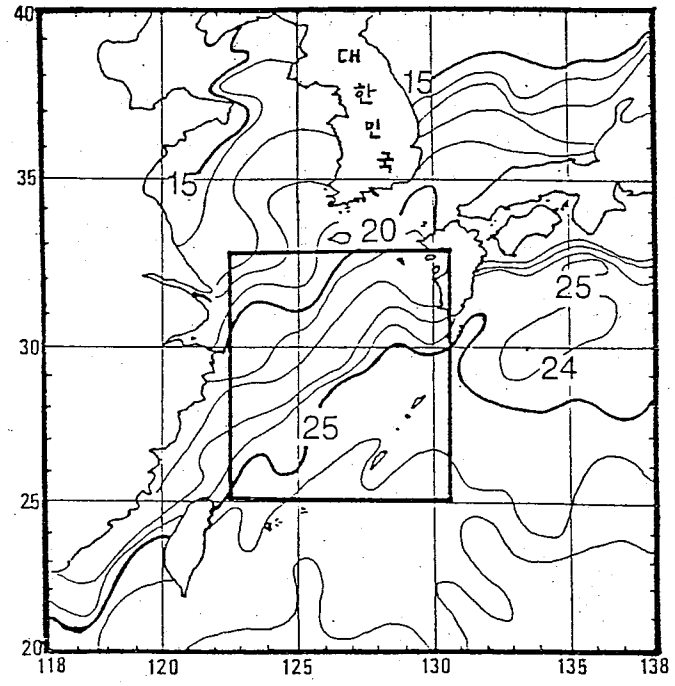

圖17　日本發佈11月11日至20日十日平均的海面溫度
（引用自苟氏，1983）

捌、簡易大氣模式

我們詳細研究如何利用3.7μm、11μm和12μm三頻道作本研究區上空的大氣水汽訂正，在不考慮雲的影響下，求出一個海面溫度由3.7μm、11μm和12μm三窗區頻道的亮度溫度線性組合表示出來的經驗公式，即求出迴歸係數A_0，A_1，A_2，A_3。由(2)式可知，當我們有某一區實際大氣溫度和水汽垂直分布及水汽的各頻道透射模式時，對應表面溫度T_s在衛星上量到的輻射強度I_ν理論值是可以算出來的。因此，大氣效應是可以藉模擬方法算出來的（Deschamps et al, 1980）。換句話說，(24)式的係數A_0，A_1，A_2，A_3是可以用理論模擬算出來的。本文就是用理論模擬先算出係數A_0，A_1，A_2，A_3，進而求得經過水汽訂正的海面溫度。

更進一步說，求㉔式的水汽訂正公式，可由二個方法得到：㈠將衛星觀測值的亮度溫度和相對應的船測海面溫度代入㉔式，求出A_0, A_1, A_2, A_3。㈡將實際溫度和水汽剖面加到透射模式裡來作模擬，並假設海面溫度（T_S）與探空剖面最低點之大氣溫度（T_{air}）的差值小於5°K，然後設定各種T_S值，經由⑵式算出衛星觀測值（亮度溫度$T_B(\nu_i)$），再算出係數A_0, A_1, A_2, A_3。後者就是所謂的理論模擬。因爲我們研究區海域缺乏足夠與衛星資料相對應的船測海面溫度，用理論模擬導出㉔式的係數A_0, A_1, A_2, A_3是最可行的方法。

洪氏等人（1985）曾隨機取用澎湖的冬季和夏季探空剖面各20組，並應用北美空軍地球物理實驗室（AFGL）所發展出來的大氣透射模式（LOWTRAN-5）程式套來驗證Strong and McClain（1984）的經驗公式，發現有的理想，有的誤差嚴重。

本文使用理論模擬，但模擬過程中未使用LOWTRAN-5的透射模式，只用了Barton（1983）的各頻道吸收係數計算公式，算出各頻道的透射函數後，再作理論模擬。步驟如下：

㈠計算溫度、水汽垂直分布：

我們首先使用研究範圍附近10個測站（圖7）的探空資料計算其氣溫和混合比平均值的垂直分布，以代表研究區內大氣的溫度和水汽含量的分布概況（圖18和圖19）。

㈡計算各頻道水汽吸收係數：

採用Bignell（1970）計算水汽連續吸收係數的公式：

$$k_\nu = k_1 p + k_2 e$$

算出3.7μm、11μm、12μm三頻道的水汽吸收係數。其中k_ν是單位質量的水汽吸收係數，k_1是線強外緣的吸收係數，k_2是指數型（e_j— type）吸收係數，e是水汽壓。各頻道的k_1、k_2值如表1（Barton, 1983）所示。

表1　各頻道水汽吸收係數值（Barton, 1983）

	12.0	11.4	10.8	3.7
k_1 ($gm^{-1}cm^2atm^{-1}$)	0.024	0.020	0.016	0.020
k_2 ($gm^{-1}cm^2atm^{-1}$)	12.1	9.8	8.0	4.0

㈢計算各頻道的光程：

依光程的定義：

$$\tau_\nu(p) = \int_0^p k_\nu(p) \frac{q(p)}{g} dp$$

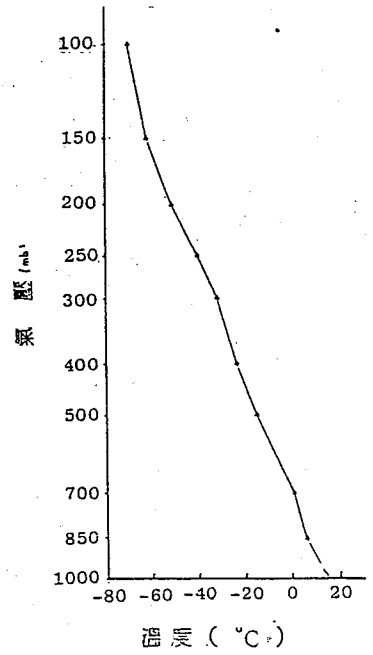

圖18　平均溫度探空圖

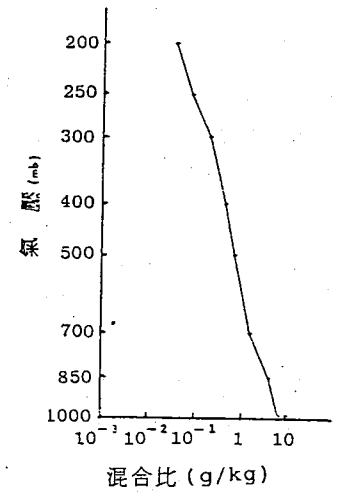

圖19　平均混合比探空圖

將前二步驟算出的k_ν（p）、q（p）代入上式，就可算出各頻道的光程$\tau_{3.7}$（p）、τ_{11}（p）、τ_{12}（p）（足號3.7、11、12分別代表3.7μm、11μm、12μm）。然後可計算透射函數。

㈣計算相當輻射強度：

若給定大量的表面溫度T_S、視角θ，就可算出3.7μm、11μm、12μm三頻道的相當輻射強度$I_{3.7}$、I_{11}、I_{12}。此處依本文的情形T_S由15℃到32℃，每0.25℃給定一個值，θ由0°到30°，每0.5°給定一個值。

㈤計算相當亮度溫度：

由算出的相當輻射強度（大量的三頻道輻射強度值），可求得大量的T_B（3.7）、T_B（11）、T_B（12）。在此大量的數值，乃是爲了作統計迴歸用的。

㈥計算迴歸係數：

將步驟㈣和㈤的大量T_S及T_B（3.7）、T_B（11）、T_B（12）代入㉔式，即：

$$T_S = A_0 + A_1 T_{B_1} + A_2 T_{B_2} + A_3 T_{B_3} \qquad (25)$$

用多重線性迴歸的方法可求出A_0, A_1, A_2, A_3四個係數。

㈦求海面溫度：

將1983年11月19日1924Z的衛星三頻道的亮度溫度代入㉕式，就可求得經過水汽訂正的海面溫度。

玖、水汽訂正的結果

在說明水汽訂正的研究結果以前，我們先討論一下水汽訂正值和亮度溫度及視角之間的關係。圖20是視角在 30° 以內時 11 μm 的水汽訂正值（即海面溫度和 11 μm 亮度溫度間的差值，我們用 ΔT_{11} 表示）和11 μm亮度溫度之間的關係。我們發現，隨着11μm亮度溫度的增加，其水汽訂正值也隨着增加，但在視角在 30 °以內的情況下，其水汽訂正值幾乎沒有顯著的變化，在圖中不能顯示出來。

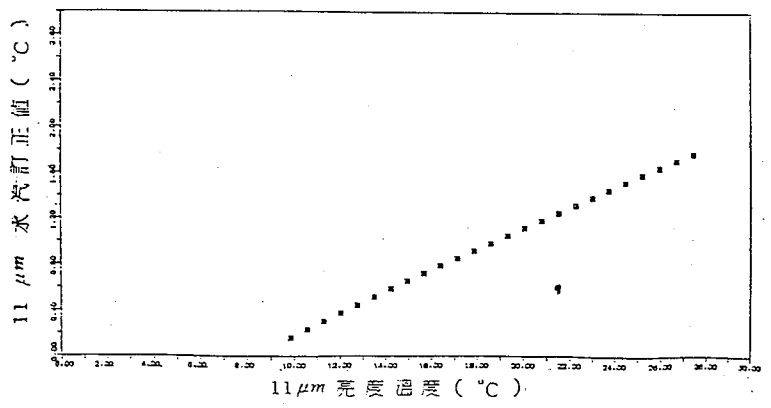

圖 20　視角在 30° 以內時的 11 μm 水汽訂正值隨其亮度溫度的變化

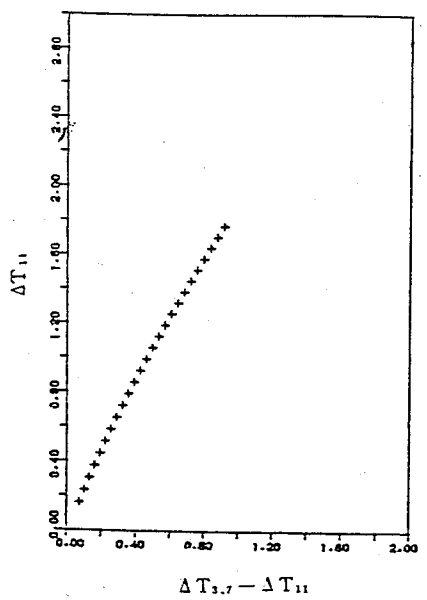

圖 21　ΔT_{11} 隨（$\Delta T_{3.7} - \Delta T_{11}$）的變化

圖21顯示 ΔT_{11} 隨 $\Delta T_{11} - \Delta T_{3.7}$ 呈線性增加。這張圖和 Barton（1983）的結果（圖 22）非常類似。但圖21中顯示，對同樣的 $\Delta T_{11} - \Delta T_{3.7}$ 值而言，ΔT_{11} 較小。

圖23表示 ΔT_{12} 隨 $\Delta T_{11} - \Delta T_{12}$ 呈線性增加，這個結果也和Baton（1983）的結果（圖24）相似，但圖 23 的 ΔT_{12} 較大。圖 25 表示 ΔT_{11}（$\theta = 0°$）和 ΔT_{11}（$\theta = 0°$）$- \Delta T_{11}$（$\theta = 50°$）之關係。圖 26 是 Barton（1983）得到的結果。這兩張圖無法比較。

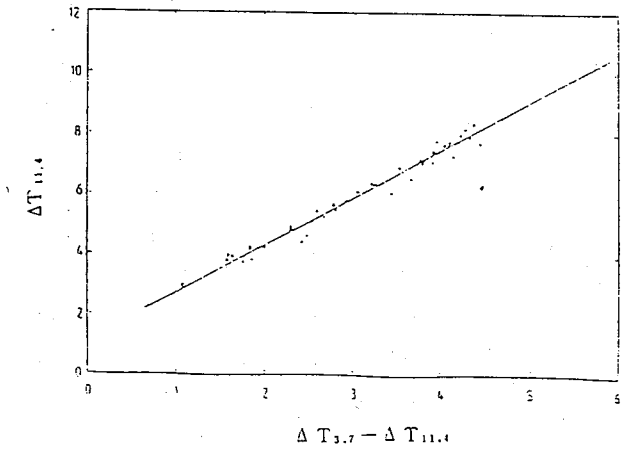

圖 22　$\Delta T_{11.4}$ 隨（$\Delta T_{3.7} - \Delta T_{11.4}$）的變化（Barton, 1983）

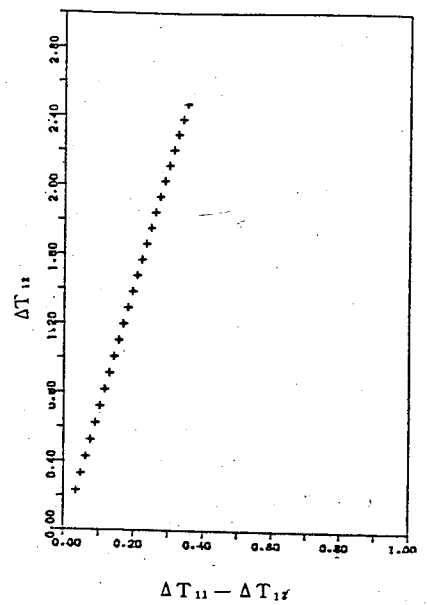

圖 23　ΔT_{12} 隨 $\Delta T_{11} - \Delta T_{12}$ 的變化

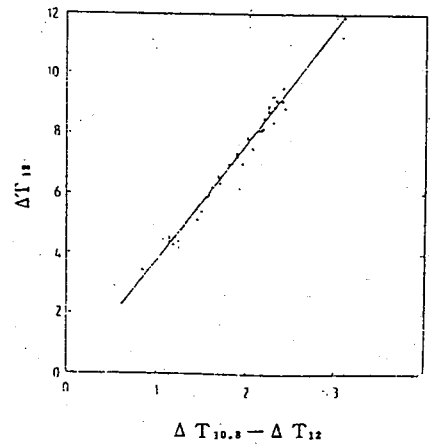

圖 24　ΔT_{12} 隨 ($\Delta T_{10.8} - \Delta T_{12}$) 的變化
(Barton, 1983)

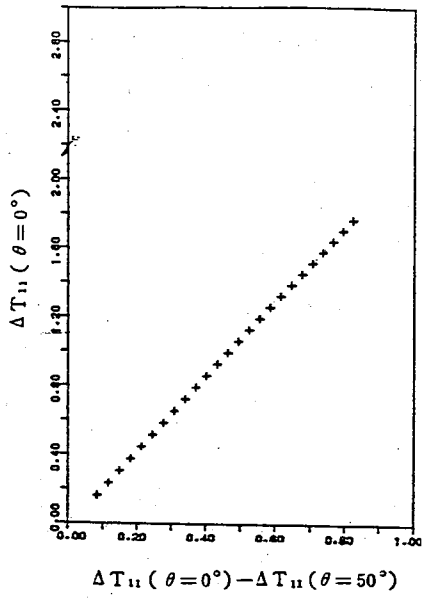

圖 25　ΔT_{11} ($\theta = 0°$) 隨 ΔT_{11} ($\theta = 0°$ $- \Delta T_{11}$ ($\theta = 50°$) 的變化

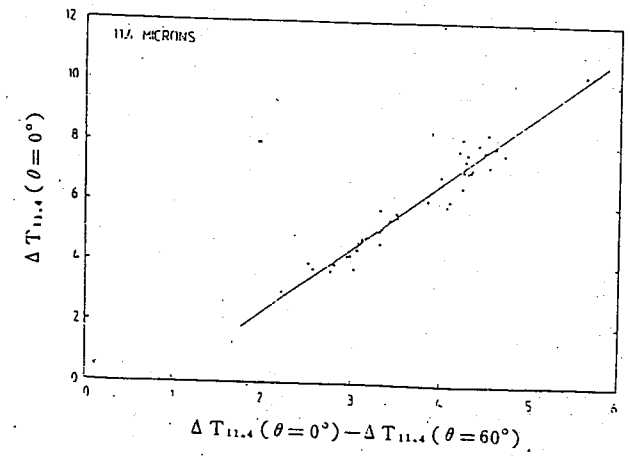

圖 26　$\Delta T_{11.4}$ ($\theta = 0°$) 隨 $\Delta T_{11.4}$ ($\theta = 0°$) − $\Delta T_{11.4}$ ($\theta = 60°$) 的變化 (Barton, 1983)

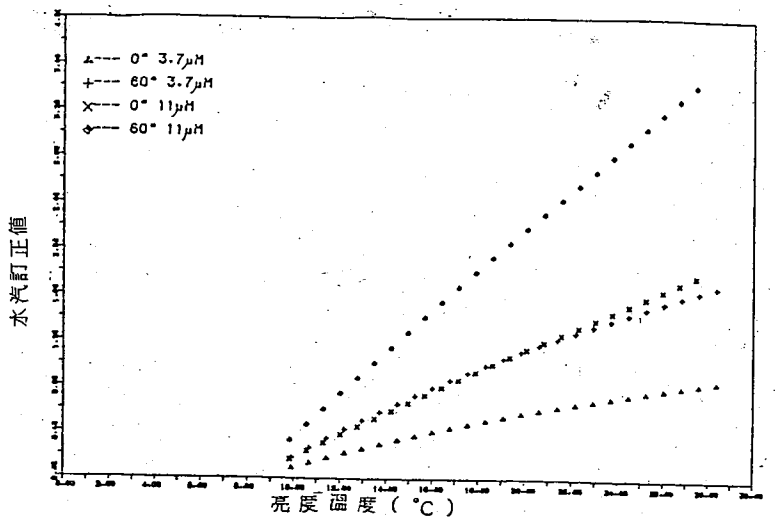

圖 27　3.7μm 和 11μm 在視角爲 0° 時 60° 時的亮度溫度與水汽訂正值的關係

圖 27 表示 3.7μm和 11μm 頻道的水汽訂正值和亮度溫度之間的關係。可以看出，11μm的水汽訂正值一般說來比 3.7μm 大。我們知道，就地表放射率、雲以及水汽吸收等觀點而言，11μm 頻道所受到的影響都比 3.7μm大（曾氏，1983）。

利用 3.7μm、11μm、12μm三頻道，以理論模擬的方法作水汽訂正，所得到的海面溫度和亮度溫度組合關係式爲：

$$Ts = 0.6119 + 1.9061\,T_{B_{3.7}} + 0.1091\,T_{B_{11}} - 1.0652\,T_{B_{12}} \qquad (26)$$

換句話說，(26)式的各係數爲：$A_0 = 0.6119$，$A_1 = 1.9061$，$A_2 = 0.1091$，$A_3 = -1.0652$。

我們將 1983 年 11 月 19 日 1924Z 的衞星資料：3.7μm、11μm、12μm亮度溫度，代入上面的關係式，就可得到經過水汽訂正後的海面溫度，如圖 28（每 5°C劃一等溫線）所示。

水汽訂正後的溫度由 18°C 左右到 29°C左右，較未作水汽訂正的 3.7μm頻道亮度溫度高出 3.6 ℃到16 ℃（雲區）左右。等溫線型態、溫度梯度仍和未作水汽訂正前的情形（圖9 及圖 11 ）相類似，唯雲區變化較大。

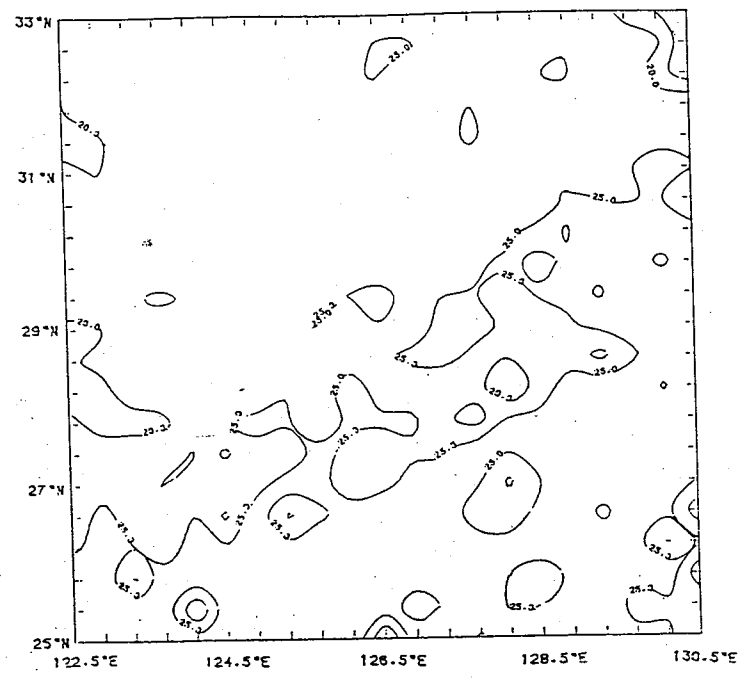

圖 28　水汽訂正後的海面溫度

國外有許多人也從事多頻道濾雲法的研究，例如Strong and Clain (1984)，Barton (1983)，Deschamps and Phulpin (1980)。他們得到的迴歸係數A_0，A_1，A_2，A_3，如表 2 所示。本研究也曾用他們的迴歸方程進行水汽訂正，求得訂正後的海面

溫度。可是結果並不理想，誤差相當大。其原因是顯而易見的。因爲他們得到的迴歸方程只適用於某一定的地理區域和季節，當然並不一定適用於本文的個案。

表 2　海面溫度和亮度溫度關係式的各個係數和國外學者所做結果之表較

	A_0	A_1	A_2	A_3	
W.I.C. NOAA-7 (C)	0.6119	1.9061	0.1091	−1.0652	
Strong & McClain (1984) NOAA-7(NIGHT)	1.2237	1.0170	0.97	−0.97	
Barton (1983)	−0.07	0	3.830	−2.83	0.2-0.6
Niabus 5 Barton (1981)	1.25	1.70	0	−0.70	0.23
Deschamps & Phulpin (1980)	0.14	1.002	1.126	−1.128	0.95
	2.02	1.481	−0.481	0	0.83
For selected	1.46	1.331	0	−0.33	0.71
Standard atm.	−2.18	0	3.626	−2.626	2.03
	0.94	0.966	0.739	−0.705	0.70
Far mean	2.01	1.473	−0.473	0	0.78
Monthly atm.	1.54	1.295	0	−0.29	0.66
NOAA - 7	−1.28	0	3.098	−2.098	1.87

拾、結　語

前面的分析可以明顯的告訴我們，多窗區頻道濾雲法能夠將那些被部分雲遮蔽的視場濾除掉部份雲的雜訊，而得到眞實的海面溫度，同時也可求到對應的雲頂溫度。然而，在使用這濾雲法之前，必須將視場的各頻道衞星資料作準確的大氣訂正，才能得到合理的海面溫度和雲頂溫度。

本文用理論模擬來作多窗區頻道水汽訂正的研究，可以得到一個由三頻道亮度溫度線性組合表示的關係式，藉此也求到了經過水汽訂正的海面溫度，只是溫度偏高了一些。這似乎和我們在作理論模擬時所用的透射函數有關；因爲本文並沒有使用 LOWTRAN-5 或像 Barton (1983)所使用的透射模式，僅簡單的用了水汽連續吸收帶的各頻道吸

收係數，計算在十個測站平均溫度和水汽垂直分布狀況下（水汽含量只計算到 200mb），地表輻射強度所能到達衛星上的量。由此所求出的各頻道水汽訂正值比Barton（1983）或Deschamps and Phulpin（1980）的水汽訂正值小一些，因此使得在求(25)式的係數A_1，A_2，A_3時，有A_1過大及A_2偏小的情形發生，進而導出的海面溫度就有偏高的趨勢。

另一方面，我們把國外學者所作的經驗式代入本研究的個案，發現沒有二個結果是非常接近的；而在溫度數值及等溫線型態上，似乎利用 3.7μm、11μm、12μm三頻道亮度溫度組合的式子，求出的結果比用 3.7μm、11μm、12μm任二頻道亮度溫度組合的式子求出的結果要好。而且用11μm、12μm二頻道亮度溫度求出的海面溫度顯然太低，故這個式子並不能適用。我們得到了一個結論：不能隨便取用國外的經驗式子來作我們研究區域的水汽訂正，必須有本研究區上空大氣完整而詳細的氣溫、水汽垂直分布資訊，加上有完全的各頻道透射模式，才能求得適合我們自己研究區域水汽訂正的經驗式。

多窗區頻道濾雲法可在有部分雲遮蔽的情形下使用，以濾除雲的影響，求得眞實的海面溫度及雲頂溫度；而多頻道水汽訂正法可在晴天時使用，求得一個由三頻道亮度溫度線性組合表示的經驗式，進而求出經過水汽訂正後的晴天海面溫度。

經由本文的研究，知道這二種方法都可求得精確的海面溫度。用3.7μm、11μm二頻道來濾雲時，必須先對這二頻道作準確的大氣訂正，才能用濾雲法來濾除雲的雜訊。當然，若能有事先判別雲高的方法，而對不同高度的雲分別來濾雲，將更能提高此濾雲法的精度。另外，本文所使用的理論模擬，以 3.7μm、11μm、12μm三頻道來作水汽訂正，需要有完整而詳細的溫度和水汽探空剖面，再加上有精確的各頻道透射模式，將可求得一個適於我們自己研究區的水汽訂正經驗公式，以便求得晴天的海面溫度。在我們沒有和衛星相對應的精確船測海溫資料時，用理論模擬來求適用我們自己海域附近的水汽訂正公式，是相當可行的辦法。

拾壹、致　　謝

本研究是在國科會專題計畫NSC73-0202-M001-01 的支持下完成的。中央研究院計算機中心提供電子計算機使用上的方便，本計畫才得以順利完成全部計算工作。在這裡本計畫工作人員表達最深摯的謝意。

參 考 文 獻

曾忠一，1983：大氣遙測原理與應用。中央氣象局出版，287 頁。

洪理強、顏泰崇、邱爾文、陳世照，1985：氣象衛星及多譜掃瞄遙測海面溫度分布與烏魚汛期關係之研究。遙感探測第五期，27－47。

曹幼民，1982：氣象衛星遙測資料之應用——海面溫度之求取。中國文化大學地學研究所碩士論文，59 頁。

苟潔予，1984：利用氣象衛星資料求取海面溫度及參數。中國文化大學地學研究所碩士論文，54 頁。

劉瑞貞，1984：衛星遙測海面溫度之初步研究。國立臺灣大學海洋研究所碩士論文。

Anding, D. and R. Kauth, 1970 : Estimation of sea surface temperatures from space. Rem. Sens. Environ., 1, 217-220.

Barton, I. J., 1983 : Dual channel satellite measurements of sea surface temperature. Quart. J. Roy. Meteor. Soc., 109, 365-378.

Bignell, K. J., 1970 : The water-vapor infrared continuum. Quart. J. Roy. Meteor. Soc., 96, 390-403.

Deschamps, P. Y. and T. Phulpin, 1980 : Atmospheric correction of infrared measurements of sea surface temperature of infrared measurements of sea surface temperature using channels at 3.7, 11 and 12 μm. Bound. Layer Meteor., 18, 131-143.

Kneizys, F. X., E. P. Shettle, W. O. Gallery, J. H. Chetwynd, Jr., L. W. Abreu, J. E. A. Selby, R. W. Fenn and R. A. McClatchey, 1980 : Atmospheric Transmittance / Radiance Computer Code LOWTRAN 5. AFGL-TR-80-0067, Air Force Geophysics Lab., Hanscom AFB, Massachusetts, North America, 233 pp.

_____, _____, _____, _____, _____, _____, S. A. Clough and R. W. Fenn, 1983 : Atmospheric Transmittance / Radiance Computer Code LOWTRAN 6. AFGL-TR-83-0187, 200 pp, Air Force Geophysics Laboratory, Hanscom AFB, Mass., North America.

McMillin, L. M., 1978 : An Improved technique for obtaining clear radiances from cloud contaminated radiances. Mon. Wea. Rev., 106, 1590-1597.

_____, and C. Dean, 1982 : Evaluation of a new operational technique for producing clear radiance. J. Appl. Meteor., 21, 1005-1014.

Prabhakara, C., G. Dalu and V. G. Kunde, 1974 : Estimation of sea surface temperature from remote sensing in the 11- to 13- μm window region, J. Geophys. Res., 79, No. 33, 5039-5044.

Rao, P. K., W. L. Smith and. Koffler, 1972 : Global sea surface temperature distribution determined from an environmental satellite. Mon. Wea. Rev., 100, 10-14.

Schwalb, A., 1978 : The TIROS-N/NOAA A-G Satellite Series. NOAA Tech. Mem. NESS-95, National Environmental Satellite Service, Washington, D. C., North America.

Smith, W. L., P. K. Rao, R. Koffler and W. R. Curtis, 1970 : The determination of sea-surface temperature from satellite high resolution infrared window radiation measurements. Mon. Wea. Rev., 98, 604-611.

Strong, A. E. and E. P. McClain, 1984 : Improved ocean surface temperatures from space — comparisons with drifting buoys. Bull. Amer. Meteor. Soc., 65, 138-142.

INFRARED SENSING OF CLOUD PARAMETER AND SEA SURFACE TEMPRATURE FROM SATELLITES

Chung-yi Tseng

Academia Sinica and National Taiwan University

Yi-cheng Huang

National Taiwan University

ABSTRACT

Cloud filtering and water vapor correction are two main problems in the infrared sensing of sea surface temperature from satellites. A screening procedure is devised to detect unreliable radiance data and determine whether a field of view is clear, partly cloudy or completely overcast. Then the multiple spectral window method is applied to determine the cloud top temperature along with the sea surface temperature.

The AVHRR on the NOAA-7 satellite carries three window channels at 3.7 μm, 11 μm at 12 μm. More precise corrections for water vapor can be achieved using the radiances measured by those channels. We use simple transmittance / radiance model to calculate the window channel radiances, given the temperature and water vapor profile, sea surface temperatures, and viewing angles. Then we establish a regression model to relate the sea surface temperature with brightness temperatures. The sea surface temperatures thus obtained are in good agreement with thosed obtained from the geosynchronous satellite GMS-2.

VARIATIONAL INITIALIZATION AND DETERMINATION OF WEIGHTING FACTORS

Chung-yi Tseng

Institute of Physics, Academia Sinica

Nankang 11529, Taipei, Taiwan, Republic of China

The variational optimization technique is used to develop an operational scheme for the initialization of meteorological fields in the numerical weather prediction. A method of determining a unique value of the weighting factors is proposed for the variational analysis. The linear balance equation is employed to maintain the balance between the mass and wind fields. A case study has been made to investigate the applicability of the proposed scheme to synoptic data in the East Asia area.

The variational formalism is given as follows :

$$\bar{o}\iint\{\alpha(u-\tilde{u})^2+\alpha(v-\tilde{v})^2+\beta(\phi-\tilde{\phi})^2+2\lambda' B(u,v,\phi)\}\,dxdy/m^2=0$$

where the strong constraint is the linear balance equation :

$$B(u,v,\phi)=m^2\left(\frac{\partial}{\partial x}\frac{fv}{m}-\frac{\partial}{\partial y}\frac{fu}{m}\right)-m^2\nabla^2\phi=0$$

m is the image scale factor and all the other symbols have their usual meaning. The resulting analysis equations take the form

$$\nabla \lambda = \frac{1}{m}(\phi - \widetilde{\phi})$$

$$\nabla^2\phi - \frac{f^2}{m}\frac{1}{\alpha/\beta}(\phi - \widetilde{\phi}) = \frac{\partial}{\partial x}\frac{f\widetilde{v}}{m} - \frac{\partial}{\partial y}\frac{f\widetilde{u}}{m} + \frac{2f}{\alpha/\beta}\left(\frac{\partial f}{\partial x}\frac{\partial \lambda}{\partial x} + \frac{\partial f}{\partial y}\frac{\partial \lambda}{\partial y}\right)$$

$$\frac{u}{m} = \frac{\widetilde{u}}{m} - \frac{f}{\alpha/\beta}\frac{\partial \lambda}{\partial y} \qquad \frac{v}{m} = \frac{\widetilde{v}}{m} + \frac{f}{\alpha/\beta}\frac{\partial \lambda}{\partial x}$$

with the natural boundary conditions

$$\phi = \widetilde{\phi} \quad \lambda' = 0$$

where $\lambda = \beta \lambda'$. The equations are coupled elliptical differential equations of of Helmholtz type subject to the Dirichlet boundary conditions and amenable to solution by the relaxation method. The weighting factors can be determined as follows :

$$\alpha = \frac{1}{\sigma^2_{uv}} \qquad \beta = \frac{1}{\sigma^2_{\phi}}$$

$$\sigma^2_{u,v} = \frac{1}{2}(\sigma^2_u + \sigma^2_v) \quad \sigma^2_u = \overline{(u - \widetilde{u})^2} \quad \sigma^2_v = \overline{(v - \widetilde{v})^2} \quad \sigma^2_{\phi} = \overline{(\phi - \widetilde{\phi})^2}$$

where the overbar represents the average over all the grid points.

This variational formalism is very simple and has been studied by many investigators previously. However, the most difficult problem is how to determine a reasonable value of the weight ratio α/β. In this study we calculate the value of the weight ratio by an iteration method. It is found that for some initial values the weight ratio varies greatly with the number of iteration. An example is shown in Fig. 1 for 500mb data. For other initial values the weight ratio changes only slightly. We take the optimal weight as the one which changes the least in the iteration process. Consequently, the optimal value for 500mb data is 85.08 m^2/s^2. Thus, by this method we can find a unique value of the weight ratio for each pressure level.

The general pattern of the adjusted height and wind fields is quite the same as the observed fields. However, there is some difference in the numerical values, since the adjusted fields satisfy the balance equation, while

the observed fields do not. The variance spectrum analysis of the height fields indicates that the short wave components have been completely suppressed, while the long wave components remain intact. Thus, the dynamic constraint has an effect of smoothing and filtering.

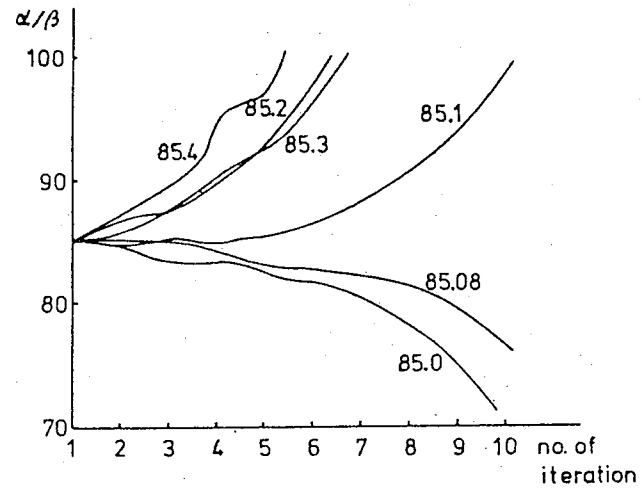

Fig. 1 The weight ratio as a function of the number of iteration for various initial values.

Published in the Extended Abstracts Submitted for the International Symposium on Variational Methods in Geosciences, Norman, Oklahoma, U. S. A. October 15-17, 1985, P. 35-37.

Annual Report of the Institute of Physics, Academia Sinica, Vol. 15, 1985

SYMMETRY BREAKING IN THE TWO-PARAMETER KADANOFF RENORMALIZATION-GROUP TRANSFORMATION*

Chin-Kun Hu

Institute of Physics, Academia Sinica, Nankang,

Taipei, Taiwan, R.O.C.

ABSTRACT

We prove that, when applied to square-lattice Ising models with 90° rotation symmetry, the renormalization-group transformation in the Kadanoff variational method with two variational parameters p_1 and p_2 breaks the 90° rotation symmetry if $|p_1| \neq |p_2|$. Thus it is inappropriate to apply this method to the spin model with 90° rotation symmetry, e.g. the Baxter model.

* Published in phys Lett. Vol. 109A, 51-52 (1985).

MULTISITE-CORREIATED PERCOLATION AND ISING MODELS WITH MULTISPIN INTERACTIONS*+

Chin-Kun Hu

Institute of Physics, Academia Sinica, Nankang,

Taiwan, Taiwan 11529, Republic of China

ABSTRACT

We extend the concept of site percolation and bond percolation to multisite percolation in which each active element in the random process involves more than two sites. We show that the partition function of the Ising model with multisite interactions of strength J_m is the generating function of a multisite-correlated percolation model. From this connection, we conclude that the phase transition of the Ising model with multispin interactions is also a percolation transition. Based on such connection, we define nonpercolating geometrical factor g_f and percolating geometrical factor g_p which depend only on geometrical properties of the system. The thermal properties of the Ising model with multispin interactions may be derived simply from g_f and g_p. The theory is confirmed by an exact calculation for a one dimensional model with four-spin interactions.

* Part of this paper was presented at Workshop on Statistical Physics, Academia Sinica, Taipei, Taiwan, R. O. C.

+ Published in Chinese J. Phys. (Taipei) vol. 23, 47-63 (1985).

PERCOLATION, GEOMETRICAL FACTOR, AND THERMAL PROPERTIES OF AN ISING MODEL WITH ANTIFERROMAGNETIC AND FERROMAGNETIC INTERACTIONS*

Chin-Kun Hu

Institute of Physics, Academia Sinica,

Nankang, Taipei, Taiwan 11529

Republic of China

ABSTRACT

Many solid state systems, e.g. ferromagnet and antiferromagnet, binary alloy, atoms or molecules on surfaces, may be represented by Ising-like spin models. Using a new idea to define " clusters " for Ising-like spin models, in this paper we formally show that the partition function of an Ising model with antiferromagnetic and ferromagnetic interactions may be written as the generating function of a dichromatic bondcorrelated percolation model so that the phase transition of the former corresponds the percolation transition of the later.

Based on such connection, we define nonpercolating geometrical factor g_f and percolating geometrical factor g_p for the spin model, which depend only on the geometrical properties of the system. With certain reasonable assumptions about the behavior of g_f and g_p, we may show that thermal properties of the spin model may be deduced simply from the logarithm of such geometrical factors and their first and second derivatives.

* Presented at Second R. O. C. - R. O. K. Symposium on Solid State Physics, Taipei, Taiwan, April 20-21, 1985

GEOMETRICAL FACTOR AND THERMAL PROPERTIES OF LATTICE GAS MODELS*

Chin-Kun Hu **

Institute of Physics, Academia Sinica,

Nankang, Taipei, Taiwan 11529

Republic of China

ABSTRACT

Many gas-liquid systems may be represented by lattice gas models which are mathematically equivalent to Ising-like spin models. Using a new idea to define " clusters " for Ising-like spin models, we have formally shown that many Ising-like spin models have corresponding correlated percolation models[1]. Based on such connection, we can define nonpercolating geometrical factor g_f and percolating geometrical factor g_p for each spin model, which depend only on the geometrical properties of the system. In this paper, we propose that thermal properties of a spin model, i.e. a lattice gas model, can be deduced simply from the logarithm of such geometrical factors and their derivatives. Our idea is confirmed by exact calculations for many one-dimensional systems.

1. C. - K, Hu, Phys. Rev. B29, 5103-5108, 5109-5116 (1984); Physica 119A, 609 (1983); J. Phys. A 16, L321 (1983); Chin. J. Phys. (Taipei) 22, No. 1, 1 (1984), No. 4, 1(1984).

* Presented at IUPAP Conference : Conference on Mathematical Problems from the Physics of Fluids, Roma, June 5 - 12, 1985.

**Supported in part by National Science Council of the Republic of China under contract No. NSC 74-0208-Mool-11.

GEOMETRICAL FACTOR AND THERMAL PROPERTIES OF A SUBLATTICE DILUTE POTTS MODEL*

Chin-Kun Hu

Institute of Physics, Academia Sinica, Nankang,

Taipei. Taiwan 11529, Republic of China

ABSTRACT

Based on the connection between a sublattice dilute q-state Potts model (SDQPM) and a correlated percolation model, we define nonpercolating geometrical factor g_f and a percolating geometrical factor g_p, which depend only on q and geometrical properties of the system. The thermal properties of the SDQPM may be derived simply from g_f and g_p. The theory is confirmed by an exact calculation for one-dimensional SDQPM and may be extended to other interacting systems.

* Published in Phys. Rev. B Vol 32, no. 11, (1985).

AXIALLY SYMMETRIC KALUZA-KLEIN DYONS AND NONLINEAR SIGMA-MODELS *

S. C. Lee

Institute of Physics, Academia Sinica

Taipei, Taiwan 115.

Republic of China

ABSTRACT

We show that the main part of the field equations for axially symmetric Kaluza-Klein dyons reduces to that of a nonlinear sigma-model on symmetric spaces when these models are generalized in a suitable way. As a result, we derive Lax pairs of the Belinskii-Zakharov type as well as the Pohlmeyer-Eichenherr-Forger type. The well-known four-dimensional axially symmetric stationary fields of Einstein and Einstein-Maxwell equations become special cases of ours.

* Published in Lett Nuovo Cimento 44, 133 (1985).

Annual Report of the Institute of Physics, Academia Sinica, Vol. 15, 1985

ABELIAN KALUZA-KLEIN MONOPOLES AND DYONS AS COMPLETELY INTEGRABLS SYSTEMS *

S. -C. Lee

Institute of Physics, Academia Sinica

Taipei Taiwan 115,

Republic of China

S.-L. Lou

Department of Physics, National Tsing Hua University

Hsinchu, Taiwan 300, Republic of China

ABSTRACT

We derive Lax equations for spherically symmetric Kaluza-Klein monopoles and dyons in 4 + K dimensions with internal space isomorphic to an Abelian Lie group. Apart from a constraint, which we show can always be satisfied, the field equations are thus completely integrable.

* Published in Lett Nuovo Cimento 44, 69 (1985).

CURVATURE TENSOR FOR KALUZA-KLEIN THEORIES WITH HOMOGENEOUS FIBERS*

C. -C. Chiang, S. -C. Lee, and G. Marmo
Institute of Physics, Academia Sinica, Taipei, Taiwan 115,
Republic of China

S. -L. Lou

Department of Physics, National Tsing Hua University, Hsinchu,
Taiwan 300, Republic of China

ABSTRACT

We give explicit formulas for all components of the Riemanian connection and curvature tensor for a class of metrics which describe low-energy deformations in Kaluza-Klein theories with homogeneous fibers.

* Published in Phys. Rev. D 32, 1364 (1985).

GENERALIZED NEUGEBAUER-KRAMER TRANSFORMATIONS FOR NONLINEAR SIGMA MODELS*

S. -C. Lee

In Institute of Physics, Academia Sinica
Taipei, Taiwan 11529, Republic of China

ABSTRACT

We consider the solutions of vacuum Einstein equations in $4+K$ dimensions with $2+K$ commuting Killing vectors and show that this system possesses a series of discrete symmetries $I^{(q)}$ generalizing the the Neugebauer-Kramer transformation which corresponds to the $K=0$ case. When conjugated with the dual symmetry, we obtain a series of continuous symmetries generalizing the I_1 transformation of Neugebauer. we argue that the discrete symmetries are in fact symmetries for any generalized nonlinear sigma models.

* to appear in Physics Lett. B.

SPHERICALLY SYMMETRIC KALUZA-KLEIN MONOPOLES AND DYONS IN 4+K DIMENSIONS*

S. -C. Lee

Institute of Physics, Academia Sinica

Taipei, Taiwan 115, Republic of China

ABSTRACT

We show that the field equations for spherically symmetric abelian Kaluza-Klein monpoles and dyons in 4 + K dimensions can be completely integrated. The explicit integration can be carried out by purely algebraic procedures.

* to appear in Classical and Quantum Gravity.

SOME RECENT RESULTS IN HIGHER DIMENSIONAL GRAVITY

S. -C. Lee

Institute of Physics, Academis Sinica

Taipei, Taiwan 11529, Republic of China

ABSTRACT

We consider the axially symmetric vacuum Einstein equations in 4 + K dimensions under the Kaluza-Klein ansatz. The equivalence to a generalized nonlinear sigma model is established. The Belinskii-Zakharov one soliton transformation is shown to be of the form $I_2 I^{(q)} I_2$ where I_2 is the dual symmetry and $I^{(q)}$ is a series of discrete symmetries generalizing the Neugebauer-Kramer mapping. $I^{(q)}$'s are also symmetries for any generalized nonlinear sigma models on symmetric spaces.

* to appear in Proceedings of the X IV International Colloquium on Group Theoretical Methods in Physics.

SPHERICALLY SYMMETRIC KALUZA-KLEIN MONOPOLES AND DYONS IN 4+K DIMENSIONS*

S. -C. Lee

Institute of Physics, Academia Sinica

Taipei, Taiwan 115, Republic of China

ABSTRACT

We show that the field equations for spherically symmetric abelian Kaluza-Klein monpoles and dyons in 4 + K dimensions can be completely integrated. The explicit integration can be carried out by purely algebraic procedures.

* to appear in Classical and Quantum Gravity.

Annual Report of the Institute of Physics, Academia Sinica, Vol. 15, 1985

SOME RECENT RESULTS IN HIGHER DIMENSIONAL GRAVITY

S. -C. Lee

Institute of Physics, Academis Sinica

Taipei, Taiwan 11529, Republic of China

ABSTRACT

We consider the axially symmetric vacuum Einstein equations in 4 + K dimensions under the Kaluza-Klein ansatz. The equivalence to a generalized nonlinear sigma model is established. The Belinskii-Zakharov one soliton transformation is shown to be of the form $I_2 I^{(q)} I_2$ where I_2 is the dual symmetry and $I^{(q)}$ is a series of discrete symmetries generalizing the Neugebauer-Kramer mapping. $I^{(q)}$'s are also symmetries for any generalized nonlinear sigma models on symmetric spaces.

* to appear in Proceedings of the X IV International Colloquium on Group Theoretical Methods in Physics.

GENERALIZED NONLINEAR SIGMA MODELS ON SYMMETRIC SPACES*

S. -C. Lee

Institute of Physics, Academia Sinica, Taipei, Taiwan 115,

Republic of China

ABSTRACT

We point out that the nonlinear sigma models on symmetric spaces as considered by Eichenherr and Forger can be generalized to include a larger class of models possessing dual symmetry. The well-known axially symmetric gravitational vacuum and electrovac poblems as well as the axially symmetric Kaluza-Klein dyons fall into this class.

* Published in Phys. Lett. 158B, 413 (1985).

LAGRANGIAN DYNAMICS ON HIGHER-DIMENSIONAL SPACES WITH APPLICATIONS TO KALUZA-KLEIN THEORIES*

C - C. Chiang, S - C. Lee, and G. Marmo

Institute of Physics, Academia Sinica, Taipei, Taiwan,

Republic of China

ABSTRACT

We review and apply the method of Lagrangian dynamics to particle motion in higher-dimensional spaces. We discuss in detail the case of a Kaluza-Klein theory with coset spaces as fiber. While the total metric we use in general need not allow for Killing vectors, we require that the restriction to the fiber does. We find that for general Jordan-Thiry scalar fields, the geodesic motion in total space is not describable in terms of particle motion in the base manifold with the usual internal charges. The cases when this is possible are discussed. We also consider the geodesic motion in the Sorkin-Gross-Perry Kaluza-Klein monopoles. We find all the conserved quantities and the equations can be integrated by quadrature.

* Published in J. Math. Phys. 26 (5), 1083 (1985)

SOME DYNAMICAL PROPERTIES OF THE PION IN $\pi^+ \to e^+ \nu \gamma$ AND $\pi^+ \to e^+ e^+ e^- \nu$ DECAYS *

Ching-Yieh Lee

Institute of Physics, Academia Sinica, Nankang, Taipei, Taiwan 115

Republic of China

ABSTRACT

We investigate some of the dynamical properties of the pion by explicitly calculating the γ and ξ parameters in $\pi^+ \longrightarrow e^+ \nu \gamma$ and $\pi^+ \longrightarrow e^+ e^+ e^- \nu$ decays within the relativistic quark model, nucleon-loop approximation, and the σ model. One of the purposes in this study is to clarify a sign ambiguity raised recently in the prediction of γ within the quark model. The second purpose is to give some precise predictions for ξ, which has not yet been discussed extensively. The last purpose in this analysis involves a possible connection between ξ and chiral-symmetry breaking. Within the σ model, this parameter is found to depend logarithmically upon m_π, the explicit-breaking parameter of the symmetry.

* Published in Phys.. Rev. D32, 658 (1985).

ANOTHER LOOK AT $Z \longrightarrow \ell \bar{\ell} \gamma$ DECAY *

Ching-Yieh Lee

Institute of Physics

Academia Sinica

Nankang, Taipei, Taiwan 115, R.O.C.

ABSTRACT

We first make some comments on the angular distribution of the photon observed in the anomalous $Z \to \ell \bar{\ell} \gamma$ decay, and then, calculate explicitly the lowest-order one-loop contribution within the standard electroweak model. It is finally pointed out that, possibly in some composite models with hyper-strong coupling, large electromagnetic moments for Z may exist to accommodate the anomalous decay rate without violating the present accuracy of the g-2 factors of the electron and muon.

* To be published in Phys. Rev. D 32, (December 1, 1985).

ELECTRICAL AND MAGNETICAL PROPERTIES OF AISI 304 AND 430 STAINLESS STEELS*

Y. D. Yao （姚永德）
Institute of Physics, Academia Sinica
Taipei, Taiwan, R.O.C

ABSTRACT

The electrical resistivity ρ of commercial AISI type number 304 and 430 stainless steels was investigated as a function of the absolute temperature T between 4K and 1,300 K. The magnetization was studied at both 77K and 300K in an applied magnetic field up to 6 KG. These experimental results will be discussed from the viewpoint of current theories of electrical conduction in iron-based multi-metallic systems.

* Published in Proc. Ann. Conf. of Chinese Soc. Mat. Sci., p. 20 (1985).

MAGNETORESISTANCE OF Fe-RICH Fe-Pd ALLOYS*

S. U. Jen (任盛源) and Y. D. Yao (姚永德)
Institute of Physics
Academia Sinica
Taipei, Taiwan,
R. O. C.

ABSTRACT

The anisotropic magnetoresistance ratio $\Delta\rho/\rho_0 = (\rho - \rho_0) / \rho_0$ of a series of Fe-Rich FePd alloys samples has been studied as a function of the absolute temperature T from 10K to 300K. The experimental results are discussed from the view point of the two-current model. The analysis based on the Matthiessen's rule has been used to describe the temperature dependence of $\Delta\rho/\rho_0$. In addition, the concentration dependence of the residual resistivity of these alloy samples is discussed in terms of the validity of the Nordheim's rule.

* Accepted for publication in Chinese J. Physics, Vol. 23, (1985).

ELECTRICAL AND MAGNETIC PROPERTIES OF FeAlMnC ALLOYS*

Y. D. Yao (姚永德) and S. U. Jen (任盛源)
Institute of Physics, Academia Sinica
Taipei, Taiwan, R. O. C.

ABSTRACT

Electrical resistivity of four FeAlMnC alloy samples has been studied as a function of the temperature between 4K and 1,300K. The magnetization was measured at 77K and 300K. Double resistivity minima have been observed. The resistivity minimum near 40K is associated with the magnetic transition from a mixed or frustrated state towards a ferromagnetic state. The resistivity minimum near 400K disappears after high temperature annealing ; this suggests that it is nonmagnetic in origin.

* Accepted for publication in J. Magnetism and Magnetic Materials (1986).

SPECIFIC HEAT STUDY OF Ni-Cu ALLOYS NEAR THE CURIE TEMPERATURE*

S. K. Lee
Physics Department, Fu Jen University
Taipei, Taiwan, R. O. C.
Y. D. Yao (姚永德) and C. Chiang (蔣 炯)
Institute of Physics, Academia Sinica
Taipei, Taiwan, R. O. C.

ABSTRACT

The specific heat of nickel-copper alloys containing 0.0, 4.6, 9.3, 14.0 and 18.8 at. % Cu has been studied near the Curie temperature. The effective critical exponents of specific heat were analyzed using a simple power law; our results show that the value of the effective critical exponents depends on the concentration of impurities. Higher-order correction techniques are definitely necessary for analyzing the universality and symmetry of the critical exponents of specific heat.

* Published in Chinese J. Physics, Vol. 22, No. 4, p. 54 (1984).

VALENCE FLUCTUATION OF $Ce_{0.5}Rh_3B_2$ WITH THE NEW $La_{1-x}Rh_3B_2$-TYPE STRUCTURE *

H. C. Ku, Y. B. You, L. J. Ma, H. Y. Chao
Department of Physics, National Tsing Hua University,
Hsinchu, Taiwan, R. O. C.

Y. D. Yao （姚永德）
Institute of Physics, Academia Sinica, Taipei, Taiwan, R. O. C.

ABSTRACT

Ternary borides with the new disordered $La_{1-x}Rh_3B_2$-type structure ($0 < x \leqq 0.5$) are reported with the general formula $RE_{0.5}Rh_3B_2$ (RE = La, Ce, Pr or Nd). Unit cell volume data indicate that $Ce_{1-x}Rh_3B_2$ exhibits valence fluctuation. High temperature resistivity measurements on $La_{1-x}Rh_3B_2$ exhibit an abrupt drop around 950 K, which indicate that these new compounds are high-temperature metastable compounds.

* Published in Journal of Magnetism and Magnetic Materials 47, 573 (1985).

ELECTRICAL RESISTIVITY OF AMORPHOUS AND CRYSTALLIZED $(Fe\text{-}Mn)_{80}B_{14}Si_6$ BETWEEN 300 AND 1200 K*

Y. D. Yao[a] (姚永德), M. M. Yih[b] and S. T. Lin[c]

a) Institute of Physics, Academia Sinica, Taipei, Taiwan, R. O. C.
b) Physics Department, Tamkung University, Taipei, Taiwan, R. O. C.
c) Physics Department, Chengkung University, Tainan, Taiwan, R. O. C.

ABSTRACT

Electrical resistivity ρ of amorphous and crystallized $Fe_{80-x}Mn_xB_{14}Si_6$ alloys (x = 0, 2, 4, 6, 10, 12, 14, 16, 20) has been studied as a function of temperature T between 300 and 1200 K. Using heating rates of ~ 2 K/min., the slopes of the ρ vs T curves are positive for all the alloys below the crystallization temperature. Near the crystallization temperature the quantity of ρ decreases abruptly for these alloys with the Mn content < 16 at. %, and this decreases with increasing the Mn content. However, for the alloys with x = 16 and 20, the quantity of ρ increases abruptly near the crystallization temperature; and then followed by an abruptly decreasing. At high temperatures (≧ 1100 K), the electrical resistivity of these alloys with the Mn content ≧ 10 at. % shows an anomalous increase; this is explained by the fast diffusibility of the alloys near the melting point. The electrical resistivity of the alloys with x = 0 and 2 does not show any anomalous increase for temperatures ~ 1250 K. This suggests that the melting point of the alloys is decreased with increasing the Mn content from 2 to 10 at.%. In the crystalline state, our data show that ρ is a monotonically increased function of T between 300 and 1100 K. Each of the ρ vs T curves exhibits a well-defined knee around the Cruie temperature T_c. T_c of these alloys is determined by the ρ / dT vs T analysis. Our data shows that the values of T_c are decreased with increasing the Mn content.

* Published in Rapidly Quenched Metals (eds. : S. Steeb and H. Warlimont) Elsevier Sci. Pub. p. 1051 (1985).

MAGNETORESISTANCE AND MAGNETIZATION OF Fe-RICH Fe-Pd ALLOYS*

S. U. Jen (任 盛 源) and Y. D. Yao (姚 永 德)
Institute of Physics, Academia Sinica,
Taipei, Taiwan, R. O. C.

ABSTRACT

A series of Fe-Pd alloys were made. The magnetic moment was measured at 77K and 300K, and the magnetoresistance ratio $\Delta\rho/\rho_0$ was measured over the temperature range from 10 K to 300 K. Atomic moment n_B increases in the range $0 < x < 0.9$ at. % and decreases as (12 - N_e^{Pd} - 2x) in the range $10 < x < 30$ at. %. By extending $\Delta\rho/\rho_0$ to 4K, the spin-up and spin-down resistivities were computed for dilute Fe-Pd.

* Accepted for publication in J. Magnetism and Magnetic Materials (1986).

A RAMAN STUDY OF THE PHASE TRANSITIONS OF SOLID CARBON TETRABROMIDE*

W. S. Tse, N. T. Liang, W. W. Lin and P. Y. Chiang
Institute of Physics, Academia Sinica
Taipei, Taiwan (115), R.O.C.

ABSTRACT

The Raman spectrum of cyrstalline carbon tetrabromide has been studied at various temperatures above and below the order-disorder phase transition near 320K. Changes in the lattice and stretching region spectra at temperature near T_c show that there are two phases separated by first order transition. The phase transition was found to be associated with the softening of a low frequency lattice Raman mode.

* Chem phys. Lelt., 119, 67 (1985)

THE ENHANCEMENT OF RESONANCE RAMAN SCATTERING FROM CRYSTAL VIOLET DEPOSITED ON ISLAND Ag FILMS*

Y. C. Chou

Department of Physics, National Tsing Hua University

Hsinchu, Taiwan 300, Republic of China

N. T. Liang, and W. S. Tse

Institute of Physics, Academia Sinica

Nankang, Taipei, Republic of China

ABSTRACT

The observed thickness dependence and excitation profiles of the surface enhanced resonance Raman scattering (SERRS) from crystal violet (CV) on Ag films demonstrated the importance of surface roughness and chemical effects. Using different normalization schemes in studying the excitation profile of SERRS we were able to identify that there are three multiplicative contributions to the observed giant enhancement, they are the electromagnetic effect, the molecular resonance effect and the charge transfer effect originated from the strong electronic interaction between CV and the metal islands.

* Accepted for publication : J. Raman Spectro.,

RAMAN SPECTRA OF SOLID TITANIUM TETRABROMIDE*

W. S. Tse and W. W. Lin

Institute of Physics, Academia Sinica

Taipei, Taiwan, R.O.C.

ABSTRACT

The vibrational spectra of polycrystalline titanium tetrabromide at various temperatures between 80K and 300K have been investigated by Raman spectroscopic techniques. The observed modes are discussed in terms of the known molecular and crystal structure.

* Accepted for publication : PNSC : part A.

THE FLOW OF ROUND BUOYANT JETS DISCHARGING VERTICALLY INTO A CROSS FLOW OF STRATIFIED FLUID*

Robert R. Hwang and T. P. Chiang

Institute of Physics, Academia Sinica and
Department of Naval Architecture, National Taiwan University
Taiwan, Republic of China

ABSTRACT

In this study, combining with dimensional analysis, the integral approach which consistes of integrating the equations of continuity, motion and density deficit across the jet cross section works to investigate the time average behavior of a vertical round buoyant jet in a uniform cross flow of stably stratified density. The model predicts the vertical rise and the dilution of the jet as a function of horizontal position. A comprehensive experimental program performed in a flume was also conducted to enable verification of the calculating relationships. Results show that the comparisons between the numerical calculation and the laboratory experiment are favorable.

* Proceedings of Intern. Symp. on Refined Flow Modelling and Turbulence Measurements, The Univ of Iowa, A11-1-10, 16-18 September, 1985.

大氣密度層流中背面波形成之研究*

黃 榮 鑑
中央研究院 物理研究所
台灣大學造船工程研究所

摘 要

本文經由連續方程式、芮維－史托克運動方程及密度擴散方程式，利用數值分析以變向隱式法（ alternattve direction implicit scheme ）的差分方法建立數值模式，探討二維度層變流體通過半橢圓之柱體及半圓柱體等障礙物時背面波之形成及流場流況的變化情形。引生的流場變化分三區（即形成於障礙體上游的阻滯區，形成於障礙體下游之分離區以及上述二區外之場內區）分別加以研討。

結果顯示背面波的形成及發展受流場的密度福祿數F、雷諾數R及障礙體的高寬比ε所影響。F值減小將使分離區的發展受到壓抑，背面波的發展也將加快，容易造成流場的不穩定，並且使阻滯區向上游延伸。ε小的障礙體，分離區不容易形成，背面波的發展也較快，同時流況受R值的影響相當明顯。減小ε及R值，阻滯區的長度將增長，但並不十分明顯，而R值及ε值的增加將促使近分離區的發展，有助於流場的穩定。

* 發表於大氣科學，第十二期，7-22 頁，1985

AUTHOR INDEX

Annual Report of the Institute of Physics, Academia Sinica, Vol. 15, 1985

本集刊每年出版一次

非　賣　品

中央研究院

物理研究所集刊

第十五卷

發行人：林　爾　康

編輯者：中央研究院物理研究所集刊編輯委員會

出版者：中央研究院物理研究所　臺北市南港區

印刷者：天宏印刷事業有限公司

電　話：七六五五七七七

中華民國七十四年十二月出版